

**Proceedings of the Eleventh Lomonosov
Conference on Elementary Particle Physics**



Particle Physics in Laboratory, Space and Universe

Editor

Alexander I Studenikin

Particle Physics in Laboratory, Space and Universe

This page intentionally left blank

Faculty of Physics of Moscow State University



Proceedings of the Eleventh Lomonosov
Conference on Elementary Particle Physics

Particle Physics in Laboratory, Space and Universe

Moscow, Russia

21 – 27 August 2003

Editor

Alexander I Studenikin

*Department of Theoretical Physics
Moscow State University, Russia*



NEW JERSEY • LONDON • SINGAPORE • BEIJING • SHANGHAI • HONG KONG • TAIPEI • CHENNAI

Published by

World Scientific Publishing Co. Pte. Ltd.

5 Toh Tuck Link, Singapore 596224

USA office: 27 Warren Street, Suite 401-402, Hackensack, NJ 07601

UK office: 57 Shelton Street, Covent Garden, London WC2H 9HE

British Library Cataloguing-in-Publication Data

A catalogue record for this book is available from the British Library.

PARTICLE PHYSICS IN LABORATORY, SPACE AND UNIVERSE

Copyright © 2005 by World Scientific Publishing Co. Pte. Ltd.

All rights reserved. This book, or parts thereof, may not be reproduced in any form or by any means, electronic or mechanical, including photocopying, recording or any information storage and retrieval system now known or to be invented, without written permission from the Publisher.

For photocopying of material in this volume, please pay a copying fee through the Copyright Clearance Center, Inc., 222 Rosewood Drive, Danvers, MA 01923, USA. In this case permission to photocopy is not required from the publisher.

ISBN 981-256-162-5

Printed in Singapore.

**Moscow State University
Faculty of Physics
Interregional Centre for Advanced Studies**

*Dedicated to the 70th Anniversary of
Faculty of Physics
of Moscow State University*



Mikhail Lomonosov
1711-1765

**ELEVENTH
LOMONOSOV
CONFERENCE
ON
ELEMENTARY
PARTICLE
PHYSICS**

Moscow, August 21-27, 2003

Sponsors

Russian Foundation for Basic Research
Ministry of Industries, Science and Technologies of Russia

Supporting Institutions

Faculty of Physics of Moscow State University
Interregional Centre for Advanced Studies
Joint Institute for Nuclear Research (Dubna)
Institute of Theoretical and Experimental Physics (Moscow)
Institute for Nuclear Research (Moscow)

International Advisory Committee

E.Akhmedov (ICTP, Trieste & Kurchatov Inst.,Moscow),
 V.Berezinsky (LNGS, Gran Sasso),
 S.Bilenky (JINR, Dubna),
 J.Bleimaier (Princeton),
 M.Danilov (ITEP, Moscow),
 G.Diambrini-Palazzi (Univ. of Rome),
 A.Dolgov (INFN, Ferrara & ITEP, Moscow),
 V.Kadyshevsky (JINR, Dubna),
 S.Kapitza (EAPS, Moscow)
 A.Logunov (IHEP, Protvino),
 V.Matveev (INR, Moscow),
 P.Nowosad (Univ. of Sao Paulo),
 L.Okun (ITEP, Moscow),
 V.Rubakov (INR, Moscow),
 D.Shirkov (JINR, Dubna),
 J.Silk (Univ. of Oxford),
 A.Skrinsky (INP, Novosibirsk),
 A.Slavnov (MSU & Steklov Math.Inst, Moscow)
 A.Smirnov (ICTP, Trieste & INR, Moscow),
 P.Spillantini (INFN, Florence),

Organizing Committee

V.Bagrov (Tomsk State Univ.),
 V.Belokurov (MSU), V.Braginsky (MSU),
 A.Egorov (ICAS, Moscow), D.Galtsov (MSU),
 A.Grigoriev (MSU & ICAS, Moscow),
 P.Kashkarov (MSU), A.Kataev (INR, Moscow),
 O.Khrustalev (MSU), V.Mikhailin (MSU & ICAS, Moscow)
 A.Mourao (IST/CENTRA, Lisbon),
 N.Narozhny (MEPHI, Moscow),
 A.Nikishov (Lebedev Physical Inst., Moscow),
 N.Nikiforova (MSU), V.Ritus (Lebedev Physical Inst., Moscow),
 Yu.Popov (MSU) , V.Savrin (MSU),
 D.Shirkov (JINR, Dubna), Yu.Simonov (ITEP, Moscow),
 A.Sissakian (JINR,Dubna),
 A.Studenikin (MSU & ICAS, Moscow),
 V.Trukhin (MSU)

**Moscow State University
Interregional Centre for Advanced Studies
Centre of International Educational Projects
Ministry of Science and Education of Russia**

**FIFTH
INTERNATIONAL
MEETING
ON PROBLEMS
OF INTELLIGENTSIA
“INTELLIGENTSIA
and EDUCATION”**

Moscow, August 27, 2003

Presidium of the Meeting

V.A.Sadovnichy (MSU) - Chairman

V.V.Belokurov (MSU)

J.Bleimaier (Princeton)

G.Diambrini-Palazzi (Univ. of Rome)

V.G.Kadyshevsky (JINR)

S.P.Kapitza (Russian Academy of Sciences)

N.S.Khrustaleva (Ministry of Science and Education, Russia)

V.V.Mikhailin (MSU)

A.I.Studenikin (MSU & ICAS) - Vice Chairman

V.I.Trukhin (MSU)

S.V.Volkov (Orthodox St.Tikhon's Inst.)

This page intentionally left blank

FOREWORD

The 11th Lomonosov Conference on Elementary Particle Physics was held at the Moscow State University (Moscow, Russia) on August 21-27, 2003. The conference was dedicated to the 70th Anniversary of the Faculty of Physics of the Moscow State University.

The conference was organized by the Faculty of Physics of the Moscow State University and the Interregional Centre for Advanced Studies and supported by the Joint Institute for Nuclear Research (Dubna), the Institute of Theoretical and Experimental Physics (Moscow), and the Institute for Nuclear Research (Moscow). The Ministry of Industries, Science and Technologies of Russia, the Russian Foundation for Basic Research sponsored the conference.

It was more than twenty years ago when the first of the series of conferences (from 1993 called the "Lomonosov Conferences"), was held at the Department of Theoretical Physics of the Moscow State University (June 1983, Moscow). The second conference was held in Kishinev, Republic of Moldavia, USSR (May 1985).

After the four years break this series was resumed on a new conceptual basis for the conference programme focus. During the preparation of the third conference (that was held in Maykop, Russia, 1989) a desire to broaden the programme to include more general issues in particle physics became apparent. During the conference of the year 1992 held in Yaroslavl it was proposed by myself and approved by numerous participants that these irregularly held meetings should be transformed into regular events under the title "Lomonosov Conferences on Elementary Particle Physics". Since then at subsequent meetings of this series a wide variety of interesting things both in theory and experiment of particle physics, field theory, astrophysics, gravitation and cosmology were included into the programmes. It was also decided to enlarge the number of institutions that would take part in preparation of future conferences.

Mikhail Lomonosov (1711-1765), a brilliant Russian encyclopaedias of the era of the Russian Empress Catherine the 2nd, was world renowned for his distinguished contributions in the fields of science and art. He also helped establish the high school educational system in Russia. The Moscow State University was founded in 1755 based on his plan and initiative, and the University now bears the name of Lomonosov.

The 6th Lomonosov Conference on Elementary Particle Physics (1993) and all of the subsequent conferences of this series were held at the Moscow State University on each of the odd years. Publication of the volume "Particle Physics, Gauge Fields and Astrophysics" containing articles written on the basis of presentations at the 5th and 6th Lomonosov Conferences was supported by the Accademia Nazionale dei Lincei (Rome, 1994). Proceedings of the 7th and 8th Lomonosov Conference (entitled "Problems of Fundamental Physics" and "Elementary Particle Physics") were published by the Interregional Centre for Advanced Studies (Moscow, 1997 and 1999). Proceedings of the 9th and 10th

Lomonosov Conferences (entitled “Particle Physics at the Start of the New Millennium” and “Frontiers of Particle Physics”) were published by World Scientific Publishing Co. (Singapore), in 2001 and 2003, correspondently.

The physics programme of the 11th Lomonosov Conference on Elementary Particle Physics (August, 2003) included review and original talks on wide range of items such as electroweak theory, fundamental symmetries, tests of standard model and beyond, neutrino and astroparticle physics, heavy quark physics, non-perturbative QCD, quantum gravity effects, physics at the future accelerators. Totally there were more than 250 participants with 93 talks including 37 plenary (40-35 min) talks, 45 session (25-20 min) talks and 11 brief (15 min) reports.

Following the tradition that has started in 1995, each of the Lomonosov Conferences on particle physics has been accompanied by a conference on problems of intellectuals. The 5th International Meeting on Problems of Intelligentsia held during the 11th Lomonosov Conference (27 August, 2003) was dedicated to discussions on the issue “Intelligentsia and Education”. The four papers presented at the meeting are included into this volume.

The success of the events was due in a large part to contributions of the International Advisory Committee and Organizing Committee. On behalf of these Committees I should like to warmly thank the session chairpersons, the speakers and all of the participants of the 11th Lomonosov Conference and the 5th International Meeting on Problems of Intelligentsia.

We are grateful to the Rector of the Moscow State University, Victor Sadovnichy, the Dean of the Faculty of Physics of the Moscow State University, Vladimir Trukhin, the Director of the Joint Institute for Nuclear Research, Vladimir Kadyshevsky, the Director of the Institute for Nuclear Research, Victor Matveev, the Vice Director of the Institute of Theoretical and Experimental Physics, Mikhael Danilov, and the Vice Deans of the Faculty of Physics of the Moscow State University, Anatoly Kozar and Pavel Kashkarov for the support in organizing these two conferences.

I should like to thank Andrey Kataev, Lev Okun, and Yuri Simonov for their help in planning of the scientific programme of the meeting. Special thanks are due to Giorgio Capon, Tim Hallman, Fabienne Kunne, Giovanni Lamanna and Charles Young for their valuable help in inviting speakers for the topical sessions of the conference.

Furthermore, I am very pleased to mention Andrey Egorov, the Scientific Secretary of the conference, and Alexander Grigoriev for their very efficient work in preparing and running the meeting.

These Proceedings were prepared for publication and sponsored by the Faculty of Physics of the Moscow State University and the Interregional Centre for Advanced Studies with support by the Ministry of Industries, Science and Technologies of Russia and the Russian Foundation for Basic Research.

Alexander Studenikin

CONTENTS

Neutrino Physics

KamLAND Antineutrino Detector—Status and Perspective <i>E. Yakushev</i>	1
Long Baseline Neutrino Experiments <i>T. Kobayashi</i>	10
Precision Measurements from the NOMAD Experiment <i>R. Petti</i>	20
From the Extreme Universe Space Observatory (EUSO) to the Extreme Energy Neutrino Observatory <i>S. Bottai and P. Spillantini</i>	26
Theory of Neutrino Oscillations <i>C. Giunti</i>	35
Quiet or Active Sun and the Neutrino Properties <i>S. Turck-Chieze</i>	45
Generalized Dirac–Pauli Equation and Spin Light of Neutrino in Magnetized Matter <i>A. Grigoriev, A. Studenikin and A. Ternov</i>	55
Effects of Heavy Majorana Neutrinos at Lepton–Proton Colliders <i>A. Ali, A. V. Borisov and D. V. Zhuridov</i>	66
Radiative Neutrino Decay in Magnetic Field at Finite Density of Medium <i>A. I. Ternov and P. A. Eminov</i>	71
Beta Decay in External Field and Neutrino Mass <i>O. Dorofeev and A. Lobanov</i>	76
Neutrino Oscillations and Neutrino Physics at Super-Kamiokande <i>K. S. Ganezer</i>	80

Astroparticle Physics and Cosmology

Astroparticle Physics with AMS02 <i>V. Zhukov</i>	82
Neutralino Annihilation in Small-Scale Clumps in the Galactic Halo <i>V. S. Berezinsky, V. I. Dokuchaev and Yu. Eroshenko</i>	92
Big Bang Nucleosynthesis: A Brief Review <i>F. L. Villante</i>	99
Gravitational Microlensing and Dark Matter in Our Galaxy: 10 Years Later <i>A. F. Zakharov</i>	106
The Gravitational Wave Detectors on the Earth at the Era of the VIRGO Start Up <i>F. Ricci</i>	116
Conformal Gravitation and Evolution of Galaxies <i>B. Barbashov, P. Flin, V. Pervushin and A. Zorin</i>	130
Quantum Tunnelling of a Rotating Universe <i>M. Fil'chenkov</i>	135
On the Problem of Uniqueness of Energy–Momentum Tensor of Gravitational Field <i>A. I. Nikishov</i>	140
Singularities Electrodynamics with a “Magnetic” Charge in Spaces of various Dimension <i>S. V. Kopylov and G. P. Cherny</i>	148
CP Violation and Rare Decays	
Direct CP Violation Measurements with the NA48 Experiment: Status and Perspectives <i>M. Scarpa</i>	153
Recent NA48 Results on Rare Kaon Decays <i>G. Collazuol</i>	163

On the Relative Strength of Direct CP Violation in $K_L \rightarrow 2\pi$ and $K^\pm \rightarrow \pi^\pm \pi^\pm \pi^\mp$ Decays <i>E. Shabalin</i>	169
Hadron Physics	
Hadron Physics in BABAR <i>G. D. Lafferty</i>	173
Selex-E781 Results on Doubly Charmed Baryon Family <i>M. Iori</i>	181
Law of Large Numbers and Asymptotic of Phase Space Integral <i>J. Manjavidze, A. Sissakian and N. Shubitidze</i>	186
The Gottfried Sum Rule: Theory VS Experiment <i>A. L. Kataev</i>	194
Small-x Behaviour of the Nonsinglet and Singlet Structure Functions g_1 <i>M. Greco</i>	201
Static Potentials in QCD: What Information We Can Get <i>V. I. Shevchenko</i>	202
Light and Heavy Baryons in the Nonperturbative QCD <i>I. M. Narodetskii and M. A. Trusov</i>	209
Evaluation of the Higher Twist Contribution to the Moments of Proton Structure Functions F_2 and g_1 <i>M. Osipenko, S. Simula, G. Ricco, G. Fedotov, E. Golovach, B. Ishkhanov, E. Isupov and V. Mokeev</i>	216
Thermal QCD Condensates in the Hadron Resonance Gas Model <i>N. O. Agasian and S. M. Fedorov</i>	221
The Structure Function of B Mesons <i>G. Ricciardi</i>	226
Integral Representation for Structure Functions and Target Mass Effects <i>I. L. Solovtsov</i>	231

Nonperturbative Effects in the Hadronic Decay of the Tau-Lepton <i>O. Solovtsova</i>	237
Physics at Accelerators and Studies in SM and Beyond	
Higgs Searches at LEP <i>A. Kiiskinen</i>	243
Search for Higgs Bosons with the ATLAS Detector <i>S. Gentile</i>	253
Results on B Physics at LEP <i>J. Salt</i>	263
Four-Fermion Physics at LEP <i>E. Graziani</i>	273
Anomalous Gauge Couplings at LEP-2 <i>O. Yushchenko</i>	280
Fermion- and Photon-Pair Production at LEP-2 <i>M. Winter</i>	287
Tau and Two-Photon Physics at BABAR <i>J. Williams</i>	294
Initial State Radiation Studies at the $\Upsilon(4S)$ using the BABAR Detector <i>J. McKenna</i>	303
Semileptonic B Decays in BABAR <i>A. Sarti</i>	310
Perspectives of the Study of Double Pomeron Exchange at the LHC <i>J. P. Guillaud and A. Sobol</i>	316
New Developments in Quantum Field Theory	
Discrete Heavy Physics <i>J. Wudka</i>	323

The Problem of Monopoles in the Standard and Family Replicated Models <i>L. V. Laperashvili and H. B. Nielsen</i>	331
Conditional Density Matrix in the Context of Noncontextuality <i>V. Belokurov, O. Khrustalev, V. Sadovnichy and O. Timofeevskaya</i>	338
Hyperfine Splitting of the Ground State in Muonic Hydrogen <i>A. P. Martynenko</i>	348
Evolution of Angular Distribution of Polarization Components for Synchrotron Radiation under Changes of Particle Energy <i>V. G. Bagrov, D. M. Gitman, V. B. Tlyachev and A. T. Jarovoi</i>	355
Synchrotron Radiation of Relativistic Electron Bunches <i>V. A. Bordovitsyn, V. G. Bulenok and T. O. Pozdeeva</i>	363
New Approach for Description of P-, T-non-invariant States in Elementary Particle Physics <i>O. Kosmachev</i>	368
Studies of Exotic Phenomena	
The Generation of Exotic Quasiparticles <i>V. Skvortsov and N. Vogel</i>	373
New Kind of Electromagnetic Radiation <i>N. Perevozchikov and V. Sharichin</i>	383
Problems of Intelligentsia	
The Intelligentsia & Progress <i>J. K. Bleimaier</i>	388
The Developing of the Scientific Knowledge and the Change of the Human Condition <i>G. Diambriini-Palazzi</i>	394
A Book: Has it Got a Future? <i>H. Westerheide</i>	405

Scientific Societies in Moscow University <i>V. Mikhailin</i>	408
Conference Programme	413
List of Participants	419

KamLAND Antineutrino Detector – Status and Perspective

E.Yakushev ^a

*Department of Physics and Astronomy
University of Alabama, Tuscaloosa, Alabama, 35487, USA*

On behalf of KamLAND collaboration

Abstract. KamLAND, 1 kton liquid scintillator detector, was constructed in Japan by international collaboration for detection of $\bar{\nu}_e$'s from nuclear reactors. KamLAND operation started in January of 2002. After accumulation of 162 ton-yr (145.1 days) of experimental data the ratio of the number of observed inverse β -decay events to the expected number of events without oscillation was found to be $0.611 \pm 0.085(\text{stat}) \pm 0.041(\text{syst})$ for $\bar{\nu}_e$ energies > 3.4 MeV. In case of CPT is invariant, this result has demonstrated that solution to the solar neutrino problem located in the LMA region. Due underground location, low own background, and high sensitivity KamLAND is also effective or can be effective in future for detection of geo neutrinos, solar neutrinos, relic neutrinos and for search of some rare processes as for example nucleon decay.

1 KamLAND Detector

KamLAND was designed and built to search for the oscillation of $\bar{\nu}_e$'s produced by distant nuclear reactors of commercial power plants. KamLAND has been constructed at former Kamiokande [1] detector cavity located under Ikenoyama mountain in central Japan. Rock shielding equal to 2700 m.w.e. provides as low as 0.34 Hz of cosmic-ray muons detection rate in the entire detector volume.

The detector scheme is presented on Fig. 1. Spherical balloon made from transparent composite film holds 1 kton of liquid scintillator (LS) which is the neutrino target and detector. A buffer of dodecane and isoparaffin oils between the balloon and a spherical stainless-steel containment vessel shields the inner detector from radiation from constructive materials and outside. An array of 1879 photomultiplier tubes (PMTs), mounted on the inner surface of the containment vessel, completes the inner detector (ID) system. The containment vessel is surrounded by a 3.2 kton water-Čerenkov detector with 225 20-inch PMTs. This outer detector (OD) absorbs γ -rays and neutrons from the surrounding rock and provides a tag for cosmic-ray muons.

The primary ID trigger threshold is set at 200 PMT hits, corresponding to about 0.7 MeV. This threshold is lowered to 120 hits for 1 msec after the primary trigger to observe lower energy delayed activity. The OD trigger threshold is set to provide $> 99\%$ tagging efficiency.

2 Antineutrino sources and antineutrino detection in KamLAND

After pioneer reactor $\bar{\nu}_e$'s detection by Reines and Cowan a number of such experiments were performed (at L \sim 10-1000 m) for search a possible oscilla-

^ae-mail: yakushev@bama.ua.edu

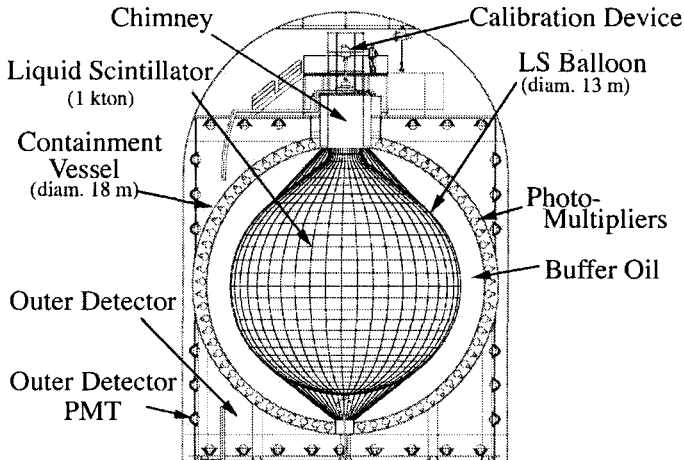


Figure 1: Schematic diagram of the KamLAND detector.

tion signal. No signature of disappearance of electron $\bar{\nu}_e$ flux or distortion of expected energy spectrum was found. These results plays important role in interpretation of KamLAND data, since it was demonstrated that calculated total fluxes agrees with measured ones on level better then 3% and experimental shapes are in agreement with calculations.

KamLAND detector is uses commercial reactors in Japan as free source of $\bar{\nu}_e$'s. There are 54 commercial reactors in Japan. 70GW (7% of world total) power corresponding to 80% of neutrino flux at KamLAND generated by plants located at distance from 130 to 240 km. The long baseline enables KamLAND to address the oscillation solution of the ‘solar neutrino problem’ using reactor $\bar{\nu}_e$'s under laboratory conditions. Instantaneous thermal power generation, burn-up and fuel exchange records for all Japanese commercial power reactors are provided by the power companies. The fission rate for each fissile element is calculated from these data, resulting in a systematic uncertainty in the $\bar{\nu}_e$ flux of less than 1%. The contribution to the $\bar{\nu}_e$ flux from Korean reactors is estimated to be $(2.46 \pm 0.25)\%$. Other reactors around the world give an average $(0.70 \pm 0.35)\%$ contribution.

The inverse β -decay reaction, $\bar{\nu}_e + p \rightarrow e^+ + n$, is utilized to detect $\bar{\nu}_e$'s in LS. The detection of the e^+ and the 2.2 MeV γ -ray from neutron capture on a proton in delayed coincidence is a powerful tool for reducing background.

3 KamLAND calibration and event reconstruction

The inner detector is calibrated with γ -ray sources of ^{68}Ge , ^{65}Zn , ^{60}Co , and Am-Be, deployed on different depths at inner detector.

These sources provide calibration energies in the 0.5 to 4.4 MeV region. Fig. 2 (a) shows the fractional deviation of the reconstructed energies from the source energies. The ^{68}Ge and ^{60}Co sources emit two coincident γ -rays and are plotted at an average energy in Fig. 2 (a). The observed energy resolution is $\sim 7.5\%/\sqrt{E(\text{MeV})}$.

The energy calibration is augmented with studies of ^{40}K and ^{208}Tl (which are contaminants in the detector), Bi-Po sequential decays, the spallation products ^{12}B and ^{12}N , and γ 's from thermal neutron captures on protons and ^{12}C . The energy scale exhibits less than 0.6% variation in time during the entire data run.

The source positions are reconstructed from the relative times of PMT hits. Energy-dependent radial adjustments are used to reproduce the known source positions to ~ 5 cm.

4 Data selection for reactor antineutrino analysis

For first results on antineutrino detection in KamLAND [2] 145.1 days of live time data were used.

4.1 Antineutrino candidate selection

The criteria for selection of $\bar{\nu}_e$ events are (1) a fiducial volume cut ($R < 5$ m), (2) a time correlation cut ($0.5 \mu\text{sec} < \Delta T < 660 \mu\text{sec}$), (3) a vertex correlation cut ($\Delta R < 1.6$ m), (4) a delayed energy window cut ($1.8 \text{ MeV} < E_{\text{delay}} < 2.6 \text{ MeV}$), and (5) a cut on the delayed vertex position requiring it to be more than 1.2 m from the central vertical axis (to eliminate background from thermometers deployed in this region used to monitor LS temperature). The

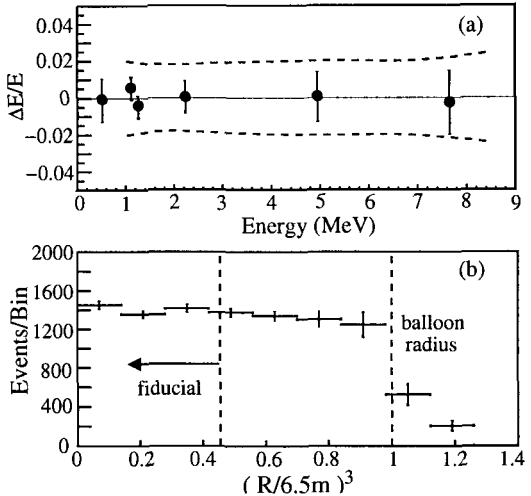


Figure 2: (a) The fractional difference of the reconstructed average γ energies and average source energies. The dashed line shows the systematic error. (b) The R^3 vertex distribution of 2.2 MeV neutron capture γ 's.

efficiency associated with criteria (2)-(5) and the effect of (1) on the delayed vertex is $(78.3 \pm 1.6)\%$. $\bar{\nu}_e$'s emitted by ^{238}U and ^{232}Th decays in the Earth, 'geo-neutrinos' ($\bar{\nu}_{\text{geo}}$), contribute low-energy events with $E_{\text{prompt}} < 2.49$ MeV. However the abundances of U and Th and their distributions in the Earth are not well known. To avoid ambiguities from $\bar{\nu}_{\text{geo}}$'s we employ (6) a prompt energy cut, $E_{\text{prompt}} > 2.6$ MeV.

4.2 Background events

Low-energy γ -rays from ^{208}Tl entering from outside the balloon are potential sources of background in the range up to 3 MeV and are strongly suppressed by the fiducial volume cut (1). From studies of Bi-Po sequential decays, the equilibrium concentrations of ^{238}U and ^{232}Th in the LS are estimated to be $(3.5 \pm 0.5) \times 10^{-18}$ g/g and $(5.2 \pm 0.8) \times 10^{-17}$ g/g, respectively. The observed background energy spectrum constrains the ^{40}K contamination to be less than 2.7×10^{-16} g/g. The accidental background, obtained from the observed flat distribution in the delayed time window 0.020-20 sec, is 0.0086 ± 0.0005 events for the present data set.

At higher energies, the background is dominated by spallation products from energetic muons. Single neutrons are efficiently suppressed by a 2-msec veto following a muon. Most fast neutrons are produced by energetic muons which pass through both the OD and the surrounding rock. This background is evaluated by detecting delayed coincidence events with a prompt signal associated with a muon detected only by the OD. To estimate the number of background events due to neutrons from the surrounding rock, the OD-associated rate is scaled by the relative neutron production and neutron shielding properties of the relevant materials. We estimate that the total background is less than 0.5 events for the entire data set.

Decays of most radioactive spallation products are effectively suppressed by requiring a delayed neutron signal. Neutron emitters like ^8He and ^9Li are eliminated by two time/geometry cuts: (a) a 2-sec veto is applied for the entire fiducial volume following a showering muon (with more than ~ 3 GeV energy deposition), (b) for the remaining muons, delayed events within 2 sec and 3 m from a muon track are rejected. The efficiency of these cuts is calculated from the observed correlation of spallation neutrons with muon tracks. The remaining ^8He and ^9Li background is estimated to be 0.94 ± 0.85 .

As shown in Table 1 the total number of expected background events is 0.95 ± 0.99 , where the fast neutron contribution is included in the error estimate.

Distribution of spallation neutron capture events was used for fiducial volume estimation. Uniformity of these events demonstrated on Fig. 2 (b).

Table 1: Background summary.

Background	Number of events
Accidental	0.0086 ± 0.0005
$^9\text{Li}/^8\text{He}$	0.94 ± 0.85
Fast neutron	< 0.5
Total B.G. events	0.95 ± 0.99

4.3 Systematic uncertainties

Table 2: Estimated systematic uncertainties (%).

Total LS mass	2.13	Reactor power	2.05
Fiducial mass ratio	4.06	Fuel composition	1.0
Energy threshold	2.13	Time lag	0.28
Efficiency of cuts	2.06	ν spectra [3]	2.48
Live time	0.07	Cross section [4]	0.2
Total systematic error			6.42%

5 Expected and experimental result

Number of expected reactor antineutrino events for data set under consideration in case of no neutrino oscillations was estimated to be 86.8 ± 5.6 . After applying the prompt and delayed energy cuts to neutrino candidates (see Fig. 3), 54 events remain as the final sample.

The ratio of the number of observed reactor $\bar{\nu}_e$ events to that expected in the absence of neutrino oscillations is $\frac{N_{obs} - N_{BG}}{N_{expected}} = 0.611 \pm 0.085(\text{stat}) \pm 0.041(\text{syst})$.

The probability that the KamLAND result is consistent with the no disappearance hypothesis is less than 0.05%. Fig. 4 shows the ratio of measured to expected flux for KamLAND as well as previous reactor experiments as a function of the average distance from the source.

The observed prompt energy spectrum is shown in Fig. 5.

6 Impact of KamLAND results on neutrino oscilation parameters

The neutrino oscillation parameter region for two-neutrino mixing is shown in Fig. 6. The best fit to the KamLAND data in the physical region yields $\sin^2 2\theta = 1.0$ and $\Delta m^2 = 6.9 \times 10^{-5} \text{ eV}^2$ while the global minimum occurs slightly outside of the physical region at $\sin^2 2\theta = 1.01$ with the same Δm^2 . The 95% C.L. allowed regions from the spectrum shape analysis are shown in

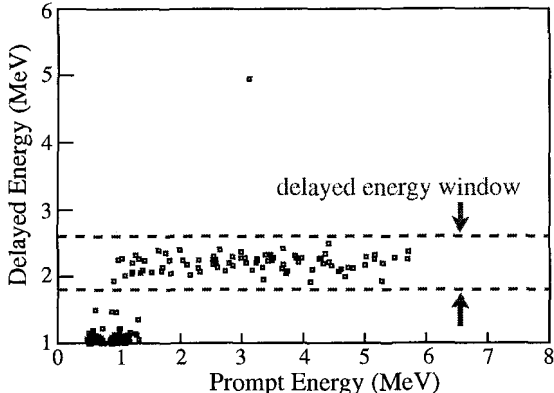


Figure 3: Energy distribution of reactor $\bar{\nu}_e$ candidates. One event with delayed energy around 5 MeV is consistent with a thermal neutron capture γ on ^{12}C .

Fig. 6. The allowed regions displayed for KamLAND correspond to $0 < \theta < \frac{\pi}{4}$ consistent with the solar LMA solution, but for KamLAND the allowed regions in $\frac{\pi}{4} < \theta < \frac{\pi}{2}$ are identical [7].

KamLAND results demonstrated reactor $\bar{\nu}_e$ disappearance at a high confidence level (99.95%). Since negligible reduction of $\bar{\nu}_e$ flux expected from the SMA, LOW and VAC solar neutrino solutions, the LMA region is the only remaining oscillation solution consistent with the KamLAND result and CPT invariance.

7 Search for $\bar{\nu}_e$'s from the Sun in KamLAND

As it was explained in beginning, KamLAND was designed to study the flux of reactor $\bar{\nu}_e$'s. While the reactor $\bar{\nu}_e$ spectrum has endpoint at 8.5 MeV, spectrum of ^8B solar neutrinos extends to 15 MeV. As a result, KamLAND data may be used to search for $\bar{\nu}_e$'s in the solar neutrino flux over an energy range largely free of reactor $\bar{\nu}_e$ events.

Events reconstruction for high energy inverse β -decay events is similar to described above for reactor anti-neutrino events. Energy scale was extended in investigated region with study of the β -spectra of cosmogenically produced ^{12}B and ^{12}N .

There are several mechanism which could lead to a $\bar{\nu}_e$ component in the solar flux incident on the Earth. Electron neutrinos with a non-zero transition magnetic moment can evolve into $\bar{\nu}_\mu$'s or $\bar{\nu}_\tau$'s propagating through magnetic field in the solar core. These neutrinos can evolve into $\bar{\nu}_e$'s via flavor oscillation. There is also neutrino decay, in which a heavy neutrino mass eigenstate decays into a lighter anti-neutrino mass eigenstate [8, 9].

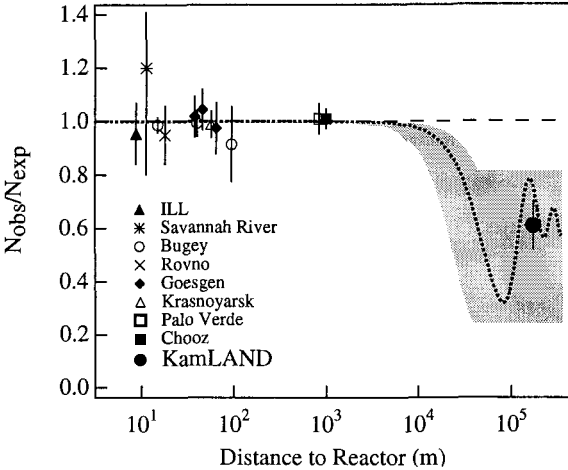


Figure 4: The ratio of measured to expected $\bar{\nu}_e$ flux from reactor experiments [5]. The solid dot is the KamLAND point plotted at a flux-weighted average distance. The shaded region indicates the range of flux predictions corresponding to the 95% C.L. LMA region found in a global analysis of the solar neutrino data [6]. The dotted curve corresponds to $\sin^2 2\theta = 0.833$ and $\Delta m^2 = 5.5 \times 10^{-5} \text{ eV}^2$ [6] and is representative of recent best-fit LMA predictions while the dashed curve shows the case of small mixing angles (or no oscillation).

No $\bar{\nu}_e$ events in the energy range from 8.3 to 14.8 MeV were found in the 185.5 live-day of KamLAND data set. As result we have obtained a flux limit of solar $\bar{\nu}_e$ to be less than $3.7 \cdot 10^{-2} \text{ cm}^2 \text{s}^{-1}$ (90% C.L.), assuming an un-oscillated ${}^8\text{B}$ neutrino energy spectrum.

8 Prospects for KamLAND measurements

In early 2003, many reactors in Japan were powered down for an inspection. Expected non-oscillated neutrino flux in KamLAND was reduced by about factor of two for few months. Such a changes helps to understand better of backgrounds and to check previous results. It's also provide a great opportunity for confirmation of geo neutrino signal.

In more far perspective, KamLAND will continue to collect data and reduce systematic error with using new 4π calibration system. Fig. 7 demonstrates sensitivity of KamLAND for 5 years of data taking. New power reactor (Shika-2) in 88 km from KamLAND with a thermal power of 3.926 GWth is under construction and is planned to start operation in 2006. Expected contribution of that reactor to better understanding of oscillation parameters demonstrated on Fig. 7.

${}^7\text{Be}$ solar neutrino observation is in plans for second stage of KamLAND which will required an additional purification of LS.

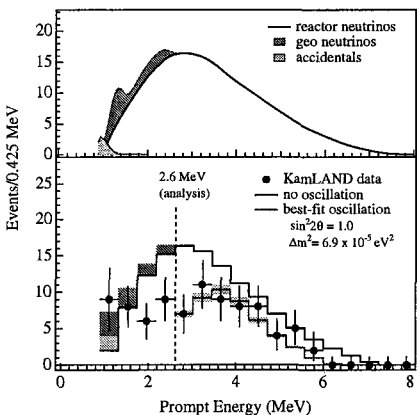


Figure 5: Upper panel: Expected $\bar{\nu}_e$ energy spectrum. Lower panel: Energy spectrum of the observed prompt events and expected no oscillation spectrum.

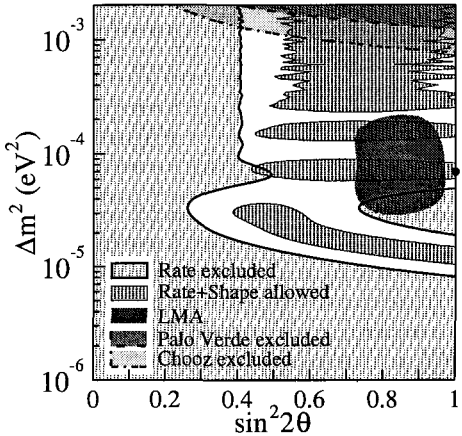


Figure 6: Allowed regions of neutrino oscillation parameters for the rate analysis and the combined rate and shape analysis from KamLAND [2] at 95% C.L. The thick dot indicates the best fit to the KamLAND data in the physical region: $\sin^2 2\theta = 1.0$ and $\Delta m^2 = 6.9 \times 10^{-5} \text{ eV}^2$.

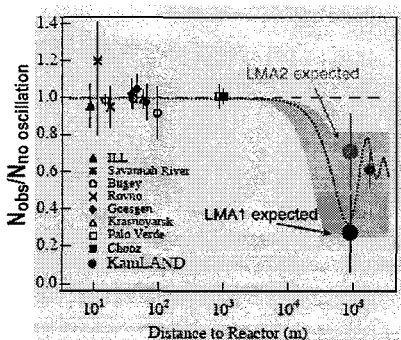
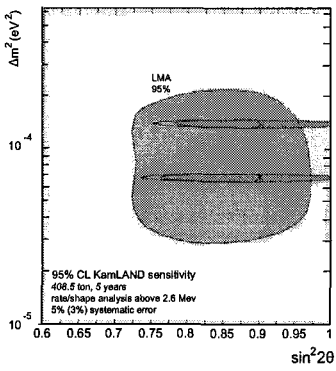


Figure 7: Future of KamLAND: Expected sensitivity of KamLAND after 5 years of data (left picture); and Sensitivity to LMA1 versus LMA2 solution for 3 years of data taking before and after operation of new reactor (Shika-2) will be started (right picture).

Acknowledgments

The KamLAND experiment is supported by the COE program of Japanese Ministry of Education, Culture, Sports, Science and Technology, and funding from the United States Department of Energy. The reactor data are provided by courtesy of the following electric associations in Japan; Hokkaido, Tohoku, Tokyo, Hokuriku, Chubu, Kansai, Chugoku, Shikoku and Kyushu Electric Power Companies, Japan Atomic Power Co. and Japan Nuclear Cycle Development Institute. Kamioka Mining and Smelting Company has provided service for activities in the mine.

References

- [1] K. S. Hirata et al., *Phys. Rev.* **D** 38, 448 (1988).
- [2] KamLAND collaboration, *Phys. Rev. Lett.* 90, 021802 (2003)
- [3] ^{235}U : K. Schreckenbach et al., *Phys. Lett.* **B** 160, 325 (1985); $^{239,241}\text{Pu}$: A. A. Hahn et al., *Phys. Lett.* **B** 218, 365 (1989); ^{238}U : P. Vogel et al., *Phys. Rev.* **C** 24, 1543 (1981).
- [4] P. Vogel and J. F. Beacom, *Phys. Rev.* **D** 60, 053003 (1999);
- [5] Particle Data Group, *Phys. Rev.* **D** 66, 010001-406 (2002).
- [6] G. L. Fogli et al., *Phys. Rev.* **D** 66, 053010 (2002).
- [7] A. de Gouvea, A. Friedland, H. Murayama, *Phys. Lett.* **B** 490, 125 (2000).
- [8] J. F. Beacom and N. F. Bell, *Phys. Rev.* **D** 65, 113009 (2002)
- [9] XG. He et al., *Phys. Rev.* **D** 38, 1317 (1988); A. Acker et al., *Phys. Lett.* **B** 285, 371 (1992); A. Joshipura et al., *Phys. Rev.* **D** 66, 113008 (2002); C. W. Kim and W. P. Lam, *Mod. Phys. Lett.* **A** 5, 297 (1990).

LONG BASELINE NEUTRINO EXPERIMENTS

Takashi Kobayashi ^a

Institute for Particle and Nuclear Studies, High Energy Accelerator Research Organization (KEK), 1-1 Oho, Tsukuba, 305-0801, Japan

Abstract. On-going and future long baseline neutrino experiments are reviewed.

1 Introduction

As seen in the discoveries of neutrino oscillations in atmospheric and solar neutrinos [1–3], the recent development of the neutrino physics is remarkable and properties of neutrino are gradually being revealed. In order to understand the whole properties of neutrino, many long baseline (LBL) neutrino oscillation experiments are being performed, constructed, or planned.

These LBL experiments could be categorized into 3 types as following [4]:

1st generation experiments: Set the primary goal to confirm the results from atmospheric neutrino observation by searching for signals of ν_μ disappearance and/or ν_τ appearance.

2nd generation experiments: Put the highest priority on the discovery of ν_e appearance, the only mode remaining unknown. Since the experiments are designed and optimized after the SK results, Δm^2 region to be searched for is small. In order to maximize discovery potential, neutrino beam with narrow energy spread are produced and the peak of the spectrum are tunned at the oscillation maximum.

3rd generation experiments: Purposes of the experiments are search for CP violation in neutrino sector and/or determination of mass hierarchy from measurement of matter effect. The experiments for those purposes require multi-MW proton beam and \sim Mton detector.

In this report, these LBL experiments are reviewed but neutrino factory is not covered.

2 First generation experiments

There is one running experiment, K2K and three constructing experiments, MINOS in US and ICARUS and OPERA in Europe.

2.1 K2K experiment

The K2K (KEK-to-Kamioka) experiment is the first LBL experiment [5], in which ν_μ beam is produced at KEK and detected by Super-Kamiokande (SK) at 250 km from KEK.

^ae-mail: takashi.kobayashi@kek.jp

The neutrino beam of K2K is almost pure ν_μ beam generated from decay of mesons (mainly pions) produced by irradiating protons on a target. Proton beam extracted from 12-GeV proton synchrotron (PS) hits the target once every 2.2 s in 1.1 μs width and number of protons in a spill is 6×10^{12} . The positive secondary particles are focused toward the direction of SK by a pair of pulsed magnetic horns [6] and are lead into a decay volume of 200m long. They decay into neutrinos during flight in the decay volume. The purity of ν_μ is 98% and mean energy of the neutrinos is 1.3 GeV. In order to measure properties of neutrino beam just after production, neutrino detectors are placed in KEK site, 300 m from the production target.

The K2K experiment started physics run in June 1999. By the summer of 2001, 5.6×10^{19} protons were delivered to the production target. After the accident of SK, K2K resumed in Dec. 2002 and 2.5×10^{19} more protons on target (POT) were delivered by the end of June 2003. The period before and after the SK accident are called K2K-I and K2K-II, respectively. The results based on K2K-I data, which corresponds to 4.8×10^{19} analyzed POT, are presented.

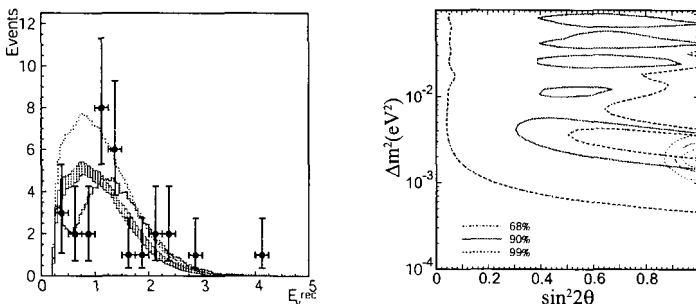


Figure 1: (Left) The E_{ν}^{rec} distribution for $1R\mu$ sample. Points with error bars are data. Box histogram is expected spectrum without oscillations, where the height of the box indicates the size of systematic error. The solid line is the best fit spectrum. These histograms are normalized to data by the number of events observed. The dashed line shows the expectation without oscillations normalized to the expected number of events $1R\mu$ events. (Right) Allowed regions of oscillation parameters. Dashed, solid and dot-dashed lines are 99%, 90% and 68.4% C.L. contours, respectively. Thick lines are K2K results and thin lines are from SK atmospheric neutrino observation. The best fit points for K2K and SK are indicated by the filled star and open star, respectively.

Signature of the neutrino oscillation of ν_μ disappearance mode is a suppression in the number of events and a characteristic spectrum distortion. Number of events fully contained (FC) in the inner detector and distribution of neutrino energies for single ring μ -like ($1R\mu$) events are used to probe the ν_μ disappearance. The neutrino energy of the $1R\mu$ events are calculated using the observed momentum of the muon, assuming 2-body kinematics of charged-current (CC) quasi-elastic interactions ($\nu_\mu + n \rightarrow \mu + p$), and neglecting Fermi

momentum. Observed number of FC events in K2K-I is 56 and the E_ν^{rec} distribution for 29 1R μ events are plotted by points in Fig. 1. Expected number of FC events without oscillation is estimated to be $80.1^{+6.2}_{-5.4}$ events. The oscillation parameters which describe the observation best are found to be at $(\sin^2 2\theta, \Delta m^2) = (1.0, 2.8 \times 10^{-3} \text{ eV}^2)$. Probability that there is no oscillation is found to be less than 1%. Allowed region for the oscillation parameters are evaluated and shown in Fig. 1 (right). At maximum mixing, $\sin^2 2\theta = 1$, the mass squared difference is constrained to be within $\Delta m^2 = 1.5 \sim 3.9 \times 10^{-3} \text{ eV}^2$ at 90% confidence level.

Electron neutrino appearance at same Δm^2 region as atmospheric neutrino oscillation is searched for for the first time. Electron neutrino events are selected by requiring fully contained, single electron-like (showering) ring with visible energy greater than 100MeV and no decay electron associated. Efficiency to select CC interactions from the oscillated ν_e is 57 % for $\Delta m^2 = 2.8 \times 10^{-3} \text{ eV}^2$. To select electron-like event, both the Cherenkov ring pattern and opening angle are required to be consistent with an electron event. PID parameters are defined based on the ring pattern and opening angle and the distributions of the parameters for data and MC are plotted in Fig. 2 (left). Distributions of data are con-

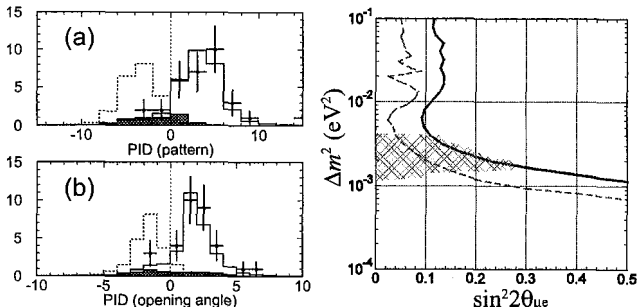


Figure 2: (Left) Distributions of PID parameters for 32 single-ring events based on (a) Cherenkov ring pattern, and (b) Cherenkov opening angle. The distributions for the data (closed circles), oscillated ν_μ MC with $(\sin^2 2\theta, \Delta m^2) = (1.0, 2.8 \times 10^{-3} \text{ eV}^2)$ (solid histograms) and expected ν_e signal with full mixing (dashed histograms) are shown. Shaded histograms are the NC component of ν_μ MC. (Right) The confidence interval for the mixing angle $\sin^2 2\theta_{\mu e}$ at 90% C.L. as a function of Δm^2 for K2K (solid line) and CHOOZ (dashed line). Area to the right of each curve is excluded. Hatched area is allowed region by SK atmospheric neutrino 3-flavor analysis.

sistent with the oscillated ν_μ MC with $(\sin^2 2\theta, \Delta m^2) = (1.0, 2.8 \times 10^{-3} \text{ eV}^2)$.

One event is selected as an electron candidate, while expected background is estimated to be 2.4 ± 0.6 events. The background is dominated by neutral current (NC) π^0 production (1.7 events). Since no significant signal events over the background is observed, upper bound on the mixing angle is set and plotted in Fig. 2. Neutrino oscillations from ν_μ to ν_e are excluded for $\sin^2 2\theta_{\mu e} (\simeq \frac{1}{2} \sin^2 2\theta_{13}) > 0.15$ at $\Delta m^2 = 2.8 \times 10^{-3} \text{ eV}^2$ at 90% C.L.

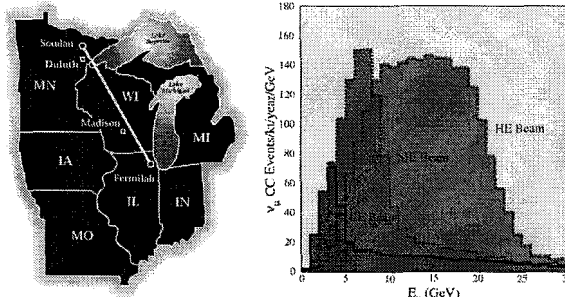


Figure 3: (Left) MINOS overview. (Right) Expected energy spectra for ν_μ CC interactions without oscillations.

2.2 MINOS and CNGS-OPERA/ICARUS projects

MINOS is a LBL experiment in US which is now under construction aiming to start experiment in the beginning of 2005 [7]. The ν_μ beam is produced at FNAL using 120-GeV Main Injector (MI) and detected by a detector placed in the Soudan mine after 735 km travel as in Fig. 3. The main purposes of the experiment is to investigate the ν_μ disappearance phenomenon in detail at Δm^2 region suggested by atmospheric neutrino observation, and to determine the oscillation parameters precisely.

The beam is conventional horn-focused wide-band beam. By choosing different setting of the distances between target, 1st horn, and 2nd horn, neutrino energy regions can be selected as shown in Fig. 3. The far detector in the Soudan mine is a magnetized Iron and scintillator sandwich detector with Iron thickness of 2.5 cm. To measure properties of neutrinos just after production, near detector with the same configuration as the far detector is placed. The fiducial masses of the near and far detectors are 980 t and 5,400 t, respectively. Expected number of CC interactions is about 2,500/yr in the fiducial volume of the far detector. The far detector construction finished on July 10, 2003, and the first protons on target is expected in December 2004.

The CERN neutrino beam to Gran Sasso (CNGS) is a project to produce high energy ν_μ beam using 400-GeV CERN-SPS and send toward Gran Sasso laboratory at 732 km from CERN [8]. Mean energy of ν_μ is \sim 17 GeV. Two detectors are planned to be placed in Gran Sasso, namely, OPERA [9] and ICARUS [10]. The goal of these experiments is to detect ν_τ interactions which is changed from ν_μ due to oscillation (ν_τ appearance). The OPERA detector consists of 206k bricks of Emulsion Cloud Chamber, which is a sandwich of 1-mm thick Pb plates and emulsion sheets. Total mass of the ECC is 1.7 kt. The ECC part is followed by a magnetic spectrometer with electronic tracking system. The τ events from CC ν_τ interactions are identified by event topology, a kink in a track caused by $\tau \rightarrow \mu$ decay. The ICARUS detector is 3-kt liquid

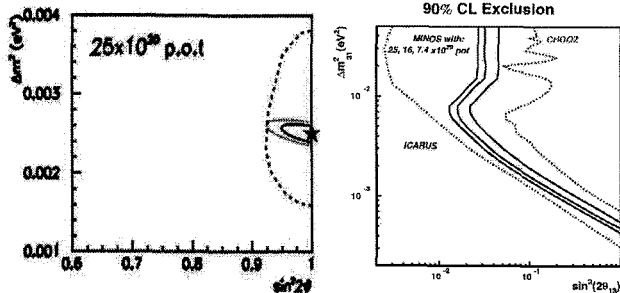


Figure 4: (Left) MINOS sensitivity on ν_μ disappearance. (Right) Sensitivities of MINOS and ICARUS on ν_e appearance.

Argon time projection chamber. The τ events are selected using distributions of kinematic variables. A 300 t prototype was constructed and performances was tested.

Expected sensitivities of MINOS, ICARUS and OPERA for ν_μ disappearance and ν_e appearance are summarized in Fig. 4. In 5 years of MINOS, precision of the oscillation parameters reaches about 5% and 2×10^{-3} eV 2 for $\sin^2 2\theta$ and Δm^2 , respectively. Expected number of signal and background events for the ν_τ appearance search are 17.2 and 1.06 for the OPERA experiment and 11.9 and 0.7 events for ICARUS experiment (1.5 kt fiducial) in 5 years of running at the $\Delta m^2 = 2.5 \times 10^{-3}$ eV 2 .

3 Future Next Generation Projects

3.1 Project in Japan: T2K experiment

In Japan, construction of a MW proton accelerator complex, now called as

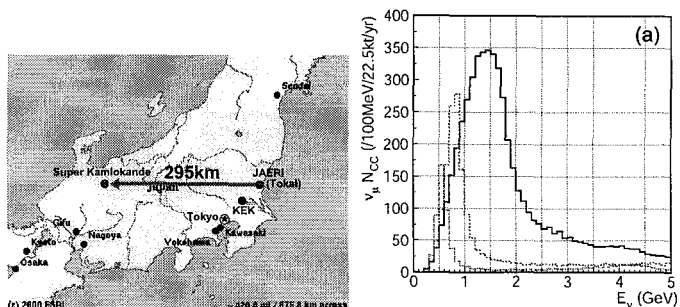


Figure 5: (Left) Locations of JAERI-Tokai site and SK. (Right) Expected spectrum of CC interactions at SK. The solid (black), dashed (red) and dotted (blue) histograms are OA1.5°, OA2° and OA3°, respectively.

J-PARC (Japan Proton Accelerator Research Complex), is going on at JAERI-Tokai site aiming the completion by March, 2008 [11]. The T2K (Tokai-to-Kamioka) experiment is a next generation LBL neutrino oscillation experiment in which ν_μ beam is produced using the 50 GeV proton synchrotron in J-PARC and sent to SK with 295 km flight distance (Fig. 5) [12]. At the first phase of the project, the power of the 50 GeV PS is 0.75 MW and SK will be used as a far detector. In the future, PS upgrade up to 4 MW and 1-Mt “Hyper-Kamiokande” [13] are envisaged. The main goals of the first phase are discovery of ν_e appearance and the precision measurements of oscillation parameters in ν_μ disappearance.

One of the special features of T2K is the first application of “off-axis” (OA) beam which can produce low energy high intensity ν_μ beam with adjustable sharp peak in the energy spectrum [14]. The position of the peak will be tunned at energy of oscillation maximum to maximize the sensitivity. The expected ν_μ spectrum at SK without oscillation is plotted in Fig. 5. The ν_e to ν_μ flux ratio is as small as 0.2% at the peak energy of ν_μ spectrum. Expected numbers of interactions at SK with 2° off-axis is about 3000 for CC interactions in fiducial volume of 22.5 kt in 1 year. In order to monitor the neutrino beam and to predict the flux and spectrum at SK, muon monitor behind the beam dump and front neutrino detector at 280 m from the production target will be installed.

The budget for the 1st phase T2K experiment including beamline and the near detector is approved by the government and facility construction started in April 2004. Construction will take 5 years and the first proton beam on target is scheduled in the beginning of 2009.

3.2 Projects in US

At FNAL, a new 2nd generation OA experiment called NO ν A is proposed [4]. The experiment will share the same beam line as MINOS experiment and place a far detector at 810 km from production target and 12 km off from the beam axis. The OA angle is 14.8 mr. The expected spectra are shown in Fig. 6. The proposed detector is a 50-kt medium-Z sandwich detector with particle board absorber and liquid scintillator strip detectors. The NC π^0 background is identified by event topology, that is the existence of two tracks with different starting points. Possible schedule is that construction will be started in Oct. 2006, data taking with 25% partial detector will start in Sept. 2008 and detector construction will complete in Sept. 2010.

Possibility to upgrade the beam power of MI is also being discussed at FNAL [15]. The idea is to replace the current 8-GeV booster by a 8-GeV rapid-cycling synchrotron or 2 MW 8-GeV superconducting LINAC. It increases the power of MI up to about 2 MW.

There is another interest to conduct a (very) LBL experiment proposed at

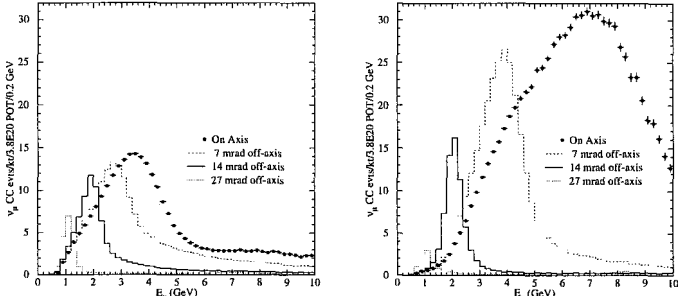


Figure 6: Energy spectra of CC events expected at a far detector location 735km from FNAL at various OA angles for the NuMI low-energy beam setting (left) and the medium-energy setting (right) [4].

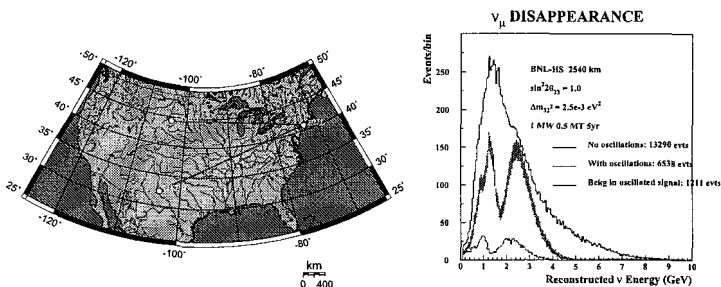


Figure 7: (Left) Locations of BNL and possible detector sites Homestake and WIPP at 2540 and 2880 km from BNL, respectively. (Right) Expected spectrum of detected events in a 0.5-Mt detector at 2540 km from BNL including quasi-elastic signal and CC-single pion background in 5 years of running. The top histogram is without oscillations; the middle error bars are with oscillations and the bottom histogram is the contribution of the background to the oscillated signal only. This plot is for $\Delta m_{32}^2 = 0.0025 \text{ eV}^2$.

BNL in which the neutrino beam is produced by 28 GeV AGS upgraded to 1 MW and detected by a water Cherenkov detector of 500 kt or more at more than 2000 km [16]. The locations of BNL and possible detector sites and expected neutrino spectra are shown in Fig. 7. One special feature of this experiment is that the neutrino energy and the distance are chosen so that the second oscillation maximum can be measured. This gives the sensitivity on solar parameters θ_{12} and Δm_{12}^2 and higher sensitivity on CPV than experiments at first oscillation maximum.

3.3 Projects in Europe

In Europe, there is an idea of future LBL experiment in which the neutrino beam is produced by Super Proton Linac (SPL) and detected by a detector at Modane laboratory in Furejus tunnel, 130 km from CERN [17]. The proposed SPL is a 2.2 GeV linac with 4 MW beam power operated at 75-Hz repetition

rate and 1.5×10^{14} protons/pulse. The neutrino beam is a conventional wide-band beam and the expected neutrino spectrum at the detector site is plotted in Fig. 8. The expected neutrino spectrum ranges $\lesssim 500$ MeV which matches

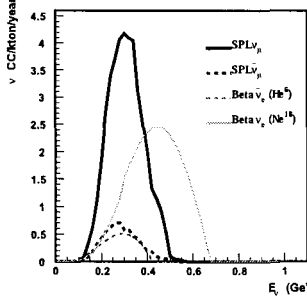


Figure 8: Energy spectra of CC interactions from super- and beta-beam at CERN

with the oscillation maximum of ~ 300 MeV at $\Delta m^2 = 3 \times 10^{-3}$ eV 2 . Currently two types of detector technology are under consideration, i.e., water Cherenkov detector of SK type and liquid scintillator detector of LSND/MiniBooNE type. The detector fiducial mass is supposed to be 40 kt in early phase.

Also at CERN, a possibility to produce sub-GeV ν_e or $\bar{\nu}_e$ beam with a novel method, beta beam [18]. The method uses beta decays of accelerated radioactive ions. Expected spectra are also shown in Fig 8.

3.4 Summary of experiments

Current and planned (superbeam) LBL experiments are summarized in Table 1. As can be seen in the L/L_{osci} column, neutrino energy and the baseline length in most of the 2nd generation experiments are chosen so that the neutrino energy matches at the oscillation maximum.

Table 1: Summary of (super)beam LBL experiments. The column “FM” is the fiducial mass of far detector. The letters in “status” column mean “A”: accelerator, “B”: neutrino beam line, “D”: far detector, and the meaning of the symbols are \odot : in operation, \circ : construction, Δ : design.

	E_p (GeV)	Power (MW)	E_{ν} (GeV)	L (km)	L/L_{osci}	FM (kt)	#CCint (/yr)	status		
								A	B	D
K2K	12	0.005	1.3	250	0.47	22.5	30	running		
MINOS	120	0.4	3.5	730	0.51	5.4	2.5k	start 2005		
ICARUS						2.35	6.5k	start 2006		
OPERA	400	0.3	17	732	0.10	1.65	4.6k			
T2K-I	50	0.75	0.7	295	1.02	22.5	3k	\circ	\circ	\odot
NO ν A	120	0.4	2.0	810	0.82	50	4.6k	\odot	\circ	Δ
T2K-II	50	4.0	0.7	295	1.02	540	480k	Δ	Δ	Δ
Super-AGS	28	1.3	1.5	2540	4.1	500	16k	Δ	Δ	Δ
SPL-Furejus	2.2	4.0	0.26	130	1.21	40	650	Δ	Δ	Δ

*1 : The definition of neutrino oscillation length is $L_{osci} = \frac{\pi}{2} \cdot \frac{\langle E_{\nu} \rangle}{1.27 \Delta m^2}$ for $\Delta m^2 = 3 \times 10^{-3}$ eV 2 .

3.5 Sensitivities

In Fig. 9, sensitivities on ν_e appearance of two second generation experiments are drawn with the current upper bound from CHOOZ experiment [19]. The LBL experiments extend the current limit more than an order of magnitude. The expected sensitivity on CP violation in the 2nd phase T2K project is

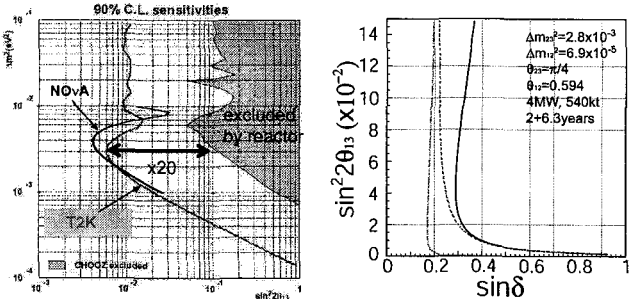


Figure 9: (Left) Expected 90% sensitivity on ν_e appearance. (Right) Expected 3 σ discovery region of $\sin \delta$ as a function of $\sin^2 2\theta_{13}$ in the phase II of T2K project. The (blue) dotted curve is the case of no background and only statistical error of signal, (red) dashed one is 2% error for the background subtraction, and (black) solid curve is the case that systematic errors of both background subtraction and signal detection are 2%.

plotted in Fig. 9. If $\sin^2 2\theta_{13}$ is of the order of 0.01 or larger, the CP violation phase δ can be discovered down to $\sim 20^\circ$.

4 Summary

On-going and future LBL experiments with conventional beam have been reviewed. The pioneering experiment K2K have established a methodology of LBL experiment, and is confirming the atmospheric neutrino results. Other 1st generation experiments under construction will be on-line within 1 or 2 years. For the medium near future of 5~10 years, experiments optimized to discover ν_e appearance, T2K and NO ν A are planned. The T2K experiment is approved and the first beam will be in Jan. 2009. For more future, several possibilities to search for CP violation and to determine mass hierarchy with a multi-MW proton driver and a \sim Mt detector are being seriously discussed. Neutrino physics will continue to be exciting for coming several 10 years.

Acknowledgments

The author greatly acknowledge organizers of the conference, especially Prof. A. Studenikin, for giving me a chance to present this talk and for patience in waiting my very late preparation of the proceedings.

- [1] Y.Fukuda *et al* , Phys. Rev. Lett. **81**, 1562 (1998), Phys. Rev. Lett. **85**, 3999 (2000)
- [2] Q.R. Ahmad *et al* , Phys. Rev. Lett. **89**: 011301 (2002); S. Fukuda *et al* , Phys. Lett. **B539**:179-187,2002.
- [3] K. Eguchi *et al.*, Phys. Rev. Lett. **90**, 021802 (2003).
- [4] <http://www-off-axis.fnal.gov/> ; G. Feldman,
http://www.bnl.gov/physics/superbeam/docs/APS1_Mar_04.pdf,
 presentation at workshop “*Neutrino Super Beam, Detectors and Proton Decay*”, Mar. 3-5, 2004, BNL.
- [5] S. H. Ahn *et al.*, Phys. Lett. B **511**, 178 (2001); M. H. Ahn *et al.*, Phys. Rev. Lett. **90**, 041801 (2003).
- [6] M. Ieiri *et al.*, “Magnetic horn for a long-baseline neutrino oscillation experiment at KEK”, *Prepared for 11th Symposium on Accelerator Technology and Science, Hyogo, Japan, 21-23 Oct 1997*.
- [7] D. Michael, Nucl. Phys. Proc. Suppl. **118**, 189 (2003); K. Lang, Proceedings of *International Workshop on Astroparticle and High-Energy Physics (AHEP-2003)*, Valencia, Spain, 14-18 Oct 2003.
- [8] G. Acquistapace *et al.*, CERN-98-02; R. Baldy *et al.*, CERN-SL-99-034-DI.
- [9] M. De Serio, in proceedings of *International Workshop on Astroparticle and High-Energy Physics (AHEP-2003)*, Valencia, Spain, 14-18 Oct 2003; M. Komatsu, Nucl. Instrum. Meth. A **503**, 124 (2003).
- [10] F. Arneodo *et al.*, Nucl. Instrum. Meth. A **461**, 324 (2001).
- [11] <http://j-parc.jp>
- [12] Y. Itow, *et al* , hep-ex/0106019, <http://neutrino.kek.jp/jhfnu>
- [13] M. Koshiba, *Phys. Rep.* **220**, 229 (1992); K. Nakamura, *Neutrino Oscillations and Their Origin*, (Universal Academy Press, Tokyo, 2000), p. 359.
- [14] D. Beavis *et al* , Proposal of BNL AGS E-889 (1995).
- [15] <http://www-bd.fnal.gov/pdriver/>
- [16] M. V. Diwan *et al.*, Phys. Rev. D **68**, 012002 (2003); M. Diwan *et al.*, arXiv:hep-ex/0305105; <http://www.neutrino.bnl.gov/>
- [17] J.J. Gomes Cadenas *et al* , (hep-ph/0105297), May 2001; A. Blondel *et al* , CERN-NUFACT-NOTE-095, Oct. 2001.
- [18] P. Zucchelli, Phys. Lett. B **532**, 166 (2002); <http://beta-beam.web.cern.ch/beta-beam/>
- [19] M. Apollonio *et al.*, Eur. Phys. J. C **27**, 331 (2003).

PRECISION MEASUREMENTS FROM THE NOMAD EXPERIMENT

R.Petti ^a

CERN, 1211 Geneva 23, Switzerland

Abstract. The NOMAD experiment collected unprecedent neutrino data samples, matching both the large statistics of massive calorimeters and the reconstruction quality of bubble chambers. A review of the currently ongoing measurements is presented.

1 Introduction

The NOMAD experiment was designed to search for ν_τ appearance from neutrino oscillations in the CERN wide-band neutrino beam produced by the 450 GeV proton synchrotron. The detection of an oscillation signal in NOMAD relied on the identification of the τ lepton from ν_τ charged-current (CC) interactions using kinematic criteria. This required a fine-grained detector with good energy and momentum resolution in order to achieve a precise measurement of all visible final-state particles. In addition, large statistics and refined analysis schemes were needed to explore oscillation probabilities of the order of 10^{-4} .

The single-particle reconstruction and lepton identification capability of the NOMAD detector allowed the search for ν_τ appearance in most of the leptonic and hadronic τ decay channels [1] and also to look for $\nu_\mu \rightarrow \nu_e$ oscillations [2]. No evidence for oscillations was found from the analysis of the full data sample.

A second phase of the NOMAD analysis started after the completion of the oscillation searches, with the aim of exploiting the high quality of the available neutrino data samples for precise measurements of cross-sections and particle production. This analysis activity could benefit from the beam and detector studies performed for the oscillation searches.

2 Detector and data samples

The NOMAD detector (Figure 1) is described in detail in Ref. [3]. Inside a 0.4 T magnetic field there is an active target consisting of drift chambers (DC) [4] with a fiducial mass of about 2.7 tons and a low average density (0.1 g/cm^3). The main target, 405 cm long and corresponding to about one radiation length, is followed by a transition radiation detector (TRD) [5] for electron identification, a preshower detector (PRS), and a high resolution lead-glass electromagnetic calorimeter (ECAL) [6]. A hadron calorimeter (HCAL) and two stations of drift chambers for muon detection are located just after the downstream part of the magnet coil. An iron-scintillator sampling calorimeter

^ae-mail: Roberto.Petti@cern.ch

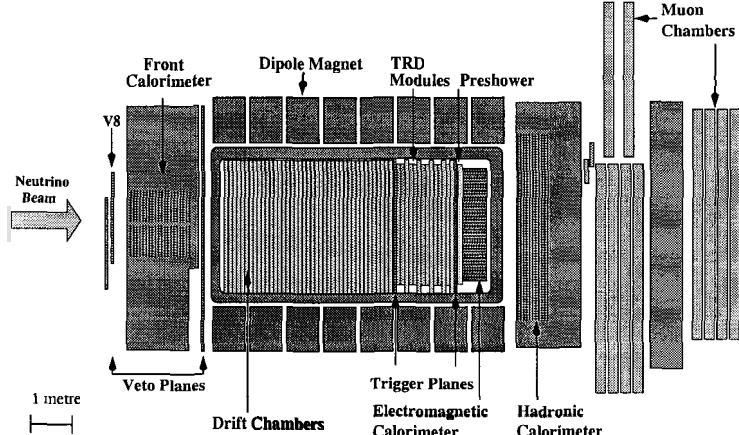


Figure 1: Side view of the NOMAD detector.

with a fiducial mass of about $17t$ (FCAL) is located upstream of the central part of the NOMAD target. The detector is designed to identify leptons and to measure muons, pions, electrons and photons with comparable resolutions. Momenta are measured in the DC with a resolution:

$$\frac{\sigma_p}{p} \simeq \frac{0.05}{\sqrt{L[m]}} \oplus \frac{0.008 \times p[GeV/c]}{\sqrt{L[m]^5}}$$

where L is the track length and p is the momentum. The energy of electromagnetic showers, E , is measured in the ECAL with a resolution:

$$\frac{\sigma_E}{E} = 0.01 \oplus \frac{0.032}{\sqrt{E[GeV]}}.$$

From recent beam computations [7], the relative composition of CC events in NOMAD is estimated to be $\nu_\mu, \bar{\nu}_\mu, \nu_e, \bar{\nu}_e = 1.00 : 0.0227 : 0.0154 : 0.0016$, with average neutrino energies of 45.4, 40.8, 57.5, and 51.5 GeV, respectively. Neutrinos are produced at an average distance of 625 m from the detector.

The NOMAD experiment collected data from 1995 to 1998. Most of the running, for a total exposure of 5.1×10^{19} protons on target (pot), was in neutrino mode. This resulted in three distinct data samples, according to the different targets: $1.3 \times 10^6 \nu_\mu$ CC interactions from the drift chambers (mainly carbon), $1.5 \times 10^6 \nu_\mu$ CC interactions from the region of the magnet coil (mainly aluminium) located in front of the DC and $1.2 \times 10^7 \nu_\mu$ CC interactions from FCAL (iron). Table 2 shows a comparison with the existing data from other experiments.

Experiment	Target mass	Exposure p.o.t.	Statistics ν_μ CC	Type
CDHS	750 t	5.2×10^{18}	10^7	massive calorimeter
CHARM II	547 t	9.0×10^{18}	10^7	massive calorimeter
BEBC	various	various	5.7×10^4	bubble chambers
E531	91 kg	2.0×10^{19}	3.8×10^3	emulsions
CCFR	690 t	1.0×10^{18}	1.0×10^6	massive calorimeter
NuTeV	690 t	1.3×10^{18}	1.3×10^6	massive calorimeter
CHORUS	770 Kg	5.06×10^{19}	1.0×10^5	emulsions
NOMAD	2.7 t		1.3×10^6	C, DC
	few t	5.10×10^{19}	1.5×10^6	Al, coil
	17.7 t		1.2×10^7	Fe, FCAL

Table 1: Summary of main neutrino data samples presently available.

3 Precision measurements

Significant efforts were performed in order to further improve the quality of data for precision measurements. A complete reprocessing of the raw data allowed a better reconstruction and the recovery of additional samples (in particular events originating in the front coil of the magnet). In addition, new large statistics Monte Carlo simulations were produced, after a detailed tuning of the generator using NOMAD data. This resulted in a reduction of systematic uncertainties with respect to the oscillation searches.

The physics potential of the NOMAD data samples is extremely rich and several physics topics are currently under study. A brief summary of the main measurements is given in the following sections.

3.1 Determination of $\sin^2 \theta_W$

A precise determination of the weak mixing angle from νN Deep Inelastic Scattering (DIS) is in progress. The value of $\sin^2 \theta_W$ is obtained from the ratio of Neutral (NC) to Charged Current neutrino interactions:

$$\mathcal{R}_\nu = \frac{\sigma_{NC}}{\sigma_{CC}}$$

In order to reduce systematic uncertainties, a simultaneous fit to both \mathcal{R}_ν and the CC differential cross-section $d\sigma_{CC}^2/dxdQ^2$ is performed. The analysis consists in classifying the events as NC and CC, providing the measured experimental ratio $\mathcal{R}_\nu^{\text{exp}}$. The knowledge of the detection efficiencies and of the experimental resolutions provides then the cross-section values.

The identification of CC interactions is based upon two *independent* criteria. First, events containing tracks (of any charge) which can be matched to

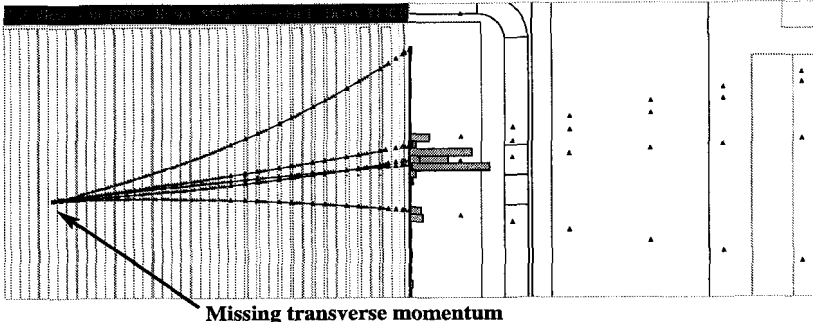


Figure 2: Example of a NC candidate event selected from NOMAD data (run 12389, event 55918). Solid lines represent the reconstructed charged tracks (with DC hits). The energy deposition of individual ECAL cells is also shown by the shaded bins on the right.

segments in the external muon chambers are flagged as ν_μ CC. A kinematic tagging of the leading lepton is then applied to all events failing the previous requirement. This second tagging is provided by a multidimensional likelihood function [1] and is applied to negative tracks only. The procedure provides two substantial advantages. A CC event failing any of the two complementary criteria has a second possibility to be tagged as CC, thus resulting in a reduction of the corresponding systematic uncertainty by one order of magnitude. In addition, the kinematic tagging is very efficient on electrons from ν_e CC events which are mostly identified without the use of any specific detector requirement. This in turn reduces systematic uncertainties from the ν_e beam content to a negligible level. The fraction of unidentified ν_μ CC events is about 2%. Figure 2 shows an example of an event tagged as NC in the data.

In principle, the theoretical model enters both in the Monte Carlo simulations used for the efficiency corrections and in the final fit to extract $\sin^2 \theta_W$. However, a refined Data Simulator technique [1] is used to extract all efficiencies from the data themselves, for both NC (with a NC-simulator) and CC (with a CC-simulator), through the expression $\epsilon = \epsilon_{MC} \times \epsilon_{DS}/\epsilon_{MCS}$, where ϵ_{MC} , ϵ_{DS} and ϵ_{MCS} are the efficiencies extracted from the Monte Carlo, the Data Simulator and the Monte Carlo Simulator. The model largely cancels in the ratio $\epsilon_{MC}/\epsilon_{MCS}$. As a result, experimental efficiencies are stable against changes in the simulations.

The analysis is "blind" and the value of $\sin^2 \theta_W$ will be extracted only after all systematic effects are fully understood.

The interest of the analysis increased after the publication of the final measurement of $\sin^2 \theta_W$ by the NuTeV collaboration [8], reporting a deviation of about 3σ with respect to the Standard Model predictions. That result triggered many discussions [9] on its possible interpretations and it appears desirable to

have an independent measurement from neutrino interactions.

3.2 Cross-sections and structure functions

The present knowledge of neutrino cross-sections is rather nonuniform. In the region $E_\nu > 30$ GeV, where data from the large massive calorimeters (CCFR, NuTeV) are available, the uncertainty is about 2%. This increases to about 20% at lower energies, due to the limited statistics of bubble chamber experiments. The average energy of the ν_μ flux in NOMAD was 24.3 GeV (minimum energy 5 GeV), thus allowing to cover the critical region with large statistics data. Measurements of both the total σ_{CC}^{tot} and the differential $d\sigma_{CC}^2/dx dQ^2$ cross-sections are ongoing as part of the $\sin^2 \theta_W$ analysis. In addition, a large sample of quasi-elastic ν_μ interactions provides an accurate measurement of the corresponding cross-section for $E_\nu > 5$ GeV.

The sample of events ($1.2 \times 10^7 \nu_\mu$ CC) originating in the forward iron calorimeter is used to measure the charm dimuon production in neutrino using 12000 identified dimuon events from charm. It is also used to measure the CC ν Fe cross-section.

The NOMAD cross-section data can also be used to extract the structure functions F_2 and xF_3 . The average Q^2 is about 15 GeV 2 , with events extending to the few GeV 2 region. In addition, it is possible to study nuclear effects in neutrino structure functions by comparing the results with C, Al and Fe targets.

3.3 Modelling

The determination of $\sin^2 \theta_W$ from \mathcal{R}_ν required the development of a refined modelling of neutrino interactions. A NLO (or NNLO when applicable) QCD calculation is performed to obtain the neutrino-nucleon structure functions. The approach used is the one described in [10]. New fits to available data from charged lepton scattering on p and D (BCDMS, SLAC, NMC, JLab), focused on the low Q^2 region, are performed to extract parton distributions, high twist terms and the corresponding uncertainties [11].

A model of nuclear effects on structure functions is included [12]. This has been defined on the basis of charged lepton nuclear data and checked against cross-section data. It includes shadowing, off-shell, Fermi motion and binding energy and non isoscalarity corrections.

A new evaluation of electroweak radiative corrections to structure functions is also used [13]. Results are checked against an independent calculation [14] to estimate systematic uncertainties.

A detailed tuning of fragmentation parameters is extracted with the analysis of individual tracks in the hadronic system reconstructed in ν_μ CC data.

The charm production parameters are extracted from a dedicated NLO analysis of NOMAD FCAL dimuon data. In addition, results are further combined

with available data from other experiments (both with neutrinos and e^+e^-).

4 Summary

The NOMAD experiment has collected 1.3×10^6 , 1.5×10^6 and 1.2×10^7 ν_μ CC interactions on carbon, aluminium and iron targets, respectively. Precise measurements of neutrino cross-sections and structure functions, including a determination of $\sin^2 \theta_W$, started after the completion of the oscillation searches. The program includes the development of a detailed model to describe νN scattering events, taking into account higher order QCD calculations, nuclear effects, radiative electroweak corrections, fragmentation and charm production.

Acknowledgments

The author would like to thank the organizers of the conference for the pleasant stay and for their assistance.

References

- [1] P. Astier et al. *Nucl. Phys.* **B** 611, 3 (2001).
- [2] P. Astier et al. *Phys. Lett.* **B** 570, 19 (2003).
- [3] J. Altegoer et al. *Nucl. Instr. and Meth.* **A** 404, 96 (1998).
- [4] M. Anfreville et al. *Nucl. Instr. and Meth.* **A** 481, 339 (2002).
- [5] G. Bassompierre et al. *Nucl. Instr. and Meth.* **A** 403, 363 (1998);
G. Bassompierre et al. *Nucl. Instr. and Meth.* **A** 411, 63 (1998).
- [6] D. Autiero et al. *Nucl. Instr. and Meth.* **A** 372, 556 (1996); D. Autiero et al. *Nucl. Instr. and Meth.* **A** 373, 358 (1996); D. Autiero et al. *Nucl. Instr. and Meth.* **A** 387, 352 (1997); D. Autiero et al. *Nucl. Instr. and Meth.* **A** 411, 285 (1998); D. Autiero et al. *Nucl. Instr. and Meth.* **A** 425, 188 (1999).
- [7] P. Astier et al. *Nucl. Instr. and Meth.* **A** 515, 800 (2003).
- [8] G. Zeller et al. *Phys.Rev.Lett.* 88, 091802 (2002).
- [9] S. Davidson, S. Forte, P. Gambino, N. Rius and A. Strumia, hep-ph/0112302; W. Melnitchouk and A. Thomas, hep-ex/0208016; S. Kulagin, hep-ph/0301045; K. McFarland and S. Moch, hep-ph/0306052; B. Dobrescu and R. Ellis, hep-ph/0310154.
- [10] S. Alekhin, *Phys. Rev.* **D** 67, 114002 (2003).
- [11] S. Alekhin, S. Kulagin and R. Petti, *paper in preparation*.
- [12] S. Kulagin and R. Petti, *paper in preparation*.
- [13] A. Arbuzov, D. Bardin and L. Kalinovskaya, *paper in preparation*.
- [14] K. Diener, S. Dittmaier and W. Hollik, hep-ph/0310364.

FROM THE EXTREME UNIVERSE SPACE OBSERVATORY (EUSO) TO THE EXTREME ENERGY NEUTRINO OBSERVATORY

S. Bottai^a, P. Spillantini^b

University and INFN, Florence, Italy

Abstract. The physics of Cosmic Rays of Extreme Energy will be deeply investigated by the next generation of space detectors (EUSO, KLYPVE,..). For the Extreme Energy neutrino astronomy such detectors will probably exhibit a lack of statistics and a further increase of sensitivity will be necessary for this goal. The increase on neutrino events statistics is discussed with respect to different detector layout

1 Introduction

The discovery of cosmic ray particles with energy greater than 10^{20} eV (Extreme High Energy Cosmic Rays -"EHECR") [1] has opened a new perspective for Astrophysics showing the existence of either unexpected extremely powerful acceleration mechanisms ("bottom-up") or more fundamental phenomena of emission/creation closely related to the primordial structure of the Universe ("top-down"). Furthermore if EHECR are hadrons or nuclei, the energy loss due to their interaction with the cosmic microwave background radiation (Greisen-Zatsepin-Kuzmin cut-off (GZK)) raises the fundamental question concerning the distance travelled by such particles. In case of uniform distribution of sources in the Universe, due to GZK cut-off, the observed spectrum should end around 10^{20} eV. In general if sources yield hadronic EHECR, they produce as well photons and neutrinos of comparable energy. Furthermore the GZK mechanism will guarantee a neutrino flux which arise from the interaction of protons with the cosmic microwave background radiation [8] (Fig. 1). Such neutrinos (called GZK neutrinos) are able to travel for almost the entire universe and carry the information about very far Extreme Energy proton sources. Their detection will open a new window in neutrino astronomy, complementary to neutrino astronomy performed by neutrino telescopes at lower energy. The GZK neutrino direction will be almost the same than proton direction and the angular deviation respect to the sources direction will be affected by the intergalactic magnetic fields encountered by the protons. Due to the very small value of the EECR and neutrino fluxes, their detection require the indirect observation through their atmospheric induced showers (EAS) and very large detectors. The outcoming generation of such EECR detectors plans to look at the EAS from space observatories. From the space it is possible to observe the fluorescence light emitted in the terrestrial atmosphere by the gigantic showers produced by extreme energy cosmic rays. Several experiments have been

^ae-mail: bottai@fi.infn.it

^be-mail: piero.spillantini@fi.infn.it

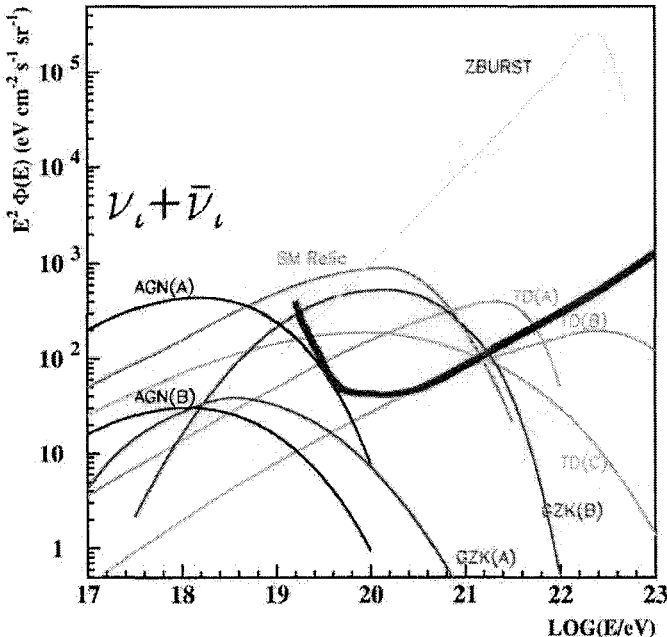


Figure 1: Fluxes of neutrinos from various models. GZK (B) and GZK(A) are respectively the "maximum" and "minimum" GZK neutrino fluxes per flavour considered in this work. The broad line is the EUSO limit.

proposed for performing such an observation from orbiting spacecrafts (AIR-WATCH concept): TUS [2] on board of a Russian satellite, OWL [3] (proposed by NASA physicists) on board of two satellites in order to obtain a stereoscopic view of the shower, KLYPVE [2] on board of the Russian section of the International Space Station (ISS) and EUSO [6] as external payload attachment to the European module Columbus of the ISS. One of the most advanced project from a point of view of the official approval and financial support is the EUSO project, and in the following we will concentrate on it our attention. In section 2 the EUSO project will be shortly described while in sections 3,4 the EUSO parameters will be used as a "reference unit" for discussing the possibility of extending the sensitivity of such detection technique.

2 The EUSO project

The perspective of installing an adequate observing device on board of the ISS was suggested several years ago [4] and considered in the framework of

the Airwatch concept [5]. The potentiality seemed very promising, given the enormous area of the terrestrial surface observable from the ISS. The mass of the air insisting on this surface is $\approx 200 \cdot 10^{12}$ t, an enormous target not only for the study of extreme energy cosmic rays, but also sufficient for acting as an observatory for extreme energy neutrinos. At the end of 1999 the call for proposal issued by the European Space Agency (ESA) for the F2/F3 missions gave the occasion of proposing the EUSO experiment on board of a free flyer (as required by ESA). When, in February 2000, ESA selected the EUSO experiment for an accommodation study on board of the ISS, it was like a "return to the future", i.e. a return to the initial consideration of the ISS as a suitable vehicle for this kind of observations, with the perspective of a promising extension of the EUSO experimental approach in the future. EUSO is a space mission devoted to the investigation of EECRs and will observe the fluorescence signal looking downwards the dark Earth's atmosphere from 400-430 km altitude. EUSO has been approved by the European Space Agency ESA for a Phase A study concerning its accommodation as external payload on the International Space Station (ISS), with a goal for flight in 2008-2010. The instrument consists of a UV telescope with large collecting area and wide field of view (FOV) 60° based on a double Fresnel lens system, a high segmented focal detector, and an on-board image processing acting as a trigger.

EUSO is a collaborating effort of many research groups from Europe, USA and Japan and it has been designed to operate for more than 3 years mission lifetime.

Fresnel lenses will be used for the main optics system which will provide the formation of the shower image on the focal plane. An angular resolution of 0.1° and a full Field of View of 60° are the operational characteristics of the lens. The present detector design foresees a lens system with an entrance pupil diameter of 2.3m. The required angular resolution of 0.1° correspond to a ground spatial resolution of 0.8 km and yields the pixel diameter at about 5 mm. This figure leads to a total number of pixels of the order of $2 \cdot 10^5$. In order to prevent light of undesirable wavelengths from reaching the focal surface a band-pass filter in the wavelength comprises from 300 to 400 nm is planned for the instrument. A cover mechanism as a shutter or an iris, will be installed on the lens side to protect the optics elements and the focal surface in the diurnal orbit phase and from the pollution produced during the scheduled periodic Shuttle docking on the ISS. At present, the optical sensors that meets closely the requirements of pixel size, gain, fast response time, low weight and small dimension, has been identified in a couple of commercial multi-anode photomultiplier manufactured by Hamamatsu, series R8900-03-M36. These devices, which exhibit a very low cross talk and good response gain uniformity, are equipped with a bi-alkali photocatode and an UV transmitting window that assure an average Quantum Efficiency of 20%, a collection efficiency at first

dynode of about 70%. With the help of a weak focusing electrostatic potential after the photocathode such MAPMT device exhibit an overall sensitive area close to 80% respect to physical area, which reach around 95% with the help of a proper designed lens optically connecttd to the MAPMT. The expected background due to nightglow light is around 0.5 detected photoelectrons (PE) in one EUSO integration gate $GTU = 2500\text{ns}$ per pixel while the signal is $\approx 10\text{PE}$ for $E = 10^{20}\text{eV}$ Such detector configuration exhibit an energy threshold close to $5 \cdot 10^{19}\text{eV}$.

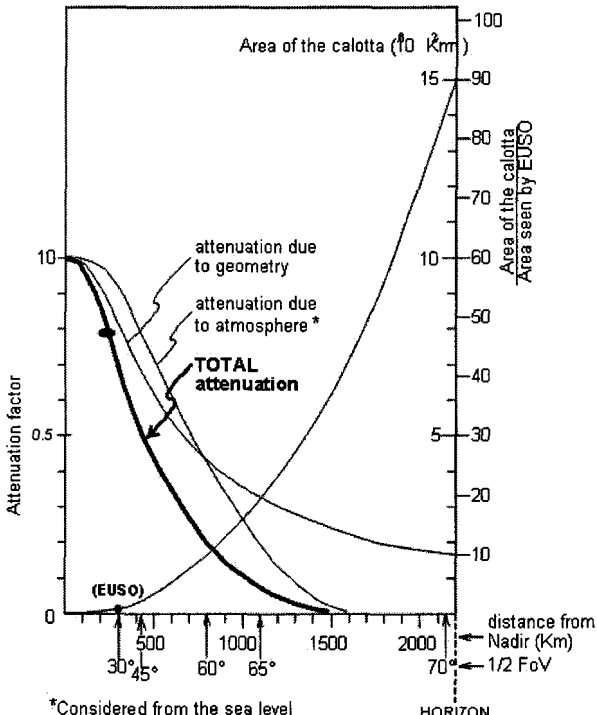


Figure 2: Attenuation factors normalized at Nadir (left scale). Area of the observable terrestrial surface from an altitude of 400 km as a function of the distance of the circumference of this surface from the Nadir direction (right scale).

3 Increasing the detector sensitivity

Let's now assume EUSO on ISS as a starting point and a "unity" of measurement for discussing the potentiality of a detection system on board of the ISS that could cover the whole Field of View (FOV) from the Nadir up to the hori-

zon observed from the ISS. Assuming the average altitude of the ISS at 400 km, the full coverage FOV is 140.8° , the area of the corresponding observed terrestrial surface $\approx 1.5 \cdot 10^7 \text{ km}^2$, and the mass of the corresponding volume of air $\approx 150 \cdot 10^{12} \text{ t}$, i.e. ≈ 90 times the air target observed by EUSO. For expanding EUSO in the direction of the realization of a neutrino observatory we can act in two directions: (a) going down in the energy threshold for the observation of the atmospheric showers, thus profiting of the expected increase of the rates in the lower energy region, where the flux is much higher; (b) and/or increasing the FOV for including in the observation as much as possible area of the terrestrial surface.

In order to decrease the energy threshold we can both increase the diameter of the optical system collecting the fluorescence light, and the efficiency of the sensors in converting this light in an electric signal. The calculation of the lowering of the energy threshold is performed here requiring that, at the threshold, the signal to noise ratio $\text{Signal}/\sqrt{\text{Signal} + \text{background}}$ in one pixel and one time gate $\Delta T = 2500\text{ns}$ is fixed by the value it has for EUSO at $E = 5 \cdot 10^{19} \text{ eV}$.

In Fig.2 is reported the area of the observable terrestrial surface from an altitude of 400 km as a function of the distance of the circumference of this surface from the Nadir direction (the scale is that at the right side, given both in 10^6 km^2 and in "EUSO units"). In order to obtain the corresponding annual counting rates it must be taken into account several effects:

1) - The attenuation of the light signal due to the distance 'd' between the emission point and the detector. Because the length of the portion of shower seen in an angular pixel of the detector increases as d , while the signal attenuates as d^{-2} , the signal diminishes as d^{-1} (see in Fig.2 the curve of the signal amplitude normalized to the amplitude at Nadir, the scale is that at left side).

2) - The absorption of the light by the atmosphere. At the Nadir the atmosphere transparency is ≈ 0.56 . By increasing the angle of view from the Nadir direction the thickness of the air to be crossed by the light increases. Due to the Earth curvature it increases much faster than for the observation of a flat surface. Furthermore, since it appears as power in an exponential function, the corresponding transparency of the atmosphere rapidly falls to zero. It is less than 2% already halfway between the Nadir and the horizon (the curve in Fig.2 is normalized to the Nadir transparency; the scale is at the left side). The total transparency normalized to the Nadir is given by the product of the two above effects, and is reported in Fig.2 on the same left side scale. We calculate that expanding the FOV from 60° to 90° results in a factor 3 for the number of detected events.

There are several other effects that should be taken into account and could further worsen the experimental situation at the increase of the distance from

the Nadir direction. The most relevant are the signal/noise ratio, worsening as d^{-1} , and the increase of the terrestrial surface observed in a single angular pixel (it reaches $4 \cdot 180 \text{ km}^2$ at the horizon) that could de-localize the position of the signal on the terrestrial surface and give difficulties for the corrections to be applied for the local atmospheric and light emission conditions. However, because these effects strongly depend by the detail of the detection system, they will not be considered in the following, living to the real project how to take care of them.

4 Neutrino detection

Downward electron, muon and tau neutrinos interact through deep inelastic scattering with the nucleons of the atmosphere, generating :

- a) an electromagnetic plus an hadronic detectable shower in case of ν_e charged current (CC) interaction
- b) an hadronic shower plus a muon in case of ν_μ charged current (CC) interaction
- c) an hadronic shower plus a tau (which in turns can give rise to an other shower at the point of its decay) in case of ν_τ charged current (CC) interaction
- d) an hadronic shower plus a neutrino for the neutral current (NC) interactions of all the flavours.

The easier events to detect will be ν_e charged currents, where all the neutrino energy goes in the shower injected at the point of interaction. Since muons and taus are difficult to detect all the other cases are properly detected only by their hadronic showers which carry only a fraction of the neutrino energy. Due to the high fluctuations expected in the energy sharing between hadrons and leptons this effect does not really lead to a clear energy threshold for NC and ν_μ, ν_τ CC, but rather in a smooth increase of detection efficiency starting from the threshold [9]. For EUSO the ratio between detected events of all flavour and ν_e interactions is around 2 for equal abundance of the 3 flavour (equal fluxes are expected in case of neutrino oscillation). Hence the total detected events for all flavour will be between 2 times and 3 times ν_e events for a general detector with a lower threshold. The selection between neutrino and nuclei showers will be performed using the ability of neutrinos to penetrate deeply in the atmosphere [9]. The detection efficiency above the energy threshold for ν_e charged current (CC) is taken here to be 30% [9] and the duty cycle 10% (including inefficiencies due to clouds [9]). For neutrino expected fluxes we have considered the GZK neutrinos calculated in ref [8] for several hypothesis on the primary protons spectrum and sources distribution. Here we report two extreme cases giving rise to high and low fluxes respectively (Fig. 3) This GZK neutrinos are a guaranteed component expected at the extreme energies. To avoid to become "model dependent", no other neutrino sources will be

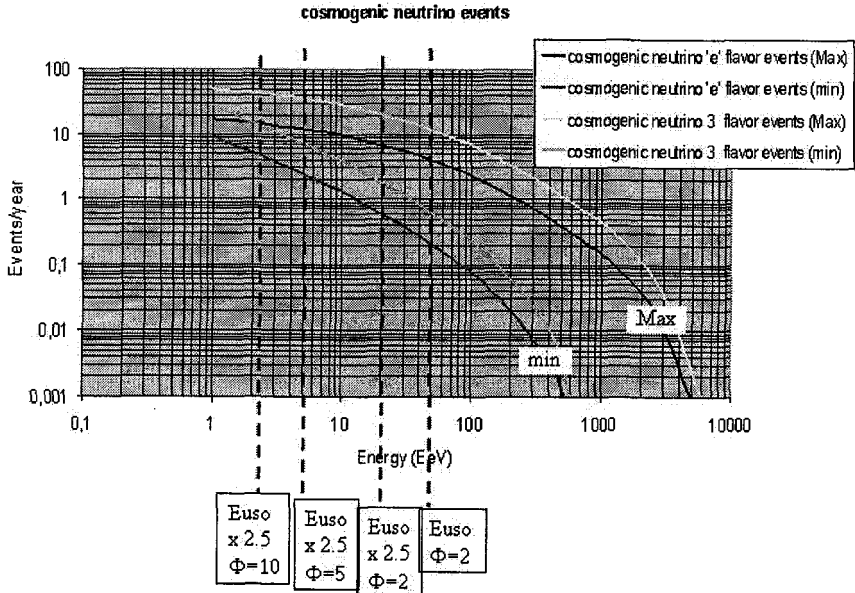


Figure 3: Detected neutrinos from GZK origin as a function of the energy threshold for a detector with $FOV = 60^\circ$ from 400km altitude. Vertical lines show EUSO threshold together with threshold resulting from larger sensor efficiency $Q_{eff} = 0.5 = 2.5Q_{eff}^{EUSO}$ and larger diameter of the entrance pupil of the optical system. The upper *min* and *Max* curves correspond to the 3 flavor events, the lower *min* and *Max* curves correspond to the 1 flavor events.

considered. In fact, also if potentially supplying much more abundant neutrino fluxes (such as the neutrino's foreseen in the "Top-Down" processes, or those connected in some models to the Gamma Ray Bursts (GRB's)), the previsions for their fluxes are much more uncertain. As pointed out in [10] the tau leptons, created by CC ν_τ interactions inside the Earth, because of their relative long decay length at high energy, could emerge from the Earth surface and eventually decay inside the atmosphere as fully horizontal events. Such kind of events could be detected with full efficiency by atmospheric shower detectors as upward going showers. In ref [10] is calculated the ratio between such neutrino events and downward ν_e charged current (CC) events as a function of threshold. For very high threshold ($E_{th} > 10^{19} eV$) such tau events are much less abundant than downward ν_e (CC), but for energy around $E_{th} \approx 10^{18} eV$

	<u>EUSO like</u>		<u>Multi-mirror</u>		
H (km)	400		400		
Total FoV ($^{\circ}$)	60		90		
Radius on ground (km)	235		413		
Area on ground (10^3 km^2)	173		536		
Pixel on ground (km * km)	0.8×0.8		1.6×1.6		
Φ pixel on detector (cm)	0.6		2.0		
" " with corrector			1.2		
Area/pixel (\approx n. of pixels)	270k		238k		
Pupil diameter (m)	2.0	2.0	5.0	7.5	10.0
Photo detection efficiency	20%	50%	50%	50%	50%
E threshold (EeV)	50	20	5.5	3.2	2.3
Proton events/year,					
GKZ + uniform source distrib.	1200	8000	300k	900k	1800k
with $E_p > 100 \text{ EeV}$	100	100	310	310	310
Neutrino events per year (\approx min)	0.6	1.5	18	30	42
Neutrino events per year (\approx Max)	12	18	108	120	138

Figure 4: Table resuming the performance of various detector configuration.

their rate is equal or even more abundant than that downward events and they will give rise to an additional neutrino signal of comparable statistical significance.

5 Conclusions

The expected rate for GZK neutrinos and several detector layout are given in Fig 4. The increase of sensor efficiency up to 0.5, of optical system diameter to $D \geq 5m - 7m$ and of detector field of view to $\text{FOV}=90^{\circ}$ results in a detector which provides a minimum of several tens of detected neutrinos for the almost guaranteed GZK ν fluxes, enough to act as a Neutrino Observatory.

The increase of the detector FOV is probably not possible with only one detector unit. A number of identical wide FOV systems could be assembled on board of the ISS looking at different but nearby Earth atmospheric portion. The following devices could have general structure (optics + mechanics) identical to the first one, greatly decreasing the needed work, the realization time and possibly the prices.

Also the possibility to release several detector units as free flyers should be taken into account.

References

- [1] D. J. Bird et al.: Phys. Rev. Lett. 71 (1993) 3401; N. Hayashida et al.: Phys. Rev. Lett. 73 (1994) 3491. M. Takeda et al. Phys. Rev. Lett. 81 (1998) 1163
- [2] B.A. Khrenov et al. "Space program KOSMOPETL" Metepec 2000, Observing ultrahigh energy cosmic rays from space and earth 57-75
- [3] R.E. Streitmatter for the OWL collaboration. "Orbiting Wide Angle Light-Collectors (OWL) : Observing Cosmic Rays from Space" College Park 1997, Observing giant cosmic ray air showers 95-107.
- [4] P.Spillantini, 'First International Symposium on Airwatch', Catania, Jan.30-Febr.2, 1997.
- [5] J.Linsley et al., "Space Air Watch: Observation of the Earth Atmosphere from ISSA Space Station", 25-th International Cosmic Ray Conference, Durban 1997, proc. OG.10.6.20
- [6] L. Scarsi et al., "Extreme Universe Space Observatory", proposal to ESA for the F2/F3 missions ; ESA and EUSO Team, "Extreme Universe Space Observatory - Report on the accommodation of EUSO on the Columbus Exposed Payload Facility" ESA/MSM-GU/2000.462/AP/RDA December 2000, O. Catalano et al. ICRC 2003 HE1.5 pg. 1081
- [7] G.K.Garikov et al., "Russian plans for ISS", AIP Conf. Proc., 433 (1998) 108-116; "Camera for detection of Cosmic Rays of energy more than 10 EeV on the ISS orbit", AIP Conf. Proc., 433 (1988) 403-417.
- [8] Oleg E. Kalashev et al. Phys.Rev.D66:063004,2002
- [9] S. Bottai, S. Giurgola , "Downward neutrino induced EAS with EUSO detector" ICRC 2003 pg 1113, HE1.5
- [10] S. Bottai, S. Giurgola, Astropart.Phys.18:539-549,2003

THEORY OF NEUTRINO OSCILLATIONS

Carlo Giunti^a

*INFN, Sezione di Torino, and Dipartimento di Fisica Teorica, Università di Torino,
Via P. Giuria 1, I-10125 Torino, Italy*

Abstract. We review critically the main assumptions on which the standard theory of neutrino oscillations is based. We show that all assumptions are realistic, except the so-called “equal momentum assumption”, which however is irrelevant. We briefly review the covariant plane-wave derivation of neutrino oscillations and a quantum field theoretical wave packet model of neutrino oscillations. We show that both approaches lead to the standard expression for the oscillation phase. The wave packet model allows also to describe the coherence of the oscillations and the localization of the production and detection processes.

1 Introduction

The possibility of neutrino oscillations was discovered by Bruno Pontecorvo in the late 50’s following an analogy with kaon oscillations [1, 2]. Since at that time only one *active* neutrino was known, Pontecorvo invented the concept of a *sterile* neutrino [3], which is a neutral fermion which does not take part to weak interactions. The muon neutrino was discovered in 1962 in the Brookhaven experiment of Lederman, Schwartz, Steinberger *et al.* [4], which followed a proposal made by Pontecorvo in 1959 [5]. Then, it became clear that oscillations between different active neutrino flavors are possible if neutrinos are massive and mixed particles. Indeed, in 1967 [3] Pontecorvo predicted the solar neutrino problem as a possible result of $\nu_e \rightarrow \nu_\mu$ (or $\nu_e \rightarrow \nu_{\text{sterile}}$) transitions before the first measurement of the solar electron neutrino flux in the Homestake experiment [6], and in 1969 Gribov and Pontecorvo discussed in detail the possibility of solar neutrino oscillations due to neutrino mixing [7].

However, in these and other papers written before 1976 the probability of neutrino oscillations was not calculated in a rigorous way, but simply estimated on the basis of the analogy with kaon oscillations. As a result, the phase of the oscillations was correct within a factor of two.

The standard theory of neutrino oscillations was developed in 1976 by Eliezer and Swift [8], Fritzsch and Minkowski [9], Bilenky and Pontecorvo [10] (see the beautiful review in Ref. [11]) on the basis of the following four assumptions that will be discussed critically in this report:

- (A1) Neutrinos are ultrarelativistic particles.
- (A2) Neutrinos produced or detected in CC weak interaction processes are described by the flavor states

$$|\nu_\alpha\rangle = \sum_k U_{\alpha k}^* |\nu_k\rangle , \quad (1)$$

^ae-mail: giunti@to.infn.it

where U is the unitary mixing matrix, $\alpha = e, \mu, \tau$, and $|\nu_k\rangle$ is the state of a neutrino with mass m_k .

- (A3) The propagation time is equal to the distance L traveled by the neutrino between production and detection.
- (A4) The massive neutrino states $|\nu_k\rangle$ in Eq. (1) have the same momentum, $p_k = p \simeq E$ (“equal momentum assumption”), and different energies, $E_k = \sqrt{p^2 + m_k^2} \simeq E + m_k^2/2E$, where E is the neutrino energy neglecting mass effects and the approximations are valid for ultrarelativistic neutrinos.

In Section 2 we briefly review the main points of the standard theory of neutrino oscillations. In Sections 3–6 we discuss critically the four assumptions listed above. In Section 7 we review the covariant derivation of the neutrino oscillation probability in the plane wave approach [12–15]. In Section 8 we review the quantum field theoretical wave packet model presented in Ref. [16]. Finally, in Section 9 we present our conclusions.

2 Standard theory of neutrino oscillations

In the plane wave approximation the states $|\nu_k\rangle$ of massive neutrinos are eigenstates of the free Hamiltonian with definite energy eigenvalues E_k . Therefore, their time evolution is given by the Schrödinger equation, whose solution is

$$|\nu_k(t)\rangle = e^{-iE_k t} |\nu_k\rangle. \quad (2)$$

Using assumption (A2), from Eq. (1) the time evolution of the flavor states is given by

$$|\nu_\alpha(t)\rangle = \sum_{\beta=e,\mu,\tau} \left(\sum_k U_{\alpha k}^* e^{-iE_k t} U_{\beta k} \right) |\nu_\beta\rangle, \quad (3)$$

which, for $t > 0$, is a superposition of different flavors if the mixing matrix is non-diagonal. The coefficient of the flavor state $|\nu_\beta\rangle$ is the amplitude of $\nu_\alpha \rightarrow \nu_\beta$ transitions, whose squared absolute value gives the probability

$$P_{\nu_\alpha \rightarrow \nu_\beta}(t) = |\langle \nu_\beta | \nu_\alpha(t) \rangle|^2 = \left| \sum_k U_{\alpha k}^* e^{-iE_k t} U_{\beta k} \right|^2. \quad (4)$$

Using the equal-momentum assumption (A4), the energy of the k^{th} massive neutrino component is given by $E_k = \sqrt{p^2 + m_k^2}$, which can be approximated to $E_k \simeq p + m_k^2/2p$ in the case of ultrarelativistic neutrinos following from assumption (A1). Moreover, assumption (A3) allows to replace the usually

unknown propagation time t with the usually known distance L traveled by the neutrino between production and detection. The final result for the oscillation probability can be written as

$$P_{\nu_\alpha \rightarrow \nu_\beta}(L) = \sum_k |U_{\alpha k}|^2 |U_{\beta k}|^2 + 2\text{Re} \sum_{k>j} U_{\alpha k}^* U_{\beta k} U_{\alpha j} U_{\beta j}^* \exp\left(-i \frac{\Delta m_{kj}^2 L}{2E}\right), \quad (5)$$

where $\Delta m_{kj}^2 = m_k^2 - m_j^2$ and $E = p$ is the neutrino energy neglecting mass contributions. In Eq. (5) we have separated the expression for the flavor transition probability into a constant term and a term which oscillates as a function of the distance L . The oscillating term is the most interesting one from a quantum mechanical point of view, because it is due to the interference between the different massive neutrino components, whose existence requires coherent production and detection. On the other hand, the constant term is experimentally very important, because it gives the average probability of flavor transitions, which is the measured one when the oscillating term is not present because of lack of coherence or when the oscillating term is not measurable because it is washed out by the average over the energy resolution of the detector or the distance uncertainty.

Let us now examine critically one by one the four assumptions (A1)–(A4) that lead to the result (5).

3 Assumption (A1): ultrarelativistic neutrinos

The assumption (A1) is correct, because neutrino masses are smaller than about one eV (see Refs. [17, 18]) and only neutrinos with energy larger than about 100 keV can be detected.

Indeed, neutrinos are detected in:

1. Charged-current or neutral-current weak processes which have an energy threshold larger than some fraction of MeV. This is due to the fact that in a scattering process $\nu + A \rightarrow \sum_X X$ with A at rest, the squared center-of-mass energy $s = 2E_\nu m_A + m_A^2$ (neglecting the neutrino mass) must be bigger than $(\sum_X m_X)^2$, leading to $E_\nu^{\text{th}} = \frac{(\sum_X m_X)^2}{2m_A} - \frac{m_A^2}{2}$. For example:
 - $E_\nu^{\text{th}} \simeq 0.233$ MeV for $\nu_e + {}^{71}\text{Ga} \rightarrow {}^{71}\text{Ge} + e^-$ in gallium solar neutrino experiments (see Ref. [18]).
 - $E_\nu^{\text{th}} \simeq 0.81$ MeV for $\nu_e + {}^{37}\text{Cl} \rightarrow {}^{37}\text{Ar} + e^-$ in the Homestake [6] solar neutrino experiment.
 - $E_\nu^{\text{th}} \simeq 1.8$ MeV for $\bar{\nu}_e + p \rightarrow n + e^+$ in reactor neutrino experiments (see Ref. [18]).

- $E_\nu^{\text{th}} \simeq 2.2 \text{ MeV}$ in the neutral-current process $\nu + d \rightarrow p + n + \nu$ used in the SNO experiment to detect active solar neutrinos [19].
2. The elastic scattering process $\nu + e^- \rightarrow \nu + e^-$, whose cross section is proportional to the neutrino energy ($\sigma(E_\nu) \sim \sigma_0 E_\nu / m_e$, with $\sigma_0 \sim 10^{-44} \text{ cm}^2$). An energy threshold of some MeV's is needed in order to have a signal above the background. For example, $E_\nu^{\text{th}} \simeq 5 \text{ MeV}$ in the Super-Kamiokande [20] solar neutrino experiment.

As we will see, the ultrarelativistic character of neutrinos implies the correctness of the assumptions (A2) and (A3) and the irrelevance of the assumption (A4), which is not realistic.

4 Assumption (A2): flavor states

In Ref. [21] it has been shown that the assumption (A2) is not exact, because the amplitude of production and detection of the massive neutrino ν_k is not simply given by $U_{\alpha k}^*$ (see also Refs. [14, 16]). However, in the ultrarelativistic approximation the characteristics of the production and detection processes that depend on the neutrino mass can be neglected, leading to a correct approximate description of flavor neutrinos through the states (1).

5 Assumption (A3): $t = L$

The assumption (A3) follows from the ultrarelativistic approximation, because ultrarelativistic particles propagate almost at the velocity of light. However, in the standard theory of neutrino oscillations massive neutrinos are treated as plane waves, which are limitless in space and time. In order to justify the assumption (A3) it is necessary to treat massive neutrinos as wave packets [22], which are localized on the production process at the production time and propagate between the production and detection processes at a velocity close to the velocity of light. Such a wave packet treatment [16, 22–24] yields the standard formula for the oscillation length. In addition, the different group velocities of different massive neutrinos imply the existence of a coherence length for the oscillations, beyond which the wave packets of different massive neutrinos do not jointly overlap with the detection process [25, 26].

The wave packet treatment of neutrino oscillations is also necessary for a correct description of the momentum and energy uncertainties necessary for the coherent production and detection of different massive neutrinos [24, 27, 28], whose interference generates the oscillations.

The physical reason why the substitution $t = L$ is correct can be understood by noting that, if the massive neutrinos are ultrarelativistic and contribute coherently to the detection process, their wave packets overlap with the detection

process for an interval of time $[t - \Delta t, t + \Delta t]$, with

$$t = \frac{L}{\bar{v}} \simeq L \left(1 + \frac{\overline{m^2}}{2E^2} \right), \quad \Delta t \sim \sigma_x, \quad (6)$$

where \bar{v} is the average group velocity, $\overline{m^2}$ is the average of the squared neutrino masses, σ_x is given by the spatial uncertainties of the production and detection processes summed in quadrature [23] (the spatial uncertainty of the production process determines the size of the massive neutrino wave packets). The correction $L\overline{m^2}/2E^2$ to $t = L$ in Eq. (6) can be neglected, because it gives corrections to the oscillation phases which are of higher order in the very small ratios m_k^2/E^2 . The corrections due to $\Delta t \sim \sigma_x$ are also negligible, because in all realistic experiments σ_x is much smaller than the oscillation length $L_{kj}^{\text{osc}} = 4\pi E/\Delta m_{kj}^2$, otherwise oscillations could not be observed [22, 24, 27, 28]. One can summarize these arguments by saying that the substitution $t = L$ is correct because the phase of the oscillations is practically constant over the interval of time in which the massive neutrino wave packets overlap with the detection process and it is given by

$$\phi_{kj}(L) = \frac{\Delta m_{kj}^2 L}{2E} = 2\pi \frac{L}{L_{kj}^{\text{osc}}}, \quad (7)$$

plus negligible corrections of higher order in the neutrino masses.

6 Assumption (A4): equal momentum

Let us discuss now the assumption (A4), which has been shown to be unrealistic in Refs. [24, 29] on the basis of simple relativistic arguments. Indeed, the relativistic transformation of energy and momentum implies that the equal momentum assumption cannot hold concurrently in different inertial systems. On the other hand, the probability of flavor neutrino oscillations is independent from the inertial system adopted for its measurement, because the neutrino flavor is measured by observing charged leptons whose character is Lorentz invariant (*e.g.* an electron is seen as an electron in any system of reference). Therefore, the probability of neutrino oscillations is Lorentz invariant [13, 30] and must be derived in a covariant way. In fact, the oscillation probability has been derived without special assumptions about the energies and momenta of the different massive neutrino components both in the plane wave approach [12–15] and in the wave packet treatment [22–24, 29].

7 Covariant derivation of neutrino oscillations

Let us briefly describe the covariant derivation of the neutrino oscillation probability in the plane wave approach, in which the massive neutrino states in

Eq. (1) evolve in space and time as plane waves:

$$|\nu_k(x, t)\rangle = e^{-iE_k t + ip_k x} |\nu_k\rangle. \quad (8)$$

Substituting Eq. (8) in Eq. (1) and expressing the $|\nu_k\rangle$ on the right-hand side in terms of flavor states ($|\nu_k\rangle = \sum_{\beta=e,\mu,\tau} U_{\beta k}^* |\nu_\beta\rangle$), we obtain

$$|\nu_\alpha(x, t)\rangle = \sum_{\beta=e,\mu,\tau} \left(\sum_k U_{\alpha k} e^{-iE_k t + ip_k x} U_{\beta k}^* \right) |\nu_\beta\rangle, \quad (9)$$

which shows that at a distance x and after a time t from the production of a neutrino with flavor α , the neutrino is a superposition of different flavors (if the mixing matrix is not diagonal). The probability of flavor transitions in space and time is given by

$$P_{\nu_\alpha \rightarrow \nu_\beta}(x, t) = |\langle \nu_\beta | \nu_\alpha(x, t) \rangle|^2 = \left| \sum_k U_{\alpha k} e^{-iE_k t + ip_k x} U_{\beta k}^* \right|^2, \quad (10)$$

which is manifestly Lorentz invariant.

Considering ultrarelativistic neutrinos, we apply now the assumption (A3), $t = x = L$, where L is the distance traveled by the neutrino between production and detection. The phase in Eq. (10) becomes

$$E_k t - p_k x = (E_k - p_k) L = \frac{E_k^2 - p_k^2}{E_k + p_k} L = \frac{m_k^2}{E_k + p_k} L \simeq \frac{m_k^2}{2E} L. \quad (11)$$

It is important to notice that Eq. (11) shows that the phases of massive neutrinos relevant for the oscillations are independent from any assumption on the energies and momenta of different massive neutrinos, as long as the relativistic dispersion relation $E_k^2 = p_k^2 + m_k^2$ is satisfied. This is why the standard derivation of the neutrino oscillation probability gives the correct result, in spite of the unrealistic equal momentum assumption (A4).

Using the phase in Eq. (11), the oscillation probability as a function of the distance L has the standard expression in Eq. (5). Let us notice that the expression (5) is still Lorentz invariant, as shown in Ref. [30], because L is not the instantaneous source-detector distance but the distance traveled by the neutrino between production and detection.

8 Wave packet model

Several wave packet models of neutrino oscillations have been devised, with similar results, in the framework of Quantum Mechanics [22–24, 26, 29, 31] and Quantum Field Theory [16, 32–35] (see Ref. [28] for a comprehensive review).

Here we briefly review the main points of the quantum field theoretical wave packet model presented in Ref. [16], which is based on the assumption in Quantum Field Theory that free particle are described by wave packets constructed as appropriate superpositions of states in the momentum Fock space of the corresponding free field.

The wave packet describing a neutrino created with flavor α in the process

$$P_I \rightarrow P_F + \ell_\alpha^+ + \nu_\alpha \quad (12)$$

is given by

$$|\nu_\alpha\rangle \propto \langle P_F, \ell_\alpha^+ | -i \int d^4x \mathcal{H}_I(x) |P_I\rangle, \quad (13)$$

where we have considered the first order perturbative contribution of the effective weak interaction hamiltonian $\mathcal{H}_I(x)$. The states $|P_I\rangle$, $|P_F\rangle$, $|\ell_\alpha^+\rangle$ that describe the particles taking part to the localized production process have the wave packet form

$$|\chi\rangle = \int d^3p \psi_\chi(\vec{p}; \vec{p}_\chi, \sigma_{p\chi}) |\chi(\vec{p}, h_\chi)\rangle \quad (\chi = P_I, P_F, \ell_\alpha^+), \quad (14)$$

where \vec{p}_χ is the average momentum, $\sigma_{p\chi}$ is the momentum uncertainty, determined by the interactions with the surrounding medium, and h_χ is the helicity. Approximating the momentum distributions $\psi_\chi(\vec{p}; \vec{p}_\chi, \sigma_{p\chi})$ with gaussian functions, the integrals in the expression (13) for the neutrino state can be calculated analitically, leading to

$$|\nu_\alpha\rangle = N_\alpha \sum_k U_{\alpha k}^* \int d^3p e^{-S_k^P(\vec{p})} \sum_h \mathcal{A}_k^P(\vec{p}, h) |\nu_k(\vec{p}, h)\rangle, \quad (15)$$

where N_α is a normalization factor, $\mathcal{A}_k^P(\vec{p}, h)$ is the amplitude of production of a neutrino with mass m_k , momentum \vec{p} and helicity h , and the function $e^{-S_k^P(\vec{p})}$ enforces energy-momentum conservation within the momentum uncertainty due to the momentum distributions of P_I , P_F , ℓ_α^+ . The spatial width σ_{xP} of the neutrino wave packet is related to its momentum uncertainty

$$\sigma_{xP}^2 = \sigma_{pP_I}^2 + \sigma_{pP_F}^2 + \sigma_{p\ell_\alpha^+}^2 \quad (16)$$

by the minimal Heisenberg uncertainty relation $\sigma_{xP}\sigma_{pP} = 1/2$.

Let us consider the detection of a neutrino with flavor β through the charged-current weak process

$$\nu_\beta + D_I \rightarrow D_F + \ell_\beta^-, \quad (17)$$

at a space-time distance (\vec{L}, T) from the production process, where the neutrino created with flavor α is described by a state obtained by acting on $|\nu_\alpha\rangle$ in

Eq. (15) with the space-time translation operator $\exp(-i\hat{E}T + i\vec{\hat{P}} \cdot \vec{L})$, where \hat{E} and $\vec{\hat{P}}$ are the energy and momentum operators, respectively:

$$|\nu_\alpha(\vec{L}, T)\rangle = N_\alpha \sum_k U_{\alpha k}^* \int d^3 p e^{-iE_{\nu_k}(\vec{p})T + i\vec{p} \cdot \vec{L}} e^{-S_k^P(\vec{p})} \sum_h A_k^P(\vec{p}, h) |\nu_k(\vec{p}, h)\rangle. \quad (18)$$

The detection amplitude is given by

$$\mathcal{A}_{\alpha\beta}(\vec{L}, T) = \langle D_F, \ell_\beta^- | -i \int d^4 x \mathcal{H}_I(x) | D_I, \nu_\alpha(\vec{L}, T)\rangle. \quad (19)$$

The transition probability as a function of the distance \vec{L} is given by the average over the unmeasured time T of $|\mathcal{A}_{\alpha\beta}(\vec{L}, T)|^2$. In the realistic case of ultrarelativistic neutrinos the final result for the flavor transition probability is

$$P_{\alpha\beta}(L) = \sum_k |U_{\alpha k}|^2 |U_{\beta k}|^2 + 2\text{Re} \sum_{k>j} U_{\alpha k}^* U_{\beta k} U_{\alpha j} U_{\beta j}^* \exp \left[-2\pi i \frac{L}{L_{kj}^{\text{osc}}} - \left(\frac{L}{L_{kj}^{\text{coh}}} \right)^2 - 2\pi^2 \kappa \left(\frac{\sigma_x}{L_{kj}^{\text{osc}}} \right)^2 \right], \quad (20)$$

where $L_{kj}^{\text{osc}} = 4\pi E / \Delta m_{kj}^2$ are the standard oscillation lengths and $L_{kj}^{\text{coh}} = 4\sqrt{2\omega} E^2 \sigma_x / |\Delta m_{kj}^2|$ are the coherence lengths. The quantities κ and ω , which are usually of order one, depend on the production and detection processes [16]. The total spatial coherence width σ_x is given by

$$\sigma_x^2 = \sigma_{xP}^2 + \sigma_{xD}^2. \quad (21)$$

The form of the flavor transition probability in Eq. (20) is consistent with the results obtained with other wave packet models in the framework of Quantum Mechanics [22–24, 26, 29, 31] and Quantum Field Theory [32–35]. One can see that the standard value of the oscillation phase is confirmed, in agreement with the discussion in the previous Sections. In addition, the wave packet treatment produced a coherence term and a localization term.

The coherence term $\exp[-(L/L_{kj}^{\text{coh}})^2]$ suppresses the oscillations due to Δm_{kj}^2 when $L \gtrsim L_{kj}^{\text{coh}}$, because the wave packets of the massive neutrino components ν_k and ν_j have separated so much that they cannot be absorbed coherently in the detection process.

The localization term $\exp[-2\pi^2 \kappa (\sigma_x / L_{kj}^{\text{osc}})^2]$ suppresses the oscillations due to Δm_{kj}^2 if $\sigma_x \gtrsim L_{kj}^{\text{osc}}$. This means that in order to measure the interference of the massive neutrino components ν_k and ν_j the production and detection processes must be localized in space-time regions much smaller than the oscillation

length L_{kj}^{osc} . In practice this requirement is easily satisfied by all neutrino oscillation experiments, because the space-time coherence regions of the production and detection processes are usually microscopic, whereas the oscillation length is usually macroscopic.

The localization term is important for the distinction of neutrino oscillation experiments from experiments on the measurement of neutrino masses. As first shown by Kayser in Ref. [27], neutrino oscillations are suppressed in experiments able to measure the value of a neutrino mass, because the measurement of a neutrino mass implies that only the corresponding massive neutrino is produced or detected.

Kayser's [27] argument goes as follows. Since a neutrino mass is measured from energy-momentum conservation in a process in which a neutrino is produced or detected, from the energy-momentum dispersion relation $E_k^2 = p_k^2 + m_k^2$ the uncertainty of the mass determination is

$$\delta m_k^2 = \sqrt{(2E_k\delta E_k)^2 + (2p_k\delta p_k)^2} \simeq 2\sqrt{2}E\sigma_p, \quad (22)$$

where the approximation holds for realistic ultrarelativistic neutrinos and $\sigma_p = 1/2\sigma_x$ is the momentum uncertainty. If $\delta m_k^2 < |\Delta m_{kj}^2|$, the mass of ν_k is measured with an accuracy better than the difference Δm_{kj}^2 . In this case the neutrino ν_j is not produced or detected and the interference of ν_k and ν_j is not observed. The localization term in the oscillation probability (20) automatically implements Kayser's mechanism, because $\sigma_x/L_{kj}^{\text{osc}}$ can be written as $\Delta m_{kj}^2/4\sqrt{2}E\sigma_p$. If $\delta m_k^2 < |\Delta m_{kj}^2|$, the localization term in Eq. (20) suppresses^b the interference of ν_k and ν_j .

9 Conclusions

In conclusion, we have shown that the probability of neutrino oscillations can be derived in a covariant way in the plane wave approach starting from realistic assumptions. We have also presented a derivation of neutrino oscillations in a quantum field theoretical wave packet approach. In both cases we obtained the standard expression for the oscillation phase. The wave packet approach allows also to describe the coherence of the oscillations and the localization of the production and detection processes.

- [1] B. Pontecorvo, Sov. Phys. JETP **6**, 429 (1957).
- [2] B. Pontecorvo, Sov. Phys. JETP **7**, 172 (1958).
- [3] B. Pontecorvo, Sov. Phys. JETP **26**, 984 (1968).
- [4] G. Danby *et al.*, Phys. Rev. Lett. **9**, 36 (1962).

^bUsing the arguments presented by M. Beuthe in Ref. [35], it is possible to show that κ is always of order one.

- [5] B. Pontecorvo, Sov. Phys. JETP **37**, 1236 (1960).
- [6] Homestake, B. T. Cleveland *et al.*, Astrophys. J. **496**, 505 (1998).
- [7] V. N. Gribov and B. Pontecorvo, Phys. Lett. **B28**, 493 (1969).
- [8] S. Eliezer and A. R. Swift, Nucl. Phys. **B105**, 45 (1976).
- [9] H. Fritzsch and P. Minkowski, Phys. Lett. **B62**, 72 (1976).
- [10] S. M. Bilenky and B. Pontecorvo, Nuovo Cim. Lett. **17**, 569 (1976).
- [11] S. M. Bilenky and B. Pontecorvo, Phys. Rept. **41**, 225 (1978).
- [12] R. G. Winter, Lett. Nuovo Cim. **30**, 101 (1981).
- [13] C. Giunti and C. W. Kim, Found. Phys. Lett. **14**, 213 (2001), hep-ph/0011074.
- [14] S. M. Bilenky and C. Giunti, Int. J. Mod. Phys. **A16**, 3931 (2001), hep-ph/0102320.
- [15] C. Giunti, (2003), hep-ph/0311241, IFAE 2003, Lecce, 23–26 April 2003.
- [16] C. Giunti, JHEP **11**, 017 (2002), hep-ph/0205014.
- [17] S. M. Bilenky, C. Giunti, J. A. Grifols, and E. Masso, Phys. Rept. **379**, 69 (2003), hep-ph/0211462.
- [18] C. Giunti and M. Laveder, (2003), hep-ph/0310238.
- [19] SNO, Q. R. Ahmad *et al.*, Phys. Rev. Lett. **89**, 011301 (2002), nucl-ex/0204008.
- [20] SuperKamiokande, S. Fukuda *et al.*, Phys. Rev. Lett. **86**, 5651 (2001), hep-ex/0103032.
- [21] C. Giunti, C. W. Kim, and U. W. Lee, Phys. Rev. **D45**, 2414 (1992).
- [22] C. Giunti, C. W. Kim, and U. W. Lee, Phys. Rev. **D44**, 3635 (1991).
- [23] C. Giunti and C. W. Kim, Phys. Rev. **D58**, 017301 (1998), hep-ph/9711363.
- [24] C. Giunti, Found. Phys. Lett. **17**, 103 (2004), hep-ph/0302026.
- [25] S. Nussinov, Phys. Lett. **B63**, 201 (1976).
- [26] K. Kiers, S. Nussinov, and N. Weiss, Phys. Rev. **D53**, 537 (1996), hep-ph/9506271.
- [27] B. Kayser, Phys. Rev. **D24**, 110 (1981).
- [28] M. Beuthe, Phys. Rept. **375**, 105 (2003), hep-ph/0109119.
- [29] C. Giunti, Mod. Phys. Lett. **A16**, 2363 (2001), hep-ph/0104148.
- [30] C. Giunti, (2003), physics/0305122.
- [31] K. Kiers and N. Weiss, Phys. Rev. **D57**, 3091 (1998), hep-ph/9710289.
- [32] C. Giunti, C. W. Kim, J. A. Lee, and U. W. Lee, Phys. Rev. **D48**, 4310 (1993), hep-ph/9305276.
- [33] C. Giunti, C. W. Kim, and U. W. Lee, Phys. Lett. **B421**, 237 (1998), hep-ph/9709494.
- [34] C. Y. Cardall, Phys. Rev. **D61**, 073006 (2000), hep-ph/9909332.
- [35] M. Beuthe, Phys. Rev. **D66**, 013003 (2002), hep-ph/0202068.

QUIET OR ACTIVE SUN AND THE NEUTRINO PROPERTIES

S. TURCK-CHIEZE ^a

Service d'Astrophysique DAPNIA/CEA, CE Saclay, 91190 Gif sur Yvette, France

Abstract. The Sun and the Supernovae are very interesting MeV neutrino sources and remarkable examples of symbiosis between astrophysics and particle physics researches. Thanks to helioseismology, we have now reached a clear characterization of the solar central plasma and consequently, we put strong constraints on the solar core temperature. We deduce a prediction of the most energetic neutrino fluxes with a high degree of confidence. Neutrino detections have also solved challenging questions, as the detection of the different flavors of neutrinos. The present impressive agreement between prediction of the seismic solar model and SNO detection leads to an unambiguous evidence for a solution of the neutrino puzzle and a clear demonstration of the presence of solar neutrino oscillations. It is now worth to notice that the main role of seismology is to build a dynamical view of the stellar interiors. The description of the magneto-hydrodynamical processes is nowadays the present objective for a renewal of the stellar discipline. This year, important results on the Sun constitute a real breakthrough towards a dynamical vision of the Sun from which we may hope to extract complementary solar neutrino properties. I comment here on the real interest to look for other neutrino properties with the solar source of neutrinos and give preliminary results.

1 Introduction

The Sun is the second source of neutrinos of the universe after the cosmological one. It is a unique case for which we have today 30 years of observations corresponding to two different approaches neutrinos and acoustic modes. To check the Sun we have 3 helioseismic ground networks and 3 spatial experiments aboard SoHO running since 7 years. The Sun emits neutrinos through the weak interaction, the different sources are recalled in table 1. The difference of energy of these different sources, has contributed to complicate the interpretation of the results as the gallium (threshold: 0.24 MeV) and the chlorine (threshold: 0.8 MeV no detection of pp neutrinos) experiments detect simultaneously neutrinos from different sources. Only Superkamiokande and SNO detect one source of neutrinos, those emitted by the marginal ppIII chain, largely dependent on the solar internal plasma.

2 Standard solar model and neutrino emitted fluxes

Theoretical emitted fluxes for the different sources of neutrinos, described in table 1, are extracted from solar models which describe the temporal and radial evolution of the Sun in the classical framework of stellar evolution. These models do not introduce any condition on the kinematics of the reactions, the energy dependence of the neutrino fluxes is deduced from the knowledge of the nuclear processes. We use in the solar models a mean energy for each source. By

^ae-mail: cturck@cea.fr

Table 1: Nuclear processes leading to neutrino emission.

ppI chain: $p + p \rightarrow D + e^+ + \nu_e$ (pp neutrinos) $p + p + e^- \rightarrow D + \nu_e$ (pep neutrinos)
ppII chain: ${}^7Be + e^- \rightarrow {}^7Li + \nu_e$ (7Be neutrinos)
ppIII chain: ${}^7Be + p \rightarrow {}^8B$ ${}^8B \rightarrow {}^8Be^* + e^+ + \nu_e$ ${}^8Be^* \rightarrow {}^{24}He$ (8B neutrinos) $p + {}^3He \rightarrow \nu_e + e^+ + {}^4He$ (hep neutrinos)
CNO I cycle: ${}^{13}N \rightarrow {}^{13}C + e^+ + \nu_e$ (${}^{13}N$ neutrinos) ${}^{15}O \rightarrow {}^{15}N + e^+ + \nu_e$ (${}^{15}O$ neutrinos)
CNO II cycle: ${}^{17}F \rightarrow {}^{17}O + e^+ + \nu_e$ (${}^{17}F$ neutrinos)

solving the four structure equations (see [1] for details) of stellar evolution, one performs an *ab initio* complete calculation which requires a good description of the nuclear and atomic processes. From the structural equations, we extract temperature, density, pressure and composition for the different shells of the present Sun and consequently the neutrino emitted fluxes. One may notice that the energy sum rule which allows to extract without detailed calculations the pp neutrino flux from the present observed luminosity is explicitly contained in the third equation of stellar evolution. So, independently of the change of flavor, about $6.5 \cdot 10^{10} \nu_e$ reach the earth /cm²/s coming from the fundamental pp interaction which produces $1.68 \cdot 10^{38} \nu_e$ /s. This main source of neutrinos coming from the Sun has unfortunately a small neutrino energy and this flux has never been measured totally and alone. The other sources are smaller: typically $1.3 \cdot 10^{37}$ /s for 7Be neutrinos $1.3 \cdot 10^{34}$ /s for 8B , $1.3 \cdot 10^{36}$ /s for ${}^{13}N$, $1.1 \cdot 10^{36}$ /s for ${}^{15}O$, the ${}^{17}F$ one is extremely small. These secondary sources are directly proportional to the density in the range of emission and are largely temperature dependent, typically $T^8 - T^{10}$ for 7Be neutrinos and $T^{18} - T^{24}$ for 8B neutrinos and other sources, so they significantly depend on the solar structure and the characteristics of the plasma.

The above representation of the Sun is the most economical way to describe a star and supposes that there is no important effect of rotation and magnetic field. In this framework, we introduce in the model 3 observed quantities: the luminosity of the Sun at an age of 4.55 Gyr from the beginning of the hydrogen burning, the solar radius and the detailed element composition for nuclei greater than helium coming from the photosphere determination and compared to meteoritic ones. We use also the helioseismic observed helium [2] to determine the present relative composition. The only adjusted variable is the initial helium content in order to reproduce these superficial observations at the present time.

Table 2: Location in the Sun where the knowledge of some specific elements can check, through the mentioned quantities, some particular processes. From [5]

radius	element	quantities	physical processes	problem solved
0.98	4He	Γ_1	microscopic diffusion	[2]
0.71	^{16}O	κ	transition R/C	[3]
0.70	7Li	c^2 , rotation	nuclear process, turbulence magnetic processes	[4] no
0.57	9Be	c^2	nuclear process, turbulence	[4]
0.25	3He	c^2 , density	mixing?	[5]
0.05	7Be	c^2 , density	mixing?	[5]
< .1	^{56}Fe	κ	central temperature?	[6]

The helioseismic probe is used, since 1988, in our publications to check if :

- these hypotheses are correct,
- they can help to improve the quality of the physics included
- extra processes must be introduced.

Table 2 summarizes the different processes and locations where helioseismology can check the quality of the models. This is the reason why the solar model and the physical processes included in the equations through the composition, the nuclear reaction rates, the equation of state and the opacity coefficients, have received a lot of attention these last 15 years. Helioseismic results are now used also to predict correct neutrino fluxes, through seismic models [6, 7].

3 Checking the solar interior through acoustic waves

Acoustic waves are generated by the surface granulation and may propagate inside the whole Sun. The travel depends on their initial velocity. They generate very slight motions in the atmosphere of the Sun which are visible and detectable. As these perturbations are small and as the Sun is reasonably spherical, we can formally treat this information through a perturbed theory. The Sun, as a self-gravitating sphere of compressible gas, oscillates around its equilibrium state with a period of about 5-min. These oscillations are interpreted as a superposition of waves propagating inside the star (acting as a resonant cavity), and forming standing waves: the eigenmodes of vibration. A general description of the corresponding equations may be found in [1] or in [8]. Up to now, we exploit two variables extracted from the spatial instruments GOLF (Global oscillations at low frequency [9]) and MDI (Michelson Doppler Imager [10]) located aboard SoHO, namely the sound speed profile and the internal rotation profile. The first one can be compared to the one extracted from up-to-dated solar models. It allows to improve these models

if the agreement is not satisfactory as a lot of phenomena have very specific signatures (table2). The rotation profile is today the only way to quantify the macroscopic phenomena. We must have also a description of the internal magnetic field but today, we put mainly limits due to the difficulty to extract such quantity with acoustic modes.

Using the sound speed profile to constrain the high energy neutrino fluxes is extremely demanding. Effectively the acoustic modes are mainly sensitive to the surface effects and the variation of the sound speed is small in time and space. To get a constraint on the central temperature of a fraction of %, we need to get the central sound speed at a fraction of .1%, which allows constraints on physical quantities at a level of several % [5]. This has been achieved with SoHO. In parallel to the progress on neutrino detections, major efforts have been carried out to improve the quality and the accuracy of the seismic indicators. The difficulty to get reliable values for investigating the physics of the solar core is due by three phenomena:

- the stochastic excitation
- the influence of the solar cycle
- the asymmetry of the mode distribution due to the interaction of the mode with the solar background.

A comparison of the 3 different instruments aboard SoHO has contributed to identify the biases in the data determination [11], [12]. We have then analyzed the consequences on the extracted physics [7, 13, 14]. SoHO has effectively allowed to detect modes of low frequency which have a long lifetime and cavities in which the indirect deterioration coming from the stochastic excitation and the effect of the solar cycle is reduced. Consequently the quality of the information extracted from the central solar region has been improved by an order of magnitude and reached the level required for establishing quantitatively the neutrino fluxes for all the sources (see figure 1 of [7]).

Nowadays, we have reached a stage where we can describe the mean behavior of the solar core, but we have not yet reached the dynamical aspect of it, which necessitates the detection of gravity modes.

4 The Sun, a laboratory for plasma physics

Since 1988, our group has controlled the emitted solar neutrino fluxes, in confronting the solar theoretical structure to the seismic one. Constant progress has been noticed on the determination of our fluxes Table 3 shows the evolution with time of our ${}^8\text{B}$ neutrino flux prediction. In 2001, we have reached the needed accuracy to finish to investigate all the different points mentioned in table 2. During the same period of time, the prediction of Bahcall and collaborators has varied from 5.8 to $6.6 \text{ } 10^6 \text{ cm}^{-2}\text{s}^{-1}$, then, using the same helioseismic constraints, they have converged to comparable numbers. This last year, the

Table 3: Evolution with time of the 8B neutrino flux in $10^6 \text{ cm}^{-2} \text{s}^{-1}$, of the central temperature in 10^6 K , initial helium in mass fraction, and problem solved

8B flux	Tc	Y initial	problem solved	reference
3.8 ± 1.1	15.6	0.276	CNO opacity, ${}^7Be(p, \gamma)$	[15]
4.4 ± 1.1	15.43	0.271	CNO Fe abundances, screening	[16, 17]
4.82	15.67	0.273	microscopic diffusion	[18]
4.82	15.71	0.272	turbulence tachocline	[4]
4.72	15.67		central mixing ?, pp	[5]
4.98 ± 0.73	15.74	0.276	seismic model	[6]
5.07 ± 0.76	15.75	0.277	seismic model, magnetic field	[7]
4.05	15.55	0.265	reduced abundance CNO	[19]
SNO results: 5.44 ± 0.99 [20] $5.09 \pm 0.44(\text{stat}) \pm 0.45(\text{syst})$ [21]				
$5.27 \pm 0.27(\text{stat}) \pm 0.38(\text{syst.})$ [22]				

carbon, nitrogen and oxygen have been reestimated [23, 24] and reduced of about 30% which has an impact on the neutrino flux (see table 3).

I shall recall here the main highlights of our work: 1) use of a proper determination of the interaction between photons and all the elements; 2) use of the best abundance determination for the heavy elements; 3) a proper description of the microscopic diffusion and of mixing in the radiation-convection transition partly inhibiting the microscopic diffusion; 4) a proper description of the plasma for the determination of the nuclear interaction including screening; 5) the discussion of the existence or not of a potential mixing in the very central core; 6) the proper description of the pp reaction rate and introduction of the relativistic effect in the equation of state.

Including progress on theoretical, instrumental and observational sides, we have finally produced seismic theoretical models which present a similar sound speed profile than the observed one in the radiative zone [6, 7]. Figure 1a shows one of them. From this model we are confident to quantify the neutrino fluxes with the best information on the solar interior even the density profile is not totally satisfactory. This model is certainly not a physical model of the Sun. Figure 1b shows strong deviation and demonstrates that these models cannot properly define the central temperature.

A flux of 4.95 ± 0.72 (5.25) $10^6 \text{ cm}^2/\text{s}$ for the 8B neutrinos (with magnetic effect) has been determined [6, 7] with an error bar of only 14%, including physics beyond standard hypotheses. The perfect agreement of this prediction with the SNO detections is determinant to solve the neutrino puzzle and to demonstrate that astrophysical representation of stars becomes to be quantitative.

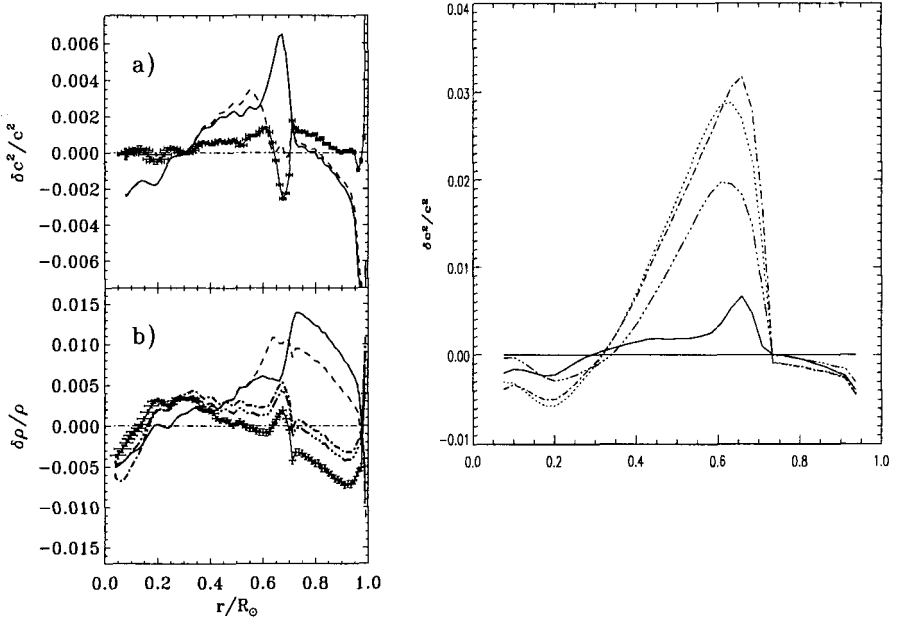


Figure 1: a) Relative differences between (a) the square of the sound speed and (b) the density deduced for the Sun using the GOLF/MDI frequencies [12, 14] and those of different Saclay models. We compare a standard solar model [18] (continuous curve), the same with turbulent diffusion [4] (dashed curve), and seismic model [5] (points with error bars joined by straight lines). Superimposed on the density profile, two other models, one with the $(^3\text{He}, ^4\text{He})$ reaction rate reduced by 10% (dot-dot dashed curve), the other with the CNO cycle reaction rates reduced by 70% (dot-dash-dotted curve). b) New standard solar models (non continuous lines) including the new estimate of the CNO abundances, from [19].

The story of solar neutrinos may stop here but it will be dangerous to do so, and the astrophysical perspectives (see below) encourage to continue solar neutrino observations at low energy. Thanks to helioseismology, we hope to improve our representation of the Sun. The radial electron and neutron density profiles of our seismic model is on our web site <http://www-dapnia.cea.fr/Phys/Sap/Documents/soleil/solarmodel.html> and may be used for any work on neutrino oscillations.

5 The Sun is not standard

Helioseismology has also revealed that the Sun is not standard. Effectively, the main objectives of this probe is to go beyond the simple representation which neglects the effects of the macroscopic motions. The history of the angular momentum evolution is crucial to understand the dynamo process and the range of internal magnetic field which is an essential property of the solar plasma and also which leads to the activity of the Sun.

Due to the solar rotation and magnetic field, the frequencies of two modes of the same degree ℓ and order n are splitted in m components varying between $\pm\ell$. The corresponding splitting contains information on the internal rotation. Differential rotation is now well established in the convective zone. The region of the transition between radiation and convection, is called the tachocline due to the rapid evolution of this differential rotation towards a rigid rotation. Turbulent mixing appears in this region due to horizontal motions as a consequence of the meridional circulation in the convective zone. The rotation profile is now extracted down to the limit of the nuclear core, typically 0.2 R_\odot , without ambiguity thanks to the longevity, the stability and the position of the SoHO satellite [25]. The radiative zone rotates as a solid body with a constant rate. Such a profile is only understandable with the introduction of a magnetic field in the radiative zone which is probably the main responsible of this profile. It is why we have introduced rather crudely a magnetic field of $3 \cdot 10^7$ G near 0.2 solar radius in our last neutrino prediction to estimate the sensitivity of the neutrino prediction to this term. The effect is small and its introduction even improves the agreement with the solar neutrino detection. Our next step will consist to perform a complete MHD calculation but a quantitative calculation is difficult as the order of magnitude of the magnetic field is not sufficiently known and the numerical exercise must be validated. MHD calculations have been already developed in the convective zone to reproduce the differential rotation profile [26].

The best way to extract dynamical motions in the radiative zone will come from the gravity waves. Several attempts to detect them have been unsuccessful due to the weakness of their amplitudes at the surface. We have performed a complete analysis of the GOLF data for a long observation of 2-3 and then 5 years to look for multiplet gravity modes with a velocity of no more than 2 mm/s at the surface of the Sun. We have proposed gravity mode candidates for which multiplets appear with more than 90% confidence level when the Sun is quiet [27]. The evolution with time of the observed patterns could be compatible with a small core rotating with a different axis than the rest of the radiative zone and a higher rotation rate (see figure 2). This work will be continue during the whole SoHO mission and we hope, before the end of the observations, scheduled for 2007, to confirm or not such detection.

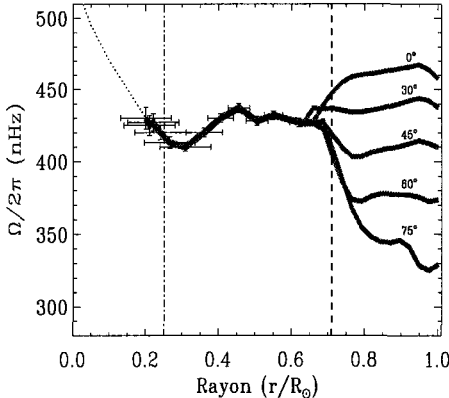


Figure 2: Rotation profile in the solar interior obtained from GOLF and MDI.

6 An opportunity to discover other neutrino properties ?

We know already that looking for new neutrino properties will be difficult but not excluded as the Sun is a richer source than generally considered. As the neutrino fluxes are rather well established, it is interesting to look for effects during the travelling of neutrinos in the Sun, as for example some RSF phenomena due to magnetic interaction. Of course, it seems that we can explain most of the observations through MSW effect but Kamland [28] gives only a probability of disappearance for neutrinos greater than 3.4 MeV, compatible with SNO results, the smaller value at low energy is not yet confirmed and Borexino is strongly waited for this reason. As mentioned by [29], small inconsistencies may be interesting to look at. Low time variability of the counting rates is not so easy to detect. One way to progress is to try to correlate neutrino detections to some solar indicator.

In [7], we have given some limits on the magnetic field in different regions of the Sun. Based on these values, we can look for a limit on the magnetic neutrino moment down to $\mu_\nu = 3 \cdot 10^{-12} \mu_B$ in the transition region between radiation and convection. We also give some probabilities on the RSFP transition for estimated magnetic field. Other recent analyzes have been also performed by [30, 31] with an other spirit.

Our present objectives are to look for some properties of the solar plasma which may play a role on the neutrino propagation or transformation. Previous works mention possible correlation between variabilities of the Sun and the neutrino counting rate [32] and references therein. An other approach is to try to put some constraints on the magnetic field from the properties of neutrino

oscillations [33]. Presently, we have analyzed the Superkamiokande 10 days data and note significant peaks around half the rotation of the Sun as was mentioned by [32], and some others with a period around the rotation, but the spectrum is not unambiguous. We have also studied the correlation between the neutrino dataset (SK and SAGE) and magnetic indicators. We may note some anticorrelation (at a small rate) with a delay of several hundred days, which may translate some internal interaction. Migration from the tachocline may take this time. A more convincing anti correlation is noticed with SAGE data, as was previously mentioned [34]. This may be explained by the effect of a real disappearance (contrary to the case of SK), is it the signature of another source of reduction due to magnetic variation during the solar cycle ?. We consider that all the effects are not sufficiently significant to be convincing, it could be partly due to the duration of individual data set. It is why I have recommended in last May, at the LowNu03 conference, to deliver datasets of 5 days for Superkamiokande and SNO and to try to extract data from GALLEX and SAGE, at the same time and with recurrence of less than 25 days (it is unfortunately difficult just now). We know that the magnetic activity evolves strongly at the scale of days.

We will continue this study this year and hope that Gallium experiments will continue with increased statistics to help to look for interesting properties of neutrinos.

Acknowledgments

This work has been strongly supported by ESA and CNES. I would like to thank particularly strongly my main collaborators A.S. Brun, S. Couvidat, H. Dzitko, R. A. Garcia, I. Lopes and P. Nghiem who have actively participated to these different works.

References

- [1] Turck-Chièze, S., Däppen, W., Fossat, E., Provost, J., Schatzman, E. & Vignaud, D., *Physics Rep.* **230**, (2-4) 57-235 (1993)
- [2] Vorontsov, S. V., *Astron. Zh.* **68**, 808 (1991) (English translation: *Sov. Astron.* **35** 400).
- [3] Christensen-Dalsgaard, J., Gough, D.O., Thompson, M. J., *ApJ* **378**, 413 (1991)
- [4] Brun, S., Turck-Chièze, S., Zahn, J.P., *ApJ* **525**, 1032 (1999)
- [5] Turck-Chièze, S., Nghiem, P. , Couvidat, S., & Turcotte, S., *Sol. Phys* **200**, 323 (2001)
- [6] Turck-Chièze, S., et al., *ApJ* **555**, L69 (2001)
- [7] Couvidat, S., Turck-Chièze, S., Kosovichev, A., *ApJ* **599**, 1434 (2003)

- [8] Turck-Chièze, S., *International workshop on Astroparticle and high energy physics*, JHEP, Valencia (2004)
- [9] Gabriel, A. H., Grec, G., Robillot, J.M., Roca-Cortes, T., Turck-Chièze, S. et al., *Sol. Phys.* **162**, 61 (1995)
- [10] Scherrer, P. H., et al., *Sol. Phys.* **162**, 129 (1995)
- [11] Toutain, T. et al., *Sol. Phys.* **175**, 31 (1997)
- [12] García, R. A., et al., *Sol. Phys.* **200**, 361 (2001)
- [13] Basu, S., Turck-Chièze, S., Berthomieu, G. et al., *ApJ* **535**, 1078 (2000)
- [14] Bertello, L., et al. *ApJ.* **537** L143 (2000)
- [15] Turck-Chièze, S., Cahen, S., Cassé, M. & Doom, C., *ApJ.* **335**, 415 (1988)
- [16] Turck-Chièze, S. & Lopes, I., *ApJ.* **408**, 347(1993)
- [17] Dzitko, H., Turck-Chièze, S., Delbourgo-Salvador, P., & Lagrange, G., *ApJ.* **447**, 428(1995)
- [18] Brun, S., Turck-Chièze, S., Morel, P., *ApJ.* **506**, 913(1998)
- [19] Turck-Chièze, S., et al., *Phys. Rev. Lett.* submitted
- [20] Ahmad, Q.R., et al., *Phys. Rev. Lett.* **87**, 11301 (2001)
- [21] Ahmad, Q. R. et al., in *Phys. Rev. Lett.* **89** 071301 (2002)
- [22] Ahmed, S. N. and the SNO collaboration, (2003) nucl-ex/0309004.
- [23] Lodders, K., *ApJ.* **591**, 1220, (2003)
- [24] Turck-Chièze, S. in *Solar composition and its evolution, from core to corona* ed. S. Steiger, *Space Science Review* 125, (1998)
- [25] Couvidat, S., García, R. A., Turck-Chièze, S., et al. *ApJ* **597**, L77(2003)
- [26] Brun, A. S. & Toomre, J., *ApJ* **570**, 865(2002)
- [27] Turck-Chièze, S., García, R. A., Couvidat, S. et al., *ApJ* **604** (2004)
- [28] Eguchi, K., et al., *Phys. Rev. Lett.* **90**, 021802 (2003)
- [29] de Holanda, P. C. & Smirnov, A., hep-ph/0307266 and 0309299
- [30] Pulido, J., in *Astrop. Phys.* **18**, 173 (2002)
- [31] Chauhan, B. C., Pulido, J., *Phys. Rev. D* **68**, 3015(2003)
- [32] Sturrock, P. A., *ApJ.* **594**, 1102 (2003)
- [33] Burgess, C., et al., *ApJ.* **588**, L65 (2003)
- [34] Gavryuseva, E. & Gavryusev, V., *Proceedings of the second solar cycle & Space weather Euroconferences* ESA SP-477, 221 (2003)

GENERALIZED DIRAC-PAULI EQUATION AND SPIN LIGHT OF NEUTRINO IN MAGNETIZED MATTER

Alexander Grigoriev ^a, Alexander Studenikin ^b, Alexei Ternov ^c

Physics Faculty of Moscow State University, 119992 Moscow, Russia

Abstract. We consider propagation of a massive neutrino in matter within the quantum approach based on the two equations for the neutrino field: the first one is the Dirac-Pauli equation for a massive neutrino in an external magnetic field generalized on the inclusion of effects of the background matter; the second one is the modified Dirac equation derived directly from the neutrino-matter interaction Lagrangian. On the basis of these two equations the quantum theory of a neutrino moving in the background matter is developed (the exact solutions of these equations are found and classified over the neutrino spin states, the corresponding energy spectra are also derived). Using these solutions we study within the quantum approach the spin light of neutrino ($SL\nu$) in matter with the effect of a longitudinal magnetic field being also incorporated. In particular, the $SL\nu$ radiation rate and total power are derived. The use of the generalized Dirac-Pauli equation also enables us to consider the $SL\nu$ in matter polarized under the influence of strong magnetic field.

1 Introduction

Recently in a series of our papers [1–3] we have developed the quasi-classical approach to the massive neutrino spin evolution in the presence of external electromagnetic fields and background matter. In particular, we have shown that the well known Bargmann-Michel-Telegdi (BMT) equation [4] of the electrodynamics can be generalized for the case of a neutrino moving in the background matter and being under the influence of external electromagnetic fields. The proposed new equation for a neutrino, which simultaneously accounts for the electromagnetic interaction with external fields and also for the weak interaction with particles of the background matter, was obtained from the BMT equation by the following substitution of the electromagnetic field tensor $F_{\mu\nu} = (\mathbf{E}, \mathbf{B})$:

$$F_{\mu\nu} \rightarrow E_{\mu\nu} = F_{\mu\nu} + G_{\mu\nu}, \quad (1)$$

where the tensor $G_{\mu\nu} = (-\mathbf{P}, \mathbf{M})$ accounts for the neutrino interactions with particles of the environment. The substitution (1) implies that in the presence of matter the magnetic \mathbf{B} and electric \mathbf{E} fields are shifted by the vectors \mathbf{M} and \mathbf{P} , respectively:

$$\mathbf{B} \rightarrow \mathbf{B} + \mathbf{M}, \quad \mathbf{E} \rightarrow \mathbf{E} - \mathbf{P}. \quad (2)$$

We have also shown how to construct the tensor $G_{\mu\nu}$ with the use of the neutrino speed, matter speed, and matter polarization four-vectors.

Within the developed quasi-classical approach to the neutrino spin evolution we have also considered [5–7] a new type of electromagnetic radiation by a neutrino moving in the background matter in the presence of electromagnetic and/or gravitational

^ae-mail: ax.grigoriev@mail.ru

^be-mail: studenik@srd.sinp.msu.ru

^ce-mail:A_Ternov@mail.ru

fields which we have named the "spin light of neutrino" ($SL\nu$). The $SL\nu$ originates, however, from the quantum spin flip transitions and for sure it is important to revise the calculations of the rate and total power of the $SL\nu$ in matter using the quantum theory. Note that within the quantum theory the radiation emitted by a neutrino moving in a magnetic field was also considered in [8].

In this paper we should like to present a reasonable step forward, which we have made recently [9], in the study of the neutrino interaction in the background matter and external fields. The developed quantum theory of a neutrino motion in the presence of the background matter is based on the two equations for the neutrino wave function. The first equation is obtained in the generalization of the Dirac-Pauli equation of the quantum electrodynamics under the assumption that matter effects can be introduced through the substitution (1). The second of these equations is derived directly from the neutrino interaction Lagrangian averaged over the particles of the background. In the limit of the constant matter density, we get the exact solutions of these equations, classify them over the neutrino helicity states and determine the energy spectra, that depend on the helicity.

Although the neutrino energy spectra in matter correspondent to the two equations are not equal, the difference of energies of the opposite neutrino helicity states, predicted in the linear approximation in the matter density by the two equations, are equal. Then with the use of the obtained neutrino quantum states in matter we develop the quantum theory of the $SL\nu$ and calculate the emitted photon energy, the rate and power of the radiation in matter accounting for the emitted photons polarization. The generalized Dirac-Pauli equation enables us to include the contribution from the longitudinal magnetic field and also to account for the effect of the matter polarization.

2 Neutrino wave function and energy spectrum in matter

In this section we discuss the two quantum equations for a massive neutrino wave function in the background matter. The two wave functions and energy spectra, that correspond to these two equations, are not the same. However, the results for the $SL\nu$ photon energy, the rate and the power obtained on the basis of these two equations in the lowest approximation over the matter density (see Section 3), are equal.

2.1 Modified Dirac-Pauli equation for neutrino in matter

To derive a quantum equation for the neutrino wave function in the background matter we start with the well-known Dirac-Pauli equation for a neutral fermion with non-zero magnetic moment. For a massive neutrino moving in an electromagnetic field $F_{\mu\nu}$ this equation is given by

$$\left(i\gamma^\mu \partial_\mu - m - \frac{\mu}{2} \sigma^{\mu\nu} F_{\mu\nu} \right) \Psi(x) = 0, \quad (3)$$

where m and μ are the neutrino mass and magnetic moment^d, $\sigma^{\mu\nu} = i/2(\gamma^\mu \gamma^\nu - \gamma^\nu \gamma^\mu)$.

^dFor the recent studies of a massive neutrino electromagnetic properties, including discussion on the neutrino magnetic moment, see Ref. [10]

Now let us consider the case of a neutrino moving in the presence of matter without any electromagnetic field in the background. Our goal is to study the spin-light photon emission in the process of the neutrino transition between the two quantum states with opposite helicities in the presence of matter. Since the calculation of the $SL\nu$ rate and power are performed below (in Section 3) within the lowest approximation over the density of the background matter, we are interested now in the difference of energies of the two neutrino states with opposite helicities in the presence of matter. The quantum equation for the neutrino wave function, appropriate for this task, can be obtained from (3) with application of the substitution (1) which now becomes

$$F_{\mu\nu} \rightarrow G_{\mu\nu}. \quad (4)$$

Thus, we get the quantum equation for the neutrino wave function in the presence of the background matter in the form [9]

$$\left(i\gamma^\mu \partial_\mu - m - \frac{\mu}{2} \sigma^{\mu\nu} G_{\mu\nu} \right) \Psi(x) = 0, \quad (5)$$

that can be regarded as the modified Dirac-Pauli equation. The generalization of the neutrino quantum equation for the case when an electromagnetic field is present, in addition to the background matter, is discussed below in Section 2.2. Here we should like to note that Eq.(5) is derived under the assumption that the matter term is small. This condition is similar to the condition of smallness of the electromagnetic term in the Dirac-Pauli equation (3) in the electrodynamics.

The detailed discussion on the evaluation of the tensor $G_{\mu\nu}$ is given in [1–3]. We consider here the case of the electron neutrino moving in the unpolarized matter composed of the only one type of fermions of a constant density. For a background of only electrons we get

$$G^{\mu\nu} = \gamma \rho^{(1)} n \begin{pmatrix} 0 & 0 & 0 & 0 \\ 0 & 0 & -\beta_3 & \beta_2 \\ 0 & \beta_3 & 0 & -\beta_1 \\ 0 & -\beta_2 & \beta_1 & 0 \end{pmatrix}, \quad \gamma = (1 - \beta^2)^{-1/2}, \quad \rho^{(1)} = \frac{\tilde{G}_F}{2\sqrt{2}\mu}, \quad (6)$$

$$\tilde{G}_F = G_F(1 + 4 \sin^2 \theta_W),$$

where $\beta = (\beta_1, \beta_2, \beta_3)$ is the neutrino three-dimensional speed, n denotes the number density of the background electrons, G_F is the Fermi constant, and θ_W is the Weinberg angle. Note that the neutrino magnetic moment simplifies in Eq.(5). From (39) and the two equations, (3) and (5), it is possible to see that the term $\mathbf{M} = \gamma \rho^{(1)} n \beta$ in Eq.(5) plays the role of the magnetic field \mathbf{B} in Eq.(3). Therefore, the Hamiltonian form of (5) is

$$i \frac{\partial}{\partial t} \Psi(\mathbf{r}, t) = \hat{H}_G \Psi(\mathbf{r}, t), \quad (7)$$

where

$$\hat{H}_G = \hat{\alpha} \mathbf{p} + \hat{\beta} m + \hat{V}_G, \quad (8)$$

and

$$\hat{V}_G = -\frac{\tilde{G}_F}{2\sqrt{2}} \frac{n}{m} \hat{\beta} \Sigma \mathbf{p}, \quad (9)$$

here \mathbf{p} is the neutrino momentum.

Let us now determine the energies of the two different neutrino helicity states in matter. For the stationary states of Eq.(7) we get

$$\Psi(\mathbf{r}, t) = e^{-i(Et - \mathbf{p}\mathbf{r})} u(\mathbf{p}, E), \quad (10)$$

where $u(\mathbf{p}, E)$ is independent on the spacial coordinates and time. Upon the condition that Eq.(5) has a non-trivial solution, we arrive to the energy spectrum of different helicity states in the background matter [9]:

$$E = \sqrt{\mathbf{p}^2 + m^2 \left(1 - s \frac{\alpha p}{m}\right)^2}. \quad (11)$$

where

$$\alpha = \frac{1}{2\sqrt{2}} \tilde{G}_F \frac{n}{m}. \quad (12)$$

It is important that the energy (11) in the background matter depends on the state of the neutrino longitudinal polarization (helicity), i.e. the negative-helicity and positive-helicity neutrinos with equal momentum \mathbf{p} have different energies.

Note that in the relativistic energy limit the negative-helicity neutrino state is dominated by the left-handed chiral state ($\nu_- \approx \nu_L$), whereas the positive-helicity state is dominated by the right-handed chiral state ($\nu_+ \approx \nu_R$). For the relativistic neutrinos one can derive, using Eq.(9), the probability of the neutrino spin oscillations $\nu_L \leftrightarrow \nu_R$ with the correct form of the matter term [1–3] (for the further details see Section 2.2).

The procedure, similar to one used for the derivation of the solution of the Dirac equation in vacuum, can be adopted for the case of the neutrino moving in matter. We apply this procedure to Eq.(7) and arrive to the final form of the wave function of a neutrino moving in the background matter [9]:

$$\Psi_{\mathbf{p},s}(\mathbf{r}, t) = \frac{e^{-i(Et - \mathbf{p}\mathbf{r})}}{2L^{\frac{3}{2}}} \begin{pmatrix} \sqrt{1 + \frac{m-s\alpha p}{E}} & \sqrt{1 + s \frac{p_3}{p}} \\ s\sqrt{1 + \frac{m-s\alpha p}{E}} & \sqrt{1 - s \frac{p_3}{p}} e^{i\delta} \\ s\sqrt{1 - \frac{m-s\alpha p}{E}} & \sqrt{1 + s \frac{p_3}{p}} \\ \sqrt{1 - \frac{m-s\alpha p}{E}} & \sqrt{1 - s \frac{p_3}{p}} e^{i\delta} \end{pmatrix}, \quad (13)$$

where L is the normalization length and $\delta = \arctan p_y/p_x$. In the limit of vanishing density of matter, when $\alpha \rightarrow 0$, the wave function of Eq.(13) transforms to the solution of the Dirac equation in the vacuum.

Calculations on the basis of the modified Dirac-Pauli equation (5) enables us to reproduce, to the lowest order of the expansion over the matter density, the correct energy difference between the two neutrino helicity states in matter. Therefore, the quantum theory of the $SL\nu$ in the lowest approximation over the matter density can be developed using this equation (see Section 3). However, in order to derive the correct absolute values for the two neutrino helicity states in matter, we investigate in Section 2.3 the neutrino quantum states on the basis of the modified Dirac equation that we obtain from the corresponding neutrino interaction Lagrangian.

2.2 Modified Dirac-Pauli equation in magnetized matter

We should like to note that it is easy to generalize the Dirac-Pauli equation (3) (or (5)) for the case when a neutrino is moving in the magnetized background matter [9]. For this case (i.e., when the effects of the presence of matter and a magnetic field on neutrino have to be accounted for) the modified Dirac-Pauli equation is

$$\left\{ i\gamma^\mu \partial_\mu - m - \frac{\mu}{2} \sigma^{\mu\nu} (F_{\mu\nu} + G_{\mu\nu}) \right\} \Psi(x) = 0, \quad (14)$$

where the magnetic field \mathbf{B} enters through the tensor $F_{\mu\nu}$. If a constant magnetic field present in the background and a neutrino is moving parallel (or anti-parallel) to the field vector \mathbf{B} , then the corresponding neutrino energy spectrum can be obtained within the procedure discussed above in the previous section. In particular, the neutrino energy and wave function in the magnetized matter can be obtained from (11) and (13) by the following redefinition

$$\alpha \rightarrow \alpha' = \alpha + \frac{\mu B_{\parallel}}{p}, \quad (15)$$

where $B_{\parallel} = (\mathbf{B}\mathbf{p})/p$. Thus, the neutrino energy in this case reads [9]

$$E = \sqrt{\mathbf{p}^2 + m^2 \left(1 - s \frac{\alpha p + \mu B_{\parallel}}{m} \right)^2}. \quad (16)$$

For the relativistic neutrinos the expression of Eq.(16) gives, in the linear approximation over the matter density and the magnetic field strength, the correct value (see [1, 3]) for the energy difference of the two opposite helicity states in the magnetized matter:

$$\Delta_{eff} = \frac{\tilde{G}_F}{\sqrt{2}} n + 2 \frac{\mu B_{\parallel}}{\gamma}. \quad (17)$$

that confirms our previous result of refs. [1, 3].

2.3 Modified Dirac equation for neutrino in matter

The absolute value of the energy of the neutrino helicity states in the presence of matter can be obtained on the basis of the modified Dirac equation that we derive below directly from the neutrino interaction Lagrangian. For definiteness, we consider again the case of the electron neutrino propagating through moving and polarized matter composed of only electrons (the electron gas). The generalizations for the other flavour neutrinos and also for more complicated matter compositions are just straightforward.

Assume that the neutrino interactions are described by the extended standard model supplied with $SU(2)$ -singlet right-handed neutrino ν_R . We also suppose that there is a macroscopic amount of electrons in the scale of a neutrino de Broglie wave length. Therefore, the interaction of a neutrino with the matter (electrons) is coherent. In this case the averaged over the matter electrons addition to the vacuum

neutrino Lagrangian, accounting for the charged- and neutral-current interactions, can be written in the form

$$\Delta L_{eff} = -f^\mu \left(\bar{\nu} \gamma_\mu \frac{1 + \gamma^5}{2} \nu \right), \quad f^\mu = \frac{G_F}{\sqrt{2}} \left((1 + 4 \sin^2 \theta_W) j^\mu - \lambda^\mu \right), \quad (18)$$

where the electrons current j^μ and electrons polarization λ^μ are given by

$$j^\mu = (n, n\mathbf{v}), \quad (19)$$

and

$$\lambda^\mu = \left(n(\zeta\mathbf{v}), n\zeta \sqrt{1 - v^2} + \frac{n\mathbf{v}(\zeta\mathbf{v})}{1 + \sqrt{1 - v^2}} \right). \quad (20)$$

The Lagrangian (18) accounts for the possible effect of the matter motion and polarization. Here n , \mathbf{v} , and ζ ($0 \leq |\zeta|^2 \leq 1$) denote, respectively, the number density of the background electrons, the speed of the reference frame in which the mean momentum of the electrons is zero, and the mean value of the polarization vector of the background electrons in the above mentioned reference frame. The detailed discussion on the determination of the electrons polarization can be found in [1–3].

From the standard model Lagrangian with the extra term ΔL_{eff} being added, we derive the following modified Dirac equation [9] for a neutrino moving in the background matter,

$$\left\{ i\gamma_\mu \partial^\mu - \frac{1}{2} \gamma_\mu (1 + \gamma_5) f^\mu - m \right\} \Psi(x) = 0. \quad (21)$$

This is the most general equation of motion of a neutrino in which the effective potential $V_\mu = \frac{1}{2}(1 + \gamma_5)f_\mu$ accounts for both the charged and neutral-current interactions with the background matter and also for the possible effects of the matter motion and polarization. It should be noted here that the modified effective Dirac equations for a neutrino with various types of interactions with the background environment were used previously in [12–18] for the study of the neutrino dispersion relations and derivation of the neutrino oscillation probabilities in matter. If we neglect the contribution of the neutral-current interaction and possible effects of motion and polarization of the matter then from (21) we can get corresponding equations for the left-handed and right-handed chiral components of the neutrino field derived in [13]. The similar equation for a neutrino in the background of non-moving and unpolarized neutrons was also used in [19, 20].

Upon the condition that the equation (21) has a non-trivial solution, we arrive to the energy spectrum of a neutrino moving in unpolarized background matter at rest:

$$E_\epsilon = \epsilon \sqrt{\mathbf{p}^2 \left(1 - s\alpha \frac{m}{p} \right)^2 + m^2} + \alpha m. \quad (22)$$

The quantity $\epsilon = \pm 1$ splits the solutions into the two branches that in the limit of the vanishing matter density, $\alpha \rightarrow 0$, reproduce the positive and negative-frequency solutions, respectively. Note that again the neutrino energy in the background matter depends on the state of the neutrino longitudinal polarization, i.e. in the relativistic

case the left-handed and right-handed neutrinos with equal momenta have different energies.

Although the obtained neutrino energy spectrum (22) does not reproduce the one of Eq.(11), an equal result for the energy difference $\Delta E = E(s = -1) - E(s = +1)$ of the two neutrino helicity states can be obtained from both of the spectra in the low matter density limit $\alpha \frac{pm}{E_0^2} \ll 1$:

$$\Delta E \approx 2m\alpha \frac{p}{E_0}, \quad (23)$$

where we use the notation $E_0 = \sqrt{p^2 + m^2}$. It should be also noted that for the relativistic neutrinos the energy spectrum for the neutrino helicity states of Eq.(22) in the low density limit reproduces the correct energy values for the neutrino left-handed and right-handed chiral states:

$$E_{\nu_L} \approx E(s = -1) \approx E_0 + \frac{\tilde{G}_F}{\sqrt{2}}n, \quad (24)$$

and

$$E_{\nu_R} \approx E(s = +1) \approx E_0, \quad (25)$$

as it should be for the active left-handed and sterile right-handed neutrino in matter.

For the wave function of a neutrino in the background matter given by Eq.(21) we get:

$$\Psi_{\epsilon, \mathbf{p}, s}(\mathbf{r}, t) = \frac{e^{-i(E_\epsilon t - \mathbf{p}\mathbf{r})}}{2L^{\frac{3}{2}}} \begin{pmatrix} \sqrt{1 + \frac{m}{E_\epsilon - \alpha m}} & \sqrt{1 + s \frac{p_3}{p}} \\ s \sqrt{1 + \frac{m}{E_\epsilon - \alpha m}} & \sqrt{1 - s \frac{p_3}{p}} e^{i\delta} \\ s\epsilon \sqrt{1 - \frac{m}{E_\epsilon - \alpha m}} & \sqrt{1 + s \frac{p_3}{p}} \\ \epsilon \sqrt{1 - \frac{m}{E_\epsilon - \alpha m}} & \sqrt{1 - s \frac{p_3}{p}} e^{i\delta} \end{pmatrix}, \quad (26)$$

Obviously, in the limit of vanishing density of matter, when $\alpha \rightarrow 0$, the wave function (26) transforms to the solution of the Dirac equation for a neutrino in the vacuum.

3 Spin light of neutrino in matter and magnetic field

The proposed quantum equations (5),(14) and (21) for a neutrino moving in the background matter establish a basis for a new method in the investigation of different processes with participation of neutrinos in the presence of matter and external electromagnetic fields. As an example, we should like to study of the ($SL\nu$) in the magnetized matter and develop the *quantum* theory of this effect.

Within the quantum approach, the corresponding Feynman diagram of the $SL\nu$ in matter is the standard one-photon emission diagram with the initial and final neutrino states described by the "broad lines" that account for the neutrino interaction with matter and the external electromagnetic field. From the usual neutrino magnetic moment interaction, it follows that the amplitude of the transition from the neutrino initial state ψ_i to the final state ψ_f , accompanied by the emission of a photon with a momentum $k^\mu = (\omega, \mathbf{k})$ and a polarization \mathbf{e}^* , can be written in the form

$$S_{fi} = -\mu \sqrt{\frac{2\pi}{\omega L^3}} 2\pi \delta(E_f - E_i + \omega) \int d^3x \bar{\psi}_f(\mathbf{r}) (\hat{\Gamma} \mathbf{e}^*) e^{i\mathbf{k}\mathbf{r}} \psi_i(\mathbf{r}), \quad (27)$$

where

$$\hat{\Gamma} = i\omega \{ [\Sigma \times \boldsymbol{\kappa}] + i\gamma^5 \Sigma \}. \quad (28)$$

Here $\boldsymbol{\kappa} = \frac{\mathbf{k}}{\omega}$ is the unit vector pointing in the direction of the emitted photon propagation. The delta-function stands for the energy conservation. Performing the integrations over the spatial co-ordinates, we can recover the delta-functions for the three components of the momentum. In the lowest order of the expansion over the density of the background matter, the properties of the $SL\nu$ (in particular, the rate and radiation power), obtained on the basis of Eqs. (5) and (21), are the same. This is because, as it has been already mentioned, the difference of the energies of the two neutrino helicity states, calculated with use of Eqs. (5) and (21), are equal. The additional effect from a magnetic field (if it is also present in the background environment) can be accounted for if one describes the neutrino on the basis the modified Dirac-Pauli equation of Eq.(14). Note that the $SL\nu$ in the presence of a magnetic field can have interesting applications for magnetized astrophysical media.

Let us suppose that the weak interaction of the neutrino with the electrons of the background is indeed weak. Thus, in wide ranges of densities of matter and strengths of the magnetic field that are appropriate for the astrophysical applications, we can expand the energy (16) over $\alpha' \frac{pm}{E_0^2} \ll 1$ and in the liner approximation get for the emitted photon energy

$$\omega = (s_f - s_i) \alpha' m \frac{\beta}{1 - \beta \cos \theta}, \quad (29)$$

where θ is the angle between $\boldsymbol{\kappa}$ and the direction of the neutrino speed β .

From the above consideration it follows that the only possibility for the $SL\nu$ to appear is provided in the case when the neutrino initial and final states are characterized by $s_i = -1$ and $s_f = +1$, respectively. Thus we conclude, on the basis of the quantum treatment of the $SL\nu$ in the magnetized matter, that in this process the relativistic left-handed neutrino is converted to the right-handed neutrino and the emitted photon energy is given by

$$\omega = \frac{\beta}{1 - \beta \cos \theta} \omega_0, \quad (30)$$

where we use the notation

$$\omega_0 = \frac{\tilde{G}_F}{\sqrt{2}} n \beta + 2 \frac{\mu B_{||}}{\gamma}. \quad (31)$$

Note that the photon energy depends on the angle θ and also on the value of the neutrino speed β . In the case of $\beta \approx 1$ and $\theta \rightarrow 0$ we confirm the estimation for the emitted photon energy in the background matter obtained in [5]. If the effect of the background matter is subdominant and the main contribution to the $SL\nu$ is given by the magnetic field term, then from Eq.(30) we obtain the corresponding result of ref. [8] where the $SL\nu$ in the presence of a magnetic field was considered.

For the spin light transition rate in the lowest order approximation over the parameter $\alpha' \frac{pm}{E_0^2}$ we get [9]

$$\Gamma_{SL} = \mu^2 \omega_0^3 \int \frac{S \sin \theta}{(1 - \beta \cos \theta)^4} d\theta, \quad (32)$$

where

$$S = (\cos \theta - \beta)^2 + (1 - \beta \cos \theta)^2. \quad (33)$$

The corresponding expression for the radiation power is

$$I_{SL} = \mu^2 \omega_0^4 \int \frac{S \sin \theta}{(1 - \beta \cos \theta)^5} d\theta. \quad (34)$$

Performing the integrations in Eq.(32) over the angle θ , we obtain for the rate

$$\Gamma_{SL} = \frac{8}{3} \mu^2 \omega_0^3 \gamma^2. \quad (35)$$

For the total radiation power from Eq.(34) we get,

$$I_{SL} = \frac{8}{3} \mu^2 \omega_0^4 \gamma^4. \quad (36)$$

From the obtained result of Eq.(35) by switching off the contribution from the magnetic field one can get the $SL\nu$ rate in matter (see also [7]). This result exceeds the value of the neutrino spin light rate derived in [5] by a factor of two because here the neutrinos in the initial state are totally left-handed polarized, whereas in [5] the case of initially unpolarized neutrinos (i.e., an equal mixture of the left- and right-handed neutrinos) is considered.

4 Summary and conclusion

We have developed the quantum approach to description of a neutrino moving in the background matter on the basis of the generalized Dirac-Pauli and modified Dirac equations. In the low matter density limit the two equations give equal values for the energy difference of the opposite neutrino helicity states in matter. The use of the generalized Dirac-Pauli equation also enables us to account for the effect of the longitudinal magnetic field. In the derivation of the Dirac-Pauli equation (see (5) and (14)) it has been supposed that the matter parameter is small,

$$\alpha \frac{pm}{E_0^2} = \frac{1}{2\sqrt{2}} \tilde{G}_F \frac{np}{E_0^2} \ll 1. \quad (37)$$

However, due to the fact that even for the extremely dense matter with $n = 10^{37} \text{ cm}^{-3}$ one gets $\frac{1}{2\sqrt{2}} \tilde{G}_F n \sim 1 \text{ eV}$, the restriction (37) does not forbid to use the generalized Dirac-Pauli equation even for a very dense medium of neutron stars if the neutrino has the relativistic energy. It should be noted that in the derivation of the modified Dirac equation (21) no any restrictions of this kind has been made.

On the basis of these two equations the quantum treatment of a neutrino moving in the presence of the background matter has been realized with the effect of the longitudinal magnetic field being incorporated. Within the developed quantum approach, the emission rate and power of the $SL\nu$ in magnetized matter has been calculated accounting for the emitted photons polarization. The existence of the neutrino-self polarization effect in the process of the spin light radiation in the background matter

and magnetic field has been shown. The photon energy, in the case when the both effects of the background matter and longitudinal magnetic field are important, has been derived for the first time. The photon energy depends on the density of matter, the value of the neutrino magnetic moment, the strength of the magnetic field and also on the direction of the neutrino propagation in respect to the magnetic field \mathbf{B} orientation. The $SL\nu$ radiation and the corresponding neutrino self-polarization effect, due to the significant dependence on the matter density and the magnetic field strength, are expected to be important in different astrophysical dense media and in the early Universe.

In conclusion, let us consider the case when the background magnetic field is strong enough so that the following condition is valid

$$B > \frac{p_F^2}{2e}, \quad (38)$$

where $p_F = \sqrt{\mu^2 - m_e^2}$, μ and m_e are, respectively, the Fermi momentum, chemical potential, and mass of electrons. Then all of the electrons of the background occupy the lowest Landau level (see, for instance, [11]), therefore the matter is completely polarized in the direction opposite to the unit vector \mathbf{B}/B . From the general expression for the tensor $G_{\mu\nu}$ (see the second paper of [1]) we get

$$G^{\mu\nu} = \gamma n \left\{ \rho^{(1)} \begin{pmatrix} 0 & 0 & 0 & 0 \\ 0 & 0 & -\beta_3 & \beta_2 \\ 0 & \beta_3 & 0 & -\beta_1 \\ 0 & -\beta_2 & \beta_1 & 0 \end{pmatrix} + \rho^{(2)} \begin{pmatrix} 0 & -\beta_2 & \beta_1 & 0 \\ \beta_2 & 0 & -\beta_0 & 0 \\ -\beta_1 & \beta_0 & 0 & 0 \\ 0 & 0 & 0 & 0 \end{pmatrix} \right\}, \quad (39)$$

$$\rho^{(2)} = -\frac{G_F}{2\sqrt{2}\mu}.$$

On the basis of the modified Dirac-Pauli equation (14) with the tensor $G_{\mu\nu}$ given by (39) it is possible to consider the $SL\nu$ in the case when the neutrino is moving in the completely polarized matter parallel (or anti-parallel) to the magnetic field vector \mathbf{B} . The neutrino energy and wave function in such a case can be obtained from (11) and (13) by the following redefinition

$$\alpha \rightarrow \tilde{\alpha} = \alpha \left[1 - \frac{\text{sign} \left(\frac{B_{||}}{B} \right)}{1 + \sin^2 4\theta_W} \right] + \frac{\mu B_{||}}{p}. \quad (40)$$

The second term in brackets in Eq.(40) accounts for the effect of the matter polarization. It follows, that the effect of the matter polarization can reasonably change the total matter contribution to the neutrino energy (16). The emitted $SL\nu$ photon energy is determined in this case by (30) with

$$\omega_0 = \frac{G_F}{\sqrt{2}} n \left[\beta (1 + \sin^2 4\theta_W) - \text{sign} \left(\frac{B_{||}}{B} \right) \right] + 2 \frac{\mu B_{||}}{\gamma}. \quad (41)$$

Consequently, the effect of the matter polarization significantly influence the rate and radiation power of the $SL\nu$.

References

- [1] A.Egorov, A.Lobanov, A.Studenikin, Phys.Lett. B491 (2000) 137; A.Lobanov, A.Studenikin, Phys.Lett.B515 (2001) 94.
- [2] M.Dvornikov, A.Studenikin, JHEP 09 (2002) 016.
- [3] A.Studenikin, Phys.Atom.Nucl. 67 (2004) 993, hep-ph/0306280, hep-ph/0407010.
- [4] V.Bargmann, L.Michel, V.Telegdi, Phys.Rev.Lett. 2 (1959) 435.
- [5] A.Lobanov, A.Studenikin, Phys.Lett.B564 (2003) 27;
- [6] M.Dvornikov, A.Grigoriev, A.Studenikin, Int.J.Mod.Phys.D (2005), in press, hep-ph/0406114;
- [7] A.Lobanov, A.Studenikin, Phys.Lett.B601 (2004) 171.
- [8] A.Borisov, V.Zhukovsky, A.Ternov, Sov.Phys.J. 31 (1988) 228.
- [9] A.Studenikin, A.Ternov, hep-ph/0410296, hep-ph/0410297.
- [10] M.Dvornikov, A.Studenikin, Phys.Rev.D 69 (2004) 073001; JETP 99 (2004) 254.
- [11] H.Nunokawa, V.Semikoz, A.Smirnov, J.Valle, Nucl.Phys.B501, 17 (1997).
- [12] L.N.Chang, R.K.Zia, Phys.Rev.D38 (1988) 1669. Phys.Rev.Lett.64 (1990) 115.
- [13] J.Pantaleone, Phys.Lett.B268 (1991) 227; Phys.Rev.D46 (1992) 510.
- [14] K.Kiers, N.Weiss, Phys.Rev.D56 (1997) 5776; K.Kiers, M.Tytgat, Phys.Rev.D57 (1998) 5970.
- [15] P.Mannheim, Phys.Rev.D 37 (1988) 1935.
- [16] D.Nötzold, G.Raffelt, Nucl.Phys.B307 (1988) 924.
- [17] J.Nieves, Phys.Rev.D 40 (1989) 866.
- [18] W.Haxton, W-M.Zhang, Phys.Rev.D 43 (1991) 2484.
- [19] M.Kachelriess, Phys.Lett.B426 (1998) 89.
- [20] A.Kusenko, M.Postma, Phys.Lett.B545 (2002) 238.

EFFECTS OF HEAVY MAJORANA NEUTRINOS AT LEPTON-PROTON COLLIDERS

A. Ali^a

Deutsches Elektronen-Synchrotron DESY, Hamburg, Germany

A.V. Borisov^b, D.V. Zhuridov^c

Faculty of Physics, Moscow State University, 119992 Moscow, Russia

Abstract. We discuss the prospects of detecting the processes $e^+p \rightarrow \bar{\nu}_e \ell^+ \ell'^+ X$ and $\nu_e p \rightarrow e \ell^+ \ell'^+ X$ ($\ell, \ell' = e, \mu, \tau$) under the conditions of the present ep collider HERA and of future colliders. These high-energy processes are assumed to be mediated by the exchange of heavy Majorana neutrinos (HMN). We consider two simple scenarios for the HMN mass spectrum: the effective singlet ($m_1 \ll m_2 < m_3 \dots$) and the effective doublet ($m_1 < m_2 \ll m_3 \dots$). For the latter case, the cross section includes information about CP -violating phases.

Introduction

At the moment there are experimental evidences for nonzero neutrino masses [1, 2]. The nature of neutrino mass, whether it is Dirac or Majorana, is one of the fundamental and still unsolved problems in particles physics. A Dirac neutrino carries a lepton number distinguishing a particle from an antiparticle. In contrast to that, a Majorana neutrino is identical to its own antiparticle. The Majorana mass term in the total Lagrangian does not conserve lepton number, but changes its value by two units. Therefore Majorana neutrinos can lead to various lepton number violating processes. For example, they induce same-sign dilepton production in collisions at high energies: $pp \rightarrow \ell^\pm \ell'^\pm X$ [3], $e^+p \rightarrow \bar{\nu}_e \ell^+ \ell'^+ X$ [4] etc.

In theories extending the Standard Model the seesaw mechanism is often used to provide a natural generation of small neutrino masses (for a review, see, e.g., [5, 6]). Unlike the usual way of Dirac mass generation through weak SU(2)-breaking, this mechanism doesn't need extremely small Yukawa couplings ($\lesssim 10^{-12}$). For three families of leptons and s right-handed SU(2) singlets the seesaw mechanism leads to 3 light and s heavy massive Majorana neutrino states

$$\nu_\ell = \sum_{i=1}^3 \tilde{U}_{\ell i} \nu_i + \sum_{j=1}^s U_{\ell j} N_j,$$

where ν_ℓ is a neutrino of definite flavor ($\ell = e, \mu, \tau$), the coefficients $\tilde{U}_{\ell i}$ and $U_{\ell j}$ form the leptonic mixing matrices.

Heavy mass states give a relatively small contribution to neutrino flavor states. Nevertheless effects of light and heavy Majorana neutrinos (HMN)

^ae-mail: ahmed.ali@desy.de

^be-mail: borisov@ave.phys.msu.su

^ce-mail: jouridov@mail.ru

compete in lepton number violating processes, because small values of the mixing parameters $U_{\ell j}$ for heavy neutrinos N_j may be compensated by smallness of the masses of light neutrinos ν_i .

The process $e^+ p \rightarrow \bar{\nu}_e \ell^+ \ell'^+ X$

In this report, we investigate the possibilities of observation of the process

$$e^+ p \rightarrow \bar{\nu}_e \ell^+ \ell'^+ X \quad (1)$$

and its cross symmetric process $\nu_e p \rightarrow e \ell^+ \ell'^+ X$ (X denotes hadron jets) under the conditions of the present ep collider HERA (DESY) [1] and of future ep colliders. We assume that these processes at high energies

$$\sqrt{s} \gg m_W$$

are mediated by HMN. The leading-order Feynman diagram for the process (1) is shown in Fig. 1. (There is also a crossed diagram with interchanged lepton lines.) For calculating the cross sections, we use the leading effective vector-boson (EVB) approximation [7] neglecting transverse polarizations of W bosons and quark mixing. For this case, cross sections for the process and the crossed channel turn to be equal. As an observation criteria for the process we have chosen the condition

$$\sigma L \geq 1,$$

where σ denotes the cross section and L is the integrated luminosity per year for a collider.

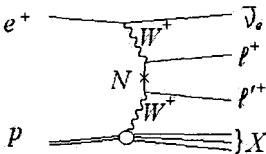


Figure 1: Feynman diagram for the process $e^+ p \rightarrow \bar{\nu}_e \ell^+ \ell'^+ X$ mediated by the HMN, N .

We should note that lepton-proton collisions are free of the Standard Model background [4] in contrast to the proton-proton collisions [8].

Effective Singlet Case

At first we take the simplest pattern of the HMN mass spectrum

$$m_1 \ll m_2 < m_3 \dots$$

$(m_{N_i} \equiv m_i)$ assuming the condition to be held

$$\sqrt{s} \ll m_2.$$

The cross section

$$\sigma_1 = C \left(1 - \frac{1}{2} \delta_{\ell\ell'}\right) |U_{\ell 1} U_{\ell' 1}|^2 \left(\frac{m_1}{m_W}\right)^2 \int_{y_0}^1 \frac{dy}{y} \int_y^1 \frac{dx}{x} p(x, xs) h\left(\frac{y}{x}\right) \omega\left(\frac{ys}{m_1^2}\right) \quad (2)$$

for the process is determined by the convolution of three functions given in [3]: $p(x, xs)$, the quark distribution density having a fraction x of the proton momentum evaluated at the scale $Q^2 = xs$, h , the normalized luminosity of W^+W^+ pairs in the quark-lepton system, and ω , the normalized cross section for the subprocess $W^+W^+ \rightarrow \ell^+\ell'^+$. Here, $y_0 = 4m_W^2/s$ and the characteristic constant C has the value

$$C = G_F^4 m_W^6 / (8\pi^5) = 0.80 \text{ fb.} \quad (3)$$

In the numerical calculation we have used the set of parton distributions CTEQ6 [9]. Using the bounds on the mixing parameters $U_{\ell N}$ from precision electroweak data [10]

$$\sum_N |U_{eN}|^2 < 6.6 \times 10^{-3}, \sum_N |U_{\mu N}|^2 < 6.0 \times 10^{-3}, \sum_N |U_{\tau N}|_{eff}^2 < 3.1 \times 10^{-3} \quad (4)$$

and the constraint from the neutrinoless double beta decay [11]

$$\left| \sum_N U_{eN}^2 m_N^{-1} \right| < 5 \times 10^{-5} \text{ TeV}^{-1}$$

(the sum is over the heavy neutrinos), we find that the process is practically unobservable at HERA even with a very optimistic luminosity ($\sqrt{s} = 318 \text{ GeV}$, $L = 1 \text{ fb}^{-1}$) and also at the projected supercollider VLHC (see, e.g., [12]) ($\sqrt{s} = 6320 \text{ GeV}$, $L = 1.4 \text{ fb}^{-1}$). For example, for $m_1 \sim 1 \text{ TeV}$, we get $\sigma L \sim 10^{-10}$ (10^{-3}) for HERA (VLHC). For a possible detection of the process, the luminosity and/or the energy of the ep -collider should be substantially increased. Taking for example the luminosity $L = 100 \text{ fb}^{-1}$, the observation of the most probable events ($\mu\tau$ and $\mu\mu$) is possible if $\sqrt{s} > 23 \text{ TeV}$. For $\sqrt{s} = 25 \text{ TeV}$ such a collider will be sensitive to a range of neutrino masses about 1–3 TeV.

Effective Doublet Case

We consider also the neutrino mass spectrum of the effective doublet type

$$m_1 < m_2 \ll m_3 \dots$$

with the bound on energy $\sqrt{s} \ll m_3$. In this scenario, the cross section for the process (1)

$$\sigma_2 = \frac{C}{2} \int_{y_0}^1 \frac{dy}{y} \int_y^1 \frac{dx}{x} p(x, xs) h\left(\frac{y}{x}\right) W\left(\frac{ys}{m_1^2}, \frac{ys}{m_2^2}\right) \quad (5)$$

includes the normalized cross section for the subprocess

$$W(t_1, t_2) = m_W^{-2} [\rho_1^2 m_1^2 \omega(t_1) + 2c\rho_1\rho_2 m_1 m_2 \Omega(t_1, t_2) + \rho_2^2 m_2^2 \omega(t_2)], \quad (6)$$

which contains the individual contributions of the neutrinos N_1 and N_2 , $\omega(t_i)$, and the interference of the two, $\Omega(t_1, t_2)$, where

$$\begin{aligned} \Omega(t_1, t_2) &= 2 - \frac{1}{t_1 + t_2 + t_1 t_2} \left[\frac{t_2(t_1^2 - 2t_1 t_2 - 2t_2)}{t_1(t_1 - t_2)} \ln(1 + t_1) + (t_1 \leftrightarrow t_2) \right]; \\ \omega(t) &= \lim_{t' \rightarrow t} \Omega(t, t') = 2 + \frac{1}{1+t} - \frac{2(3+2t)}{t(2+t)} \ln(1+t). \end{aligned}$$

The mixing parameters for different $\ell\ell'$ channels of the process are

$$\rho_i = \sqrt{2 - \delta_{\ell\ell'}} |U_{\ell i} U_{\ell' i}|, \quad c = \cos \delta_{\ell\ell'}$$

with

$$\delta_{\ell\ell'} = \phi_1 - \phi_2 \in [0, 2\pi), \quad \phi_i = \arg(U_{\ell i} U_{\ell' i}).$$

The phases $\delta_{\ell\ell'}$ carry information about CP-violation. We assume the satu-

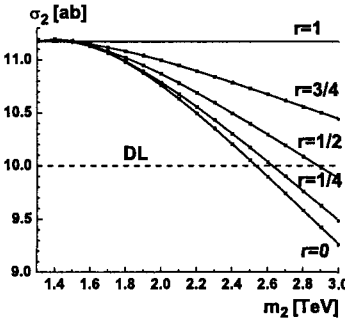


Figure 2: The dependence of σ_2 (in attobarn) on m_2 (in TeV) plotted for $r = 0, 1/4, 1/2, 3/4, 1$ with $\sqrt{s} = 25$ TeV, $m_1 = 1.3$ TeV and $c = 1$. The horizontal line DL is the discovery limit.

ration of the upper bound $B = 6.0 \times 10^{-3}$ in the second sum in (4) only by the first two terms, i.e., $|U_{\mu 1}|^2 = rB$, $|U_{\mu 2}|^2 = (1-r)B$ with $r \in [0, 1]$. Then for the most probable $\mu\mu$ channel we obtain

$$\sigma_2 = A(r^2 f_1 + 2cr\bar{r}F_{12} + \bar{r}^2 f_2), \quad \bar{r} = 1 - r, \quad (7)$$

where $f_i = f(s, m_i)$ and $F_{ij} = F(s, m_i, m_j)$ are expressed through obvious convolutions of the functions ω and Ω with h and p , respectively (see Eq. (5)), the constant A has the value $A = 1.4 \times 10^{-5}$ fb. For $r = 1$ ($r = 0$), only a single neutrino N_1 (N_2) contributes to the cross section which is reduced to the form given in Eq. (2). Generalization to the case of n neutrinos is straightforward.

In our calculations, we have chosen the following values for the parameters: $\sqrt{s} = 25$ TeV, $m_1 = 1.3$ TeV, $c = 1$. The cross section (7) as a function of m_2 for various fixed values of r is shown in Fig. 2. For the almost degenerate doublet ($m_1 \simeq m_2$) case and/or for the case of small mixing with N_2 ($r \simeq 1$), the cross section σ_2 is close to σ_1 , the cross-section for the effective singlet case. But we should note that for the case of destructive interference of the two almost degenerate massive states (e.g., for $m_2 \simeq m_1$, $r = 1/2$, $c = -1$), the cross section is vanishingly small.

Acknowledgments

We thank Dmitri Peregoudov for help in numerical calculations.

References

- [1] Particle Data Group Collab.: K. Hagiwara et al., *Phys. Rev.* **D66**, 010001 (2002).
- [2] C. Giunti, E-print Archive: hep-ph/0310238;
A.Yu. Smirnov, E-print Archive: hep-ph/0311259.
- [3] A. Ali, A.V. Borisov, N.B. Zamorin, in “*Frontiers of Particle Physics*” (Proceedings of the 10th Lomonosov Conference on Elementary Particle Physics), ed. by A. Studenikin (World Scientific, Singapore, 2003) p. 74.
- [4] M. Flanz, W. Rodejohann, K. Zuber, *Phys. Lett.* **B473**, 324 (2000);
W. Rodejohann, K. Zuber, *Phys. Rev.* **D62**, 094017 (2000).
- [5] P. Langacker, *Nucl. Phys. B (Proc. Suppl.)* **100**, 383 (2001).
- [6] B. Kayser, E-print Archive: hep-ph/0211134.
- [7] S. Dawson, *Nucl. Phys.* **B249**, 42 (1985);
I. Kuss, H. Spiesberger, *Phys. Rev.* **D53**, 6078 (1996).
- [8] A. Datta, M. Guchait, D.P. Roy, *Phys. Rev.* **D47**, 961 (1993).
- [9] J. Pumplin, D.R. Stump, J. Huston, H.L. Lai, P. Nadolsky, W.K. Tung,
E-print Archive: hep-ph/0201195.
- [10] E. Nardi, E. Roulet, D. Tommasini, *Phys. Lett.* **B344**, 225 (1995).
- [11] G. Belanger, F. Boudjema, D. London, H. Nadeau, *Phys. Rev.* **D53**, 6292 (1996).
- [12] M. Blaskiewicz et al., Fermilab Report TM-2158, 29 June 2001;
F.M.L. de Almeida Jr., Y.A. Coutinho, J.A. Martins Simões, M.A.B. do Vale, *Phys. Rev.* **D65**, 115010 (2002).

RADIATIVE NEUTRINO DECAY IN MAGNETIC FIELD AT FINITE DENSITY OF MEDIUM

A. I. Ternov^a

*Department of Theoretical Physics, Moscow Institute for Physics and Technology,
Dolgoprudny 141700, Russia*

P. A. Eminov

*Department of Physics, Moscow State Institute of Electronics and
Mathematics (Technical University), Bol'shoi Trekhsvyatitel'skii per. 3/12, 109028,
Moscow, Russia*

Abstract. In the framework of one-loop approximation of Standard Model the probability of radiative decay of a massive Dirac neutrino has been calculated in an intensive external constant magnetic field in existence of a dense medium. This probability is analyzed at different values of a medium density and energy of an initial neutrino. It was found out that in important for astrophysical applications case of degenerate electron gas the rate of decay of a massive neutrino in a medium essentially increases under the influence of an ultrastrong magnetic field.

Among different mechanisms of creation and decay of massive neutrino, the processes which take place in strong external electromagnetic fields with nonzero temperature as well as nonzero medium density should be specially pointed out [1, 2]. When the factors mentioned are taken into account then, on one hand, the results of quantum process analysis become more informative and, on the other hand, such an approach enables the physical effects observed in real laboratory experiments as well as at astrophysical conditions to be predicted and explained with a high degree of reliability.

It should be mentioned that non-linear quantum effects in hot and dense media can become apparent in the fields considerably weaker than in vacuum [3]. In actual astrophysical conditions radiation, absorption and propagation of neutrino often occur in a medium and simultaneously at the presence of strong magnetic fields. For example, in modern models of neutron stars the core of a star (with its thickness about 0.1 of its radius) appears as crystal lattice of the ions "immersed" in highly degenerate gas of relativistic electrons: the density of electrons $n \leq 10^{38} \text{ cm}^{-3}$, the temperature $T \sim 10^6 \div 10^9 \text{ K}$ and the strength of magnetic field $H \sim 10^{12} \div 10^{14} \text{ G}$ [4].

In this paper, the theory of radiation effects in hot and dense medium in the presence of external gauge field is used for evaluating the probability of radiative decay of relativistic massive neutrino in magnetized electron-positron gas.

Within the framework of one-loop approximation of the standard Glashow-Salam-Weinberg model with lepton mixing the main contribution in amplitude of the process $\nu_i \rightarrow \nu_j + \gamma$ is given by the diagram with virtual W boson.

In the contact approximation, the evident expression for the matrix element

^ae-mail: a_ternov@mail.ru

of the process of neutrino decay reads

$$S_{ij} = -i \frac{4eG_F}{\sqrt{2}} \sum_{a=e,\mu,\tau} U_{ia} U_{ja}^* \int d^4x d^4x' \bar{\nu}_j(x) \times \text{Sp} [\gamma_\mu L G^a(x, x') \gamma^\alpha A_\alpha(x') G^a(x', x)] \gamma^\mu L \nu_i(x), \quad (1)$$

where $L = \frac{1}{2}(1 + \gamma^5)$, $G^a(x, x')$ is the temporal Green function of ideal lepton-antilepton gas, which permits one to calculate precisely the influence of medium and external field on the probability of the process we are interested in, G_F is the Fermi constant, $\nu_i(x)$, $\nu_j(x)$ are the wave functions of the initial and final neutrinos with masses m_i and m_j , respectively, and U_{ia} is the unitary mixing matrix of leptons.

From formula (1), one obtains the following representation for the decay amplitude:

$$S_{ij} = S_{ij}^{(1)} + S_{ij}^{(2)},$$

where $S_{ij}^{(1)}$ is a pure field contribution to amplitude of the process (see [5–8]) and $S_{ij}^{(2)}$ is the contribution of the decay amplitude, dependent on the influence of finite temperature and the medium density.

We consider the mixing matrix in (1) to be equal to unit matrix because we are interested, first of all, in a possible catalytic role of effects caused by the influence of media and intensive magnetic field on the decay probability. Taking into account possible applications to physics of pulsars, we use the following conditions:

$$\begin{aligned} T &\ll E_F = \mu(T=0), \quad 2eH > \mu^2 - m_e^2, \\ H &\gg H_0 = m_e^2/e \simeq 4.41 \cdot 10^{13} \text{ G}. \end{aligned} \quad (2)$$

Physically conditions (2) correspond to a situation where only the ground energy level with principal quantum number $n' = 0$ is occupied by electrons of the medium and the main contribution to the probability of the process is given by their transitions into intermediate states also with zero principal quantum number.

At first we investigate the dependence of differential probability $dw/d\Omega$ of the process $\nu_i \rightarrow \nu_j + \gamma$ from a density of a medium and from energy of initial neutrino. (The exact expression for $dw/d\Omega$ is represented in our paper [2].)

In case when a neutrino is nonrelativistic ($|\mathbf{q}| \ll m_i$), and when electron gas is also nonrelativistic, that is, $(\frac{\mu}{m_e})^2 - 1 \ll 1$, the angular distribution of photons has the feebly expressed anisotropy: photons with the angles between their momenta and the direction of magnetic field satisfying the condition $0 < \theta < \pi/2$ are escaping with greater probability than in opposite directions (See figure 1a). This property of probability distribution is the consequence of parity nonconservation in weak interactions.

This situation becomes more typical in a dense medium ($\mu/m_e \gg 1$). In this case practically all the photons are radiated into a narrow cone, its axis is the direction of the magnetic field (See figure 1b).

At relativistic energies of initial massive neutrino a new maximum appears in an angular distribution of escaping photons: photons are radiated with high probability as well under small angles to momentum of an initial neutrino (See figure 1c). This property is the consequence of Doppler effect and is characteristic for an angular distribution of electromagnetic radiation of relativistic particles (in particular, for synchrotron radiation [9]). It should be noted that maximum of an angle distribution of photons practically along the direction of the magnetic field also remains for relativistic neutrino.

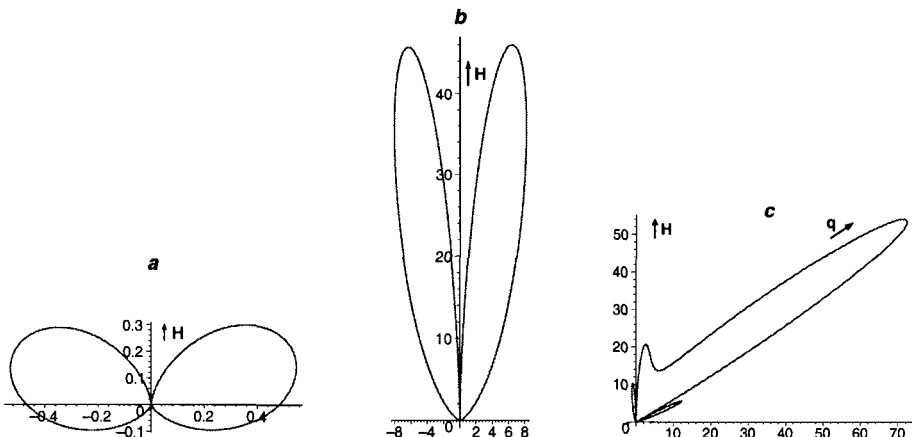


Figure 1: The angular distribution of probability of radiation of photons. Graph a: low density of a medium ($\mu/m_e \simeq 1.0001$) and nonrelativistic neutrinos ($q_0/m_i \simeq 1.0001$). Graph b: high density of a medium ($\mu/m_e \simeq 6$) and nonrelativistic neutrinos ($q_0/m_i \simeq 1.0001$). Graph c: high density of a medium ($\mu/m_e \simeq 10$) and moderately relativistic neutrinos ($q_0/m_i \simeq 7$). On the graph the magnitude $\frac{dw}{d\Omega} \frac{1}{w_0}$, where $w_0 = (eH)^2 (eG_F)^2 m_i / (2\pi)^6$, is figured. The angle between the momentum of initial neutrino and the direction of magnetic field is $\psi = \pi/3$.

The total probability of the process can be presented as the sum

$$w = w_1 + w_2 + w_{12},$$

where w_1 is a contribution resulting from the pure field amplitude $S_{ij}^{(1)}$, w_2 is a contribution originating from the amplitude $S_{ij}^{(2)}$, it corresponds to coherent scattering of neutrino on electrons and positrons of a medium, which one is accompanied by radiation of a photon, and w_{12} is a contribution stipulated by the interference of the field and plasma amplitudes.

For nonrelativistic neutrino in the limit case of rather low density of electron

gas, one obtains

$$\begin{pmatrix} w_1 \\ w_2 \\ w_{12} \\ w \end{pmatrix} \simeq w_0 \begin{pmatrix} \frac{2}{3} \\ -\frac{16}{15} (\gamma_F^{\frac{2}{3}} - 1) \\ -\frac{8}{5} (\gamma_F^{\frac{2}{3}} - 1)^{1/2} \\ \frac{2}{3} \end{pmatrix}, \quad \gamma_F^2 - 1 \ll 1, \quad (3)$$

where

$$w_0 = \frac{(eH)^2 (eG_F)^2}{(2\pi)^5} m_i, \quad \gamma_F = \frac{\mu}{m_e}.$$

It is worth noting that in nonrelativistic limit, the main contribution to the total probability of the process provides by the term w_1 arising from the field amplitude $S_{ij}^{(1)}$.

In the case of nonrelativistic neutrino and relativistic electron gas, the result looks like

$$\begin{pmatrix} w_1 \\ w_2 \\ w_{12} \\ w \end{pmatrix} \simeq w_0 \begin{pmatrix} \frac{2}{3} \\ 4 \ln(2\gamma_F) - 5 \\ -\frac{8}{3} \\ 4 \ln(2\gamma_F) - 7 \end{pmatrix}, \quad \gamma_F \gg 1. \quad (4)$$

It follows from (3) and (4) that in the case of nonrelativistic neutrino the contribution of the effect of finite density to the total probability of the process increases strongly with the increase in the medium density and it becomes the main contribution. Thus in a logarithmic approximation where

$$\ln(\gamma_F) = \ln(\mu/m_e) \gg 1,$$

the main contribution to the probability of the process is defined just by the plasma amplitude $S_{ij}^{(2)}$.

The dependence of the probability of the process on the angle ψ between the neutrino momentum and the magnetic field direction becomes essential with the increase in the energy of decaying neutrino. In the limit case of relativistic neutrino and arbitrary density of electron gas, we obtain the following asymptotic expressions for the total probability of decay:

$$w = w_0 \frac{q_0}{m_i} \begin{cases} \sin^2 \psi \cos^2 \psi, & \gamma_F \gg 1, \\ \sin^2 \psi (1 - \cos \psi)^2, & \gamma_F^2 - 1 \ll 1, \end{cases} \quad (5)$$

where q_0 is the energy of initial neutrino.

For comparison, in figure 2 dependencies of the total probability of decay on the angle ψ between the relativistic neutrino momentum and the magnetic field direction in dense medium and without a medium are shown. Note that in [2] the vector of the magnetic field was shown by mistake in the opposite direction. It should also be noted that our result for w_1 in formula (5) is in

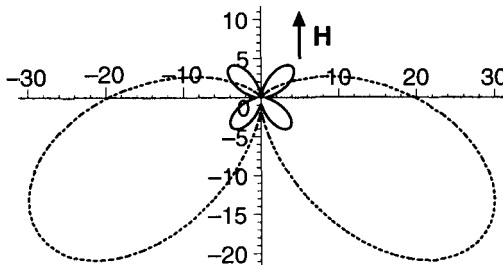


Figure 2: Integral probability of decay $\nu_i \rightarrow \nu_j + \gamma$ as a function of the angle between the initial neutrino momentum and the magnetic field direction ($q_0/m_i \simeq 20$) in dense medium ($\mu/m_e \simeq 15$, solid line) and without medium (dashed line). On the graph the magnitude w/w_0 , where $w_0 = (eH)^2 (eG_F)^2 m_i / (2\pi)^5$ is indicated.

agreement with the similar result of study [8], where the probability of the massive neutrino decay in superstrong magnetic field was calculated.

In summary, we state that our investigation of radiative decay of neutrino in degenerate magnetized plasma makes it clear that both the angular distribution of radiating photons and the total probability of decay depend essentially on the medium density, neutrino energy and external field strength. This result can be considered as an additional proof that in order to produce correct analysis of physical phenomena at different astrophysical conditions it is necessary to take into account, simultaneously, the effect of external field, finite temperature and medium density.

References

- [1] A.V. Borisov, V.Ch. Zhukovskii, A.S. Vshivtsev, P.A. Eminov *Usp. Fiz. Nauk.* **167** (1997) 241.
- [2] A.I. Ternov, P.A. Eminov *J. Phys. G* **29** (2003) 357.
- [3] A.E. Shabad *Tr. Fiz. Inst. Akad. Nauk SSSR.* (1988) 5.
- [4] V.M. Lipunov *Astrophysics of Neutron Stars* (Nauka, Moscow), 1987.
- [5] D.V. Galtsov, N.S. Nikitina *Zh. Eksp. Teor. Fiz.* **62** (1972) 2008; V.V. Skobelev *ibid* **108** (1995) 3.
- [6] L.A. Vasilevskaya, A.A. Gvozdev, N.V. Micheyev *Yad. Fiz.* **57** (1994) 124; *Phys. Rev. D* **54** (1996) 5674.
- [7] V.Ch. Zhukovskii, P.A. Eminov, A.E. Grigoruk *Mod. Phys. Lett. A* **11** (1996) 3113.
- [8] M. Kachelriess, G. Wunner *Phys. Lett. B* **390** (1997) 263.
- [9] A.A. Sokolov, I.M. Ternov *Radiation from Relativistic Electrons* (AIP, New York), 1986 [Russian original: *Relyativistskiy Elektron*, Nauka, Moscow, 1983].

BETA DECAY IN EXTERNAL FIELD AND NEUTRINO MASS

O.Dorofeev, A.Lobanov^a

Physics Faculty of Moscow State University, 119992 Moscow, Russia

Abstract. The results of the investigation of electromagnetic field effects on the process of beta decay are used for analyzing experimental data on direct neutrino mass search.

The investigation of the effect of electromagnetic fields on the process of beta decay was started long ago. In particular, the effect of plane-wave fields on this process was discussed in [1–3]. The obtained results indicate that beta spectrum is strongly affected by electromagnetic radiation. On the other hand spectral distribution of β -electrons is most sensitive to neutrino mass m_ν . In papers [1–3] the emphasis was made on very strong fields. In our work we consider very weak fields and their effect on beta spectrum.

Let us choose the monochromatic circularly polarized plane wave with frequency ω and intensity E as the model of external field and suppose that $\omega \ll m_\nu$. Then the total probability of the allowed β -decay for the model with massive Dirac neutrino is:

$$\frac{W}{\tilde{W}} = \frac{\xi^2}{4} \left\{ \int_{t_1}^{t_2} dt \int_{y_1}^{\varepsilon_0 - \mu} dy \Phi(t, y) + \Theta(\xi_0 - \xi) \int_{t_0}^{t_1} dt \int_{y_1}^{y_2} dy \Phi(t, y) \right\}. \quad (1)$$

Here

$$\begin{aligned} \Phi(t, y) &= (t + y)y(\varepsilon_0 - y) [(\varepsilon_0 - y)^2 - \mu^2]^{1/2} [\xi^2 + (y - t)^2]^{-3/2}, \\ t_0 &= 1, \quad \xi_0 = [2(\varepsilon_0 - \mu - 1)]^{1/2}, \quad \beta = (1 - 1/t^2)^{1/2}, \end{aligned} \quad (2)$$

where

$$\xi = eE/m\omega, \quad \mu = m_\nu/m, \quad t = p^0/m, \quad \varepsilon_0 = (M_i - M_f)/m, \quad (3)$$

and e, m, p^0 are the charge, mass and total energy of β -electron. The lower and upper limits of the integral (1) are given by

$$\begin{aligned} t_{1,2} &= (\varepsilon_0 - \mu)(1 + \xi^2/2) \mp \xi(1 + \xi^2/4)^{1/2} [(\varepsilon_0 - \mu)^2 - 1]^{1/2}, \\ y_{1,2} &= t[1 + \xi^2/2 \mp \xi(1 + \xi^2/4)^{1/2}\beta]. \end{aligned} \quad (4)$$

For the neutron and approximately for tritium we have $\tilde{W} = G_F^2 m^5 (1 + 3\alpha_0^2)/2\pi^2$, where α_0 is the ratio of the axial and vector constants of weak interaction, and G_F is the Fermi constant.

The behavior of the spectrum is illustrated by plots in Fig. 1 – 5, where W_0 is the total probability of beta decay without external field.

^ae-mail: lobanov@th466.phys.msu.su

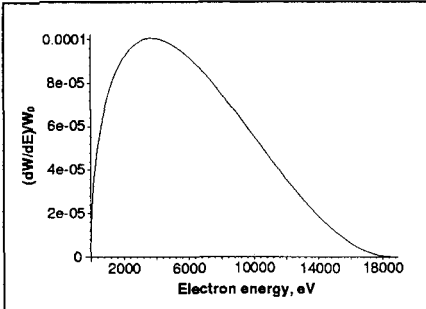
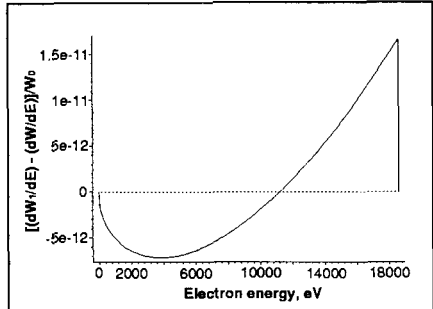
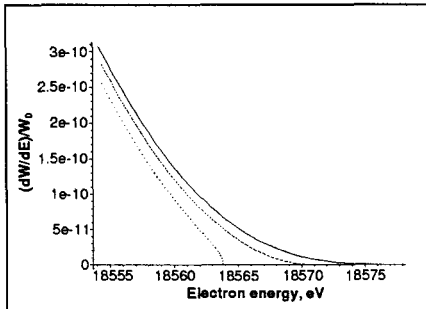
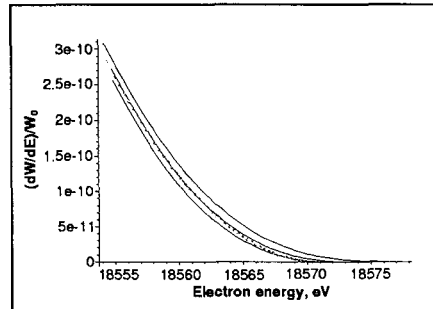


Figure 1: Tritium beta spectrum.

Figure 2: Tritium beta spectrum: $m_\nu = 0$; W corresponds to $\xi = 0$, W_1 corresponds to $\xi = 0.00005$.Figure 3: Tritium beta spectrum near its end point: dashed line corresponds to $m_\nu = 0$, $\xi = 0$; dotted line corresponds to $m_\nu = 6.8$ eV, $\xi = 0$; solid line corresponds to $m_\nu = 0$, $\xi = 0.00005$.Figure 4: Tritium beta spectrum near its end point: circles correspond to $\xi = 0$, $m_\nu = 0$; solid lines correspond to $\xi = 0.00005$, $m_\nu = 0$; 5.1 eV; 6.8 eV.

When $\xi \ll 1$,

$$t_{max} \approx \varepsilon_0 - \mu + \xi(\varepsilon_0^2 - 1)^{1/2}. \quad (5)$$

Eq. (5) allows us to evaluate the field strength, which is required to observe the effect. If the shift of the spectrum end point induced by neutrino mass is equal to the shift induced by external field, one has

$$E\lambda = \frac{2\pi}{\sqrt{\varepsilon_0^2 - 1}} m_\nu. \quad (6)$$

Here E is the radiation field strength (V/m), λ is the wavelength of radiation (m), and m_ν is the neutrino mass (eV).

For tritium $\varepsilon_0 \approx 1.03634$, and the shift of the spectrum end point induced by neutrino mass ~ 1 eV is equal to the shift induced by microwave radiation with the strength $\sim 10\text{-}100$ V/m.

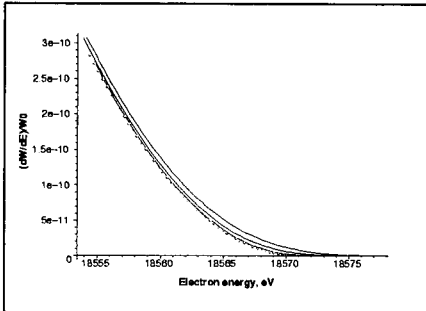


Figure 5: Tritium beta spectrum near its end point: circles correspond to $\xi = 0$, $m_\nu = 0$; solid lines correspond to $m_\nu = 0$, $\xi = 0.00005$; 0.000034 ; 0.000017 .

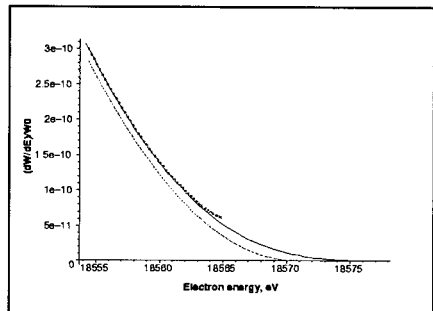


Figure 6: Tritium beta spectrum near its end point: dashed line corresponds to $\xi = 0$, $m_\nu = 0$; solid line corresponds to $\xi = 0.00005$, $m_\nu = 0$; circles correspond to $\xi = 0$, $m_{eff}^2 = -25$ eV².

For $t < t_1$ and $t > t_1$ analytical expressions for beta spectrum are different. If $\mu = 0$, $\xi \ll 1$, $\varepsilon_0 - t \ll 1$, $t < t_1$ the following approximation exists (Fig. 6):

$$\frac{d(W_{eff}/\tilde{W})}{dt} = t\sqrt{t^2 - 1} \left[2(\varepsilon_0 - t)^2 - (\varepsilon_0 - t)\sqrt{(\varepsilon_0 - t)^2 - \mu_{eff}^2} \right], \quad (7)$$

where

$$\mu_{eff}^2 = 2\xi^2 \left[\frac{\varepsilon_0}{\sqrt{\varepsilon_0^2 - 1}} \ln \left(\varepsilon_0 + \sqrt{\varepsilon_0^2 - 1} \right) - 1 \right]. \quad (8)$$

This approximation was used for analyzing experimental data [4, 5] (the so called “negative neutrino mass squared”). Thus the electromagnetic radiation could be the reason for experimentally observed anomaly in tritium beta spectrum.

Using the Curie plot

$$C \sim \sqrt{\frac{dW/dt}{t(t^2 - 1)^{1/2}}}, \quad (9)$$

we can make the representation of our results more obvious (Fig. 7).

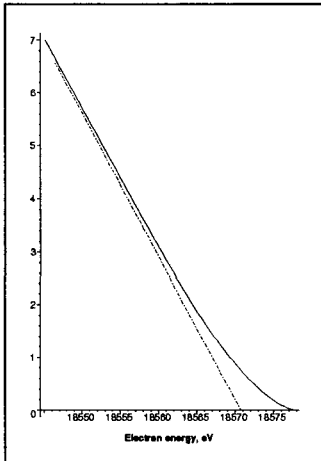


Figure 7: Curie plot for tritium in arbitrary units: solid line corresponds to $m_\nu = 0$, $\xi = 0.00005$; dashed line corresponds to $m_\nu = 0$, $\xi = 0$.

The numerical estimations demonstrate that the shift in the tritium beta spectrum, which corresponds to neutrino mass ~ 1 eV (the limiting accuracy of experiments [4,5]), can be compensated by a microwave radiation field with the strength of the order tens of V/m. In planned experiment KATRIN [6,7], in which the measurement accuracy is supposed to be of the order of 0.1 eV, this can be produced by fields with the strength of the order units of V/m, which is comparable with background values.

In the analysis of the experimental data, one should investigate the role of possible external sources of radiation, as well as radiation of beta electrons. In fact, since in chambers of experimental setups there exist constant magnetic fields with the magnitude of the order units of Tesla, maximum of β -electron electromagnetic radiation belongs to cm-range.

It should be noted that in a more detailed investigation it is necessary to allow for effects related to the energy loss due to transitions to excited states of molecular tritium (see [8]), but in our opinion this factor cannot change main conclusions of the present work.

- [1] Ternov I.M., Rodionov V.N., Lobanov A.E., and Dorofeev O.F. *Pisma v Zh. Eksp. Teor. Fiz.* 37 (1983) 288.
- [2] Ternov I.M., Rodionov V.N., Dorofeev O.F., Lobanov A.E., and Pavlova O.S. *Yad. Fiz.* 39 (1984) 1125.
- [3] Ternov I.M., Rodionov V.N., Zhulego V.G., Lobanov A.E., Pavlova O.S., and Dorofeev O.F. *J. Phys. G* 12 (1986) 637.
- [4] Weinheimer Ch., Degenddag B., Bleile A. et al. *Phys. Lett. B* 460 (1999) 219.
- [5] Lobashev V.M., Aseev V.N., Belesev A.I. et al, *Phys.Lett.B* 460 (1999) 227.
- [6] KATRIN Collaboration, Osipowicz A. et al. *hep-ex/0109033* (2001).
- [7] Weinheimer Ch. *hep-ex/0210050* (2002).
- [8] Jonsell S. and Monkhorst H. *J. Phys. Rev. Lett.* 76 (1996) 4476.

NEUTRINO OSCILLATIONS AND NEUTRINO PHYSICS AT SUPER-KAMIOKANDE

Kenneth S. Ganezer ^a for the Super-Kamiokande Collaboration

Department of Physics, California State University Dominguez Hills, Carson, CA 90747 USA

Recent measurements from Super-Kamiokande on atmospheric, solar, and possible supernova neutrinos with emphasis on neutrino oscillations, are given here. Results of two and three flavor oscillation analyses are summarized for atmospheric and solar neutrinos from Super-K-I. A brief synopsis of data analysis for Super-K-II, the post accident phase of SK, is also given. Future plans for Super-K are briefly mentioned.

The results presented at the conference and also the recent developments can be found in the following papers:

- [1] S Desai et al. (the Super-Kamiokande collaboration), Phys.Rev.D70 (2004) 083523, Erratum-ibid Phys.Rev.D70 (2004) 109901.
- [2] Y.Ashie et al. (the Super-Kamiokande collaboration), Phys.Rev.Lett.93 (2004) 101801.
- [3] D.W.Liu et al. (the Super-Kamiokande collaboration), Phys.Rev.Lett.93 (2004) 021802.
- [4] M.B.Smy et al. (the Super-Kamiokande collaboration), Phys.Rev. D (Rap.Comm.) 69 (2004) 011104, 15.
- [5] J.Yoo et al. (the Super-Kamiokande collaboration), Phys.Rev.D68 (2003) 092002.
- [6] Y. Gando et al. (the Super-Kamiokande collaboration), Phys.Rev.Lett.90 (2003) 171302.
- [7] Y.Fukuda et al. (the Super-Kamiokande collaboration), Nucl. Instrum. Meth. Phys. Res.A 501 (2003) 418.
- [8] M.Malek et al. (the Super-Kamiokande collaboration), Phys.Rev.Let. 90 (2003) 061101.

^ae-mail: kganezer@csudh.edu

- [9] S.Fukuda et al. (the Super-Kamiokande collaboration), ApJ.Lett.578 (2002) 317.
- [10] S.Fukuda et al. (the Super-Kamiokande collaboration), Phys.Lett.B539 (2002) 179.
- [11] S.Fukuda et al. (the Super-Kamiokande collaboration), Phys. Rev. Lett. 86 (2001) 5651.
- [12] S.Fukuda et al. (the Super-Kamiokande collaboration), Phys. Rev. Lett. 86 (2001) 5656.
- [13] K.Ganezer, Int.J.Mod.Phys.A16S1B (2001) 855.
- [14] E.Blaufuss et al. (the Super-Kamiokande collaboration), Nucl. Inst. & Meth. Phys. Res.A458 (2001) 636.
- [15] Y.Fukuda et al. (the Super-Kamiokande collaboration), Phys. Rev. Lett. 85 (2002) 3999.
- [16] Y.Fukuda et al. (the Super-Kamiokande collaboration), Phys.Lett.B467 (1999) 185.
- [17] K.Ganezer, in: Proc.of the 26th Int.Cosmic Ray Conf., Salt Lake City, Utah, V.2 (1999).
- [18] Y.Hayato et al. (the Super-Kamiokande collaboration), Phys. Rev. Lett. 83 (1999) 1529.
- [19] T.Futagami et al., Phys.Rev.Lett. 82 (1999) 5194.
- [20] Y.Fukuda et al., Phys.Rev.Lett.82 (1999) 2430.
- [21] Y.Fukuda et al., Phys.Lett.B452 (1999) 418.
- [22] Y.Fukuda et al., Phys.Rev.Lett.82 (1999) 2644.
- [23] M. Nakahata et al., Nucl. Inst. & Meth. Phys. Res. A421 (1999) 113.
- [24] M.Shiozawa et al., Phys.Rev.Lett.81 (1998) 3319.
- [25] Y.Fukuda et al., Phys.Rev.Lett.81 (1998).
- [26] Y.Fukuda et al., Phys.Lett.B433 (1998) 9.
- [27] Y. Fukuda et al., Phys. Rev. Lett. 81, (1998) 1158.
- [28] Y.Fukuda et al.,Phys.Lett.B436 (1998) 33.
- [29] V.Barger et al., Phys.Rev.D65 (2002) 053016.
- [30] M.C.Gonzalez-Garcia and Y.Nir, Rev.Mod.Phys.75 (2003) 345.
- [31] Q.R.Ahmed et. al. (the SNO collaboration), Phys.Rev.Lett.87 (2001) 071301; Q.R.Ahmed et. al. (the SNO collaboration), Phys.Rev.Lett.89 (2002) 011301.
- [32] Q.R.Ahmed et. al. (the SNO collaboration), Phys.Rev.Lett.89 (2002) 011302.
- [33] K. Eguchi et. al. (the KamLAND collaboration), submitted to Phys.Rev.Lett., arXiv:hep-ex/0212021.
- [34] J.F.Beacom, R.N.Boyd, A.Mezzacappa, Phys.Rev.D63 (2001) 073011.

ASTROPARTICLE PHYSICS WITH AMS02

V.Zhukov ^a

on behalf of AMS02 collaboration

Institut für Experimentelle Kernphysik, Universität Karlsruhe (TH), P.O. Box 6980, 76128 Karlsruhe, Germany and

Institute of Nuclear Physics, Moscow State University, 119992 Moscow, Russia

Abstract. The Alpha Magnetic Spectrometer (AMS) scheduled for flight on board of International Space Station will measure cosmic ray energy spectrum and chemical composition up to TeV range. In this review we discuss a discovery potential of this detector in the highlight of recent experimental data and developments in theory.

1 Introduction

There are few important ingredients in our understanding of the Universe which motivate new experiments.

Experimental data proves that the universe consists mostly of matter, at least in our ~ 20 Mpc neighborhood [1]. The observations of element abundances are favored to $\frac{N_B}{N_\gamma} \sim 3 \cdot 10^{-10}$ contrary to expected $\sim 10^{-18}$ from the baryon symmetric universe. Different baryogenesis scenarios predict such asymmetry but the exact ratio of the cosmic matter to antimatter is unknown parameter. This ratio can be estimated from the chemical composition of cosmic rays.

Cold Dark Matter (CDM) makes up $\sim 23\%$ of the energy of the universe in comparison with $\sim 5\%$ for the baryonic matter, as deduced from the temperature anisotropies in the Cosmic Microwave Background in combination with the Hubble parameter and the density fluctuations in galaxies [2,3]. According to the inflation model [4] the CDM has played an important role during formation of structures acting as a seed for the baryonic matter. There is an evidence of the CDM Halo around galaxies from the stars rotation curves. However the spatial distribution of the CDM is unknown and can be estimated nowadays only from N-body cosmological simulations [5].

Supersymmetric(SUSY) extension of Standard Model(SM) cures the SM hierarchy and fine tuning problems [6]. It predicts a stable neutral particle which can be a candidate for the non baryonic CDM. There are no solid experimental evidence of the existance of SUSY particles. If the relic CDM is a supersymmetric neutralino it can annihilate. The stable decay products are neutrinos, photons, protons, antiprotons, electrons and positrons which can be observed in cosmic rays. The anisotropy of the signal, if exists, can tell us about the CDM distribution.

Production and propagation of cosmic rays (CR), especially at super high energies, is still very much unknown. Chemical composition of CR is relatively

^ae-mail: zhukov@ekp.physik.uni-karlsruhe.de

well known from the satellite and balloon experiments up to ~ 10 GeV/nucleon but above this only energy spectrum is measured by the ground based extensive air shower arrays. There are few knees in this spectrum which can be related to the changes in the composition. Current galactic models correctly predict element abundances but calculate too few antiprotons, too few hard positrons and too few hard gammas [7, 8] in respect to existing experimental data. Precise CR measurements are needed to improve the models.

Measurement of cosmic ray energy spectra and composition are the main objective of the next decade space born experiments like AMS02, GLAST, Pamela. They will extend energy range up to hundreds GeV with typical geometrical acceptances of $0.9m^2\text{sr}$, $1.2m^2\text{sr}$ (only for gamma rays) and $0.002m^2\text{sr}$ respectively.

2 AMS02 detector

The AMS02 is an experiment planned on board of International Space Station for at least three years mission starting from ~ 2007 [9]. The precursor flight in 1998 on board of shuttle Discovery have demonstrated feasibility of the detector design. The detector inherits most of the components from accelerator experiments, see Figure 1, and consists of:

Superconductive magnet with the maximum dipole field of 0.87 T. The 2.3 tonnes magnet is cooled down to 1.8K by 2500 liters of superfluid He.

Eight layers of double sided silicon tracker with a total area of $6.2m^2$ in the magnet aperture are measuring particle tracks with an accuracy of 17μ in the bending and $30\mu\text{m}$ in the opposite plane. The rigidity $R = \frac{p_c}{Z_e}$ is reconstructed with a resolution better then 4% below 100GV. The Tracker can be used for particle identification ($\frac{dE}{dx} \propto Z^2$) and gamma detection through the pairs conversion.

The Time of Flight (ToF) scintillator hodoscope, with two planes on top and two at the bottom of the Tracker, is used for trigger, velocity measurements with $\frac{\Delta\beta}{\beta} \sim 3.5\%$ and estimation of ionization losses up to GeV range.

The Transition Radiation Detector(TRD) on top of the AMS provides e/h separation with a factor of 100-1000 in the range of E=1-250GeV and an additional tracking. The TRD is built from 20 layers of 6mm Kapton straw tubes filled with Xe/CO₂ and interposed with 22mm fleece radiator.

The ring imaging Cherenkov detector (RICH) is installed bellow the Tracker and uses 2cm thick Aerogel radiator with n=1.035 and the pixel type PMT array. The RICH measures velocity up to 20 Gev with an accuracy of $\frac{\Delta\beta}{\beta} \sim 0.1\%$ and absolute charge for particle ($N_{ph} \propto Z^2$) up to Z=26 with a resolution of $\sigma=0.2$.

The $65 \times 65\text{cm}^2$ electromagnetic calorimeter (ECAL) at the bottom of AMS has 18 x-y planes of scintillators fibers grooved in the lead plates with the

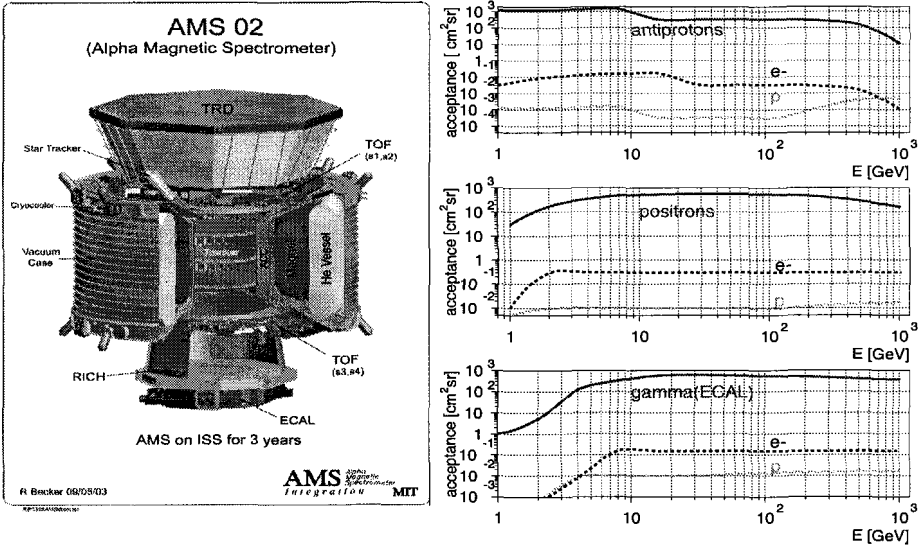


Figure 1: Sketch of *AMS02* and simulated acceptances for signals and backgrounds.

total thickness of $16X_0$ and the weight of 640kg. The ECAL measures lepton energies with a resolution of $dE/E = 0.03 + \frac{0.13}{\sqrt{E[\text{GeV}]}}$ and provides lepton/h separation ~ 1000 up to 1TeV.

The acceptance of the detector to different astroparticles is defined by the geometrical acceptance and the efficiency of particle reconstruction. The selection criteria are optimized by MC simulations in order to keep the significance $S = \frac{N_{\text{signal}}}{\sqrt{N_{\text{signal}} + N_{\text{bkg}}}}$ high. Figure 1 shows the simulated acceptances for antiprotons, positrons and gamma together with the background acceptances [10]. In the range of 1-400 GeV the typical reconstructed acceptance is in the order of $0.05\text{m}^2\text{sr}$.

3 Antimatter search

The mechanism of the baryonic symmetry breaking prior to baryons formation was proposed by Sakharov [11] and based on three obligatory conditions: baryon charge violation, C(CP) violation and deviation from thermal equilibrium. The violation of baryonic number is naturally followed from Grand Unified Theories where leptons and quarks are considered to be members of one gauge group and the B-violating decay of massive $M_x \geq 10^{14}\text{GeV}$ gauge boson is responsible for the baryon asymmetry. The C and CP violation already exists in the SM although the strength observed in the $K^o - \bar{K}^o$ system is not enough

to explain the existing asymmetry. The departure from thermal equilibrium at $T \sim M_x$ is needed to prevent back recombination and is a consequence of the expansion of the universe. The classical model of baryogenesis does not predict any primordial antimatter. However there are models which do not exclude the existence of antimatter in space and explain existing asymmetry. For example the spontaneous baryogenesis [12] predicts macroscopically large separated domains of the primordial antimatter with the mass of $10^3 - 10^5 M_\odot$. Such local antimatter clusters can survive in the halo of our galaxy and can be the source of antimatter in CR. The expected fraction of antihelium is $\overline{He}/He \sim 10^{-8} - 10^{-6}$ at $E > 0.5 \text{ GeV/n}$. If such domains had existed during primordial nucleosynthesis they would affect light elements abundances by annihilation with the matter [13], see figure 2. There are other models like SUSY condensate baryogenesis where the excessive baryonic charge can be accumulated during inflation and then released by decays to baryons. Depending on the CP violation this model can produce different amount of antimatter. Another source of large amount of antimatter can be evaporation of primordial antimatter black holes. The residuals of the not collapsed antimatter around the black holes can produce extra radiation due to annihilation [12] and detected. In this model heavy antimatter can be produced up to iron. All these models are rather speculative and are waiting for experimental confirmation.

The antiparticles can be directly observed in cosmic rays. The background is caused by antiparticles produced in secondary nuclear interactions of ordinary CR. The production rate is estimated to be $\frac{\bar{p}}{p} \sim 10^{-5}$, $\frac{\overline{^3He}}{^3He} \sim 10^{-14}$, $\frac{\overline{^4He}}{^4He} \sim 10^{-20}$. For antihelium the expected signal from antimatter domains is about 6 orders of magnitude larger but the measured antihelium flux can be significantly lower due to propagation.

For the direct observation of antinucleus one needs a magnetic spectrometer for charge sign measurements and a RICH for the absolute charge reconstruction. Main experimental background is coming from the secondary interactions with the detector material, multiple scattering in the spectrometer and can be significantly suppressed by the anticoincidence counters and optimization of selection cuts. For AMS02 the expected background rejection for antihelium is $\geq 10^9$. Figure 2 shows a summary of the experimental search of antihelium in CR and expectation for the AMS02 experiment. There are also experimental limits for heavier antiparticles with $2 < Z \leq 6 : \frac{\bar{N}}{N} \leq 3.10^{-5}$ in the rigidity range of 1-140GV [14].

Antimatter can be detected indirectly; annihilation of antimatter with the matter will produce a characteristic γ -ray spectrum with a peak near 1 Mev from the $\pi^{0,\mp}$ decays and steepening cutoff at $\sim 1 \text{ GeV}$. The diffusive γ spectrum measured by COMPTEL and EGRET [1] in the energy range 1MeV-20GeV shows no such behavior and can be explained by the normal production mechanism

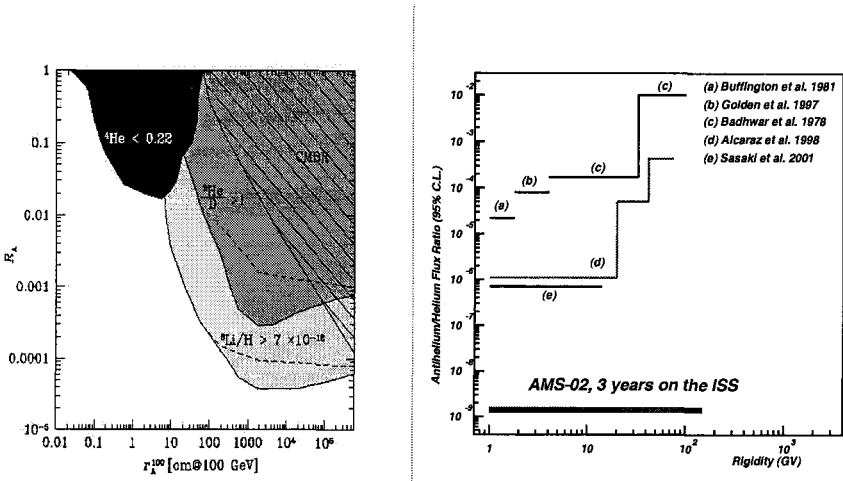


Figure 2: *Left plot shows limits on the antimatter to matter ratio versus size of antimatter domains after Big Bang at $T = 100\text{GeV}$. [13]. Shaded regions are excluded by light element abundances. On the right are the experimental limits and the expectation for AMS02.*

4 Cosmic rays production and propagation

The sources of charged and neutral cosmic rays are believed to be supernovae and their remnants, pulsars, stellar winds, etc. Such sources can accelerate charged particles up to 10^{16}GeV , higher energies are probably of extragalactic origin and produced by Active Galactic Nuclei. The primary source function usually is taken as a power-law: $Q(p) \propto (\frac{R}{R_o})^{-2.1-2.4}$ for nucleons. Charged particles accelerated near the sources propagate in the interstellar medium and galactic magnetic field where they can loose energy by ionization (mostly protons and nucleons), bremsstrahlung, synchrotron and inverse Compton (mostly for electrons and positrons) or gain energy via diffusive reacceleration and produce secondary particles and γ -rays by radioactive decay, fragmentation and radiation. Propagation usually is described as a diffusion and convection in spatial coordinates with a diffusion coefficient $D_x = \beta D_o(R/R_o)^\delta$, \vec{V}_c -convection velocity and reacceleration in the momentum phase space with the D_p (v_A), where v_A is the Alfen speed. The fragmentation and decay are characterized by characteristics times τ_f and τ_d . For each charged component propagation can be written as [17]:

$$\frac{\partial \varphi}{\partial t} = q(\vec{r}, p) + \vec{\nabla}(D_x \vec{\nabla} \varphi - \vec{V}_c \varphi) + \frac{\partial}{\partial p} p^2 D_p \frac{\partial}{\partial p} \frac{1}{p^2} \varphi - \frac{\partial \varphi}{\partial p} [\dot{p} \varphi - \frac{p \vec{V} \vec{V}_c \varphi}{3}] - \frac{1}{\tau_f} \varphi - \frac{1}{\tau_d} \varphi$$

The parameters α , D_o , δ , D_p , \vec{V}_c together with the galactic halo size z_h define the model which provides information about the cosmic ray fluxes and

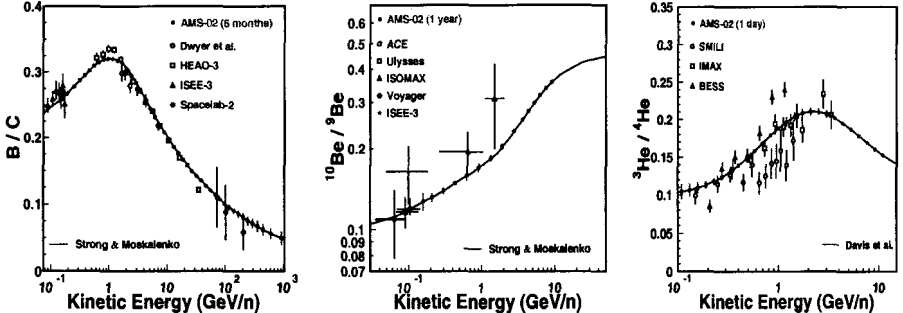


Figure 3: *Ratios of abundances calculated by [17], recent experimental data and expectations for AMS02.*

element abundances. Most of these parameters can be constrained by the isotopic distributions in cosmic rays. Diffusion parameters and primary source spectrum can be estimated from the secondary to primary nucleons ratios: B/C ($^{12}\text{C} \rightarrow ^{10}\text{B}, ^{11}\text{B}$), sub-Fe/Fe. The size of galaxy and V_c can be defined from ratios of secondary long/short lived isotopes $^{10}\text{Be}/^{9}\text{Be}$, $^{26}\text{Al}/^{27}\text{Al}$, $^{12}\text{Cl}/^{13}\text{Cl}$ used as a “radioactive clock”. The ratio $^{3}\text{He}/^{4}\text{He}$ and abundances of K capture isotopes are sensitive to the interstellar density. In figure 3 the experimental data for the B/C , $^{10}\text{Be}/^{9}\text{Be}$, $^{3}\text{He}/^{4}\text{He}$ and calculation from [17] are shown. Such model tuned to the existing experimental data can perfectly describe observed element abundances but fails to reproduce the antiproton and with less extent the positron spectra (see Figure 5).

The gamma rays has two components: from point sources and diffusive emission. The point sources have a big variety of energy spectra's but contributes only a few percent to the total gamma flux. The AMS02 will be able to identify direction of incoming γ rays in 10-200GeV range with an acceptance of $\sim 0.05\text{m}^2\text{sr}$ a) in the Tracker through $\gamma \rightarrow e^+e^-$ conversion with a resolution of $< 0.1^\circ$ b) in the ECAL with a resolution of $\sim 2.5^\circ$. The diffusive component can be split on the isotropic extragalactic one with a spectrum $E^{-2.1}$ and the anisotropic galactic emission $\propto E^{-2.7}$ produced by π^0 decays, bremsstrahlung of charged components and inverse Compton on interstellar radiation fields. The propagation model generates too few galactics in the range of 2-50GeV [8].

The explanation of the observed excesses would require introduction of the “Local Bubble Hypothesis” for antiprotons and harder electron and nucleon spectrum in the production sites for gammas.

The AMS02 will measure precisely the chemical composition and gamma rays up to the TeV range.

5 Indirect Dark Matter search

There are many arguments to consider a weakly interacting massive particle(WIMPS) as a CDM candidate [15]. These particles have been produced abundantly after the Big Bang and freeze-out at $T \sim m_\chi/20$. Since then they participate in the structure formation and should have a significant relic density concentrated in the galactic halos. Local density of the spherically symmetric CDM halo is expected to be $\rho_0 = 0.3\text{--}0.7 \text{ GeV/cm}^3$ and the WIMPS can be detected directly by registering nuclear recoil from elastic scattering of WIMPS in the low noise Earth based detectors [15]. There is no confirmed evidence of such signal yet.

The CDM can be detected in space indirectly through the WIMPs annihilation. The stable products of the WIMPS annihilation can be observed as an excess in CR spectra, especially for positrons, antiprotons and gamma where background is small [18]. The signal flux can be calculated as:

$$\frac{dF_i}{dE} = \frac{1}{m_\chi^2} \int \int \rho^2(l) dl \sum_k <\sigma v>_k A(e)_k^i G(E, e)_i de,$$

where m_χ is the WIMPS mass, $\rho(l)$ -distribution of the CDM, $<\sigma v>_k$ - averaged for all WIMPS velocities cross section of k-annihilation channel, $A(e)_k^i$ - hadronization function of the i-stable particle and the $G(E, e)_i$ is a propagation Green function for i-charged particle. For gamma rays $G = 1$ and the integration of $\rho(l)$ is done along line of sight. The hadronization function is relatively well known and can be calculated, the propagation part also can be calculated for the defined model as discussed above. The unknowns are the annihilation cross section, mass m_χ and the CDM distribution.

Supersymmetry [6] suggests a good candidate for CDM and provides tools to calculate the cross sections. It presupposes a symmetry between fermions and bosons and doubling of the particle spectrum. The 'sparticles' and normal particles have an opposite specific charge R and in the R-conservation scenario the lightest sparticles(LSP) should be stable. The SUSY is broken since none of sparticles have been observed i.e. they should be heavier than their SM partners. The supergravity inspired breaking term assume a common mass $m_{1/2}$ for the gauginos and another common mass m_0 for the scalars at the GUT scale, which is determined by the unification of the gauge couplings. In addition, the ratio of the vacuum expectation values of the two Higgs doublets, $\tan \beta$, the trilinear couplings A_0 and sign of Higgs mixing μ are free parameters. These parameters define the mass spectrum and can be constrained by existing limits on Higgs mass $m_h > 114.6 \text{ GeV}$ and electroweak symmetry breaking data $a_\mu, b \rightarrow X_s \gamma$ [16]. The Constrained Minimal SuperSymmetry Model (CMSSM) implies that the LSP is a bino-like neutralino χ with the mass $m_\chi \sim 0.4m_{1/2}$. The neutralino is a Majorana particle and can self annihilate through Z, A

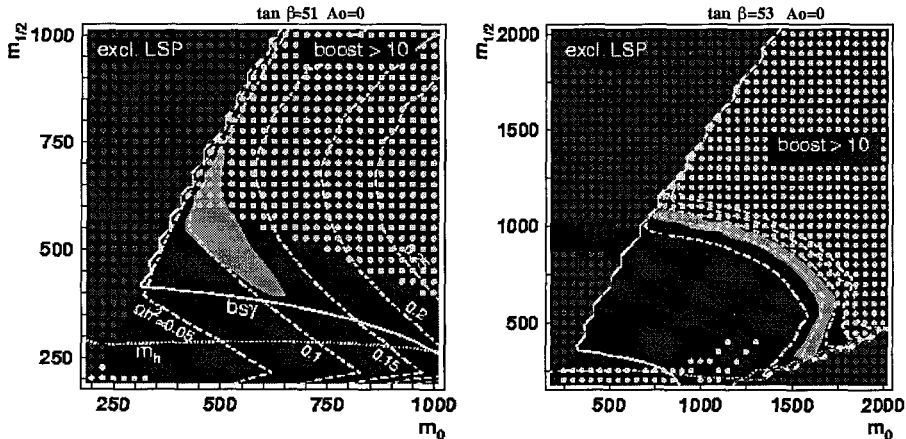


Figure 4: The allowed region in the CMSSM model with $A_o = 0$ and $\tan \beta = 51$ (left), $\tan \beta = 53$ right. The light shaded field is the WMAP region and the $\Omega_{cdm} h^2$ contours with 0.05 steps are indicated. The left excluded region is where LSP is $\tilde{\tau}$ and the low $m_{1/2}$ are excluded by EWSB data. Black dots are the resonance region. The simultaneous fit of gamma, positron and antiprotons fluxes by the model with the neutralino annihilation in the NFW halo profile excludes region where boost factors > 10 is needed.

and sfermion exchange into SM quarks, leptons and W^+W^- , ZZ pairs in the tree level and to $Z\gamma$, $\gamma\gamma$ in one loop diagramms. The parameter space can be further constrained if one will use WMAP results [2] which require $0.016 < \Omega_{cdm} h^2 < 0.024$ and exclude region where LSP is a charged $\tilde{\tau}$, see figure 4. The WMAP limits are satisfied only at large $\tan \beta > 50$ where the resonance region $m_A \sim 2m_\chi$ becomes important. The $\langle \sigma v \rangle$ is increasing with $\tan^2 \beta$ and decreasing as $1/m_{1/2}^2$.

The CDM distribution in the galactic haloes at large r can be constrained from the rotation curves which implies $\rho(r) \propto r^{-2}$. The most important central region can be obtained from cosmological N-body simulations which produce a wide range of profiles [5]. The spherical profiles can be described by a general Navarra-Frenk-White(NFW) type approximation [19]:

$$\rho(r) = \rho_a \left(\frac{r}{a}\right)^{-\gamma} \left[1 + \left(\frac{r}{a}\right)^\alpha\right]^{\frac{1-\beta}{\alpha}},$$

where $(\alpha, \beta, \gamma) = (1, 3, 1)$ and concentration parameter $a=10\text{kpc}$ for the cusped NFW profile, $(2, 2, 0)$ and $a=4\text{kpc}$ corresponds to the more flat isothermal profile without singularity in the center. Since the $F \propto \rho^2$ most of signal is coming from dense regions i.e. galactic center. The CDM halo can have eccentricity up to 0.5 [20] and can rotate [21]. This rotation can involve only a part of the CDM halo “frozen” in the galactic arms with baryonic matter. Moreover the

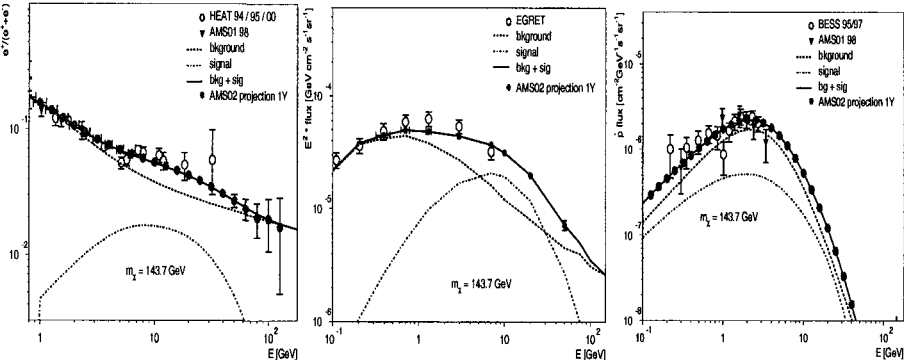


Figure 5: *Positron, gamma and antiproton spectra: experimental data and calculation of CR backgrounds calculated with [17]. The fluxes from neutralino annihilation and expectations for AMS02 are shown. The CMSSM parameters $m_{1/2} = 350$, $m_0 = 500$, $\tan\beta = 50$ and $NFW(1,3,1,10kpc)$ halo profile were used*

CMD distribution can be clumpy which may significantly extent the flux from annihilation [18] although this so called 'boost factor' is likely below 10 [22,23]. The structure and dynamics of the CDM halo can be studied by analysing gamma anisotropy from neutralino annihilation.

Simultaneous study of all components will be possible in the AMS02. Figure 5 shows the energy spectra from neutralino annihilation calculated with the NFW profile and $m_\chi \sim 144\text{GeV}$, backgrounds calculated with [17] and recent experimental data. The contribution from neutralino can explain existing excesses in the positron, gamma and antiproton fluxes. The boost factors are close and are equal to 1.5, 1.1 and 1. respectively. Models with larger m_χ will require larger boost factors or more clumpy halo. The AMS02 will be able to detect such signal after one year of operation with significances around 100, 30 and 60 for positrons, gamma and antiprotons. For positrons and gamma the energy spectrums will have a specific bump depending on neutralino mass, for antiprotons the shape at lower energy is similar to the backgrounds which makes it difficult to distinguish. There is another signal signature which can not be missed: $m_\chi \rightarrow \gamma\gamma, Z\gamma$ produces monochromatic gamma rays with $E_\gamma = m_\chi$, $m_\chi - m_z^2/4m_\chi$. The cross section for this channel is by an order of magnitude smaller and the AMS02 acceptance is not enough to see the signal for the standard NFW type profile unless there are clumps and the boost factor is above 10.

6 Conclusion

The AMS02 detector will measure precisely the cosmic ray energy spectra in the range of 1GeV-1TeV and chemical composition up to Z=26 with the reconstructed acceptance of $\sim 500\text{cm}^2\text{sr}$. Measurements of antiparticle and gamma fluxes can make a major breakthrough in study of Antimatter and Supersymmetric Dark Matter and rule out or confirm a big set of theoretical models.

Acknowledgments

I thank Prof. Wim de Boer, A.Strong, D.Kazakov, V.Choutko, G.Lamanna, C.Sander and A.Pukhov for useful discussions.

References

- [1] S.Kappadath *Astron.Astrophys.Suppl.Ser.***120**, 619 (1996).
- [2] D.N.Spergel et al. *astro-ph/0302209* .
- [3] L.Verde et al. *astro-ph/0302218*.
- [4] A.Linde *Phys.Lett.B* **129** 177 (1983).
- [5] B.Moore et al. *Astroph.J.* **542** L19 (1999).
- [6] W.de Boer *Prog. Part. Nucl. Phys.* **33** 201 (1994).
- [7] I.V.Moskalenko et al. *Astrophys. J.* **565** 28 (2002).
- [8] A.W.Strong et al. *Astrophys. J.* **537** 763 (2000).
- [9] M.Aguilar et al.(AMS collaboartion) *Phys.Rep* **366**, 331 (2002).
- [10] V.Choutko *Nuclear Physics B..Suppl.***113**, 170 (2002).
- [11] D.Sakharov *Pis'ma Z.Exp.Theor.Fiz.* **5** 32, (1967).
- [12] A.Dolgov *Nucl.Phys.Proc.Suppl.***95** 42-6 (2001).
- [13] J.B.Rehm, K.Jedamzik *Phys.Rev. D* **63** 043509, (2001).
- [14] M.Cristinzini et al.(AMS collaboartion) *Proc.27th ICRC*, 1703 (2002).
- [15] L.Bergstrom *hep-ph/0002126*.
- [16] W.de Boer et al. *hep-ph/0309029*.
- [17] A.Strong, I.Moskalenko *astro-ph/9812260*.
- [18] E.Baltz et al. *astro-ph//0211239*.
- [19] J.Navarro et al. *Astroph.J.* **490** 493, (1997).
- [20] Y.P.Jing, Y.Sito. *astro-ph/0202064*.
- [21] V.Debattista *astro-ph/0203381*.
- [22] V.Berezinsky, V.Dokuchaev, Y.Eroshenko *astro-ph/0301551*.
- [23] F.Stoehr et al. *astro-ph/0307026*.

NEUTRALINO ANNIHILATION IN SMALL-SCALE CLUMPS IN THE GALACTIC HALO

V. S. Berezinsky^{†‡ a}, V. I. Dokuchaev^{† b} and Yu. Eroshenko^{† c}

[†]*Institute for Nuclear Research, Russian Academy of Sciences, Moscow, Russia*

[‡]*Laboratori Nazionali del Gran Sasso, INFN, Italy*

Abstract. The enhancement of annihilation signal due to Dark Matter (DM) clumpiness in the Galactic halo, valid for arbitrary DM particles, is described. The mass spectrum of small-scale DM clumps with $M \leq 10^3 M_\odot$ is calculated with tidal destruction of the clumps taken into account within the hierarchical model of clump structure. The mass distribution of clumps has a cutoff at M_{\min} due to diffusion of DM particles out of a fluctuation and free streaming. In the case of neutralino (considered as a pure bino) is a DM particle, $M_{\min} \sim 10^{-8} M_\odot$. The evolution of density profile in a DM clump does not result in the singularity because of formation of the core under influence of tidal interaction. The number density of clumps as a function of their mass, radius and distance to the Galactic center is presented. For observationally preferable value of index of primeval fluctuation spectrum $n_p \approx 1$, the enhancement of annihilation signal is described by factor 2 - 5 for different density profiles in a clump.

1 Introduction

Both analytic calculations [2, 3] and numerical simulations [4–6] predict the existence of dark matter clumps in the Galactic halo. The density profile in these clumps according to analytic calculations [7–10] and numerical simulations [5, 11] is $\rho(r) \propto r^{-\beta}$. An average density of the dark matter (DM) in a galactic halo itself also exhibits a similar density profile (relative to a galactic center) in the both approaches. In the analytic approach of Gurevich and Zybiv (see review [10] and references therein) the density profiles are predicted to be universal, with $\beta \approx 1.7 - 1.9$ for clumps, galaxies and two-point correlation functions of galaxies. In the numerical simulations the density profiles can be evaluated only for the relatively large scales due to the limited mass resolution.

A central cusp (around the central supermassive black hole) in the Galactic halo and the smaller scale clumps result in the enhancement of DM annihilation rate and thus in the stronger signals in the form of gamma-rays, radio emission, positrons and antiprotons. The gamma-ray and radio signal from central cusp in the Galactic halo has been first discussed in [12, 13]. Recently this problem was examined in [14–18]. The enhancement of DM annihilation rate due to the clumpiness of DM halo was first pointed out in [2]. Neutralino annihilation in clumps can result in the very large diffuse gamma-ray flux [19] in the model of the clumpy DM by Gurevich et al. [3]. Calculations of positron and antiproton production in the clumpy DM halo have been performed e. g. in [14] (see

^ae-mail: berezinsky@lngs.infn.it

^be-mail: dokuchaev@inr.npd.ac.ru

^ce-mail: erosh@inr.npd.ac.ru

also [20–22]). The annihilation of DM in the clumps has been studied also in [23–28]. The synchrotron flux from DM annihilation products in clumps in the presence of the Galactic magnetic field is considered in [29]. Constraints on the DM clumpiness in the halos from heating of the disk galaxies is examined in [30, 31].

2 Small-scale clumps in the Galactic halo

The small-scale self-gravitating DMCs (or simply clumps), may be formed in the early universe due to several mechanisms. These DMCs may be formed (i) by the growth of the adiabatic or isothermal fluctuations (originated at inflation) during the matter-dominated epoch; or (ii) from the density fluctuations in the models with topological defects (cosmic strings and domain walls) [2]; or (iii) during the radiation dominating era from the nonlinear isothermal fluctuations (originated by phase transitions in early Universe) [32] or from the large amplitude adiabatic fluctuations [33].

Small-scale clumps are formed only if the fluctuation amplitudes in the spectrum are large enough at the corresponding small scales. The inflation models predict the power-law primeval fluctuation spectrum. If the power-law index $n_p \geq 1$, DMCs are formed in a wide range of scales. During the universe expansion the small clumps are captured by the larger ones, and the larger clumps consist of the smaller ones and of continuously distributed DM. The convenient analytic formalism, which describes statistically this hierarchical clustering, is the Press-Schechter theory [34] and its extensions, in particular ‘excursion set’ formalism developed by Bond et al. [35] (for the clear introduction see [36]). However, this theory does not include the important process of the tidal destruction of small clumps inside the bigger ones. We take into account this process and obtain the mass function for the small-scale DMCs in the Galactic halo. In the case of the power-law spectrum only a small fraction of the captured clumps survives, but even this small fraction is enough to dominate the total annihilation rate in the Galactic halo.

In the hierarchical theory of large-scale structure formation in the Universe the first formed objects have some minimal mass M_{\min} . The value of this mass is determined by the spectrum of initial fluctuations and by the properties of DM particles [3, 37]. This value is crucial for calculation of the DM annihilation rate. The estimates of M_{\min} existing in the literature for neutralino DM are substantially different, from $M_{\min} \sim 10^{-12} M_\odot$ in [38] to $M_{\min} \sim (10^{-7} - 10^{-6}) M_\odot$ in [39].

We consider only the most conservative case of adiabatic fluctuations which enter the non-linear stage of evolution at the matter dominated epoch with the inflation-induced initial power-law power spectrum.

CDM particles at high temperature $T > T_f \sim 0.05 m_\chi$ are in the thermody-

namical (chemical) equilibrium with cosmic plasma, when their number density is determined by temperature. After freezing at $t > t_f$ and $T < T_f$, the DM particles remain for some time in *kinetic* equilibrium with plasma, when the temperature of CDM particles T_χ is equal to temperature of plasma T , but number density n_χ is determined by freezing concentration and expansion of the universe. At this stage the CDM particles are not perfectly coupled to the cosmic plasma.

Collisions between a CDM particle and fast particles of ambient plasma result in exchange of momenta and a CDM particle diffuses in the space. Due to diffusion the DM particles leak from the small-scale fluctuations and thus their distribution obtain a cutoff at the minimal mass M_D . When the energy relaxation time for DM particles τ_{rel} becomes larger than the Hubble time $H^{-1}(t)$, the DM particles get out of the kinetic equilibrium. This conditions determines the time of kinetic decoupling t_d . At $t \geq t_d$ the CDM matter particles are moving in the free streaming regime and all fluctuations on the scale of

$$\lambda_{\text{fs}} = a(t_0) \int_{t_d}^{t_0} \frac{v(t') dt'}{a(t')} \quad (1)$$

and smaller are washed away (here $a(t)$ is the scaling factor of expanding universe and $v(t)$ is velocity of a DM particle at epoch t). The corresponding minimal mass at epoch t_0 , $M_{\text{fs}} = (4\pi/3)r\rho\chi(t_0)\lambda_{\text{fs}}^3$, is much larger than M_D . Numerical calculations below (for neutralino) show that M_D is close to M_{min} from [38] and M_{fs} to M_{min} from [39]. The calculation of the minimal mass M_{min} in the mass spectrum of fluctuations is obviously model dependent. As the DM particle we shall consider the neutralino χ , for which we take the pure bino state ($\chi = \tilde{B}$). As calculations show the temperature of kinetic decoupling for a reasonable range of parameters is $T_d \sim 100$ MeV. As a result we find:

$$t_d = 3.5 \cdot 10^{-5} \left(\frac{m_\chi}{100 \text{ GeV}} \right)^{-1/2} \left(\frac{\tilde{M}}{1 \text{ TeV}} \right)^{-2} \left(\frac{g_*}{10} \right)^{-3/4} \text{ s}, \quad (2)$$

and

$$T_d = 150 \left(\frac{m_\chi}{100 \text{ GeV}} \right)^{1/4} \left(\frac{\tilde{M}}{1 \text{ TeV}} \right) \left(\frac{g_*}{10} \right)^{1/8} \text{ MeV}, \quad (3)$$

where g_* is number of degrees of freedom. We calculate [40] the diffusion coefficient using the method given in [41] (§12). The resulting value determines the minimal mass in the density perturbation spectrum due to diffusion of neutralinos from a fluctuation:

$$M_D = 4.3 \cdot 10^{-13} \left(\frac{m_\chi}{100 \text{ GeV}} \right)^{-15/8} \left(\frac{\tilde{M}}{1 \text{ TeV}} \right)^{-3/2} \left(\frac{g_*}{10} \right)^{-15/16} M_\odot. \quad (4)$$

After the moment of kinetic decoupling t_d , neutralinos move freely in the expanding universe background, $a(t)d\vec{x} = \vec{v}(t)dt$, where \vec{x} is comoving particle coordinates. Free streamig define the minimal mass:

$$M_{\min} = 1.5 \cdot 10^{-8} \left(\frac{m_\chi}{100 \text{ GeV}} \right)^{-15/8} \left(\frac{\tilde{M}}{1 \text{ TeV}} \right)^{-3/2} \left(\frac{g_*}{10} \right)^{-15/16} M_\odot. \quad (5)$$

We use the following parametrization of the density profile in a clump:

$$\rho_{\text{int}}(r) = \begin{cases} \rho_c, & r < R_c; \\ \rho_c \left(\frac{r}{R_c} \right)^{-\beta}, & R_c < r < R; \\ 0, & r > R. \end{cases} \quad (6)$$

In [10] the relative core radius of the clump is estimated as $x_c = R_c/R \simeq \delta_{\text{eq}}^3 \ll 1$ from consideration of the perturbation of the velocity field due to damped mode of the cosmological density perturbations. Here δ_{eq} is an initial density fluctuation value at the end of radiation dominated epoch. In [19] the core is produced for spherically symmetric clump by inverse flow caused by annihilation of DM particles. We show [40] that these phenomena are not the main effects and that much stronger disturbance of the velocity field in the core is produced by tidal forces. The tidally induced relative core radius is

$$x_c \simeq \frac{\pi^{25/3} 3^{13/3}}{5^3} G \rho_{\text{eq}} t_{\text{eq}}^2 \nu^{-2} f^2(\delta_{\text{eq}}) \simeq 0.3 \nu^{-2} f^2(\delta_{\text{eq}}), \quad (7)$$

where ν is the height of the peak density in units of dispersion (the peak-height) $\nu = \delta_{\text{eq}}/\sigma_{\text{eq}}(M)$, $\sigma_{\text{eq}}(M) \equiv \sigma(t_{\text{eq}}, M)$ and function $\delta_{\text{eq}} \sim O(1)$. The variance $\sigma_{\text{eq}}(M) = \sigma_{(0)}$ in the small scale range is found in [42] (see also [43]).

The growth of fluctuations in the non-linear regime we study in the framework of the Press-Schechter theory of hierarchical clustering [34, 36] with the tidal interactions included as the new element [40]. The resulting differential fraction of mass in the form of clumps which escape the tidal destruction in the hierarchical objects is $\xi(n, \nu) d\nu dm/m$ with $\xi(n, \nu) \simeq (2\pi)^{-1/2} e^{-\nu^2/2} (n + 3)y(\nu)$. Here n is an effective perturbation power spectrum index and function $y(\nu) \sim 0.1$ is weakly depends on β . By integrating over ν , we obtain the integral distribution of clumps $\xi_{\text{int}} \simeq 0.01(n + 3)$. This means that, for different n , about $0.1 - 0.5\%$ of clumps survive the stage of tidal destruction in each logarithmic mass interval $\Delta \ln M \sim 1$.

3 Enhancement of DM annihilation signal

We provided the numerical calculations of the enhancement factor η due to DM clumpiness in the Galactic halo for annihilation signal by taking into account the distribution of DM clumps over their masses M and radii R and

the distribution of clumps in the galactic halo [40]. This enhancement factor is a function of the minimal clump mass M_{\min} , for clump density profile with index $\beta = 1$ and for different indices n_p of primeval perturbation spectrum. Numerically $\eta = 5$ for $M_{\min} = 2 \cdot 10^{-8} M_\odot$ and $n_p = 1.0$. It strongly increases at smaller M_{\min} and larger n_p . For example, for $n_p = 1.1$ and $n_p = 1.2$ at the same $M_{\min} = 2 \cdot 10^{-8} M_\odot$, enhancement becomes tremendously large, $\eta = 130$ and $\eta = 4 \cdot 10^3$, respectively. Our approach is based on the hierarchical clustering model in which smaller mass objects are formed earlier than the larger ones, i. e. $\sigma_{\text{eq}}(M)$ diminishes with the growing of M . This condition is satisfied for objects with mass $M > M_{\min} \simeq 2 \cdot 10^{-8} M_\odot$ only if the primordial power spectrum has the value of the power index $n_p > 0.84$. In this case the enhancement of the annihilation signal in fact is absent, $\eta \simeq 1$, for $n_p < 0.9$.

4 Conclusion

We have calculated the number density of the small-scale clumps in the Galactic halo and their distribution over masses M , radii R and distances to the Galactic Center in the framework of the standard cosmological model with the primeval density perturbation $P(k) \propto k^{n_p}$ taken from the inflation models with $n_p \simeq 1$ (the Harrison-Zeldovich spectrum). The most important element of our calculations is inclusion of the tidal interactions, which result in the formation of the clump core and destruction of small-scale clumps. In spite of small surviving probability, $\xi \sim 0.1 - 0.5\%$, clumps in most cases provide the dominant contribution to the annihilation rate in the halo.

The enhancement of the annihilation signal can be characterized by ratio $\eta = (I_{\text{cl}} + I_{\text{hom}})/I_{\text{hom}}$, where I_{cl} is the annihilation signal from the clumps, and I_{hom} - from homogeneously distributed DM particles with the NFW density profile in the Galactic halo. Practically for all allowed values of primeval perturbation spectrum index $n_p \geq 1.0$ the annihilation signal from clumps gives the dominant contribution. This result does not depend on the properties of DM particles.

The clumps which give the dominant contribution to the annihilation signal have approximately the following properties in the case $n_p = 1$: The mass $M \sim M_{\min}$ and $\nu \sim 2.5$, the radius $R \simeq 3.6 \cdot 10^{15}$ cm and the radius of the core $R_c \simeq 1.8 \cdot 10^{14}$ cm, the mean internal density of the clump $\bar{\rho}_{\text{int}} \simeq 2.5 \cdot 10^{-22}$ g cm $^{-3}$, the fraction of the halo mass in the form of these clumps $\xi_{\text{int}} \sim 0.002$, and the mean number density of these clumps in the halo $n_{\text{cl}} \sim 25$ pc $^{-3}$.

Recently HEAT collaboration detected excessive flux of cosmic ray positrons at energy $E \sim 10$ GeV [44]. According to [45], if this positron flux is produced by annihilation of neutralinos the enhancement factor of order of 30 is needed. The calculations presented here show that such enhancement can be reached in the considered scenario at extreme combination of parameters.

Acknowledgments

V.D. and Yu.E. are supported in part by the RFBR grants No. 03-02-16436-a and 02-02-16762-a.

References

- [1] A. Shemi, T. Piran, *Astrophys. J.* 365, L55 (1990).
- [2] J. Silk and A. Stebbins, *Astrophys. J.* 411, 439 (1993).
- [3] A. V. Gurevich, K. P. Zybin, and V. A. Sirota, *Sov.Phys.Usp.* 167, 913 (1997).
- [4] B. Moore et al., *Astrophys.J.Lett.* 524, L19 (1999).
- [5] S. Ghigna, B. Moore, F. Governato, G. Lake, T. Quinn, and J. Stadel, *Astrophys.J.* 544, 616 (2000).
- [6] A. Klypin, S. Gottlober, A. V. Kravtsov, and A. M. Khokhlov, *Astrophys.J.* 516, 530 (2002).
- [7] E. Bertschinger, *Astrophys.J.Suppl.* 58, 39 (1985).
- [8] Y. Hoffman and J. Shaham, *Astrophys.J.* 297, 16 (1985).
- [9] B. S. Ryden and J. E. Gunn, *Astrophys.J.* 318, 39 (1987).
- [10] A. V. Gurevich and K. P. Zybin, *Sov.Phys.Usp.* 165, 723 (1995).
- [11] J. F. Navarro, C. S. Frenk, and S. D. M. White, *Astrophys.J.* 462, 563 (1996).
- [12] V. S. Berezinsky, A. V. Gurevich, and K. P. Zybin, *Phys.Lett.* B294, 221 (1992).
- [13] V. Berezinsky, A. Bottino, and G. Mignola, *Phys.Lett.* B325, 136 (1994).
- [14] L. Bergstrom, J. Edsjo, P. Gondolo, and P. Ulio, *Phys.Rev.* D59, 043506 (1999).
- [15] P. Gondolo and J. Silk, *Phys.Rev.Lett.* 83, 1719 (1999).
- [16] P. Ullio, H. Zhao, and M. Kamionkowski, *Phys.Rev.* D64, 043504 (2001).
- [17] G. Bertone, G. Sigl, and J. Silk, *Mon.Not.R.Astron.Soc.* 337, 98 (2002).
- [18] D. Merritt, M. Milosavljevic, L. Verde, and R. Jimenez, *Phys.Rev.Lett.* 88, 191301 (2002).
- [19] V. Berezinsky, A. Bottino, and G. Mignola, *Phys. Lett.* B391, 355 (1997).
- [20] G. Jungman and M. Kaminkowski *Phys.Rev.* D49, 2316 (1994).
- [21] A. Bottino, C. Favero, N. Fornengo, and G. Mignola *Astropat.Phys.* 3, 77 (1995).
- [22] A. Bottino, F. Donato, N. Fornengo, and P. Salati, *Phys.Rev.* D58, 123503 (1998).
- [23] R. Aloisio, P. Blasi, and A. V. Olinto, astro-ph/0206036.
- [24] A. Tasitsiomi and A. V. Olinto, *Phys.Rev.* D66, 083006 (2002).
- [25] J. E. Taylor and J. Silk, submitted to *Mon.Not.R.Astron.Soc.*; astro-ph/0207299.

- [26] L. Bergstrom, J. Edsjo, and P. Ulio, *Phys.Rev.* D58, 083507 (1998).
- [27] L. Bergstrom, J. Edsjo, and C. Gunnarsson, *Phys.Rev.* D63, 083515 (2001).
- [28] P. Ullio, L. Bergstrom, J. Edsjo, and C. Lacey, *Phys.Rev.* D66, 123502 (2002).
- [29] P. Blasi, A. V. Olinto, and C. Tyler, astro-ph/0202049.
- [30] B. L. Carr and C. C. Lacey, *Astrophys.J.* 316, 23 (1987).
- [31] E. Ardi, T. Tsuchiya, and A. Burkert, astro-ph/0206026.
- [32] E. W. Kolb and I. I. Tkachev, *Phys.Rev.* D50, 769 (1994).
- [33] V. I. Dokuchaev and Yu. N. Eroshenko, *JETP* 94, 5 (2002).
- [34] W. H. Press and P. Schechter, *Astrophys.J.* 187, 425 (1974).
- [35] J. R. Bond, S. Cole, G. Efstathiou, and N. Kaiser, *Astrophys.J.* 379, 440 (1991).
- [36] C. Lacey and S. Cole, *Mon.Not.R.Astron.Soc.* 262, 627 (1993).
- [37] J. E. Gunn et al., *Astrophys.J.* 223, 1015 (1978).
- [38] K. P. Zybin, M. I. Vysotsky, and A. V. Gurevich, *Phys.Lett.* A260, 262 (1999).
- [39] D. J. Schwarz, S. Hofmann, and H. Stocker, *Phys.Rev.* D64, 083507 (2001).
- [40] V. S. Berezinsky, V. I. Dokuchaev, and Yu. N. Eroshenko, *Phys.Rev.* D68, 103003 (2003).
- [41] L. D. Landau, E. M. Lifshits, and L. P. Pitaevsky, *Course of Theoretical Physics: Physical kinetics*, vol. 10, (Pergamon Press, 1981).
- [42] E. V. Bugaev and K. V. Konishchev, *Phys.Rev.* D65, 123005 (2002).
- [43] C. Schmid, D. J. Schwarz, and P. Widerin, *Phys.Rev.* D59, 043517 (1999).
- [44] S. Coutu et al., (HEAT-pbar Collaboration), in *Proceedings of 27th ICRC* (2001).
- [45] E. A. Baltz, J. Edsjoet, K. Freese, and P. Gondolo, astro-ph/0211239.

BIG BANG NUCLEOSYNTHESIS: A BRIEF REVIEW

F.L. Villante^a

Dipartimento di Fisica and Sezione INFN di Ferrara, Via del Paradiso 12, I-44100
Ferrara, Italy

Abstract. We briefly review the physics of Big Bang Nucleosynthesis (BBN), discussing theoretical and observational uncertainties in primordial abundances determinations. We present, moreover, some recent results on active-sterile neutrino oscillations in the early universe and on their effects on BBN.

1 Introduction

Big Bang Nucleosynthesis (BBN) is one of the solid pillars of the standard cosmological model. The theory predicts that relevant abundances of light elements, namely ^2H , ^3He , ^4He and ^7Li , have been produced during the first minutes of the evolution of the Universe. The predictions span about 9 orders of magnitude and are in reasonable agreement with observations. Theoretical calculations are well defined and very precise. However, comparison of theoretical results with observational data is not straightforward because the data are subject to poorly known evolutionary effects and systematic errors. Still, even with these uncertainties, BBN permits to constraint important cosmological parameters and to derive restrictions on the properties of elementary particles and, in particular, of neutrinos.

2 The Physics of BBN

To understand BBN, we must follow the histories of nucleons in the early universe. This is usually done by using numerical codes. However, the main features of BBN can be obtained by simple analytic arguments^b.

Primordial nucleosynthesis occurs at temperatures $T \leq 1$ MeV, which are small with respect to nucleon masses. At these temperatures, the number of nucleons is simply equal to the initial baryon asymmetry of the universe. This quantity is usually parametrized in terms of the *present* baryon to photon ratio:

$$\eta \equiv (N_B - N_{\bar{B}})/N_\gamma , \quad (1)$$

which is related to the baryon density of the Universe by $\Omega_B h^2 = 3.7 \cdot 10^7 \eta$.

The neutron to proton ratio is controlled by the weak processes which interconvert neutron and proton ($n + e^+ \leftrightarrow p + \bar{\nu}_e$ and related reactions). As

^ae-mail: villante@fe.infn.it

^bDue to space limitations, we provide, in this paper, a limited reference list. For a more complete list of references see [1, 2].

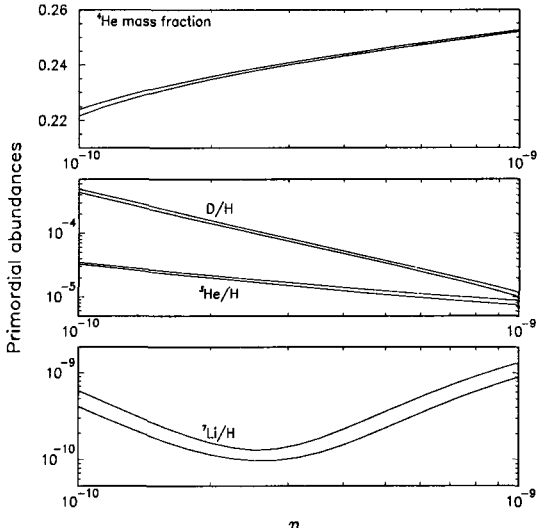


Figure 1: Primordial light element abundances as predicted by standard BBN. The widths of the bands correspond to theoretical uncertainties.

long as the rate of these processes, $\Gamma_W \sim G_F^2 T^5$, is larger than the expansion rate the universe, $H \sim \sqrt{g_* G_N} T^2$ (where g_* counts the total number of relativistic degrees of freedom of the early universe), neutrons and protons are in chemical equilibrium. The neutron abundance, $X_n \equiv n_n/(n_n + n_p)$, is thus given by $X_n = [1 + \exp(\Delta m/T + \xi_e)]^{-1}$, where $\Delta m = 1.29$ MeV is the neutron-proton mass difference and $\xi_e = \mu_e/T$ is the dimensionless chemical potential of electron neutrinos (in standard BBN ξ_e is assumed to be negligible).

When the temperature T drops below $T_f = 0.6 - 0.7$ MeV, the np conversion rate, Γ_W , becomes smaller than the expansion rate the universe ($\Gamma_W \leq H$) and chemical equilibrium can no longer be maintained. The neutron abundance evolves only due to neutron decay, according to $X_n \simeq X_n(T_f) \exp(-t/\tau_n)$, where τ_n is the neutron lifetime. The “freeze-out” temperature T_f scales as $T_f \propto g_*^{1/6}$ and thus is sensitive to the particle content of the early universe. The deviations of g_* from the standard value, $g_* = 10.75$, are usually described in terms of an *equivalent* number of massless neutrinos $N_\nu \neq 3$ according to:

$$g_* = 10.75 + \frac{7}{4}(N_\nu - 3). \quad (2)$$

The larger is g_* (or equivalently N_ν), the earlier is the freeze-out of the neutron abundance, at an higher value, and hence, the larger is the ^4He abundance produced in BBN.

When the temperature of the universe is equal to $T_N \simeq 0.06 - 0.07$ MeV neutrons and protons start to react each other to build up light nuclei. The

exact value of T_N depends on the baryon to photon ratio η . Deuterium, in fact, must be produced in appreciable quantity before the other reactions can proceed at all. Due to the large number of photons per baryon, photodissociation of deuterium is not suppressed until the temperature decreases to $T_N \sim B_d/(15 - \ln \eta)$, where $B_d = 2.2\text{MeV}$ is the deuterium binding energy.

Once deuterium is formed, nucleosynthesis begins and light nuclei are produced rapidly. Essentially all available nucleons are quickly bound into ^4He , which is the most tightly bound light nuclear species. In addition, substantial amounts of ^2H , ^3He and ^4He are produced (see fig. 1). No heavy elements ($A > 8$) are produced, due both to Coulomb-barrier suppression and to the absence of stable isotopes with $A = 5$ and $A = 8$.

Theoretical predictions are affected by uncertainties at the level of 0.2% for ^4He , 5% for ^2H and ^3He and 15% for ^7Li . These are due to uncertainties in the weak rates (which are “normalized” to the measured neutron lifetime $\tau_n = 885.7 \pm 0.8$ s) and in the values of the relevant nuclear reaction rates.

3 Observational Data

The abundances of light elements synthesized in the Big Bang have been subsequently modified through chemical evolution of the astrophysical environments where they are measured. The observational strategy is to identify sites which have undergone as little chemical processing as possible and rely on empirical methods to infer the primordial abundances. For example, measurements of deuterium are made in quasar absorption line systems (QAS) at high redshift; if there is a “ceiling” to the abundance in different QAS then it can be assumed to be the primordial value. The ^4He abundance is measured H II regions in blue compact galaxies (BCGs) which have undergone very little star formation. Its primordial value, Y_p , is inferred either by using the associated nitrogen or oxygen abundance to track the stellar production of helium, or by simply observing the most metal-poor objects. Closer to home, the observed uniform abundance of ^7Li in the hottest and most metal poor Pop II stars in our Galaxy is believed to reflect its primordial value.

As observational methods have become more sophisticated, the situation has become more, instead of less, complex. Relevant discrepancies, of a systematic nature, have emerged between different observers. The present situation for ^2H and ^4He (looking from outside by a non-expert) can be summarized as it follows:

Deuterium

Recent determinations in QAS report values of D/H in the range $D/H \sim 2 - 4 \times 10^{-5}$. However, the dispersion among the different determinations is not consistent with errors in the single measurements (see [7] for detailed discussion). We will use, in the following, the value $D/H = 2.78_{-0.38}^{+0.44} \times 10^{-5}$

given in [7], which is the weighted mean of the log D/H values given by [3–7]. The quoted error is the 1σ error in the mean, given by the standard deviation of the five log D/H values divided by $\sqrt{5}$. This error is used instead of the usual error in the weighted mean, in order to take into account the “anomalous” dispersion of deuterium data.

Helium-4

Independent determinations of Y_p have a statistical errors at the level of 1 – 2% but differ among each others by about $\sim 5\%$. In particular, by using independent data sets, Olive and Steigman [8] and Olive et al. [9] have obtained $Y_p = 0.234 \pm 0.003$, while Izotov et al. [10] and Izotov and Thuan [11] have found $Y_p = 0.244 \pm 0.002$. The discrepancy between different determinations is possibly related to different description of the complex physical processes acting in H II regions. For our estimates, we will use the central values for Y_p reported above ($Y_p = 0.234$ and $Y_p = 0.244$), and the error estimate $\Delta Y_p = 0.005$, which is obtained from the dispersion of the various Y_p determinations.

4 Cosmological Parameters from BBN

The deuterium abundance $D/H = 2.78_{-0.38}^{+0.44} \times 10^{-5}$ can be used to determine the baryon density of the universe. As discussed in [7], the quoted value corresponds to $\eta = 5.9 \pm 0.5 \times 10^{-10}$ (in standard BBN) or, equivalently, to $\Omega_B h^2 = 0.0214 \pm 0.0020$. The error budget is dominated by the observational uncertainties which are about a factor 3 larger than uncertainties in theoretical prediction.

The obtained value for $\Omega_B h^2$ has to be compared with independent determination of the baryon density of the universe. In particular with the result $\Omega_B h^2 = 0.0224 \pm 0.0009$ obtained from a combined fit to the cosmic microwave background (CMB) and large scale structure (LSS) data [12]. The agreement of these two independent determinations is extremely important because they rely on completely different physical phenomena. We note that CMB (and LSS) are presently more accurate than BBN in determining the baryon density of the universe.

The value of η deduced from deuterium can be used, in standard BBN, to predict the abundance of the other elements and to compare with observations. One obtains $Y_p = 0.2476 \pm 0.0010$, ${}^3\text{He}/\text{H} = 1.04 \pm 0.06 \times 10^{-5}$ and ${}^7\text{Li}/\text{H} = 4.5 \pm 0.9 \times 10^{-10}$ (see [7]). It is evident that there is tension between the quoted values and the observational results. The “predicted” abundance for ${}^4\text{He}$ is higher than the “high” helium value of Izotov et al. [10, 11]. Moreover, the “predicted” ${}^7\text{Li}$ abundance is a factor 2-3 larger with respect to the present observational results [13]. The origin of these differences has to be clarified. They could be due to systematic errors in the measurements or to evolutionary effects (e.g. ${}^7\text{Li}$ depletion) or they could be a real indication for non-standard effects in BBN.

In particular, the present D and ${}^4\text{He}$ data seems to favour an equivalent number of neutrino families $N_\nu \leq 3$. In order to understand the present situation, it is useful to combine the deuterium value $D/\text{H} = 2.78_{-0.38}^{+0.44} \times 10^{-5}$, with the “low” helium abundance, $Y_p = 0.234 \pm 0.005$, or with the “high” helium abundance, $Y_p = 0.244 \pm 0.005$. The error $\Delta Y_p = 0.005$ is the “estimated” systematic error in ${}^4\text{He}$ measurements (see above). If we fit these data in the plane (η, N_ν) , we obtain the bound $N_\nu = 2.3 \pm 0.5$ (1σ) in the first case, and $N_\nu = 2.8 \pm 0.5$ (1σ) in the second. In both cases, the central values are below three, even if the errors are large enough to allow for the standard value $N_\nu = 3$. The described results clearly indicate that a large number of effective neutrinos is disfavoured. One can conclude, in principle, that an upper bound on the number of *extra* neutrinos, $\delta N_\nu \equiv N_\nu - 3$, is $\delta N_\nu \leq 0.3$. It is clear, however, that the situation is quite delicate. The error $\Delta N_\nu = 0.5$ is completely dominated by systematic error in ${}^4\text{He}$ measurements. For this reason, we believe that, at present stage, a more safe upper bound on the number of extra neutrinos is $\delta N_\nu \leq 1$. Hopefully in the near future we will be able to derive a stronger limit.

5 BBN and Neutrino Oscillations

Effects of neutrino oscillations on BBN are much different if only active neutrinos are mixed, if only one active and one sterile neutrino are mixed or if we consider the more “complete” case of mixing between three active and one sterile neutrino.

Mixing between active neutrinos

If neutrinos are in thermal equilibrium with vanishing chemical potentials, mixing between active neutrinos does not introduce any deviation from standard BBN results. The situation is more interesting if neutrinos are degenerate. In particular, it was shown recently [14] that, for the mixing parameters which explain the solar neutrino problem ($\delta m^2 \simeq 7 \cdot 10^{-5} \text{ eV}^2$ and $\tan^2 \theta \simeq 0.4$) and the atmospheric neutrino anomaly ($\delta m^2 \simeq 2.5 \cdot 10^{-3} \text{ eV}^2$ and $\tan^2 \theta \approx 1$), asymmetries in the muonic and/or tauonic neutrino sectors would produce, through oscillations, an asymmetry into the electronic neutrino sector. This means that, in presence of oscillations, the BBN bounds on the chemical potential of electron neutrinos applies to all neutrino flavours, i.e. $|\xi_a| < 0.1$ for $a = e, \mu, \tau$.

Mixing between one active and one sterile neutrino

The problem of active-sterile neutrino oscillations in the early universe is quite complex and has been discussed in many papers starting from 1990 (see [1] for a complete list of references). There are three possible effects on BBN. First is the production of additional neutrino species in the primeval plasma, leading

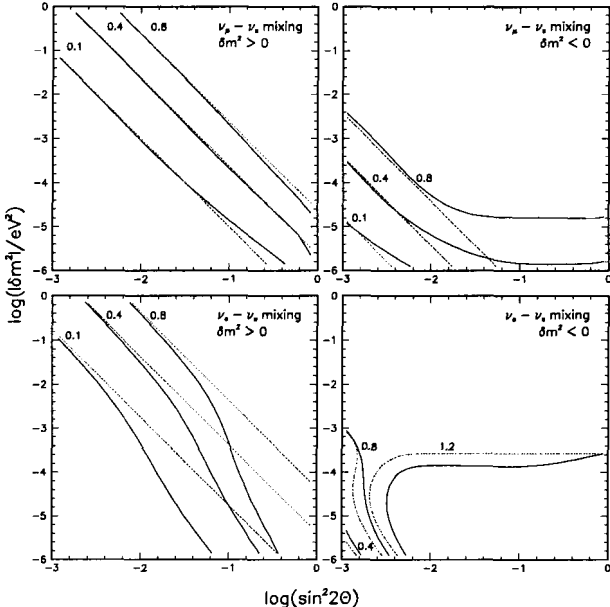


Figure 2: BBN bounds on active-sterile neutrino mixing. Solid lines correspond to numerical results. Red dotted lines correspond to analytic approximate results. See [15] for details

to $N_\nu > 3$. The second effect is a depletion of the number density of electronic neutrinos which results in a higher neutron freezing temperature^c. The third effect is a generation of large lepton asymmetry due to oscillations between active and sterile species.^d

The problem was recently re-considered in [15] both analytically and by solution of the complete system of integro-differential kinetic equations. Earlier derived bounds have been re-analyzed and significantly different results have been found in the resonance case. The results of [15] are shown in Fig. 2. The effect on BBN is expressed in term of variation of the effective number of neutrinos ΔN_ν . It is evident that an observational bound on extra neutrinos much better than unity, say $\delta N_\nu < 0.3$, could give very restrictive limits on active-sterile neutrino mixing. Unfortunately, the present observational bound $\delta N_\nu \leq 1.0$ is not accurate enough to put relevant constraints.

Three active and one sterile neutrinos

It is practically established now that all active neutrinos are mixed with parameters given by the Large Mixing Angle solution to solar neutrino problem

^cIf mixing between active neutrinos is absent, this effect would manifest itself only in the case of $(\nu_e - \nu_s)$ -mixing

^dThis effect takes place only for very weak mixing, much smaller than the experimental bound and is not considered in the following.

($\delta m^2 \simeq 7 \cdot 10^{-5}$ eV 2 and $\tan^2 \theta \simeq 0.4$) and by atmospheric neutrino data ($\delta m^2 \simeq 2.5 \cdot 10^{-3}$ eV 2 and $\tan^2 \theta \approx 1$). Existence of fast transitions between ν_e , ν_μ , and ν_τ may noticeably change BBN bounds on mixing with sterile neutrinos, especially for small values of mass difference. In particular, due to oscillations between active neutrinos, a deficit of ν_μ or ν_τ would be efficiently transformed into a deficit of ν_e , leading to stronger bounds on active-sterile mixing. The effects of mixing between active neutrinos on the BBN bounds on a possible active-sterile admixture has been investigated in detail in [15].

6 Conclusion

Comparison of BBN theoretical results with observational data is not straightforward because the data are subject to poorly known evolutionary effects and systematic errors. Still, even with these uncertainties, BBN permits to constrain important cosmological parameters, like e.g. the baryon density $\Omega_B h^2$, the effective number neutrino families N_ν , etc. The present bound on the number of extra neutrinos species δN_ν is about unity and is not accurate enough to put relevant constraints on active-sterile neutrino mixing. If this limit could be reduced in the next future, say to $\delta N_\nu < 0.3$, very restrictive limits on active-sterile admixture could be obtained.

References

- [1] A. D. Dolgov: Phys. Rept. **370**, 333 (2002)
- [2] F. L. Villante and A. D. Dolgov: arXiv:hep-ph/0310138
- [3] S. Burles and D. Tytler: Astrophys. J. **507**, 732 (1998).
D. Tytler and S. Burles: astro-ph/9606110.
- [4] S. Burles and D. Tytler: Astrophys. J. **499**, 699 (1998)
D. Tytler, X. M. Fan and S. Burles: Nature **381**, 207 (1996)
- [5] J. M. O'Meara et al: Astrophys. J. **552**, 718 (2001)
- [6] M. Pettini and D. V. Bowen: Astrophys. J. **560**, 41 (2001)
- [7] D. Kirkman et al.: arXiv:astro-ph/0302006.
- [8] K. A. Olive and G. Steigman: Astrophys. J. Suppl. **97**, 49 (1995)
- [9] K. A. Olive, E. Skillman and G. Steigman, Astrophys. J. **483**, 788 (1997)
- [10] Y. I. Izotov et al.: Astrophys. J. Suppl. **108**, 1 (1997).
- [11] Y. I. Izotov and T. X. Thuan: Astrophys. J. **500**, 188 (1998).
- [12] D. N. Spergel et al. Astrophys. J. Suppl. **148**, 175 (2003)
- [13] S. G. Ryan et al: Astrophys. J. **530**, L57 (2000)
P. Bonifacio and P. Molinaro, Mon. Not. Roy. Astron. Soc. **285**, 847 (1997)
- [14] A. D. Dolgov et al: Nucl. Phys. B **632**, 363 (2002)
- [15] A. D. Dolgov and F. L. Villante: arXiv:hep-ph/0308083.

GRAVITATIONAL MICROLENSING AND DARK MATTER IN OUR GALAXY: 10 YEARS LATER

A.F. ZAKHAROV^a

*Institute of Theoretical and Experimental Physics, 117259, B. Cheremushkinskaya,
25, Moscow, Russia*

Astro Space Centre of Lebedev Physics Institute, Moscow, Russia

Abstract. Foundations of standard theory of microlensing are described, namely we consider microlensing stars in Galactic bulge, the Magellanic Clouds or other nearby galaxies. We suppose that gravitational microlenses lie between an Earth observer and these stars. Criteria of an identification of microlensing events are discussed. We also consider such microlensing events which do not satisfy these criteria (non-symmetrical light curves, chromatic effects, polarization effects). We describe results of MACHO collaboration observations towards the Large Magellanic Cloud (LMC) and the Galactic bulge. Results of EROS observations towards the LMC and OGLE observations towards the Galactic bulge are also presented. Future microlensing searches are discussed.

A standard microlens model is based on a simple approximation of a point mass for a gravitational microlens. Gravitational lensing (gravitational focusing) results from the effect of light bending by a gravitating body (the phenomenon was discussed by I. Newton, but in the framework of Newtonian gravity a formal derivation of the light bending angle was published by J. Soldner [1]).

In the framework of general relativity (GR) using a weak gravitational field approximation the correct bending angle is described by the following expression derived by Einstein in 1915 just after his formulation of GR

$$\delta\varphi = -\frac{4GM_*}{c^2 p}. \quad (1)$$

The derivation of the famous Einstein's formulae for the bending angle of light rays in gravitational field of a point mass M_* is practically in all monographs and textbooks on general relativity and gravity theory (see, for example books [2, 3]).

The law was firstly confirmed by Sir A. Eddington for observations of light ray bend by the Solar gravitational field near its surface. The angle is equal to $1.75''$, therefore Einstein prediction was confirmed by observations very soon after its discovery.

The gravitational lens effect is a formation of several images instead of one (see details in [4, 5]). We have two images for a point lens model (Schwarzschild lens model). The total square of the two images is larger than a source square. The ratio of these two squares is called gravitational lens amplification A . That is a reason to call gravitational lensing as gravitational focusing. The angular distance between two images is about angular size of so-called Einstein's cone.

^ae-mail: zakharov@itep.ru

The angular size of Einstein's cone is proportional to the lens mass divided by the distance between a lens and an observer. Therefore, if we consider a gravitational lens with typical galactic mass and a typical galactic distance between a gravitational lens and an observer then the angular distance between images will be about few angular seconds; if we suppose that a gravitational lens has a solar mass and a distance between the lens and an observer is about several kiloparsecs then an angular distance between images will be about angular millisecond.

If a separation angle is $\sim 1''$, then one may observe two images in optical band although this problem is a complex one, but one cannot observe directly two images by Earth's observer in the optical band if a separation angle is $\sim 0.001''$. Therefore, the microlensing effect is observed on changing of a luminosity of a source S ^b.

If the source S lies on the boundary of the Einstein cone, then we have $A = 1.34$. Note, that the total time of crossing the Einstein cone is T_0 . Sometimes the microlensing time is defined as a half of T_0 we suppose that $D_d < D_{ds}$ (here we assume that D_{ds} is the distance from the source S to the lens D ; D_d is the distance from the lens D to the observer O ; D_s is the distance from the source S to the observer O)

$$T_0 = 3.5 \text{ months} \cdot \sqrt{\frac{M}{M_\odot}} \frac{D_d}{10 \text{ kpc}} \cdot \frac{300 \text{ km/s}}{v},$$

where v is the perpendicular component of a velocity of a dark body. If we suppose that the perpendicular component of a velocity of a dark body is equal to $\sim 300 \text{ km/s}$ (that is a typical stellar velocity in Galaxy), then a typical time of crossing Einstein cone is about 3.5 months. Thus, a luminosity of a source S is changed with the time.

We will give numerical estimations for parameters of the microlensing effect. If the distance between a dark body and the Sun is equal to $\sim 10 \text{ kpc}$, then the angular size of Einstein cone of the dark body with a solar mass is equal to $\sim 0.001''$ or the linear size of Einstein cone is equal to about 10 astronomical units. It is clear that since typical distances between two images are about Einstein diameters therefore is very difficult to resolve the images by ground based telescopes at least in an optical band. It was a reason that both Einstein and Chwolson thought if gravitational lenses and sources are stars then separation angle is very small to be detectable. However, recently, a direct method to measure Einstein angle ϕ_E was proposed to resolve double images generated by microlensing with an optical interferometer (say VLTI) [6](see also [7] for a

^bSince the angle is very small Einstein and Chwolson thought that gravitational lens effect could not be detectable if sources and lenses are stars. Now there are chances to measure such angles in IR band therefore there is a giant development of observational facilities.

discussion). Moreover, it is plan to launch astrometrical space probe, American SIM^c and European GAIA^d, these instruments will have precisions about 10 micro arc seconds and could determine Einstein radii for any microlensing events.

Astrometric microlensing or motions of visible images due to influence of a gravitational field of microlenses was analyzed in number of papers [8–19], although light bending in gravitational field was discussed by I. Newton (actually that is the same effect but authors presented detailed analysis and pushed new ideas to use the phenomenon to detect even invisible astronomical objects by shifts of images for background sources). An optical depth of microlensing for distant quasars was discussed for different locations of microlenses (see, for example, [20] and references therein).

For observations of extragalactic gravitational lens a typical time for changes of light curve is very long ($\sim 10^5$ years) for its direct observations. Therefore, extragalactic gravitational lenses are discovered and observed by resolving different optical components (images) since typical angular distances between images are about some angular seconds because of a great mass of a gravitational lens. If a gravitational lens is a galaxy cluster then the angular distances between images may be about several minutes. For an identification of gravitational lenses, observers compare typical features and spectra of different images. It is clear that one cannot to resolve different components during microlensing but it is possible to get and analyze a light curve in different spectral bands.

One of the basic criterion for microlensing event identification is the symmetry of a light curve. If we consider a spherically symmetric gravitational field of a lens, a point source and a short duration of microlensing event then the statement about the symmetry of a light curve will be a strong mathematical conclusion, but if we consider a more complicated distribution of a gravitational field lens or an extensive light source then some deviations of symmetric light curves may be observed and (or) the microlensing effect may be chromatic [4,5].

More than 70 years ago it was found that densities of visible matter is about 10% of total density in galactic halos (the invisible is called as dark matter (DM) [21, 22])^e. Thus baryonic density is a small fraction of total density of the Universe. Probably galactic halos is "natural" places to store not only baryonic DM, but non-baryonic DM also. If DM forms objects with masses in the range $[10^{-5}, 10] M_\odot$ microlensing could help to detect such objects. Thus, before intensive microlensing searches it was a dream that microlensing investigations could help us to solve DM problem for Galactic halo at least.

For the first time a possibility to discover microlensing using observations of

^c<http://sim.jpl.nasa.gov/whatis/>

^d<http://astro.estec.esa.nl/GAIA>

^eNow it is known that the matter density (in critical density units) is $\Omega_m = 0.3$ (including baryonic matter $\Omega_b \approx 0.05 - 0.04$, but luminous matter $\Omega_{lum} \approx 0.001$), Λ -term density $\Omega_\Lambda = 0.7$.

star light curves was discussed in the paper by Byalko in 1969 [23]. Systematic searches of dark matter using typical variations of light curves of individual stars from millions observable stars started after Paczynski's discussion of the halo dark matter discovery using monitoring stars from Large Magellanic Cloud (LMC) [24]. We remark that in the beginning of the nineties new computer and technical possibilities providing the storage and processing of huge volume of observational data were appeared and it promoted at the rapid realization of Paczynski's proposal. Griest suggested to call the microlenses as Machos (Massive Astrophysical Compact Halo Objects) [25]. Besides, MACHO is the name of the project of observations of the US-English-Australian collaboration which observed the LMC and Galactic bulge using 1.3 m telescope of Mount Stromlo observatory in Australia.^f

The first papers about the microlensing discovery were published by the MACHO collaboration [26] and the French collaboration EROS (Expérience de Recherche d'Objets Sombres) [27].^g

First papers about the microlensing discovery toward Galactic bulge were published by US-Polish collaboration (Optical Gravitational Lens Experiment), which used 1.3 m telescope at Las Campanas Observatory. Since June 2001, after second major hardware upgrade OGLE entered into its third phase, OGLE III as a result the collaboration observes more than 200 millions stars observed regularly once every 1 – 3 nights. Last two years OGLE III detected more than four hundreds microlensing event candidates each year [29].^h

MOA (Microlensing Observations in Astrophysics) is collaboration involving astronomers from Japan and New Zealand [30, 31].ⁱ

To investigate Macho distribution in another direction one could use searches toward M31 (Andromeda) Galaxy lying at 725 kpc (it is the closest galaxy for an observer in the Northern hemisphere). In nineties two collaborations AGAPE (Andromeda Gravitational Amplification Pixel Experiment, Pic du Midi, France)^j and VATT started to monitor pixels instead of individual stars [28, 33]. These teams reported about discoveries of several microlensing event candidates.

The event corresponding to microlensing may be characterized by the following main features, which allow to distinguish the microlensing event and a stellar variability [4, 34, 35].

- Since the microlensing events have a very small probability, the events

^fMACHO stopped since end 1999.

^gEROS experiment stopped in 2002 [28].

^h<http://www.astrouw.edu.pl/ogle/ogle3/ews/ews/html>

ⁱ<http://www.roe.ac.uk/%7Eiab/alert/alert/alert/html>

^jNew collaboration, POINT-AGAPE started in 1999 and uses INT (2.5 m Isaac Newton Telescope) [54].

should never repeat for the same star. The stellar variability is connected usually with periodic (or quasi-periodic) events of the fixed star.

- In the framework of a simple model of microlensing when a point source is considered, the microlensing effect must be achromatic (deviations from achromaticity for non-point source were considered, for example in the paper by Bogdanov & Cherepashchuk [36]), but the proper change of luminosity star is connected usually with the temperature changes and thus the light curve depends on a colour.
- The light curves of microlensing events are symmetric, but the light curves of variable stars are usually asymmetric (often they demonstrate the rapid growth before the peak and the slow decrease after the peak of a luminosity).
- Observations of microlensing events are interpreted quite well by the simple theoretical model, but some microlensing events are interpreted by more complicated model in which one can take into account that a source (or a microlens) is a binary system, a source has non-vanishing size, the parallax effect may take place.

The typical features of the light curve of the first microlensing event observed by the MACHO collaboration in the LMC are shown in Fig. 1, where the light curves are shown for two spectral bands (a more recent MACHO fit to the observed amplification of this event gives $A_{\max} = 7.2$). The light curve (in two bands) is fitted by the simple model well enough, but the ratio of luminosities for the bands is shown in the lower panel of figure (the ratio shape is adjusted with the event achromaticity). However, one can note that near the maximal observable luminosity the theoretical curve fits the data of observations not very well.

Now one can carry out accurate testing the achromaticity and moreover the stability of the source spectrum during a microlensing event with the Early Warning systems implemented both by the MACHO and OGLE collaborations. This allows one to study the source properties using large telescopes and to organize intense follow-up studies of light curves using telescope network around the globe.

In addition to the typical properties of individual microlensing events, Roulet and Mollerach note that the population of observed events should have the following statistical properties [4, 34].

- Unlike a star variability microlensing events should happen with the same probability for any kind of star therefore the distribution of microlensing

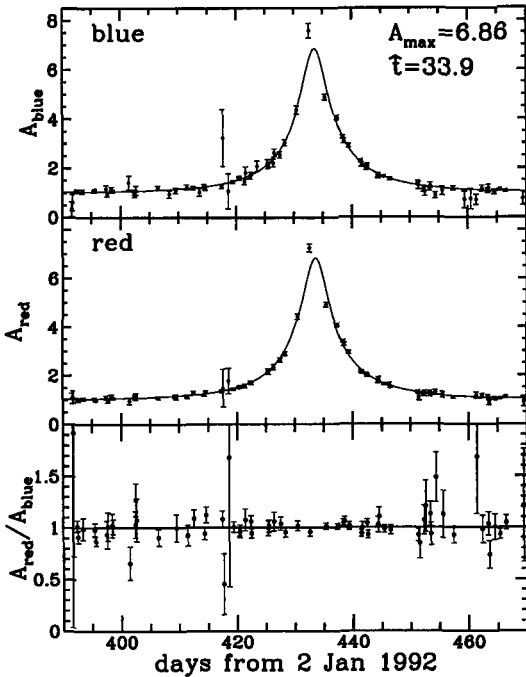


Figure 1: The first microlensing event which was detected by the MACHO collaboration during microlensing searches towards LMC [26].

events should correspond to the distribution of observed stars in the color-magnitude diagrams.^k

- The distribution of the maximal amplification factor A_{max} should correspond to a uniform distribution of the variable $u_{\min} = 1/b$ (b is the dimensionless impact parameter).
- The distributions of the amplification A_{max} and the microlensing event time T should be uncorrelated.

Since for the microlens searches one can monitor several million stars for several years, the ongoing searches have focused on two targets: a) stars in the Large and Small Magellanic Clouds (LMC and SMC) which are the nearest galaxies having lines of sight which go out of the Galactic plane and well across

^kHowever, Roulet and Mollerach noted that for observations in the bulge since observed stars have non-negligible spread along the line of sight, the optical depth is significantly larger for the star lying behind the bulge, thus the lensing probabilities should increase for the fainter stars [34].

the halo; b) stars in the Galactic bulge which allow to test the distribution of lenses near to the Galactic plane.^l

Let us cite well established results of microlensing searches and discuss the questions for which we have now different answers which do not contradict to the observational data. Now it is generally recognized that the microlensing searches towards the Galactic bulge or nearby galaxies are very important for solutions of a lot of problems in astronomy and cosmology. As Paczynski noted, the most important is the consensus that the microlensing phenomenon has been discovered [37]. Now it is impossible to tell which part of the microlensing event candidates is actually connected with the effect since probably there are some variable stars among the event candidates, it could be stellar variability of an unknown kind."^m

1. Observed light curves are achromatic and their shapes are interpreted by simple theoretical expressions very well, however, there is not complete consent about "very well interpretation" since even for the event candidate MACHO # 1 the authors of the discovery proposed two fits. Dominik and Hirshfeld suggested that the event could be fitted perfectly in the framework of the binary lens model [38, 39], but Gurevich et al. assumed that the microlensing event candidate could be caused by a non-compact microlens [40]."ⁿ
2. As expected, binary lenses have been detected and the observed rate of the events correspond to expected value.
3. As expected, the parallax effect has been detected.
4. Since the observed optical depth is essentially greater than the estimated value, the independent confirmation of the Galactic bar existence was done.
5. Using photometric observations of the caustic-crossing binary lens microlensing event EROS BLG-2000-5, PLANET collaboration reported about the first microlens mass determination, namely the masses of these components are $0.35 M_{\odot}$ and $0.262 M_{\odot}$ and the lens lies within 2.6 kpc of the Sun [47].
6. Bennett et al. discovered gravitational microlensing events due to stellar mass black holes [48]. The lenses for events MACHO-96-BLG-5 and MACHO-96-BLG-6 are the most massive, with mass estimates $M/M_{\odot} = 6^{+10}_{-3}$ and $M/M_{\odot} = 6^{+7}_{-3}$, respectively.

^lIn this paper we do not discuss microlensing for distant quasars.

^mThe microlensing event candidates proposed early by the EROS collaboration (#1 and #2) and by the MACHO collaboration (#2 and #3) are considered now as the evidence of a stellar variability [37].

ⁿMicrolensing by non-compact objects considered also in papers [41–46].

Now the following results are generally accepted:

1. The optical depth towards the Galactic bulge is equal to $\sim 3 \times 10^{-6}$, so it is larger than the estimated value [49].
2. Analysis of 5.7 years of photometry on 11.9 million stars in LMC by MACHO collaboration reveals 13 – 17 microlensing events [50] (recent results of the MACHO collaboration on could find in [51]). The optical depth towards the LMC is equal to $\tau(2 < \hat{t} < 400 \text{ days}) = 1.2_{-0.3}^{+0.4} \times 10^{-7}$, so, it is smaller than the estimated value. The maximum likelihood analysis gives a MACHO halo fraction $f=0.2$. Alcock et al. (2000b) gives also estimates of the following probabilities $P(0.08 < f < 0.5) = 0.95$ and $P(f = 1) < 0.05$. The most likely MACHO mass $M \in [0.15, 0.9]M_\odot$, depending on the halo model and total mass in MACHOs out 50 kpc is found to be $9_{-3}^{+4} \times 10^{10} M_\odot$. EROS collaboration gives a consistent conclusion, namely, this group estimates the following probability $P(M \in [10^{-7}, 1]M_\odot \& f > 0.4) < 0.05$ [52, 53]. However, these conclusions are based on assumptions about mass and spacial distributions of microlenses but generally speaking these distributions are still unknown.

However there are different suggestions (which are not contradicted to the observational data) about the following issues [37]:

What is the location of objects which dominate microlensing observed towards the Galactic bulge?

Where are the most microlenses for searches towards LMC? The microlenses may be in the Galactic disk, Galactic halo, the LMC halo or in the LMC itself. *Are the microlenses stellar mass objects or are they substellar brown dwarfs?*

What fraction of microlensing events is caused by binary lenses?

What fraction of microlensing events is connected with binary sources?

Paczynski suggested that we shall have definite answers for some presented issues after some years and since the optical depth towards the Galactic bulge is essentially greater than the optical depth towards the LMC, we shall have more information about the lens distribution towards the Galactic bulge, however, probably, some problems in theoretical interpretation will appear after detections of new microlensing event candidates [37].

The main result of the microlensing searches is that the effect predicted theoretically has been confirmed. This is one of the most important astronomical discoveries.

When new observational data would be collected and the processing methods would be perfected, probably some microlensing event candidates lost their status, but perhaps new microlensing event candidates would be extracted among analyzed observational data. So, the general conclusion may be done. The very important astronomical phenomenon was discovered, but some quantitative parameters of microlensing will be specified in future. However, the

problem about 80% of DM in the halo of our Galaxy is still open (10 years ago people believe that microlensing could give an answer for this problem). Thus, describing the present status Kerins wrote adequately that now we have "Machos and clouds of uncertainty" [54].

I thank prof. A.I. Studenikin for his kind invitation to present this contribution at the XI Lomonosov Conference on Elementary Particle Physics.

References

- [1] J.G. Soldner, *Berliner Astron. Jahrbuch*, **1804**, 161 (1804).
- [2] L.D. Landau, E. M. Lifshitz, 1975, *The Classical Theory of Fields*, Pergamon Press, Oxford (1975).
- [3] C. Möller, *The Theory of Relativity* Oxford, Clarendon Press, 1972.
- [4] A.F. Zakharov, *Gravitatsionnie linzi i microlinzi (Gravitational Lenses and Microlenses)* Janus-K, Moscow (1997).
- [5] A. F. Zakharov, M.V. Sazhin, *Phys. Usp.*, **41**, 945 (1998).
- [6] F. Delplancke, K. Gorski, A. Richichi, *Astron. and Astrophys.*, **375**, 701 (2001).
- [7] B. Paczynski, *Preprint astro-ph/0306564* (2003).
- [8] E. Hog, I.D. Novikov, A.G. Polnarev, *Astron. and Astrophys.*, **294**, 287 (1995).
- [9] M.A. Walker, *Astrophys. J.*, **453**, 37 (1995).
- [10] M. Miyamoto, Y. Yoshii, *Astron. J.*, **110**, 1427 (1995).
- [11] M.V. Sazhin, *Pis'ma v Astron. Zhurn.*, **22**, 647 (1996).
- [12] M.V. Sazhin et al., *Monthly Notices Roy. Astron. Soc.*, **300**, 287 (1998).
- [13] A.F. Boden, M. Shao, D. Van Buren, *Astrophys. J.*, **502**, 538 (1998).
- [14] B. Paczynski, *Astrophys. J.*, **494**, L23 (1998).
- [15] M. Honma, *Publ. Astron. Soc. Japan*, **53**, 223 (2001).
- [16] M. Honma, T. Kurayama, *Astrophys. J.*, **568**, 717 (2002).
- [17] R. Takahashi, *Astrophys. J.*, **595**, 418 (2003).
- [18] G.F. Lewis, R.A. Ibata, *Astrophys. J.*, **501**, 478 (1998).
- [19] M. Treyer, J. Wambsganss, *Preprint astro-ph/0311519*.
- [20] A.F. Zakharov, L. Č. Popović, P. Jovanović, *Astron. & Astrophys.* (accepted); *astro-ph/0403254* (2004).
- [21] J. Oort, *Bull. Astron. Instit. Heth.*, **6**, 249 (1932).
- [22] F. Zwicky, *Helvetica Physica Acta*, **11**, 110 (1933).
- [23] A.V. Byalko, *Astron. Zhurn.*, **46**, 998 (1969).
- [24] B. Paczynski, *Astrophys. J.*, **304**, 1 (1986).
- [25] K. Griest, *Astrophys. J.*, **366**, 412 (1991).
- [26] C. Alcock et al., *Nat.*, **365**, 621 (1993).
- [27] E. Aubourg et al., *Nat.*, **365**, 623 (1993).
- [28] M. Moniez, *Cosmological Physics with Gravitational Lensing*, eds.

J. Trân Thành Vân, Y. Mellier & M. Moniez, Proc. of the XXXVth Rencontres de Moriond, EDP Sciences, 3, 2001.

- [29] A. Udalski, *Acta Astron.*, **51**, 175 (2002).
- [30] I.A. Bond et al., *MNRAS*, **327**, 868 (2001).
- [31] J. Skuljan, *Publ. Astron. Obs. Belgrade*, **75**, 37 (2003)
- [32] E. Kerins et al., *Preprint astro-ph/0002256* (2000).
- [33] Y. Le Du, *Cosmological Physics with Gravitational Lensing*, eds. *J. Trân Thành Vân, Y. Mellier & M. Moniez*, Proc. of the XXXVth Rencontres de Moriond, EDP Sciences, 65, 2001.
- [34] E. Roulet, S. Mollerach, *Phys. Rep.* **279**, 2 (1997).
- [35] A.F. Zakharov, *Publ. Astron. Obs. Belgrade* **75**, 27 (2003); *astro-ph/0212009*.
- [36] M.B. Bogdanov, A.M. Cherepashchuk, *Pis'ma v Astron. Zhurn.*, **21**, 570 (1995).
- [37] B. Paczynski, *Ann. Rev. Astron. & Astrophys.*, **34**, 419 (1996).
- [38] M. Dominik, A.C. Hirshfeld, *Astron. and Astrophys.*, **289**, L31 (1994).
- [39] M. Dominik, A.C. Hirshfeld, *Preprint DO-TH 95/19*, Dortmund (1995).
- [40] A.V. Gurevich, K.P. Zybin, V.A. Sirota, *Phys. Lett. A* **214**, 232 (1996).
- [41] A.F. Zakharov, *Phys. Lett. A*, **250**, 67 (1998).
- [42] A.F. Zakharov, *Astron. Rep.*, **43**, 325 (1999).
- [43] A.F. Zakharov, *Dark Matter in Astro- and Particle Physics*, ed. *H. V. Klapdor-Kleingrothaus*, Proc. of the Intern. Conf. DARK-2000, Springer, 364 (2001).
- [44] A.F. Zakharov, *Cosmological Physics with Gravitational Lensing*, eds. *J. Trân Thành Vân, Y. Mellier & M. Moniez*, Proc. of the XXXVth Rencontres de Moriond, EDP Sciences, 57 (2001).
- [45] A.F. Zakharov, M. V. Sazhin, *JETP Letters*, **63**, 937 (1996).
- [46] A.F. Zakharov, M. V. Sazhin, *JETP* **83**, 1057 (1996).
- [47] J.H. An et al., 2002, *Astroph. J.*, **572**, 521 (2002)
- [48] D.C. Bennett et al., *Astroph. J.*, **579**, 639 (2002).
- [49] C. Alcock et al., *Astroph. J.*, **541**, 734 (2000).
- [50] C. Alcock et al., *Astroph. J.*, **542**, 281 (2000)
- [51] P. Popowski al., *Preprint astro-ph/0304464* (2003).
- [52] T. Lasserre et al., 2000, *Astron & Astroph.*, **355**, L39 (2000).
- [53] T. Lasserre, 2001, *Dark Matter in Astro- and Particle Physics with Gravitational Lensing*, ed. *H. V. Klapdor-Kleingrothaus*, Proc. of the Intern. Conf. DARK-2000, Springer, 342, 2001.
- [54] E. Kerins, *Cosmological Physics with Gravitational Lensing*, eds. *J. Trân Thành Vân, Y. Mellier & M. Moniez*, Proc. of the XXXVth Rencontres de Moriond, EDP Sciences, 43, 2001.

THE GRAVITATIONAL WAVE DETECTORS ON THE EARTH AT THE ERA OF THE VIRGO START UP

Fulvio Ricci^a

Department of Physics, University of Rome La Sapienza and I.N.F.N. Sezione di Roma , 00185 Roma, Italy

Abstract. We recall briefly the experimental strategies for the detection of Gravitational Waves and the status of the various detectors in the world. Then we review the G. W. astrophysical signals and the experimental limits set by the GW detectors in data taking. Finally we recall the status of the VIRGO experiment and the main results obtained in the present commissioning phase of this detector.

1 Introduction

Ten years ago, Hulse and Taylor were awarded the Nobel Prize for the discovery and scientific exploitation of the binary system of stars PSR1913+16. This system assures us that the general relativity theory is reliable for most source models and it remains our best test of the radiative properties of gravity. This strong evidence of the existence of gravitational waves (GW) is indirect and supports the experimental effort to directly detect gravitational radiation. This activity started 30 years ago with the first resonant antenna made by J. Weber and it has greatly expanded in the last decade. In the past many groups around the word developed sophisticated detectors with sensitivity to gravitational radiation dimensionless strain amplitude h less than 10^{-18} .

However, theoretical studies about GW sources [1], [2] suggest that the construction and operation of more sensitive antennas, functioning together and in coincidence with other kinds of detectors is required. Although there is a high level of uncertainty about amplitude and rate of the GW signals, the scientific community estimates that the new detectors like VIRGO and LIGO should be able to see few events per year when they reach their first sensitivity goals, ranging to $h \sim 10^{-21}$ for the amplitude of GW bursts of 1 ms of duration.

At present the scientific perspectives in this field are evolving rapidly. The construction of the kilometer size antennas on the Earth is finished and in particular LIGO has presented already the first scientific results. Moreover, the resonant detectors, as ALLEGRO in Louisiana, EXPLORER at CERN and NAUTILUS and AURIGA in Italy and NIOBE in Australia have set significant upper limits for various astrophysical sources. Thus, in the following we review the status of art of this field. We recall briefly the basic principle of the two detection strategies of GW and the status of the various antennas in the world. Then we review the expected GW signals and the present experimental limits set by the experiments on the Earth and we present one unexpected by product of this research. Finally we will discuss the status of VIRGO and the main results obtained during the first commissioning phase.

^ae-mail: fulvio.ricci@roma1.infn.it

2 The Gravitational Wave detectors on the Earth

Gravitational wave are space-time ripples propagating in the Universe; they determine a local change in the space time metric that is probed by the detectors of this kind of radiation. In the framework of General Relativity the gravitational radiation is quadrupolare, transversal and characterised by two fundamental states of polarisation, h_+ and h_\times . When the radiation is impinging perpendicular to a ring of free masses, it determines on it a deformation similar to that due to a tidal force: the masse distances along the two normal axis x and y change in phase opposition and the amplitude of the metric tensor perturbation h is directly related to the induced strain along one direction $h = 2\Delta L/L$, where L is the ring diameter.

2.1 The resonant detectors

The equation of geodetic deviation of two free falling masses is the basis for all the experiments on GW detection. The concept of a resonant antenna is well represented by a pair of free falling masses joined by a spring. In the case of a real detector the GW strain is applied on an elastic body that vibrates on its quadrupolar mode. The first antenna developed by J. Weber was an 1.5 ton aluminium cylinder operated at room temperature [3]. This kind of detector is still operated by the Moscow university group (the SNAIL antenna) at a sensitivity level of $h = 7 \cdot 10^{-17}$ [4]. Today's cryogenic GW detectors are due to a visionary intuition of W. M. Fairbank: use of low temperature reduces thermal noise, and opens the way to the superior performance of super conductive electronics. The construction of three cryogenic detectors started in 1969-70 in Stanford, Louisiana State and Rome Universities. Two of them are still in operation, EXPLORER, installed at CERN and operated by the Rome group, and the antenna ALLEGRO of the Louisiana State University. They have been simultaneously on line for about 18 months, beginning June 1991. Later these two antennas collected data in coincidence with NIOBE, the 1-ton niobium bar installed in Australia, and the two italian ultra-cryogenic detectors NAUTILUS located in Frascati and AURIGA in Legnaro.

The GW cross-section of the resonant antenna increases with the mass M of the elastic body while the signal to noise ratio (SNR) increases by increasing the acoustic quality factor Q of the vibration mode and by decreasing the detector temperature T . The detector bandwidth and sensitivity depends on the transducer performances and at present a great effort is devoted to increase the transducer coupling factor β that takes into account the conversion efficiency of the mechanical energy of the vibration mode to an electromagnetic signal. As an example we show in the figure the sensitivity change of NAUTILUS as function of β . NAUTILUS is equipped with a high performance capacitive transducer and the coupling factor β can be tuned by changing the bias electric

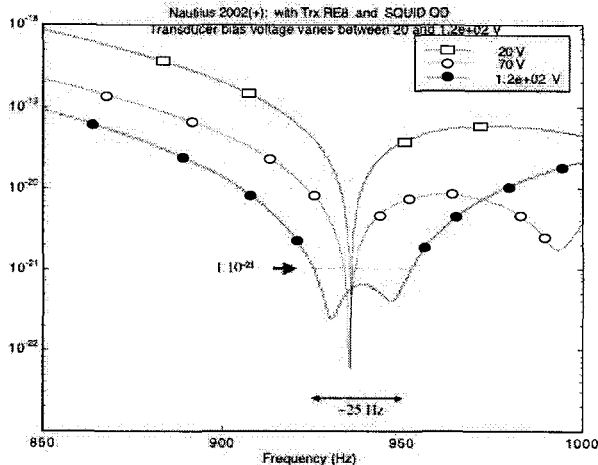


Figure 1: The bandwidth expansion of the resonant antenna NAUTILUS as function of the electromagnetic coupling of the transducer with the bar.

field in the capacitor. At it is shown in the figure they can achieve a bandwidth of the order of 25 Hz. Recently (December 2003) the AURIGA detector restarted the data taking with the antenna equipped with a new transducer highly coupled to the bar. The preliminary measurements show a noise floor lower than $5 \cdot 10^{-21} \text{ Hz}^{-1/2}$ between 855 and 950 Hz which demonstrate the possibility to increase the detector bandwidth up to 100 Hz [5].

2.2 The GW interferometers

The pioneering idea of an electromagnetic signal travelling between free test masses and probing the space-time curvature in the region between them can be found in a paper by Pirani in 1956 [6]. A Michelson interferometer belongs to this fundamental scheme. Its output signal Φ is proportional to ΔL so that the arm length L play the role of amplification factor of the Gravitational signal h . To increase the optical path, the light travelling in each interferometer arm is trapped before the recombination for a typical storage time τ by one Fabry Perot cavity of finesse F . The traveling time of the light introduces a high frequency cut-off in the response of the interferometer to the impinging GW. For this reason the detection efficiency smoothly decreases for GW frequencies higher than the inverse of the cavity storage time. For $F \sim 50$ and for a kilometer length arm the detector bandwidth results extended from few Hz to several KHz. Various sources of noise limit the antenna performances in the detector bandwidth. In the high frequency region the light shot noise dominates

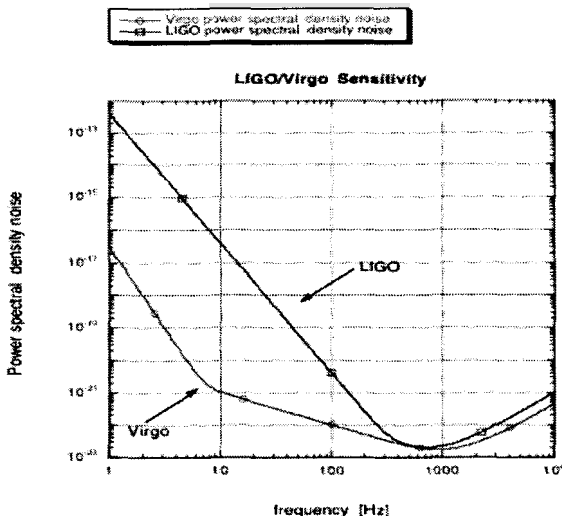


Figure 2: Sketch of the sensitivity curves of LIGO I and VIRGO. The main difference is the extension of the detector bandwidth in the low frequency range for VIRGO is obtained using the super attenuator suspension of the mirrors.

and it is compensated by increasing the light power in the cavity, in the low and in the middle range of frequency the thermal noise of the mirror and its suspension system define the sensitivity limit, while the low frequency cut-off of the sensitivity curve is due to seismic motion. The value of this low frequency cut-off depends on the suspension performances; thanks to the use of the super attenuator suspension, the bandwidth of the Italian-French detector VIRGO installed in Cascina (Italy), is expected to be a factor ten larger than those of the two US-LIGO detectors installed in Louisiana and in the Washington state. To give a quantitative idea of the sensitivity gain due to the suspensions we have sketched in the figure the sensitivity curves of LIGO I and VIRGO computed on the base of the design parameter of the two detectors . We have to point out that this difference between the two detectors will hold just in the first phase of operation of LIGO since the US project has approved already the implementation of high performance suspensions for the advanced LIGO II phase.

To complete the world scenario of the GW interferometers we have to recall that the 300-m interferometer TAMA, installed near Tokyo(Japan), is taking data since 1999, while the 600-m antenna GEO, the anglo-german detector in Hannover (Germany), is operated in the so called *signal recycling* configuration that permits to tune and increase the detector sensitivity in a smaller

bandwidth.

3 GW signals and the present experimental upper limits

The most powerful sources of gravitational waves should be characterized by large internal masses in non-spherical motion with high velocity. The most interesting case is when the gravity field of the source is strong, but in this situation the evaluation of the mass quadrupole moment is difficult and even its definition in terms of the standard Cartesian coordinates is not adequate. Different formalism and various level of approximations have been set trying to reduce the high non-linearity of the Einstein equations and various groups of numerical relativity are developing more realistic simulations taking advantage of the development of supercomputing facilities.

The emission process is characterized in terms of the gravitational wave luminosity L_G derived from the mass quadrupole formula:

$$L_G = \frac{G}{5c^5} \sum_{kh} \left(\frac{d^3}{dt^3} D_{kh} \right)^2$$

where $G = 6.667 \cdot 10^{-11} m^2 kg^{-1}s^{-2}$ is the gravitational constant, and c is the velocity of light. L_G is a linear function of the third derivative of the mass quadrupole moment D_{hk} and the luminosity coefficient $G/5c^5 = 5.5 \cdot 10^{-54} m^{-2} kg^{-1}s^3$ is so low that waves astrophysical objects are the only possible sources.

It is interesting to correlate the source luminosity with the flux detected on Earth F_E and the amplitude of the metric tensor perturbation h . This is done generally by presuming an isotropic emission and therefore

$$F_E = \frac{L_G}{4\pi r^2}$$

where r is the distance of the detector from the source. Probably most sources rotate to the respect of an axis along which in principle the radiation is weakly concentrated, so the factor 4π is an indicative value.

When we consider the simple case of a wave with a single relevant Fourier component at the angular frequency ω , the relation between F_E and h is deduced using the previous formulae and it can be shown that

$$h = \frac{1}{\omega} \sqrt{\frac{16\pi G}{c^3}} F_E$$

It is usual to classify the sources in two classes: aperiodic and periodic sources. In the class of aperiodic emissions we include all kinds of star collapses, as the Supernova explosions and the coalescent binary systems. A significant emission of a GW radiation is expected also from periodic sources such as the double star binary systems and spinning stars such as the pulsars.

3.1 The Supernovae

Type II Supernovae represent the core collapse of a massive star and the shock -driven rebound expansion of an optically luminous shell. The amount of GW radiation emitted depends on the kinetic energy of the non-spherical motion and the main-source of non-sphericity of the collapse comes from the star rotation. Depending on the initial conditions, the system may evolve and break in two or several neutron stars that coalesce again with a rapid spiraling and emission gravitational radiation. If the mass of the core is up to a certain critical value (between 1.4 and 3 solar masses, M_\odot) the collapse continues to form a black hole. In this case the shock wave driving the explosive rebound of the surrounding material should be weak. The external envelope will fall back, the neutrino emission and diffusion through the external material causes an expansion time scale from millisecond to second. In the final stage the collapse take place on a free fall time scale and the emission of millisecond pulses of gravitational radiation occurs.

It is usually estimated that the event rate of supernovae is one in ten to thirty years per galaxy.

Different authors have derived the characteristics of the gravitational signal in different scenarios. For collapse to form black holes, Thorne [1] gives rough numerical estimates for the value of h and for the frequency ν :

$$\nu \approx \frac{c^3}{5\pi Gm} \approx 1.3 \cdot 10^4 \frac{M_\odot}{M} \quad Hz$$

$$h \approx \sqrt{\frac{15\Gamma}{2\pi}} \frac{G}{c^2} \frac{M}{r} \quad Hz$$

where M_\odot is the solar mass. The conversion efficiency Γ of the rest mass to gravitational radiation is uncertain. Theoretical estimates give a range of values from 10^{-4} to 10^{-8} . This is due to the fact that the estimate depends on the collapse model and its initial conditions, such as the angular momentum.

If we consider 1 kHz as frequency reference value (corresponding to $13 M_\odot$) we get a strain signal $h \simeq 10^{-18}$ by assuming a source at the galactic center (10 kpc) and an optimistic conversion efficiency $\Gamma = 10^{-4}$.

In the present experimental scenario the most significant upper limits for burst detection have been set by the IGEC collaboration, the cooperative effort of all the groups working with resonant detectors. They analysed data taken in coincidence in the time period 1997-2000 with the antennas ALLEGRO, AURIGA, EXPLORER, NAUTILUS and NIOBE. The total span of time of the analysis was 1460 days (~ 4 years). They derived upper limit curves for the GW burst rate in the spectral sensitivity range from 10^{-21} to $10^{-19} (Hz)^{-1/2}$. They obtained similar results both in the case of full sky search and looking just toward the Galaxy center [7].

Recently the LIGO Scientific Collaboration released the first upper limit based on the data of the first scientific run S1 of the LIGO interferometers [8]. The result is less stringent than IGEC but it concerns a different frequency interval: their upper limit curves range from 10^{-19} to $10^{-17} \text{ (Hz)}^{-1/2}$.

On the base of these results we conclude that *there is no detection of g.w. bursts above $h \sim 2 \cdot 10^{-18}$ in a full sky blind search.* This corresponds to absence of events associated to conversion of $\sim 0.02 M_{\odot}$ in G.W. in our Galaxy.

3.2 The inverse problem for bursts: the crucial role of a world-wide network

Once the first detection has been performed, the main problem to be solved is the extraction of all the physics informations hidden in the event, the so-called inverse problem. A short burst of GW has 4 unknowns variables:

- the two angular coordinates that define the source position on sky
- the strain amplitude h that is a function of time - the polarisation angle that is also a function of time

Each detector returns at any time the response and the time of arrival so that with n detectors we have $2n - 1$ data values. However, at present the two LIGO detectors are very similar in orientation, so the problem is degenerate. This orientation choice was done in order to optimize the rejection of spurious event, but it does not help for solving the inverse problem. LIGO on its own can determine a source location annulus on sky, but it can not separate the strain amplitude and the polarization angle. With LIGO plus VIRGO (or GEO) we have four data just determining the source location on sky. The four interferometers should return six data but, since the GEO-VIRGO baseline is short (3 ms of time delay between the signals detected in by GEO and VIRGO), just five data are useful. However we conclude that this world-wide network can perform an over characterization of the wave.

3.3 Coalescent binaries

If we consider two compact stars as neutron stars (NS) or black holes (BH) in a circular orbit of radius r with angular frequency ω and masses m_1, m_2 it can be shown that the g. w. luminosity is

$$L_G = \frac{32}{5} \frac{G}{c^5} \left(\frac{m_1 m_2}{m_1 + m_2} \right) r^4 \omega^6$$

The radiation decay of the orbit causes the stars to collide or to tidally disrupt one another. The strength of the gravitational signal at the Earth emitted during the orbit spiraling is derived by considering an r.m.s. average over the detector orientation and the source:

$$h \simeq 1.02 \cdot 10^{-23} \left(\frac{m_1 m_2}{m_1 + m_2} \right) (m_1 + m_2)^{\frac{2}{3}} \left(\frac{\nu}{100} \right)^{\frac{2}{3}} \frac{100}{r}$$

where r is measured in Mpc and the m_1, m_2 in solar masses M_\odot . The time-scale for decay of the orbit is given by:

$$\frac{\nu}{\dot{\nu}} = 7.97 \left(\frac{m_1 m_2}{m_1 + m_2} \right)^{-1} (m_1 + m_2)^{-\frac{2}{3}} \left(\frac{\nu}{100} \right)^{-\frac{8}{3}} \quad [s]$$

The wave from the system is a well defined quasi sinusoidal function increasing in frequency and amplitude towards the final coalescence. This waveform, called chirp, is accurately predictable in the framework of Newtonian dynamics including the post-Newtonian corrections at the third order ($(v/c)^{11/2}$) [9].

Since the frequency ν , h and $\frac{\nu}{\dot{\nu}}$ are measurable quantities, Schultz [10] noticed that from the quantity $(h \frac{\nu}{\dot{\nu}})$ it is possible to derive r independently from the star masses m_1 and m_2 . This ability to measure r is almost unique in astronomy. From the experimental point of view, the precise measurement of h implies, as for the burst detection case, the use of a network of detectors (four at least) to reconstruct the direction of the source and its orientation in the sky.

If the signal shape and amplitude of the coalescing phase are very well known today, the event rate is poorly estimated due to insufficient statistics. Because of the higher emission only systems which are orbiting closer, are considered. Thus, on the basis of the pulsar birth rate and pulsar statistics the estimation rate is about 10^{-4} yr^{-1} in the Galaxy. Assuming that $\simeq 10^5$ galaxies are within 100 Mpc and that bursts are detectable out to that distance, then an occurrence rate of 10 events per year seems realistic.

Most of the energy released in the final collapse is in the neutrino burst which is impossible to detect because of the event distance from the Earth. Thus, the gravitational radiation is probably the clearest signal that we expect to receive from these phenomena. To carry on coincidences with signals of a different nature emitted during the process, it has been proposed to look at the gamma ray bursts that should be coming from the conversion of a relevant fraction of the neutrino burst. If a coincidence is found between gamma rays and gravitational wave events, given the large distances involved, the speed of the gravitational waves can be measured with an impressive accuracy.

An antenna with larger bandwidth is more efficient in detecting this kind of signal, so that significant upper limits for emission from NS/NS systems has been derived using the data taken by the Japan detector TAMA and from the LIGO S1 data. To get the upper limit LIGO uses as triggers the data of the 4-km interferometer installed in Hannford comparing it to the data of the similar antenna in Livingstone. The observation time is $T_{obs} = 295.3$ hours and they estimate the detection efficiency e via a Monte Carlo ($e = 35\%$). Thus, they present an upper limit for NS/NS events in the Milky way at the 90% of confidence of 170 events/year in a mass range $1 - 3 M_\odot$ [11].

The most recent result of the Japanese group that analyse the TAMA data for searching chirp signals, indicates that they are able to detect events up to 42.2 kpc at signal to noise ratio (SNR) equal to 10 and $e = 60\%$ for galactic

events. The 90 % confidence level upper limit released by the collaboration, is 49 events/year in the mass region of $1 - 2 M_{\odot}$ and 29 events/year in the region $1 - 3 M_{\odot}$.

3.4 The quasi monochromatic signals

Pulsars and other rotating neutron stars can be sources of periodic gravitational waves, if they have non symmetric distortions in their crust. The very low spin-down tells us that the distortion cannot be large. However, the presence of glitches in the rotation period of some pulsars is interpreted as the release of crustal distortion, and the asymmetry in the star magnetic field can also contribute to the star deformation.

By assuming a simple ellipsoidal geometry of eccentricity

$$e = \frac{(a - b)}{\sqrt{a \cdot b}}$$

with a and b the two principal axis in the equatorial plane and I the moment of inertia, we get for the luminosity

$$L_G = \frac{288GI^2e^2\omega^6}{45c^5}$$

We notice here that the radiation will be emitted at twice the spinning frequency.

An example is provided by the Crab Pulsar PSR 0532 which spins at ~ 30 Hz at 2 kpc from the Earth ($1 \text{ pc} \approx 3.86 \cdot 10^{16} \text{ m}$). Under reasonable assumptions for the e value, we evaluate h ranging between $10^{-26} - 10^{-28}$.

Presently about 1600 pulsars have been observed within the Milky way, clearly concentrated along the galactic plane. Among them, it exists a subset of 100 stars that have a rotation frequency higher than 4 Hz up to 640 Hz. These pulsars radiate gravitational waves in the frequency range of an interferometric detectors like VIRGO and an optimistic evaluation of the expected upper limits to the GW amplitude shows that few of them could be detected mainly in the frequency range of 10 - 100 Hz. In the figure we report the sensitivity curve of VIRGO in the case of an integration time of 1 year. The GW signal from the pulsar are computed in the very optimistic scenario that the pulsar energy loss is due to the GW emission only.

The first attempt to detect GW signals from a pulsar was done by Hirakawa at university of Tokyo [14]. After several years of experimental effort, the Japanese collaboration of KEK and university of Tokyo took data with a 1.2 tons resonant antenna, cooled at 4 K and tuned to the double of the rotation frequency of the Crab pulsar. Data collected in May 1993 give the one standard deviation upper limit of $h \leq 2 \cdot 10^{-22}$ at 60 Hz for an averaged time of 1900

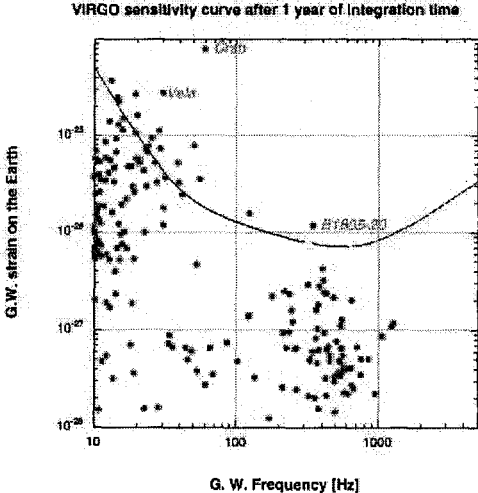


Figure 3: The VIRGO sensitivity curve for continuous signals and the expected pulsar signals computed assuming that the pulsar slowing down is due to the GW emission only.

hours [15]. However this result is still far from the upper bound due to the radio astronomical observations $h \ll 10^{-24}$.

Indeed few significant upper limit exist: one of them was obtained using 95.7 days of EXPLORER data and looking at continuous signals coming from the galactic center. In this case they look at signals inside a small frequency interval, $921.32 \leq f \leq 921.38$ Hz, and they have [12]

$$h_{max}^{(EXPL.)} \leq 3 \cdot 10^{-24}$$

The same group has carried on also a two days full sky search getting [13]

$$h_{max}^{(EXPL.)} \leq 2.8 \cdot 10^{-23}$$

Moreover, recently the TAMA group tried to observe the signal coming from a hypothetic compact object spinning at 934.908 ± 0.05 Hz inside the remenant of the Supernovae 1987a. They based the analysis on 1200 hours of the TAMA data obtaining [16]

$$h_{max}^{(TAMA)} \leq 5 \cdot 10^{-23}$$

Finally, LIGO and GEO groups focused their attention on the pulsar PSR J1939 located at 3.6 kpc of distance. Combining data taken during 408 hours

by LIGO and GEO at $f = 1283.86$ Hz, they performed an elegant analysis reporting [17] the following final result:

$$\begin{aligned} h_{max}^{(GEO-600)} &\leq 3 \cdot 10^{-21}, \quad h_{max}^{(LIGO-H2km)} \leq 5 \cdot 10^{-22}, \\ h_{max}^{(LIGO-H4km)} &\leq 3 \cdot 10^{-22}, \quad h_{max}^{(LIGO-L4km)} \leq 2 \cdot 10^{-22} \end{aligned}$$

It corresponds to an upper limit for the pulsar eccentricity $\epsilon \leq 7 \cdot 10^{-5}$. However, also in this case we have to notice that the radio observations of the PSR J1939 indicate an upper limit for the GW amplitude on the Earth of $h_{max} \sim 10^{-27}$.

3.5 Stochastic background

Among the possible sources of gravitational radiation, a stochastic background is one of the most interesting, as it might give information on the very early stages of the Universe and its formation.

Several sources of this kind of signal have been considered. We recall here the overlapping bursts due to gravitational collapses and coalescence binary systems. In this case we speak about stochastic background of astrophysical origin, the result of unresolved processes of gravitational collapses at red-shift z ranging from 2 to 5.

It should exist also the stochastic background of cosmological origin, that results the processes happened immediately after the Big-Bang. If measured, it will allow to discriminate various cosmological models. This *stochastic signal* is expressed usually in terms of Ω , the ratio of the gravitational wave energy density to the critical density ρ_c needed for a closed universe. The chances to detect the stochastic background foreseen in the framework of classical inflationary model are extremely weak. However in the context of the string cosmology the detection seems to be more probable. Veneziano et al. [18] computed the background of the relic gravitons left by an early, pre-big bang cosmological epoch, whose existence in the past of our Universe is suggested by the duality symmetries of string theory.

The GW detection strategy is based on the correlation of the output of two GW detectors, so that the measured quantity is

$$S_{h_{12}}(f) = (3H^2/4^2 f^3)\Omega_{gw}$$

the cross spectrum of the interferometer strain which depends on

$$\Omega_{gw}(f) = (1/\rho_c) \frac{d\Omega}{d(\ln f)}$$

where

$$\rho_c = \frac{3H^2}{8\pi G} = 1.8 \cdot 10^{-9} \quad \frac{J}{m^3}$$

and $H = 10^5 \text{ m s}^{-1} \text{ Mpc}^{-1}$ is the Hubble constant.

The string cosmology predictions give higher values for Ω_{gw} in the frequency range of the detectors on the Earth and a significant deviation of the spectral behavior of Ω_{gw} from the expected one of the standard cosmology.

In the first operation phase of the km-scale interferometer we expect to have a sensitivity in the range of $\Omega_{gw} \sim 1 \cdot 10^{-6}$, just below the nucleo synthesis bound, while for the advanced detectors (like LIGO II) the perspectives are to gain two order of magnitudes in Ω_{gw} .

Among the present experimental limits we cite those obtained by the resonant antennas: during a dedicated run of NAUTILUS and EXPLORER the Rome group tuned the detectors in such at the same resonance frequency. At $f \sim 907 \text{ Hz}$ they have $\Omega_{gw} \leq 60$ ($S_{h_{12}}^{1/2} \leq 1 \cdot 10^{-22} \text{ Hz}^{-1/2}$) [19].

Recently the two LIGO interferometers achieved a better result in a different frequency range. For $40 \leq f \leq 314 \text{ Hz}$ they have $\Omega_{gw} \leq 23$ (the upper limit is set on a f^{-3} power spectrum of gravitational waves) [20].

All these limits concern audio frequency intervals and they can not be compared to the result of time noise analysis of radio signals emitted by Pulsars [21]. In this case it is possible to explore the frequency region around $f \simeq 4 \cdot 10^{-9} \text{ Hz}$ getting a significant limit for Ω_{gw} at the level of

$$\Omega_{gw} \leq 1 \cdot 10^{-8} \quad (S_{h_{12}}^{1/2} \leq 2.1 \cdot 10^{-10} \text{ Hz}^{-1/2})$$

4 Elementary particles and gravitational wave detectors

We conclude this review of the GW experimental results discussing an unexpected byproduct of this research. One interesting, although unconventional, use of a GW antenna is as a elementary particle detector: high-energy cosmic rays passing through the bar material lose energy that locally heats the bar. This produces a thermal expansion that can excite the mode, generating an event in the antenna. The excitation process has been studied for many types of incident particles, and among them for nuclearites, a possible aggregate of quarks that has been proposed as a dark matter candidate [22]. The analysis, applied to the data of EXPLORER, has made it possible to set a new upper limit on the flux of nuclearites with velocity larger than 10^{-3} c and mass larger than 10^{-16} kg , a region of parameter space not accessible by traditional underground particle detector.

5 The VIRGO start-up

During the years 2001 and 2002, the 3 km VIRGO arms were under construction and the experimental activity was focused on a short interferometer (CITF) mounted in the central area of the site. Each mirror of the CITF was suspended

CITF sensitivity improvements

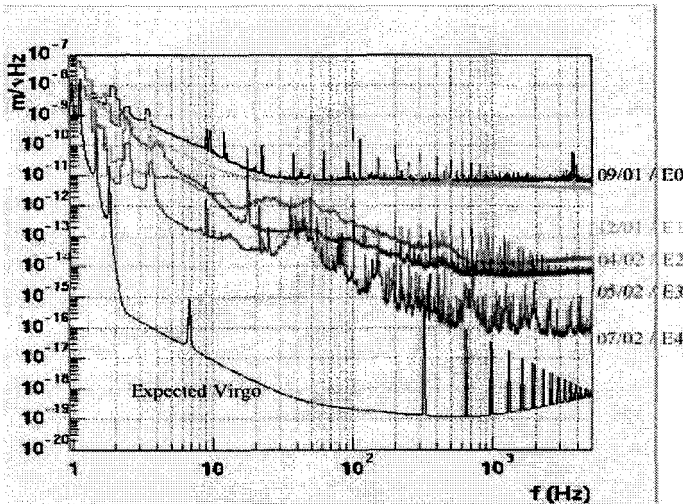


Figure 4: The improvements of the CITF sensitivity curve in the various engineering runs and the target sensitivity of VIRGO.

in vacuum to a super attenuator chain. They were aligned in a standard Michelson configuration plus the power recycling cavity. The suspensions, the control electronic and data acquisition were those of the 3km VIRGO. The main goals of experiment was to test the the various VIRGO subsystems and to take data in stable conditions in order to perform a careful detector characterization.

We carried on five different engineering runs (ER) with very high duty cycle of the detector. In the two first runs the interferometer was set in a simple Michelson configuration while in the three others the recycling cavity was alined and locked. In particular we had a duty cycle 98% for the run ER 0, 85% for ER 1, 98% for ER 2, 96% for ER 3 and 73 % for the final run ER4. This was the first time that the final VIRGO injection system of the laser light was integrated into the CITF. The low duty cycle of ER4 was due to problem of control of the light injection system probably related to the back scattered light from recycling mirror.

In the figure we summarize the performances of the CITF for the various runs [23]. At present the construction of VIRGO is over and, thanks to the experience gained with the CITF, the 3 km Fabry-Perot arms of VIRGO are already looked in a stable configuration. We plan to achieved in 2004 the complete optical configuration so that we will start the data taking of scientific interest.

6 Conclusion

In this paper we have reviewed briefly the status of the GW detectors and the possible sources of gravitational wave signals. We have summarized also the first significant scientific results obtained by the various groups in the world.

Detecting gravitational waves is still one of the main challenges in physics for the years to come. The astrophysical observations based on the detection of transient signals will imply at least three antennas of similar sensitivities running in coincidence. Thus, we conclude that the cooperative effort of all the experimental groups is crucial in order to extract all physics information from the detected GW radiation.

References

- [1] K. Thorne K., in *300 years of Gravitation*, ed. by S.W. Hawking and W. Israel ed., Cambridge Univ. Press 1987
- [2] S.Bonazzola and J.A.Marck, *Ann. Rev.Nucl.Part.Sci.*, **45**, 655, (1994)
- [3] J. Weber, *Phys. Rev. .* **117**, 306, (1960)
- [4] V. Rudenko, in "*Frontiers of Neutrino Astrophysics*" ed. by Y. Suzuki, K. Nakamura , Universal Academy Press, 1993
- [5] preliminary communication: see <http://www.auriga.lnl.infn.it/>
- [6] F.A.E. Pirani, *Act. Phys. Pol.* **15**, 389, (1956)
- [7] P. Astone et al., *Phys. Rev. D* **68**, 022001 (2003)
- [8] B.Abbott et al, *preprint gr-qc/0312056 v3* , 6 Jan 2004.
- [9] L.Blanchet et al., *Class. Quant. Grav.* **13**, (1996)
- [10] B.Schutz, *Nature* **323**, 310, (1986)
- [11] B.Abbott et al, *preprint gr-qc/0308069 v2* , 21 Aug 2003.
- [12] P. Astone et al., *Phys. Rev. D* **65**, 022001 (2002)
- [13] P. Astone et al., *Phys. Rev. D* **65**, 042003 (2002)
- [14] H. Hirakawa,K. Narihara, M.K. Fujimoto, *Jour. Phys. Soc. Jpn.* **41**, 1093 (1976)
- [15] T. Suzuki, in "*Gravitational Wave Experiments*" Proceedings of the 4th Amaldi Conference on Gravitational Wave, ed. by E. Coccia, G. Pizzella, F. Ronga, Word Scientific Singapore, 1995
- [16] Soida et al., *Class. Quant. Grav.* **20**, S645 (2003).
- [17] B.Abbott et al, *preprint gr-qc/gr-qc/0308050 v2* , 14 Aug 2003.
- [18] R. Brustein, M. Gasperini, M. Giovannini, G. Veneziano, *Phys. Lett. B* **361**,45, (1995)
- [19] P. Astone et al., *Astron. Astrophys.* **351**, 811 (1999)
- [20] B.Abbott et al., *preprint gr-qc/0312088 v1* , 19 Dec 2003.
- [21] S.E. Thorsett, R.J.Dewey, *Phys. Rev. D* **53**, 3468 (1996)
- [22] P. Astone et al., *Phys. Rev. D* **47** 4770, (1993)
- [23] Acernese et al., *Astropar. Phys.* in press (2004)

CONFORMAL GRAVITATION AND EVOLUTION OF GALAXIES

B. Barbashov, P. Flin, V. Pervushin ^a, and A. Zorin

*BLTP, Joint Institute for Nuclear Research, 141980 Dubna, Russia,
Pedagogical University, Institute of Physics, 25-406 Kielce, Poland,
Physics Faculty of Moscow State University, 119992 Moscow, Russia*

Abstract. A conformal-invariant version of the Einstein general relativity and Standard Model is considered, where the dilaton plays the role of both the Planck mass and the Higgs one. The identification of the dilaton with a time of the field space of events helps us to solve problems of energy, time, homogeneity, horizon, cosmic initial data, and singularity. The theory describes in the relative units (i.e. conformal quantities) the latest astrophysical data on the Supernova luminosity-distance – redshift relations, primordial nucleosynthesis, value of Cosmic Microwave Background-temperature, baryon asymmetry and energy budget of the universe, including the visual baryon matter. We show that the cosmic evolution of dilaton masses can form galaxies by their capture by the central gravitation field. This capture of galaxies leads to their ellipsoidal trajectories and anisotropy of the local velocity field of nearby galaxies. The Dark Matter halos can be explained by the cosmic evolution of galaxies.

1 Introduction

Beginning with the pioneer papers by Friedmann and ending with the last papers on inflationary model of the Hot Universe Scenario, all observational data are interpreted in the theoretical cosmology as some evidence of the expanding universe.

In the papers [1–6] these new data are considered as evidence of conformal symmetry of the laws of nature that do not depend not only on initial data but also on the units of their measurement. In conformal-invariant theory all measurable quantities are identified with the conformal variables and coordinates (including conformal time η , temperature T_c , running masses $m(\eta)$, coordinate distance), so that the z-history of temperature becomes the z-history of masses.

The purpose of the present paper is the description of the results and consequences of the *relative measurement standards* which expand together with the universe.

2 Theory

The action of the modern unified theory can be rewritten in the form that does not depend on the choice of the measurement units with the dilaton w instead

^ae-mail: pervush@thsun1.jinr.ru

of masses [1–3]:

$$S[w|F] = \int d^4x \sqrt{-g} \{ w^2 [\partial_\mu Q \partial^\mu Q - R(g)/6] - \partial_\mu w \partial^\mu w + \mathcal{L}_H + \mathcal{L}_{SM} \} \quad (1)$$

where $\mathcal{L}_H = -\lambda [|\Phi|^2 - y_h^2 w^2]^2$ is the Higgs potential and $y_h \sim 10^{-17}$.

The fixation of the dilaton $w(x^0, x^i) = M_{\text{Planck}} \sqrt{3/8\pi}$ leads to the conventional GR and SM with the running volume $V = V_f(t)$, and it remembers the Ptolemaeus fixation of the position of the Earth in the Newton mechanics. The fixation of the volume $V = V_c$ with the running masses $w(x^0, x^i) = \varphi(x^0)$ corresponds to the choice of the relative units and conformal variables of the observational cosmology and quantum field theory. In terms of the relative quantities the universe moves in the field world space $[\varphi|F]$ along a hypersurface, where each observer has two sets of measurable quantities corresponding to two observers of a relativistic particle in the “rest frame” and “comoving one”. The “rest frame” there corresponds a field set $[\varphi|F]$ of measurable quantities (the energy identified with the dilaton canonical momentum $E = P_\varphi$, mass φ and density of a number of particles $n = \sum_q a_q^+ a_q$ with a set of quantum numbers q), and the “comoving frame” – geometrical set $[\eta|G]$ of measurable quantities (time interval η and initial data of the density of the Bogoliubov quasiparticles b_q, b_q^+). The Hubble law $\varphi(\eta)$ plays the role of a relativistic transformation connecting two these sets [3]. Thus, one can see that the conformal quantities and the identification of the dilaton with the evolution parameter in the field world space $[\varphi|F]$ solve a set of problems of cosmology (energy, time, homogeneity, horizon, cosmic initial data, singularity, particles, and their cosmological creation from vacuum) by analogy with the solving the similar problems for a relativistic particle in Minkowskian space [3, 5].

3 Astrophysical data in the relative units

In terms of the relative units and the conformal interval we reveal that all masses including the Planck mass are scaled by the cosmic scale factor. It was shown [1–3] that the relative units give Conformal Cosmology with a completely different physical picture of the evolution of the universe than the absolute units of the Standard Cosmology. The temperature history of the expanding universe copied in the relative units looks like the history of evolution of masses of elementary particles in the cold universe with a constant temperature of the cosmic microwave background.

The best fit to the data included 42 high-redshift Type Ia supernovae [8] and the reported farthest supernova SN1997ff [9] requires a cosmological constant $\Omega_\Lambda = 0.7$ $\Omega_{\text{ColdDarkMatter}} = 0.3$ in the case of Standard Cosmology,

whereas in Conformal Cosmology these data are consistent with the dominance of the stiff state of free scalar field Q (1) compatible with nucleosynthesis $[z_{\text{cosmic}} + 1]^{-1}|_{(\text{Supernova})}(\eta) = \sqrt{1 + 2H_0(\eta - \eta_0)}$, $H_0\ell(z) = z + z^2/2$, $m(z) = 5 \log [H_0\ell(z)] + \mathcal{M}$ [3].

There are list arguments in favor of that the cosmological particle creation from vacuum in the conformal-invariant unified theory can explain a genesis of observed matter in the Universe and describe the cosmic energy density budget of observational cosmology [3, 4].

At the moment $\eta_I = 1/2H_I$ of the lifetime of the universe, when masses of W-, Z- vector bosons become the order of the Hubble parameter $M_I = H_I$, the Standard Model shows us an effect of their intensive cosmological creation from the geometric Bogoliubov vacuum [3, 4].

The distribution functions of the longitudinal $\mathcal{N}^{\parallel}(x, \tau)$ vector bosons demonstrate us large contribution of relativistic momenta. Their temperature T can be estimated from the equation in the kinetic theory for the time of establishment of this temperature

$$\eta_{\text{relaxation}}^{-1} \sim n(T) \times \sigma \sim H,$$

where $n(T) \sim T^3$ and $\sigma \sim 1/M^2$ is the cross-section.

This kinetic equation and values of the initial data $M_I = H_I$ give the temperature of relativistic bosons [3, 4]

$$T \sim (M_I^2 H_I)^{1/3} = (M_0^2 H_0)^{1/3} \sim 2.7K$$

as a conserved number of cosmic evolution compatible with the Supernova data [8, 9]. We can see that this calculation gives the value surprisingly close to the observed temperature of the CMB radiation $T = T_{\text{CMB}} = 2.73$ K. The primordial mesons before their decays polarize the Dirac fermion vacuum and give the baryon asymmetry frozen by the CP – violation, so that $n_b/n_\gamma \sim X_{CP} \sim 10^{-9}$ and $\Omega_b \sim \alpha_{\text{qed}} / \sin^2 \theta_{\text{Weinberg}} \sim 0.03$ [4].

4 Cosmic evolution of galaxies

The energy $E(\eta) = \frac{p_r^2}{2m_0a(\eta)} + \frac{P_\theta^2}{2m_0a(\eta)r^2} - \frac{\alpha}{r}$ of a particle with the running mass $m(\eta) = a(\eta)m_0$ (where p_r, P_θ are radial and orbital momenta) is not conserved in the contrast to the energy of particle with a constant mass in the Newtonian mechanics. If the scale factor $a(\eta)$ increases, the energy runs from its positive values to negatives ones. There is a moment of a time $\eta = \eta_I$ when the energy is equal to zero. It is just the moment of the capture of a galaxies. At the time of capture the zero initial data $E_I = p_{rI} = 0$ lead to the orbital velocity $v_I = P_\theta/m_I r_I = \alpha/P_\theta$ that does not depend on the initial radius $r_I \sim 1/m_I$ having different values for different masses m_I . This capture leads to ellipsoidal

trajectories [7]. These trajectories can explain recently reported [10] anisotropy of the local velocity field of nearby galaxies; see Figs. 1, 2.

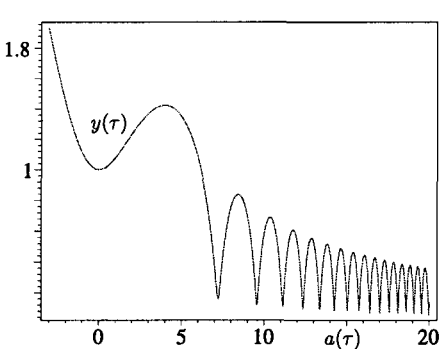


Figure 1: Graph of function $y(\tau) = r(\tau)/r_0$, where τ is the product of the time and the Hubble parameter.

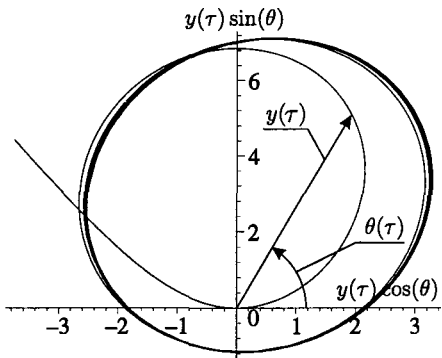


Figure 2: Graph of function $a(\tau)y(\tau)$ in the plain (x, y) .

The Dark Matter trajectories $\dot{R} = \ddot{R} = 0$ ($R = a(t)r, dt = a(\eta)d\eta$) for considered stiff state [2] gives us the rotation curve $v = [r_g/(2R) + 2(HR)^2]^{1/2}$ instead of the Newtonian one $v = [r_g/(2R)]^{1/2}$. So that the Hubble velocity in the region $R \geq R_{\text{cr}} = [r_gH^{-2}]^{1/3}$ can reproduce the contribution of the Dark Matter halo [4], see Fig. 3.

5 Conclusion

In this paper a theory of gravitation is presented, which is invariant under conformal transformations and leads to specific applications in cosmology, which in particular allow an alternative new interpretation of the type Ia supernova data and eliminate the cosmological constant problem. The observed z-history of the universe is reinterpreted within a non-expanding universe cosmology of varying dilaton masses.

We have seen that the cosmic evolution of the dilaton masses forms galaxies and their clusters and the evolution of the universe plays the role inscribed to Cold Dark Matter.

The framework of conformal cosmology presented here allows the consistent development of a conformal theory of cosmological perturbations. Such an approach will be developed in the near future and can be tested with the observations of the fluctuations of the CMBR. This approach should then also be extended to the process of recombination and element synthesis.

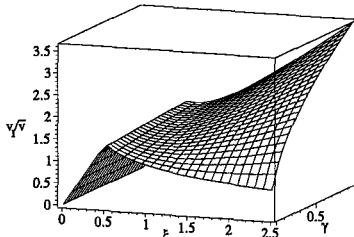


Figure 3: The dependence of the circular velocity of a galaxy v_I on its radius $\xi = R/(2R_{\text{size}})$, where R_{size} is the size of an object (cluster), $\gamma = (R_{\text{size}}/R_{\text{cr}})^3$ and $R_{\text{cr}} = [r_g H^2]^{1/3} = 10^{20} M^{1/3}$ cm is the value of the radius for which the Newton velocity coincides with the Hubble one, M - is the mass of an object in the solar one. At $\gamma = 0$ the exact rotational curve coincides with the Newton one. For $\xi = 0.5$ and $\gamma = 1/8$ $R_{\text{size}} = R_{\text{cr}}/2$ is close to the size of our Galaxy ($R_{\text{size}} = 10^{23}$, $M^{1/3} \leq 10^4$), and the rotational curve with taking into account the Hubble velocity can essentially decrease the contribution of the Dark Matter halo. The size of large cluster ($R_{\text{size}} = 10^{25}$ sm, $M \leq 10^5$) is even larger than the one of range of validity of the Newton theory $R_{\text{cr}} = 10^{20} M^{1/3}$ cm, in this case the Hubble velocity can play the role inscribed to Cold Dark Matter halo [4].

Acknowledgments

The authors are grateful to Profs. D. Blaschke, D.V. Gal'tsov, and S.I. Vinitsky for fruitful discussions and D. Behnke and A.A. Gusev for helpness.

References

- [1] M. Pawłowski, V.V. Papoyan, V.N. Pervushin, and V.I. Smirichinski, *Phys. Lett. B* 444, 293 (1998).
- [2] D. Behnke, D.B. Blaschke, V.N. Pervushin, and D.V. Proskurin, *Phys. Lett. B* 530, 20 (2002); [gr-qc/0102039].
- [3] V.N. Pervushin, D.V. Proskurin, and A.A. Gusev, *Grav. & Cosmology* 8, 181 (2002); D. Blaschke *et al.*, *Yad. Fiz.* v.67, issue 5, p.1 (2004); [hep-th/0206246].
- [4] B.M. Barbashov, A.G. Zorin, V.N. Pervushin, P. Flin, Preprint JINR P2-2002-295, submitted in *Theor. Math. Phys.*.
- [5] M. Pawłowski, V.N. Pervushin, *Int. J. Mod. Phys. A* 16, 1715 (2001); [hep-th/0006116].
- [6] B.M. Barbashov, V.N. Pervushin, D.V. Proskurin, *Phys. Part. and Nucl.* v.34, issue 7, p.138 (2003).
- [7] M. Biernacka, P. Flin, V. Pervushin, and A. Zorin, *Part. and Nucl., Lett.* v.119, issue 2, p.65 (2004); [astro-ph/0206114].
- [8] A.G. Riess *et al.*, *Astron. J.* 116, 1009 (1998); S. Perlmutter *et al.*, *Astrophys. J.* 517, 565 (1999).
- [9] A.G. Riess *et al.*, *Astrophys. J.* 560, 49 (2001); [astro-ph/0104455].
- [10] I.D. Karachentsev, D.I. Makarov, *Astrofizika* 44, 1 (2001).

QUANTUM TUNNELLING OF A ROTATING UNIVERSE

M.Fil'chenkov ^a

*Peoples' Friendship University of Russia, 6 Miklukho-Maklaya Street, Moscow
117198, Russia*

Abstract. The problem of rotation of the astronomical objects remains open so far. Its resolution is expected to be found in the framework of quantum cosmology. Raychaudhuri's equation of a homogeneous universe with acceleration, expansion, shear and rotation is considered. Its quantization results in Wheeler-DeWitt's equation for a multicomponent model of the tunnelling universe. The primordial rotation may both decrease and increase the tunnelling factor depending on contributions of angular momenta of the components with different equations of state.

1 Introduction

The problem of rotation in astronomy remains open so far [1]. The existing mechanisms cannot provide observable specific angular momenta of spiral galaxies. On the other hand, Birch's upper limit on the angular velocity of the Universe [2] is sufficient for assuming a cosmological origin of the rotation of cosmological objects.

2 Model

A homogeneous universe with rotation is described by Raychaudhuri's equation [3]:

$$\dot{\theta} + \frac{1}{3}\theta^2 - A_{;i}^i + 2\sigma^2 - 2\omega^2 = -\frac{4\pi G}{c^2}(\varepsilon + 3p), \quad (1)$$

where θ is the expansion, A^i is the acceleration, σ is the shear, ω is the angular velocity, ε is the energy density and p is the pressure.

The above quantities are given by the formulae:

$$\theta = \frac{3\dot{a}}{a}, \quad (2)$$

$$A^i = c\alpha\theta(u^i - g^{0i}), \quad (3)$$

$$\sigma = \begin{cases} \frac{\Sigma}{a^3}, & -\frac{1}{3} < \alpha \leq \frac{1}{3}, \\ 0, & -1 \leq \alpha \leq -\frac{1}{3}; \end{cases} \quad (4)$$

$$\frac{1}{c^2}(p + \varepsilon)a^5\omega = J = const, \quad (5)$$

$$p = \alpha\varepsilon, \quad (6)$$

where a is the scale factor, u^i is the 4 velocity, g^{ik} is the metric tensor.

^ae-mail: fil@crosna.net

For multicomponent quasi-Friedmann metrics, i.e. with $1 - g^{00} \ll 1$ and

$$\sigma^2 \ll \omega^2 \ll \frac{2\pi G\varepsilon}{c^2}, \quad (7)$$

$$\dot{\varepsilon}a + 3(\varepsilon + p)\dot{a} = 0 \quad (8)$$

being satisfied, Raychaudhuri's equation admits the first integral as follows

$$\begin{aligned} \frac{\dot{a}^2}{2} - a^2 \sum_{n=0}^6 \frac{1}{1 - (\frac{n}{3} - 1)(1 - g^{00})} &\left\{ -\frac{4\pi G}{3c^2} \frac{(n-2)\varepsilon_n}{2-n - \frac{4(\frac{n}{3}-1)(1-g^{00})}{1-(\frac{n}{3}-1)(1-g^{00})}} \right. \\ &+ \frac{1}{3} \frac{\omega_n^2}{n-4 - \frac{2(\frac{n}{3}-1)(1-g^{00})}{1-(\frac{n}{3}-1)(1-g^{00})}} + \frac{1}{6} \frac{\sigma_n^2}{1 + \frac{(\frac{n}{3}-1)(1-g^{00})}{1-(\frac{n}{3}-1)(1-g^{00})}} \left. \right\} \\ &+ \frac{kc^2}{2} \sum_{n=0}^6 B_n \left(\frac{a}{r_0} \right)^{\frac{4(\frac{n}{3}-1)(1-g^{00})}{1-(\frac{n}{3}-1)(1-g^{00})}} = 0, \end{aligned} \quad (9)$$

where

$$\varepsilon_n = \varepsilon_0 B_n \left(\frac{r_0}{a} \right)^n, \quad (10)$$

$$\omega_n^2 = \frac{9c^4 J_n^2}{\varepsilon_0^2 r_0^{10} n^2 B_n^2} \left(\frac{r_0}{a} \right)^{2(5-n)} \quad (J_0 = \omega_0 = 0), \quad (11)$$

$$\sigma_n^2 = \begin{cases} 0 & n = 0, 1, 2 \\ \frac{\Sigma_n^2}{a^6} & n = 3, 4, 5, 6, \end{cases} \quad (12)$$

$$\sum_{n=0}^6 B_n = 1, \quad (13)$$

$$n = 3(1 + \alpha), \quad (14)$$

$$\frac{1}{r_0^2} = \frac{8\pi G\varepsilon_0}{3c^4}, \quad (15)$$

$$k = 0, \pm 1, \quad (16)$$

k is the model parameter, ε_0 is the vacuum energy density, r_0 is de Sitter's horizon, B_n are defined by the formula

$$\varepsilon = \varepsilon_0 \sum_{n=0}^6 B_n \left(\frac{r_0}{a} \right). \quad (17)$$

3 Quantization

The universe has been created as a result of some quantum tunnelling. Quantization is performed by substituting the generalized momentum [4]

$$P = \frac{da}{d\eta}, \quad (18)$$

where

$$ad\eta = cdt, \quad (19)$$

η is the conformal time, by the operator

$$\hat{P} = \frac{1}{i} l_{pl}^2 \frac{d}{da}, \quad (20)$$

where l_{pl} is the the Planckian length. Then (9) takes the form of Wheeler-DeWitt's equation

$$\frac{d^2\psi}{da^2} - V(a)\psi = 0, \quad (21)$$

where ψ is the wave function,

$$\begin{aligned} V(a) = & \frac{1}{l_{pl}^4} \left\{ k a^2 \sum_{n=0}^6 B_n \left(\frac{a}{r_0} \right)^{\frac{4(\frac{n}{3}-1)(1-g^{00})}{1-(\frac{n}{3}-1)(1-g^{00})}} \right. \\ & - a^4 \left[-\frac{8\pi G}{3c^4} \sum_{n=0}^6 \frac{(n-2)\varepsilon_n}{(2-n) \left[1 - (\frac{n}{3}-1)(1-g^{00}) \right] - 4(\frac{n}{3}-1)(1-g^{00})} \right. \\ & - \frac{2}{3c^2} \sum_{n=0}^6 \frac{\omega_n^2}{(4-n) \left[1 - (\frac{n}{3}-1)(1-g^{00}) \right] - 2(\frac{n}{3}-1)(1-g^{00})} \\ & \left. \left. + \frac{1}{6c^2} \sum_{n=0}^6 \sigma_n^2 \right] \right\}. \end{aligned} \quad (22)$$

Using the formula

$$V(a) = \frac{2m_{pl}}{\hbar^2} [U(a) - E], \quad (23)$$

we reduce (21) to a Schrödinger-like form

$$-\frac{\hbar^2}{2m_{pl}} \frac{d^2\psi}{da^2} + [U(a) - E]\psi = 0. \quad (24)$$

In case Friedmann's world contains only de Sitter's vacuum ($p = -\varepsilon$), strings ($p = -\frac{1}{3}\varepsilon$) and radiation ($p = \frac{1}{3}\varepsilon$), for a slow rotation of dust ($p = 0$) and perfect gas ($p = \frac{2}{3}\varepsilon$) we have

$$E = \frac{m_{pl}c^2}{2} \left(\frac{r_0}{l_{pl}} \right)^2 \left(\frac{3B_4}{4-g^{00}} + \frac{2J_3 2c^2}{3\varepsilon^2 r_0^8 B_3^2} \right), \quad (25)$$

$$U(a) = \frac{m_{pl}c^2 a^2}{2l_{pl}} \left[k - B_2 - \frac{a^2}{r_0^2} \left(\frac{B_0}{6-5g^{00}} + \frac{18J_5^2 c^2}{25\varepsilon^2 r_0^8 B_5^2} \frac{1}{5-2g^{00}} \right) \right] \quad (26)$$

provided that

$$1 - g^{00} \ll 1, \quad B_3 \ll \frac{J_3^2 c^2}{\varepsilon^2 r_0^8 B_3^2} \ll B_4, \quad B_5 \ll \frac{J_5^2 c^2}{\varepsilon^2 r_0^8 B_5^2} \ll B_0, \quad B_1 = B_6 = 0.$$

4 Tunnelling Approach

The universe is born as a result of tunnelling through the potential barrier whose width and height are given by the formulae

$$a_2(E = 0) = r_0 \sqrt{\frac{k - B_2}{\frac{B_0}{6-5g^{00}} + \frac{18J_5^2 c^2}{25\varepsilon_0^2 r_0^8 B_5^2 (5-2g^{00})}}}, \quad (27)$$

$$U_{max} = \frac{m_{pl}c^2}{8} \frac{(k - B_2)^2}{\frac{B_0}{6-5g^{00}} + \frac{18J_5^2 c^2}{25\varepsilon_0^2 r_0^8 B_5^2 (5-2g^{00})}} \quad (28)$$

respectively. The tunnelling factor (the universe's birth probability) is given by Gamow's formula

$$D = \exp\left\{-\frac{2}{\hbar} \left| \int_{a_1}^{a_2} \sqrt{2m(E - U)} da \right| \right\}, \quad (29)$$

where $m = m_{pl}$, $U(a_1) = U(a_2) = E$. Calculating the integral in (29) near U_{max} , we have [5]

$$D = \exp \left\{ -\pi \left(\frac{r_0}{l_{pl}} \right)^2 \frac{\left| \frac{(k-B)^2}{4 \left[\frac{B_0}{6-5g^{00}} + \frac{18J_5^2 c^2}{25\varepsilon_0^2 r_0^8 B_5^2 (5-2g^{00})} \right]} - \frac{3B_4}{4-g^{00}} + \frac{2J_3^2 c^2}{3\varepsilon_2 r_0^8 B_3^2} \right|}{\sqrt{2(k - B_2)}} \right\}. \quad (30)$$

Near U_{max} , i.e. provided that

$$\frac{3B_4}{4-g^{00}} - \frac{(k-B_2)^2}{4 \left[\frac{B_0}{6-5g^{00}} + \frac{18J_5^2c^2}{25\varepsilon_0 r_0^8 B_5^2 (5-2g^{00})} \right]} \ll \frac{2J_3 c^2}{3\varepsilon_0 r_0^8 B_5^2},$$

we obtain

$$D = \exp \left\{ -\frac{\pi}{c^2 l_{pl}^2} \frac{\left| \frac{j_3^2}{3B_3^2} - \frac{27j_5^2 B_4 (6-5g^{00})}{25B_0 B_5^2 (4-g^{00})(5-2g^{00})} \right|}{\sqrt{\frac{3B_0 B_4}{(6-5g^{00})(4-g^{00})}}} \right\}, \quad (31)$$

where $j_n = \frac{c^2 J_n}{\varepsilon_0^2 r_0^3}$ is the specific angular momentum. From (22) it is easy to see that

$$k(1-g^{00}) \sum_{n=0}^6 B_n \left(\frac{n}{3} - 1 \right) = \frac{3j_4^2}{32r_0^2 c^2 B_4^2}. \quad (32)$$

This means that a deviation from Friedmann's geometry $1-g^{00}$ depends on the specific angular momentum of radiation and the model parameter. Thus the tunnelling factor depend on specific angular momenta of dust j_3 , perfect gas j_5 and radiation j_4 , with the two latter being able to increase the universe's birth probability as compared to Friedmann's case.

5 Conclusion

We have shown that a slow rotation of the multicomponent quasi-Friedmann world results both in and decrease and increase in the possibility of its quantum birth, depending on the equation of state of its components. The model geometry is related to the angular momentum of radiation.

Acknowledgments

I am grateful to A.I. Studenikin for providing me the possibility of participating in the 11th Lomonosov Conference on Elementary Particle Physics.

References

- [1] Li-Xin Li, *Gen. Relat. Grav.* 30, 497 (1998).
- [2] P.Birch, *Nature* 298, 451 (1982).
- [3] A.Raychaudhuri, *Phys. Rev.* 98, 1123 (1955).
- [4] M.Fil'chenkov, in "*Frontiers of Particle Physics*" (Proceedings of the 10th Lomonosov Conference on Elementary Particle Physics), ed. by A.Studenikin, World Scientific Singapore, 284, 2003.
- [5] I.Dymnikova, M.Fil'chenkov, *Phys. Lett.* **B** 545, 214 (2002).

ON THE PROBLEM OF UNIQUENESS OF ENERGY-MOMENTUM TENSOR OF GRAVITATIONAL FIELD

A.I.Nikishov ^a

*I.E.Tamm Department of Theoretical Physics, P.N.Lebedev Physical Institute,
117924, Leninsky Prospect 53, Moscow, Russia.*

*Abstract.*For an island-like distribution of matter the gravitational energy-momentum tensor is defined according to Weinberg as a 'source of metric'. If this source is formed by self-interactions of gravitons, so that nonphysical degrees of freedom are excluded, then this source is a reasonable candidate for the energy-momentum tensor of gravitational field. The disastrous influence of the nonphysical degrees of freedom is demonstrated by comparing the gravitational energy-momentum tensors in the harmonic, isotropic and standard frames for the Schwarzschild solution. The harmonic frame is clearly preferable for defining the gravitational energy-momentum tensor.

1 The gravitational energy-momentum tensor as the source of metric

There are several arguments in favor of non-localizability of the energy of the gravitational field, see §20.4 in [1]. They do not seem convincing.

Following [2], we consider the case when

$$g_{\mu\nu} = \eta_{\mu\nu} + h_{\mu\nu}, \quad \eta_{\mu\nu} = \text{diag}(-1, 1, 1, 1) \quad (1)$$

and $h_{\mu\nu} \rightarrow 0$ quickly enough when $x \rightarrow \infty$, but it is not assumed that $h_{\mu\nu} \ll 1$ everywhere. The wave equation for $h_{\mu\nu}$ is

$$\begin{aligned} h_{\mu\nu,\lambda}{}^\lambda - h^\lambda{}_{\mu,\lambda\nu} - h^\lambda{}_{\nu,\lambda\mu} + h_{,\mu\nu} + \eta_{\mu\nu}(h_{\sigma\lambda}{}^{\sigma\lambda} - h_{,\lambda}{}^\lambda) = \\ -16\pi G(T_{\mu\nu} + t_{\mu\nu}), \quad h \equiv h_\lambda{}^\lambda; \quad h_{,\sigma} \equiv \frac{\partial}{\partial x^\sigma}. \end{aligned} \quad (2)$$

Here $t_{\mu\nu}$ is the gravitational energy-momentum tensor.

In general relativity eq. (2) is the Einstein equation with

$$8\pi G t_{\mu\nu} = R_{\mu\nu} - \frac{1}{2}g_{\mu\nu}R - R_{\mu\nu}^{(1)} + \frac{1}{2}\eta_{\mu\nu}R^{(1)\lambda}{}_\lambda, \quad (3)$$

see equations (7.6.3) and (7.6.4) in [2]. Indices in $h_{\mu\nu}$, $R_{\mu\nu}^{(1)}$ and $\frac{\partial}{\partial x^\sigma}$ are raised and lowered with the help of η , while indices of true tensors, such as $R_{\mu\nu}$ are raised and lowered with the help of g as usual. $R_{\mu\nu}^{(1)}$ is a linear in $h_{\mu\nu}$ part of $R_{\mu\nu}$:

$$R_{\mu\nu}^{(1)} = \frac{1}{2}[h_{,\mu\nu} - h^\lambda{}_{\mu,\lambda\nu} - h^\lambda{}_{\nu,\lambda\mu} + h_{\mu\nu,\lambda}{}^\lambda], \quad (4)$$

^aE-mail: nikishov@lpi.rue-mail: erosh@inr.npd.ac.ru

$$h = \eta^{\mu\nu} h_{\mu\nu} \quad , \quad R^{(1)} = \eta^{\mu\nu} R_{\mu\nu}^{(1)}.$$

As shown in [2], tensor (3) has all the necessary properties of a gravitational energy-momentum tensor. The same is true even if the general relativity is not assumed i.e. $t_{\mu\nu}$ has not the form (3). Nevertheless, $t_{\mu\nu}$ as defined in (3) has one drawback: it depends on a coordinate system in an inadmissible way. I shall demonstrate this for the gravitational field of a spherically symmetric body and then indicate how, in my opinion, to correct the situation.

To begin with, we write down some of metrics outside the body.

1. Standard Schwarzschild

$$d\tau^2 = \left(1 - \frac{2GM}{r}\right) dt^2 - r^2(\sin^2 \theta d\varphi^2 + d\theta^2) - \frac{dr^2}{1 - \frac{2GM}{r}}. \quad (5)$$

2. Harmonic ($R = r - GM$)

$$\begin{aligned} d\tau^2 = & \frac{1 - \frac{GM}{R}}{1 + \frac{GM}{R}} dt^2 - \left(1 + \frac{GM}{R}\right)^2 R^2(\sin^2 \theta d\varphi^2 + d\theta^2) \\ & - \frac{1 + \frac{GM}{R}}{1 - \frac{GM}{R}} dR^2. \end{aligned} \quad (6)$$

3. Isotropic ($r = \rho(1 + \frac{GM}{\rho})^2$)

$$d\tau^2 = \left(\frac{1 - \frac{GM}{2\rho}}{1 + \frac{GM}{2\rho}}\right)^2 dt^2 - \left(1 + \frac{GM}{2\rho}\right)^4 [d\rho^2 + \rho^2(\sin^2 \theta d\varphi^2 + d\theta^2)]. \quad (7)$$

4. Eddington frame

$$d\tau^2 = dt^{*2} - \frac{2GM}{r^*}(dr^* + dt^*)^2 - dr^{*2} - r^{*2} d\Omega. \quad (8)$$

It is remarkable that in this frame $g_{\mu\nu}$ linearly depends upon G. Although all frames are equal, at least for our purpose there is a frame that is "more equal than others".

Now we go back to equation (2) and consider space region where $T_{\mu\nu} = 0$. Then the equation tell us that if we know $h_{\mu\nu}$, we can obtain $t_{\mu\nu}$. Using this, we get the gravitational energy-momentum tensors in the harmonic, isotropic and standard Schwarzschild frames. Instead of spherical coordinates in (5-7) we use below the rectangular ones and denote the space coordinates by x_i , $x_i x_i = r^2$, $i = 1, 2, 3$ in all three frames.

2 The harmonic frame

In this frame the gravitational energy-momentum tensor was obtained in [4]. We have

$$h_{00} = \frac{-2\phi}{1-\phi}, \quad h_{ij} = (-2\phi + \phi^2)\delta_{ij} + \frac{1-\phi}{1+\phi}\phi^2 \frac{x_i x_j}{r^2},$$

$$h_{0i} = 0, \quad \phi = -\frac{GM}{r}. \quad (9)$$

$$8\pi G t_{00}^{har} = \frac{1}{r^2} [-2 - \phi^2 + \frac{4}{1+\phi} - \frac{2}{(1+\phi)^2}], \quad t_{0i}^{har} = 0; \quad (10)$$

$$8\pi G t_{ij}^{har} = \frac{x_i x_j}{r^4} \left(-2\phi^2 + 2 - \frac{1}{1+\phi} - \frac{1}{(1+\phi)^2} + \frac{1}{1-\phi} + \frac{1}{(1-\phi)^2} - \frac{2}{(1-\phi)^3} \right) + \frac{\delta_{ij}}{r^2} \left(\phi^2 - \frac{1}{1+\phi} + \frac{1}{(1+\phi)^2} + \frac{1}{1-\phi} - \frac{3}{(1-\phi)^2} + \frac{2}{(1-\phi)^3} \right) \quad i, j = 1, 2, 3. \quad (11)$$

We see that the energy-momentum tensor has singularities at $r = GM$, when $\phi = -1$.

For $\phi \ll 1$ we get

$$8\pi G r^2 t_{00}^{har} \Big|_{\phi \ll 1} = -3\phi^2 + 4\phi^3 + \dots; \quad (12)$$

$$8\pi G t_{ij}^{har} \Big|_{\phi \ll 1} = 7 \frac{\phi^2}{r^2} \left(\delta_{ij} - \frac{2x_i x_j}{r^2} \right) + 6 \frac{\phi^3}{r^2} \left(\delta_{ij} - \frac{5}{3} \frac{x_i x_j}{r^2} \right) + \dots. \quad (13)$$

Defining $\tilde{h}^{\mu\nu}$ by

$$\tilde{g}^{\mu\nu} \equiv (-g)^{1/2} g^{\mu\nu} = \eta^{\mu\nu} + \tilde{h}^{\mu\nu}, \quad g = \det g_{\mu\nu}, \quad (14)$$

we get the harmonic condition in the form

$$\tilde{h}^{\mu\nu}_{,\nu} = 0. \quad (15)$$

This condition is the analogue of Lorentz condition in electrodynamics. It exclude the nonphysical degrees of freedom and the simplest assumption is that in our case it exclude all the nonphysical degrees. In this case the rectangular harmonic frame is the preferred system, the use of which has been advocated by Fock [5]. In general relativity we have

$$\tilde{g}^{ik} = \delta_{ik} - \phi^2 \frac{x_i x_k}{r^2}, \quad (16)$$

see §58 in [5]. This expression can be obtained also from the second order of perturbation expansion, considered in [6] using quantum tree graphs.

If general relativity is not assumed, we have instead of (16)

$$\tilde{g}^{ik} = \delta_{ik} - \alpha\phi^2 \frac{x_i x_k}{r^2}, \quad (17)$$

where α is a coefficient of order one. It is determined by a chosen 3 graviton vertex. The higher terms in the expansion (17), i.e. terms with ϕ^n and $\phi^n \frac{x_i x_k}{r^2}$, $n > 2$ are absent due to (15). Indeed, as seen from the relations

$$\left(\frac{1}{r^n}\right)_{,j} = -\frac{nx_j}{r^{n+2}}, \quad \left(\frac{x_i x_j}{r^n}\right)_{,j} = \frac{x_i(4-n)}{r^n},$$

only term $\phi^2 \frac{x_i x_k}{r^2} = G^2 M^2 x_i x_k / r^4$ is compatible with (15).

Using (17) and letting g_{00} to be arbitrary for the time being, we can express g_{ik} through it. First, from (17) we find

$$\det \tilde{g}^{ik} = 1 - \alpha\phi^2. \quad (18)$$

Then we have

$$\det \tilde{g}^{\mu\nu} = \tilde{g}^{00} \det \tilde{g}^{ik} = g. \quad (19)$$

Then, using $\tilde{g}^{00} = \sqrt{(-g)} g^{00} = \sqrt{-g}/g_{00}$, we obtain from (18) and (19)

$$\sqrt{-g} = -\frac{1 - \alpha\phi^2}{g_{00}}.$$

From definition $\tilde{g}^{ik} \tilde{g}_{kj} = \delta_{ij}$ we find

$$\tilde{g}_{kj} = \delta_{kj} + \frac{\alpha\phi^2}{1 - \alpha\phi^2} \frac{x_k x_j}{r^2}. \quad (20)$$

Finally, we have

$$g_{ik} = \sqrt{-g} \tilde{g}_{ik} = -\frac{1}{g_{00}} [(1 - \alpha\phi^2)\delta_{ik} + \alpha\phi^2 \frac{x_i x_k}{r^3}]. \quad (21)$$

Assuming $g_{00} = -\exp(2\phi)$, obtained in [7] from heuristic considerations, we get $g_{\mu\nu}$ and $t_{\mu\nu}$ regular everywhere except $r = 0$. The same form of g_{00} appears in general relativity for a model of a spherical body considered in the cylindrical coordinates, see eq. (8.30) in [8].

In any case, from perihelion precession we know that in G^2 approximation $g_{00} = -(1 + 2\phi + 2\phi^2)$. Then (21) in this approximation gives

$$g_{ik} = [1 - 2\phi + (2 - \alpha)\phi^2]\delta_{ik} + \alpha\phi^2 \frac{x_i x_k}{r^2}. \quad (22)$$

In general relativity $\alpha = 1$. If we want to preserve the coordinate condition (15) in a more general approach, then g_{ik} must still have the form (22).

3 Isotropic frame

In this frame

$$\begin{aligned} h_{00} &= \frac{4}{1 - \frac{\phi}{2}} - \frac{4}{(1 - \frac{\phi}{2})^2}, \\ h_{ij} &= \delta_{ij} \left[-2\phi + \frac{3}{2}\phi^2 - \frac{1}{2}\phi^3 + \frac{\phi^4}{16} \right], \quad h_{0i} = 0. \end{aligned} \quad (23)$$

Here ϕ has the same form as in (9). From here we get

$$\begin{aligned} h_{ij,km} &= \delta_{ij} \frac{x_k x_m}{r^4} [-6\phi + 12\phi^2 - \frac{15}{2}\phi^3 + \frac{3}{2}\phi^4] + \\ &\quad \frac{\delta_{ij}\delta_{km}}{r^2} [2\phi - 3\phi^2 + \frac{3}{2}\phi^3 - \frac{1}{4}\phi^4], \end{aligned} \quad (24)$$

$$\begin{aligned} h_{00,ij} &= \frac{\delta_{ij}}{r^2} \left[\frac{4}{1 - \frac{\phi}{2}} - \frac{12}{(1 - \frac{\phi}{2})^2} + \frac{8}{(1 - \frac{\phi}{2})^3} \right] + \\ &\quad \frac{x_i x_j}{r^4} \left[-\frac{4}{1 - \frac{\phi}{2}} - \frac{4}{(1 - \frac{\phi}{2})^2} + \frac{32}{(1 - \frac{\phi}{2})^3} - \frac{24}{(1 - \frac{\phi}{2})^4} \right]. \end{aligned} \quad (25)$$

and

$$h = -\frac{4}{1 - \frac{\phi}{2}} + \frac{4}{(1 - \frac{\phi}{2})^2} + 3[-2\phi + \frac{3}{2}\phi^2 - \frac{1}{2}\phi^3 + \frac{1}{16}\phi^4], \quad (26)$$

Using these expressions in (4), we find

$$R_{00}^{(1)} = \frac{1}{2}h_{00,ii} = \frac{1}{r^2} \left[\frac{4}{1 - \frac{\phi}{2}} - \frac{20}{(1 - \frac{\phi}{2})^2} + \frac{28}{(1 - \frac{\phi}{2})^3} - \frac{12}{(1 - \frac{\phi}{2})^4} \right], \quad (27)$$

$$\begin{aligned} R_{ij}^{(1)} &= \frac{x_i x_j}{r^4} \left[\frac{2}{1 - \frac{\phi}{2}} + \frac{2}{(1 - \frac{\phi}{2})^2} - \frac{16}{(1 - \frac{\phi}{2})^3} + \frac{12}{(1 - \frac{\phi}{2})^4} - 3\phi + 6\phi^2 - \right. \\ &\quad \left. \frac{15}{4}\phi^3 + \frac{3}{4}\phi^4 \right] + \frac{\delta_{ij}}{r^2} \left[-\frac{2}{1 - \frac{\phi}{2}} + \frac{6}{(1 - \frac{\phi}{2})^2} - \frac{4}{(1 - \frac{\phi}{2})^3} + \phi - \frac{3}{4}\phi^3 + \frac{1}{4}\phi^4 \right] \end{aligned} \quad (28)$$

Finally, we obtain from (3) (the first two terms on the r.h.s. of (3) disappear because we use the exact solution of the Einstein equation and consider the region of space without matter)

$$8\pi G r^2 t_{00}^{iso} = -3\phi^2 + 3\phi^3 - \frac{3}{4}\phi^4, \quad \phi = -\frac{GM}{r}, \quad t_{0i}^{iso} = 0; \quad (29)$$

(this is an exact expression for t_{00}^{iso}) and similarly

$$8\pi G t_{ij}^{iso} = \frac{x_i x_j}{r^4} \left[-\frac{2}{1 - \frac{\phi}{2}} - \frac{2}{(1 - \frac{\phi}{2})^2} + \frac{16}{(1 - \frac{\phi}{2})^3} - \right.$$

$$\begin{aligned} & \frac{12}{(1 - \frac{\phi}{2})^4} + 3\phi - 6\phi^2 + \frac{15}{4}\phi^3 - \frac{3}{4}\phi^4] + \frac{\delta_{ij}}{\rho^2}[-\frac{2}{1 - \frac{\phi}{2}} + \frac{14}{(1 - \frac{\phi}{2})^2} - \\ & \frac{24}{(1 - \frac{\phi}{2})^3} + \frac{12}{(1 - \frac{\phi}{2})^4} - \phi + 3\phi^2 - \frac{9}{4}\phi^3 + \frac{1}{2}\phi^4]. \end{aligned} \quad (30)$$

For $\phi \ll 1$ we have

$$8\pi G t_{ij}^{iso}|_{\phi \ll 1} = 7\frac{\phi^2}{r^2} \left(\delta_{ij} - 2\frac{x_i x_j}{r^2} \right) + \frac{9}{2} \frac{\phi^3}{r^2} \left(\delta_{ij} - \frac{5}{3} \frac{x_i x_j}{r^2} \right) + \dots \quad (31)$$

We note now that $t_{\mu\nu}^{iso}$ is regular everywhere, except at $r = 0$. This can be expected because the metric in (7) is regular. The transformation from the harmonic frame to the isotropic one is also regular transformation (as well near horizon): $R = \rho(1 + \frac{GM}{2\rho})^2 - GM$. So there is no reason for disappearance of singularities in $t_{\mu\nu}^{iso}$. If we assume that $h_{\mu\nu}^{har}$ is formed only by the physical degrees of freedom, we may consider $t_{\mu\nu}^{har}$ as a correct tensor and interpret the disappearance of singularity in $t_{\mu\nu}^{iso}$ as foul play of nonphysical degrees of freedom.

From (12-13) and (29), (31) we see that in ϕ^2 approximation $t_{\mu\nu}^{har}$ coincides with $t_{\mu\nu}^{iso}$. This is in agreement with the fact that $h_{\mu\nu}^{(2)iso}$, (i.e. $h_{\mu\nu}^{iso}$ in the ϕ^2 approximation) can be obtained from $h_{\mu\nu}^{(2)har}$ by gauge transformation

$$\begin{aligned} h_{ij}^{(2)har} - h_{ij}^{(2)iso} &= \frac{1}{2}G^2 M^2 \left(\frac{\delta_{ij}}{r^2} - \frac{2x_i x_j}{r^4} \right) = \frac{1}{4}G^2 M^2 (\Lambda_{i,j} + \Lambda_{j,i}), \\ \Lambda_i &= \frac{x_i}{r^2}. \end{aligned} \quad (32)$$

Here

$$h_{ij}^{(2)har} = \phi^2 \left(\delta_{ij} + \frac{x_i x_j}{r^2} \right), \quad h_{ij}^{(2)iso} = \frac{3}{2} \phi^2 \delta_{ij},$$

see (9) and (23). The gauge transformation does not changes the source and may be interpreted as a change of frame, but *not visa versa*. The linear approximation in $h_{\mu\nu}$, i.e. $h_{\mu\nu}^{(1)}$ produces the ϕ^2 approximation in the source (see equation (7.6.15) in [2]) and that is why $t_{\mu\nu}^{(2)}$ coincide in both frames.

4 Standard frame

In this case we have

$$h_{00} = -2\phi, \quad h_{ij} = \frac{x_i x_j}{r^2} \left(\frac{1}{1 + 2\phi} - 1 \right). \quad (33)$$

Simple calculations give

$$\begin{aligned}
h_{ij,kl} = & \frac{x_i x_j x_k x_l}{r^6} \left[-8 + \frac{3}{1+2\phi} + \frac{3}{(1+2\phi)^2} + \frac{2}{(1+2\phi)^3} \right] + \frac{1}{r^4} (\delta_{il} x_j x_k + \\
& \delta_{jl} x_i x_k + \delta_{kl} x_i x_j + \delta_{ik} x_j x_l + \delta_{jk} x_i x_l) [2 - \frac{1}{1+2\phi} - \frac{1}{(1+2\phi)^2}] + \\
& \frac{1}{r^2} (\delta_{ik} \delta_{jl} + \delta_{jk} \delta_{il}) [\frac{1}{1+2\phi} - 1]. \tag{34}
\end{aligned}$$

As in previous Section we find

$$8\pi G t_{00}^{st} = \frac{1}{r^2} \left[-1 + \frac{2}{1+2\phi} - \frac{1}{(1+2\phi)^2} \right], \tag{35}$$

$$8\pi G t_{00}^{st}|_{\phi \ll 1} = \frac{1}{r^2} [-4\phi^2 + 16\phi^3 + \dots], \tag{36}$$

and

$$\begin{aligned}
8\pi G t_{ij}^{st} = & \frac{x_i x_j}{r^4} \left[1 - 3\phi - \frac{1}{2(1+2\phi)} - \frac{1}{2(1+2\phi)^2} \right] + \\
& \frac{\delta_{ij}}{r^2} \left[\phi - \frac{1}{2(1+2\phi)} - \frac{1}{2(1+2\phi)^2} \right], \tag{37}
\end{aligned}$$

$$8\pi G t_{ij}^{st}|_{\phi \ll 1} = 4 \frac{\phi^2}{r^2} \left(\delta_{ij} - \frac{2x_i x_j}{r^2} \right) - 12 \frac{\phi^3}{r^2} \left(\delta_{ij} - \frac{5}{3} \frac{x_i x_j}{r^2} \right) + \dots. \tag{38}$$

Comparing (36) and (38) with corresponding expressions in harmonic frame, see (12) and (13), we note that there is a difference even in ϕ^2 approximation. This means that $h_{\mu\nu}^{(2)st}$ cannot be obtained from $h_{\mu\nu}^{(2)har}$ by gauge transformation because the latter do not affect $t_{\mu\nu}$ calculated with $h_{\mu\nu}$ in linear approximation. The small difference in radial coordinates in these systems [see the transition from (5) to (6)], i.e. $r - R = GM$, can't be responsible for the essential differences in the energy-momentum tensors when $R, r \gg GM$. The blame must be laid upon the violation of the coordinate condition (15), i.e. on the nonphysical degrees of freedom.

Finally, we note that in the considered static field in space without matter the conservation law $t^{\mu\nu}_{,\nu}$ takes the form $t_{ij,j} = 0$ outside the horizon. Each term in the expansion of $t_{ij,j}$ in power series of ϕ must satisfy the conservation law and this dictates up to a constant factor the form of the n -th term of the expansion:

$$\frac{\phi^n}{r^2} \left(\delta_{ij} - \frac{n+2}{n} \frac{x_i x_j}{r^2} \right).$$

5 Conclusion

We see that the energy-momentum tensor of gravitational field requires the existence of privileged coordinate system and there are some grounds to assume that the rectangular harmonic frame is such a system. Of course, any other frame is also good if we deal with covariant quantities, but the energy-momentum tensor must be properly transformed from the privileged system. It seems reasonable to expect that in the region of applicability of any theory, its energy-momentum tensor should be finite. More exactly we expect that the total gravitational energy in space outside a radius r must be finite. In general relativity, with definitions of $t_{\mu\nu}$ which seems reasonable, this energy goes to $-\infty$ when $r \rightarrow GM$ [9,4]. So the consideration of possible deviations from general relativity are of interest, cf [10].

Acknowledgments

This work was supported in part by the Russian Foundation for Basic Research (projects no. 00-15-96566 and 02-02-16944).

References

1. Misner C.W., Thorne K.S., Wheeler J.A., *Gravitation*, Sam Francisco (1973).
2. Weinberg S., *Gravitation and Cosmology*, New York (1972).
3. Schwinger J., *Particle, Sources and Fields*, Addison-Wesley Publishing Company, Reading (1970).
4. Nikishov A.I. gr-qc/0002038; Bulletin of the Lebedev Physics Institute, N12, pp. 45-49 (1999).
5. Fock V., *The Theory of Space-Time and Gravitation*. (2-nd revised edition, Pergamon Press, New York, 1964.)
6. Duff M.J., Phys. Rev. **D**, V. **7**, 2317 (1972).
7. Dehnen H., Hönl H. and Westpfahl, Ann. der Phys. **6**, 7 Folge, Band 6, Heft 7-8, S. 670 (1960).
8. Synge J.L., *Relativity: The General Theory*, Amsterdam (1960).
9. Dehnen H. Zeit. für Phys., **179** Band, 1 Heft, S. 76 (1964).
10. Nikishov A.I., gr-qc/9912034; Part. and Nuclei, **32**, p. 5 (2001).

SINGULARITIES ELECTRODYNAMICS WITH A “MAGNETIC” CHARGE IN SPACES OF VARIOUS DIMENSION

S.V. Kopylov ^a, G.P. Cherny ^b

^a STE "Brainstorm", 26-9 Konstantinov Street, 129626 Moscow, Russia
^b Moscow Bauman State Technical University, 5 Second Baumanskaya Street,
105005 Moscow, Russia

Abstract. The results of experiments on detection of magnetic charges have been negative up to now. Nevertheless experimental and theoretical investigations in this direction are going on. The basic purpose of the present work is to explain the structure of sources of an electromagnetic field usually associated with magnetic charges. Multidimensional spaces is used as a methodical approach. Such an approach allows us to differentiate the general properties from those inherent only to space of a concrete dimension.

1 Equations

The equations of electrodynamics in vacuo, as known, has the form:

$$\partial_\mu \mathbf{F}^{\mu\nu} = \mathbf{j}^\nu, (\partial_\nu \mathbf{j}^\nu = \mathbf{0}) \quad (1),$$

$$\varepsilon^{\mu\nu\rho\lambda} \partial_\mu \mathbf{F}_{\rho\lambda} = \mathbf{0} \quad (2).$$

For a dual tensor $\tilde{F}^{\mu\nu} = \varepsilon^{\mu\nu\rho\lambda} F_{\rho\lambda}$ we shall obtain a more symmetric form:

$$\partial_\mu \mathbf{F}^{\mu\nu} = \mathbf{j}^\nu, (\partial_\nu \mathbf{j}^\nu = \mathbf{0}) \quad (3),$$

$$\partial_\mu \tilde{\mathbf{F}}^{\mu\nu} = \tilde{\mathbf{j}}^\nu, (\partial_\nu \tilde{\mathbf{j}}^\nu = \mathbf{0}) \quad (4).$$

A full symmetry is achieved by introducing a current of magnetic charges \tilde{j}^ρ , [1]:

$$\partial_\mu \mathbf{F}^{\mu\nu} = \mathbf{j}^\nu, (\partial_\nu \mathbf{j}^\nu = \mathbf{0}) \quad (5),$$

$$\partial_\mu \tilde{\mathbf{F}}^{\mu\nu} = \tilde{\mathbf{j}}^\nu, (\partial_\nu \tilde{\mathbf{j}}^\nu = \mathbf{0}) \quad (6).$$

2 Specific properties of electrodynamics for n=4

The space of dimension 4 is characterized by a coincidence of the rank of the tensor $F^{\mu\nu}$ with the rank of a dual tensor $\tilde{F}^{\mu\nu}$ [2]. In particular, the relations (5,6) prove to be invariant under dual transformations as [1,3]:

$$\mathbf{F}^{\mu\nu} \mapsto \mathbf{F}^{\mu\nu} \cos(\alpha) + \tilde{\mathbf{F}}^{\mu\nu} \sin(\alpha),$$

^ae-mail: KopSV@mail.ru

$$\begin{aligned}\tilde{\mathbf{F}}^{\mu\nu} &\mapsto -\mathbf{F}^{\mu\nu} \sin(\alpha) + \tilde{\mathbf{F}}^{\mu\nu} \cos(\alpha), \\ \mathbf{j}^\nu &\mapsto \mathbf{j}^\nu \cos(\alpha) + \tilde{\mathbf{j}}^\nu \sin(\alpha), \\ \tilde{\mathbf{j}}^\nu &\mapsto -\mathbf{j}^\nu \sin(\alpha) + \tilde{\mathbf{j}}^\nu \cos(\alpha).\end{aligned}$$

Below, we consider electrodynamics in spaces of arbitrary dimension (n).

$$\partial_\mu \mathbf{F}^{\mu\nu} = \mathbf{j}^\nu, (\partial_\nu \mathbf{j}^\nu = \mathbf{0}) \quad (7),$$

$$\begin{aligned}\varepsilon^{\overbrace{\lambda\mu\nu\rho\tau\dots\xi}^n} \partial_\lambda \mathbf{F}_{\mu\nu} &= \overbrace{\tilde{\jmath}^{\rho\tau\dots\xi}}^{n-3}, \\ (\partial_\rho \tilde{\jmath}^{\rho\tau\dots\xi} = \mathbf{0}) \quad (8).\end{aligned}$$

The form of equation (7) is independent of space dimension . In equation (8) the rank pseudotensor changes in the right side of the equation, since the rank completely antisymmetric Levi-Civita pseudotensor varies with the change of space dimension.

The relation (8) can be always presented as:

$$\begin{aligned}\varepsilon^{\overbrace{\lambda\mu\nu\rho\tau\dots\xi}^n} \partial_\lambda \mathbf{F}_{\mu\nu} &= \varepsilon^{\lambda\mu\nu\rho\tau\dots\xi} \mathbf{J}_{\lambda\mu\nu}, \\ (\partial_\rho \varepsilon^{\lambda\mu\nu\rho\tau\dots\xi} \mathbf{J}_{\lambda\mu\nu} = \mathbf{0}) \quad (9).\end{aligned}$$

Here $J_{\lambda\mu\nu}$ is a completely antisymmetric tensor of the third rank dual to the tensor $\tilde{\jmath}^{\rho\tau\dots\xi}$. The number of components $J_{\lambda\mu\nu}$ is equal to $C_n^3 = C_n^{n-3}$, that is to the number of components of the tensor $\tilde{\jmath}^{\rho\tau\dots\xi}$.

3 Potentials

The current vector j^ν corresponds to a vector potential A^ν . $F^{\mu\nu}$ is set as $F^{\mu\nu} = \partial_\mu A^\nu - \partial_\nu A^\mu$. Equations (8) prove to equal zero identically. Equations (7) give $\square A^\nu = j^\nu$ provided $\partial_\nu A^\nu = 0$, which is in agreement with the condition on j^ν of equations (7): $\partial_\nu j^\nu = 0$. The condition $\partial_\nu A^\nu = 0$ is always valid, since $F^{\mu\nu} = \tilde{F}^{\mu\nu}$ at $A^\mu \rightarrow \tilde{A}^\mu = A^\mu + \partial^\mu \phi$, where ϕ is an arbitrary scalar function.

Similarly we shall assign $J_{\lambda\mu\nu}$ to the potential $f^{\sigma\mu\nu}$ where $f^{\sigma\mu\nu}$ completely antisymmetric tensor of the third rank. Thus: $F^{\mu\nu} = \partial_\sigma f^{\sigma\mu\nu}$. In this representation equations (7) are identically equal to zero. Equations (8), or, that too - (9), thus will take the form:

$$\begin{aligned}\varepsilon^{\overbrace{\lambda\mu\nu\rho\tau\dots\xi}^n} \partial_\lambda \partial^\sigma \mathbf{f}_{\sigma\mu\nu} &= \varepsilon^{\lambda\mu\nu\rho\tau\dots\xi} \mathbf{J}_{\lambda\mu\nu}, \\ (\partial_\rho \varepsilon^{\lambda\mu\nu\rho\tau\dots\xi} \mathbf{J}_{\lambda\mu\nu} = \mathbf{0}) \quad (10).\end{aligned}$$

Just as for the potential A^μ we have: $F^{\mu\nu} = \check{F}^{\mu\nu}$ at $f_{\sigma\mu\nu} \rightarrow \check{f}_{\sigma\mu\nu} = f_{\sigma\mu\nu} + \partial^\rho \Pi_{\rho\sigma\mu\nu}$, where $\Pi_{\rho\sigma\mu\nu}$ is a completely antisymmetric tensor of the fourth rank.

Take advantage of this freedom and we shall impose on $f_{\sigma\mu\nu}$ of additional condition of a kind: $\partial_\rho \varepsilon^{\lambda\mu\nu\rho\tau\dots\xi} f_{\lambda\mu\nu} = 0$. It can be always made due to an arbitrariness of $\Pi_{\rho\sigma\mu\nu}$.

It is possible to show that under this condition equation (10) takes the form:

$$\begin{aligned}\lambda\mu\nu &= \varepsilon^{\lambda\mu\nu\rho\tau\dots\xi} \mathbf{J}_{\lambda\mu\nu}, \\ (\partial_\rho \varepsilon^{\lambda\mu\nu\rho\tau\dots\xi} \mathbf{J}_{\lambda\mu\nu}) &= 0\end{aligned}\quad (11).$$

Or, which is the same,

$$\begin{aligned}\square \mathbf{f}_{\lambda\mu\nu} &= \mathbf{J}_{\lambda\mu\nu}, \\ (\partial_\rho \varepsilon^{\lambda\mu\nu\rho\tau\dots\xi} \mathbf{J}_{\lambda\mu\nu}) &= 0\end{aligned}\quad (12).$$

From the relation obtained it is seen that the above condition on $f_{\lambda\mu\nu}$ is in agreement, as is in the case with A^μ , with the requirement for the current: $\partial_\rho \varepsilon^{\lambda\mu\nu\rho\tau\dots\xi} J_{\lambda\mu\nu} = 0$ equations (12).

4 Sources

The electric current density j_μ for the case of a local charge has the form $j_\nu = e\delta(x-x_0)du_\nu/dt$. Similarly, a local source of the field $f_{\lambda\mu\nu}$ should take the form $J_{\lambda\mu\nu} = g\delta(x-x_0)\{s_{\lambda\mu}du_\nu/dt\}$. Here e and g are constants, and $\{ \}$ - is antisymmetrization of a tensor. Thus as a source of $f_{\lambda\mu\nu}$ should be considered the antisymmetrized tensor of a spin density tensor.

The Lagrangian of interaction takes the form:

$$\mathbf{L}_{\text{int}} = \mathbf{f}^{\lambda\mu\nu} \mathbf{J}_{\lambda\mu\nu} \quad (13).$$

4.1 Spinor field ($n = 4$)

For Dirac's bispinors in the case of $n=4$ we have [4]:

$$\mathbf{L}_{\text{int}} = \mathbf{f}^{\lambda\mu\nu} \bar{\Psi} \gamma_5 \gamma_\lambda \gamma_\mu \gamma_\nu \Psi \quad (14).$$

Or, which is the same, $L_{\text{int}} = B^\nu \bar{\Psi} \gamma_5 \gamma_\nu \Psi$, where B^ν is a pseudo-vector. Thus $\partial_\nu \bar{\Psi} \gamma_5 \gamma_\nu \Psi = 0$, i.e. such an interaction is connected with an axial current. For the axial current in quantum field theory, it is known [5], that

$$\partial_\nu \bar{\Psi} \gamma_5 \gamma_\nu \Psi = 2m \bar{\Psi} \gamma_5 \Psi + e^2 / 16\pi^2 \tilde{F}_{\mu\nu} F^{\mu\nu} \quad (15).$$

Hence it is clear that even for $m = 0$ such a current is not conserved due to the presence of an axial anomaly $\tilde{F}_{\mu\nu} F^{\mu\nu}$.

4.2 Vector field ($n = 4$).

For a vector field [6], in four - dimension space, we obtain $J_{\lambda\mu\nu} = \{S_{\lambda\mu\nu}\}$ and the requirement of the current divergence being equal to zero results in the relation

$$\varepsilon^{\lambda\mu\nu\rho} \partial_\rho \{S_{\lambda\mu\nu}\} = \tilde{\mathbf{F}}_{\mu\nu} \mathbf{F}^{\mu\nu} = 0 \quad (16).$$

Thus, we again come to a dependence on the axial anomaly.

4.3 Scalar field.

For a scalar field, whose spin equals zero it is possible to estimate the role of an orbital moment: $M_{\mu\nu}^\rho$. Since [4]

$$\mathbf{M}_{\mu\nu}^\rho = \mathbf{x}_\mu \mathbf{T}_\nu^\rho - \mathbf{x}_\nu \mathbf{T}_\mu^\rho \quad (17),$$

where $T_{\mu\nu}$ - is the symmetric energy momentum tensor, then the contraction

$$\mathbf{L}_{\text{int}} = \{\mathbf{M}_{\mu\nu}^\rho\} \mathbf{f}_\rho^{\mu\nu} = 0 \quad (18).$$

4.4 Case of $n \neq 4$.

For spinor fields in the case of $n=6$ we have [7]:

$$\mathbf{L}_{\text{int}} = \mathbf{f}^{\lambda\mu\nu} \bar{\Psi} \Gamma_\lambda \Gamma_\mu \Gamma_\nu \Psi \quad (19).$$

Or, which is the same,

$$\mathbf{L}_{\text{int}} = \mathbf{B}^{\rho\sigma\tau} \bar{\Psi} \Gamma_7 \Gamma_\rho \Gamma_\sigma \Gamma_\tau \Psi \quad (20),$$

where $B^{\rho\sigma\tau}$ - is the pseudotensor dual to the tensor $f^{\lambda\mu\nu}$. Thus we should have $\partial_\rho \bar{\Psi} \Gamma_7 \Gamma_\rho \Gamma_\sigma \Gamma_\tau \Psi = 0$.

Therefore only for $n = 4$ the source takes the form of a pseudo-current (pseudo-vector) which simplifies some calculations. In a general case it is a pseudotensor.

4.5 Poincarés Group.

To Poincarés group correspond two basic Casimir operators:

$$\begin{aligned} \mathbf{P}_\mu \mathbf{P}^\mu &= \mathbf{m}^2, \\ \mathbf{W}_\mu \mathbf{W}^\mu &= \mathbf{m}^2 s(s+1); \\ \text{here: } \mathbf{W}^\mu &= \varepsilon^{\mu\nu\rho\sigma} \mathbf{M}_{\nu\rho} \mathbf{P}_\sigma. \end{aligned} \quad (21)$$

In field theory P_μ is related to the A_μ procedure of lengthening the derivative: $P_\mu \longrightarrow P_\mu - eA_\mu$.

By analogy it would be possible to construct: $\{M_{\nu\rho}P_\sigma\} \longrightarrow \{M_{\nu\rho}P_\sigma\} - gf_{\nu\rho\sigma}$. However W_ν does not generate the equations of motion distinct from the equations related to P_ν .

An absence of such equations of motion, in our opinion, is a principal reason why there arises a problem of field source existence of $f_{\sigma\mu\nu}$.

Acknowledgments

We are grateful to A.I. Studenikin for providing for us the possibility of participating in the 11th Lomonosov Conference on Elementary Particle Physics.

References

- [1] A.A. Sokolov, I.M. Ternov, V.Ch. Zhukovsky et al., "Gauge Fields", (Moscow University Publishers, Moscow), 49, 1986.
- [2] Y.S. Vladimirov, "Frame of Reference in the Theory of Gravitation", (Energoizdat, Moscow), 234, 1982.
- [3] V.I. Strazhev, L.M. Tomil'chik, "Electrodynamics with a Magnetic Charge", (Science and Engineering, Minsk), 32, 1975.
- [4] N.N. Bogoliubov, D.V. Shirkov, "Introduction to Quantized Field Theory", (Nauka, Moscow), 30, 1984.
- [5] Encyclopedia of Physics, (Soviet Encyclopedia, Moscow), 1, 87, 1988.
- [6] N.Cabibbo, E.Ferrari, *Nuovo Cimento*, **23**, 1147 (1962).
- [7] S.V. Kopylov, in "Frontiers of Particle Physics" (Proceeding of the 10th Lomonosov Conference on Elementary Particle Physics), ed. by A. Studenikin, World Scientific Singapore, 304, 2003.

DIRECT CP VIOLATION MEASUREMENTS WITH THE NA48 EXPERIMENT: STATUS AND PERSPECTIVES

M.Scarpa ^{a b}

INFN and University of Ferrara, Ferrara, Italy

Abstract. Direct CP violation in neutral Kaon system has been studied at NA48 through the measurement of $Re(\epsilon'/\epsilon)$. The decay rates of neutral kaons $K_{L,S}$ in two pions ($\pi^0\pi^0, \pi^+\pi^-$) were measured using two collinear beams, the four decay modes were collected concurrently. The final result, covering the full data sample collected from 1997 to 2001, is $(14.7 \pm 2.2) \times 10^{-4}$ showing a clean evidence of direct CP violation in neutral Kaon system. Year 2003 data taking has been devoted to high statistics study of charged kaon decays using simultaneous K^+ and K^- beams, and an upgraded NA48 setup: NA48/2. The main goal is to measure the CP-violating asymmetry in the linear slope of the $K^\pm \rightarrow \pi^\pm\pi^+\pi^-$ decays with an accuracy of about 10^{-4} .

1 CP violation in Kaon system

1.1 CP violation in neutral Kaon system

If CP is conserved the mass eigenstates K_S and K_L ($c\tau_S = 2.6786\text{cm}$, $c\tau_L = 15.51\text{m}$ [1]) should be pure CP eigenstates: K_1 ($CP = +1$) and K_2 ($CP = -1$). As a consequence K_L should not decays into $\pi\pi$ ($CP = +1$). But in 1964 the forbidden K_L decays in the opposite CP state $\pi^+\pi^-$ were recorded by Christenson, Cronin, Fitch and Turlay [2]. The observed CP violation effect was of order $\approx 2 \times 10^{-3}$.

The effect, called *Indirect* CP violation, is due to $K^0 - \bar{K}^0$ (flavour eigenstates) mixing. Mass eigenstates are not pure CP eigenstates: $K_S \approx K_1 + \epsilon K_2$, $K_L \approx K_2 + \epsilon K_1$ where $\epsilon \approx 2 \times 10^{-3}$ is the *indirect* CP violation parameter.

If the mixing is the only source of CP violation then the ratios of CP violating / CP conserving decay amplitudes η_{+-} and η_{00}

$$\eta_{+-} \equiv \frac{A(K_L \rightarrow \pi^+\pi^-)}{A(K_S \rightarrow \pi^+\pi^-)} , \quad \eta_{00} \equiv \frac{A(K_L \rightarrow \pi^0\pi^0)}{A(K_S \rightarrow \pi^0\pi^0)} \quad (1)$$

should be both equal to ϵ . CP violation in neutral kaon system is dominated by mixing but there could also be a *direct* CP violation contribution, occurring in the decay process itself. *Direct* CP violation requires two interfering amplitudes, two different weak phase-shifts and two different strong phase-shifts: in neutral kaon system it can be seen through the interference of $\pi\pi$ final states with different isospin ($\pi\pi$ can have isospin $I=0$ or $I=2$).

Taking into account the *direct* CP violation the *CP violating / CP conserving* ratios can be expressed as

^ae-mail: marcella.scarpa@cern.ch

^bon behalf of the NA48 Collaboration

$$\eta_{+-} \approx \epsilon + \epsilon' , \quad \eta_{00} \approx \epsilon - 2\epsilon' \quad (2)$$

where ϵ' is the *direct* CP violation parameter^c. Therefore direct CP violation can be demonstrated measuring $\epsilon' \neq 0$. Being $\epsilon' \ll \epsilon$ it is convenient to measure the double ratio R, realated to $Re(\epsilon'/\epsilon)$ by [3]:

$$R = |\eta_{00}/\eta_{+-}|^2 = \frac{\Gamma(K_L \rightarrow \pi^0\pi^0)\Gamma(K_S \rightarrow \pi^+\pi^-)}{\Gamma(K_S \rightarrow \pi^0\pi^0)\Gamma(K_L \rightarrow \pi^+\pi^-)} \approx 1 - 6Re(\epsilon'/\epsilon) \quad (3)$$

1.2 CP violation in charged Kaon system

In charged kaon system, free from mixing, a manifestation of direct CP violation would be any difference between the K^+ and K^- decay matrix elements [4]. The matrix element for $K^\pm \rightarrow (3\pi)^\pm$ (B.r. $(5.576 \pm 0.031)\%$ [1]) can be parametrized as

$$|M(u, v)|^2 \propto 1 + gu + hu^2 + kv^2 \quad (4)$$

where $u = (s_3 - s_0)/m_\pi^2$, $v = (s_1 - s_2)/m_\pi^2$, $s_0 = (s_1 + s_2 + s_3)/3$, $s_i = (P_K - P_i)^2$, P_K and P_i the 4-momenta of kaon and pion (i=3 for the odd pion, having opposite sign to the decaying kaon) [4].

In case of CP conservation the coefficient g^+, h^+, k^+ and g^-, h^-, k^- , for K^+ and K^- respectively, must be the same. Direct CP violation can be measured through the asymmetry in the slope describing the linear dependence of the decay probabilities on the u variable of the Dalitz plot:

$$A_g = \frac{g^+ - g^-}{g^+ + g^-} \quad (5)$$

In the analogous way A_g^0 is the asymmetry parameter for $K^\pm \rightarrow \pi^0\pi^0\pi^\pm$ (B.r. $(1.73 \pm 0.04)\%$).

2 NA48: $Re(\epsilon'/\epsilon)$ measurement

Up to year 2001 $Re(\epsilon'/\epsilon)$ measurement, through the double ratio R, has been the main NA48 item [5]. In order to achieve a precision of $\approx 2 \times 10^{-4}$ several millions of $K_L \rightarrow \pi\pi$ are required ($K_L \rightarrow \pi\pi$ are only 0.3% of K_L decays) and systematic uncertainties have to be minimized. In the double ratio R:
- contributions from systematic effects can be canceled if they are symmetric on Long/Short or Charge/Neutral modes

^c $\epsilon' = \frac{i}{\sqrt{2}} Im \frac{A_2}{A_0} \exp(i(\delta_2 - \delta_0))$, where $A(K_0 \rightarrow \pi\pi, I) = A_I \exp(i\delta_I)$, $A(\overline{K_0} \rightarrow \pi\pi, I) = A_I^* \exp(i\delta_I)$ and δ_I are strong phases

- fluxes, inefficiency, dead time, accidental effects cancel in case of concurrent decays.

Differences between K_S and K_L acceptances $a_{L,S}(p, z)$, function of momentum and vertex position along beam direction, can be minimized if K_L and K_S have similar spectra, obtained using kaons with energy in the range (70,170)GeV, and the decays are

- in the same decay volume,
- coming from quasi-collinear beams,

Moreover being $\tau_L \approx 600 \times \tau_S$ the K_S and K_L have very different decay lengths, this imply a big difference on the total acceptance for K_S and K_L , even if for a given decay position the acceptances are the same. As a consequence a big correction on R would be needed (red stars in Fig. (1)). To avoid this the K_L events are weighted, offline on a event by event basis, by means of a proper lifetime function obtaining similar distributions for K_S and K_L (Fig. (2)). Through the weighting the acceptance correction almost cancels in the double ratio (black dots in Fig. (1)), even if the statistical error on R increases by about 35%. To be insensitive to remaining difference in K_L and K_S spectra, the analysis is performed in bins of kaon energy, 5Gev each.

Summarizing, in order to minimize systematic uncertainties, the experiment has been designed to have collinear K_L and K_S beams and to collect the four decay modes ($K_{L,S} \rightarrow \pi^0\pi^0, \pi^+\pi^-$) simultaneously and in the same fiducial volume. Therefore, once subtracted the background, the double ratio reduces to double ratio of number of decays:

$$R = \frac{N(K_L \rightarrow \pi^0\pi^0)N(K_S \rightarrow \pi^+\pi^-)}{N(K_S \rightarrow \pi^0\pi^0)N(K_L \rightarrow \pi^+\pi^-)} \quad (6)$$

where the *first order* corrections ($\approx 1\%$) have been canceled and the remaining *second order* (few per mille) corrections ΔR due to residual asymmetries (like remaining backgrounds, trigger inefficiency and so on) have to be estimated. In year 2001 run (≈ 90 days) $1.55 \times 10^6 K_L \rightarrow \pi^0\pi^0$ have been collected.

2.1 NA48 beams and detector

NA48, located in the CERN North Area, makes use of protons extracted from SPS to produce the *far* (K_L) and *near* (K_S) beams: the primary protons impinge on a first target producing the *far* beam, while part of the non interacting protons are deviated toward a second target (*near*) slightly displaced on the vertical axis ($\approx 7cm$) w.r.t the far beam axis (Fig. (3)). Along the proton secondary path is placed a tagging station (Tagger) to record the crossing time of each proton going to the K_S target. The coincidence ($\pm 2ns$) between the time of the event (from the detector) and the time of the nearest proton in

the Tagger labels the decay as K_S . The two beams enter the same fiducial volume, roughly 6m downstream the *near* target and 126m from *far* target, so that decaying kaons from *near* and *far* beam are K_S and K_L respectively.

The beginning of the fiducial volume is defined by an anticounter (AKS), located on the K_S beam path, used to reject all the $K_S \rightarrow \pi\pi$ decays occurred upstream. The two beam axis converge at the center of the electromagnetic calorimeter (LKr) located $\approx 120m$ downstream. Seven rings of counters surround the fiducial volume in order to record escaping photons thus reducing $K_L \rightarrow 3\pi^0$ background. Muon counters, at the end of the beam line, are used as a veto to reduce the $K_{\mu 3}$ background. The main subdetectors for charged and neutral decays are (Fig. (4)):

- charged decays: magnetic spectrometer. A dipole magnet providing 265 MeV p_t kick, two drift chambers upstream and two downstream of it. Each drift chamber is equipped with 4 views (2 staggered planes each) orthogonal to the beam axis (Z) and oriented at $0^\circ, 90^\circ, -45^\circ, +45^\circ$. Each plane houses 256 sense wires, 1cm spaced. The track momentum resolution is $\sigma(p)/p = 0.48\% \oplus 0.009p\%$ (p in GeV/c).
- neutral decays: Liquid Krypton electromagnetic calorimeter. It is a quasi-homogeneous detectors filled with an active volume of $\sim 10m^3$ of liquid Krypton. Several performances are required since $2\pi^0$ decays are reconstructed through their 4ys detection. 13212 cells ($2 \times 2cm^2 \times 127cm$) are defined by electrodes in a structure of longitudinal projective towers pointing toward the center of the decay region. The energy resolution is $\sigma(E)/E = \frac{(3.2 \pm 0.2)\%}{\sqrt{E}} \oplus \frac{(9 \pm 1)\%}{E} \oplus (0.42 \pm 0.05)\%$

2.2 $\pi^+\pi^-$ detection and reconstruction

$K_{L,S} \rightarrow \pi^+\pi^-$ events are triggered by the two levels *charged trigger* (efficiency $\approx 98.7\%$). The first level reduces the rate to 100kHz by a coincidence of charged hodoscope signals in opposite quadrants, hit multiplicity in the first chamber (integrated over 200ns) and total energy from calorimeters (LKr+HAC). The second level trigger is based on hardware coordinate builder reconstructing tracks from drift chambers (1,2, and 4) data.

Charged selection is based on tracks, momenta and invariant mass. The $\pi^+\pi^-$ invariant mass resolution is about 2.5 MeV (Fig. (5)) and the applied cut is at 3σ . In November 1999 all the four drift chambers were damaged by the implosion of the beam pipe but they have been rebuilt and were ready for the run in year 2001. The new chambers' resolution, as shown in Fig. (5) is in agreement with 1998 and 1999 data.

In order to reduce effects from uncertainties in magnetic field and multiple scattering in the definition of the fiducial region the kaon energy is calculated

by the $\pi^+\pi^-$ opening angle (θ) and tracks energy ratio:

$$E_K^2 = \frac{C}{\theta^2} \{ m_K^2 - C m_\pi^2 \} \quad , \quad C = 2 + \frac{E_{\pi 1}}{E_{\pi 2}} + \frac{E_{\pi 1}}{E_{\pi 2}} \quad (7)$$

Charged energy understandig is reduced to chambers' geometry knowledge and can be checked reconstructing the position of the AKS anticounter for not vetoed $\pi^+\pi^-$ ($\Delta z = 2$ cm).

The background, due to K_L semileptonic decays in which an electron or a muon is identified as a pion, are suppressed by μ -veto counters and the E/p cut, where E is the energy of the cluster associated to the track in the calorimeter. Λ decays are suppressed cutting on tracks momentum asymmetry while the cut on kaon transverse momentum ($P_T^2 < 200$ (MeV/c) 2) removes three-body decays with a missing neutrino. A detailed description of the cuts can be found in [3, 5, 6]

2.3 $\pi^0\pi^0$ detection and reconstruction

$K_{L,S} \rightarrow \pi^0\pi^0$ events are triggered by the *neutral trigger* which operates on Lkr informations such as energy deposit and number of energy peaks, and distance of the decay vertex from the calorimeter. The electronics is implemented in a pipeline which makes the trigger free from dead time. The efficiency is almost 100% (99.9%) fot both K_S and K_L .

$K_{L,S} \rightarrow \pi^0\pi^0$ selection is based on LKr data on photon showers: energy and position, minimum distance between photons, matching of photon pairs invariant mass with nominal π^0 mass. From the four detected photons in the calorimeter, the distance D of the decay from the calorimeter is given by:

$$D = \frac{\sqrt{\sum E_i E_j \times (r_{ij})^2}}{M_K} \quad (8)$$

where E_i are the photons energies and r_{ij} the distances between photons in the calorimeter. The two photons invariant mass is:

$$m_{ij} = \frac{\sqrt{E_i E_j} \cdot r_{ij}}{D} \quad (9)$$

In order to find the best shower pairing a χ^2 variable ($R_{ellipse}$ Fig. (7)) of the two photons invariant masses w.r.t. the π^0 mass is constructed. A cut on the χ^2 is applied to suppress $3\pi^0$ decays with missing or overlapping photons. Events with extra photons in time are rejected.

The calorimeter energy scale is adjusted to match the AKS nominal position, reconstructed from the $K_S \rightarrow \pi^0\pi^0$ decay distribution (Fig. (8)).

2.4 Accidental activity

Accidental activity in the beams can induce event losses. Being the K_L beam intensity roughly 10^5 times the K_S one the event losses due to K_S beam are negligible. Moreover event losses show a linear dependence on K_L beam instantaneous intensity, as verified in year 2001 data.

The accidental activity effect cancels to first order in R but a difference in losses between charged and neutral or Long and Short can lead to a residual correction to R:

$$\Delta R \approx \Delta(\pi^+\pi^- - \pi^0\pi^0) \times \Delta(K_L - K_S) \quad (10)$$

The difference between neutral and charged losses is minimized by applying dead time conditions to all the modes. Dead time conditions are due mainly to the drift chamber multiplicity limit, these conditions are recorded and applied offline to all the events. The difference in the accidental activity seen by K_L and K_S events is small by design being the two beams simultaneous.

To estimate residual illumination difference^d random events overlayed to $\pi\pi$ Montecarlo and data events have been used.

2.5 Data samples and Results

Year 2001 has been the last one devoted to $\text{Re}(\epsilon'/\epsilon)$, it has been useful no only to accumulate more statistics but also to perform a better studies on accidental activity effects.

Thanks to the end of LEP activities a longer spill (Table (1)) was infact delivered to NA48 with lower momentum protons (400GeV/c) giving lower instantaneous intensity in the detector. New beam monitors, to study accidental activity at short time scale, and new drift chambers were installed.

	98-99	2001
proton momentum (GeV/c)	450	400
SPS cycle time (s)	14.4	16.8
spill length (effective) (s)	2.4 (1.7)	5.2 (3.6)
duty cycle	0.17	0.31
K_L beam intensity (ppp)	$\approx 1.5 \times 10^{12}$	$\approx 2.4 \times 10^{12}$
K_S beam intensity (ppp)	$\approx 3 \times 10^7$	$\approx 5 \times 10^7$

Table 1: Beam proprieties, years 1998-99 and 2001

Due to all these improvements a better understanding of accidental activity and related items have been reached improving their corrections to R as shown in Table (2)

^d K_S and K_L beams are still separated by about 1 cm at the first drift chamber: this could induce a difference on charged events from K_L and K_S

	98-99	2001
$\pi^+\pi^-$ background	$16.9 \pm 3.0_{(syst.)}$	$14.2 \pm 3.0_{(syst.)}$
$\pi^0\pi^0$ background	$-5.9 \pm 2.0_{(syst.)}$	$-5.6 \pm 2.0_{(syst.)}$
beam scattering	$-9.6 \pm 2.0_{(syst.)}$	$-8.8 \pm 2.0_{(syst.)}$
Tagging inefficiency α_{SL}	$\pm 3.0_{(syst.)}$	$\pm 3.0_{(syst.)}$
Accidental tagging α_{LS}	$8.3 \pm 3.4_{(stat.)}$	$6.9 \pm 2.8_{(stat.)}$
$\pi^+\pi^-$ scale	$2.0 \pm 2.8_{(syst.)}$	$\pm 2.8_{(syst.)}$
$\pi^0\pi^0$ scale	$\pm 5.8_{(syst.)}$	$\pm 5.3_{(syst.)}$
AKS inefficiency	$1.1 \pm 0.4_{(syst.)}$	$1.2 \pm 0.3_{(syst.)}$
Acceptance	$26.7 \pm 4.1_{(stat.)}$ $\pm 4.0_{(syst.)}$	$21.9 \pm 3.5_{(stat.)}$ $\pm 4.0_{(syst.)}$
$\pi^+\pi^-$ trigger inefficiency	$-3.6 \pm 5.2_{(stat.)}$	$5.2 \pm 3.6_{(stat.)}$
Accidental activity intensity diff. illumination diff.	$\pm 3.0_{(syst.)}$ $\pm 3.0_{(stat.)}$	$\pm 1.1_{(syst.)}$ $\pm 3.0_{(stat.)}$
K_S in time activity	$\pm 1.0_{(syst.)}$	$\pm 1.0_{(syst.)}$
Total	$+35.9 \pm 8.1_{(stat.)} \pm 9.6_{(syst.)}$	$+35.0 \pm 6.5_{(stat.)} \pm 9.0_{(syst.)}$

Table 2: Different years corrections on R. Corrections and systematic uncertainties on R are reported in 10^{-4} units.

The corrected double ratio for the 2001 data is $R_{2001} = 0.99181 \pm 0.00147_{stat} \pm 0.00110_{syst}$; where part of the systematic error (± 0.00065) comes from the statistics on control samples. NA48 results are stable along the different samples:

sample	$K_L \rightarrow \pi^0\pi^0$	$\text{Re}(\epsilon'/\epsilon)$
1997	0.5M	$(15.3 \pm 2.3) \times 10^{-4}$ [3]
1998-99	3M	$(15.0 \pm 2.7) \times 10^{-4}$ [6]
2001	1.5M	$(13.7 \pm 3.1) \times 10^{-4}$ [5]

and the final result is $\text{Re}(\epsilon'/\epsilon) = (14.7 \pm 2.2) \times 10^{-4}$ [5]

3 NA48/2: A_g measurement

NA48/2 main goal is to search for CP violation in $K^\pm \rightarrow \pi^\pm \pi^\pm \pi^\mp$ decays measuring the direct CP violating asymmetry $A_g = (g^+ - g^-)/(g^+ + g^-)$; where $g^{+,-}$ are the slope parameters describing the linear dependence of $K^{+,-}$ decay probabilities on the u kinematic variable of the Dalitz plots. The u variable is linearly related to the energy of the odd pion^e in the centre of mass system:

$$u = (2M_K/m_\pi^2)(M_K/3 - E_\pi^*) \quad (11)$$

Any variation in the ratio

$$R(u) = \frac{\int dv |M^+(u, v)|^2}{\int dv |M^-(u, v)|^2} \quad (12)$$

^ethe pion having the opposite sign to that of the dacying kaon

as a function of u , would show evidence of direct CP violation [4].

The experiment is designed to reach sensitivity of about 10^{-4} , limited by statistics rather than systematics. The corresponding asymmetry A_g^0 in $K^\pm \rightarrow \pi^0 \pi^0 \pi^\pm$ will be measured too, with a sensitivity again limited by statistics. Moreover high statistics Ke4 can be analyzed allowing the $\pi - \pi$ scattering lenght parameter a_0^0 to be measured with an accuracy of better than 1×10^{-2} , which permits to measure the $q\bar{q}$ condensate postulated by the Chiral Perturbation Theory. The present knowledge of several rare decays can be extended as well.

To achieve the required sensitivity, as it has been done for $Re(\epsilon'/\epsilon)$ measurement, all possible sources of asymmetries have to be minimized. In order to do that the simultaneous K^+ and K^- beams are derived from the same target, K^+ and K^- decaying in the same fiducial volume, the field in the spectrometer is frequently alternated in sign.

A new beam line using a novel design has been built downstream the NA48- K_L target position to transport simultaneously the K^+ and K^- beams, produced by the 400GeV/c primary protons from SPS impinging on the beryllium target (Fig. (9)). The average kaon momentum is 60GeV/c for both K^+ and K^- (r.m.s. $\pm 3.8\%$), selected by their passage through two vertical deflection magnets with opposite-sign field and a pair of collimators (TAX) which have two similar openings and also serve as a dump for the remaining primary protons [4]. Two further vertical deflection magnets return the two beams onto a common axis. A system of quadrupole is used to focused particle of each sign in both planes in order to have small spot size beams at the spectrometer, thus minimizing the transverse scale of any structure within the beam spots. Moreover by regular inversion of the achromats any remaining structures inside the beam spots is exchanged between K^+ and K^- . Other improvement have been done and new detectors (KABES, 3 station of TPC-type detector using MICROMEGAS) have been installed (see [7]).

The proposed statistic should be reach with the 2004 run, while analysis is already started on 2003 data corresponding to roughly 50% of the planned statistics. During 2003 run the positive flux at the exit of the final collimator was estimated to be 3.8×10^7 particle per pulse of which 2.2×10^6 were K^+ . While negative particle flux was 2.6^7 ppp of which 1.3×10^6 were K^- . The number of charged kaons reconstructed $K^\pm \rightarrow (3\pi)^\pm$ per spill was roughly 1.3×10^4 .

Acknowledgments

I would like to thank the NA48/1/2/ collaboration: it is a pleasure to be in such a nice team. Many thanks to the PS,SPS,CERN people and machines for the protons.

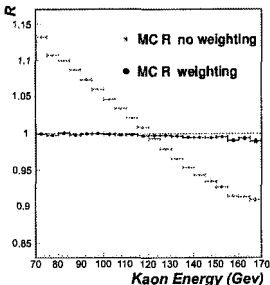


Figure 1: Acceptance effect on R (20 energy bins, 5 GeV each) estimated by MC

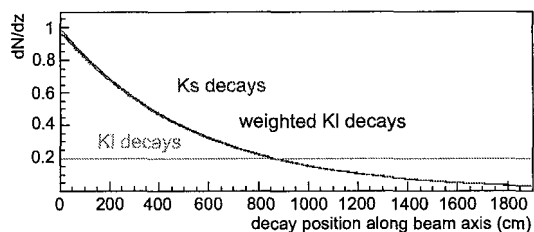


Figure 2: Decays position along beam axis for K_L , K_S and weighted K_L decays

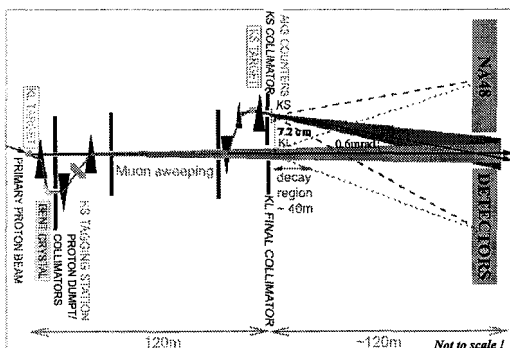


Figure 3: NA48 beams setup

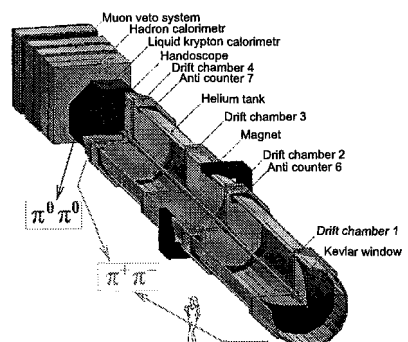


Figure 4: NA48 detector

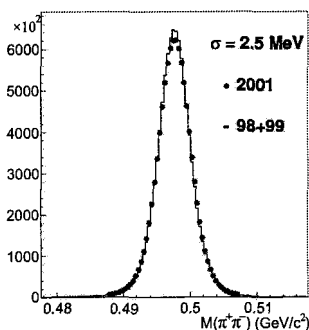


Figure 5: $\pi^+\pi^-$ inv. mass

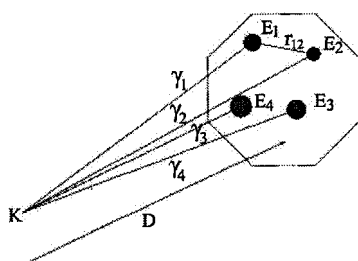


Figure 6: Decay distance D computed from 4 γs in Lkr

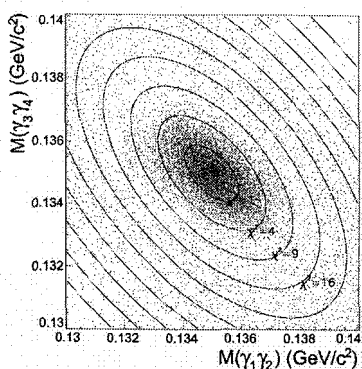


Figure 7: $K_S \rightarrow \pi^0\pi^0$ candidates in the the two reconstructed $m_{\gamma\gamma}$ space

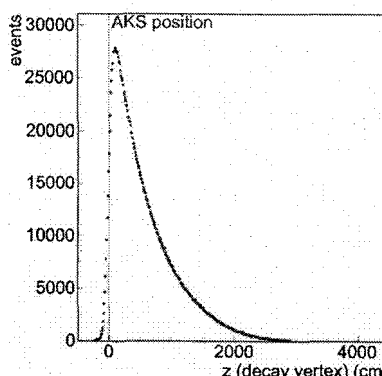


Figure 8: $\pi^0\pi^0$ vertex distribution

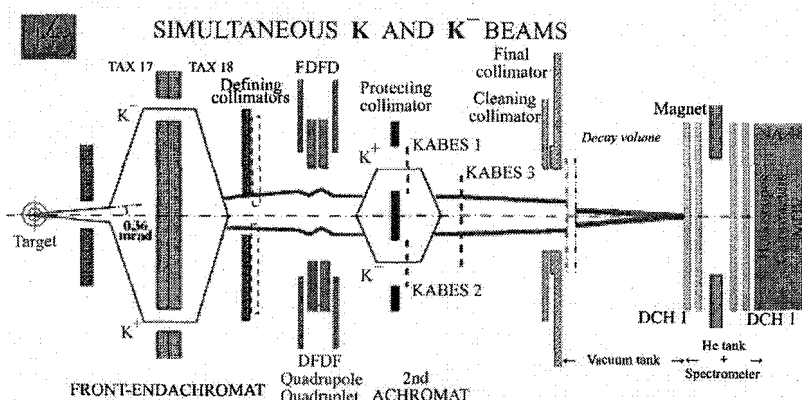


Figure 9: Vertical view of the simultaneous K^+ and K^- beam, not to scale. Outside achromats the beam lines are separated for clarity, in reality displacement is less than 1mm

References

- [1] K.Hagiwara *et al.* [Particle Data Group], *Phys.Rev. D* 66, 10001 (2002).
- [2] J.H.Christenson *et al.*, *Phys.Rev.Lett.* 13, 138 (1964).
- [3] V.Fanti *et al.*, *Phys.Lett. B* 465 ,335 (1999).
- [4] J.R.Batley *et al.*, *CERN/SPSC 2000-003* (2000).
- [5] J.R.Batley *et al.*, *Phys.Lett. B* 544 ,92 (2002).
- [6] A.Lai *et al.*, *Eur. Phys. J. C* 22 ,231 (2001).
- [7] NA48/2 Collaboration, *CERN/SPSC 2003-033* (2003).

RECENT NA48 RESULTS ON RARE KAON DECAYS

G.Collazuol^a, on behalf of the NA48 collaboration

Scuola Normale Superiore, Piazza dei Cavalieri 7 - 56100 Pisa - Italy

Abstract. New measurements of rare K_S decays from the NA48 experiment are reported. From data taken in the year 2000 a search for $K_S \rightarrow \pi^0\pi^0\pi^0$ decays is being performed. The preliminary limits on the CP violating parameter η_{000} and on the CPT violating parameter $Im \delta$ are discussed. From data taken in 2002 a search for the decay $K_S \rightarrow \pi^0e^+e^-$ has been made. The final result is reported, which consists in the observation of 7 events with a background of 0.15 events.

1 Introduction

The NA48 experiment at the CERN SPS has been designed for a precise measurement of the direct CP violation parameter $Re(\epsilon'/\epsilon)$ [1], but several special run periods have been performed for investigations in rare K_L K_S and neutral hyperon decays. Two neutral beams were used, produced respectively at one 'far' target ~ 120 m upstream the decay region, so that K_L decays dominate, and at one 'near' target, ~ 6 m upstream the decay region where mainly K_S hyperons decays are available, with only a small component of K_L decays.

During the year 2000, data were collected for searching CP violation in $K_S \rightarrow \pi^0\pi^0\pi^0$ decays from the 'far' and 'near' beams. In the year 2002 a very high intensity beam was exploited to search the decay $K_S \rightarrow \pi^0e^+e^-$.

2 The NA48 detector

The main two elements of the NA48 setup are a charged particle magnetic spectrometer and a liquid krypton electromagnetic calorimeter. The quasi-homogeneous and fully active liquid Krypton ionization chamber measures the electromagnetic showers with a time resolution of 300 ps for a single shower, an energy resolution of $\sigma(E)/E = 3.2\%/\sqrt{E} + 9\%/E + 0.42\%$ and a transverse position resolution is $\simeq 1$ mm. The corresponding mass resolution at the π^0 mass is 1 MeV/ c^2 . The spectrometer includes two drift chambers before a dipole magnet and two after and has a momentum resolution of $\sigma_p/p = 0.48\% + 0.01\% \times p$ (p in GeV/ c), which translates into a resolution of 3 MeV/ c^2 when reconstructing the kaon mass in $K_S \rightarrow \pi^+\pi^-$ decays. Time resolution below 200 ps on charged tracks is obtained by a scintillators hodoscope. A detailed description of the whole NA48 setup can be found elsewhere [1].

3 Observation of the rare decay $K_S \rightarrow \pi^0e^+e^-$

In order to access the short distance information from $K_L \rightarrow \pi^0e^+e^-$, whose topical physical interest is the extraction of the CP violation parameter $Im(\lambda_t) =$

^ae-mail: gianmaria.collazuol@cern.ch

$Im(V_{td}V_{ts}^*)$, it is necessary to study the $K_S \rightarrow \pi^0 e^+ e^-$ reaction.

Besides a negligible CP conserving amplitude, the decay $K_L \rightarrow \pi^0 e^+ e^-$ has two interfering CP violating amplitudes, which originate respectively from $K^0 - \bar{K}^0$ mixing via a decay of the CP-even component of the K_L (K_1) -indirect CP violation- and from short distance physics -direct CP violation-.

The total CP-violating branching ratio of $K_L \rightarrow \pi^0 e^+ e^-$ can be written as [2]:

$$BR(K_L \rightarrow \pi^0 e^+ e^-)_{CPV} \times 10^{12} \simeq 15.3 a_S^2 - 6.8 a_S \left(\frac{Im(\lambda_t)}{10^{-4}} \right) + 2.8 \left(\frac{Im(\lambda_t)}{10^{-4}} \right)^2 \quad (1)$$

This equation shows that the sensitivity to $Im(\lambda_t)$ depends on the parameter a_S which is related to the $K_S \rightarrow \pi^0 e^+ e^-$ brancin fraction as follows:

$$B(K_S \rightarrow \pi^0 e^+ e^-) = 5.2 \times 10^{-9} a_S^2. \quad (2)$$

Currently, the upper limit of the $BR(K_L \rightarrow \pi^0 e^+ e^-)$ is 5.1×10^{-10} [3]. This together with the present upper limit $BR(K_S \rightarrow \pi^0 e^+ e^-) < 1.4 \times 10^{-7}$ [4] gives a bound on $Im(\lambda_t)$ [5], but not competitive with respect to other constraints obtained from b-physics.

A search for the decay $K_S \rightarrow \pi^0 e^+ e^-$ has been made using data collected during 89 days in 2002 with a very high intensity K_S beam (about 3 orders of magnitude greater than used before). A total amount of 4.4×10^{10} K_S decays were collected in the fiducial decay region.

The signal channel $K_S \rightarrow \pi^0 e^+ e^-$ was studied by selecting decays where an electron-positron pair was accompanied by two additional clusters in the LKr. For the analysis of the data, signal and control regions were defined. These regions were masked while the cuts to reject the background were tuned using both data and Monte Carlo simulation.

Four quantities related to the decay vertex were computed.

- *neutral vertex*. The longitudinal vertex position was computed from the energies and positions of the four clusters in the LKr by imposing the kaon mass, as invariant mass of four particles. Then the invariant mass of the two photons, $m_{\gamma\gamma}$ was obtained. The proper lifetime was also computed from the position of the neutral vertex.
- π^0 *vertex*. The π^0 vertex position was computed in a similar way, but using only the two photon clusters and imposing the π^0 mass.
- *charged vertex*. The position of the charged vertex, obtained by matching the kaon line of flight with the tracks, was then used to compute $m_{ee\gamma\gamma}$, the invariant mass of the four decay products.
- *track vertex*. The track vertex is at the position of the closest distance of approach of the two tracks.

The signal (control) region was defined in the plane $m_{ee\gamma\gamma}$ VS $m_{\gamma\gamma}$ as rectangular box centered around the kaon and the π^0 masses and with a width of 2.5 (6) times the resolutions.^b

Among a large number of possible background channels the most dangerous follows:

- i) K_S into two π^0 with a missing photon and a Dalitz π^0 decay or a gamma conversion. By rejecting events with invariant electron-positron or electron-gamma mass below $0.165 \text{ MeV}/c^2$ the background was highly reduced (fig. 1).
- ii) K_S or K_L radiative decays in two electrons and two gammas (Greenlee background). This was precisely measured in the data collected by NA48 in 2001 from a pure K_L beam (fig. 2).
- iii) fragments from two primary decays which happen to coincide in time and space and fall into the signal box. Given the very good time resolution of the detector, this background is measured in out of time side bands and extrapolating the result in the signal region.

After the background estimation (summarised in Fig. 3), the control region was unmasked to estimate the final background contribution to the signal. No events were found in the control region, consistent with the background prediction of 0.33 events. The resulting estimate of the total background in the signal region was $0.15^{+0.10}_{-0.04}$ events.

When the signal region was unmasked seven events were found (fig. 4), corresponding to a signal of $6.85^{+3.8}_{-1.8}$. The probability that such a signal is consistent with background is $\sim 10^{-10}$, we therefore interpret the signal as the first observation of the $K_S \rightarrow \pi^0 e^+ e^-$ decays.

After correcting signal for the acceptance (extrapolated to the full m_{ee} spectrum) and dividing by the flux, the branching ratio resulted:

$BR(K_S \rightarrow \pi^0 e^+ e^-) = (5.8^{+2.8}_{-2.3}(\text{stat}) \pm 0.8(\text{syst})) \times 10^{-9}$ where the systematic error is dominated by the uncertainty in the acceptance extrapolation to the full m_{ee} spectrum. The parameter $|a_S|$ is then measured to be:

$$|a_S| = (1.06^{+0.26}_{-0.21}(\text{stat}) \pm 0.07(\text{syst})) \quad (3)$$

Using the measured value of $|a_S|$ and the global fit for $Im(\lambda_t)$ one obtains

$$BR(K_L \rightarrow \pi^0 e^+ e^-)_{CPV} \simeq (17.2_{\text{indirect}} \pm 9.4_{\text{interference}} + 4.7_{\text{direct}}) \times 10^{-12}. \quad (4)$$

where it can be observed that, as a prediction of the Standard Model, the direct CP violated component in the decay $K_L \rightarrow \pi^0 e^+ e^-$ is small with respect to

^bThe resolutions, $\sigma_{m_{ee\gamma\gamma}} = 6.5 \text{ MeV}/c^2$ and $\sigma_{m_{\gamma\gamma}} = 1 \text{ MeV}/c^2$, were studied in the channel $K_S \rightarrow \pi^0 \pi_D^0$ with Dalitz decay of the π^0 and with Monte Carlo simulation.

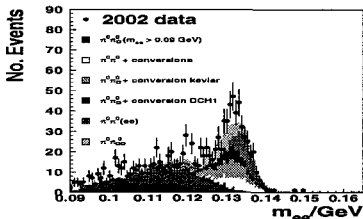


Figure 1: Distributions of m_{ee} for data and Monte Carlo after all the cuts have been applied.

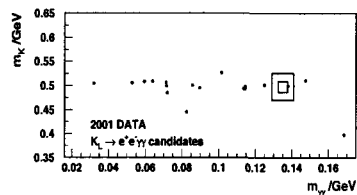


Figure 2: Scatter plot of $m_{ee\gamma\gamma}$ versus $m_{\gamma\gamma}$ for events selected as $K_L \rightarrow e^+e^-\gamma\gamma$ in the 2001 data.

Source	control region	signal region
$K_S \rightarrow \pi_D^0 \pi_D^0$	0.03	< 0.01
$K_L \rightarrow ee\gamma\gamma$	0.11	0.08
Accidentals	0.19	0.07
Total bkg	0.33	0.15

Figure 3: Summary of the background estimate.

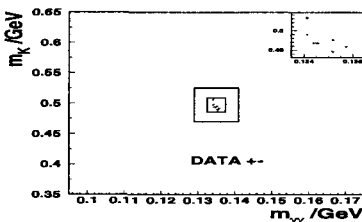


Figure 4: Scatter plot of $m_{ee\gamma\gamma}$ versus $m_{\gamma\gamma}$ for events passing all the cuts described in the text. The regions of 3σ and 6σ are shown.

the indirect component. Only if the sign of a_S turns out to be negative then $\text{BR}(K_L \rightarrow \pi^0 e^+ e^-)$ retains some sensitivity to $\text{Im}(\lambda_t)$ through the interference term.

4 Search for the CP violating Decay $K_S \rightarrow \pi^0 \pi^0 \pi^0$ and measurement of η_{000}

CP violation in $K^0 \rightarrow 2\pi$ decays is firmly established and the parameters which describe it (η_\pm , η_{00} and ϵ'/ϵ) are precisely measured [6], [7], [8]. CP violation in $K_S \rightarrow 3\pi$ is equally allowed in the Standard Model (SM) but has been investigated in much less detail owing to the difficulty of the measurements. The equivalent of η_{00} for $K_S \rightarrow 3\pi^0$ decays is $\eta_{000} = A(K_S \rightarrow 3\pi^0)/A(K_L \rightarrow 3\pi^0)$, which in the SM is $\eta_{000} = \epsilon + i\text{Im } a_1/\text{Re } a_1$, where a_1 is the isospin 1 amplitude for $K^0 \rightarrow \pi^0 \pi^0 \pi^0$ and $\epsilon = 2/3\eta_\pm + 1/3\eta_{00}$.

A search for the decay of K_S into $3\pi^0$ has been made using data collected during the year 2000 run. The intensity of $3\pi^0$ decays in the 'near' target beam is measured as a function of the proper decay time, and information on η_{000} is extracted by measuring the $K_S - K_L$ interference term. The acceptance correction is done by normalising the data using $3\pi^0$ decays collected from the far target beam, where the $K_S - K_L$ interference is completely negligible. Data were first collected from the far target (more than 10^7 $3\pi^0$ decays) and subsequently from the near target (5.6×10^6 $3\pi^0$ decays). Beam intensities were tuned in order to have similar rate of particle in the detectors, thus minimizing

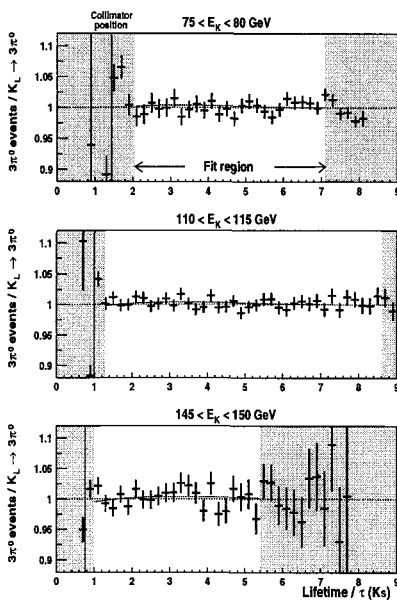


Figure 5: The ‘near’/‘far’ ratio corrected for the beam geometry is shown for three energy bins.

	$Re \eta_{000} (10^{-2})$	$Im \eta_{000} (10^{-2})$
Acceptance	± 0.3	± 0.8
Dilution	± 0.3	± 0.4
Accidentals	± 0.1	± 0.6
Fit	± 0.1	± 0.2
Energy Scale	± 0.1	± 0.1
Total	± 0.5	± 1.1

Figure 6: Systematics errors

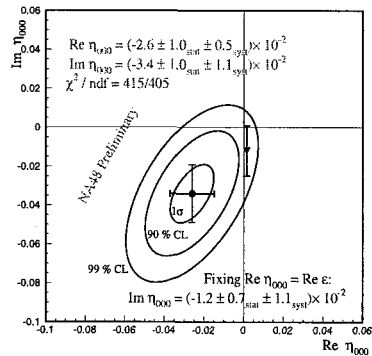


Figure 7: Results of the η_{000} fit.

the effects due to accidental activity. Trigger criteria and detector conditions were kept as much the same as possible during the ‘far’ and ‘near’ data taking period. Monte Carlo simulation is used only to correct for the residual geometrical difference between the two beams. In order to account for the different decay energy spectra of kaon generated from the ‘near’ and ‘far’ beams, the analysis is done fitting the data in 5 GeV wide energy bins according to the function:

$$f(E, t) = \frac{NEAR}{FAR} = A(E)[1 + |\eta_{000}|^2 e^{(\Gamma_L - \Gamma_S)t} + 2D(E)e^{\frac{1}{2}(\Gamma_L - \Gamma_S)t} (Re \eta_{000} \cos \Delta mt - Im \eta_{000} \sin \Delta mt)] \quad (5)$$

where $A(E)$ are normalization constants and $D(E)$ is the so called $K^0 - \bar{K}^0$ dilution describing the excess of produced K^0 over \bar{K}^0 ^c.

The (preliminary) result of the fit is:

^cThe dilution values measured by the NA31 experiment [9] are used (adjusting them to take into account the different production angle and proton energy)

$$\begin{aligned} Re \eta_{000} &= -2.6 \pm 1.0(stat) \pm 0.5(syst) \times 10^{-2} \\ Im \eta_{000} &= -3.4 \pm 1.0(stat) \pm 1.0(syst) \times 10^{-2} \end{aligned} \quad (6)$$

with a correlation coefficient of $\rho \simeq 0.8$. The systematic errors are dominated by the uncertainties on acceptance, kaon dilution and accidental activity (see Fig. 6). The corresponding confidence limits are shown in Fig. 7. Turning this result into an upper limit on the branching fraction, we get $BR(K_S \rightarrow \pi^0\pi^0\pi^0) < 1.4 \times 10^{-6}$ at 90%CL. The result is consistent with CP conservation with a probability of 5%.

To avoid the correlation of the parameters, we have also imposed CPT conservation, which fixes $Re \eta_{000} = Re \epsilon \simeq 1.6 \times 10^{-3}$. Then the fit yields $Im \eta_{000} = -1.2 \pm 0.7(stat) \pm 1.1(syst) \times 10^{-2}$ and $BR(K_S \rightarrow \pi^0\pi^0\pi^0) < 3.0 \times 10^{-7}$ at 90%CL, which is compatible with the SM prediction of $\sim 3 \times 10^{-9}$ and improves the current limit by about 50 times.

Finally, this result improves the limit on CPT violation via the Bell-Steinberger unitarity relation, which connects the CPT violating phase δ with the CP violating amplitudes for the various K_S and K_L decays. So far the limiting quantity has been the precision on η_{000} [10].

Taking into account the NA48 results, we obtain:

$$Im \delta = (-1.2 \pm 3.0) \times 10^{-5} \quad (7)$$

which represents an improvement of about 40% with respect to previous result [11] Now the main limitation comes from the knowledge of η_{+-} parameter.

Assuming CPT Conservation in the semi-leptonic K^0 decays, the phase of δ is fixed and the measurement translates into a new limit on the $K^0\bar{K}^0$ mass difference:

$$M_K^0 - M_{\bar{K}^0} = (-1.7 \pm 4.2) \times 10^{-19} GeV \quad (8)$$

References

- [1] J.R. Batley *et al.*, *Phys. Lett.* **B 544** (2002) 97.
- [2] G. D'Ambrosio, G. Ecker, G. Isidori, and J. Portoles, *Journal of High Energy Physics* **08** (1998) 004.
- [3] A. Alavi-Harati *et al.*, *Phys. Rev. Lett.* **86** (2001) 397.
- [4] A. Lai *et al.*, *Phys. Lett.* **B 514** (2001) 253.
- [5] G. Isidori, *International Journal of Modern Physics A* **17** (2002) 3078.
- [6] K. Hagiwara *et al.*, *Phys. Rev. D* **66** (2002) 010001.
- [7] J. R. Batley *et al.*, *Phys. Lett.* **B 544** (2002) 97.
- [8] A. Alavi-Harati *et al.*, *Phys. Rev. D* **67** (2003) 012005.
- [9] R. Carosi *et al.*, *Phys. Lett.* **B 237** (1990) 303.
- [10] I. I. Bigi and A. I. Sanda, *Phys. Lett.* **B 466** (1999) 33.
- [11] A. Angelopoulos *et al.*, *Phys. Lett.* **B 444** (1998) 52.

ON THE RELATIVE STRENGTH OF DIRECT CP VIOLATION IN $K_L \rightarrow 2\pi$ and $K^\pm \rightarrow \pi^\pm \pi^\pm \pi^\mp$ DECAYS

Evgeny Shabalin^a

*State Research Center. Institute for Theoretical and Experimental Physics, 117218
Moscow, Russia*

Abstract. It is shown that contrary to the case of $K_L \rightarrow 2\pi$ decays where the direct CP violation is suppressed because of partial cancellation between the so-called QCD and electroweak penguin contributions in the amplitude, in decays $K^\pm \rightarrow 3\pi$, the effects of both contributions are summed.

1 Introduction

In decays $K_L \rightarrow 2\pi$, the CP invariance is violated by two mechanisms: due to $\Delta S = 2$ transitions $K^0 \longleftrightarrow \bar{K}^0$ and due to direct CP violation in $\Delta S = 1$ transition $K^0 \rightarrow 2\pi$. In the last case, a strength of direct CP violation is characterized by parameter ε' . At present, experimentally, $\varepsilon' = (1.66 \pm 0.16)10^{-3}\varepsilon$, where ε characterizes a strength of indirect CP violation in $\Delta S = 2$ transitions.

The theoretical estimates of ε' are very uncertain allowing $\varepsilon'/\varepsilon = (1.5 \div 31.6)10^{-4}$ [1] and one of the reasons of such large uncertainty is an absence of the reliable calculation of two contributions into ε' : the first – from the QCD penguin operators and the second – from electroweak penguin (EWP) operators. The contributions of these operators into ε' cancell partially one another.

We show that in the case of $K^\pm \rightarrow \pi^\pm \pi^\pm \pi^\mp$ decay, a contribution of QCD penguin operators is increased by EWP contribution. And, therefore, CP effects are enhanced in $K^\pm \rightarrow 3\pi$ decays.

2 The scheme of calculation

A theory of $\Delta S = 1$ non-leptonic decays is based on the effective lagrangian [2]

$$L(\Delta S = 1) = \sqrt{2}G_F \sin \theta_C \cos \theta_C \sum c_i O_i \quad (1)$$

where O_i are the 4-quark operators and c_i are Wilson's coefficients. A definition of O_{1-6} can be found in [2], [3] and a set of these operators is sufficient for description of the CP-even part of the amplitudes. To calculate the CP-odd parts, it is necessary to add

$$O_7 = \frac{3}{2} \bar{s} \gamma_\mu (1 + \gamma_5) d \cdot \left(\sum_{q=u,d,s} e_q \bar{q} \gamma_\mu (1 - \gamma_5) q \right) \quad (\Delta I = 1/2, 3/2) \quad (2)$$

^ae-mail: shabalin@heron.itep.ru

$$O_8 = -12 \sum_{q=u,d,s} e_q (\bar{s}_L q_R) (\bar{q}_R d_L), \quad e_q = \left(\frac{2}{3}, -\frac{1}{3}, -\frac{1}{3} \right), \quad (\Delta I = 1/2, 3/2) \quad (3)$$

The coefficients c_{5-8} have the imaginary parts necessary for CP violation. After the Fierz reordering transformations, the operators $O_{7,8}$ acquire the form

$$O_7 = -\bar{s}(1 - \gamma_5)u \cdot \bar{u}(1 + \gamma_5)d - \frac{3}{8}O_5; \quad O_8 = 3O_7. \quad (4)$$

The bosonization of these operators can be done using the relations [4]

$$\bar{q}_j(1 + \gamma_5)q_k = -\frac{1}{\sqrt{2}}F_\pi r \left(U - \frac{1}{\Lambda^2} \partial^2 U \right)_{kj}; \quad U = \frac{F_\pi}{\sqrt{2}} \exp(i\sqrt{2}\hat{\pi}/F_\pi) \quad (5)$$

where

$$r = 2m_\pi^2/(m_u + m_d), \quad F_\pi \approx 93 \text{ MeV} \quad (6)$$

and $\hat{\pi}$ is 3×3 matrix of the nonet of pseudoscalar mesons. Representing $M(K \rightarrow 2\pi)$ in the form

$$M(K_1^0 \rightarrow \pi^+ \pi^-) = A_0 e^{i\delta_0} - A_2 e^{i\delta_2} \quad (7)$$

$$M(K_1^0 \rightarrow \pi^0 \pi^0) = A_0 e^{i\delta_0} + 2A_2 e^{i\delta_2} \quad (8)$$

$$M(K^+ \rightarrow \pi^+ \pi^0) = -\frac{3}{2}A_2 e^{i\delta_2} \quad (9)$$

we obtain

$$A_0 = G_F F_\pi \sin \theta_C \cos \theta_C \frac{m_K^2 - m_\pi^2}{\sqrt{2}} \cdot [c_1 - c_2 - c_3 + \frac{32}{9}\beta(Re\tilde{c}_5 + iIm\tilde{c}_5)] \quad (10)$$

$$A_2 = G_F F_\pi \sin \theta_C \cos \theta_C \frac{m_K^2 - m_\pi^2}{\sqrt{2}} \cdot [c_4 + i\frac{2}{3}\beta\Lambda^2 Im\tilde{c}_7(m_K^2 - m_\pi^2)^{-1}] \quad (11)$$

where

$$\tilde{c}_5 = c_5 + \frac{3}{16}c_6; \quad \tilde{c}_7 = c_7 + 3c_8; \quad \beta = \frac{2m_\pi^4}{\Lambda^2(m_u + m_d)^2}.$$

From data on widths of $K \rightarrow 2\pi$ decays we obtain

$$c_4 = 0.328; \quad c_1 - c_2 - c_3 + \frac{32}{9}\beta Re\tilde{c}_5 = -10.13. \quad (12)$$

At $c_1 - c_2 - c_3 = -2.89$ [2], $\frac{32}{9}\beta Re\tilde{c}_5 = -7.24$.

Using the general relation

$$\varepsilon' = ie^{i(\delta_2 - \delta_0)} \left[-\frac{ImA_0}{ReA_0} + \frac{ImA_2}{ReA_2} \right] \cdot \left| \frac{A_2}{A_0} \right| \quad (13)$$

and the experimental value $\varepsilon' = (3.78 \pm 0.38)10^{-6}$ we come to the relation

$$-\frac{Im\tilde{c}_5}{Rec_5} \left(1 - \Omega_{\eta,\eta'} + 24.36 \frac{Im\tilde{c}_7}{Im\tilde{c}_5} \right) = (1.63 \pm 0.16) \cdot 10^{-4}. \quad (14)$$

where $\Omega_{\eta,\eta'}$ takes into account the effects of $K^0 \rightarrow \pi^0\eta(\eta') \rightarrow \pi^0\pi^0$ transitions.

Introducing the notation

$$-\frac{Im\tilde{c}_5}{Rec_5} = x \frac{Im\lambda_t}{s_1}, \quad \frac{24.36}{1 - \Omega_{\eta,\eta'}} \cdot \frac{Im\tilde{c}_7}{Im\tilde{c}_5} = -y \quad (15)$$

and using [7]

$$Im\lambda_t/s_1 \approx s_2 s_3 \sin \delta = \frac{(1.2 \pm 0.2)10^{-4}}{0.223} \quad (16)$$

we can write eq.(14) for the case $\Omega_{\eta,\eta'} = 0.25 \pm 0.08$ in the form

$$x(1 - y) = 0.40(1 \pm 0.22). \quad (17)$$

We have one equation with two variables. To move farther, we are enforced to apply to existing theoretical estimates of one of these variables.

In terms of notations in [5]

$$y = \frac{\Pi_2}{\omega} / \Pi_0 (1 - \Omega_{\eta,\eta'}) \quad (18)$$

In [6], the central value of y is $y \approx 0.5$ and, consequently $x = 0.80 \pm 0.18$. This result looks as the reliable one. A very close result: $x = 0.71 \pm 0.27$ can be derived from the result $(\varepsilon'/\varepsilon)_{EWP} = (-12 \pm 3)10^{-4}$ [6] taking $(\varepsilon'/\varepsilon)_{exp} = (16.6 \pm 1.6)10^{-4}$. But it should be noted that the previous estimates of Imc_5/Rec_5 were rather different. In particular, according to [7] $x = 1.4 \pm 0.28$. An estimate of x can be extracted also from the papers [8] - [10]: $x \approx 2$ [8]; $x = 2.8$ [9]; $x = 5.5$ [10]. Such difference of the theoretical estimates of x makes very desirable an investigation of CP-effects in $K^\pm \rightarrow 3\pi$ decays where, contrary to $K_L \rightarrow 2\pi$ decays, the electroweak penguin (EWP) contributions increase CP effects.

3 Decay $K^\pm \rightarrow \pi^\pm\pi^\pm\pi^\mp$

To p^4 approximation [3]

$$|M(K^\pm \rightarrow \pi^\pm\pi^\pm\pi^\mp(p_3))|^2 \sim 1 + \frac{g}{1 + a^2} (1 + ab \pm a(b_{KM} - a_{KM}))Y + \dots \quad (19)$$

where

$$a_{KM} = \left[\frac{32}{9} \beta Im\tilde{c}_5 + 4\beta Im\tilde{c}_7 \left(\frac{3\Lambda^2}{2m_K^2} + 2 \right) \right] / c_0 \quad (20)$$

$$b_{KM} = \left[\frac{32}{9} \beta Im\tilde{c}_5 + 8\beta Im\tilde{c}_7 \right] / (c_0 + 9c_4) \quad (21)$$

$$\frac{1}{2}g = -\frac{3m_\pi^2}{2m_K^2}(1 + 9c_4/c_0), \quad Y = (s_3 - s_0)/m_\pi^2 \quad (22)$$

$$c_0 = c_1 - c_2 - c_3 - c_4 + \frac{32}{9}\beta Re\tilde{c}_5 = -10.46 \quad (23)$$

and a, b are the CP-even imaginary parts of the amplitude arising due to rescattering of the final mesons. Numerically [3]

$$a = 0.1626, \quad b = 0.762 \quad (24)$$

The CP-odd difference of the slope parameters g^+ and g^- is

$$R_g \equiv \frac{g^+ - g^-}{g^+ + g^-} = \frac{a(b_{KM} - a_{KM})}{1 + ab} \quad (25)$$

For $\Omega_{\eta,\eta'} = 0.25$ we find

$$(R_g) = 0.039 \frac{Im\tilde{c}_5}{Re\tilde{c}_5} \left(1 - 11.95 \frac{Im\tilde{c}_7}{Im\tilde{c}_5} \right) = -(3.0 \pm 0.5) 10^{-5} x \left(1 - \frac{0.11 \pm 0.025}{x} \right). \quad (26)$$

Comparing eqs.(14) and (26) we conclude that in $K^\pm \rightarrow 3\pi$ decays, EWP contributions increase CP-odd effects.

Measuring R_g , one obtain a possibility to determine the true relation between QCD and EWP contributions into CP violation in Kaon decays.

References

- [1] T.Hambye et al., *Nucl.Phys.B* **564** 391 (2000)
- [2] M.A.Shifman, A.I.Vainshtein, V.I.Zakharov, *Zh.Eksp.i Teor.Fiz. (JETP)* **72** 1277 (1977)
- [3] E.Shabalin, *hep-ph/0305320 v1* (2003)
- [4] W.A.Bardeen, A.J.Buras, J.-M.Gerard, *Nucl.Phys.B* **293** 787 (1987)
- [5] T.Hambye, S.Peris, E.de Rafael, *hep-ph/0305104 v2* (2003).
- [6] J.F.Donoghue, E.Golovich, *Phys.Lett. B* **478** 172 (2000)
- [7] M.B.Voloshin, preprint ITEP-22. M.,(1981)
- [8] S.Bertolini et al., preprint SISSA 102/95/EP (1995)
- [9] A.J.Buras, M.Jamin, M.Lautenbacher, *Nucl.Phys. B* **408** 209 (1993)
- [10] S.Bertolini, J.O.Eeg, M.Fabbrichesi, *Nucl.Phys. B* **449** 197 (1995)

HADRON PHYSICS IN BABAR

G.D.Lafferty ^a

Department of Physics and Astronomy, The University of Manchester, Manchester M13 9PL, UK

Abstract. Some recent results in hadron physics from the BaBar experiment are discussed. In particular, the observation of two new charmed states, the $D_{sJ}^{*+}(2317)$ and the $D_{sJ}^{*+}(2457)$, is described, and results are presented on the first measurement of the rare decay mode of the B meson, $B^0 \rightarrow \pi^0\pi^0$.

1 The BaBar experiment

The BaBar detector [1] is a general purpose, solenoidal, magnetic spectrometer at the PEP-II asymmetric-energy e^+e^- storage rings at the Stanford Linear Accelerator Center. Since 1999 the detector has been taking data at centre-of-mass energies on, and just below, the peak of the $\Upsilon(4S)$ resonance, colliding 9 GeV electrons with 3.1 GeV positrons. The main purpose of the experiment is to measure CP-violation in the B-meson system. However the e^+e^- collisions are also a copious source of light-flavour and charm $q\bar{q}$ pairs and also of τ -lepton pairs. This allows for a rich and varied programme of hadron physics in the experiment.

Up until 2002, BaBar had accumulated some 91 fb^{-1} of e^+e^- collision data, recorded both on and off the $\Upsilon(4S)$ resonance. During 2003, a further 35 fb^{-1} was added to the sample. With annihilation cross sections of about 1.3 nb for up-type quark pairs, 0.3 nb for down-type quarks and 0.9 nb for tau-pairs, there are correspondingly large data sets. In this short paper, I discuss two particular recent BaBar analyses, one topic from charm spectroscopy and one from rare hadronic B-meson decays.

The BaBar detector combines a precision silicon vertex-tracker with a drift chamber, both having dE/dx capability, a Cherenkov radiation detector (the DIRC), a caesium iodide electromagnetic calorimeter and an iron flux-return system, for the 1.5 T solenoidal magnetic field, instrumented as a muon detector. BaBar thus has precision vertexing and tracking capability together with excellent particle identification for all species of stable particles, including K_s^0 , and for $\pi^0 s$.

2 Charmed meson spectroscopy: the new D_{sJ} states

One of the most remarkable of recent results in particle physics has been BaBar's discovery of a new charmed, strange meson, the $D_{sJ}^{*+}(2317)^+$ [2]. While most new particles start life as dubious, two or three standard-deviation bumps on mass spectra (for example, the proposed pentaquark states that came to

^ae-mail: George.Lafferty@man.ac.uk

light at about the same time as the D_{sJ}), the $D_s^*(2317)^+$ was first seen as a dramatic peak of many standard deviations. Indeed, it is an interesting question as to why it escaped detection for so long. There is a lesson for us all to expect the unexpected.

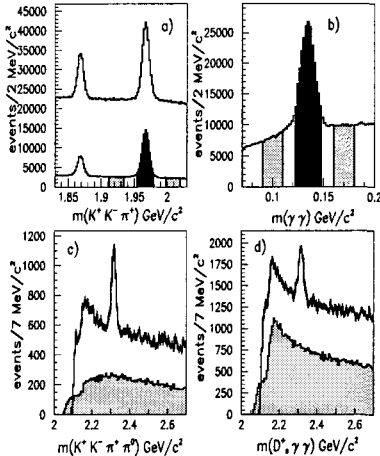


Figure 1: (a) The distribution of $K^+K^-\pi^+$ mass for all candidate events. Additional selection criteria have been used for the lower histogram. (b) The two-photon mass distribution from $D_s^+\pi^0$ candidate events. The D_s^+ and π^0 signal and sideband regions are shaded. (c) The $D_s^+\pi^0$ mass for candidates in the D_s^+ signal (top histogram) and $K^+K^-\pi^+$ sideband regions (shaded histogram) of (a). (d) The $D_s^+\gamma\gamma$ mass for signal D_s^+ candidates and a photon pair from the π^0 signal region of (b) (top histogram) and the sidebands region of (b) (shaded histogram).

The BaBar analysis used 91 fb^{-1} of data to investigate the inclusively-produced $D_s^+\pi^0$ mass spectrum. The technique was to combine charged particles from the decay $D_s^+ \rightarrow K^+K^-\pi^+$, measured in the tracking detectors, with π^0 candidates reconstructed from pairs of photons detected in the electromagnetic calorimeter. The kaon candidates were identified based on their Cherenkov radiation and their specific energy loss. Various cuts were applied to ensure a clean sample on a low background. The upper histogram in figure 1(a) shows the mass spectrum of the selected $K^+K^-\pi^+$ combinations. The two peaks are from the D^+ and D_s^+ mesons. The lower histogram of figure 1(a) shows the effect of selecting for the $\phi(1020)$ in K^+K^- or the $K^*(892)$ in $K^-\pi^+$. This plot shows the D_s^+ peak and sideband regions used in the subsequent analysis.

Figure 1(b) shows the spectrum of $\gamma\gamma$ pairs associated with the selected events, with peak and sideband regions indicated. Signal D_s^+ candidates are combined with π^0 candidates to give the spectrum of figure 1(c). The shaded

part shows the spectrum when π^0 candidates are combined with sideband entries in the $K^+K^-\pi^+$ mass spectrum. The dramatic peak near $2.32 \text{ GeV}/c^2$ is the new state, the $D_{sJ}^*(2317)^+$. Figure 1(d) shows the result of combining the D_s^+ candidates with the π^0 signal (unshaded) and sideband (shaded) regions.

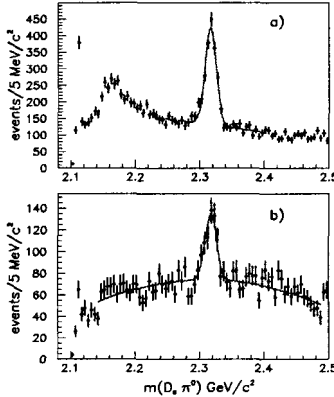


Figure 2: The $D_s^+\pi^0$ mass for (a) the decay $D_s^+ \rightarrow K^+K^-\pi^+$ and (b) the decay $D_s^+ \rightarrow K^+K^-\pi^+\pi^0$. The curves are from fits described in the text.

Figure 2 shows the mass spectrum of $D_s^+\pi^0$ candidates for two different D_s^+ decay modes and for some restricted kinematic ranges. The curves show fits using Gaussian functions, plus polynomials to describe the background. Consistent results are obtained from the two D_s^+ decay modes for the mass and the Gaussian width of the new peak. The fit in figure 2(a) yields a mass of $2316.8 \pm 0.4 \text{ MeV}/c^2$ and a Gaussian width of $\sigma = 8.6 \pm 0.4 \text{ MeV}/c^2$. Analysis of subchannels shows that this $D_{sJ}^*(2317)^+$ state is, as expected, seen in both the $\phi\pi^+$ and $\bar{K}^{*0}K^+$ decay modes of the D_s^+ . The fitted Gaussian width is consistent with the mass resolution, so the intrinsic width of the $D_{sJ}^*(2317)$ is small, with $\Gamma < 10 \text{ MeV}/c^2$.

Monte Carlo simulations have been used to verify that the $2.32 \text{ GeV}/c^2$ peak cannot be due to a reflection from some other charm state, nor from pion/kaon misidentification. The decay angular distribution is consistent with being flat, as expected for a spin-0 particle or for an unpolarized particle of any spin.

No evidence for other decay modes of the $D_{sJ}^*(2317)^+$ has been found. Figure 3 shows, for example, $D_s^+\gamma$, $D_s^+\gamma\gamma$ and $D_s^+\pi^0\gamma$ mass spectra for a number of cuts and selections, as described in the figure caption. While peaks are seen for $D_s^*(2112)^+$ and another apparent new state near $2.46 \text{ GeV}/c^2$, there is no indication in any of these channels for the $D_{sJ}^*(2317)^+$.

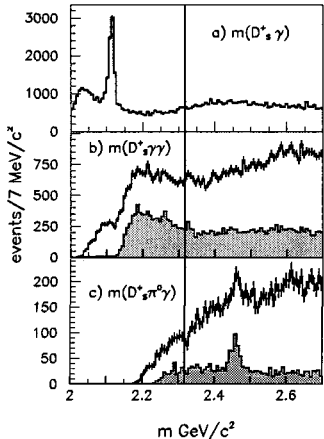


Figure 3: The mass distribution for (a) $D_s^+\gamma$ and (b) $D_s^+\gamma\gamma$ after excluding photons from the signal region of figure 1(b). (c) The $D_s^+\pi^0\gamma$ mass distribution. The lower histograms of (b) and (c) correspond to $D_s^+\gamma$ masses that fall in the $D_s^*(2112)^+$ signal region. The vertical line indicates the $D_{sJ}^*(2317)^+$ mass.

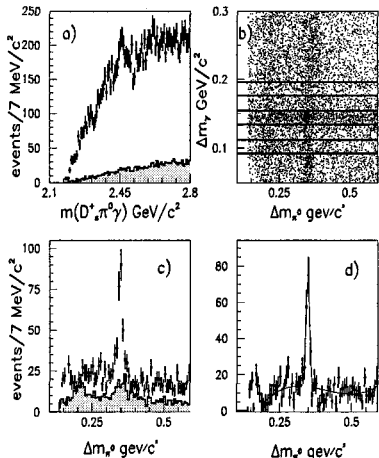


Figure 4: (a) The mass distribution for all selected $D_s^+\pi^0\gamma$ combinations. The shaded region is from D_s^* sidebands ($1.912 < m(K^+K^-\pi^+) < 1.933 \text{ GeV}/c^2$). (b) The value of Δm_γ versus Δm_{π^0} for all combinations. The horizontal lines indicate three ranges of Δm_γ . (c) The Δm_{π^0} mass distribution for the middle range of Δm_γ (points) and for the average of the upper and lower ranges (shaded histogram). (d) The difference between the two distributions shown in (c). The curve shows the fit described in the text.

At the time of publication of the discovery of the $D_{sJ}^*(2317)^+$ by BaBar, there was some uncertainty as to the nature of the second new peak at $2.46 \text{ GeV}/c^2$. The complexity of the overlapping kinematics of the $D_s^*(2112)^+ \rightarrow D_s^+\gamma$ and $D_{sJ}^*(2317)^+ \rightarrow D_s^+\pi^0$ decays needed further study to rule out the possibility of a kinematic artefact in $D_s^+\pi^0\gamma$ near $2.46 \text{ GeV}/c^2$. Subsequent work by Belle [3], CLEO [4] and BaBar [5] has confirmed the $D_{sJ}^*(2458)^+$ as a second, new charm state.

To investigate the $D_s^+\pi^0\gamma$ spectrum, D_s^+ candidates decaying to $K^-K^+\pi^+$ were used, from $c\bar{c}$ events recorded at centre-of-mass energy near 10.6 GeV , as described above. These candidates were combined with π^0 and γ candidates, as described in [5]. Figure 4(a) shows the resulting mass distribution, with a clear peak at $2.4 \text{ GeV}/c^2$. The background under the peak comes from several sources, which can be described in terms of mass differences: $\Delta m_\gamma = m(D_s^+\gamma) - m(D_s^+)$ and $\Delta m_{\pi^0} = m(D_s^+\pi^0) - m(D_s^+\gamma)$. The distributions of these are shown in the scatter plot of figure 4(b), indicating some kinematic effects that could possibly conspire to produce the peak at $2.4 \text{ GeV}/c^2$. The upper distribution of 4(c) shows $D_s^+\gamma\pi^0$ combinations corresponding to the $D_s^*(2112)^+$ signal region, and the shaded region to the corresponding sidebands. A fit to the subtracted distribution in figure 4(d) gives a narrow signal at $\Delta m_{\pi^0} = 346.2 \pm 0.9 \text{ MeV}/c^2$.

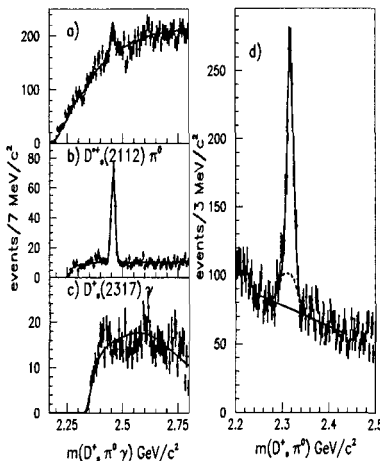


Figure 5: Maximum likelihood fit results overlaid on the $D_s^+\pi^0\gamma$ mass with (a) no weights, and after applying weights for (b) $D_s^*(2112)^+\pi^0$ and (c) $D_{sJ}^*(2317)^+\gamma$. (d) The mass spectrum of $D_s^+\pi^0$ (with no γ requirement). The solid curve is the fit described in detail in [5]. The dashed and lower solid curves are the contributions from $D_{sJ}^*(2458)^+$ decays and combinatorial background.

An unbinned maximum likelihood fit was used to disentangle the possible decay modes of the new state, the $D_{sJ}^*(2458)^+$, and to obtain reliable measures of the signal parameters. Full details of the fit are given in [5], and some results are shown in figure 5. The caption to the figure describes the distributions and the curves.

The measured mass of the $D_{sJ}^*(2458)^+$ is $2458.0 \pm 1.4 \text{ MeV}/c^2$ which agrees with the Belle result [3], but is two standard deviations lower than that obtained by CLEO [4]. The measured width of the state is consistent with the experimental resolution. The yield relative to that of the $D_{sJ}^*(2317)^+$ also agrees with Belle, but is smaller than the yield reported by CLEO.

3 Rare B-meson decays

Determination of the angle α of the Unitarity Triangle using $B \rightarrow \pi\pi$ decays requires the use of isospin relations [6] between the amplitudes for the decays $B^0(\bar{B}^0) \rightarrow \pi^+\pi^-$, $B^0(\bar{B}^0) \rightarrow \pi^0\pi^0$ and $B^\pm \rightarrow \pi^\pm\pi^0$. The main contributions to the $\pi^0\pi^0$ channel come from colour-suppressed tree and gluonic penguin amplitudes, and the branching fraction has been calculated in a number of QCD models. For example, in a QCD factorisation model [7], the prediction is 0.3×10^{-6} . On the other hand, phenomenological fits to data on charmless B decays [8] give results in the range $(1.6 - 2.5) \times 10^{-6}$.

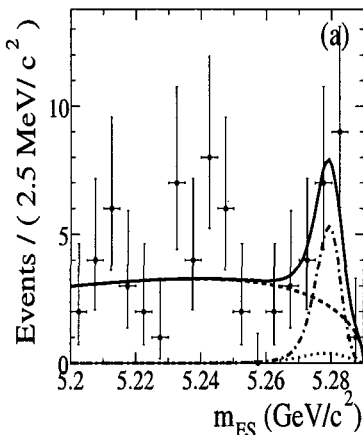


Figure 6: The distribution of m_{ES} for candidates in the $B \rightarrow \pi^0\pi^0$ signal data sample that satisfy an optimized requirement on the signal probability, based on all variables except m_{ES} . The solid line shows the projection of the maximum-likelihood fit, with the dotted and dashed curves showing some non-signal contributions, as described in [9].

The BaBar study [9] used (124 ± 1) million $\Upsilon(4S) \rightarrow B\bar{B}$ events, together with 12 fb^{-1} of data collected 40 MeV below the $\Upsilon(4S)$ peak. Candidate π^0 mesons were formed from selected photon pairs, reconstructed in the electromagnetic calorimeter, with invariant masses within 3σ of the π^0 mass, where the resolution σ is about $8 \text{ MeV}/c^2$ for high-momentum π^0 mesons. B-meson candidates were formed from combinations of two π^0 candidates. Two variables, used to isolate the $B \rightarrow \pi^0\pi^0$ signal, rely on the kinematic constraints for B meson pairs produced at the $\Upsilon(4S)$: these are the beam-energy-substituted mass, given by $m_{\text{ES}} = \sqrt{(s/2 + \mathbf{p}_i \cdot \mathbf{p}_B)^2/E_i^2 - \mathbf{p}_B^2}$, and the energy balance, given by $\Delta E = E_B - \sqrt{s}/2$. In these expressions, \sqrt{s} is the total e^+e^- centre-of-mass energy, (E_i, \mathbf{p}_i) is the four-momentum of the initial e^+e^- system in the lab frame, and (E_B, \mathbf{p}_B) is the lab four-momentum of the B candidate. The ΔE resolution for signal is about 80 MeV.

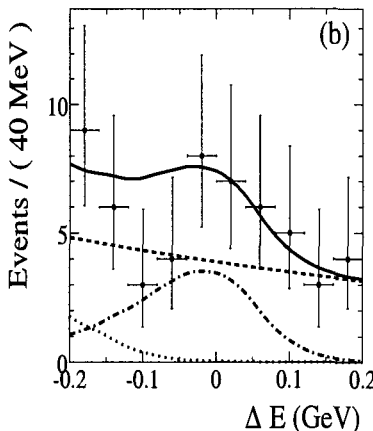


Figure 7: The distribution of ΔE for candidates in the $B \rightarrow \pi^0\pi^0$ signal data sample that satisfy an optimized requirement on the signal probability, based on all variables except ΔE . The solid line shows the projection of the maximum-likelihood fit, with the dotted and dashed curves showing some non-signal contributions, as described in [9].

Background sources of such pairs of π^0 mesons include $e^+e^- \rightarrow q\bar{q}$ events, where a π^0 from each quark jet can randomly combine to mimic a B decay. This background is suppressed using a cut on the angle between the sphericity axis of the B candidate and that of the rest of the tracks and photon candidates in the event. Background also comes from $B^\pm \rightarrow \rho^\pm\pi^0 \rightarrow \pi^\pm\pi^0\pi^0$ decays, in which the charged pion is emitted nearly at rest in the B rest frame.

An extended, unbinned maximum likelihood fit was used to measure the number of signal $B \rightarrow \pi^0\pi^0$ events, with, as inputs, the m_{ES} and ΔE variables

together with a Fisher discriminant, optimised to separate signal from background. The probability density functions for the fit were determined using both data and Monte Carlo simulation. Figures 6 and 7 show some projections of the fit. The fit gave a result of 46 ± 13 signal events in the sample, corresponding to a branching fraction $\text{BR}(\text{B} \rightarrow \pi^0\pi^0) = (2.1 \pm 0.6) \times 10^{-6}$. The significance of the signal was measured using the change in the likelihood value between the nominal fit and one with the signal yield fixed to zero. With statistical errors only, the significance is 4.7σ . An alternative event-counting analysis, with a lower efficiency, gave a consistent result. A large number of possible sources of systematic error were considered, leading to an expected systematic error of ± 3 signal events. This reduces the significance of the result to 4.2σ . The final branching ratio is then $\text{BR}(\text{B} \rightarrow \pi^0\pi^0) = (2.1 \pm 0.6 \pm 0.3) \times 10^{-6}$. This result is larger than some theoretical predictions, including those of the QCD factorisation model.

4 Conclusions

Hadron physics at BaBar is still at an early stage. In the first phases of the experiment, most attention was devoted to the physics of CP-violation. However the data sets contain copious amounts of $q\bar{q}$ and $\tau^+\tau^-$ events, which will lead to an increasing, and varied, programme of hadron physics studies.

Acknowledgments

I would like to thank the committee of the 11th Lomonosov conference, and particularly Alexander Studenikin, for organising such a stimulating and interesting conference. I also thank the entire BaBar Collaboration and our PEP II colleagues; it is their work that is reported here.

References

- [1] B. Aubert et al., BaBar Collaboration, *Nucl.Instr.Meth* A497, 1 (2002).
- [2] B. Aubert et al., BaBar Collaboration, *Phys.Rev.Lett* 90, 242001 (2003).
- [3] P. Krokovny et al., Belle Collaboration, submitted to *Phys.Rev.Lett* 92, 012002 (2004).
- [4] D. Besson et al., CLEO Collaboration, *Phys.Rev.* D68, 032002 (2003).
- [5] B. Aubert et al., BaBar Collaboration, *Phys.Rev.D* 69, 031101 2004.
- [6] M. Gronau and D. London, *Phys.Rev.Lett* 65, 3381 (1990).
- [7] See references [7] cited in [9].
- [8] See references [8] cited in [9].
- [9] B. Aubert et al., BaBar Collaboration, *Phys.Rev.Lett* 91, 241801 (2003).

SELEX-E781 RESULTS ON DOUBLY CHARMED BARYON FAMILY

M.Iori ^a

Departement of Physics,

University of Rome P.zza A. Moro 5 00185 Rome, Italy

Abstract. The SELEX experiment (E781) is a 3-stage magnetic spectrometer for a high statistics study of hadroproduction of charm baryons out to large x_F using 650 GeV/c Σ^-, π^- and p beams. The main features of the spectrometer are a high precision silicon vertex system and powerful particle identification provided by TRD and RICH. The mass of states with cc-diquark, Ξ_{cc}^{++} , Ξ_{cc}^+ was observed for first time, their masses are consistent with theoretical considerations. Production mechanisms and angular momentum are also investigated.

1 The eightfold way SU(4) for J=1/2 and 3/2 baryons

The SU(4) multiplet predicts the existence of baryons with one, two or three c -quarks. In particular in the double-charm level for $J=1/2$ we expect [1] three particles having two c -quarks: $\Xi_{cc}^+(cc\bar{d})$, $\Xi_{cc}^{++}(cc\bar{u})$ and $\Omega_{cc}^+(cc\bar{s})$. Several authors, using different approaches [3-7], predict a mass in the interval 3500-3700 MeV/ c^2 for $J=1/2$ as shown in Table 1. The production mechanism for double-charm was evaluated by Gunter and Saleev assuming only a charm excitation in proton and the $c+c \rightarrow (cc)+g$ diagram. This approach, applicable to the case when the momentum transfer is larger than $cc\bar{q}$ baryon mass, is not appropriate for the p_t range (< 3 GeV/ c) in most fixed target experiments.

2 The Selex experiment

The SELEX experiment at Fermilab uses a 3-stage magnetic spectrometer. The 600 GeV/c Hyperon beam of negative polarity contains roughly equal fractions of Σ^- and π^- . The positive beam is composed of 92% of protons and the rest π^+ 's. Beam particles are identified by a Transition Radiation detector (BTRD). The spectrometer was designed to study charm production in the forward hemisphere with good mass and decay vertex resolution for charm momentum in a range of 100-500 GeV/ c . The vertex region is composed of 5 targets (2 Cu and 3 C). The total target thickness is 5% of λ_{int} for protons and the targets are separated by 1.5 cm. Downstream of the targets there are 20 silicon planes with a strip pitch of 20-25 μm disposed in X,Y,U and V views. The M1 and M2 magnets effect a momentum cutoff of 2.5 GeV/ c and 15 GeV/ c respectively. A RICH detector, filled with Neon at room temperature and pressure, provides a single track ring radius resolution of 1.4% and 2σ K/π separation up to about 165 GeV/ c . A computational filter uses tracks identified by the RICH and linked to the vertex silicon by the PWCs to make a full reconstruction of the

^ae-mail: maurizio.iori@roma1.infn.it

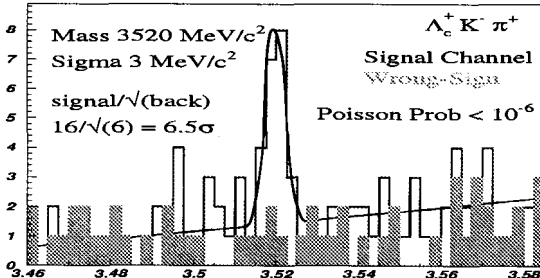


Figure 1: The $\Lambda_c^+ K^- \pi^+$ mass distribution in $5 \text{ MeV}/c^2$ bins. The shaded region is the wrong-sign combination $\Lambda_c^+ K^+ \pi^-$ mass distribution. The fit is a Gaussian plus a linear background

secondary vertex. Events consistent with only a primary vertex are rejected. A layout of the spectrometer can be found elsewhere [8]. The charm trigger is very loose. It requires a valid beam track, two tracks of charge opposite to the beam with momentum $> 15 \text{ GeV}/c$, two high momentum tracks linked to the Silicon vertex detector, and unconnected to all other tracks from the primary vertex. We triggered on about 1/3 of all the inelastic interactions. About 1/8 of them are written on tape for a final sample of about $0.9 \cdot 10^9$ events. In the analysis secondary vertices were reconstructed if the χ^2 of all tracks was inconsistent with single primary vertex. The RICH detector labelled all particles above $25 \text{ GeV}/c$. and it gives a good separation π/K for track momentum of $100 \text{ GeV}/c$, typical momenta for charm decay tracks (p, K). Results reported here are based on the sample of 1630 Λ_c^+ events used to measure the lifetime [9].

Table I: Estimated masses of Baryons with C=2 from several authors using quark mass combination [3], Lattice [4, 5], potential model [6] and relativistic quark model [7]; The errors are statistical. For systematic errors see the papers referenced

	$\Omega_{ccc}(ccc)$	$\Omega_{cc}(ccs)$	$\Xi_{cc}(ccu, d)$
J=3/2[3]	4925 ± 90	3840 ± 60	3695 ± 60
[4]		3730	3727
[6]			3625 ± 20
[7]			3610
J=1/2[3]			3635
[4]			3562 ± 20
[5]			3549 ± 13
[6]		3594	3478
[7]		3620	

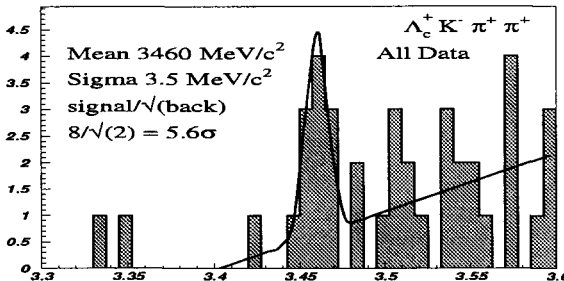


Figure 2: Ξ_{ccu}^{++} mass distribution in $7.5 \text{ MeV}/c^2$ bins.

3 Double-charm analysis

To search for double-charm baryons we required a weak decay vertex between the primary vertex and the downstream Λ_c with a strange particle (K^-) according to a Cabibbo-allowed transition . In particular we searched for decays with $Q=1$, $\Xi_{cc}^+(ccu)$ and $Q=2$, $\Xi_{cc}^{++}(ccd)$ in a mass interval of $3.2\text{-}4.0 \text{ GeV}/c^2$. The K and p decay tracks of Λ_c^+ were detected by the RICH.

3.1 $\Xi_{ccd}^+(3520)$

Fig. 1 shows the $\Lambda_c^+ K^- \pi^+$ invariant mass. In particular it shows a signal of 22 Ξ_{cc}^+ events at mass of $3520 \text{ MeV}/c^2$. The width of the peak is consistent with the simulation. The wrong-sign invariant mass (full histogram) shows a linear background behaviour and confirms the physical nature of the peak . The background in the signal region is 6 events and the significance is 6.5σ . The probability of such an excess is less than 10^{-6} . The probability that it is a fluctuation anywhere in the reconstructed mass range is less than $1.1 \cdot 10^{-4}$.

3.2 $\Xi_{ccu}^{++}(3460)$

The $\Xi_{cc}^+(ccd)$ should have an iso-doublet partner with $Q=2$. Looking in the $\Lambda_c^+ K^- \pi^+ \pi^-$ invariant mass spectrum with $7.5 \text{ MeV}/c^2$ bins we find , as shown in Fig. 2, $\Xi_{cc}^{++}(ccu)$ candidate at mass $3460 \text{ MeV}/c^2$. The width of the signal matches with the simulation. To improve the signal we require the negative track, K^- to be in forward hemisphere in the center of mass. With such a requirement we find a signal of 8 events over a background of 2 corresponding to 5.6σ . The wrong sign mass combination does not show an excess of events in this region. Simulation yields an acceptance for $\Xi_{cc}^{++}(ccu)$ which is of 50% the $\Xi_{cc}^+(ccd)$ acceptance.

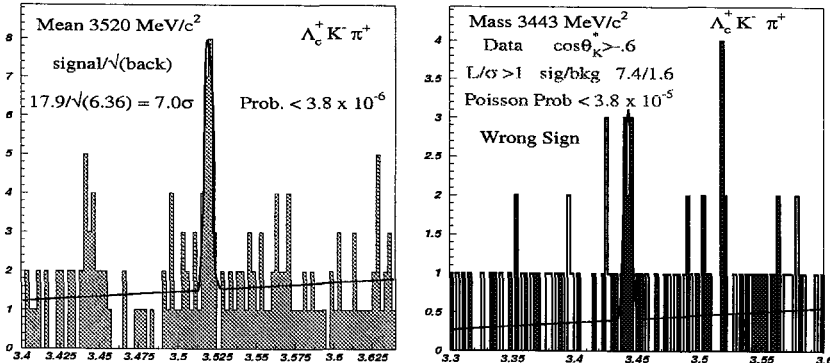


Figure 3: The histogram on left side shows $\Lambda_c^+ K^- \pi^+$ mass distribution in 5 MeV/ c^2 bins. On the right side the same histogram with $\cos \Theta_{K^*} > -0.6$. The fit gives a mass value of 3443 MeV/ c^2

3.3 Study of ccq decay anisotropy

The final state in the ccq rest frame is represented by back-to-back emission of $K\pi$ and Λ_c . The study of angular distribution of one of the decay particles provides informations about angular momentum of the parent particle. When we applied a cut of $\cos \Theta_{K^*} > -0.6$ to the Ξ_{ccd}^+ mass plot shown in Fig.1 we find the peak at 3520 MeV/ c^2 is strongly attenuated as shown by the histogram on the right side of Fig. 3. If the same cut is applied to the Ξ_{ccu}^{++} mass plot shown in Fig. 2 we do not see reduction. These results suggest the $\Xi_{ccd}^+(3520)$ and MeV/ c^2 $\Xi_{ccu}^{++}(3460)$ have angular momentum, $L > 0$ and $L = 0$ respectively.

3.4 $\Xi_{ccu}^+(3443)$

If we enlarge the Ξ_{ccd}^+ mass plot we see, as shown in the histogram on left side of Fig.3, a peak at 3450 MeV/ c^2 . When the angular cut discussed before is applied we have still find an excess of events at 3443 MeV/ c^2 .

4 Production

The Ξ_{cc}^+ and Ξ_{cc}^{++} are produced only by baryon beams (Σ^- and p). The average x_F is about 0.35. By detection efficiency evaluation the double-charm

sample corresponds to 40% of the Λ_c sample. This estimate suggests an unusual hadroproduction mechanism which might be explained within the framework of the QGS Model [10]. The FOCUS photoproduction experiment at Fermilab has looked for these states using their Λ_c sample and they see no evidence for double charm decaying into final states with Λ_c [11]. That may be suggests the content of hadronic beam plays a role in the production mechanism.

5 Summary

The SELEX Collaboration has measured for the first time the mass of two states with two c-quarks, Ξ_{cc}^+ , Ξ_{cc}^{++} . Their masses, 3520 ± 3 MeV/ c^2 and 3460 ± 3 MeV/ c^2 respectively are consistent with theoretical considerations. Further studies on angular distribution of particle in final states suggest these two states have angular momentum, $L > 0$ and $L = 0$ respectively. Also, the 3443 state is not consistent with $L=0$. A possible new state at 3443 MeV/ c^2 is found and it is consistent with $L = 1$. The double-charm baryons are produced only by baryon beam.

Acknowledgments

The author is indebted to the staff of Fermi National Accelerator Laboratory and for invaluable technical support from the staffs of collaborating institutions. He has appreciated the hospitality of University of Moscow.

References

- [1] Particle Data Group. D.E. Groom, et al. Eur. Phys. J. C15 1 (2000).
- [2] D. A. Gunter and V. A. Saleev Phys. Rev. D64 03 4006 (2001).
- [3] J. F.D. Bjorken Conf-85/69.
- [4] N. Mathur, R. Lewis and R. M. Woloshyn Phys. Rev D66 014502 (2002).
- [5] J. M. Flynn et al. JHEP 0307:066, 2003 hep-lat/0307025
- [6] V. Kiselev and A. K. Likhoded Phys. Rev. D66 034030 (2002).
- [7] D. Erbert, R. Faistov, O. Galkin and A. Martynenko, Phys. Rev D66 037501 2002.
- [8] J.S. Russ, et al., in *Proceedings of the 29th International Conference on High Energy Physics*, 1998, edited by A. Astbury et al. (Word Scientific, Singapore, 1998) Vol II, p. 1259; hep-ex/9812031.
- [9] A. Kushnirienko et al. Phys. Rev. Lett. 86 5243 (2001).
- [10] Kaidalov A. B. and Piskounova O.I. Sov. J. Nucl Phys 43 1986.
- [11] S. Ratti, talk given at 5th International Conference on Hyperons, Charm and Beauty Hadrons; Vancouver 25 Jun 2002.

LAW OF LARGE NUMBERS AND ASYMPTOTIC OF PHASE SPACE INTEGRAL

J.Manjavidze ^a, A.Sissakian ^b, N.Shubitidze ^c

Joint Institute for Nuclear Research, 141980, Dubna, Russia

Abstract. The law of large numbers is used for estimation of the longitudinal phase space integral for big value of particle numbers. A fully completed analytical expression of the phase space integral is received.

1 Introductions

In my talk I report on statistical method of estimation of the phase space integral in the case when number of particles $n -> n_{max}$. This work is small part of the big program that realize in Sissakian - Manjavidze group at JINR and devoted to the statistical description of inelastic processes at high energy, including processes with very high multiplicity.

Thermodynamical approach give as the possibility of full description of complicated system by the limited number of parameters. We use conception of thermodynamical equilibrium that means assumption of uniform distribution of energy over all degrees of freedom and fluctuations are the Gauss type.

Pioneering works of the use thermodynamical description of hadron processes belong to Fermi and Landau. Its main assumption consist in treatment the inelastic hadron collisions as dissipation of kinetic energies of colliding particles.

Interest in the events with very high multiplicity catenate with following. Fermi-Landau model badly described processes with medium multiplicity from the limitations of Non-Abelian gauge symmetries. The role of the last will be weaken when the number of particles tends yo the n_{max} . Therefore, it is important to investigate the phenomenological indications of thermalization.

So, it is actually the program of building fast events generator for correctly describing processes with very high multiplicity.

2 Asymptotic of Phase Space Integral

We propose a new method of estimation of the phase space integral at $n \rightarrow n_{max} = \sqrt{s}/m$:

$$Z_n = \int \left\{ \prod_{i=1}^n \frac{d^3 k_i}{2\sqrt{k_i^2 + m^2}} \right\} \delta^4(P - \sum k_i) f_n(k_1, \dots, k_n) \quad (1)$$

^ae-mail: joseph@nusun.jinr.ru

^be-mail: sisakian@jinr.ru

^ce-mail: shubi@nusun.jinr.ru

where f_n is the amplitude module squire, $P \equiv (E, 0, 0, 0)$ is the momentum 4-vector, i.e. we work in the center of the mass (CM) system. Such a type integrals arise when the topological cross-sections are calculated. We will examine the simplest case of separable amplitude f_n :

$$f_n(k_1, \dots, k_n) = \prod_{i=1}^n \exp(-r_0^2 k_{t,i}^2) \quad (2)$$

where $k_{t,i}$ is a transverse momentum and r_0 is a phenomenological cutting parameter. This choice means assumption that the secondaries are produced independently from each other. Limitations to small values of transverse momentum imposed by the dynamics on the collision amplitude are compatible with the present experimental evidence.

The theory of calculations of the integrals (1) have a long history [1-10].

The dominant problem descended from the presence of Dirac delta function in the integrand. In order to avoid this difficulty Kajantie and Karimaki [6] introduce Fourier transformation for δ -function and use a saddle point method for the calculating of the Fourier transform. Lurcat and Mazur [1] use Laplace transformation for integrand, normalizes it and then interprets it as a frequency function. The last approximated by the Edgeworth series and keep the first few terms only. The analogous technique with small modifications for a special case of f_n was used by Krzywicki and Bilash [2-4]. The are presence series of works, where in calculations used the method of Monte Carlo (MC) [8-10]. There is a need to note that the preceding theories represent themselves an algorithm of numerical calculations.

A base of our method consists of the expansion of (1) by terms of the universally independent functions $T_s(n)$. Then we will use the law of large numbers for $T_s(n)$. On this way we receive for Z_n completely analytical expression.

Our interest focused on the asymptotic behavior of Z_n when $n \rightarrow n_{max}$. This case corresponds to the situation when produced particles have the small momenta. We may neglect the momentum conservation law at $n \rightarrow n_{max}$ and leave only energy conservation law:

$$\delta^4 \left(P - \sum_{i=1}^n k_i \right) \rightarrow \delta \left(E - \sum_{i=1}^n \sqrt{k_i^2 + m^2} \right) \quad (3)$$

Performing integration over spherical angles, we get to the expression de-

pending from the longitudinal $k_{z,i}$ and transverse $k_{t,i}$ momentum :

$$Z_n(E) = (\pi/2)^n \int \left\{ \prod_{i=1}^n \frac{d(k_{t,i}^2) dk_z}{\sqrt{k_{t,i}^2 + k_{z,i}^2 + m^2}} e^{-r_0^2 k_{t,i}^2} \right\} \times \\ \times \delta \left(E - \sum_{i=1}^n \sqrt{k_{t,i}^2 + k_{z,i}^2 + m^2} \right) \quad (4)$$

Then we introduce the particle energy as the independent variable. We receiving result:

$$Z_n(E) = (\pi/r_0)^n [m(n_{max} - n)]^{n-1} \times \\ \times \left\{ \prod_{i=1}^n \int_0^1 dy_i F(r_0 m \sqrt{(n_{max} - n)y_i((n_{max} - n)y_i + 2)}) \right\} \delta \left(1 - \sum y_i \right) \quad (5)$$

where $F(x)$ is the Dawson integral:

$$F(x) = e^{-x^2} \int_0^x e^{t^2} dt \quad (6)$$

Let us represent the integral (6) in the following form:

$$F(r_0 m \sqrt{(n_{max} - n)y((n_{max} - n)y + 2)}) = \sqrt{y} \exp \{a_0 + a_1 y + a_2 y^2 + \dots\} \quad (7)$$

where the coefficients

$$a_s = \frac{1}{2\pi i} \int_C d\zeta \zeta^{-s-1} \ln \left\{ F(r_0 m \sqrt{(n_{max} - n)\zeta((n_{max} - n)\zeta + 2)}) / \sqrt{\zeta} \right\} \quad (8)$$

After the substitution (7) into eq. (5) we find:

$$Z_n(E) = (\pi/r_0)^n [m(n_{max} - n)]^{n-1} \left\{ \prod_{i=1}^n \int_0^1 dy_i \sqrt{y_i} \right\} \delta \left(1 - \sum y_i \right) \times \\ \times \exp \{n[a_0 + a_1 T_1(n) + a_2 T_2(n) + \dots]\} \quad (9)$$

where $T_s(n)$ is an universal function:

$$T_s(n) = \frac{1}{n} \sum_{i=1}^n y_i^s \quad (10)$$

Since we wish to calculate our integral (9) by the method of MC it is reasonable to investigate the statistical distributions of functions (10) with the

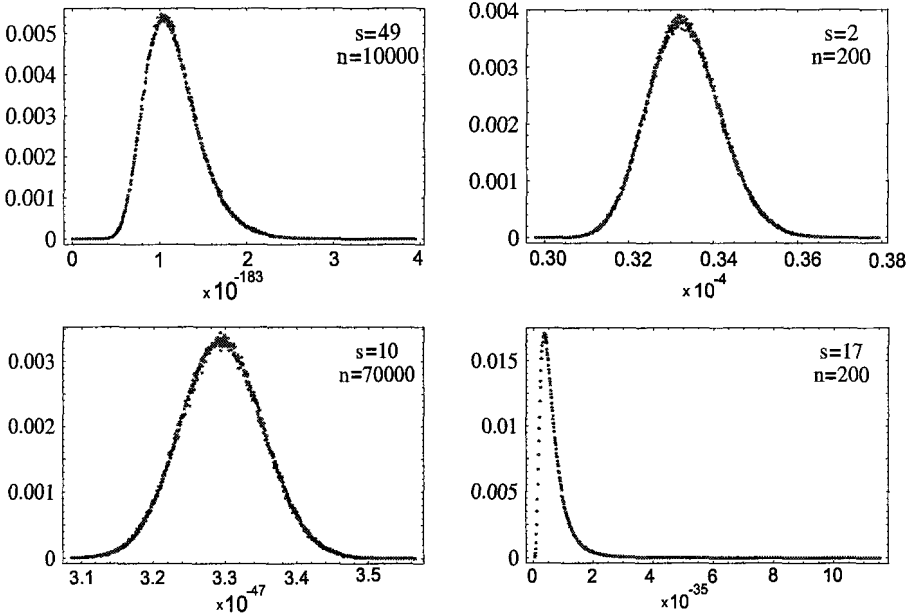


Figure 1: Examples of statistical distributions of $T_s(n)$ functions

constrain $\sum y_i = 1$. The calculations was realized for the different values of s and n . As it can be seen from Fig.1 for relatively small values of s the distribution tends to the normal type but for relatively big values of s the distribution tends to the Poisson's one.

We can not receive the exact expression for statistical distribution of functions $T_s(n)$. But we find the good approximation for their extremum:

$$\frac{1}{s+1} \left(\frac{2}{n} \right)^s \quad (11)$$

We find also the limits of the area where is grouped more significant values of $T_s(n)$:

$$\left(\frac{1}{s+1} \left(\frac{1.7}{n} \right)^s, \frac{1}{s+1} \left(\frac{2.3}{n} \right)^s \right) \quad (12)$$

Let us imagine that we calculate our integral (9) by the MC method. On every step we must randomly select the group of nonnegative numbers y_1, y_2, \dots, y_n with the constrain $\sum y_i = 1$ and substitute their to the eq. (9). As a result, the maximal number of items must contain as a functions $T_s(n)$ values $(2/n)^s/(s+1)$. Consequently, if we neglect a small contributions terms we may

change in (9) functions $T_s(n)$ by the corresponding values $(2/n)^s/(s+1)$ and carry out exponent from the integrand expression (9).

After this procedure the remainder integral has a form:

$$\left\{ \prod_{i=1}^n \int_0^1 dy_i \sqrt{y_i} \right\} \delta \left(1 - \sum_{i=1}^n y_i \right). \quad (13)$$

It is easily calculable if we pass to the hyperspherical coordinates:

$$\begin{aligned} y_1 &= \rho \cos^2(\varphi_{n-1}) \dots \cos^2(\varphi_2) \cos^2(\varphi_1) \\ y_2 &= \rho \cos^2(\varphi_{n-1}) \dots \cos^2(\varphi_2) \sin^2(\varphi_1) \\ &\vdots \\ y_{n-1} &= \rho \cos^2(\varphi_{n-1}) \sin^2(\varphi_{n-2}) \\ y_n &= \rho \sin^2(\varphi_{n-1}) \end{aligned} \quad (14)$$

The result looks as follows:

$$\left\{ \prod_{i=1}^n \int_0^1 dy_i \sqrt{y_i} \right\} \delta \left(1 - \sum_{i=1}^n y_i \right) = \frac{(\Gamma(3/2))^{n-1}}{\Gamma(3n/2)} \quad (15)$$

The final expression has a form:

$$Z_n(E) = \frac{\pi^{(3n-1)/2}}{r_0 \Gamma(3n/2)} \left[\frac{m(n_{max} - n)}{2r_0} \right]^{n-1} e^{nW(2)} \quad (16)$$

where

$$W(t) = \frac{n}{t} \int_0^{t/n} \ln \left[\frac{1}{\sqrt{y}} F \left(r_0 m \sqrt{(n_{max} - n)y((n_{max} - n)y + 2)} \right) \right] dy \quad (17)$$

Fig.2 demonstrated three graphics of $\ln(Z_n(E))/n$ for various values of parameter t in (17) - 1.7, 2.0, 2.3. As is shown in the graphic observable differences take a place for small n (< 5000). Thus, we find an area of validity of our equation (16).

Generalization for another form of f_n (2) is not a complicated procedure. It is the interesting to calculate the limit $r_0 \rightarrow 0$:

$$Q_n(E) = \lim_{r_0 \rightarrow 0} Z_n(E) \quad (18)$$

For it we use eq.(5) and because $\lim_{x \rightarrow 0} F(x)/x = 1$ receive:

$$\begin{aligned} Q_n(E) &= \pi^n m^{2n-1} (n_{max} - n)^{\frac{3}{2}n-1} \times \\ &\times \left\{ \prod_{i=0}^n \int_0^1 dy_i \sqrt{y_i((n_{max} - n)y_i + 2)} \right\} \delta(1 - \sum y_i) \end{aligned} \quad (19)$$

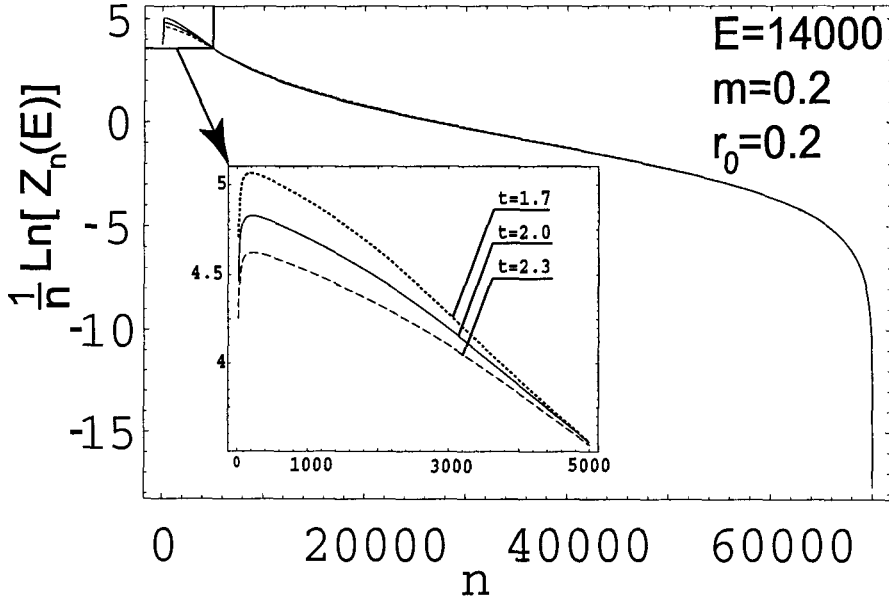


Figure 2: Behavior of $\ln(Z_n(E))/n$ for various values of parameter t

Then we expand the square root in (19) into the series:

$$\sqrt{y_i((n_{max} - n)y_i + 2)} = \exp\left\{\sum_{j=0}^{\infty} a_j y_i^j\right\} \quad (20)$$

where:

$$a_0 = \frac{1}{2} \ln(2); a_j = (-1)^{j+1} \frac{1}{2j} \left(\frac{y}{2}\right)^j \quad (21)$$

Using the analogous method we receive the following expressions for the "normalized" phase space integral $\overline{Z_n(E)}$:

$$\overline{Z_n(E)} = Z_n(E)/Q_n(E) = \left\{ \frac{1}{r_0 m \sqrt{2(n_{max} - n)}} \exp^{W(2) - U(2)} \right\}^n \quad (22)$$

where

$$U(t) = \frac{1}{2} [(2-t)\tau/(2t) + (1+1/\tau) \ln(1+\tau) - 1] \quad (23)$$

and

$$\tau = \frac{t(n_{max} - n)}{2n}$$

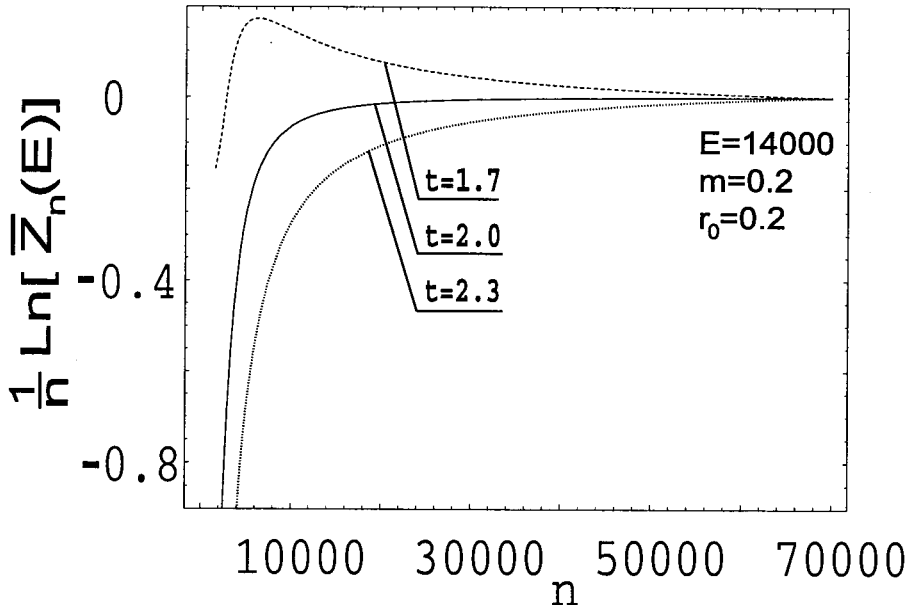


Figure 3: Behavior of $\ln(\overline{Z}_n(E))/n$ for various values of parameter t

On Fig.3 you can see the behavior of $\overline{Z}_n(E)$ for various value of the parameter t in (17) - 1.7, 2.0, 2.3.

3 Conclusion

Method of estimation phase space integral by use the law of large numbers allows to receive an analytical expression. The last is very significant when we build the fast event generator.

As would be expected, the dependence on the cutting parameter r_0 vanishes at the asymptotic on multiplicity $n \rightarrow n_{max}$ but it is essential in case when n have a finite value.

Acknowledgments

The authors wish to express their appreciation to Dr. M. Mania from Tbilisi Institute of Mathematic for many helpful discussions.

References

- [1] F.Lurcat,P.Mazur, Nuovo Cim. **31**, 140, (1964).
- [2] A.Krzywicki, Nuovo Cim., **32**, 1067, (1964).
- [3] A.Krzywicki, J. Math. Phys., **6**, 485, (1965).
- [4] A.Bialas, T.Ruijgrok, Nuovo Cim., **39**, 1061, (1965).
- [5] E.H.de Groot, Nucl. Phys., **B48**, 295, (1972).
- [6] K.Kajantie, V.Karimaki, Computer Phys. Comm., **2**, 207, (1971).
- [7] P.Pirala, E.Byckling, Computer Phys. Comm., **4**, 117, (1972).
- [8] R.A.Morrow, Computer Phys. Comm., **13**, 399, (1978).
- [9] R.Kleiss, W.J.Stirling, Computer Phys. Comm., **40**, 359, (1986).
- [10] M.M.Block, Computer Phys. Comm., **69**, 459, (1992).

THE GOTTFRIED SUM RULE: THEORY VS EXPERIMENT

A.L. Kataev ^{a, b}

*Institute for Nuclear Research of the Academy of Sciences of Russia, 117312,
Moscow, Russia*

Abstract. The current status of theoretical QCD calculations and experimental measurements of the Gottfried sum rule are discussed. The interesting from our point of view opened problems are summarised. Among them is the task of estimating the measure of light-quark flavour asymmetry in possible future experiments.

1 Introduction.

Studies of the Gottfried sum rule of charged lepton-nucleon deep-inelastic scattering [1], namely

$$I_G(Q^2, 0, 1) = \int_0^1 \frac{dx}{x} \left[F_2^{lp}(x, Q^2) - F_2^{ln}(x, Q^2) \right] \quad (1)$$

can provide the important information on the possible existence of a light antiquark flavour asymmetry in the nucleon sea. Indeed, the NMC collaboration determination [2] demonstrated that its experimental value

$$I_G^{\text{NMC}}(4 \text{ GeV}^2, 0, 1) = 0.235 \pm 0.026 \quad , \quad (2)$$

is significantly lower than the quark-parton flavour-symmetric prediction

$$I_G(Q^2, 0, 1) = \frac{1}{3} \quad . \quad (3)$$

This deviation is associated with the existence of a non-zero integrated light-quark flavour asymmetry defined as

$$FA(Q^2, 0, 1) = \int_0^1 [\bar{d}(x, Q^2) - \bar{u}(x, Q^2)] dx \quad . \quad (4)$$

In spite of the existence of detailed reviews on the subject [3, 4] we think that it is worth while to return to the consideration of the current status of knowledge of different aspects related to this sum rule.

In this report, based in part on the recent work of Ref. [5], the contributions of QCD corrections and higher-twist effects to the Gottfried sum rule are discussed first in the case of a flavour-symmetric sea. Next, the results of its experimental determination are summarised. Then we briefly outline various possibilities for determining the integral $FA(Q^2, 0, 1)$ from previous, present and future data.

^ae-mail: kataev@ms2.inr.ac.ru

^bSupported in part by RFBR Grants Nos. 03-02-17047 and 03-02-17177

2 QCD predictions.

Let us start by defining the arbitrary non-singlet (NS) Mellin moment of the difference of F_2 structure functions of charged lepton-proton and charged lepton-nucleon deep-inelastic scattering (DIS):

$$M_n^{NS}(Q^2) = \int_0^1 x^{n-2} \left[F_2^{lp}(x, Q^2) - F_2^{ln}(x, Q^2) \right] dx . \quad (5)$$

The moment with $n = 1$, namely the Gottfried sum rule, can be expressed as

$$\begin{aligned} I_G(Q^2, 0, 1) &= \int_0^1 \left[\frac{1}{3}(u_v(x, Q^2) - d_v(x, Q^2)) + \frac{2}{3}(\bar{u}(x, Q^2) - \bar{d}(x, Q^2)) \right] dx \\ &= \frac{1}{3} - \frac{2}{3} FA(Q^2, 0, 1) \end{aligned} \quad (6)$$

where $u_v(x, Q^2) = u(x, Q^2) - \bar{u}(x, Q^2)$ and $d_v(x, Q^2) = d(x, Q^2) - \bar{d}(x, Q^2)$ are the valence-quark distributions and the measure of flavour asymmetry is related to the difference of the sea-quark distributions $\bar{u}(x, Q^2)$ and $\bar{d}(x, Q^2)$ via Eq.(4).

2.1 Perturbative contributions.

Consider first the case when the sea is flavour-symmetric. In zeroth order of perturbation theory the quark-parton result of Eq.(3) is reproduced. However, the quark-gluon interactions generate non-zero corrections to I_G , defined as

$$I_G(Q^2, 0, 1) = AD(\alpha_s)C(\alpha_s) . \quad (7)$$

The anomalous dimension term is related to the anomalous dimension function of the first moment $\gamma^{n=1}(\alpha_s)$ and to the QCD β -function, namely :

$$\begin{aligned} AD(\alpha_s) &= \exp \left[- \int_{\delta}^{\alpha_s(Q^2)} \frac{\gamma^{n=1}(x)}{\beta(x)} dx \right] = 1 + \frac{1}{2} \frac{\gamma_1^{n=1}}{\beta_0} \left(\frac{\alpha_s(Q^2)}{4\pi} \right) \\ &\quad + \frac{1}{4} \left(\frac{1}{2} \frac{(\gamma_1^{n=1})^2}{\beta_0^2} - \frac{\gamma_1^{n=1}\beta_1}{\beta_0^2} + \frac{\gamma_2^{n=1}}{\beta_0} \right) \left(\frac{\alpha_s(Q^2)}{4\pi} \right)^2 . \end{aligned} \quad (8)$$

The given expansion in α_s can be obtained after taking into account that $\gamma_0^{n=1} = 0$ and setting $\delta = 0$.

The calculations of $\gamma_1^{n=1}$ [6, 7] give the following result

$$\gamma_1^{n=1} = -4(C_F^2 - C_F C_A)[13 + 8\zeta(3) - 2\pi^2] = +2.557 . \quad (9)$$

The coefficients of the QCD β -function are well-known:

$$\beta_0 = \left(\frac{11}{3} C_A - \frac{2}{3} f \right) = 11 - 0.667f \quad (10)$$

$$\beta_1 = \left(\frac{34}{3} C_A^2 - 2C_F f - \frac{10}{3} C_A f \right) = 102 - 12.667f \quad . \quad (11)$$

Here and below $C_F = 4/3$ and $C_A = 3$ and f is the number of active flavours.

The general order α_s^2 - expression for $C(\alpha_s)$ can be written down as

$$C(\alpha_s) = \frac{1}{3} \left[1 + C_1^{n=1} \left(\frac{\alpha_s}{\pi} \right) + C_2^{n=1} \left(\frac{\alpha_s}{\pi} \right)^2 \right] \quad (12)$$

where $C_1^{n=1} = 0$ [8]. The coefficient $C_2^{n=1}$ was evaluated only recently [5] by means of numerical integration of the complicated x -dependence of the two-loop contributions to the coefficient functions of DGLAP equation for DIS structure functions, calculated in Ref. [9]. The expression obtained in Ref. [5] is:

$$C_2^{n=1} = (3.695 C_F^2 - 1.847 C_F C_A) = -0.821 \quad . \quad (13)$$

Collecting now all known QCD corrections to Eq.(7) we found :

$$I_G(Q^2, 0, 1)_{f=3} = \frac{1}{3} \left[1 + 0.0355 \left(\frac{\alpha_s}{\pi} \right) + \left(-0.852 + \frac{\gamma_2^{n=1}}{64\beta_0} \right) \left(\frac{\alpha_s}{\pi} \right)^2 \right] \quad , \quad (14)$$

$$I_G(Q^2, 0, 1)_{f=4} = \frac{1}{3} \left[1 + 0.0384 \left(\frac{\alpha_s}{\pi} \right) + \left(-0.850 + \frac{\gamma_2^{n=1}}{64\beta_0} \right) \left(\frac{\alpha_s}{\pi} \right)^2 \right] \quad , \quad (15)$$

where $\alpha_s = \alpha_s(Q^2)$ and the three-loop anomalous dimension term $\gamma_2^{n=1}$ is still unknown. In Ref. [5] it was estimated using the feature observed in Ref. [12] that the n -dependence of the ratio γ_1^n/γ_2^n , obtained from three-loop terms of the the anomalous dimension functions of even moments for charged lepton-nucleon DIS, calculated in Ref. [10], and of odd moments of νN DIS, calculated in Ref. [11], can be fixed by similar approximate relation. Direct calculations of $\gamma_2^{(n=1)}$ were performed lated on in Ref. [13]. The final numerical analogs of Eq. (14) and Eq. (15) read [13]:

$$I_G(Q^2, 0, 1)_{f=3} = \frac{1}{3} \left[1 + 0.0355 \left(\frac{\alpha_s}{\pi} \right) - 0.584 \left(\frac{\alpha_s}{\pi} \right)^2 \right] \quad , \quad (16)$$

$$I_G(Q^2, 0, 1)_{f=3} = \frac{1}{3} \left[1 + 0.0384 \left(\frac{\alpha_s}{\pi} \right) - 0.565 \left(\frac{\alpha_s}{\pi} \right)^2 \right] \quad , \quad (17)$$

where the α_s^2 contribution is dominated by the numerical value of the coefficient $C_2^{n=1}$ from Eq. (13). Thus we convinced ourselves that the perturbative QCD corrections to the Gottfried sum rule are really small and cannot be responsible for violation of the flavour-symmetric prediction from the experimental value of Eq.(2).

2.2 Higher-twist terms.

The possibility that the higher-twist effects in the Gottfried sum rule might be sizable was discussed in Ref. [14]. It was argued that the next-to-leading sets of parton distributions, namely GRV94 [15], MRST98 [16] and CTEQ5 [17], failed to describe the existing experimental F_2^p - F_2^n data below $Q^2 < 7 \text{ GeV}^2$ [14]. From the point of view of the authors of Ref. [14] this might be associated with substantial higher-twist corrections, which in part are responsible for the deviation of the Gottfried sum rule result from its NMC value. However, definite results of the fits to $F_2^p - F_2^n$ data, performed in Ref. [18] with the help of the most recent Alekhin PDF set of Ref. [19] (A02), indicate that the conclusions of Ref. [14] are too optimistic. Indeed, the authors of Ref. [18] demonstrated that for the second NS moment of Eq. (5) the numerator of the $1/Q^2$ twist-4 correction is rather small, namely $H_{F_2}^{n-p} = -0.0058 \pm 0.0069 \text{ GeV}^2$. In view of this we expect that the twist-4 contribution to the first moment, namely to I_G , will be small also. Moreover, in spite of the fact that the fits of Ref. [18] reveal a definite discrepancy between x -dependence found for $H_{F_2}^{n-p}(x)$ and the predictions of the infrared renormalon (IRR) model (for a review see Ref. [20]), we think that the latter method still might give order-of-magnitude estimates of the higher-twist contributions. Note, that the IRR model is based in part on summations of the chain of fermion loop insertions to the gluon propagator and is thus related to the large f -expansion of the coefficient functions. For the polarised Bjorken sum rule these studies were made in Ref. [21] (for more recent discussions see Ref. [22]). In the case of I_G the flavour dependence does not manifest itself up to α_s^3 -corrections (see Eq. (12)). It is possible to show that in comparison with polarised Bjorken sum rule, the IRR model corrections (and therefore higher-twist effects) to the Gottfried sum rule will be damped by the additional factor $\alpha_s/(\pi N_c^2) = \alpha_s/(9\pi)$ [13]. Therefore, the Gottfried sum rule cannot receive substantial higher twist contributions.

3 Experimental situation.

The experimental determinations of the Gottfried sum rule have a rather long history, summarised in the reviews of Refs. [3,4]. In fact what is really evaluated from the experimental data is the integral

$$I(Q^2, x_{min}, x_{max}) = \int_{x_{min}}^{x_{max}} \frac{dx}{x} \left[F_2^{lp}(x, Q^2) - F_2^{ln}(x, Q^2) \right] . \quad (18)$$

In a more detailed analysis $F_2^{lp}(x, Q^2) - F_2^{ln}(x, Q^2)$ should be extrapolated to the unmeasured regions and since $F_2^{ln}(x, Q^2)$ is extracted from DIS on nuclei targets, nuclear effects should be also taken into account. However, all four experimental groups working on the direct determination of the Gottfried sum

rule from their experimental data, were not able to achieve ideal results. Indeed, the main source of experimental uncertainty results from the extrapolations of the experimental data from x_{min} to 0. Moreover, the mean Q^2 in the data are dependent on x and it is sometimes difficult to fix typical Q^2 value of the Gottfried sum rule (see Table 1.)

Group	Q^2 (GeV 2)	x_{min}	x_{max}	$I_G(Q^2, x_{min}, x_{max})$
SLAC [23]	0.1–20	0.02	0.82	0.200 ± 0.040
EMC [24]	10–90	0.02	0.8	$0.197 \pm 0.011(\text{st.}) \pm 0.083 (\text{sys.})$
BCDMS [25]	20	0.06	0.8	$0.197 \pm 0.011 (\text{st.}) \pm 0.036 (\text{sys.})$
NMC [2]	4	0.004	0.8	$0.221 \pm 0.008 (\text{st.}) \pm 0.019 (\text{sys.})$

Table 1. The existing experimental data for the integral of Eq. (18).

In spite of the fact that already the results of Ref. [23] inspired discussions of the possibility that the theoretical expression for Eq.(3) might be violated, its further determinations by EMC collaboration [24], namely

$$I_G^{\text{EMC}}(Q^2 = ?, 0, 1) = 0.235^{+0.110}_{-0.099} \quad (19)$$

within experimental error bars did not in fact demonstrate an obvious deviation from the quark-parton model prediction 1/3 (note, that in Eq.(19) Q^2 -value was not determined). A similar conclusion also applies to the analysis of the BCDMS data in Ref. [25]. Indeed, it suffers from large uncertainties at $x < 0.06$, which vary from 0.07 to 0.22. Thus the results of NMC collaboration of Eq.(2) turned out to be extremely important for understanding that flavour-asymmetry of antiquark distributions in the nucleon really exist in nature. The precision of their data even allow one to extract the value of integrated light-quark flavour asymmetry, defined by Eq.(4) [2]:

$$FA^{\text{NMC}}(4 \text{ GeV}^2, 0, 1) = 0.147 \pm 0.039 \quad . \quad (20)$$

However, even the members of NMC collaboration were not able to take into account all effects, typical for DIS. Indeed, the nuclear corrections, such as the Fermi motion, were neglected by them. In view of this, it became rather important to get an independent experimental extraction of $FA(Q^2, 0, 1)$. Quite recently this was done in an analysis of the data for Drell-Yan production in proton-proton and proton-deuteron scattering by the members of E866 collaboration. Integrating $\bar{d}(x, Q^2) - \bar{u}(x, Q^2)$ over the measured x -region they obtained [26]:

$$FA^{\text{E866}}(54 \text{ GeV}^2, 0.015, 0.35) = 0.0803 \pm 0.011 \quad . \quad (21)$$

Extrapolation this integral to the unmeasured region $0 \leq x \leq 0.015$ and assuming that the contribution for $x \geq 0.35$ is negligible, the members of E866 collaboration found that

$$FA^{\text{E866}}(54 \text{ GeV}^2, 0, 1) = 0.118 \pm 0.015 \quad (22)$$

(see Ref. [26]). Within existing error-bars this result turned out to be in agreement with Eq. (20), which is the NMC value of this integral, extracted at 4 GeV². In view of this it is possible to conclude that the value of the integrated light-quark flavour asymmetry is almost independent of Q^2 over a wide range of the momentum transfer. This demonstrates in part its non-perturbative origin.

4 Possible future prospects.

In order to calculate the characteristics of a light-quark flavour asymmetry a number of non-perturbative models have been successfully used. Among them are the meson-cloud model, instanton model, chiral-quark soliton models and others (for reviews see Refs. [3, 4]). However, to make more definite conclusions on the predictive power of these approaches more detailed experimental knowledge about the behaviour of the rate \bar{d}/\bar{u} at different values of x is needed.

The new 120 GeV Fermilab Main Injector should allow one to extend Drell-Yan measurements of \bar{d}/\bar{u} to the region of $0.02 < x < 0.7$. Moreover, the studies of the CEBAF data for F_2^D at large x can give the chance to perform more detailed combined fits of all available DIS data. The extraction of a light-quark flavour asymmetry from the fits to the data for F_2^D require the detailed treatment of nuclear effects, say in the manner of the work of Ref. [18]. Clearly, these measurements might be important for more detailed determinations of the effects of flavour-asymmetry in various sets of parton distribution functions, which at present differ in the CTEQ6M, MRST2001C and A02 sets (for their comparison at $Q^2 = (100 \text{ GeV})^2$ see Ref. [27]). As a test of their current predictive power it is rather useful to use them for calculations of the integral $FA(Q^2, 0, 1)$, as was done in Ref. [4].

Another possibility is to study light-quark flavour asymmetry in the process of νN DIS at the possible future Neutrino Factories. Indeed, as was noticed in Ref. [6] in the quark-parton model the $\bar{d} - \bar{u}$ difference can be related to the νN DIS SFs as

$$\bar{d}(x) - \bar{u}(x) = \frac{1}{2} \left[F_1^{\bar{\nu}p}(x) - F_1^{\nu p}(x) \right] - \frac{1}{4} \left[F_3^{\bar{\nu}p}(x) - F_3^{\nu p}(x) \right] \quad (23)$$

where the \bar{s} and \bar{c} distributions are neglected. At the NLO of perturbative QCD the analog of Eq.(23) was also derived [6]. Since it is known, that at the Neutrino Factories it will be possible to extract from the cross-sections of νN DIS F_1 and F_3 structure functions separately [28], the more precise νN DIS data might be useful for additional estimates of the size of the light-quark flavour asymmetry.

Acknowledgements

I am grateful to D. J. Broadhurst, G. Parente and C. J. Maxwell for the fruitful collaboration at the various stages of the described above studies. It is also the pleasure to thank A. B. Kaidalov and W. J. Stirling for useful discussions.

References

- [1] K. Gottfried, *Phys.Rev.Lett.* **18**, 1174 (1967).
- [2] M. Arneodo *et al.* [New Muon Collaboration], *Phys.Rev.* **D 50**, 1 (1994).
- [3] S. Kumano, *Phys Rept* **303**, 183 (1998).
- [4] G. T. Garvey and J. C. Peng, *Prog.Part. Nucl. Phys.* **47**, 203 (2001).
- [5] A. L. Kataev and G. Parente, *Phys. Lett.* **B 566**, 120 (2003).
- [6] D. A. Ross and C. T. Sachrajda, *Nucl.Phys.* **B 149**, 497 (1979).
- [7] G. Curci, W. Furmanski and R. Petronzio, *Nucl.Phys.* **B 175**, 27 (1980).
- [8] W. A. Bardeen, A. J. Buras, D. W. Duke and T. Muta, *Phys Rev.* **D 18**, 3998 (1978).
- [9] W. L. van Neerven and E. B. Zijlstra, *Phys Lett.* **B 272**, 127 (1991).
- [10] S. A. Larin, T. van Ritbergen and J. A. Vermaseren, *Nucl. Phys.* **B 427**, 41 (1994); S. A. Larin, P. Nogueira, T. van Ritbergen and J. A. Vermaseren, *Nucl. Phys.* **B 492**, 338 (1997).
- [11] A. Retey and J. A. Vermaseren, *Nucl Phys.* **B 604**, 281 (2001).
- [12] A. L. Kataev, G. Parente and A. V. Sidorov, hep-ph/0106221, *Phys.Part. Nucl.* **34**, 20 (2003) [*Fiz. Elem. Chast. Atom. Yadra* **34**, 43 (2003)].
- [13] D . J. Broadhurst, A. L. Kataev and C. J. Maxwell, preprint IPPP-04-11, hep-ph/0403037 (to appear in *Phys.Lett.* **B** (2004)).
- [14] A. Szczurek and V. Uleshchenko, *Phys. Lett.* **B 475**, 120 (2000).
- [15] M. Gluck, E. Reya and A. Vogt, *Z. Phys.* **C 67**, 433 (1995).
- [16] A. D. Martin, R. G. Roberts, W. J. Stirling and R. S. Thorne, *Eur. Phys. J.* **C 4**, 463 (1998).
- [17] H. L. Lai *et al.* [CTEQ Collaboration], *Eur. Phys. J.* **C 12**, 375 (2000).
- [18] S. I. Alekhin, S. A. Kulagin and S. Liuti, hep-ph/0304210.
- [19] S. Alekhin, *Phys.Rev.* **D 68** , 014002 (2003).
- [20] M. Beneke, *Phys. Rept.* **317**, 1 (1999).
- [21] D. J. Broadhurst and A. L. Kataev, *Phys.Lett.* **B 315**, 179 (1993).
- [22] D. J. Broadhurst and A. L. Kataev, *Phys. Lett.* **B 544**, 154 (2002).
- [23] S. Stein *et al.*, *Phys. Rev.* **D 12**, 1884 (1975).
- [24] J. J. Aubert *et al.* [EMC Collab.], *Nucl. Phys.* **B 293**, 740 (1987).
- [25] A. C. Benvenuti *et al.* [BCDMS Coll.], *Phys. Lett.* **B 237**, 599 (1990).
- [26] R. S. Towell *et al.* [FNAL E866/NuSea Collaboration], *Phys.Rev.* **D 64**, 052002 (2001).
- [27] A. Djouadi and S. Ferrag, CERN-TH/2003-214, hep-ph/0310209.
- [28] M. L. Mangano *et al.*, CERN-TH-2001-131, hep-ph/0105155.

SMALL-X BEHAVIOUR OF THE NONSINGLET AND SINGLET STRUCTURE FUNCTIONS g_1

Mario Greco^a

Universita' di Roma III, Via della Vasca Navale, 84 P, Rome, 00146 Italy

The explicit expressions for the singlet and non-singlet structure functions g_1 are discussed, including the total re-summation of the double logarithmic contributions and accounting for the running of the QCD coupling. We predict that asymptotically $g_1 \propto x^{-\Delta}$, with the intercepts Δ_S and $\Delta_N S$ found in agreement with experimental data.

The results presented at the conference are based on the following papers:

- [1] B.I.Ermolaev, M.Greco, S.I.Troyan, Phys.Lett.B579 (2004) 330.
- [2] B.I.Ermolaev, M. Greco, S.I.Troyan, Phys.Lett.B522 (2001) 57.
- [3] B.I.Ermolaev, M. Greco, S.I.Troyan, Nucl.Phys.B594 (2001) 71.
- [4] B.I.Ermolaev, M.Greco, S.I.Troyan, Nucl.Phys.B571 (2000) 137.

^ae-mail: greco@fis.uniroma3.it

STATIC POTENTIALS IN QCD: WHAT INFORMATION WE CAN GET

V.I.Shevchenko ^a

ITEP, B.Cheremushkinskaya, 25 Moscow 117218 Russia

Abstract. Recent accurate lattice measurements of static potentials between sources in various representations of the gauge group $SU(3)$ by G.Bali, S.Deldar and others provide a crucial test of different approaches to confinement. The Casimir scaling of the potential observed for all measured distances implies strong cancellations of higher cumulant contributions. We discuss the constraints following from these data on QCD vacuum models. We have proved, in particular, that Casimir scaling violating terms in cluster expansion correspond to exchanges by colorless glueball-like states. The contribution is based on the papers [2–5] the reader is referred to for bibliography and all technical details.

1 Introduction

Quantum Chromodynamics (QCD) is the **SU(3)** Yang-Mills theory with quarks described by the Lagrangian (up to gauge-fixing terms):

$$L = -\frac{1}{4} F_{\mu\nu}^a F_a^{\mu\nu} + \sum_q \bar{\psi}_q^i \left(i\gamma^\mu [D_\mu]_{ij} - m_q \right) \psi_j^q$$

$$F_{\mu\nu}^a = \partial_\mu A_\nu^a - \partial_\nu A_\mu^a - gf^{abc} A_\mu^b A_\nu^c$$

$$[D_\mu]_{ij} = \delta_{ij} \partial_\mu + ig [t^a]_{ij} A_\mu^a$$

Neither quarks nor gluons have been observed as isolated particles and we have strong reasons to believe that QCD is the **confining** theory.

Sometimes people speak about mass gap or dimensional transmutation phenomena. It is commonly assumed that **confinement** of color in QCD and **mass gap** property of pure gluodynamics (Yang-Mills theory without quarks) are deeply related.

Unfortunately, right now we have no operational way to formulate QCD and to perform computations beyond perturbation theory in continuum space. However, the theory can be formulated *operationally* and *nonperturbatively* on the space-time Euclidean lattice.

In lattice formulation fundamental objects are link variables U_{link}

$$U_\nu(x) = P \exp ig \int_x^{x+a\hat{\nu}} A_\mu(z) dz^\mu \in SU(N),$$

phase factors along contours C_{xy}

$$U(x; y) = \prod_{C_{xy}} U_{link} = P \exp ig \int_x^y A_\mu(z) dz^\mu,$$

^ae-mail: shevchenko@itep.ru

and Wilson loops for closed contours C

$$W_D(C) = \text{Tr}_D P \exp ig \int_C A_\mu(z) dz^\mu$$

Physically $W_D(C)$ corresponds to the propagation of a particle charged by representation D along trajectory C . Of main interest are fundamental charges (quarks) and adjoint charges (gluons).

If the sources are static, the contour $C = R \times T$ is planar and one can define **static potential** as

$$V_D(R) = - \lim_{T \rightarrow \infty} \frac{1}{T} \log \langle W_D(C) \rangle$$

This definition is up to a (perhaps, UV-diverging) constant. This constant is irrelevant if the force $dV_D(R)/dR$ is considered.

Confinement in gluodynamics corresponds to **area law** for the Wilson loop:

$$\langle W(C) \rangle \propto \exp(-\sigma S[C]) \Rightarrow V(R) = \sigma R + \dots$$

where the dots denote terms subleading at large R . Fundamental charge and anticharge attract each other with the force $\sigma \approx 14$ tons. This force (the string tension) $\sigma \approx (430 \text{ MeV})^2$ can be determined independently from the meson Regge trajectories, heavy quarkonia spectroscopy and lattice numerical simulations.

Most of phenomenological models of confinement are designed to reproduce area law for the fundamental Wilson loop. However to match correctly the lattice data on $V_D(R)$ in higher representations is much more tricky problem.

2 Static potentials for higher representations

Let us begin with some mathematical preliminaries. Representation of dimension D of $SU(N)$ is characterized by $N^2 - 1$ hermitian generators T^a which satisfy commutation relations $[T^a T^b] = i f^{abc} T^c$. Trace is normalized as $\text{Tr}_D \mathbf{1}_D = 1$.

Eigenvalue of quadratic Casimir operator $\mathcal{C}_D^{(2)}$ is defined as

$$\mathcal{C}_D^{(2)} = \delta_{ab} T^a T^b = T^a T^a = C_D \cdot \mathbf{1}_D$$

For $SU(N)$ group:

$$C_{fund} = \frac{N^2 - 1}{2N} ; \quad C_{adj} = N ; \quad d_D \stackrel{\text{def}}{=} C_D / C_{fund}$$

For $SU(3)$ irreducible representation of dimension $D = (1 + \mu)(1 + \nu)(1 + \frac{1}{2}(\mu + \nu))$ labelled by Dynkin coordinates (μ, ν) there are two primitive Casimirs given by:

$$C_D(\mu, \nu) = \frac{1}{3}(\mu^2 + \mu\nu + \nu^2 + 3\mu + 3\nu)$$

$$C_D^{(3)}(\mu, \nu) = \frac{1}{6}(\mu - \nu)(2\mu + \nu + 3)(\mu + 2\nu + 3)$$

The Wilson loop $\langle W_D(C) \rangle$ in representation D defines $V_D(R)$ and σ_D . We now come to the central question: how does $V_D(R)$ depend on (μ, ν) ?

Let us make the following important remark. At asymptotically large distances zero N -ality charges are to be screened in gluodynamics (and in full QCD all charges are eventually screened) because of string breaking:

$$\sigma_D \xrightarrow{R \rightarrow \infty} \begin{cases} 0, & \exp\left(\frac{2\pi i}{3}(\mu - \nu)\right) = 1 \\ \sigma_{fund}, & \exp\left(\frac{2\pi i}{3}(\mu - \nu)\right) \neq 1 \end{cases}$$

For example, the adjoint potential at strong coupling looks like

$$V_a(R) = \sigma_a R \cdot \theta(R_c - R) + \sigma_a R_c \cdot \theta(R - R_c)$$

so the screening happens at some critical distance R_c . Numerical estimates show, however, that gluelumps are rather heavy in units of string tensions so that $R_c \approx 1.1 - 1.3$ Fm.

Actual lattice simulations confirm the existence of linear potential window where it obeys **Casimir scaling** law [6] with an accuracy of 1-5%. One can write general parametrization of the potential

$$V_D(R) = d_D V^{(2)}(R) + d_D^2 V^{(4)}(R) + \dots$$

in terms of which the **Casimir scaling (CS)** hypothesis is easy to formulate: only linear in C_D term $V^{(2)}(R)$ is dominant.

Casimir scaling is exact and trivial in $d = 2$ Yang-Mills theory. It is also correct in $d = 4$ Yang-Mills perturbation theory at tree level (trivial) and up to two loops (less trivial) [7]. It is valid in strong coupling expansion up to the order $1/g^6$. The most important observation is the approximate CS for *confining* part of the potential measured on the lattice (see [8,9] and subsequent papers, for the full bibliography see review [4]).

A few comments about large N behavior are in order:

- String breaking is large N suppressed effect \Rightarrow CS window expands up to infinity
- $\lim_{N \rightarrow \infty} C_{adj}/C_{fund} = 2 \Rightarrow$ CS coincides with the flux counting.

- Large area and large N limits are not interchangeable

The data allows to put concrete limits on parameters of different phenomenological models of QCD vacuum [1–3]

- MIT bag model: $V_D(R) \propto \sqrt{d_D}$ at large R - $\sim 100\%$ deviation from CS
- (dilute) instanton gas model: 15-25% deviation from CS. Perhaps different pattern in dense ensemble
- (fat) center vortex model: 5-50% deviation from CS, but correct asymptotic at $R \rightarrow \infty$
- bosonic string: $\sigma R \rightarrow \sigma R - \pi/12R$ big errors at small R , low signal at large R , so it is difficult to discriminate
- interesting problem of k -strings for $SU(N)$ with $N > 3$, MQCD conjecture $\sigma_k \propto \sin(k\pi/N)$ versus CS prediction $\sigma_k \propto k(N-k)$. Notice that in both cases $\sigma_2 < 2\sigma_1$ - genuine Type I superconductor.
- finite temperature - CS is not to be spoiled for spatial loops at $T > 0$ and even at $T > T_c$. It is not clear at the moment is there D -dependence of the deconfinement temperature T_c
- Georgi-Glashow model: $SU(2)$ Yang-Mills + adjoint Higgs – no CS (only massless A_μ^3 couples to large Wilson loop). Common problem for “abelian-dominated” pictures of Yang-Mills theory. One needs eventually $SU(3)$, not $U(1)$ confinement.

It is useful to see how the CS property looks like in the language of gauge-invariant field correlators (see review [10] and references therein). The potential can be expressed in terms of correlators on the surface making use of nonabelian Stokes theorem and cluster expansion:

$$\begin{aligned} \langle W_D(C) \rangle &= \left\langle \text{Tr}_D \text{P exp } ig \int_C A_\mu(z) dz^\mu \right\rangle = \\ &= \left\langle \text{Tr}_D \mathcal{P} \exp ig \int_S G_{\mu\nu}(z, x_0) d\sigma^{\mu\nu}(z) \right\rangle = \\ &= \exp \sum_{m=2}^{\infty} i^m \Delta_D^{(m)}[S] \end{aligned}$$

where $G_{\mu\nu}(z, x_0) = U(x_0, z)F_{\mu\nu}(z)U(z, x_0)$ and the lowest (Gaussian) term $\Delta_D^{(2)}[S]$ is given by

$$\Delta_D^{(2)}[S] = \frac{1}{2} \int_S d\sigma(1) \int_S d\sigma(2) \langle \text{Tr}_D G(1)G(2) \rangle$$

According to the **Gaussian (stochastic) dominance** [11] picture on the *minimal surface* $S = S_{min}$ the Wilson loop average is saturated by $\Delta_D^{(2)}[S]$. It is easy to see that Gaussian dominance provides exact **CS** (but not vice versa, generally speaking).

Naively one could think of CS as of some exact symmetry in the whole region $R < R_c$. This cannot be a correct picture, however. Deviations from CS are to start from 4-point irreducible colorless exchanges [5]. For example

$$\begin{aligned} \delta_{a/f}^{(4)} &= \Delta_{adj}^{(4)}[S] - \frac{C_{adj}}{C_{fund}} \Delta_{fund}^{(4)}[S] = \\ &= \left(\frac{N^2}{N^2 - 1} \right) \cdot \left(\int_S d\sigma \langle \text{Tr} G(1)G(2) \cdot \text{Tr} G(3)G(4) \rangle \right. \\ &\quad \left. - \left(1 + \frac{2}{N^2 - 1} \right) \left[\int_S d\sigma \langle \text{Tr} G(1)G(2) \rangle \right]^2 \right) \end{aligned}$$

On the other hand, even the lightest glueball is rather heavy, $m_0 \approx 1.5$ GeV. Parametrically one has

$$\frac{\delta_{a/f}^{(4)}}{\Delta^{(2)}[S]} \propto \frac{\langle \alpha_s F_{\mu\nu}^a F_{\mu\nu}^a \rangle}{N^2} \cdot \left(\frac{r_0}{m_0} \right)^2$$

where r_0 is typical glueball radius and m_0 is the mass. Phenomenological values vary as

$$\langle \alpha_s F_{\mu\nu}^a F_{\mu\nu}^a \rangle = (0.04 \div 0.08) \text{ GeV}^4$$

The strong suppression of CS violating terms is evident.

The phenomenon of **CS** supports Gaussian dominance. Let us consider *connected probe*, assuming Gaussian dominance

$$\begin{aligned} \mathcal{F}_{\mu\nu}(x, x_0) &= \frac{\langle \text{Tr} iG_{\mu\nu}(x, x_0)U_{C=\partial S}(x_0, x_0) \rangle}{\langle \text{Tr} U_{C=\partial S}(x_0, x_0) \rangle} \approx \\ &\approx \int_S d\sigma_{\rho\sigma}(u) \langle \text{Tr} G_{\mu\nu}(x, x_0)G_{\rho\sigma}(u, x_0) \rangle \end{aligned}$$

so that the **CS** potential is given by

$$V(R) = \frac{1}{2} \int_S d\sigma_{\mu\nu}(x) \mathcal{F}_{\mu\nu}(x)$$

but generally $x \notin S$. In the static case $\mathcal{F}_{ij} = \epsilon_{ijk}\mathbf{B}_k$ vanishes and effective "abelian" currents are determined via "Maxwell equations" for "electric field" $\mathbf{E}_i = \mathcal{F}_{0i}$ [12]

$$\text{div } \mathbf{E} = \rho \quad ; \quad \text{rot } \mathbf{E} = \mathbf{k}$$

The typical field profiles resemble the celebrated proposal by 't Hooft and Mandelstam that QCD vacuum is **dual superconductor** (and *perfect dielectric*).

Finally, let us make a remark concerning the nonperturbative potential *at small distances*. It is interesting to check - what is the first (after Coulomb) subleading term there?

One has

$$V_D(R) = \frac{c_{-1}}{R} + c_0 + c_1 R + c_2 R^2 + \mathcal{O}(R^3)$$

Conventional OPE gives $-c_{-1} = \tilde{\alpha}_s = C_D(g^2/4\pi)$, $c_2 \propto \tilde{\alpha}_s \langle F_{\mu\nu}^a F_{\mu\nu}^a \rangle T_g$ and nonperturbative physics is soft in the sense that $c_1 = 0$. Recent lattice data indicate that possibly $c_1 \neq 0$ [13]. One can develop a phenomenological model with $\mathcal{E} = \mathcal{E}_p + \mathcal{E}_{np}$ based on the idea of *critical perturbative field* [14, 15] which defines critical distance for the color dipole

$$L_c = \left(\frac{\tilde{\alpha}_s R^2}{4\pi\kappa\epsilon} \right)^{1/6} \quad ; \quad \epsilon = \frac{\beta(\alpha_s)}{16\alpha_s} \langle F_{\mu\nu}^a F_{\mu\nu}^a \rangle$$

and the energy gain

$$\delta V_D(R) = \frac{4}{3} \sqrt{\pi \tilde{\alpha}_s \kappa \epsilon} \cdot R \propto \sqrt{C_D} \cdot R$$

The observation of such square root law on the lattice would be a clear indication of not yet observed perturbative-nonperturbative interference.

Acknowledgments

The author is thankful to FOM and Dutch National Scientific Fund (NOW) for financial support.

References

- [1] Yu.A.Simonov, *JETP Lett.* 71, 127 (2000)
- [2] V.I.Shevchenko, Yu.A.Simonov, arXiv: hep-ph/0104135
- [3] V.I. Shevchenko, Yu.A. Simonov, *Phys.Rev.Lett.* 85, 1811 (2000)
- [4] V.I.Shevchenko, Yu.A.Simonov, *Int.J.Mod.Phys. A* 18, 127 (2003).
- [5] V.I.Shevchenko, *Phys.Lett. B* 550, 85 (2002)
- [6] J.Ambjørn, P.Olesen, C.Peterson, *Nucl. Phys. B* 240, 189 (1984)

- [7] M.Peter, Phys. Rev. Lett. 78, 602 (1997), Nucl. Phys. **B** 501, 471 (1997); Y.Schröder, Phys. Lett. **B** 447, 321 (1999)
- [8] G.Bali *Nucl.Phys.Proc.Suppl.* 83, 422 (2000)
- [9] S.Deldar, *Phys.Rev.* **D** 62, 034509 (2000)
- [10] A. Di Giacomo, H.G.Dosch, V.I.Shevchenko, Yu.A.Simonov, *Phys.Rep.* 372, 319 (2002)
- [11] H.G.Dosch, *Phys.Lett.* **B** 190, 177 (1987); H.G.Dosch, Yu.A.Simonov, *Phys.Lett.* **B** 205, 339 (1988); Yu.A.Simonov, *Nucl.Phys.* **B** 307, 512 (1988)
- [12] D.S.Kuzmenko, V.I.Shevchenko, Yu.A.Simonov, *Physics-Uspekhi* 47, 5 (2004)
- [13] G.Bali, *Phys.Lett.* **B** 460, 170 (1999)
- [14] R.Akhouri, V.Zakharov, *Phys.Lett.* **B** 438, 165 (1998)
- [15] V.I.Shevchenko, arXiv: hep-ph/0301280

LIGHT AND HEAVY BARYONS IN THE NONPERTURBATIVE QCD

I.M.Narodetskii^a, M.A.Trusov^b

*Institute of Theoretical and Experimental Physics,
Russia, 117218, Moscow, Bolshaya Cheremushkinskaya str., 25*

Abstract. We review the results obtained in an Effective Hamiltonian (EH) approach for the three-quark systems. This approach furnishes the QCD consistent framework within which to study baryons. After outlining the essence of the method simple applications for the ground state baryons are explained in details. With only two parameters: the string tension $\sigma = 0.15 \text{ GeV}^2$ and the strong coupling constant $\alpha_s = 0.39$ a unified quantitative description of the ground state light and heavy baryons is achieved. The prediction of masses of the doubly heavy baryons not discovered yet are also given. In particular, a mass of 3660 MeV for the lightest Ξ_{cc} baryon is found by employing the hyperspherical formalism to the three quark confining potential with the string junction.

1 Introduction

The exploration of known and novel baryon states has important consequences for our understanding of the nature of low-energy QCD. For a long time baryons were objects of an intensive theoretical study. Both the two-body one-gluon exchange potentials and the three-quark Y-shaped confinement interaction were considered almost 30 years ago. In particular, the outstanding papers by Isgur and collaborators (see [1] and references therein) have enlightened the general structure of the baryon spectrum in good general agreement with experiment. In [1] quark dynamics was considered as a QCD motivated one and the importance of the kinematical relativistic effects has been clearly demonstrated constituent model have been derived from QCD. Therefore it is tempting to consider the Effective Hamiltonian (EH) approach in QCD (see e.g. [2]) which from one side can be derived from QCD and from another side leads to the results for the $\bar{q}q$ mesons and $3q$ baryons which are equivalent to the quark model ones with some important modifications. The EH approach contains the minimal number of input parameters: current (or pole) quark masses, the string tension σ and the strong coupling constant α_s , and does not contain fitting parameters as e.g. the total subtraction constant in the Hamiltonian. The application of EH to the meson sector [3] demonstrates that gross features of meson spectra can be calculated using the only two parameters inherent to QCD: the string tension σ and the strong coupling constant α_s . It should be useful and attractive to consider expanding of EH approach for baryons. This work focuses on the description of ground state baryons in this approach.

^ae-mail: naro@heron.itep.ru

^be-mail: trusov@heron.itep.ru

2 EH method. A brief outline

In the EH approach the effective degrees of freedom are constituent quarks, treated symmetrically, although the quark-diquark dynamics can be considered on the same footing. The initial formulation is non relativistic and is based on the auxiliary field formalism [4]. For the three constituents EH has the form

$$H = \sum_{i=1}^3 \left(\frac{m_i^2}{2\mu_i} + \frac{\mu_i}{2} \right) + H_0 + V, \quad (1)$$

where H_0 is the kinetic energy operator, V is the sum of the perturbative one-gluon exchange potentials

$$V_C(\mathbf{r}_1, \mathbf{r}_2, \mathbf{r}_3) = -\frac{2}{3}\alpha_s \cdot \sum_{i < j} \frac{1}{r_{ij}}, \quad (2)$$

and the string potential $V_{\text{string}} = \sigma l_{\min}$. The latter is proportional to a minimum length l_{\min} of the strings meeting in a Y-shaped configuration at a string junction point. The dynamical masses μ_i (analogues of the constituent ones) are expressed in terms of the current quark masses m_i from the condition of the minimum of the hadron mass $M_H^{(0)}$ as function of μ_i . Technically, this is done using the auxiliary field approach to get rid of the square root term in the Lagrangian [4]. Applied to the QCD Lagrangian, the auxiliary field technique yields the EH for hadrons (mesons, baryons, tetra- and pentaquarks, etc) depending on auxiliary fields μ_i . In practice, these fields are treated as c -numbers determined from the minimum condition:

$$\frac{\partial M_H^{(0)}(m_i, \mu_i)}{\partial \mu_i} = 0, \quad M_H^{(0)} = \sum_{i=1}^3 \left(\frac{m_i^2}{2\mu_i} + \frac{\mu_i}{2} \right) + E_0(\mu_i), \quad (3)$$

$E_0(\mu_i)$ being eigenvalue of the operator $H_0 + V$. Quarks acquire constituent masses $\mu_i \sim \sqrt{\sigma}$ due to the string interaction in (1). The EH in the form of (1) does not include any chiral symmetry breaking (CSB) effects. A possible interplay between the confinement and CSB effects should be clarified in the future.

The physical mass M_H of a hadron H is

$$M_H = M_H^{(0)} + \sum_i C_i, \quad (4)$$

where the constants C_i have the meaning of the constituent self energies which are due to constituent spin interaction with the vacuum background fields. The constants C_i play the same role as the subtraction constants in the standard phenomenological constituent quark model. In the EH method they are not the

fitting parameters but can be evaluated analytically in terms of string tension σ [5]:

$$C_i = -\frac{2\sigma}{\pi\mu_i}\eta_i, \quad (5)$$

where $\eta_q = 1$ ($q = u, d$), $\eta_s = 0.88$, $\eta_c = 0.234$, and $\eta_b = 0.052$ are the correction factors due to non-vanishing current mass of the strange, charm and bottom quarks.

Considering the Coulomb-like terms as a perturbation the eigenvalues of the EH can be found as expansions in powers of α_s . These expansions are especially simple for the nucleon containing three light quarks with the running mass equal to zero. In this case the task is greatly simplified and one can obtain analytic expressions for μ and M_N as a series in α_s . Omitting the intermediate details we quote here the result with accuracy up to α_s^2 :

$$\mu = 0.959 \cdot \sqrt{\sigma} \cdot (1 + 0.270\alpha_s + 0.117\alpha_s^2 + \dots), \quad (6)$$

$$M_N = 5.751 \cdot \sqrt{\sigma} \cdot (1 - 0.270\alpha_s - 0.039\alpha_s^2 + \dots) + 3C_q, \quad (7)$$

or

$$M_N = 6m \cdot (1 - 0.540\alpha_s - 0.083\alpha_s^2 + \dots) + 3C_q, . \quad (8)$$

As it follows from Eq. (8), the Coulomb-like correction to M_B comprises approximately 20%.

3 Hyperspherical approach

In general case the dynamical problem is solved by expanding the wave function in a hyperspherical basis. The wave function $\psi(\rho, \lambda)$ expressed in terms of the Jacobi coordinates ρ and λ can be written in a symbolical shorthand as

$$\psi(\rho, \lambda) = \sum_K \psi_{[K]}(R) Y_{[K]}(\Omega). \quad (9)$$

where $Y_{[K]}$ are eigen functions (the hyperspherical harmonics) of the angular momentum operator $\hat{K}(\Omega)$ on the 6-dimensional sphere: $\hat{K}^2(\Omega)Y_{[K]} = -K(K+4)Y_{[K]}$, with K being the grand orbital momentum. The Schrödinger equation written in terms of the variable $x = \sqrt{\mu}R$, where μ is an arbitrary scale of mass dimension which drops off in the final expressions, reads:

$$\begin{aligned} \frac{d^2\chi_K(x)}{dx^2} &+ 2 \left[E_0 - \frac{(K + \frac{3}{2})(K + \frac{5}{2})}{2x^2} \right] \chi_K(x) + \frac{1}{x} \sum_{K'} a_{KK'} \chi_{K'}(x) - \\ &- x \sum_{K'} b_{KK'} \chi_{K'}(x) = 0, \end{aligned} \quad (10)$$

with the boundary condition $\chi_K(x) \sim \mathcal{O}(x^{5/2+K})$ as $x \rightarrow 0$ and the asymptotic behavior $\chi_K(x) \sim \text{Ai}((2b_K)^{1/3}x)$ as $x \rightarrow \infty$. In Eq. (10)

$$a_{KK'} = R\sqrt{\mu} \cdot \int u_{[K]} \cdot V_{\text{Coulomb}}(\mathbf{r}_1, \mathbf{r}_2, \mathbf{r}_3) \cdot u_{[K']} \cdot d\Omega, \quad (11)$$

$$b_{KK'} = \frac{1}{R\sqrt{\mu}} \cdot \int u_{[K]} \cdot V_{\text{string}}(\mathbf{r}_1, \mathbf{r}_2, \mathbf{r}_3) \cdot u_{[K']} \cdot d\Omega, \quad (12)$$

Explicit expression of $V_{\text{string}}(\mathbf{r}_1, \mathbf{r}_2, \mathbf{r}_3)$ in terms of Jacobi variables is given in [6].

4 Ground state baryons

We use the values of $\sigma = 0.15 \text{ GeV}^2$, $\alpha_s = 0.39$, $m_q^{(0)} = 0.009 \text{ GeV}$, $m_s^{(0)} = 0.17 \text{ GeV}$, $m_c^{(0)} = 1.4 \text{ GeV}$, and $m_b^{(0)} = 4.8 \text{ GeV}$. Accuracy of the predictions of the EH method is illustrated in Table 1 in which the spin-averaged eigenvalues has been calculated from the solution of the system (10) with $K_{max} = 8$. The comparison with the results obtained using the simplest hypercentral truncation of Eqs. (10) [6] allows to quantify (rather small) systematic errors associated with this truncation, and underpins a two-parameter description of an extensive body of baryon masses.

While studying Table 1 is sufficient to have an appreciation of the accuracy of our predictions, few comments should be added. We expect an accuracy of the baryon predictions to be $\sim 5 - 10\%$ that is partly due to the auxiliary field approximation employed in the derivations of the Effective Hamiltonian itself. From this point of view the overall agreement with data is quite satisfactory. E.g. we get $\frac{1}{2}(N + \Delta)_{\text{theory}} = 1144 \text{ MeV}$ vs. $\frac{1}{2}(N + \Delta)_{\text{exp}} = 1085 \text{ MeV}$ (a 5% increase in α_s would correctly give the (N, Δ) center of gravity), $\frac{1}{4}(\Lambda + \Sigma + 2\Sigma^*) = 1242 \text{ MeV}$ vs. experimental value of 1267 MeV. We also find $\Xi_{\text{theory}} = 1336 \text{ MeV}$ (without hyperfine splitting) vs. $\Xi_{\text{exp}} = 1315 \text{ MeV}$ and $\Xi_{\text{theory}}^c = 2542 \text{ MeV}$ vs. $\Xi_{\text{exp}}^c = 2584 \text{ MeV}$. On the other hand, our study shows some difficulties in reproducing the Ω -hyperon mass.

5 Doubly heavy baryons

Doubly heavy baryons are baryons that contain two heavy quarks, either cc , bc , or bb . Their existence is a natural consequence of the quark model of hadrons, and it would be surprising if they did not exist. In particular, data from the BaBar and Belle collaborations at the SLAC and KEK B-factories would be good places to look for doubly charmed baryons. Recently the SELEX, the charm hadroproduction experiment at Fermilab, reported a narrow state at $3519 \pm 1 \text{ MeV}$ decaying in $\Lambda_c^+ K^- \pi^+$, consistent with the weak decay of the doubly charmed baryon Ξ_{cc}^+ [11]. The candidate is 6.3σ signal.

Table 1: For various $3q$ systems in column (1) we display the dynamical quark masses given by Eq. (3), the ground state eigenvalue E_0 in Eq. (10), the baryon masses including the self energy correction Eq. (4) (all in units of GeV).

baryon	m_1	m_2	m_3	E_0	M_B
qqq	0.362	0.362	0.362	1.387	1.139
qqs	0.365	0.365	0.409	1.359	1.235
qss	0.369	0.412	0.412	1.330	1.330
sss	0.415	0.415	0.415	1.302	1.422
qqc	0.400	0.400	1.475	1.138	2.448
qsc	0.402	0.445	1.476	1.112	2.529
ssc	0.447	0.447	1.478	1.085	2.608
qqb	0.420	0.420	4.828	1.044	5.809
qsb	0.421	0.465	4.828	1.017	5.883
ssb	0.466	0.466	4.829	0.990	5.956
qcc	0.420	1.501	1.501	0.877	3.637
scc	0.464	1.502	1.502	0.851	3.710
qcb	0.434	1.523	4.842	0.754	6.941
scb	0.479	1.523	4.842	0.727	7.011
qbb	0.444	4.860	4.860	0.576	10.182
sbb	0.487	4.860	4.860	0.548	10.247

The SELEX result was recently critically discussed in [12]. Whether or not the state that SELEX reports turns out to be the first observation of doubly charmed baryons, studying their properties is important for a full understanding of the strong interaction between quarks.

In Table 2 we compare the spin-averaged masses (computed without the spin-spin term) of the lowest double heavy baryons to the predictions of other models [7], [8], [9] as well as variational calculations of Ref. [10] for which the center of gravity of non-strange baryons and hyperons is essential a free parameter. Most of recent predictions were obtained in a light quark-heavy diquark model [7], [8], in which case the spin-averaged values are $M = \frac{1}{3}(M_{1/2} + 2M_{3/2})$. In general, in spite of the completely different physical picture, we find a reasonable agreement within 100 MeV between different predictions for the ground state masses of the doubly heavy baryons. Our prediction for M_{ccu} is 3.66 GeV with the perturbative hyperfine splitting $\Xi_{ccu}^* - \Xi_{ccu} \sim 40$ MeV. Note that the mass of Ξ_{cc}^+ is rather sensitive to the value of the running c -quark mass $m_c^{(0)}$.

Table 2: Comparison of various predictions for ground-state masses (in units of GeV) of doubly heavy baryons.

Baryon	Ref. [6]	Ref. [10]	Ref. [7]	Ref. [8]	Ref. [9]
Ξ_{cc}	3.66	3.69	3.57	3.69	3.70
Ω_{cc}	3.73	3.86	3.66	3.84	3.80
Ξ_{cb}	6.97	6.96	6.87	6.96	6.99
Ω_{cb}	7.03	7.13	6.96	7.15	7.07
Ξ_{bb}	10.21	10.16	10.12	10.23	10.24
Ω_{bb}	10.27	10.34	10.19	10.38	10.34

6 Conclusions

We have shown that baryon spectroscopy can be unified in a single framework of the Effective Hamiltonian which is consisted with QCD. This picture uses the stringlike picture of confinement and perturbative one-gluon exchange potential. The main advantage of this work is demonstration of the fact that it is possible to describe all the baryons in terms of the only two parameters inherent to QCD, namely σ and α_s .

Acknowledgments

This work was supported by RFBR grant # 03-02-17345 and the grant for leading scientific schools # 1774.2003.2.

References

- [1] S. Capstick and N. Isgur, *Phys. Rev. D* **34**, 2809 (1986).
- [2] For a review see Yu.A.Simonov, in *Proceedings of the XVII Autumn School Lisboa, Portugal, 24 September - 4 October 1999*, edited by L. Ferreira, P.Nogueira, and J. I. Silva-Marco, World Scientific, Singapore, 2000, 60.
- [3] A.M.Badalian, B.L.G.Bakker and V.L.Morgunov, *Phys. At. Nucl.* **63**, 1635 (2000).
- [4] A. M. Polyakov, *Gauge Fields and Strings*, Harwood Academic Publishers, 1987; L. Brink, P. Di Vecchia, and P. Howe, *Nucl. Phys* **B118**, 76 (1977).
- [5] Yu.A.Simonov, *Phys. Lett.* **B515**, 137 (2001).
- [6] I.M.Narodetskii, A.N.Plekhanov, A.I.Veselov, *JETP Lett.* **77** (2003) 58.
- [7] S. S. Gershtein *et al.*, *Phys. Rev. D* **62**, 050421 (2000).
- [8] D. Ebert *et al.*, *Phys. Rev. D* **66**, 014008 (2002).
- [9] E. Bagag *et al.*, *Z. Phys. C* **64**, 57 (1994).

- [10] I. M. Narodetskii and M. A. Trusov, *Phys. Atom. Nucl.* **65**, 917 (2002) [hep-ph/0104019].
- [11] M. Mattson *et al.*, *Phys. Rev. Lett.* **89**, 112001 (2002).
- [12] V. V. Kiselev and A. K. Likhoded, hep-ph/0208231.

EVALUATION OF THE HIGHER TWIST CONTRIBUTION TO THE MOMENTS OF PROTON STRUCTURE FUNCTIONS F_2 AND g_1

M.Osipenko^{1,2, a}, S.Simula^{3, b}, G.Ricco^{1,4}, G.Fedotov², E.Golovach², B.Ishkhanov²,
E.Isupov², V.Mokeev^{5,2}

¹ *Istituto Nazionale di Fisica Nucleare, Sezione di Genova, 16146 Genova, Italy*

² *Skobeltsyn Institute of Nuclear Physics, 119992 Moscow, Russia*

³ *Istituto Nazionale di Fisica Nucleare, Sezione Roma III, 00146 Roma, Italy*

⁴ *Dipartimento di Fisica dell'Università, 16146 Genova, Italy*

⁵ *Thomas Jefferson National Accelerator Facility, Newport News, Virginia 23606*

Abstract. We performed the measurement of the inclusive electron scattering off the proton [1, 2] in the resonance region ($W < 2.5$ GeV) at momentum transfer Q^2 below 4.5 (GeV/c)² with the CLAS detector. The large acceptance of CLAS provided an access to a large, continuous two-dimensional kinematic domain in Q^2 and x , allowing therefore an integration of the data at fixed Q^2 over x -interval. The covered x -interval at each measured Q^2 value is sufficient for an evaluation of the higher moments ($n > 2$). From these data we extracted the structure function F_2 and, by including other world data, we studied the Q^2 evolution of its moments, $M_n(Q^2)$, in order to estimate the higher twist contributions. A similar experiment with polarized proton target is completed at CLAS [3]. These new data allow an accurate determination of higher moments of the proton structure function g_1 . A preliminary phenomenological analysis [4] indicates an excess of the higher twist contribution in the spin-dependent structure function with respect to the spin-independent one.

1 Introduction

Investigation of the nucleon internal structure with electromagnetic probes provided most striking success of the strong interaction theory, QCD. Measured nucleon structure functions give an access to both parton momentum distributions as well as to the scale dependence of the parton coupling with photon. Here the former quantities, parton momentum distributions within the nucleon, are purely phenomenological observable, not derived from the first principles of QCD. Meanwhile, the scale dependence is completely determined by QCD evolution equations. Therefore, in order to compare directly QCD predictions on the nucleon structure to a measurement one has to study the scale dependence of the structure functions avoiding the problem of describing parton momentum distributions, as it was proposed in Ref. [5, 9]. This can be performed by measuring moments of the structure functions in experiment and studying their scale evolution. In the case of electron-proton scattering it implies a measurement of Q^2 evolution of the moments of proton structure functions F_2 , g_1 , F_1 and g_2 .

^ae-mail: osipenko@ge.infn.it

^be-mail: simula@roma3.infn.it

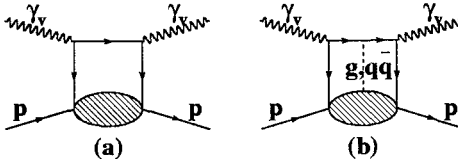


Figure 1: Twist diagrams:(a) the leading twist contribution evaluated at leading order of pQCD; (b) the contribution of higher twists, where current quark and nucleon remnant can exchange by a system of particles consisting of gluons and $q\bar{q}$ -pairs whose complexity is increasing with twist order.

The method of studying moments is based on Operator Product Expansion (OPE) of the virtual photon-nucleon scattering amplitude. This leads to the description of the complete Q^2 evolution of the moments of the nucleon structure functions. For example, n-th Cornwall-Norton non-singlet moment of the (asymptotic) structure function $F_2(x, Q^2)$ for a massless nucleon can be expanded as:

$$M_n^{CN}(Q^2) = \sum_{\tau=2k}^{\infty} E_{n\tau}(\mu, Q^2) O_{n\tau}(\mu) \left(\frac{\mu^2}{Q^2} \right)^{\frac{1}{2}(\tau-2)}, \quad (1)$$

where $k = 1, 2, \dots, \infty$, μ is the factorization scale, $O_{n\tau}(\mu)$ is the reduced matrix element of the local operators with definite spin n and twist τ , related to the non-perturbative nucleon structure. $E_{n\tau}(\mu, Q^2)$ is a dimensionless coefficient function describing the small distance behavior, which can be perturbatively expressed as a power series in the running coupling constant $\alpha_s(Q^2)$.

In order to investigate the double expansion in Eq. 1 we truncated both series: in the running coupling constant $\alpha_s(Q^2)$ up to Next to Leading Order (NLO) and in twists τ , suppressed by a power of $(\mu^2/Q^2)^{\frac{1}{2}(\tau-2)}$, up to $\tau = 6$ term. This choice is limiting the analysis to the kinematic region where these parameters are small. We fixed the value of local operator $O_{n\tau}(\mu)$ matrix element at large Q^2 , where all next-to-leading twist expansion terms were neglected. After that we explored low- Q^2 region to determine the contribution of the higher twist terms.

The higher twists are related to quark-quark and quark-gluon correlations, as illustrated by Fig. 1, and should become important at small Q^2 . In contrast to the asymptotically free quarks, the quarks interacting among themselves during the short time of the photon-proton scattering produce the higher twist terms. The importance of studying the multiparton correlations is due to the fact that they are responsible for the phenomenon of confinement and for the dynamical origin of proton mass.

The recent experiments undertaken in Thomas Jefferson National Accelerator Facility (USA) provide a large amount of data in the energy range not well explored previously. Measurements of inclusive electron scattering off polarized [3] and unpolarized [1, 2] proton targets in Hall B with maximum beam energy of 4.5 GeV allowed a precise extraction of the moments of the proton structure functions F_2 and g_1 in the range of momentum transfer, Q^2 , from 0.1 up to 4.5 (GeV/c)². These and complementary data from Deep Inelastic Scattering (DIS) were analyzed in terms of perturbative QCD (pQCD) evolution equations and OPE to create a complete picture of the proton structure at different scales.

2 Experimental moments of the structure functions

At small Q^2 values the moments contain non-negligible mass-dependent terms that produce in Eq. 1 additional M^2/Q^2 power corrections (kinematic twists), that mix with dynamical twists under the renormalization-group equations. To avoid these terms, the moments $M_n^{CN}(Q^2)$ have to be replaced by the corresponding Nachtmann moments $M_n^N(Q^2)$ which by the construction allow to keep the form of the twist expansion in Eq. 1 (see also Ref. [6]). The Nachtmann moments of the structure function F_2 given by:

$$M_n^N(Q^2) = \int_0^1 dx \frac{\xi^{n+1}}{x^3} F_2(x, Q^2) \left[\frac{3 + 3(n+1)r + n(n+2)r^2}{(n+2)(n+3)} \right], \quad (2)$$

where $r = \sqrt{1 + 4M^2x^2/Q^2}$ and $\xi = 2x/(1+r)$. In the polarized case situation is more involved since Nachtmann moments of the structure function g_1 depend on both g_1 and g_2 :

$$M_n^N(Q^2) = \int_0^1 dx \frac{\xi^{n+1}}{x^2} \left\{ g_1(x, Q^2) \left[\frac{x}{\xi} - \frac{n^2}{(n+2)^2} \frac{M^2 x^2}{Q^2} \frac{\xi}{x} \right] - g_2(x, Q^2) \frac{M^2 x^2}{Q^2} \frac{4n}{n+2} \right\}, \quad (3)$$

Because of lack of experimental data on g_2 , moments of the polarized structure function g_1 contain an intrinsic unavoidable model dependence.

The evaluation of experimental moment M_n involves the computation at fixed Q^2 of an integral over x from the corresponding structure function weighted with n -th power of x . The integral over x was computed numerically. In x intervals where data coverage was not complete we applied essentially model independent interpolation method to avoid as much as possible assumptions on x -shape of corresponding momentum distributions. This was accomplished by normalizing the interpolation function directly to experimental data located at

the edges of interpolating interval, independently for each Q^2 value. Therefore, the obtained Q^2 evolution of the moments is free of any model assumptions on the interpolating parton momentum distributions. The low- x extrapolation has been handled by using two parameterizations and estimating the difference as the systematic error. The error come out very small, thanks to the low- x data from HERA. One can note that the low- x extrapolation is only important for the lowest moment, while in higher moments, which are of the main interest of this analysis, the low- x part is strongly suppressed by a power of x .

The moments were obtained with remarkable statistical and systematic precision of the order of a few percent. In particular, higher moments ($n > 2$) have almost 100% of significant x -interval covered by high precision CLAS data and therefore have tiny error bars. This also allowed to extract the value of QCD running coupling constant $\alpha_s(M_Z^2)$ with good precision [7].

3 OPE analysis

The experimental Nachtmann moments were analyzed in terms of the following twist expansion

$$M_n^N(Q^2) = LT_n(Q^2) + HT_n(Q^2), \quad (4)$$

where $LT_n(Q^2)$ is the leading twist moment and $HT_n(Q^2)$ is the higher-twist contribution given by [8]

$$HT_n(Q^2) = a_n^{(4)} \left[\frac{\alpha_s(Q^2)}{\alpha_s(\mu^2)} \right]^{\gamma_n^{(4)}} \frac{\mu^2}{Q^2} + a_n^{(6)} \left[\frac{\alpha_s(Q^2)}{\alpha_s(\mu^2)} \right]^{\gamma_n^{(6)}} \frac{\mu^4}{Q^4}, \quad (5)$$

here the logarithmic pQCD evolution of the twist- τ contribution is accounted for by the term of LO-wise form with an effective anomalous dimension $\gamma_n^{(\tau)}$ and the matrix element $a_n^{(\tau)}$ ($O_{n\tau}(\mu)$ in Eq. 1) fixes normalization of the twist- τ term at large Q^2 .

The leading twist $LT_n(Q^2)$ term was calculated in pQCD to NLO as the sum of a non-singlet and singlet terms. Using the decoupling feature in the pQCD evolution [9] of the singlet quark and gluon densities at large x we considered a pure non-singlet evolution for $n > 2$. Therefore, for $n > 2$ leading twist contain one unknown parameter, the matrix element $O_{n\tau}(\mu)$. In order to (partly) account for the higher perturbative orders of pQCD we used Soft Gluon Resummation (SGR) technique as in [10]. The resummation of soft gluons does not introduce any further parameter in the description of the leading twist. Leading twist normalization parameter as well as the higher-twist parameters $a_n^{(4)}, \gamma_n^{(4)}, a_n^{(6)}, \gamma_n^{(6)}$, were simultaneously determined in a χ^2 -minimization procedure and reported in Refs. [1, 4].

The obtained results can be summarized as follows: 1) the contribution of the leading twist remains dominant down to Q^2 of the order of a few $(\text{GeV}/c)^2$;

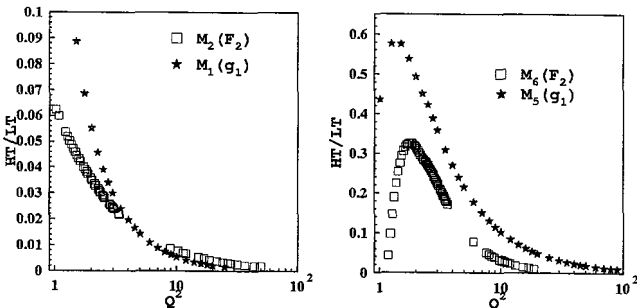


Figure 2: Ratio of the higher to leading twist contributions to the moments ($q(x)$ left panel and $x^4 q(x)$ right panel) of the proton structure functions F_2 and g_1 .

2) different higher twist terms tend to compensate each other in such a way that their sum is small even in a Q^2 region where their absolute contributions exceed the leading twist (for details see Ref. [1]); 3) the contribution of higher twists relative to the leading one is very sensitive to the parton polarization. This can be seen in the comparison of the ratio higher to leading twists for structure functions F_2 and g_1 shown in Fig. 2. The power of x in the moment is the same for both structure functions, but the ratio is different by almost factor of two at low Q^2 . For the higher Q^2 values the lowest moment of both structure functions becomes very similar, this give an idea that the enhancement of the higher twist contribution in g_1 moments is due to presence of $P_{33}(1232)$ resonance. This excited nucleon state gives strongly negative contribution to the total structure function g_1 breaking the quark-hadron duality expectations, but it quickly disappear with rising Q^2 because of the rapid fall-off of the $P_{33}(1232)$ form-factor.

References

- [1] M.Osipenko et al., *Phys.Rev.* **D67**, 092001 (2003).
- [2] M.Osipenko et al., CLAS-NOTE-2003-001.
- [3] R.Fatemi et al., *Phys.Rev.Lett.* **91**, 222002 (2003).
- [4] S.Simula, M.Osipenko, G.Ricco and M.Taiuti, *Phys. Rev.* **D65**, 034017 (2002).
- [5] M.Osipenko et al., in "Frontiers of Particle Physics" (Proceedings of the 10th Lomonosov Conference on Elementary Particle Physics), ed. by A.Studenikin, World Scientific Singapore, 136-141, 2003.
- [6] R.Roberts, "The structure of the proton", (Cambridge U.P.), 1993.
- [7] S.Simula, M.Osipenko, *Nucl.Phys.* **B675** 289 (2003).
- [8] X.Ji and P.Unrau, *Phys. Rev.* **D52**, 72 (1995); U.K.Yang and A.Bodek, *Phys. Rev. Lett.* **82**, 2467 (1999).
- [9] G.Ricco et al., *Nucl. Phys.* **B** 555, 306 (1999).
- [10] S.Simula, *Phys.Lett.* **B** 493, 325 (2000).

THERMAL QCD CONDENSATES IN THE HADRON RESONANCE GAS MODEL

N.O. Agasian^a, S.M. Fedorov^b

*Institute of Theoretical and Experimental Physics,
117218, Moscow, Russia*

Abstract. The nonperturbative QCD vacuum with two light quarks is studied at finite temperature in the framework of hadron resonance gas. Temperature dependence of the quark and gluon condensates in the confined phase is found. It is shown that the quark condensate and one half (chromo-electric component) of gluon condensate evaporate at the same temperature, which corresponds to the temperature of quark-hadron phase transition. Critical temperature is $T_c \simeq 190$ MeV when temperature shift of hadron masses is taken into account.

1. QCD at finite temperature undergoes a phase transition from hadron phase, characterized by confinement and chiral symmetry breaking, to the phase of hot quark-gluon matter. At the critical point T_c where the phase transition occurs the behavior of the thermodynamic properties of the system, such as energy density ε , specific heat, non-ideality $(\varepsilon - 3P)/T^4$, etc., are drastically changed. More than that, the phase transition in QCD is characterized by the radical rearrangement of the non-perturbative quark-gluon vacuum.

Lattice calculations for finite temperature QCD show that the deconfinement and chiral invariance restoration take place at the same temperature, and for the case of two light quarks ($N_f = 2$) critical temperature is in the interval $T_c \sim 175 \div 190$ MeV [1, 2]. From lattice QCD and from experimental data on high energy collisions it also follows that energy density of the system at quark-hadron phase transition is of the order of $\varepsilon_c \sim 1 \div 1.5$ GeV/fm³.

Recently it was demonstrated in the lattice simulations that for gauge $SU(3)$ theory without quarks and for QCD with $N_f = 2$ electric component of gluon condensate is strongly suppressed above critical temperature T_c , while magnetic component even slightly grows with temperature [3]. Also, gluon condensate at finite temperature in $SU(2)$ lattice gauge theory was studied in the earlier paper [4]. It was shown there that approximately one half of the gluon condensate does not vanish above T_c .

These results are in line with theoretical predictions of the deconfining phase transition within the "evaporation model" [5] approach. Within the framework of the effective dilaton Lagrangian at finite temperature the temperature dependence of the gluon condensate and its discontinuity at $T = T_c$ in pure-glue QCD was studied in [6]. Later in the paper [7] temperature dependence of the gauge invariant bilocal correlator of chromo-magnetic fields and spatial string tension $\sigma_s(T)$ were found analytically.

^ae-mail: agasian@heron.itep.ru

^be-mail: fedorov@heron.itep.ru

Taking into account above listed facts, one has to obtain in the framework of single approach that in QCD with $N_f = 2$ at the critical point $T_c \sim 175 \div 190$ MeV energy density reaches value $\varepsilon_c \sim 1 \div 1.5$ GeV/fm 3 , quark condensate $\langle \bar{q}q \rangle_T$ vanishes, and only one half of gluon condensate (chromo-electric component, responsible for the formation of string and confinement) "evaporates", which is required to retain magnetic confinement.

2. We will consider QCD with two light quarks. Then, knowing pressure in the hadronic phase, $P_h(T)$, and making use of Gell-Mann-Oakes-Renner (GOR) relation, one can find the temperature dependence of quark condensate

$$\frac{\langle \bar{q}q \rangle_T}{\langle \bar{q}q \rangle_0} = 1 - \frac{1}{F_\pi^2} \frac{\partial P_h(T)}{\partial m_\pi^2}, \quad (1)$$

where $F_\pi = 93$ MeV is the axial π -meson decay constant. Expression for gluon condensate $\langle G^2 \rangle_T \equiv \langle (gG_{\mu\nu}^a)^2 \rangle_T$ was derived in [8] starting from the renormalization group consideration of anomalous contribution to the energy-momentum tensor in QCD with $N_f = 2$ at finite temperature. Relation connecting gluon condensate with thermodynamical pressure in QCD is given by [8]

$$\langle G^2 \rangle_T = \langle G^2 \rangle_0 + \frac{32\pi^2}{b} \left(4 - T \frac{\partial}{\partial T} - m_\pi^2 \frac{\partial}{\partial m_\pi^2} \right) P_h(T), \quad (2)$$

where $b = 11N_c/3 - 2N_f/3$. QCD low energy theorems [9] and GOR relation, which relates mass of light quark to the π -meson mass, were used to derive (2).

Thus, knowing pressure $P_h(T)$ as a function of temperature and π -meson mass one can find temperature dependence of quark and gluon condensates in the hadronic phase.

To describe thermodynamics of QCD in the confined phase we make use of hadron resonance gas model (this model was first proposed by R. Hagedorn [10] for the description of hot strongly-interacting matter). In this approach all thermodynamic properties of the system are determined by the total pressure of relativistic Bose and Fermi gases, which describe temperature excitations of massive hadrons. The motivation of using this method is that it incorporates all essential degrees of freedom of strongly interacting matter. Moreover, the use of hadron resonances spectrum effectively takes into account interactions between stable particles. Description of multiple particle production in heavy ions collisions in the framework of hadron resonance gas [11] leads to good agreement with experimental data.

Thus, pressure in the confined phase is given by

$$P_h = T \sum_i g_i \eta_i \int \frac{d^3 p}{(2\pi)^3} \ln \left(1 + \eta_i e^{-\omega_i/T} \right), \quad (3)$$

$$\omega_i = \sqrt{p^2 + m_i^2}, \quad \eta_i = \begin{cases} +1, & \text{fermions} \\ -1, & \text{bosons} \end{cases}$$

where g_i is the spin-isospin degeneracy factor (e.g. $g_\pi = 3$, $g_N = 8$, ...). The energy density $\varepsilon_h = T \partial P_h / \partial T - P_h$ in the hadronic phase is given by

$$\varepsilon_h = \sum_i g_i \int \frac{d^3 p}{(2\pi)^3} \frac{\omega_i}{\exp(\omega_i/T) + \eta_i} \quad (4)$$

3. To study condensates in the confined phase quantitatively the knowledge about pressure P_h dependence on light quark mass, or which is the same, on π -meson mass is needed. In the framework of hadron resonance gas model it is equivalent to the knowledge of masses of all resonances as functions of pion mass. This dependence was studied numerically on the lattice, and in the paper [12] five parameters formula, inspired by bag model, was suggested. At the certain choice of parameters it accurately describes masses of all considered by the authors [12] particles

$$\begin{aligned} m_i &= N_u a_1 x \sqrt{\sigma} + \frac{m_h}{1 + a_2 x + a_3 x^2 + a_4 x^3 + a_5 x^4}, \\ a_1 &= 0.51, \quad a_2 = a_1 N_u \sqrt{\sigma} / m_h, \\ a_3 &= 0.115, \quad a_4 = -0.0223, \quad a_5 = 0.0028. \end{aligned} \quad (5)$$

Here $x \equiv m_\pi / \sqrt{\sigma}$, m_h is the physical hadron mass, N_u is the number of light quarks ($N_u = 2$ for mesons, $N_u = 3$ for baryons), $\sigma = (0.42 \text{ GeV})^2$ is the string tension.

Next, it should be taken into account that as temperature increases hadron masses change. In the framework of finite temperature conformally generalized nonlinear sigma model with light and massive hadrons [13] it was shown, that temperature shift of hadron masses can be taken into account by the following substitution

$$\begin{aligned} m_h &\rightarrow m_h (\chi_T / \chi_0), \quad m_\pi \rightarrow m_\pi \sqrt{\chi_T / \chi_0}, \\ \chi_T / \chi_0 &= (\langle G^2 \rangle_T / \langle G^2 \rangle_0)^{1/4}, \end{aligned} \quad (6)$$

where χ is the dilaton field. Different as compared to other particles dependence of π -meson mass is the reflection of its goldstone nature. In the chiral limit, $m_q \rightarrow 0$, presented relation for the hadron masses is a strict consequence of low-energy QCD theorems. Similar to (6) relations for the shift of nucleon mass were obtained using effective dilaton Lagrangian at finite baryon density [14].

4. Formulas (1)-(6) define thermodynamic properties of the system in hadronic phase and allow to calculate quark and gluon condensates in the whole region of temperatures below T_c .

We take into account all hadron states with masses below 2.5 GeV for mesons and 3.0 GeV for baryons. Altogether it amounts to 2078 states (with degeneracy

factors g_i taken into account). It is clear, that at low temperatures $T < m_\pi = 140$ MeV main contribution to the thermodynamic quantities will come from thermal excitations of π -mesons, since other states are substantially heavier and are exponentially suppressed with Boltzman factor $\propto \exp\{-m_h/T\}$. However, a great many of heavy states starts playing important role when $T > m_\pi$. In the left part of figure 1 pion contribution to the pressure is shown with dash-dotted line. It is seen, that below temperature $T = 120$ MeV pions give main contribution to the P_h . At higher temperatures main contribution comes from all other hadron states. Left part of figure 1 also shows lattice data [15] for the pressure P_h in QCD with $N_f = 2$. One can see that in the region $T < T_c$ hadron resonance gas model with the account for temperature mass shift gives good description of pressure as a function of temperature.

In the right part of figure 1 energy density ε_h as a function of temperature is presented. Value of 1 GeV/fm^3 , corresponding to the estimates for energy density at quark-hadron phase transition, is reached at temperature $T \simeq 175$ MeV, i.e. in the region of phase transition temperature, as obtained in lattice calculations (see a review [16]).

Figure 2 shows quark and gluon condensates as functions of temperature. Shaded area corresponds to zero-temperature values of gluon condensate being in the range $\langle G^2 \rangle_0 = (0.5 \div 1.0) \text{ GeV}^4$. It is important that quark condensate goes to zero at the same temperature, where half of gluon condensate evaporates. If temperature shift of hadron masses is taken into account, this temperature is $T \simeq 190$ MeV.

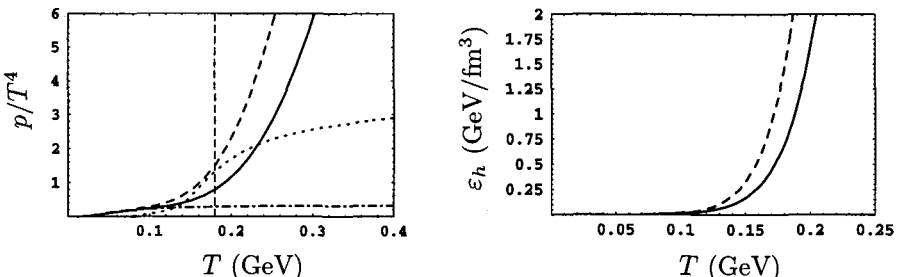


Figure 1: left: pressure P_h/T^4 as a function of temperature; right: energy density ε_h as a function of temperature. Solid line – zero temperature hadron spectrum; dashed line – spectrum with temperature shift taken into account, $\chi_T/\chi_0 = 0.84$; dash-dotted line – pion excitations only; dotted line – lattice data [15].

This work is supported by NSh-1774.2003.2 grant and by Federal Program of the Russian Ministry of Industry, Science and Technology No 40.052.1.1.1112.

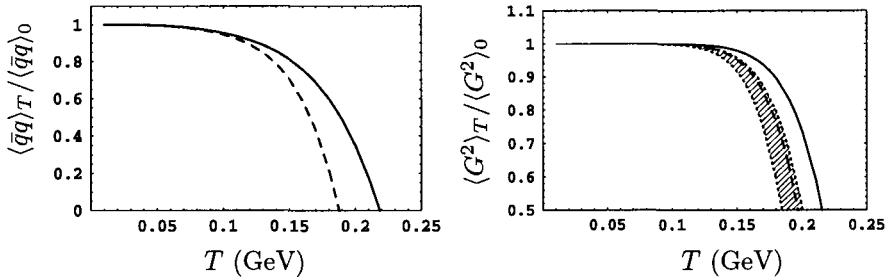


Figure 2: left: quark condensate $\langle\bar{q}q\rangle_T/\langle\bar{q}q\rangle_0$ as a function of temperature; right: gluon condensate $\langle G^2 \rangle_T/\langle G^2 \rangle_0$ as a function of temperature. Solid line – zero temperature hadron spectrum; dashed line – spectrum with temperature shift taken into account, $\chi_T/\chi_0 = 0.84$; $\langle G^2 \rangle_0 = 0.87 \text{ GeV}^4$ [17]. Shaded area – uncertainty due to zero-temperature gluon condensate value ($\langle G^2 \rangle_0 = 0.5 \div 1.0 \text{ GeV}^4$).

References

- [1] F. Karsch, E. Laermann and A. Peikert, Nucl. Phys. B **605**, 579 (2001).
- [2] Y. Nakamura, V. Bornyakov, M.N. Chernodub, et. al., hep-lat/0309144.
- [3] M. D'Elia, A. Di Giacomo, E. Meggiolaro, Phys. Rev. D **67**, 114504 (2003).
- [4] S. H. Lee, Phys. Rev. D **40**, 2484 (1989).
- [5] Y.A. Simonov, JETP Lett. **55**, 627 (1992); Phys. Atom. Nucl. **58**, 309 (1995).
- [6] N. O. Agasian, JETP Lett. **57**, 208 (1993).
- [7] N. O. Agasian, Phys. Lett. B **562**, 257 (2003).
- [8] N. O. Agasian, Phys. Lett. B **519**, 71 (2001); JETP Lett. **74**, 353 (2001).
- [9] V. A. Novikov, M. A. Shifman, A. I. Vainshtein, V. I. Zakharov, Nucl. Phys. **B191**, 301 (1981); Sov. J. Part. Nucl. **13**, 224 (1982);
- [10] R. Hagedorn, Nuovo Cim. Suppl. **3**, 147 (1965).
- [11] P. Braun-Munzinger, D. Magestro, K. Redlich and J. Stachel, Phys. Lett. B **518**, 41 (2001); J. Cleymans and K. Redlich, Phys. Rev. C **60**, 054908 (1999); Phys. Rev. Lett. **81**, 5284 (1998); F. Becattini, J. Cleymans, A. Keranen, E. Suhonen and K. Redlich, Phys. Rev. C **64**, 024901 (2001).
- [12] F. Karsch, K. Redlich and A. Tawfik, Eur. Phys. J. C **29**, 549 (2003).
- [13] N.O. Agasian, D. Ebert, E.-M. Ilgenfritz, Nucl. Phys. A **637**, 135 (1998).
- [14] N.O. Agasian, B.O. Kerbikov, V.I. Shevchenko, Phys. Rept. **320**, 131 (1999).
- [15] F. Karsch, E. Laermann and A. Peikert, Phys. Lett. B **478**, 447 (2000).
- [16] F. Karsch, Lect. Notes Phys. **583**, 209 (2002).
- [17] S. Narison, Phys. Lett. B **387**, 162 (1996).

THE STRUCTURE FUNCTION OF B MESONS

G.Ricciardi ^a

*Dipartimento di Scienze Fisiche, Universitá di Napoli "Federico II"
and I.N.F.N., 80126 Napoli, Italy*

Abstract. In semi-inclusive B decays, the structure function of B mesons, also called shape function, is required to factorize the non perturbative part of the amplitude. We compare the leading one-loop corrections to the shape function in effective theories with different regularization, in soft and collinear kinematical regions.

1 Introduction

In some kinematical regions, processes where an heavy quark in the initial state decays into a light quark in the final state can be described by effective theories. In this paper, the kinematical regions of interest are the soft and collinear regions for the light quark. They are relevant for several phenomenological reasons; let us just mention that in the $B \rightarrow X_u + l + \nu$ decay, these regions overlap with the end-point of the lepton spectrum, where the background decay $B \rightarrow X_c l \nu$ is kinematically forbidden.

The effective description can introduce additional ultraviolet and infrared divergencies in the calculation of the rate, but the physical results must reproduce the correct behavior of the QCD in the chosen kinematical regions. The important point is that, since the effective theory is basically based on cuts in the kinematical regions and on the consequent approximations, one cannot a priori discuss the effective theory without considering the regularization procedure. In fact, also the regularization procedure "cuts" into the kinematical regions in order to avoid ultraviolet divergent regions, and the two effects interplay.

One of the goal of effective theories is to simplify the description by factorizing the amplitude into perturbative and non perturbative parts. In B semi-inclusive decays, the structure function of B meson takes into account the non perturbative part of the amplitude and it is generally called shape function.

Here we will consider different approximations and regularizations in the simplified contest of leading order corrections to the shape function.

2 The shape function

Let us consider a semi-inclusive B decay with an hadronic final jet originated by a light quark. In an effective theory (ET) where the heavy b quark is taken in the HQET, the shape function is defined as [1]

$$f(k_+) \equiv \langle B(v) | h_v^\dagger \delta(k_+ - iD_+) h_v | B(v) \rangle, \quad (1)$$

^ae-mail: giulia.ricciardi@na.infn.it

where h_v is the HQET field with velocity v ($v^2 = 1$) and D is the covariant derivative, taken in the light cone coordinates. The argument of $f(k_+)$ is related to the kinematics of the process by $k_+ = -Q^2/2v \cdot Q$, where $Q \equiv m_B v - q$ and q is the momentum of non hadronic particles.

The shape function $f(k_+)$ is introduced to take care of non perturbative effects in the kinematical region with a large jet energy

$$E_X^2 \sim O(m_B^2)$$

and with an “intermediate” invariant mass

$$M_X^2 \sim O(\Lambda_{QCD} m_B).$$

In order to be meaningful, an effective theory must have the same infrared behaviour of the original, high energy theory. By computing the shape function in the double logarithmic approximation with a hard cut-off, we find indeed the same double logarithm of k_+ as in QCD. In other words, the leading IR singularity, $\log^2 k_+$, cancels in the matching constant (coefficient function), implying the factorization of infrared physics into the shape function.

However, by repeating the same calculation with dimensional regularization, it appears an additional factor of two in the term proportional to $\log^2 k_+$, implying that the double logarithm of k_+ does not cancel in the matching constant. In order to obtain a meaningful matching constant one can choose between using a non minimal subtraction [2] and adding collinear terms [3].

The shape function $f(k_-)$ receives perturbative QCD corrections which determine its evolution through a renormalization group equation [4, 5]. The starting point of the evolution (boundary value) is determined by matching ET onto full QCD. The matching constant (or coefficient function) is defined through the relation

$$f(k_+)^{QCD} = Z f(k_+)^{ET} \quad (2)$$

in which both the full QCD and the ET shape functions are computed in perturbation theory up to a prescribed accuracy.

We find useful to introduce a light-cone function $F(k_+)$ [2, 6]

$$F(k_+) \equiv \langle B(v) | h_v^\dagger \frac{1}{iD_+ - k_+ + i\eta} h_v | B(v) \rangle, \quad (3)$$

whose absorptive part is proportional to the shape function via a relation analogous to the optical theorem

$$f(k_+) = -\frac{1}{\pi} \text{Im } F(k_+). \quad (4)$$

It is easier to compute the matching constant through the relation

$$F(k_+)^{QCD} = Z F(k_+)^{ET}. \quad (5)$$

By using relation (4) and the fact that Z is real (and positive), since it is a ratio of physical rates, one can indeed derive Eq.(2).

At tree level:

$$F(k_+)^{QCD} = F(k_+)^{ET} = \frac{1}{-k_+ + i\eta}$$

implying $Z = 1$ as it should.

Up to one loop, in covariant gauges, the leading contributions come from the vertex correction diagram; we choose the Feynman gauge for simplicity, and we set the light quark mass equal to zero [7]. The computation of the light-cone function gives in QCD [2,5]

$$F(k_+)^{QCD} = \frac{1}{-k_+ + i\eta} \left(-\frac{1}{2} \right) a \log^2 \left(\frac{2m}{k_+ - i\eta} \right), \quad (6)$$

where m is the b quark mass, and $a \equiv \alpha_s C_F / \pi$. The hadronic tensor relevant to the decay is obtained by taking the imaginary part according to the optical theorem. Infrared singularities (soft & collinear) are regulated by the virtuality $Q^2 \neq 0$ of the external light quark.

In view of lattice-QCD applications, it is interesting to compute the matching constant of the shape function $f(k_+)$ in the ET regularized by a hard cut-off. A regularization with a hard cut-off Λ (HC) on the spatial loop momenta may be chosen, where

$$-\infty < l_0 < +\infty, \quad |\vec{l}| < \Lambda.$$

This regularization resembles ordinary lattice QCD regularization; we expect similar results to hold at DLA. Up to one loop, we have [2]

$$F(k_+)^{EFT} = \frac{1}{-k_+ + i\eta} \left(-\frac{1}{2} \right) a \log^2 \left(\frac{2\Lambda}{k_+ - i\eta} \right). \quad (7)$$

We take the external states in the effective theory on-shell because $k_+ \neq 0$ regulates the infrared divergences.

We explicitly see that the light-cone function (or equivalently the shape function) is ultraviolet divergent in the ET, the divergence being a double logarithm of the cut-off, while it is finite in QCD (cfr. Eq.(6)). Inserting these expressions into Eq.(5) we find

$$\begin{aligned} Z &= 1 - \frac{1}{2} a \left[\log^2 \left(\frac{2m}{k_+ - i\eta} \right) - \log^2 \left(\frac{2\Lambda}{k_+ - i\eta} \right) \right] \\ &= 1 - a \log \left(\frac{m}{\Lambda} \right) \log \left(\frac{2\sqrt{m\Lambda}}{k_+ - i\eta} \right). \end{aligned} \quad (8)$$

The double logarithm of k_+ , i.e. the leading infrared singularity, cancels in the difference of the integrals, implying the factorization of infrared physics into

the effective theory light-cone function. In particular, if we choose $\Lambda = m$ as the matching scale, we get $Z = 1$ also at one loop in DLA.

We expect the physics to be independent from the ultraviolet regulator, as long as it is large enough; therefore, we expect an evolution equation in Λ . In DLA the evolution equation leads to the well-known exponentiation of the one-loop amplitude [8]; using the previous results:

$$F(k_+)^{EFT} = \frac{1}{-k_+ + i\eta} \exp \left[-\frac{1}{2} a \log^2 \left(\frac{2\Lambda}{k_+ - i\eta} \right) \right]$$

and the QCD light-cone function is

$$\begin{aligned} F(k_+)^{QCD} &= \frac{1}{-k_+ + i\eta} \left\{ 1 - \frac{1}{2} a \left[\log^2 \left(\frac{2m}{k_+ - i\eta} \right) - \log^2 \left(\frac{2\Lambda}{k_+ - i\eta} \right) \right] \right\} \\ &\quad \exp \left[-\frac{1}{2} a \log^2 \left(\frac{2\Lambda}{k_+ - i\eta} \right) \right]. \end{aligned} \quad (9)$$

With the choice $\Lambda = m$, we have the QCD light-cone function with all large double logarithms exponentiated

$$F(k_+)^{QCD} = \frac{1}{-k_+ + i\eta} \exp \left[-\frac{1}{2} a \log^2 \left(\frac{2m}{k_+ - i\eta} \right) \right].$$

Let us now repeat the same calculation, employing this time another regularization, i.e. dimensional regularization; we find [2, 5]

$$\begin{aligned} F(k_+)^{ET} &= \frac{1}{-k_+ + i\eta} \left(-\frac{a}{2} \right) \frac{\Gamma(1+\epsilon)\Gamma(1+2\epsilon)\Gamma(1-2\epsilon)}{\epsilon^2} \left(\frac{\mu}{k_+ - i\eta} \right)^{2\epsilon} \quad (10) \\ &= \frac{1}{-k_+ + i\eta} a \left[-\frac{1}{2\epsilon^2} - \frac{1}{\epsilon} \log \left(\frac{\mu}{k_+ - i\eta} \right) - \log^2 \left(\frac{\mu}{k_+ - i\eta} \right) \right] \end{aligned}$$

where $\epsilon \equiv 2 - d/2$, d is the space-time dimension and μ is the regularization scale. The double and the simple pole are of ultraviolet nature; the finite term containing the $\log^2 k_+$ has an additional factor two with respect to the HC result (Eq.(7)) or the QCD result (Eq.(6)). Computing the coefficient function according to Eq.(5) we have

$$Z = 1 + a \left[\frac{1}{2\epsilon^2} + \frac{1}{\epsilon} \log \left(\frac{\mu}{k_+ - i\eta} \right) - \frac{1}{2} \log^2 \left(\frac{2m}{k_+ - i\eta} \right) + \log^2 \left(\frac{\mu}{k_+ - i\eta} \right) \right].$$

Unlike what happens with the HC regularization, the matching constant above contains a double logarithm of k_+ . This term does not drop, no matter what the choice of the matching scale μ is. This result has to be compared with the result (8) in the HC regularization, where the leading infrared singularity cancels in the matching at any value of Λ .

Different regularizations seem to affect the effective theory in different ways. This can be explained if we consider that the regularization itself operates a choice in the phase space, which interferes with the kinematical approximations of the effective theory. In DLA, the HC regularization sets the effective theory within the boundaries of the soft infrared kinematical region. The shape function factorizes correctly the non perturbative modes and the matching is consistent with the infrared QCD behaviour. On the other side, dimentional regularization leaves space for additional collinear modes, which need to be included in order to recover the correct matching.

References

- [1] I. I. Bigi, M. A. Shifman, N. G. Uraltsev and A. I. Vainshtein, Phys. Rev. Lett. 71, 496 (1993); A. V. Manohar and M. B. Wise, Phys. Rev. D 49, 1310 (1994); M. Neubert, Phys. Rev. D 49, 3392 (1994); 49, 4623 (1994); I. I. Bigi, M. A. Shifman, N. G. Uraltsev and A. I. Vainshtein, Int. J. Mod. Phys. A 9, 2467 (1994); T. Mannel and M. Neubert, Phys. Rev. D 50, 2037 (1994).
- [2] U. Aglietti and G. Ricciardi, Phys. Lett. B 466, 313 (1999)
- [3] C. W. Bauer, S. Fleming and M. Luke, Phys. Rev. D 63, 014006 (2000)
- [4] I. A. Korchemskaya and G. P. Korchemsky, Phys. Lett. B 287, 169 (1992); A. G. Grozin and G. P. Korchemsky, Phys. Rev. D 53, 1378 (1996).
- [5] C. Balzereit, T. Mannel and W. Kilian, Phys. Rev. D 58, 114029 (1998).
- [6] U. Aglietti and G. Ricciardi, Nucl. Phys. B 587 (2000), 363.
- [7] M. Abud, G. Ricciardi and G. Sterman, Phys. Lett. B 437:169 (1998).
- [8] R. Jackiw, Annals of Physics 48, 292 (1968); for a counter example to exponentiation see: E. Eichten and R. Jackiw, Phys. Rev. D 4, 439 (1971).

INTEGRAL REPRESENTATION FOR STRUCTURE FUNCTIONS AND TARGET MASS EFFECTS

I.L. Solovtsov ^a

*Bogoliubov Laboratory of Theoretical Physics, JINR, Dubna, Russia
International Center for Advanced Studies, GSTU, Gomel, Belarus*

Abstract. Target mass effects in the inelastic lepton-hadron scattering are studied within a method based on the Jost–Lehmann–Dyson integral representation for structure functions. It is demonstrated that, in accordance with general principles of local quantum field theory, expressions obtained for the physical structure functions depending on the target mass have a correct spectral property.

The inclusive cross section for inelastic lepton-hadron scattering is expressed as the Fourier transform of the expectation value of the current product $J(z)J(0)$ in the target state. The operator product expansion (OPE) is a powerful tool to study inelastic scattering processes. This method has been applied to define the contribution of target mass terms to the structure functions in paper [1]. Within this method the structure functions are parameterized by the quark distribution function $F(x)$ that appears with the argument $\xi = 2x/(1+\sqrt{1+4x^2}\epsilon)$ which is usually called the Nachtmann variable [2]. x is the Bjorken scaling variable $x = Q^2/2\nu = Q^2/2(q \cdot P)$ and ϵ is expressed through the target mass M and the transfer momentum Q as $\epsilon = M^2/Q^2$.

This ξ -approach leads to expressions for the physical structure functions which conflict with general spectral condition at $x = 1$. At the same time the target mass corrections become to be large at large x . This trouble with the ξ -scaling has widely been discussed in the literature (see, for example, [3–6]).

We will use the Jost–Lehmann–Dyson (JLD) [7, 8] representation for the structure function which reflects general principles of the theory [9]. We argue that in this case it is possible to get an expressions for the structure functions in terms of the quark distribution incorporating the target mass effects and having the correct spectral property. Our investigation of the inelastic lepton-hadron scattering based on the JLD representation has been started in [10] and continued in [11, 12].

The situation that an approximation can be in a confrontation with general properties is not rare event in quantum field theory. It is well known, for example, that when the renormalization group equation for the running coupling is solved directly, there arise unphysical singularities of the ghost pole type. One has to apply some additional requirements to correct this trouble. The analytic approach proposed in [13] gives a possible resolution of the ghost pole problem.^b This method combines the renormalization invariance and the Q^2 -analyticity of the Källén–Lehmann type has revealed new important properties

^ae-mail: solovtso@thsun1.jinr.ru, solovtsov@gstu.gomel.by

^bSee also [10, 14] for reviews and [15–17], where a new comparative analysis of the analytic perturbation theory and ordinary one has been performed.

of the analytic coupling. In the leading order the analytic running coupling has the form

$$\bar{a}_{\text{an}}^{(1)}(Q^2) = \frac{1}{\beta_0} \left[\frac{1}{\ln Q^2/\Lambda^2} + \frac{\Lambda^2}{\Lambda^2 - Q^2} \right], \quad (1)$$

where β_0 is the one loop coefficient of the renormalization group β -function.

The analytic coupling has no ghost pole at $Q^2 = \Lambda^2$. The first term on the right-hand side (1) preserves the standard ultraviolet behavior of the invariant coupling. The second term, which comes from the Källén–Lehmann representation and enforces the proper analytic properties, compensates the ghost pole at $Q^2 = \Lambda^2$. This term gives no contribution to the perturbative expansion. We note also that unlike in electrodynamics, the asymptotic freedom property in QCD has the effect that such nonperturbative contributions show up in the effective coupling function already in the domain of low energies and momentum transfers reachable in realistic experiments, rather than at unrealistically high energies.

The invariant analytic formulation maintaining the asymptotic freedom ultraviolet properties essentially modifies a behavior of the analytic running coupling in the infrared region by making it stable with respect to higher-loop corrections. This is radically different from the situation encountered in the standard renormalization-group perturbation theory, which is characterized by strong instability with respect to the next-loop corrections in the domain of small energy scale. The analytic perturbation theory results are much less sensitive to the choice of the renormalization scheme than those in the standard approach that allows us to reduce theoretical uncertainties drastically.

Our consideration of the inelastic lepton-hadron process based on the JLD representation for structure functions. The structure functions depend on two arguments, and the corresponding representation that accumulates the fundamental properties of the theory (such as relativistic invariance, spectrality, and causality) have a more complicated form in our analysis than in the representation of the Källén–Lehmann type for functions of one variable.^c Applications of the JLD representation to automodel asymptotic have been considered in [18].

For the function $W(\nu, Q^2)$ satisfying conditions of the covariance, spectrality, reality, Hermiticity and causality there exists a real moderately growing distribution $\psi(\mathbf{u}, \lambda^2)$ such that the JLD integral representation in the nucleon rest frame can be written as [18]

$$W(\nu, Q^2) = \varepsilon(q_0) \int d\mathbf{u} d\lambda^2 \delta[q_0^2 - (M\mathbf{u} - \mathbf{q})^2 - \lambda^2] \psi(\mathbf{u}, \lambda^2). \quad (2)$$

The weight function $\psi(\mathbf{u}, \lambda^2)$ is supported in

$$\rho = |\mathbf{u}| \leq 1, \quad \lambda^2 \geq \lambda_{\min}^2 = M^2(1 - \sqrt{1 - \rho^2})^2. \quad (3)$$

^cThe 4-dimensional integral representation has been proposed by Jost and Lehmann in [7] for the so-called symmetric case. A more general case has been considered by Dyson [8].

The physical values of ν and Q^2 , for the process under consideration, are positive. One can neglect the sign factor $\varepsilon(q_0)$ and keep the same notation for $W(\nu, Q^2)$. Taking into account that the weight function $\psi(\mathbf{u}, \lambda^2) = \psi(\rho, \lambda^2)$ is radial-symmetric we write down the JLD representation for W in the following covariant form,

$$W(\nu, Q^2) = \int_0^1 d\rho \rho^2 \int_{\lambda_{\min}^2}^{\infty} d\lambda^2 \int_{-1}^1 dz \times \delta(Q^2 + M^2 \rho^2 + \lambda^2 - 2z\rho\sqrt{\nu^2 + M^2 Q^2}) \psi(\rho, \lambda^2). \quad (4)$$

A ‘natural’ target mass dependent variable coming from the JLD representation which is different from the ξ -variable (??) is

$$s = x \sqrt{\frac{1+4\epsilon}{1+4x^2\epsilon}}. \quad (5)$$

In terms of the s -variable there arises the dispersion relation for the forward Compton scattering amplitude $T(\nu, Q^2)$ [10]

$$T(\nu, Q^2) = \frac{2}{\pi} \int_0^1 \frac{ds_1}{s_1} \frac{1}{1-(s_1/s)^2} W(\nu_1, Q^2). \quad (6)$$

The structure of this dispersion integral is similar to the structure which is appear for the x -variable. The s -moments of the structure function are the analytic functions in the complex Q^2 -plane with a cut along a negative part of the real axis.

Eq. (6) can be used to expand the Compton amplitude in the inverse powers of s . If the operator basis is chosen such that an arbitrary contraction of the tensor $\langle P|\hat{O}_{\mu_1 \dots \mu_n}|P\rangle$ with the nucleon momentum P_{μ_i} vanishes, then the operator product expansion leads to a power series for the forward Compton scattering amplitude with the expansion parameter $q^\mu q^\nu (P_\mu P_\nu - g_{\mu\nu} P^2)/(q^2)^2$, which corresponds to expanding dispersion integral (6) in powers of $1/s^2$. This relation between the analytic s -moments and the structure of the operator product expansion has been found in [10]. It should be stressed that the orthogonality requirement of the symmetric tensor $\langle P|\hat{O}_{\mu_1 \dots \mu_n}|P\rangle$ to the nucleon momentum P_{μ_i} determines its Lorentz structure unambiguously.

We represent a physical structure function $W(x, Q^2)$ in the form [11, 12]

$$W(x, Q^2) = W_0(x, Q^2) + w(x, Q^2). \quad (7)$$

The function $W_0(x, Q^2)$ is expressed via the corresponding parton distribution $F(x)$ as follows

$$W_0(x, Q^2) = \begin{cases} F(\beta_-) - F(1), & \text{if } 0 \leq x < \tilde{x}, \\ F(\beta_-) - F(\beta_+), & \text{if } \tilde{x} \leq x \leq 1. \end{cases} \quad (8)$$

Here

$$\beta_{\pm} = \frac{x\sqrt{1+4\epsilon x^2}}{1+4\epsilon x^2+4\epsilon^2 x^2} \left[1 + 2\epsilon \pm 2\epsilon \sqrt{\frac{1-x^2}{1+4\epsilon x^2}} \right] \quad (9)$$

and $\tilde{x} = 1/\sqrt{1+4\epsilon^2}$.

The function $w(x, Q^2)$ is

$$w(x, Q^2) = \int_0^1 d\beta \theta[f(\beta; x, \epsilon)] \phi(\beta; x, \epsilon), \quad (10)$$

where

$$f(\beta; x, \epsilon) = \frac{\beta}{s} \sqrt{1+4\epsilon} - 1 - 2\epsilon(1 - \sqrt{1-\beta^2}). \quad (11)$$

For the scalar quark currents function $\phi(\beta; x, \epsilon)$ in Eq. (10) is [11]

$$\phi(\beta; x, \epsilon) = \frac{1}{4\sqrt{\tau}} \theta(\tau) \theta(1-\tau) \frac{\partial}{\partial(\sqrt{\tau})} [\sqrt{\tau} F(\sqrt{\tau})], \quad (12)$$

where

$$\tau \equiv \tau(\beta; x, \epsilon) = \frac{1}{\epsilon} \left(\frac{\beta}{s} \sqrt{1+4\epsilon} - 1 \right). \quad (13)$$

The analysis of combination of the physical structure functions $F_1(x, Q^2)$ and $F_2(x, Q^2)$ which is taken in the form $2x(2W_T - W_L) = 6xF_1 - (1+4x^2\epsilon)F_2$ is similar to the scalar case.

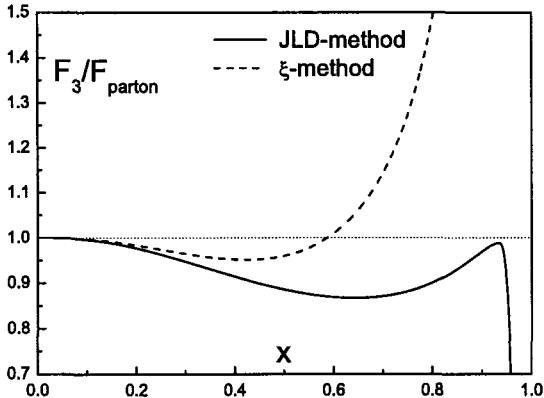


Figure 1: Ratios of xF_3 structure function with target mass correction to the parton distribution for the JLD-method (solid line) and the ξ -approach (dashed curve).

The ξ -scaling method leads to the expression

$$2x(2W_T - W_L) = \frac{2x^2}{\sqrt{1+4x^2\epsilon}} F(\xi). \quad (14)$$

The defect of this equation is that there is a mismatch at $x = 1$. The combination physical structure functions in the left hand side of Eq. (14) vanishes at $x = 1$, at the same time the right hand side does not because at $x = 1$ the variable ξ remains less than unity. Within the method based on the JLD representation it is possible to get a correct result which obeys the spectral condition.

In Fig. 1 we plot ratios of the structure function xF_3 to the parton distribution (which is taken as in [19]) for $\epsilon = 1/2$. The solid line corresponds to incorporating the target mass effects by using the JLD approach, the dashed curve reflects the method of ξ -scaling.

It has been argued that the approach based on the Jost-Lehmann-Dyson representation gives the self-consistent method of incorporating the target mass dependence into the structure function and does not lead to the conflict with the general principles.

The author would like to express their gratitude to Prof. D.V. Shirkov, Drs. A.L. Kataev, A.V. Kotikov, V.I. Lashkevich, A.V. Sidorov and O.P. Solovtsova for interest in this work and valuable discussions. Partial support of the work by the International Program of Cooperation between Republic of Belarus and JINR, the Belarus Program of Basic Research "Physics of Interactions", the grant of the Ministry of Education and the RFBR (grants 00-15-96691, 02-01-00601) is gratefully acknowledged.

References

- [1] H.Georgi, H.D.Politzer, *Phys. Rev.* **D** 14, 1829 (1976).
- [2] O.Nachtmann, *Nucl. Phys.* **B** 63, 237 (1973).
- [3] D.J.Gross, S.B.Treiman, F.A.Wilczek, *Phys. Rev.* **D** 15, 2486 (1977).
- [4] A.De Rújula, H.Georgi, H.D.Politzer, *Phys. Rev.* **D** 15, 2495 (1977).
- [5] J.L.Miramontes, J.S.Guillén, *Z. Phys.* **C** 41, 247 (1988).
- [6] R.G.Roberts, *The Structure of the Proton. Deep Inelastic Scattering* (Cambridge University Press, 1990).
- [7] R.Jost, H.Lehmann, *Nuovo Cim.* 5, 1598 (1957).
- [8] F.J.Dyson, *Phys. Rev.* 110, 1460 (1958).
- [9] N.N.Bogoliubov, D.V.Shirkov, *Introduction to the Theory of Quantum Fields* [in Russian], Nauka, Moscow (1973, 1976, 1986), English transl.: Wiley, New York (1959, 1980).
- [10] I.L.Solovtsov, D.V.Shirkov, *Theor. Math. Phys.* 120, 1220 (1999).
- [11] I.L.Solovtsov, *Part. Nucl. Lett.* 4[101], 10 (2000).
- [12] V.I.Lashkevich, I.L.Solovtsov, Proceedings of Int. School-Seminar on "Actual problems of particle physics", August 2001, Gomel, Belarus, JINR E1, 2-2002-166, Dubna, 2002, v. I, p. 298.
- [13] D.V.Shirkov, I.L.Solovtsov, JINR Rap. Comm. 2, 5 (1996); *Phys. Rev.*

Lett. 79, 1209 (1997).

- [14] I.L.Solovtsov, Proceedings of International School-Seminar “*Actual problems of particle physics*” July 30 - August 8, 1999, Gomel, Belarus, vol. I, p.175, Dubna, 2000.
- [15] K.A.Milton, O.P.Solovtsova, *Int J. Mod. Phys. A* 26, 3789 (2002).
- [16] K.A.Milton, I.L.Solovtsov, O.P.Solovtsova, *Phys. Rev. D* 65, 076009 (2002).
- [17] O.P. Solovtsova, *Theor. Math. Phys.* **134** (2003) 365.
- [18] N.N.Bogoliubov, V.S.Vladimirov, A.N.Tavkhelidze, *Theor. Math. Phys.* 12, 305 (1972).
- [19] A.L.Kataev, G.Parente, A.V.Sidorov, *Phys. Part. Nucl.* 34, 43 (2003).

NONPERTURBATIVE EFFECTS IN THE HADRONIC DECAY OF THE TAU-LEPTON

O.Solovtsova

Gomel State Technical University, October av. 48, 246746 Gomel, Belarus

Abstract. A nonperturbative approach in quantum chromodynamics is applied to analyze the low energy scale hadronic decay of the τ -lepton data. The method suggested allow us to describe well the experimental D -function down to the lowest energy scale and parameters of the ρ -meson.

1 Introduction

The experimental data on the τ -lepton decay into hadrons obtained with a record accuracy for hadronic processes [1, 2] give a unique possibility for testing QCD at low energy scale. A perturbative approximation in QCD as a rule cannot be exhaustive in the low energy region of a few GeV and a nonperturbative contribution has to be included. In comparing theoretical predictions with experimental data, it is important to connect measured quantities with “simplest” theoretical objects to check direct consequences of the theory without using model assumptions in an essential manner. Some single-argument functions which are directly connected with experimentally measured quantities can play the role of these objects. Let us mention, among functions of this sort, the correlator $\Pi(s)$, that appear in the process of e^+e^- annihilation into hadrons and the inclusive decay of the τ -lepton into hadrons, and the corresponding Adler function, $D(Q^2)$. This function defined in the Euclidean region is a smooth function, and thus it is not necessary to apply any “smearing” procedure in order to be able to compare theoretical results with experimental data. The “experimental” curve for the Adler function corresponding to the e^+e^- data and a comparative analysis has been presented in [3]. Here, we investigate the Adler function corresponding to the inclusive τ decay data. The theoretical method we will use is the nonperturbative expansion technique [4] based on the idea of variational perturbation theory [5] which, in the case of QCD, leads to a new small expansion parameter, a . Even going into the infrared region of small momenta where the running coupling becomes large and the standard perturbative expansion fails, the a -expansion parameter remains small and the approach holds valid [6].

2 Theoretical framework

The method of variational perturbation theory (VPT) leads to the following connection between the expansion parameter a and the original coupling constant, $\lambda = g^2/(4\pi)^2 = \alpha_s/4\pi = C a^2/(1-a)^3$. For all values of the coupling constant $\lambda \geq 0$ the expansion parameter a obeys the inequality $0 \leq a < 1$. The

positive parameter C plays the role of a variational parameter, which can be found by using an additional information.

The Q^2 -evolution of a is defined by the renormalization group equation,

$$\ln \frac{Q^2}{Q_0^2} = \frac{C}{2\beta_0} [f(a) - f(a_0)], \quad (1)$$

where $a_0 = a(Q_0^2)$, $\beta_0 = 11 - 2/3 N_f$ is the first coefficient of the β -function in perturbative expansion, and N_f is the number of active quarks. At the level $O(a^3)$, the function $f(a)$ has the form

$$f(a) = \frac{2}{a^2} - \frac{6}{a} - 48 \ln a - \frac{18}{11} \frac{1}{1-a} + \frac{624}{121} \ln(1-a) + \frac{5184}{121} \ln(1 + \frac{9}{2}a). \quad (2)$$

We will use a more complicated expression for the $O(a^5)$ level [7]. For any values of Q^2 , equation (1) has a unique solution $a(Q^2)$: $0 < a(Q^2) < 1$. Independently of a value a_0 , an infrared limiting value is $a(0) = 1$.

The method of the renormalization group gives a Q^2 -evolution law of the running coupling in the Euclidean region, and there is the question of how to parametrize a quantity, for example, $R(s) = \text{Im}\Pi(s + i0)/\pi$, defined for timelike momentum transfers. To perform this procedure self-consistently, it is important to maintain correct analytic properties of the correlator $\Pi(s)$ which are violated in perturbation theory (PT). Within the analytic approach [8] and the considering here nonperturbative a -expansion, it is possible to maintain such analytic properties and self-consistently determine the effective coupling in the Minkowskian region [9–11].

3 τ -decay

The ratio of hadronic to leptonic widths for the inclusive decay of the τ -lepton, R_τ , is the most precise one for extracting of the values of the fundamental QCD parameters at a low energy scale. The initial theoretical expression for R_τ contains an integral over timelike momentum

$$R_\tau = 2 \int_0^{M_\tau^2} \frac{ds}{M_\tau^2} \left(1 - \frac{s}{M_\tau^2}\right)^2 \left(1 + 2\frac{s}{M_\tau^2}\right) R(s) \quad (3)$$

which extends down to small s . R_τ -ratio and the Adler function

$$D(Q^2) = Q^2 \int_0^\infty ds \frac{R(s)}{(s + Q^2)^2} \quad (4)$$

cannot be directly calculated in the framework of standard PT. Indeed, the function $R(s)$ is parametrized by the perturbative running coupling which has

unphysical singularities (the ghost pole and corresponding cuts) and, therefore, is ill-defined in the region of small momenta.

A description of quark-antiquark systems near threshold requires us to take into account the resummation factor which summarizes the threshold singularities of the perturbative series of the $(\alpha_s/v)^n$ type. In a nonrelativistic approximation, this is the well known Sommerfeld-Sakharov factor [12,13]. The corresponding relativistic resummation factor $S(\chi)$ (χ is the rapidity which related to s by $2m \cosh \chi = \sqrt{s}$) has been found in [14]. This relativistic resummation factor reproduces both the expected nonrelativistic and ultrarelativistic limits and corresponds to a QCD-like quark-antiquark potential.

A convenient way to incorporate quark mass effects is to use an approximate expression [15,16] which can be written as

$$R(s) = T(v) [1 + g(v)r(s)] \Theta(s - 4m^2), \quad (5)$$

where $r(s)$ is the massless QCD correction,

$$T(v) = v \frac{3 - v^2}{2}, \quad g(v) = \frac{4\pi}{3} \left[\frac{\pi}{2v} - \frac{3+v}{4} \left(\frac{\pi}{2} - \frac{3}{4\pi} \right) \right], \quad v = \sqrt{1 - \frac{4m^2}{s}}. \quad (6)$$

Effective quark mass, m , which incorporate some nonperturbative contributions, turn out to be close to the constituent masses. In the description of the nonstrange vector component of the D -function we neglect the difference of the quark mass values and set $m_u = m_d = m$.

We represent $R(s)$ in the form $R(s) = R_0(s) + R_1(s)$, where

$$R_0(s) = T(v) S(\chi), \quad R_1(s) = T(v) \left[\frac{\alpha_s(s)}{\pi} g(v) - \frac{1}{2} X(\chi) \right]. \quad (7)$$

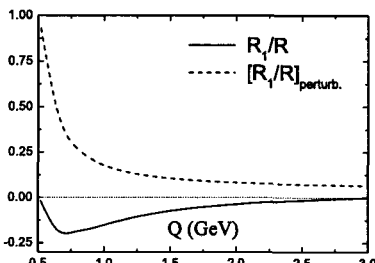


Figure 1: Relative contributions.

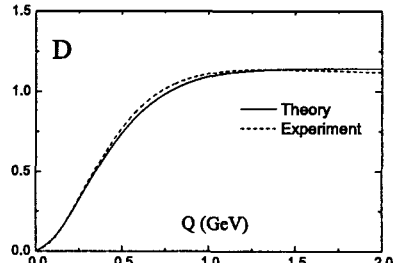


Figure 2: The "light" D -function.

In Fig. 1 we show a relative contribution of the correction R_1 defined in (7) and R_1^{PT} defined in perturbation theory. The "light" D -function corresponding

to the $f = 3$ quark world is plotted in Fig. 2. The experimental curve is obtained by using the ALEPH vector spectral function τ -data. Our result was obtained by using the value of the quark masses $m = 260$ MeV. The shape of the infrared tail of the D -function is rather sensitive to the value of these masses. We obtain the value of $R_{\tau,V} = 1.77$ in the vector channel which agrees well with the experimental data presented by the ALEPH, $R_{\tau,V}^{\text{expt}} = 1.775 \pm 0.017$ [1], and the OPAL, $R_{\tau,V}^{\text{expt}} = 1.764 \pm 0.016$ [2], collaborations.

The analysis performed lead to a good agreement with experimental data for the quark masses which are constant and close the values of the constituent quark masses. More systematic consideration has to take into account the “dynamical” nature of quark mass as, for instance, in [17,18], and to use a mass function as, for instance, coming from the Dyson-Schwinger equations [19]. It is interesting that in these cases we come to the similar results which we have received for the constant masses. Thus, the constant quark mass of order the constituent mass is an useful model “average” object which can be used in a simple analysis instead of more complicated consideration. A justification of this statement can also be received from the analysis of the QCD sum rules.

4 QCD sum rules and ρ -meson

To consider ρ -meson characteristics we use the QCD sum rules [20] with the following hadronic model for $R(s)$:

$$R^h(s) = \frac{2\pi}{g_\rho^2} m_\rho^2 \delta(s - m_\rho^2) + \left(1 + \frac{\alpha_s^{(0)}}{\pi}\right) \theta(s - s_0), \quad (8)$$

where the parameters $\alpha_s^{(0)} = 0.4 \div 0.5$ and $s_0 \simeq 1.5$ GeV 2 [20,21]. The experimental values of the ρ^0 -parameters m_ρ and g_ρ^2 reproduce well the “experimental” curve for the D -function represented in Fig. 2.

For the ρ -mass the Borel sum rules give

$$m_\rho^2 = \frac{\mathfrak{M}_1(M^2) - (1 + \alpha_s/\pi) M^4 (1 + s_0/M^2) \exp(-s_0/M^2)}{\mathfrak{M}_0(M^2) - (1 + \alpha_s/\pi) M^2 \exp(-s_0/M^2)}. \quad (9)$$

For the width we can get two expressions

$$g_{\rho 1}^2 = \frac{2\pi m_\rho^2 \exp(-m_\rho^2/M^2)}{\mathfrak{M}_0(M^2) - M^2 (1 + \alpha_s/\pi) \exp(-s_0/M^2)}, \quad (10)$$

$$g_{\rho 2}^2 = \frac{2\pi m_\rho^4 \exp(-m_\rho^2/M^2)}{\mathfrak{M}_1(M^2) - M^2 (s_0 + M^2) (1 + \alpha_s/\pi) \exp(-s_0/M^2)}, \quad (11)$$

where

$$\mathfrak{M}_k(M^2) = \int_0^\infty ds s^k \exp\left(-\frac{s}{M^2}\right) R(s). \quad (12)$$

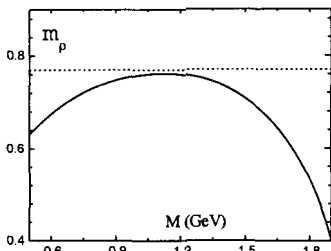


Figure 3: Behavior of $m_\rho(M)$ defined by Eq. (9). Horizontal line corresponds to the experimental value.

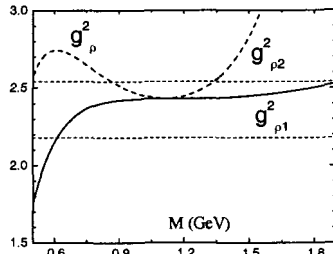


Figure 4: Behavior of $g_\rho^2(M)$ defined by Eqs. (10) and (11). Horizontal lines correspond to the experimental “corridor”.

Results coming from Eqs. (9), (10) and (11) are shown in Figs. 3 and 4. Regions of stability give values $m_\rho = 763$ MeV and $g_\rho^2 = 2.43$ which agree well with experimental data.

5 Conclusions

The method we used here is the non-perturbative approach based on the idea of variational perturbation theory which combines an optimization procedure of variational type with a regular method of calculating corrections. In the case of QCD the non-perturbative expansion parameter, a , obeys an equation whose solutions are always smaller than unity for any value of the original coupling constant. An important feature of this approach is the fact that for sufficiently small value of the running coupling the a -expansion reproduces the standard perturbative expansion, and, therefore, the perturbative high-energy physics is preserved. In moving to low energies, where ordinary perturbation theory breaks down ($\bar{\alpha}_s \simeq 1$), the parameter a remains small and we still stay within the region of applicability of the a -expansion method.

We have also used the new form of the threshold resummation factor. This relativistic factor could have a significant impact in interpreting strong-interaction physics. In many physically interesting cases, $R(s)$ occurs as a factor in an integrand, as, for example, for the case of inclusive τ decay, for smearing quantities, and for the Adler D function. Here the behavior of S at intermediate values of v becomes important.

The experimental D -function turned out to be a smooth function without visible traces of the resonance structure of $R(s)$. One can expect that this object more precisely reflects the quark-hadron duality and is convenient for comparing theoretical predictions with experimental data. Note here that any finite order of the operator product expansion fails to describe the infrared tail

of the D -function. Within the framework of nonperturbative a -expansion technique with the relativistic threshold factor, we have obtained a good agreement between our results and the experimental data down to the lowest energy scale both for Minkowskian and Euclidean quantities.

Acknowledgments

I would like to thank the Organizing Committee for the invitation. Partial support of the work by the RFBR grant 02-01-00601 is gratefully acknowledged.

References

- [1] R.Barate *et al.* (ALEPH Coll.), *Eur. Phys. J.* **C** 4, 409 (1998).
- [2] K.Ackerstaff *et al.* (OPAL Coll.), *Eur. Phys. J.* **C** 7, 571 (1999).
- [3] S.Eidelman, F.Jegerlehner, A.Kataev, O.Veretin, *Phys. Lett.* **B** 454, 369 (1999).
- [4] I.Solovtsov, *Phys. Lett.* **B** 327, 335 (1994); **B** 340, 245 (1994).
- [5] A.Sissakian, I.Solovtsov, *Phys. Part. Nucl.* 25, 478 (1994); *Phys. Part. Nucl.* 30, 461 (1999).
- [6] H.Jones, I.Solovtsov, *Phys. Lett.* **B** 349, 519 (1995).
- [7] A.Sissakian, I.Solovtsov, O.Solovtsova, *JETP Lett.* 73, 166 (2001).
- [8] D.Shirkov, I.Solovtsov, *Phys. Rev. Lett.* 79, 1209 (1997); *Theor. Math. Phys.* 120, 1220 (1999).
- [9] H.Jones, I.Solovtsov, O.Solovtsova, *Phys. Lett.* **B** 357, 441 (1995).
- [10] K.Milton, I.Solovtsov, *Phys. Rev.* **D** 55, 5295 (1997).
- [11] K.Milton, O.Solovtsova, *Phys. Rev.* **D** 57, 5402 (1998).
- [12] A.Sommerfeld, “*Atombau und Spektrallinien*”, vol. II (Vieweg, Braunschweig) 1939.
- [13] A. Sakharov, *JETP Lett.* 18, 631 (1948).
- [14] K.Milton, I.Solovtsov, *Mod. Phys. Lett.* **A** 16, 2213 (2001).
- [15] E.Poggio, H.Quinn, S.Weinberg, *Phys. Rev.* **D** 13, 1958 (1976).
- [16] T.Appelquist, H.D.Politzer, *Phys. Rev. Lett.* 34, 43 (1975); *Phys. Rev.* **D** 12, 1404 (1975).
- [17] H.D.Politzer, *Nucl. Phys.* **B** 117, 397 (1976).
- [18] L.Reinders, K.Stam, *Phys. Lett.* **B** 195, 465 (1987).
- [19] R.Alkofer, L.von Smekal, *Phys. Rep.* 353, 281 (2001);
- [20] M.Shifman, A.Vainshtein, V.Zakharov, *Nucl. Phys.* **B** 147, 385 (1979); 448 (1979); 519 (1979).
- [21] L. Reinders, H.Rubinstein, S.Yazaki, *Phys. Rep.* 127, 1 (1985).

HIGGS SEARCHES AT LEP

A.Kiiskinen ^a

Helsinki Institute of Physics, P.B. 64, 00014 Helsinki University, Finland

Abstract. A review of the Higgs particle searches performed at the LEP collider is given. Potential production processes and analysis techniques for Higgs particles within and beyond the Standard Model are described. Latest results of the four LEP collaborations are presented.

1 Introduction

1.1 Outline

The Large Electron Positron collider (LEP), at CERN, operated from 1989 to 2000. During its last year of operation it reached maximum energies of about 209 GeV. Reasonable amounts of data, about 140 pb^{-1} per experiment, were collected at energies above 206 GeV.

Higgs bosons, predicted by the Standard Model and many extended models, were searched for in the data collected by the LEP experiments. Many results of the four collaborations have been combined by the LEP Higgs Working Group [1] improving the statistics by a factor of four compared to results of individual experiments.

Some of the latest and most interesting LEP Higgs search results will be presented in this review. Some results are final, some still preliminary.

1.2 Motivation for Higgs searches

Electroweak symmetry breaking is included in the Standard Model by using the Higgs mechanism which predicts the existence of a Higgs boson. Many extensions of the Standard Model predict more Higgs bosons. Higgs bosons have been searched for at many past and present experiments but no direct evidence for their existence has been found so far. The mass of the Higgs boson is a free parameter in the Standard Model but its value has effects on some other Standard Model parameters such as the W boson and top quark masses. Fits to the presently existing Standard Model measurements clearly favour a light Higgs mass with a preferred mass value at $96 \text{ GeV}/c^2$ and the mass being below $219 \text{ GeV}/c^2$ at 95% confidence level [2], as can be seen Fig. 1.

The Standard Model has problems, such as the naturalness or hierarchy problem, and it is also not able to provide Grand Unification of forces. Therefore, many extensions and alternative theories have been developed. A popular candidate for the model beyond the Standard Model is the supersymmetry (SUSY) which solves the problems of the Standard Model by introducing superpartners

^ae-mail: ari.kiiskinen@cern.ch

for all Standard Model particles. SUSY models contain extensions also on the Higgs sector predicting the existence of five physical Higgs particles.

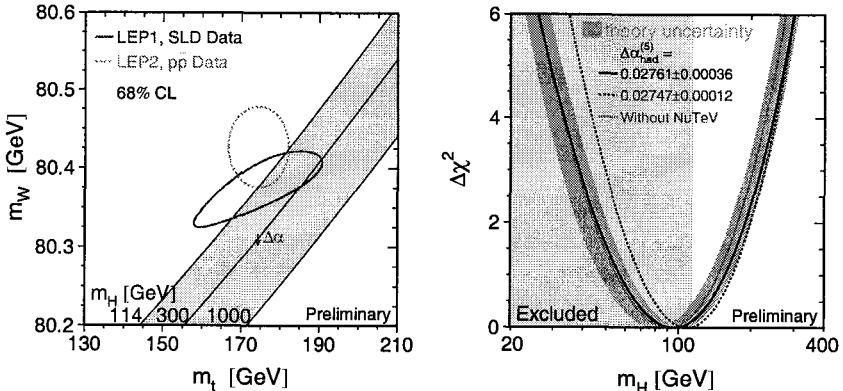


Figure 1: Figure on the left shows the indirect (LEP1 and SLD data) and direct (LEP2 and $p\bar{p}$ data) measurements of the W boson and top quark masses. Diagonal lines show the Standard Model relation between the W and top masses for different Higgs boson mass values. The figure on the right shows the $\Delta\chi^2$ curve derived from precision electroweak measurements as a function of the Higgs-boson mass, assuming the Standard Model to be the correct theory of nature. The minimum of the curve corresponds to the preferred Higgs boson mass and the shaded area below 114.4 GeV/c^2 shows the area excluded by the LEP direct searches [2].

2 Search for the Standard Model Higgs boson

2.1 Production and decay

The dominant Standard Model process for Higgs boson production in e^+e^- collisions at the LEP energies was the Higgs-strahlung process (see Fig. 2). At high Higgs masses the W boson fusion process was also expected to give a small contribution.

The branching ratios of the Standard Model Higgs boson depend on the Higgs boson mass. At the LEP energy range, the dominant decay channel was the decay into $b\bar{b}$ quark pairs. Other decays with lower significance were decays into $\tau^+\tau^-$, W^+W^- and gg (see Fig. 2).

Only b quarks and τ leptons could be identified with high efficiency and purity at LEP and those two decays were the ones with main contribution to the search results. The final state topology of the whole event in the Higgs-strahlung process depended also on the Z^0 boson decay: $q\bar{q}$, $\nu\bar{\nu}$ or l^+l^- .

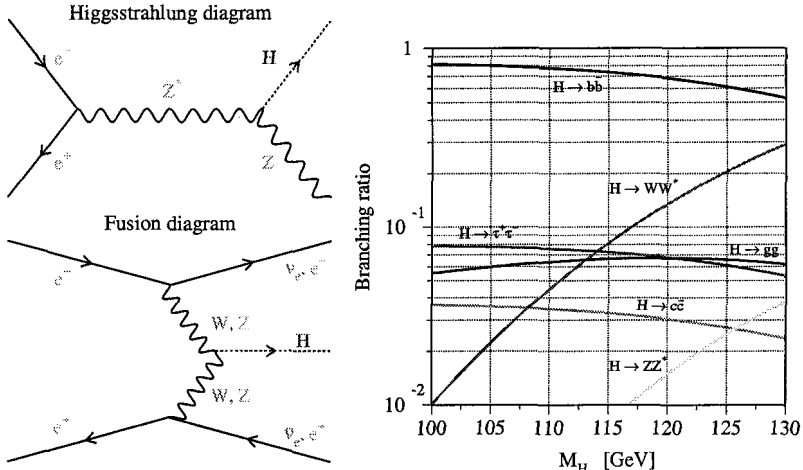


Figure 2: Feynman diagrams of the two production processes, on the left hand side, and the branching ratios as a function of the Higgs mass, on the right hand side.

2.2 Event analysis

Observed Higgs boson candidate events were compared one by one to the signal and background hypotheses. All available information, such as the Higgs boson mass, b-tag probability and event shape variables, were combined to give each event a signal over background value, s/b . The dominant backgrounds came from $e^+e^- \rightarrow Z\gamma(\gamma)$, $f\bar{f}$, WW and ZZ processes. The distributions of the s/b values for data and for a 115 GeV/ c^2 signal mass hypothesis can be seen in Fig. 3. The mass distribution of events with high s/b values is also shown in the same figure [3].

2.3 Statistical interpretation

Compatibility of the observed data with the signal+background and background only hypotheses was tested combining information from all channels and all events into one test statistic, $-2\ln Q(m_H)$.

A large number of Monte Carlo Gedanken experiments with and without signal were generated in order to obtain the probability distribution functions for $-2\ln Q(m_H)$. The observer value of $-2\ln Q(m_H)$ was then compared to the expectations. The observation and expected distributions with two hypothetical Higgs masses are shown in Fig. 4. As can be seen clearly in those two plots, a clear separation between signal and no-signal hypotheses was expected and observed for Higgs masses up to 110 GeV/ c^2 but for a Higgs mass of 115 GeV/ c^2 the result became ambiguous.

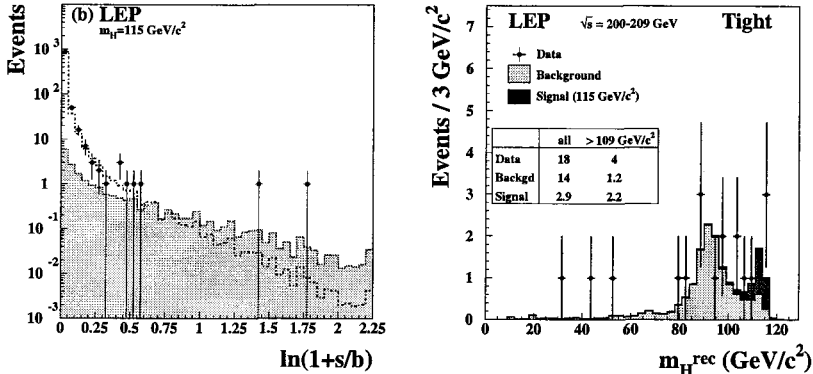


Figure 3: On the left hand side: distribution of the signal to background ratios of the observed events and simulated $115 \text{ GeV}/c^2$ signal. On the right hand side: mass distribution of observed events after a tight selection [3].

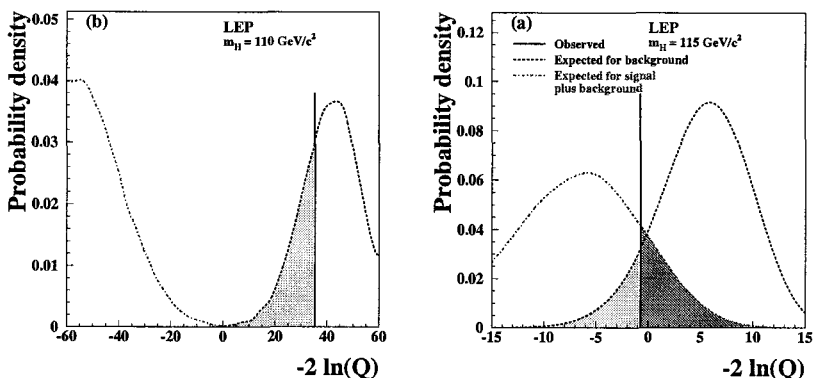


Figure 4: The observed values of $-2 \ln Q(m_H)$ and the probability distributions functions of simulated Gedanken experiments with and without signal [3] for two Higgs mass values, $110 \text{ GeV}/c^2$ and $115 \text{ GeV}/c^2$.

The confidence levels for the signal+background and background only hypotheses were obtained by integrating the expected $-2 \ln Q(m_H)$ distributions. Finally, a conservative confidence level for the signal hypothesis was obtained: $CL_s(m_H) = CL_{s+b}(m_H)/CL_b(m_H)$.

Significance of deviations from the background only hypothesis was described by the value of $1 - CL_b$ (a 5σ effect required for discovery). The compatibility

of a potential excess of candidates with the signal+background hypothesis was described by the values of CL_s .

As can be seen in Fig. 5, a 2.3σ deviation from the background only hypothesis was observed at $98 \text{ GeV}/c^2$. However, this effect was incompatible with the $98 \text{ GeV}/c^2$ Standard Model Higgs boson hypothesis which would have had a much larger cross-section. Another 1.7σ deviation was observed at around $115 \text{ GeV}/c^2$ mass. This observation had a 9% confidence level compatibility with the background only hypothesis and a 15% confidence level compatibility with the signal+background hypothesis [3].

As no signal reaching the discovery level was observed, a 95% confidence level lower mass limit for the Standard Model Higgs boson was set at $114.4 \text{ GeV}/c^2$ ($115.3 \text{ GeV}/c^2$ expected) [3].

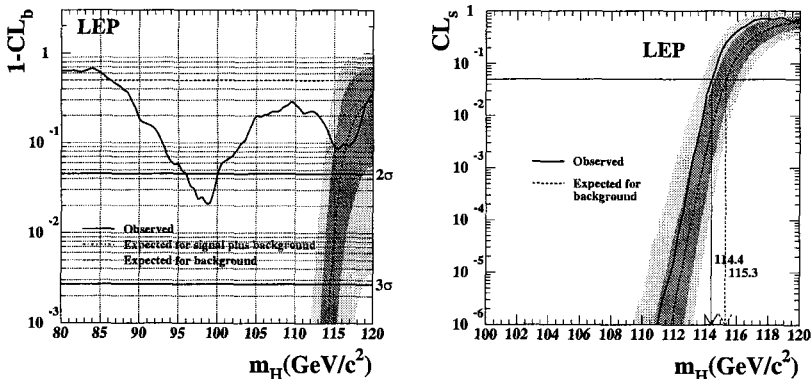


Figure 5: Observed $1 - CL_b$ and CL_s as a function of the tested Higgs mass hypothesis [3].

3 H^0 beyond the Standard Model

Allowing processes beyond the predictions of the minimal Standard Model, the Higgs boson could be produced in a Standard Model like production process but decay into a non-standard final states. One of the possible processes is the so-called flavour blind scenario in which the Higgs boson decays into light quarks or gluons. These decays would lead into hadronic final states with no b -tags. The result after combination of the four experiments is shown in Fig. 6. The preliminary Higgs boson lower mass limit is $112.9 \text{ GeV}/c^2$, assuming the Standard Model production cross-section and 100% branching fraction into hadrons [4].

In so-called fermiophobic models, the fermionic couplings of the Higgs boson are suppressed and it decays into boson pairs. The combined LEP lower mass

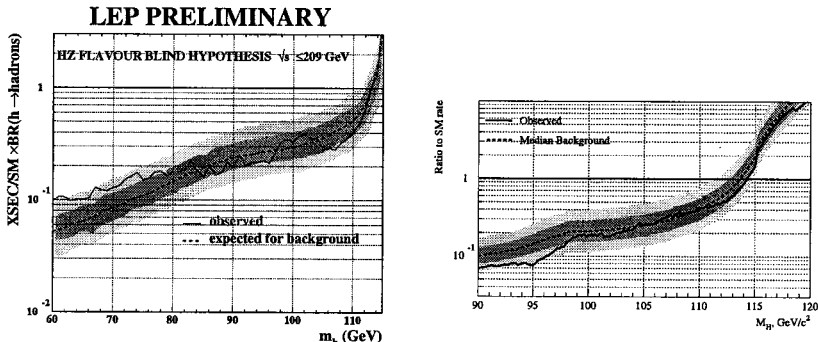


Figure 6: Cross-section exclusion for the flavour blind hypothesis on the left hand side [4]. Excluded rate of invisible Higgs decays compared to the production rate expected in the Standard Model on the right hand side [7].

limit for a Higgs boson decaying into $\gamma\gamma$ is 109.7 GeV/ c^2 [5] and the L3 limit for decay into bosons ($\gamma\gamma/WW^*/ZZ^*$) is 107 GeV/ c^2 [6].

Higgs boson could possibly also decay into invisible (or nearly invisible) particles. The search for these final states was based on reconstruction of the Z boson recoil mass. A preliminary LEP lower mass limit for a Higgs boson with Standard Model cross-section and 100% invisible decay rate is 114.4 GeV/ c^2 [7]. DELPHI has combined the results of the invisible decay with the results of the Standard Model analyses obtaining a limit of 111.8 GeV/ c^2 for any combination of invisible and standard decays [8].

4 More than one Higgs: 2HDM models

Many extensions of the Standard Model, such as supersymmetric models, contain extensions also on the Higgs sector. All such extensions must be in agreement with experimentally confirmed parts of the Standard Model.

The first elementary condition for the Higgs sector is the requirement that $\rho = \frac{m_W^2}{m_Z^2 \cos^2 \theta_w} \sim 1$. This is naturally satisfied if the Higgs sector is extended by additional doublets. Most straight forward extensions of the Higgs sector are the Two Higgs Doublet Models (2HDM) which predict five physical Higgs bosons: h^0 , H^0 , A^0 , H^+ and H^- .

Another important experimental restriction for models is the absence of flavour changing neutral currents. This condition can be satisfied by limiting the fermionic couplings of the Higgs bosons. Two options for couplings are:

- Type II: the first doublet ϕ_1 couples to down-type fermions and the second

doublet ϕ_2 couples to up-type fermions.

- Type I : only the second doublet ϕ_2 couples to fermions.

The Minimal Supersymmetric Standard Model (MSSM) is an example of a 2HDM type II. In MSSM, the production and decay modes of the Higgs bosons depend on few parameters: one free Higgs mass, $\tan\beta$ and mixing angle α . The two lightest neutral Higgs bosons are produced in two complementary processes in MSSM:

- $e^+e^- \rightarrow h^0Z^0 : \sigma_{h^0Z^0} = \sin^2(\beta - \alpha)\sigma_{HZ}^{SM}$
- $e^+e^- \rightarrow h^0A^0 : \sigma_{h^0A^0} = \cos^2(\beta - \alpha)\bar{\lambda}\sigma_{HZ}^{SM}$

where $\bar{\lambda}$ is the phase space suppression factor near the threshold.

4.1 The lightest neutral Higgs bosons in 2HDM: h^0 and A^0

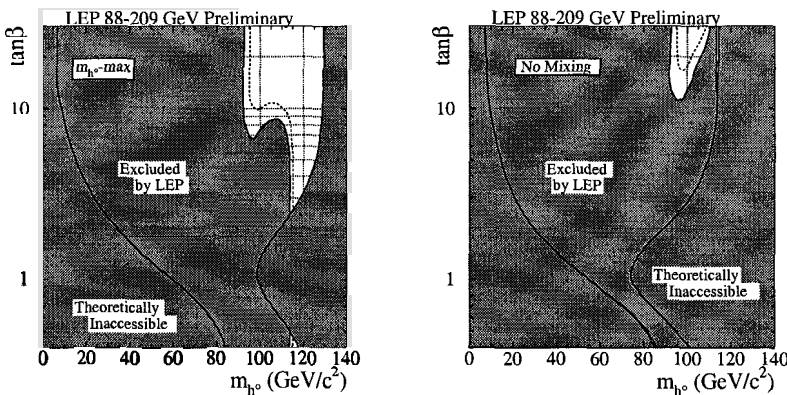


Figure 7: MSSM parameter space regions excluded by LEP in two different MSSM benchmark scenarios [9].

The two lightest neutral MSSM Higgs bosons are expected to decay dominantly into b quarks and they were searched for by using analyses similar to the Standard Model Higgs search analyses. Preliminary lower mass limits were set at $m_{h^0} > 91.0 \text{ GeV}/c^2$ and $m_{A^0} > 91.9 \text{ GeV}/c^2$ [9].

The values of the $\tan(\beta)$ parameter were also restrained (see Fig. 7). Assuming $m_{top} < 174.3 \text{ GeV}/c^2$, maximal stop-mixing and conservative values for other SUSY parameters, parameter range $0.5 < \tan(\beta) < 2.4$ was excluded [9].

h^0 and A^0 were also searched for in more general 2HDM Type II models. Different final states were analysed to scan α , β and Higgs boson masses. Limits

are given as multidimensional parameter scans or projections with different sets of parameter assumptions.

4.2 Charged Higgses

Charged Higgs bosons could be pair produced in e^+e^- collisions with masses up to half of the centre-of-mass energy. In 2HDM type II they decay into $H^+ \rightarrow \tau\nu$ or $H^+ \rightarrow cs$. This results in three possible final states: a) four c and s quark jets, b) c and s jets + τ lepton + neutrino or c) two τ leptons + two neutrinos.

A preliminary combined LEP 2HDM type II charged Higgs boson lower mass limit was set at $78.6 \text{ GeV}/c^2$ [10], as can be seen in Fig. 8.

An additional decay channel becomes possible in 2HDM type I: $H^+ \rightarrow W^*A$. W^* is virtual and the decay is allowed if the pseudoscalar Higgs A light enough. Branching fraction of this process can be large if fermionic decay is suppressed. A preliminary DELPHI limit for 2HDM type I charged Higgs boson is $76.7 \text{ GeV}/c^2$ (assuming $m_A > 12 \text{ GeV}/c^2$) [11].

4.3 Doubly charged Higgses

Left-right symmetric SUSY models with automatic R-parity conservation can have H^{++} with a mass of the order of $100 \text{ GeV}/c^2$. The dominant decay is to same sign lepton pairs.

Stringent limits exist for $H^{++} \rightarrow e^+e^+$ from high energy Bhabha exchange and for $H^{++} \rightarrow \mu^+\mu^+$ from the absence of muonium to antimuonium transitions

Searches for $e^+e^- \rightarrow H^{++}H^{--} \rightarrow \tau^+\tau^+\tau^-\tau^-$ were performed. Highest mass limit is from OPAL: $98.5 \text{ GeV}/c^2$ [12] (See Fig. 8.)

5 Other LEP Higgs searches

It was not possible to present all LEP Higgs analyses and results in this review due to limited space. Other searches include e.g. various SUSY and 2HDM parameter scans, Higgs bosons with anomalous couplings, 2HDM with CP-violation, model independent scalar boson searches and single H^\pm or $H^{\pm\pm}$ production. No evidence for Higgs bosons has been found in these searches.

More information about all LEP Higgs searches can be found in publications and web pages of ALEPH, DELPHI, L3 and OPAL collaborations and the LEP Higgs Working Group.

6 Conclusions

Many models and hypotheses have been tested at LEP. No discoveries have been made and a large number of exclusion limits has been set. Parameterspace

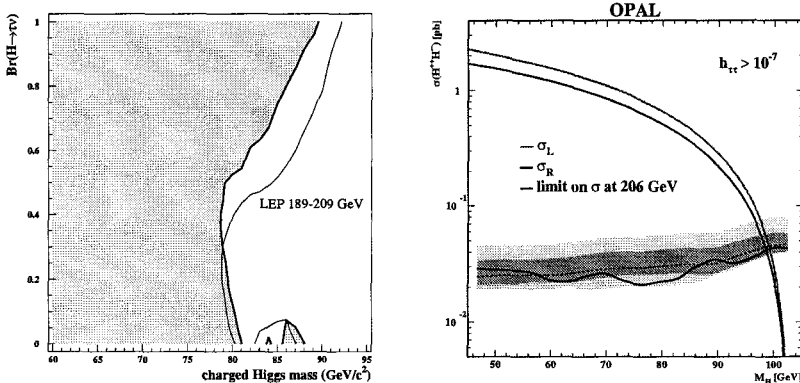


Figure 8: Preliminary LEP exclusion limits for 2HDM Type II charged Higgs boson, on the left. OPAL exclusion for the doubly charged Higgs boson, on the right.

of the Minimal Supersymmetric Standard Model (MSSM) has been restricted severely but the model has not been completely excluded.

LEP collaborations are still active and more analyses and interpretations will be still published in next few years.

Acknowledgments

The author wants to thank all members of the four LEP collaboration who have contributed to the Higgs boson searches.

References

- [1] Information about the LEP Working Group for Higgs Boson Searches and combined results can be found at:
<http://lephiggs.web.cern.ch/LEPHIGGS/www/Welcome.html>.
- [2] The LEP Collaborations ALEPH, DELPHI, L3, OPAL, the LEP Electroweak Working Group, the SLD Electroweak and Heavy Flavour Groups, "*A Combination of Preliminary Electroweak Measurements and Constraints on the Standard Model*", LEPEWWG/2003-02, hep-ex/0312023 (2003).
- [3] ALEPH, DELPHI, L3, and OPAL Collaborations, the LEP Working Group for Higgs Boson Searches, *Search for the Standard Model Higgs Boson at LEP*, CERN-EP/2003-011 (2003).
- [4] the LEP Working Group for Higgs Boson Searches, *Flavour Independent Search for Hadronically Decaying Higgs Bosons at LEP*, LHWG note

- 2001-07, hep-ex/0107034 (2001).
- [5] ALEPH, DELPHI, L3 and OPAL Collaborations, the LEP Working Group for Higgs Boson Searches, *Searches for Higgs Bosons Decaying into Photons: Combined Results from the LEP Experiments*, LHWG note 2002-02 (2002).
 - [6] P. Achard et al. (the L3 Collaboration), *Phys. Lett.* **B** 534 (2002) pp. 28-38.
 - [7] ALEPH, DELPHI, L3 and OPAL Collaborations, the LEP Working Group for Higgs Boson Searches, *Searches for Invisible Higgs bosons: Preliminary combined results using LEP data collected at energies up to 209 GeV*, LHWG note 2001-06, hep-ex/0107032 (2001).
 - [8] J.Abdallah et al (the DELPHI Collaboration), *Searches for invisibly decaying Higgs bosons with the DELPHI detector at LEP*, CERN-EP 2003-046 (2003), Accepted by Eur. Phys. J. C.
 - [9] ALEPH, DELPHI, L3 and OPAL Collaborations, the LEP Working Group for Higgs Boson Searches, *Searches for the Neutral Higgs Bosons of the MSSM: Preliminary Combined Results Using LEP Data Collected at Energies up to 209 GeV*, LHWG note 2001-04, hep-ex/0107030 (2001).
 - [10] ALEPH, DELPHI, L3 and OPAL Collaborations, the LEP Working Group for Higgs Boson Searches, *Search for Charged Higgs bosons: Preliminary Combined Results Using LEP Data Collected at Energies up to 209 GeV*, LHWG note 2001-05, hep-ex/0107031 (2001).
 - [11] M.Battaglia et al., *Search for Charged Higgs Bosons at LEP in General Two Higgs Doublet Models*, DELPHI 2003-038-CONF-658 (2003), Contributed paper for EPS 2003 and LP 2003.
 - [12] G.Abbiendi et al. (the OPAL Collaboration), *Phys. Lett.* **B** 526 (2002) 221-232.

SEARCH FOR HIGGS BOSONS WITH THE ATLAS DETECTOR

Simonetta Gentile^a

Università di Roma, "La Sapienza", Sezione di Roma1 dell'INFN, Roma, Italy

Abstract. The Large Hadron Collider experiments are designed to fully explore new physics at the TeV center-of-mass region. The performance and the discovery potential of the LHC detectors, in particular of ATLAS, for the only unobserved Standard Model particle, the Higgs boson, are discussed. The discussion includes also the supersymmetric Higgs bosons, postulated in the Minimal Supersymmetric extension to the Standard Model.

1 Introduction

For one decade, precision tests of the Standard Model of Electroweak Interactions (SM) [1] have been performed at LEP. The observed consistency provided great confidence in the validity of the SM and encouraged the use of all experimental data to predict the mass of the last unobserved particle of the model: the Higgs boson. The derived limit on its mass from electroweak fit is $m_H < 219$ GeV at 95 % Confidence Level [2]. Direct searches for the Standard Model Higgs set a lower limit on its mass $m_H > 114.4$ GeV at 95 % Confidence Level [3].

Despite the success of the precision tests of the SM, extensions of the Standard Model have been proposed, of which the most investigated is the Minimal Supersymmetric Standard Model (MSSM). This theory requires two Higgs doublets. This gives rise to five Higgs bosons: a charged scalar pair, two neutral CP-even, the lightest of which is called h , and a neutral CP-odd, A [4]. The discovery of any one of these particles is crucial to prove the validity of the model. Based on LEP data, limits on the masses of charged, H^\pm [5], and neutral Higgs bosons, h and A [6], exist over a large region of the parameter space.

Recent studies by the Tevatron experiments show a reduction in the amount of integrated luminosity needed to discover Higgs bosons at the Tevatron collider relative to previous studies. These improvements come from more optimized methods of analysis. An integrated luminosity of $4\text{-}8 \text{ fb}^{-1}$, expected to be collected by 2009, is needed for a 95% C.L. exclusion of a Higgs boson with $m_H \approx 120$ GeV [7].

One of the goals of the Large Hadron Collider (LHC) general-purpose experiments, ATLAS and CMS, is to look for the SM Higgs boson and to prove or exclude the existence of supersymmetric Higgs bosons in the parameters region not excluded by the LEP data. This ambitious program requires high performance detectors and high luminosity from the machine.

This article is organized as follows: Section 2 reviews the expected performance of one of the general-purpose detectors, ATLAS, and expected integrated

^ae-mail: simonetta.gentile@cern.ch,simonetta.gentile@roma1.infn.it

luminosities. The production of the SM Higgs in pp interactions at 14 TeV, its decay modes and the expected backgrounds are described in Section 3. The discovery potential for various integrated luminosity scenarios are discussed in Section 4 and the measurement of the Higgs properties, such as mass and couplings, in Section 5. The hunt of supersymmetric Higgs is reviewed in Section 6. The conclusions and future prospects for the future are given in Section 7.

2 Experimental tools: Large Hadron Collider, ATLAS

The Large Hadron Collider, now under construction at CERN, will collide proton beams at centre-of-mass energy of 14 TeV, with very high luminosity ($10^{33} - 10^{34} \text{ cm}^{-2}\text{s}^{-1}$). The first physics data will be collected in 2007. In the following the main features of the ATLAS detector are briefly summarized [9]:

- **Superconducting Magnet:** It is composed of: a) a solenoid, which provides a 2 T magnetic field for the inner detector, b) a barrel air toroid, consisting of eight flat coils of 25m length. The bending power for muons is typically 4 T·m and c) Two end-cap toroids, which provide a field of 6 T·m for muon momentum measurements.
- **Inner Tracking detector:** This is inside in the solenoid magnetic field and consists of 140 million Si pixels and 6 million silicon strip detectors near the interaction point, and 0.4 million strawtubes. The momentum resolution of the inner tracker for charged particle is $\frac{\sigma}{p_T} \sim 5 \times 10^{-4} p_T (\text{GeV}) \oplus 0.01$.
- **Electromagnetic Calorimeter:** This is a liquid argon-lead sampling calorimeter with accordion shape in the barrel and end-cap regions (total of about 180000 channels). The energy resolution is $\frac{\sigma}{E} \sim \frac{10\%}{\sqrt{E}}$.
- **Hadronic Calorimeter:** It is a copper-liquid argon calorimeter in the end-cap region ($\sim 10,000$ channels) and a Fe-scintillator calorimeter scintillators ($\sim 10,000$ channels) in barrel region. The liquid argon tungsten forward calorimeters extend the coverage to $|\eta| = 4.9$. The hadronic jet energy resolution is $\frac{\sigma}{E} \sim \frac{50\%}{\sqrt{E}} \oplus 0.03$.
- **Muon spectrometer:** a) 1194 precision tracking chambers made of more than $3.7 \cdot 10^6$ Monitored Drift Tubes (MDT) covering the rapidity range $|\eta| < 2.7$. The momentum resolution ranges from about 2% for 100 GeV muons to 10% for 1 TeV muons. b) 32 Cathode Strip Chambers (CSC) consisting of more than 24 thousand precision and 6 thousand transverse coordinate strips covering the most forward rapidity region ($|\eta| = 2.0 - 2.7$) in the inner most stations of the muon system. c) 596 Resistive Plate Chambers (RPC) in the barrel region ($|\eta| < 1$) and

4256 Thin Gap Chambers (TGC) in the end-cap region to provide muon triggers and to measure the second coordinate of the muon tracks.

The ATLAS detector will have excellent lepton and photon identification capabilities, and accurate energy and angular measurements over almost 4π coverage.

The expected potential will be discussed under different assumptions on the integrated luminosity:

- $\int \mathcal{L} dt = 10 \text{ fb}^{-1}$, corresponding to data collected in approximately one year of data taking at the initial LHC luminosity ($\mathcal{L} = 10^{33} \text{ cm}^{-2} \text{s}^{-1}$).
- $\int \mathcal{L} dt = 30 \text{ fb}^{-1}$, collected in 3 years at low luminosity.
- $\int \mathcal{L} dt = 100 \text{ fb}^{-1}$, collected in one year at high luminosity,
- Ultimate luminosity $\int \mathcal{L} dt = 300 \text{ fb}^{-1}$.

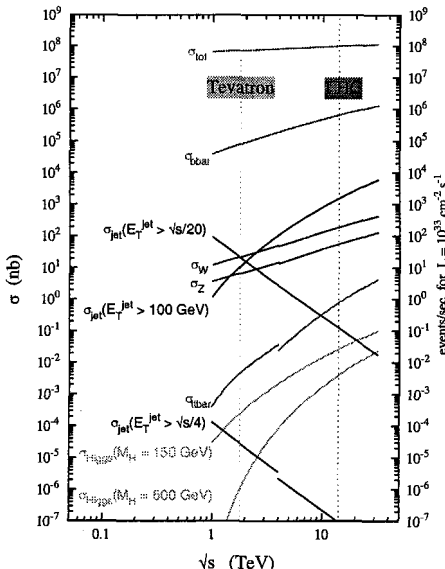


Figure 1: Cross section of various physics processes in pp and p \bar{p} collisions as a function of center-of-mass energy.

3 Standard Model Higgs: production and decays

The search for the Standard Model Higgs has been studied in ATLAS looking at a large number of different production and decay modes up 1 TeV [9]. The

difficulty to extract the Higgs signal from the huge QCD background dictates the choice of channels with leptons and photons. Fig. 1 shows that the cross-section of the QCD backgrounds is many orders of magnitude higher than the cross-section of a Higgs of mass 150 GeV. The most copious background is made of QCD jets and W, Z gauge boson production. At the LHC the production

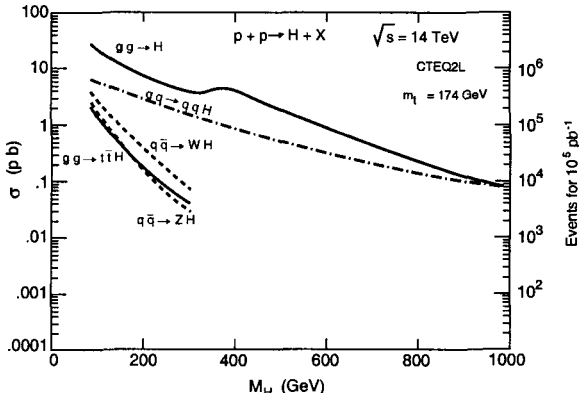


Figure 2: Higgs production cross section at LHC as a function of m_H for different production mechanism.

cross section for the Standard Model Higgs boson is dominated by gluon-gluon fusion (Fig.2); the second most important process is the fusion of vector bosons radiated from initial-state quarks. The relative contributions of the two processes depend on the Higgs boson mass. For $m_H < 2m_Z$, vector boson fusion amounts to about 20% of the total production cross section, and becomes more important with increasing mass. Other production mechanisms, such as associated production $t\bar{t}H, WH, ZH$, have cross-sections of approximately 1-10% of the gluon-gluon fusion. Fig.3 shows the Higgs decay modes as a function of m_H . The dominant decay modes are W^+W^- and ZZ for Higgs mass $m_H > 2m_Z$ and $H \rightarrow b\bar{b}$ for $m_H < 2m_Z$. Because of the large QCD background it is necessary to rely on Higgs decays that produce isolated energetic leptons or photons in the final state.

The Higgs discovery criterion used here is the so called “ 5σ signal significance”, defined as $\frac{S}{\sqrt{B}} \geq 5$, where S is the number of signal events and B the number of background events.

Recent analyses have shown the promising contribution of WW fusion in the low-mass range [10]. In this process the Higgs boson is accompanied by two jets in the forward regions of the detector, originating from the initial quarks that emit the vector bosons. In addition, central jet activity is suppressed due the lack of color exchange between the quarks. This is in contrast to most background processes, where there is color flow in the t-channel. Therefore jet

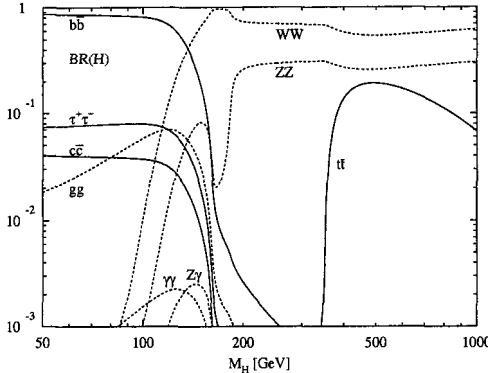


Figure 3: Higgs decay branching ratios as a function of m_H . The mass region excluded by LEP direct searches is below 114 GeV.

tagging in the forward region of the detector, with a veto of jet activity in the central region, are useful tools to enhance the signal-to-background ratio.

4 Standard Model Higgs boson discovery potential.

The LEP data favour the m_H region between 114.4 GeV and 219 GeV. In this region a combined 5σ significance can be reached by combining the decays $t\bar{t}H \rightarrow t\bar{t}b\bar{b}$, $H \rightarrow \gamma\gamma$, $H \rightarrow WW^{(*)}$, $H \rightarrow ZZ^{(*)}$. In the low mass region ($m_H < 130$ GeV) the Higgs will be searched mainly through $H \rightarrow \gamma\gamma$ and the associated production $t\bar{t}H$. Exploiting the characteristics of the WW -fusion channel it is possible to extract a very clear signal from $H \rightarrow WW^* \rightarrow \ell\nu\ell\nu$. The Higgs is produced with a pseudorapidity distribution $\Delta\eta$ of the tag jets, which allows a good separation of signal from background (Fig. 4a). Including all channels, each experiment should be able to discover a SM Higgs with only 10 fb^{-1} , expected to be collected in one year of data taking (Fig. 5).

In this region the observation of all channels is important to reach the $4\text{-}5\sigma$ significance. For heavy Higgs mass ($m_H > 2m_Z$) the search will be easier through the $H \rightarrow ZZ \rightarrow 4\ell$ gold-plated channel (Fig. 4b).

4.1 Standard Model Higgs: Parameter measurements

Although the Higgs boson discovery is possible with only $\int \mathcal{L} dt = 10 \text{ fb}^{-1}$, higher integrated luminosity is necessary to measure the Higgs parameters, e.g. mass, width, branching ratios and couplings. The ultimate luminosity, $\int \mathcal{L} dt = 300 \text{ fb}^{-1}$, is necessary to measure the Higgs mass with a precision of 0.1 % over the mass range between 130 and 450 GeV [11].

Recent results for Higgs-coupling measurements with a global fit method use all the production modes and detection channels with the ultimate luminosity.

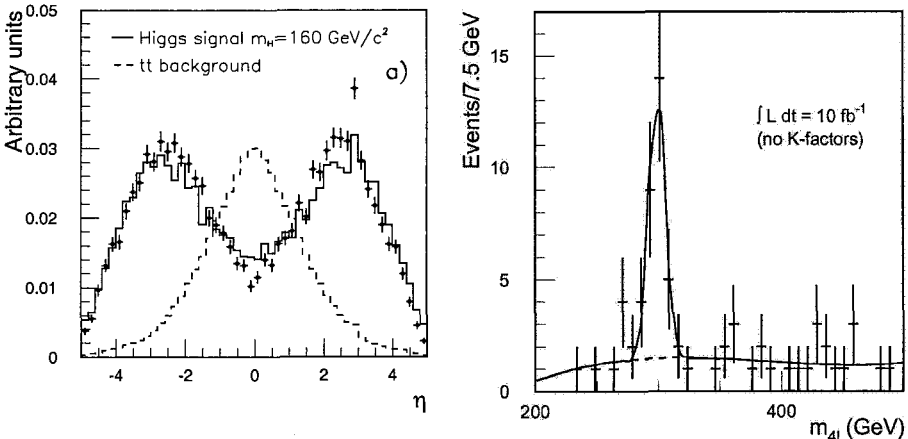


Figure 4: a) Pseudorapidity distribution of the tag jets in qqH events with $m_H=160 \text{ GeV}$ and in the $t\bar{t}$ background (left). b) Invariant mass distribution for 300 GeV Higgs signal over background in the four lepton final state for $\int \mathcal{L} dt = 10 \text{ fb}^{-1}$ (right) .

The branching ratio $H \rightarrow ZZ$ can be measured with 10-20 % accuracy for $m_H > 125 \text{ GeV}$. The Higgs couplings to Z, W, τ and top-quark can be measured with an accuracy of better than 20 %, for Higgs bosons heavier than 150 GeV.

5 Search for Minimal Supersymmetric Standard Model Higgs bosons

The prospects for the detection of the MSSM Higgs bosons at LHC have been evaluated [9, 12] in the scenario in which supersymmetric (SUSY) particle masses are large, so that the Higgs bosons do not decay in SUSY particles. At three level, all Higgs boson masses and couplings can be expressed in terms of only two parameters: m_A , the mass of the CP-odd boson, and $\tan\beta$, the ratio of the vacuum expectation values of the two Higgs doublets. Some of the SUSY Higgs decay modes are the same as for the SM Higgs boson: $h \rightarrow \gamma\gamma, t\bar{t} \rightarrow tt\bar{b}\bar{b}$.

Others modes, strongly enhanced at high $\tan\beta$, e.g. $H/A \rightarrow \tau^+\tau^-$, $H/A \rightarrow \mu^+\mu^-$, have been investigated [9]. The conclusion of these studies is that the complete region of parameter space should be accessible for the discovery of MSSM Higgs bosons, already with an integrated luminosity $\int \mathcal{L} dt = 30 \text{ fb}^{-1}$. Over a large fraction of the parameter space, more than one Higgs boson and more than one decay mode can be detected. An exhaustive summary of

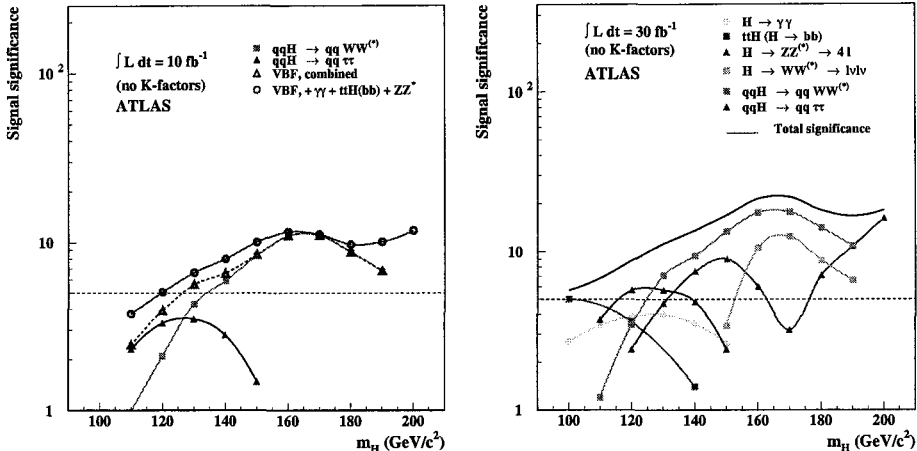


Figure 5: ATLAS sensitivity for the discovery of a Standard Model Higgs Boson for $\int \mathcal{L} dt=10 \text{ fb}^{-1}$ (left), and $\int \mathcal{L} dt=30 \text{ fb}^{-1}$ (right).

accessible decay modes can be found in Ref. [9]. The most difficult region is at moderate $\tan\beta$ and large m_A , where only the lightest Higgs boson would be observable.

As in the SM case the search for Higgs boson decay in $\gamma\gamma$ can also be performed using associated WH and ttH production. The sensitivity of these channels is shown in Fig. 6a).

From Fig. 6a) it is clear that the region with m_h approximately 100 GeV and $\tan\beta$ greater than 10 is not covered by the above mentioned decay channels of the h boson. In the most general case, considering all MSSM Higgs bosons, this region is accessible to the neutral boson H decays into $\mu^+\mu^-, \tau^+\tau^-$ and to charged boson decays $H^\pm \rightarrow \tau\nu$. Recent studies have been performed to explore this region using the channel $b\bar{b} h \rightarrow \mu^+\mu^-$ (Fig. 6b) [14, 15]. This search requires at the same time an excellent performance in μ detection and in b-tagging. Both features are offered by ATLAS.

The contributions of all channels investigated by ATLAS and CMS are summarized in Fig. 7 as 5σ contours in the m_A vs. $\tan\beta$ plane.

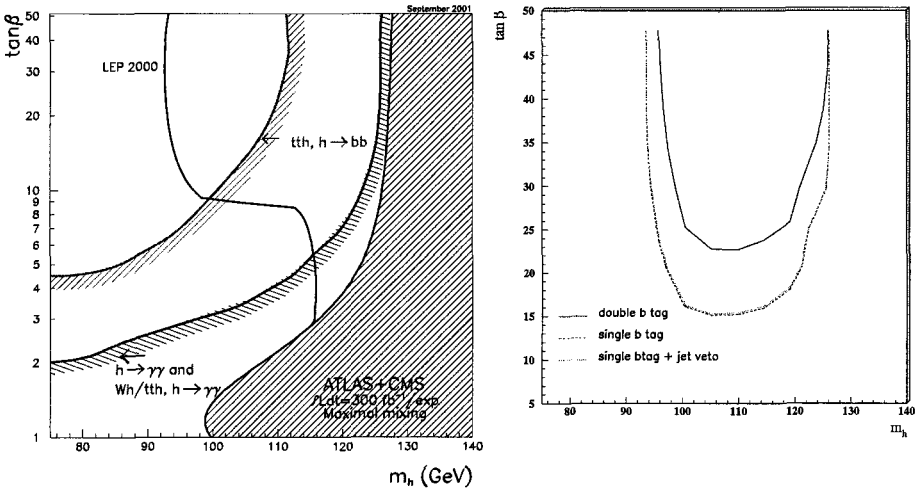


Figure 6: a) The ATLAS+CMS sensitivity for the discovery of the MSSM Higgs boson h , in case of maximal mixing. The 5σ discovery contour curves are shown in the $(\tan \beta, m_h)$ plane for the individual channels and for an integrated luminosity of 300 fb^{-1} . The LEP limits are also shown. The forbidden region is hatched [13]. b) Plot of discovery potential for the $b\bar{b}h$ channel with $h \rightarrow \mu^+\mu^-$ in the maximal mixing scenario. The curves correspond to a signal significance $\sqrt{\frac{s}{B}} = 5$. The integrated luminosity is $\int \mathcal{L} dt = 300 \text{ fb}^{-1}$.

6 Conclusions

The LHC discovery potential for the Standard Model Higgs and MSSM Higgs bosons are extremely promising already in the first year(s) of data taking if the total integrated luminosity is in the range $10-30 \text{ fb}^{-1}$. Measurements of Higgs parameters can reach a precision of 0.1-1.0% for the mass determination, 5-30% for the branching ratios and 10-40% for the couplings with $\int \mathcal{L} dt = 300 \text{ fb}^{-1}$.

Acknowledgments

I would like to thank Elzbieta Richter-Was for her useful comments and Fabiola Gianotti for the helpful discussion, detailed comments and the critical reading of manuscript.

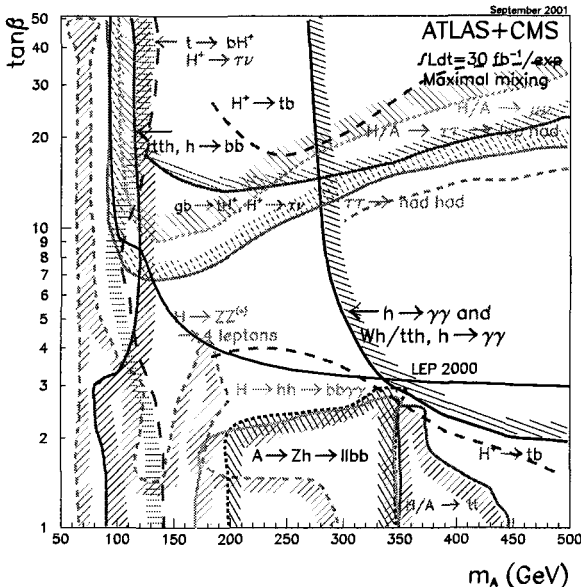


Figure 7: The ATLAS+CMS sensitivity for the discovery of the MSSM Higgs bosons, in the case of maximal mixing. The 5σ discovery curves are shown in the $(\tan\beta, m_A)$ plane for the individual channels and for an integrated luminosity of 30 fb^{-1} . The LEP limit is also shown.

References

- [1] S.L. Glashow, *Nucl.Phys.* 22, 579 (1961); S. Weinberg,, *Phys.Rev.Lett* 19, 1264 (1967); A.Salam," Elementary Particle theory",Ed.N. Svartholm (Almqvist ad Wiksell, Stockholm) (1968), 367.
- [2] The ALEPH and DELPHI and L3 and and OPAL Collaborations and the LEP Electroweak working group, CERN-EP/2002-091.
- [3] ALEPH, DELPHI, L3, OPAL, The LEP Working Group For Higgs Boson Search *Phys.Lett.* **B** 565, 61 (2003)
- [4] H.-P. Nilles, *Phys.Rep.* 1 (1984); H. E. Haber and G. L. Kane, *Phys.Rep.* 75 (1985); R. Barbieri,*Riv. Nuovo. Cim.* (1988) 11.
- [5] The ALEPH and DELPHI and L3 and and OPAL Collaborations and the LEP Higgs working group, LHWG Note 2001-05 (2001).
- [6] The ALEPH and DELPHI and L3 and and OPAL Collaborations and the LEP Higgs working group, LHWG Note 2001-04 (2001).
- [7] The CDF and and D0 Collaborations and the Tevatron Higgs Sensitivity group, FERMILAB-PUB-03/320-E (2003)

- [8] CMS Coll., Technical Proposal, report CERN/LHCC/94-38 (1994).
- [9] ATLAS Coll., ATLAS Detector and Physics Performance: Technical Design Report, Volume 2, report CERN/LHCC/99-15 (1999).
- [10] S.Asai et al., Prospect for search of a Standard Model Higgs Boson in ATLAS using Vector Boson Fusion, SN-ATLAS-2003-024.(2003)
- [11] M. Duehrssen,*Prospects for the measurement of Higgs boson coupling parameters in the mass rang 110-190 GeV*, ATL-PHYS-2003-030 (2003).
- [12] E. Richter-Was et al., *J.Mod.Phys.* 1371 (1998).
- [13] F. Gianotti, Presentation at LHC Committee 5 July 2000.
- [14] S.Gentile et al. *Search for supersymmetric neutral Higgs h in the decay h → μ⁺μ⁻ in ATLAS detector at LHC*, ATL-PHYS-2003-013,(2003).
- [15] S.Gonzales et al. *Analysis of the process pp → b̄bh/A→ μ⁺μ⁻ in MSSM with m_A > 125 GeV*, ATL-PHYS-2002-021,(2002).

RESULTS ON B PHYSICS AT LEP

J. Salt ^a

*IFIC, Edificio Institutos de Investigación, Apdo. Correos 22085, Valencia, E-46071,
Spain*

Abstract. In this talk a review of a selection of recent results on B Physics at LEP is given, in particular, the status of the determination of V_{cb} and V_{ub} CKM matrix elements and the B oscillations

1 Introduction

In the LEP era, a crucial progress has been performed in the development of b tagging techniques, in the test of the Standard Model in the fermion sector (R_b , R_c , asymmetries,etc), in the measurement of relevant quantities of b decay and production (as BR's, lifetimes, ...), studying QCD in the non-perturbative regime, searching for new Physics through virtual processes 1. The main features of the subjects which will be described in this review are the following: (1) the very high precision measurements, most of them with high statistics provided by the consideration of other useful channels, (2) the exploitation of better and performant analysis techniques and algorithms which have been applied to the data, (3) in the interpretation of the quark decays: it is necessary to understand and control theories and models which relate quark to hadrons (HQET, OPE, LQCD).

2 B decay and production properties

2.1 b fragmentation function

The main result is the extraction of the b-quark fragmentation functions $f(x_B^{prim})$, $f(x_B^{weak})$ ^b and, for first time, $f(z)$ ^c from real data 2. It has been applied an unfolding method and one can see the first central moments of the unfolded functions. In figure 1 (left) we give a comparison of the results from this analysis for x_B^{weak} compared to 2 other recent analyses from ALEPH, OPAL and SLD. The main results coming from DELPHI experiment are: (a) the results given in Table 1; results for $f(z)$ have been reconstructed for first time; (b) the Peterson et al, Kartvelishvili et al., Collins/Spiller models for non-perturbative are unable to reproduce the measurements when used in conjunction with NLL perturbative calculations; (c) using present measurements, the non-perturbative component has been extracted independently of any model assumption; therefore it can be applied in another environment

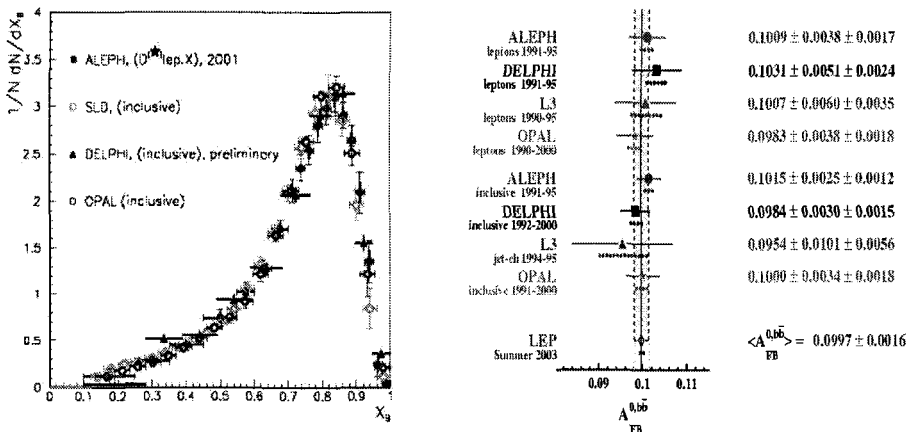
^ae-mail: Jose.Salt@ific.uv.es

^blabels 'prim' and 'weak' mean primary and decaying b-hadron

^c $x_B = 2E_B/\sqrt{s}$ and $z = (E + P_L)_B/(E + p)_b$, p_L is de hadron momentum in the direction of the b quark. $(E + p)_b$ is the sum of energy plus the momentum of the b quark just before

	Mean	Variance
$f(x_B^{prim})$	$0.7346 \pm 0.0008(stat) \pm 0.0055(syst)$	$0.0318 \pm 0.0005(stat)$
$f(x_B^{weak})$	$0.7153 \pm 0.0007(stat) {}^{+0.0049}_{-0.0052}(syst)$	$0.0300 \pm 0.0004(stat)$
$f(z)$	$0.8872 \pm 0.0012(stat) \pm 0.0054(syst)$	$0.0027 \pm 0.0001(stat)$

Table 1: Results on Fragmentation in terms of the first two central moments

Figure 1: Left: Unfolded distributions from ALEPH, OPAL, SLD and DELPHI. Right: Summary of $A_{FB}^{0,b\bar{b}}$ measurements

2.2 b forward-backward asymmetries

One of the quantities which has caused a strong controversy has been the Forward Backward Asymmetry ($A_{FB}^{b\bar{b}}$). In DELPHI experiment a special attention and a rigorous checking process concerning the systematic errors have been applied. $A_{FB}^{b\bar{b}}$ is measured at three points around the Z pole and a general procedure is followed to obtain the so-called pole asymmetry (the results for $A_{FB}^{b\bar{b}}$ have been connected to the Z pole and the effects of initial state radiation, γ and γ/Z exchange have been subtracted). OPAL (3) has repeated an update of their measurements to the Summer Conferences (4). The average of their results is (pole asymmetry): $A_{FB}^{b\bar{b}} = (9.98 \pm 0.27 \pm 0.13)\%$ In figure 1 (right) one can see the compilation of the A_{FB} measurements with the LEP average in the bottom of the plot. The value for the pole FB asymmetry is $A_{FB}^{0,b\bar{b}} = 0.0997 \pm 0.0016$.

At LEP experiments we have got the following progress on A_{FB} : (1) a

fragmentation, E_B is the reconstructed b hadron energy

second iteration has been finished on $A_{FB}^{0,b}$ using final reprocessing and the latest experimental techniques; (2) obtention of significant improvements in the experimental precision and control of the systematic uncertainties, (3) LEP and SLD averages are internally consistent; (4) 3σ difference between hadronic and leptonic mixing angle is confirmed; (5) the interpretation of Electroweak data is difficult but a 3σ difference is not dramatic.

2.3 b lifetime

LEP experiments have done a big effort in the measurement of b-hadron lifetime. Only applying arguments in which spectator effects are included in a hierarchy in the lifetime arise $\tau(B^+) > \tau(B^0) > \tau(B_s^0) > \tau(\Lambda_b^0)$ but one can formulate the problem more formally using OPE (Operator Product Expansion). The lifetime measurement relies in the resolution of the decay length and in the resolution of momentum. Elaborated neural networks based on particle identification and secondary vertex reconstruction have been developed to accurately reconstruct the b-hadron energy. Final results from DELPHI experiment 5: are given in table 2.

$\tau_{B^+} = 1.624 \pm 0.014(stat) \pm 0.018(syst)$ ps
$\tau_{B^0} = 1.531 \pm 0.021(stat) \pm 0.031(syst)$ ps
$\frac{\tau_B^+}{\tau_B^0} = 1.060 \pm 0.021(stat) \pm 0.024(syst)$

Table 2: *Summary of results on Lifetimes in DELPHI*

The result of the average b-hadron lifetime in DELPHI yields $\tau_b = (1.570 \pm 0.005(stat) \pm 0.008(syst))ps$, this value being the most precise measurement worldwide.

In the plot of figure 2 (left) one can see the b hadron lifetimes. From these results several remarks can be done: $\tau(B^+)/\tau(B^0) = 1.073 \pm 0.014$ so we have a 5.2σ difference and this effect is in agreement with the theory. Λ_b lifetime is shorter because of WA^d effect but the experimental result says that the effect is more important: $\tau(\Lambda_b)/\tau(B^0) = 0.784 \pm 0.034$, so we have a 20% difference when the proponents of the HQE model foresee that there should be at most 10% difference between b-baryon and B^0 lifetime 6.

3 Extracting the CKM matrix elements

Apart of these measurements, during the last years there has been a lot of activity focused in the determination of the parameters related to the elements of the CKM matrix 9. There are several parametrizations, for instance, the

^dWeak Annihilation

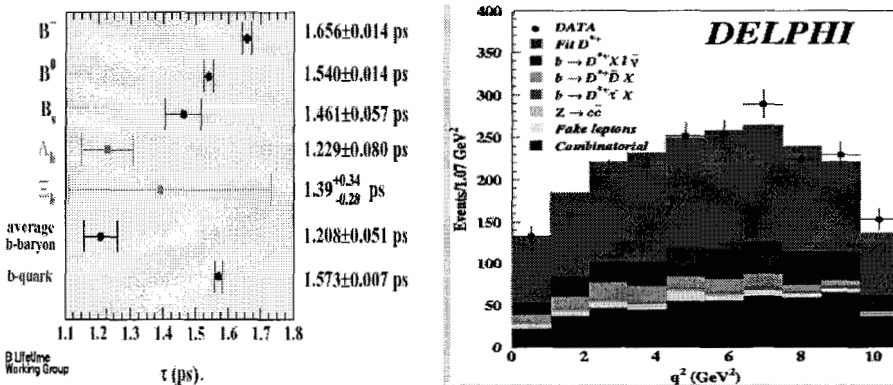


Figure 2: Left: Measurements of the lifetimes of b particles (B Lifetime Working Group), Right: Fit on real data events. All periods are combined. Only events selected within the Δ_m mass interval corresponding to the D^{*+} signal are displayed

Wolfenstein parameterization (λ, A, ρ, η). B physics studies play an important role in the determination of those parameters, as we can see in the scheme of the CKM metric for $|V_{cb}|$, $|V_{ub}|$, $|V_{td}|$ and $|V_{ts}|$.

Moreover, the determination of these parameters is also important to establish the Unitarity Triangle which include the constraints coming from the physics results obtained from experiments.

3.1 V_{cb} and V_{ub} measurements

The value of V_{cb} is extracted by studying the decay partial width for the process $\bar{B}_d^0 \rightarrow D^{*+} l^- \bar{\nu}_l$ as a function of w where $w = (M_{D^{*+}}^2 + M_{\bar{B}_d^0}^2 - q^2)/2M_{\bar{B}_d^0}M_{D^{*+}}$ by using the HQET, the differential partial width for the decay is given by $\frac{d\Gamma}{dw} = \frac{G_F^2}{48\pi^3} |V_{cb}|^2 K(w) F_{D^*}(w)$

In the Heavy Quark limit ($m_b \rightarrow \infty$) $F_{D^*}(1)$ is normalized to 1 at the point of 0 recoil. Corrections to $F_{D^*}(1)$ have been calculated to take into account the effects of finite quark masses and QCD corrections and it gives $F_{D^*}(1) = 0.91 \pm 0.04$. The shape of this form factor is parameterized in terms of the form factor slope ρ_{D^*} and the form factor ratios R_1 and R_2 [7]. From the mass difference distribution corresponding obtained for channel $D \rightarrow K\pi$ it is possible to obtain the number of D^* candidates for the signal. Three channels are considered: $D^0 \rightarrow K^-\pi^+$, $D^0 \rightarrow K^-\pi^+\pi^+\pi^-$, $D^0 \rightarrow K^-\pi^+(\pi^0)$. Applying an elaborated analysis procedure to take into account the different backgrounds we can have access to the spectrum of the q^2 variable one gets: $F_{D^*}(1)|V_{cb}| = 0.0392 \pm 0.0018$, $\rho_{A_1}^2 = 1.32 \pm 0.15$ which is the final result of the experimental procedure [8]. Performing an average within DELPHI the results

given in 3 are obtained:

$F_{D^*}(1) V_{cb} = 0.0377 \pm 0.0011_{stat} \pm 0.0019_{syst}$ ps
$\rho_{A_1}^2 = 1.39 \pm 0.10_{stat} \pm 0.33_{syst}$
$BR(\bar{B}_d^0 \rightarrow D^* + l^- \nu_l) = (5.39 \pm 0.11_{stat} \pm 0.33_{syst})\%$
$ V_{cb} = 41.4(1 \pm 0.029_{expt} \pm 0.051_{syst} \pm 0.043_{th})10^{-3}$

Table 3: Average results (DELPHI). $|V_{cb}|$ obtained by using $F_{D^*}(1) = 0.91 \pm 0.04$

The distributions of q^2 for events are shown in figure 2 (right) with the contributions for the fitted components.

In the left plot of figure 3 one can see two results from DELPHI: one is the recent result and it's tagged as 'DELPHI (excl)'. In the right plot one can appreciate the ellipse regions in the $F_{D^*}(1)|V_{cb}| - \rho_{A_1}^2$ plane.

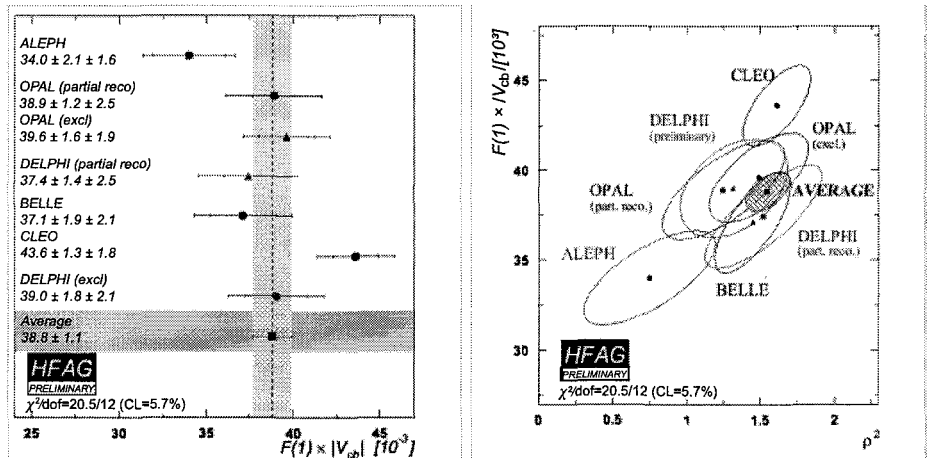


Figure 3: Comparison between the values of $F_{D^*}(1)|V_{cb}|$ and $\rho_{A_1}^2$ measured in different experiments. Results labeled as 'DELPHI (excl)' (left) and 'DELPHI (preliminary)' (right) correspond to the same analysis 8

Another possibility is to perform an inclusive measurement of $|V_{cb}|$. Using the Operator Product Expansion we can express the semileptonic amplitude as a function of V_{cb} and a set of Heavy Quark parameters as m_b , m_c , μ_π^2 , ρ_D^2 , ρ_{LS}^3 , which we are going to measure (10). To do that we evaluate the moments of 2 spectra: the spectrum of the hadronic mass in the decay $B \rightarrow X_c l \nu_l$ and the spectrum of the lepton energy.

For the hadronic mass the crucial point is to include properly the D^{**} component by using a dedicated variable. Once it has been done it is straightforward to evaluate the hadronic moments by considering the sum of D , D^* and D^{**} .

On the other hand it can be evaluated the moments of the lepton energy spectrum and to perform a 4-parameter fit by applying constraints on m_b and m_c and fixing μ_G^2 and ρ_{LS}^3 . So we obtain these results shown on the table 4 which can be used in the expression of Γ_{sl} and to obtain V_{cb} .

Parameter	<i>Value</i> \pm <i>fitting error</i> \pm <i>syst moments</i> \pm <i>syst.theo</i>
$m_b^{kin}(1GeV)$	$4.570 \pm 0.082 \pm 0.010 \pm 0.005 GeV$
$m_c^{kin}(1GeV)$	$1.133 \pm 0.134 \pm 0.019 \pm 0.020 GeV$
$\mu_\pi^2(1GeV)$	$0.382 \pm 0.070 \pm 0.031 \pm 0.020 GeV^2$
ρ_D^3	$0.089 \pm 0.039 \pm 0.004 \pm 0.010 GeV^3$

Table 4: Values of the HQE parameters obtained from the fit

The result is $V_{cb} = 42.4(1 \pm 0.015(expt) \pm 0.019(syst) \pm 0.010(th))10^{-3}$ where now we have an especific error coming from the previous determination of the Heavy Quark parameters. There is an error statistical plus systematics and a theoretical error coming from the value of α_s parameter.

As an illustration of the fit procedure one can see the 2D plots of the 2 fitted parameters with the regions constrained after the fit in figure 4.

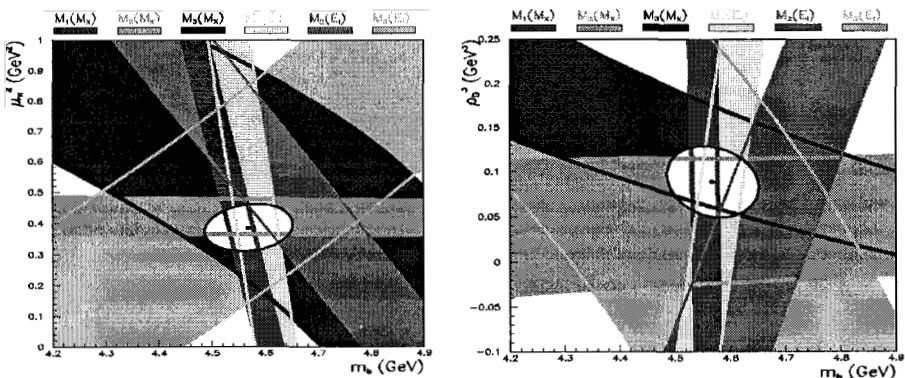


Figure 4: The projection of the constraints of the 6 measured moments on the $m_b(1GeV)$ - $\mu_\pi^2(1GeV)$ (left) and $m_b(1GeV)$ - ρ_D^3 (right) planes. The bands correspond to the total measurement accuracy and are given by keeping all the other parameters at their central values. The ellipses represent the 1 sigma contours

The ellipses give the intersection region of all these regions with an accuracy of 1 sigma. In conclusion, V_{cb} has : (a) a better experimental error , and (b) we have decreased the theoretical error by the isolation of the error coming from the determination of the Heavy Quark parameters in a so-called 'fitting error' (which is also experimental).

The situation for V_{ub} is clearly different: it's more difficult to obtain an accurate measurement due to the large background coming from $b \rightarrow c$ decays. As in the V_{cb} case we have two methods of measurements:

- inclusive: by using kinematical and topological variables one can have selected samples enriched in $b \rightarrow ul\bar{\nu}_l$ and several interesting regions are considered in which this $b \rightarrow cl\bar{\nu}_l$ is small. Then it's applied HQET implemented through OPE. The semileptonic width is expressed as $\Gamma_{sl} = BR(b \rightarrow ul\nu)/\tau_b = \gamma_{th}|V_{ub}|^2$ where γ_{th} is a function of $\alpha_s, m_D, \mu_\pi^2, 1/m_b^3$. The average for CLEO and LEP (incl) es $|V_{ub}| = (4.09 \pm 0.46 \pm 0.36)10^{-3}$
 - exclusive: based on the exclusive decays $B \rightarrow \pi l\nu_l$ and $B \rightarrow \rho l\nu$ and it is necessary to reconstruct these charmeless semileptonic decays and , then, to use the exclusive final states by means of kinematical constraints for background suppression. Theoretically, the uncertainties are of different nature and there are already described in the inclusive analysis. The probability that a final state quarks form a given meson is described by the hadronic form factors and the problem is its determination. In figure 5 (left) are compiled the measurements of V_{ub} obtained by CLEO, BaBar, Belle and LEP where the LEP measurement is the result using the hadronic mass (M_x) 6.

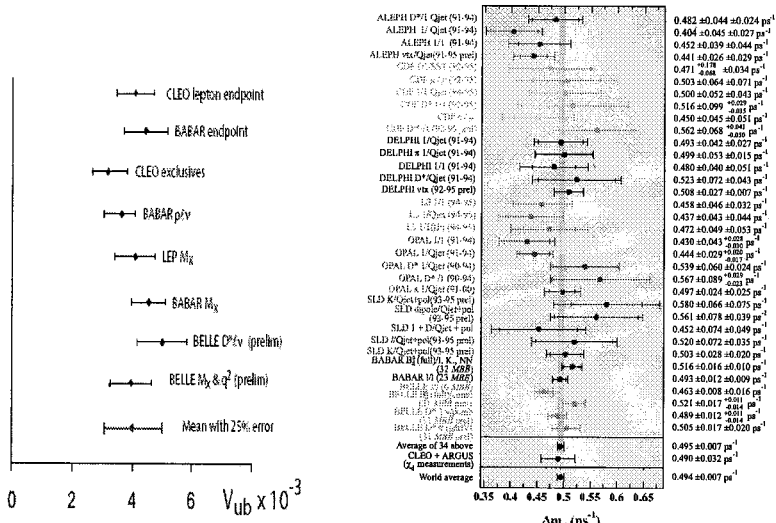


Figure 5: Left: Compilation of V_{ub} measurements 6. Right: Summary of Δm_d results obtained in each analysis (Heavy Flavour Averaging Group).

In order to give an idea of the status by averaging the CLEO, BaBar and Belle, we give the following result $|V_{ub}| = (3.90 \pm 0.16 \pm 0.53)10^{-3}$

3.2 *B oscillations*

Two studies on B oscillations have been performed in LEP 12:

- the $B_d^0 - \bar{B}_d^0$ oscillation: in figure 5 (right) one can see the compilation of 34 measurements performed at LEP, BaBar, CDF, Belle and SLD. The average of the results of CLEO and ARGUS is given. Precision of LEP, SLD and CDF is in average of about 2.8%.

Now we have new and precise measurements performed at B factories and, taking into account these results, the following world average is obtained $\Delta m_d = (0.494 \pm 0.007)ps^{-1}$ which implies a relative error of 1.4% (a factor 2 better), on top of it, the LEP results are quite in agreement with the ones extracted in b-factories. This high accuracy can not yet fully exploited due to the error on $f_B\sqrt{B_B}$, where this factor includes the information of non-perturbative QCD. More theoretical effort must be done in this aspect.

- the $B_s^0 - \bar{B}_s^0$ oscillation: the activity on this search is on the way and two reports on the latest results on B_s oscillations have been sent to the Summer Conferences (see 11): (I) an update of the results obtained in DELPHI corresponding to two published analysis13: a first analysis using leptons with high p_t relative to the jet axis in which have been applied improved semileptonic vertexing techniques and production flavour tag, and a second analysis using D_s - lepton conditions in which the proper time resolution is applied now event by event; Combining the results with the previous measurements published in DELPHI we have the following limit: $\Delta m_s > 8.5ps^{-1}$ (@95%CL) with a sensitivity of $12.0ps^{-1}$ (@ 95% CL).
(II) another important report from ALEPH experiment which contain 3 analysis based on a complementary event selection 14: one with decays of B_s , hadronic flavour fully reconstructed whose properties are small sample, excellent length and p resolution and high average purity; a second analysis based on semileptonic decays with a reconstructed D_s ; and a third analysis based on semileptonic decays inclusively selected. The result corresponding to the limit on Δm_s is $\Delta m_s > 10.9ps^{-1}$ (@95%) with a sensitivity of $15.2ps^{-1}$ (@ 95% CL).

In figure 6 (left) it is shown the results of the amplitude at $\Delta m_s = 10.0ps^{-1}$ obtained by LEP and SLD experiments (origin : B Oscillation Working Group). The world average is $\langle A(\Delta m_s = 10.0) \rangle = -0.03 \pm$

0.22ps^{-1} which is compatible with 0, and, in the plot given in figure 6 (right) one can see the behaviour of the amplitude as a function of Δm_s .

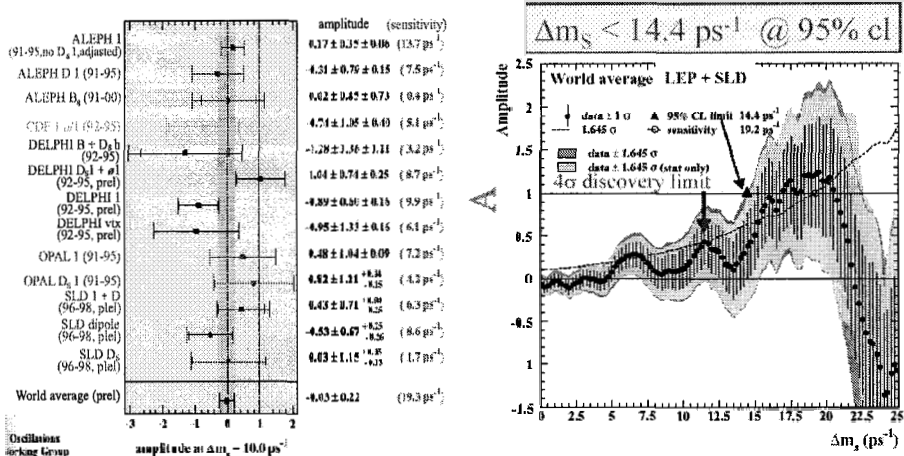


Figure 6: Left: Compilation of results on $\Delta m_s = 10.0\text{ps}^{-1}$. Right: Combined results from LEP + SLD analyses on the oscillation amplitude, as a function of Δm_s . Points with error bars are the data; lines show the 95% CL curves (in dark the systematics have been included). The dotted curve corresponds to the sensitivity

In this plot the data are displayed with 1σ error bar, the shadowed area corresponds to data $\pm 1.645\sigma$, and the curve of the sensitivity is displayed. From this information we get: (a) the limit on Δm_s (> 14.4 , world average LEP + SLD) (b) sensitivity : intersection point of the curve of sensitivity with $A=1$

4 Conclusions

LEP did so much better than anticipated, in particular on B Physics, and is still giving important results: (a) in b fragmentation function, important conclusions have been established, in particular the information in z variable for first time; (b) obtention of more accurate measurements in a lot of quantities: Forward-Backward asymmetry, b hadron lifetimes at few percent level; success for the description in OPE framework; (c) for V_{cb} , extracted with error less than 2% from inclusive, and it is limited by the theoretical uncertainty in the value of the Form Factor from exclusive analysis; (d) for V_{ub} , inclusive, pioneered by LEP, pursued at B factories, relative precision of 10%; (e) in HQET: extraction of Heavy Quark Parameters: moments analysis is being fruitful (CLEO, DELPHI,...) and more results will be available soon; (f) B_d oscillations: first time

observed at LEP and precisely measured Δm_d with high precision (less than 1% including b factories measurements) (g) B_s meson oscillates at least 30 time faster than B_d^0 : to fully exploit the measurements on neutral meson mixings further improvements are necessary on the determination of non-perturbative parameters.

Those results are important contributions in the determination of the Unitary Triangle parameters. A non negligible list of important results are not quoted here due to the lack of time, i.e. B^{**} states, B production fractions, charm counting, rare decays, etc. (see 15)

Acknowledgments

We are greatly indebted to the LEP technical collaborators and to the funding agencies for their support in building and operating the LEP detectors.

References

- [1] 'B Physics and CKM Matrix' , Memoire d'Habilitation, Achille Stocchi, LAL 03-31. July-2003
- [2] G. Barker et al., *A study of the b-quark fragmentation function with the DELPHI detector at LEP I*, DELPHI note 2002-069 CONF 603. Contributed paper for ICHEP 2002
- [3] G. Abbiendi et al. (OPAL Coll.). Phys. Lett. B **577** (2003) 18-36.
- [4] M. Elsing, *Heavy Flavour results from LEP I*, talk given in EPS 2003, Aachen.
- [5] DELPHI Coll., *A precise measurement of the B^+ , B^0 and mean b-hadron lifetime with the DELPHI detector at LEP I*, CERN-EP/2003-065; accepted by Eur. Phys. J.
- [6] S. Stone, *Experimental results in Heavy Flavour Physics*, plenary talk given in EPS 2003 , Aachen
- [7] M. Neubert, Phys. Rep. **245**, (1994) 259.
- [8] DELPHI Coll. *Measurement of V_{cb} using the semileptonic decay $\bar{B}_d^0 \rightarrow D^{*+} l^- \nu_l$* , CERN-EP / 2003-057 (accepted in EPJ)
- [9] Proceedings of the Durham CKM Workshop, April -2003
- [10] M. Battaglia et al. Phys. Letters B **556** (2003) 41-49.
- [11] G. Barker, *B production and oscillation at DELPHI*, talk given in EPS 2003 , Aachen.
- [12] W. Adam et al. (DELPHI Coll.), Phys. Lett. B **414** (1997) 382-400.
- [13] P. Abreu et al., (DELPHI Coll.), Eur. Phys. C **28** (2003) 155-173.
- [14] A. Heister et al., (ALEPH Coll.), Eur. Phys. Jour. C **29** (2003) 143-170.
- [15] 'Combined results on b-hadron production rates and decay properties', CERN-EP / 2001-050 (ALEPH,CDF,DELPHI,L3, OPAL, SLD)

FOUR-FERMION PHYSICS AT LEP

E. Graziani ^a

INFN, sezione di Roma III

*and Dipartimento di Fisica "E. Amaldi", Università degli Studi di Roma Tre
Via della Vasca Navale 84 I-00146 Roma*

Abstract. Electroweak processes with four fermions in the final state were measured extensively at LEP2 in e^+e^- collisions with centre-of-mass energies up to 209 GeV. By combining the results obtained by ALEPH, DELPHI, L3 and OPAL, the predictions from the Standard Model were probed at the level of their present accuracy.

1 Introduction

During the second part of the LEP program in 1995-2000, the centre-of-mass energy of the e^+e^- collisions was raised above the Z boson mass, reaching up to 209 GeV in the last year of operation. Integrated luminosities of about 700 pb⁻¹ were collected by each of the four LEP collaborations ALEPH, DELPHI, L3 and OPAL, mostly above the W and Z-pair production thresholds. This allowed a comprehensive measurement program of boson pair production in e^+e^- collisions and more generally of all possible four-fermion ($4f$) final states. Two of the main aims of LEP, directly validating the non-Abelian gauge structure of the Standard Model (SM) and searching for anomalous gauge boson self-couplings to access new physics beyond the SM (NP), could be pursued. Most of the measured $4f$ final states result from processes seen at LEP for the first time. Initially some of the theoretical predictions and modelling were crude. Improvements were needed to match the experimental accuracy and were challenging, especially in the case of W-pair production.

In several cases the experimental signatures of $4f$ processes are very similar to those expected for new particle production, thus providing a useful environment to test the corresponding analysis techniques.

The latest measurements of $4f$ final states arising via the production processes $e^+e^- \rightarrow WW, ZZ, Z\gamma^*, eeZ/\gamma^*, e\nu W$ are described.

2 Signal definition

The expected cross-sections of the production processes $e^+e^- \rightarrow WW, ZZ, Z\gamma^*, eeZ/\gamma^*, e\nu W$ are shown for illustration in fig.1. Two ways of defining a signal to be measured were used, either as the total cross-section in a kinematic region where the process is dominant or as that corresponding exclusively to the relevant Feynman graphs. Interference effects for identical final states were properly taken into account. In the first method kinematical cuts were chosen in order to limit theory uncertainties.

^ae-mail: graziani@roma3.infn.it

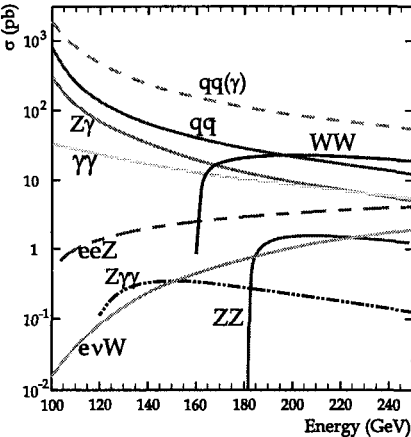


Figure 1: Cross-sections of the main two and four-fermion processes at LEP2.

3 WW production

W-boson pairs are produced at tree level via the doubly-resonant graphs shown in fig. 2. Measurements of cross-sections and decay branching ratios, using a total of about 40000 events selected by the four LEP collaborations are reported in [1]. All decay topologies $q\bar{q}q\bar{q}$, $l\nu q\bar{q}$ and $l\nu l\nu$ were analysed. The cross-sections obtained by combining all LEP results are shown in fig. 3 as a function of the centre-of-mass energy, with a comparison to theoretical expectations [2]. The results clearly favour the SM prediction where the graphs in fig. 2 involving three gauge boson couplings (TGCs) are included, hence providing strong evidence for the non-Abelian gauge group structure of the theory. The highest precision was achieved by combining the results from all energies normalised to respective expectations. The best agreement was obtained using the new YFSWW [3] and RacoonWW [4] predictions. In these two calculations all $O(\alpha)$ electroweak (EW) radiative corrections relevant to the graphs in fig. 2 were included through expansions about the W-pole (in the so-called leading and double pole approximations, respectively). They were introduced into “complete” 4f generators such as KoralW [5] and Wphact [6] to achieve a consistent description of all processes in the full phase space. The result obtained using YFSWW was

$$\frac{\sigma_{WW}}{\sigma_{YFSWW}} = 0.997 \pm 0.007(stat) \pm 0.008(syst)$$

Results with RacoonWW differed by only 0.2%, well within the estimated theory uncertainty of 0.5%. On the contrary a set of previously used predictions

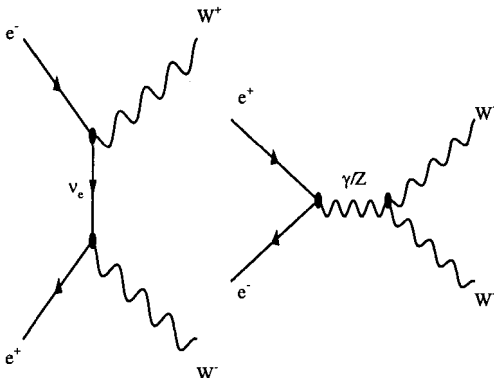


Figure 2: Feynman diagrams for on-shell WW production.

which did not include all EW radiative corrections were too high by 2%, illustrating the sensitivity to loop effects achieved in these results [7]. The main source of uncertainty was from limited precision in the modelling of QCD fragmentation and hadronisation and in background level estimates from $q\bar{q}(\gamma)$. A careful procedure was used in the combination, as these effects are correlated among the different experiments and energies [2]. The same treatment was applied to all LEP cross-section combinations described in this report.

4 ZZ production

Z-boson pair production occurs at tree level in the SM only via graphs with a t-channel electron (similar to that with a ν in fig. 2). The cross-section was measured by the four LEP collaborations using all visible decays $q\bar{q}q\bar{q}$, $\nu\bar{\nu}q\bar{q}$, $llqq\bar{q}$, $lll\bar{l}$ and $ll\nu\bar{\nu}$ [8]. The combined result shown in fig. 4 agrees well with the SM predictions. Combining all energies gave

$$\frac{\sigma_{ZZ}}{\sigma_{YFSZZ}} = 0.945 \pm 0.052$$

using YFSZZ, one of the calculations. The theoretical uncertainty, estimated to be 2%, was higher than for W-pairs (because radiative corrections were not fully included) but sufficient given measurement errors. The main correlated systematic errors, arising from the background modelling, were smaller than the statistical ones.

Reconstructing the Z-boson pairs at LEP-2 was also an important test for

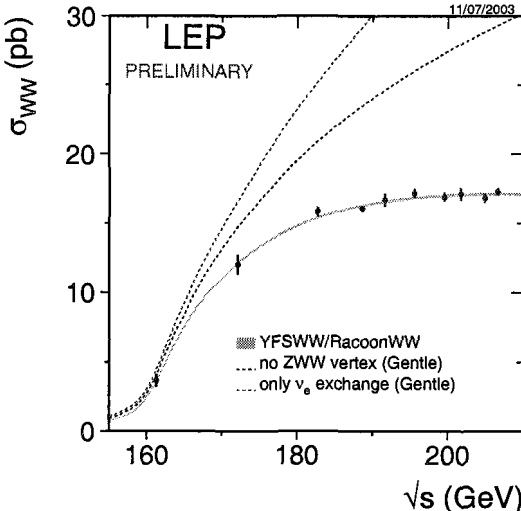


Figure 3: Combined WW cross-section measurements compared with the SM predictions. The dashed curves correspond to removing the graphs with triple gauge boson couplings.

the Higgs searches, since the analysed topologies were quasi-identical and cross-sections similarly small.

5 $Z\gamma^*$ production

Measurements of neutral boson pairs were also extended to include an off-shell photon instead of a Z. The process can then be described as a virtual radiative return to the Z, with characteristic forward-peaked production and quasi mono-energetic γ^* at the lower masses. Resulting topologies are distinctive and gave sizeable backgrounds in several searches for NP. They also led to an original search for anomalous production via neutral TGCs, using a new parametrization extended to include off-shell terms. DELPHI analysed the $\mu\mu q\bar{q}$, $eeq\bar{q}$, $\nu\nu q\bar{q}$, $lll\bar{l}$ and $q\bar{q}q\bar{q}$ final states [9] and OPAL the $\mu\mu q\bar{q}$ and $eeq\bar{q}$ [10]. Good agreement was found, see fig. 5. In final states with electrons, t-channel single-boson processes enhanced the cross-section at high and low di-electron mass. Another interesting final state, $\nu\nu q\bar{q}$ has a mono-jet topology because the γ^* mass distribution peaks at low values. The corresponding energy-averaged cross-section was measured by DELPHI to be

$$\frac{\sigma_{Z\gamma^*}}{\sigma_{WPHACT}} = 1.04^{+0.13}_{-0.12}(stat) \pm 0.04(syst)$$

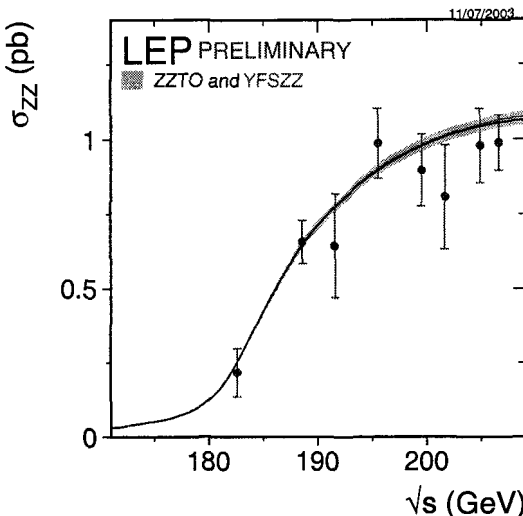


Figure 4: Combined ZZ cross-section measurements compared with the SM predictions from ZZTO and YFSZZ. The band shows the theory uncertainty.

Uncertainties in the hadronization at low $q\bar{q}$ mass and in the way to set α_{em} given the different scales involved were shown to affect predictions by up to 5% [11].

6 eeZ/ γ^* production

Neutral bosons can be produced singly via the so-called EW Compton scattering process $e^+\gamma \rightarrow e^+\gamma^*/Z$, where a quasi-real photon, radiated from one of the beam electrons, scatters off the opposite one. The signature of such events is an electron in the detector with moderate energy recoiling against the γ^*/Z system, with the other "spectator" electron mostly lost in the beam-pipe. LEP collaborations measured the $eeq\bar{q}$ and $ee\mu\mu$ final states with one electron lost. Competing "single-tag" contributions from two-photon processes were suppressed using correlations between the tag electron charge and direction. A combination of cross-sections using the ALEPH, DELPHI and L3 results [12] was performed in the high mass single-Z region, giving good agreement with expectations. Averaging over energies gave

$$\frac{\sigma_{Zee}}{\sigma_{WPHACT}} = 0.932 \pm 0.068$$

using WPHACT, one of the calculations. Uncertainties in the way to set α_{em} and from treating initial state radiation given the different scales involved af-

Measured/Predicted $Z\gamma^*$ Cross-Section DELPHI

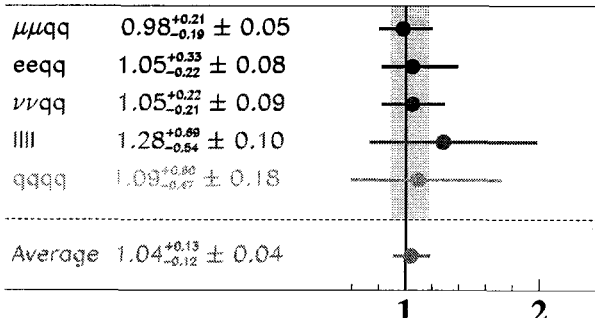


Figure 5: Ratios of measured to predicted cross-sections for individual channels contributing to the $Z\gamma^*$ process. The vertical band displays the total error in the combination.

fected the predictions at the 5% level [11]. This matched the experimental errors, though some differential effects may need to be included.

7 $e\nu_e W$ production

W-bosons can also be produced singly via EW Compton scattering processes $e^+\gamma \rightarrow \bar{\nu}_e W^+$. This involves charged TGCs, which can be probed measuring this process. As for single Z-boson production, the spectator electron is mostly lost in the beam-pipe. LEP collaborations measured all the possible final states $e\nu_e q\bar{q}$, $e\nu_e l\nu_l$ ($l = e, \mu, \tau$) with the electron lost. The main signature was the large missing energy and either a pair of acoplanar jets with mass close to m_W or a single energetic lepton. The signal was defined as the complete t-channel sub-set of $4f$ graphs within kinematic cuts specified to reduce theoretically poorly known multiperipheral contributions: $m_{q\bar{q}} > 45 \text{ GeV}/c^2$, $E_l > 20 \text{ GeV}$, $|\cos\theta_{e+}| < 0.95$. All results [13] agreed with SM expectations. Combining the cross-sections measured by all experiments at all energies gave

$$\frac{\sigma_{e\nu_e W}}{\sigma_{WPHACT}} = 0.978 \pm 0.080$$

using WPHACT, one of the calculations. Uncertainties similar to those described in the previous section for single Z-bosons affected single W-bosons.

Theoretical uncertainties were estimated to be of the order of 5%, matching the experimental precision.

8 Summary

The comprehensive $4f$ measurement program conducted at LEP has been a success. It provided a large set of original results and established experimentally the SM environment where NP searches were carried out. The experimental precision achieved was matched by the accuracy of theory, in some cases after substantial work by the theoretical community [3–7, 11]. In the case of the W-pairs the non-Abelian gauge group structure of the SM was clearly confirmed. The accuracy obtained, close to 0.5%, even allowed the SM calculation at loop level to be probed. In the case of the Z-pairs, a valuable experimental cross-check of the Higgs search at LEP-2 was made. In the case of the single-resonant boson processes SM predictions were tested in several yet unexplored regions.

References

- [1] LEP collaboration public notes ALEPH 2001-013, DELPHI 2003-054, L3 note 2756, OPAL PN-469.
- [2] The LEP Collaborations ALEPH, DELPHI, L3, OPAL, the LEP EW working group and SLD heavy flavours and electroweak groups.
- [3] S.Jadach *et al.*, Comp. Phys. Comm. **140**, 432 (2001).
- [4] A.Denner *et al.*, Nucl. Phys. **B587**, 67 (2000).
- [5] S.Jadach *et al.*, Comp. Phys. Comm. **140**, 475 (2001).
- [6] A.Ballestrero *et al.*, Comp. Phys. Comm. **152**, 175 (2003).
- [7] E.Accomando *et al.*, *Four-fermion production in e^+e^- collisions*, Reports of the working groups on precision calculations for LEP2 Physics, S.Jadach, G.Passarino, R.Pittau (eds.) CERN 200-009 (2000) 1.
- [8] LEP collaborations public notes ALEPH 2001-006, DELPHI 2003-056, L3 note 2805, OPAL Cern-EP 2003-049.
- [9] DELPHI Collaboration, A.Lipniacka *et al.*, DELPHI 2003-060.
- [10] OPAL Collaboration, G.Abbiendi *et al.*, Phys. Lett. **B544** 259 (2002).
- [11] E.Accomando *et al.*, Comp. Phys. Comm. **150**, 166 (2003).
For the hadronisation of low mass systems see M.Boonekamp, hep-ph/0111213.
- [12] OPAL Collaboration, G.Abbiendi *et al.*, Phys. Lett. **B438**, 391 (1998);
L3 Collaboration, P.Achard *et al.*, CERN-EP/2002-103;
LEP Collaboration public notes ALEPH 2002-029, DELPHI 2003-055.
- [13] L3 Collaboration, P.Achard *et al.*, Phys. Lett. **B547**, 151 (2002);
LEP Collaboration public notes ALEPH 2001-017, DELPHI 2003-055,
OPAL PN-427.

ANOMALOUS GAUGE COUPLINGS AT LEP-2

O.Yushchenko^a

Institute for High Energy Physics, Protvino, Russia

Abstract. The LEP-2 measurements of the triple gauge couplings in the charged and neutral sectors are considered. All the results are considered to be preliminary.

1 Introduction

One of the main motivations to double the LEP energy was to study the W boson properties as well as the characteristics of the W -pair production processes, such as the total cross section, the angular distributions and the helicity structure. All these measurements are intended for the test of the Standard Model (SM) and for the searches of the possible extensions.

At the core of the electroweak Standard Model is its invariance under the local non-Abelian gauge group $SU(2)_L \otimes U(1)_Y$. The existence of the triple gauge-boson couplings (TGC) is a direct consequence of the gauge structure of the theory. The measurements of the TGCs represents a fundamental test of the non-Abelian nature of the SM. The local gauge invariance imposes the strong limitations on the TGCs and their inter-dependence. Any deviations from the expected values of TGCs would be direct indications on the physics beyond the SM.

1.1 Charged Bosons Couplings

The most general phenomenological parameterization of the $\gamma(Z)W^+W^-$ vertex can be found in [1–3] (below the subscript V denotes γ or Z):

$$\begin{aligned} \Gamma_{\mu\alpha\beta}^{VWW} = g_{VWW} & \left\{ \left(1 + \Delta g_1 + \frac{\lambda_V}{2m_W^2} p^2 \right) g_{\alpha\beta}(q - \bar{q})_\mu - \frac{\lambda_V}{m_W^2} p_\alpha p_\beta (q - \bar{q})_\mu + \right. \\ & (2 + \Delta\kappa_V + \Delta g_1)(g_{\mu\beta}p_\alpha - g_{\mu\alpha}p_\beta) + \frac{\lambda_V}{m_W^2} (g_{\mu\beta}p_\alpha q^2 - g_{\mu\alpha}p_\beta \bar{q}^2) + \quad (1) \\ & \left(1 + \Delta g_1 + \frac{\lambda_V}{m_W^2} p \cdot \bar{q} \right) g_{\mu\alpha}\bar{q}_\beta - \left(1 + \Delta g_1 + \frac{\lambda_V}{m_W^2} p \cdot q \right) g_{\mu\beta}q_\alpha + \\ & \frac{\lambda_V}{m_W^2} \left[g_{\alpha\beta}p_\mu \frac{\bar{q}^2 - q^2}{2} - p_\alpha\bar{q}_\mu\bar{q}_\beta + p_\beta q_\alpha q_\mu \right] + ig_5\epsilon_{\alpha\beta\mu\gamma}(q - \bar{q})^\gamma - \\ & ig_4(g_{\mu\beta}p_\alpha + g_{\mu\alpha}p_\beta) - \tilde{\kappa}\epsilon_{\alpha\beta\mu\gamma}p^\gamma + \\ & \left. \frac{\tilde{\lambda}}{m_W^2} p^\gamma (\epsilon_{\beta\rho\gamma\mu}q^\rho\bar{q}_\alpha + \epsilon_{\rho\alpha\gamma\mu}q_\beta\bar{q}^\rho - \epsilon_{\beta\alpha\gamma\mu}q \cdot \bar{q}) \right\}, \end{aligned}$$

^ae-mail: Oleg.Iouchtchenko@cern.ch

where $g_{\gamma WW} = -e$ and $g_{ZWW} = e \cot \Theta_W$ [4].

Within the SM, at tree level, the couplings are given by $g_1^\gamma = g_1^Z = \kappa_\gamma = \kappa_Z = 1$, with all other couplings in (1) vanishing. For on-shell photons, electromagnetic gauge invariance fixes the values $g_1^\gamma = g_5^\gamma = 1$. The terms proportional to g_1^V , κ_V and λ_V conserve C and P separately, while g_5^V violates C and P but conserves CP . Other terms in (1) are connected with a possible CP violation in the bosonic sector.

The general three-boson vertex with arbitrary values of the couplings is not locally gauge invariant and this fact leads to some difficulties, such as violation of tree unitarity in scattering processes and bad divergences in loop corrections.

$SU(2) \otimes U(1)$ symmetry requirements, however, can be imposed on the general Lagrangian to ensure the absence of the most serious divergences. These requirements appear as relations among *a priori* arbitrary anomalous couplings, and reduce the number of them.

One can consider $SU(2) \otimes U(1)$ operators of high dimensions to reproduce all couplings in (1). Depending on the new physics dynamics, such operators could be generated at the mass scale Λ , with a strength which is generally suppressed by a factors like $(m_W/\Lambda)^{d-4}$ [5]. As the reduced three-boson vertex contains only $dim = 4, 6$ operators, it should be stressed that it represents the low-energy limit of the general Lagrangian expansion over relative operator strengths if only the leading terms are kept.

The final form of the $SU(2) \otimes U(1)$ relations among the TGC couplings is:

$$\Delta\kappa_\gamma = -\cot^2 \theta_W (\Delta\kappa_Z - \Delta g_1), \quad \lambda_\gamma = \lambda_Z, \quad \tilde{\kappa}_\gamma = -\cot^2 \theta_W \tilde{\kappa}_Z, \quad \tilde{\lambda}_\gamma = \tilde{\lambda}_Z. \quad (2)$$

1.2 Neutral Couplings

In addition to charged couplings $WW\gamma$ and WWZ , neutral ones can also be defined. These couplings are absent at the tree level of SM and can appear when the loop corrections are considered. The typical values of such loop corrections are generally small and are far below the possibility of the measurements.

The well known representation by Hagiwara et al. [2] gives these couplings, fixing selected bosons at mass-shell. Particular vertices at the level of $dim = 6$ operators have the form:

$$\Gamma_{\mu\alpha\beta}^{VZZ} = i \frac{s - m_V^2}{m_Z^2} \{ f_4^V (p_\alpha g_{\mu\beta} + p_\beta g_{\mu\alpha}) + f_5^V \epsilon_{\mu\alpha\beta\rho} (q - \bar{q})^\rho \}, \quad (3)$$

and

$$\Gamma_{\mu\alpha\beta}^{VZ\gamma} = i \frac{s - m_V^2}{m_Z^2} \left\{ h_1^V (\bar{q}_\mu g_{\alpha\beta} - \bar{q}_\alpha g_{\mu\beta}) + \frac{h_2^V}{m_Z^2} p_\alpha (p \cdot \bar{q} g_{\mu\beta} - \bar{q}_\mu p_\beta) \right\}$$

$$h_3^V \epsilon_{\mu\alpha\beta\rho} \bar{q}^\rho + \frac{h_4^V}{m_Z^2} p_\alpha \epsilon_{\mu\beta\rho\sigma} p^\rho \bar{q}^\sigma \Big\} \quad (4)$$

Generally speaking, this representation cannot be satisfactory for general amplitudes due to the finite width of Z -boson. Adequate treatment of neutral couplings based on the operator formalism can be found in [6]. Extending the operators dimension up to $\text{dim} = 12$ as many as 44 terms can be constructed in general case, while the explicit requirement of the local $SU(2) \otimes U(1)$ gauge invariance will again reduce the number of them.

1.3 Basic Processes

The Figure.1 represents all the processes with triple boson vertices studied at LEP-2 energies.

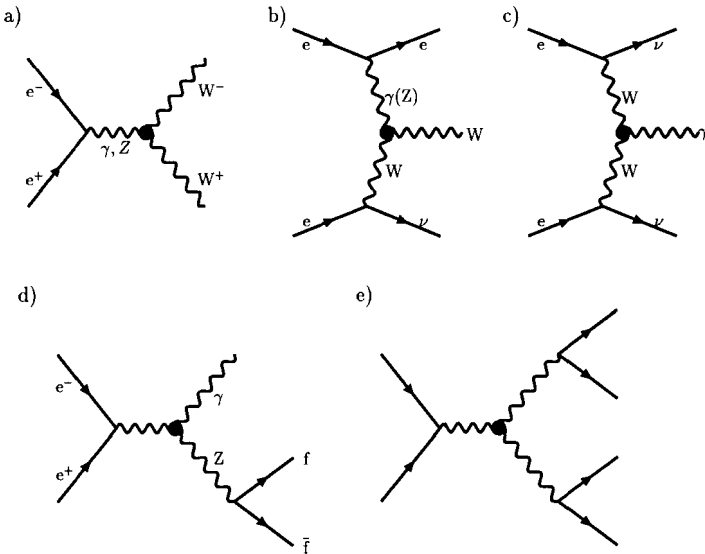


Figure 1. The basic process with anomalous couplings

The general channels with anomalous couplings and signatures are as follows:

- a) The WW production with charged couplings in the signatures:

- $WW \rightarrow q\bar{q}q\bar{q} \rightarrow 4j$
- $WW \rightarrow l\nu q\bar{q} \rightarrow l2j$
- $WW \rightarrow l\nu l\nu \rightarrow 2l$

- b) The single-W production with invisible e down the beam-pipe with charged couplings in the signatures:
 - $W \rightarrow q\bar{q} \rightarrow 2j$
 - $W \rightarrow l\nu \rightarrow l$
- c) The single- γ production with charged couplings.
- d) The single- γ production with neutral couplings.
- e) ZZ and $Z\gamma^*$ production in different signatures with neutral couplings.

The WW production process with the typical cross-section of ~ 18 pb is the main source of the information about TGCs in the charged sector. The complementary single-W topology with rather smaller cross-section (~ 0.6 pb), nevertheless, provides very high sensitivity to the coupling $\Delta\kappa_\gamma$.

The main processes, which provide us with the information concerning TGCs in the neutral sector, are $Z\gamma$ and ZZ production. The first one, with large cross-section, low background and high sensitivity to anomalous couplings, has prominent signatures that makes it easy to select the relevant final states and perform the estimation of TGCs limits.

2 LEP2 results

2.1 Charged couplings

All LEP experiments performed the search for triple gauge boson couplings in the charged sector using WW and “single-W”-induced topologies. The detailed description of the analysis methods, as well as the discussions of the systematics and particular channels sensitivity, can be found in [7–10].

The Fig.2 represents the combination of LEP results obtained in the charged sector. All the anomalous couplings are consistent with their SM expectations.

2.2 Neutral couplings

There are two classes of Lorentz invariant structures associated with neutral TGC vertices which preserve $U(1)_{\text{em}}$ and Bose symmetry, as described in [2].

The relevant final states contain the leptons and/or the quark jets from Z decays for the first class (3) of the couplings and the visible photon and lepton or quark jets pair for the second class.

The first class refers to anomalous $ZZ\gamma^*$ and ZZZ^* couplings which are accessible at LEP2 in the process $e^+e^- \rightarrow ZZ$ (see Figure.1.e). This anomalous vertex is parametrized in terms of four couplings: f_i^V with $i = 4, 5$ and $V = \gamma, Z$ (3).

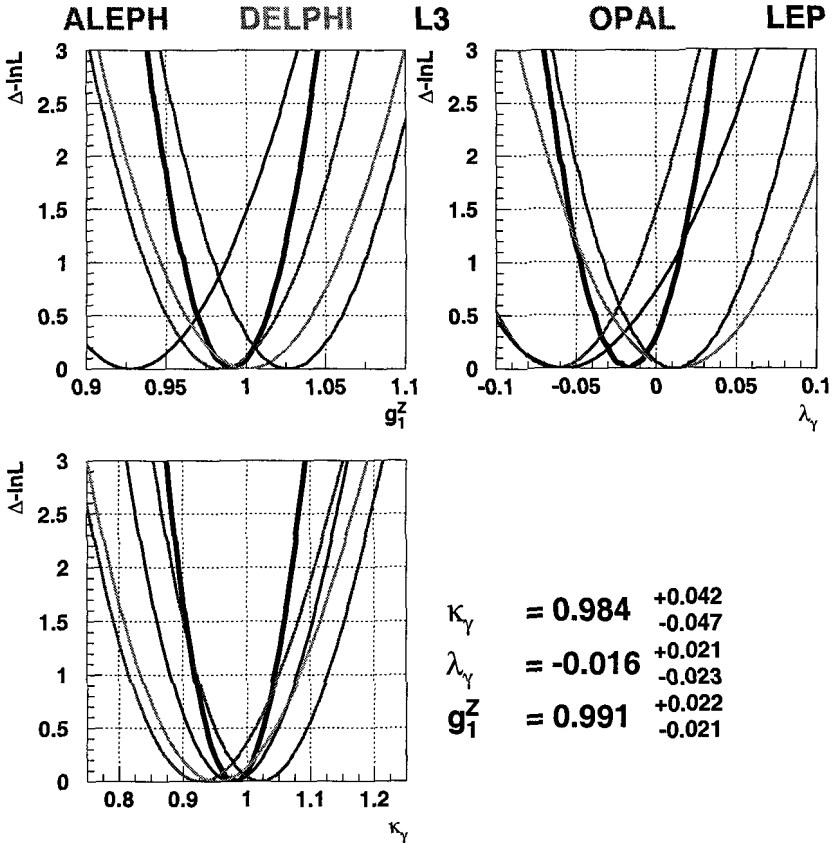


Figure 2. The $-\log \mathcal{L}$ curves of the four experiments, and the LEP combined curve for the three charged TGCs ($g_1^Z, \lambda_\gamma, \kappa_\gamma$) with $SU(2)_L \otimes U(1)_Y$ constraints. In each case, the minimal value is subtracted.

The second class refers to anomalous $Z\gamma\gamma^*$ and $Z\gamma Z^*$ couplings which are accessible at LEP in the process $e^+e^- \rightarrow Z\gamma$ (see Fig.1.d). The relevant parametrisation contains eight couplings: h_i^V with $i = 1, \dots, 4$ and $V = \gamma, Z$ (4).

In all cases the final state bosons are assumed to be on-shell, and the couplings f_4^V, h_1^V and h_2^V are CP-odd while f_5^V, h_3^V and h_4^V are CP-even.

The h_i^V and f_i^V are independent of each other. They are assumed to be real and they vanish at tree level in the Standard Model.

All relevant channels have been studied by LEP experiments. The details of the selection and analysis procedures can be found in [11] - [16].

The Table 1 represents the combination of LEP2 results in the neutral sector.

coupling	<i>s</i> -channel hauge boson	
	γ	Z
h_1	$-0.056 \div +0.055$	$-0.13 \div +0.13$
h_2	$-0.045 \div +0.025$	$-0.078 \div +0.071$
h_3	$-0.049 \div -0.008$	$-0.20 \div -0.07$
h_4	$-0.002 \div -0.034$	$-0.05 \div +0.12$
f_4	$-0.17 \div +0.19$	$-0.30 \div +0.30$
f_5	$-0.32 \div +0.36$	$-0.34 \div +0.38$

Table 1. The 1σ intervals for the neutral anomalous couplings.

In general, good agreement with the Standard Model expectations is observed. At 2σ level all the anomalous couplings are consistent with zero.

3 Conclusion

The study of the gauge sector of the Standard Model has been performed by all four LEP experiments by means of the anomalous coupling measurements. The results of the individual experiments are in good agreement and the combined LEP2 estimations are consistent with the Standard Model expectations.

Acknowledgments

I would like to thank the organizers of 11th Lomonosov Conference, Prof. A.Studenikin and Moscow State University, for a stimulating conference.

As a DELPHI collaborator I thank the DELPHI members, as well as members of all other LEP experiments for their contributions into physics analysis of LEP data and an overall detectors performance.

I also would like to thank the CERN accelerator divisions for the efficient operation and nice performance of the LEP accelerator over more than 10 years.

References

- [1] K. Gaemers and G. Gounaris, *Z. Phys. C1* (1979) 259.
- [2] K. Hagiwara, K. Hikasa, R.D. Peccei, D. Zeppenfeld, *Nucl. Phys. B282* (1987) 253.
- [3] F.A. Berends and A.I. van Sighem, hep-ph/9506391 and *Preprint INLO-PUB-7/95*.

- [4] M. Böhm, A. Denner, *Preprint CERN-PPE-92-002*
- [5] G.J. Gounaris, F.M. Renard and G. Tsirigoti, *Phys. Lett.* **B350** (1995) 212.
- [6] G.J.Gounaris, J.Layssac, and F.M.Renard, hep-ph/0005269 and *Phys. Rev.* **D62**, 073013 (2000).
- [7] The ALEPH Collaboration, *Measurement of Triple Gauge-Boson Couplings in e^+e^- collisions from 183 to 209 GeV*, ALEPH 2003-015 CONF 2003-011.
- [8] The DELPHI Collaboration, *Measurement of Charged Trilinear Gauge Boson Couplings*, DELPHI 2002-016 CONF 555.
- [9] The L3 Collaboration, *Preliminary Results on the Measurement of Triple-Gauge-Boson Couplings of the W Boson at LEP*, L3 Note 2820 (2003).
- [10] The OPAL Collaboration, *Measurement of charged current triple gauge boson couplings using W pairs at LEP*, CERN-EP 2003-042 (2003), hep-ex/0308067.
- [11] The ALEPH Collaboration, *Limits on anomalous neutral gauge couplings using data from ZZ and Z γ production between 183-208 GeV*, ALEPH 2001-061 CONF 2001-041.
- [12] The DELPHI Collaboration, *Study of Trilinear Gauge Boson Couplings ZZZ, ZZ γ and Z $\gamma\gamma$* , DELPHI 2001-097 CONF 525.
- [13] The L3 Collaboration, *Search for anomalous ZZ γ and Z $\gamma\gamma$ couplings in the process ee \rightarrow Z γ at LEP*, L3 Note 2672 (July 2001).
- [14] The OPAL Collaboration, G. Abbiendi *et al.*, *Eur. Phys. J* **C17** (2000) 13.
- [15] The L3 Collaboration, M. Acciari *et al.*, *Phys. Lett.* **B450** (1999) 281;
The L3 Collaboration, M. Acciari *et al.*, *Phys. Lett.* **B465** (2000) 363;
The L3 Collaboration, *Z Boson Pair-Production at LEP*, L3 Note 2696 (July 2001).
- [16] The OPAL Collaboration, G. Abbiendi *et al.*, *Phys. Lett.* **B476** (2000) 256;
The OPAL collaboration, *Study of Z Pair Production and Anomalous Couplings in e^+e^- Collisions at \sqrt{s} between 190 and 209 GeV*, OPAL Physics Note PN482 (July 2001).

FERMION- AND PHOTON-PAIR PRODUCTION AT LEP-2

M.Winter ^a

IReS, 23 rue du Loess, BP28, 67037 Strasbourg cedex 2, France

Abstract. The running of LEP-2 at CERN has allowed the four LEP experiments to accumulate a total of several hundred thousands of events resulting from fermion- or photon-pair production in e^+e^- collisions. Several observables were extracted from their analysis and used to test the Standard Model consistency and constrain basic parameters of models going beyond it.

1 Introduction

Fermion- and photon-pair production at LEP-2 provide a unique tool to test the Standard Model (SM) consistency at the per-cent level. They also allow to investigate (mainly virtual) manifestations of physics beyond the SM. This article summarises preliminary results of the combined analysis of the data collected with the 4 LEP experiments (ALEPH, DELPHI, L3 and OPAL).

2 Fermion-pair production

2.1 General Remarks

At tree level and within the SM, fermion-pair production results from the s-channel exchange of a photon or a Z boson in which the incoming e^+ and e^- have annihilated. In the case of e^+e^- production, the t-channel exchange adds a sizeable contribution to the cross-section.

The process has been extensively studied at LEP-1, where the Z exchange dominated widely. On the contrary at LEP-2, the photon exchange contribution is of much larger importance. As another basic difference, the cross-sections are more than two orders of magnitude smaller than at LEP-1. Moreover, initial state photon radiation (ISR), which played already an important role at LEP-1, doubles the cross-sections at LEP-2 energies.

The interpretation of the measurements first consists in comparing the measured values of physical observables extracted from the data collected for each final state, to the SM predictions in order to test its internal consistency. Second, the measured observables are used to search for (mainly virtual) manifestations of new physics.

In order to investigate the new kinematical domain accessible at LEP-2, the studies were restricted to events produced near the kinematical limit, i.e. with an e^+e^- annihilation energy ($\sqrt{s'}$) close to the collision energy (\sqrt{s}). Because of the sizeable ISR, only about a quarter of the total sample collected is produced with $\sqrt{s'}$ exceeding 85 % of \sqrt{s} .

^ae-mail: marc.winter@ires.in2p3.fr

The final states studied are those made of e^+e^- , $\mu^+\mu^-$, $\tau^+\tau^-$, $q\bar{q}$, $b\bar{b}$ or $c\bar{c}$ pairs. The event selections are similar to those applied at LEP-1, completed by an additional cut on $\sqrt{s'}$, set to 85 % or 90 % of \sqrt{s} , depending on the final state considered. The value of $\sqrt{s'}$ is estimated for each event by computing the fermion-pair or the propagator invariant mass.

Depending on the final state considered, the physical observables extracted from the data are the total and differential cross-sections (σ and $d\sigma/d\cos\theta$), forward-backward asymmetries (A_{FB}) and R ratios^b. The observables calculated for each final state are listed in table 1.

observable	e^+e^-	$\mu^+\mu^-$	$\tau^+\tau^-$	$q\bar{q}$	$b\bar{b}/c\bar{c}$
σ	YES	YES	YES	YES	NO
$d\sigma/d\cos\theta$	YES	YES	YES	NO	NO
A_{FB}	YES	YES	YES	NO	YES
R	NO	NO	NO	NO	YES

Table 1: Physical observables determined for each final state.

The data used for the analysis were collected from 1995 through 2000 at mean collision energies ranging from ~ 130 GeV to ~ 207 GeV. The total integrated luminosity is close to 700 pb^{-1} , out of which almost 50 % were collected near 200 GeV and above. The results shown, which rely on the combination of the data collected with the 4 LEP experiments, are still incomplete and ought to be considered as preliminary. The combination was performed with an extensive treatment of the different types of correlations [1].

2.2 Comparison of the measured observables to the SM predictions

Figure 1 shows how the measured total cross-sections for $\mu^+\mu^-$, $\tau^+\tau^-$ and $q\bar{q}$ production and the $\mu^+\mu^-$ and $\tau^+\tau^-$ forward-backward asymmetries compare to the SM expectations at different collision energies. The measurements agree with the SM over the full kinematical domain.

Similarly, the differential cross-sections for $\mu^+\mu^-$, $\tau^+\tau^-$ and e^+e^- production were also well reproduced by the SM predictions, as well as the R ratio and forward-backward asymmetries for $b\bar{b}$ and $c\bar{c}$ production.

Next, the fit performed at LEP-1 providing the Z mass (M_Z) was repeated within the S-matrix formalism [2], which allows to fit cross-sections and asymmetries without fixing the γZ interference to its SM value. This approach is

^bwhere θ is the production angle of the outgoing fermion w.r.t. the direction of the incoming e^- , $A_{FB} = \frac{N_{\cos\theta>0} - N_{\cos\theta<0}}{N_{\cos\theta>0} + N_{\cos\theta<0}}$ and $R_{b,c} = \frac{\sigma_{b\bar{b},c\bar{c}}}{\sigma_{q\bar{q}}}$.

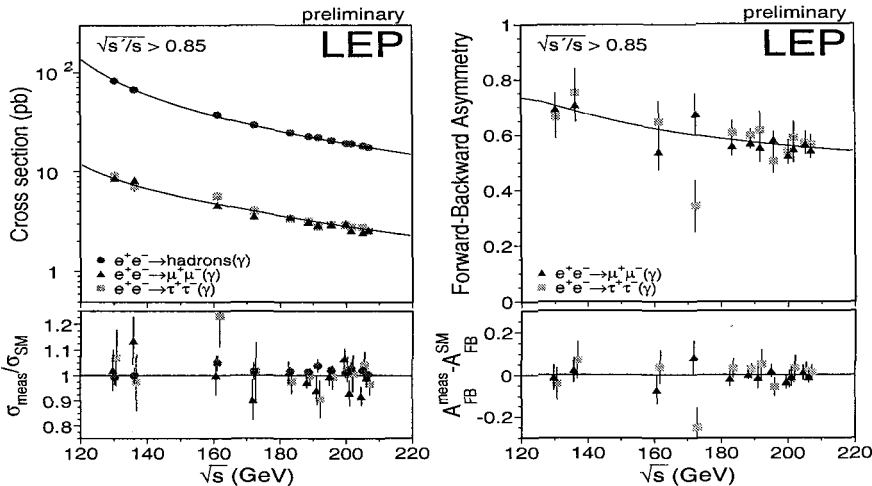


Figure 1: Top: measured cross-sections (left) and asymmetries (right) compared to SM predictions (full line). Bottom: ratio between measured and predicted values.

therefore less model dependent, at the expense of a reduced statistical accuracy since it relies on at least 3 additionnal free parameters. The fit result is $M_Z = 91.1869 \pm 0.0023 \text{ GeV}/c^2$, a value which confirms the LEP-1 result ($M_Z = 91.1876 \pm 0.0021 \text{ GeV}/c^2$) and is nearly as precise, due to the strong constraint on the γZ interference imposed by the LEP-2 data.

2.3 Constraints on models going beyond the SM

Several phenomenological frameworks going beyond the SM were investigated. The results shown here concentrate on contact interactions, additionnal gauge bosons and low scale quantum gravity. A more comprehensive review is available [1], which includes also results on lepto-quarks.

Contact interactions were investigated by adding an effective Lagrangian term to the SM component [3], which allows to expand the differential cross-section in terms of a parameter ϵ ($=1/\Lambda^2 c$):

$$\frac{d\sigma}{dcos\theta} = A(s, t) + B(s, t) \cdot \epsilon + C(s, t) \cdot \epsilon^2$$

where A, B and C are well defined functions. The parameter ϵ was fitted to the full set of observables determined for each final state (see table 1). The 95 % C.L. limits on Λ extracted from most of the final states are shown on figure 2 in the case of negative and positive deviations from the SM expectation, and assuming that the unknown coupling g^2 entering the Lagrangian amounts to

^cwhere Λ stands for the typical energy scale of the contact interactions.

4π (see [3]). 8 different models were considered, each corresponding to different helicity couplings between the initial and final state currents. Depending on the model, the limits range from a few TeV to about 20 TeV.

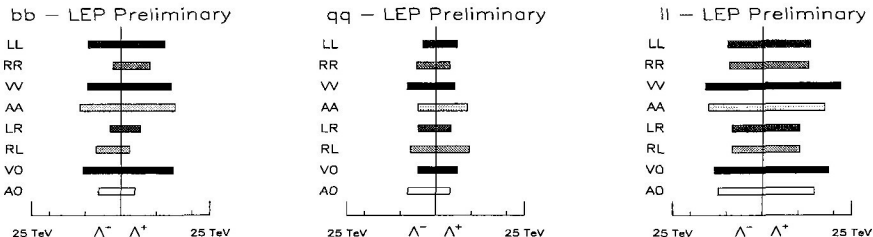


Figure 2: 95 % C.L. limits on the energy scale, Λ^\pm , of the contact interactions extracted from $q\bar{q}$, $b\bar{b}$ and charged lepton pairs (i.e. $\mu^+\mu^-$ and $\tau^+\tau^-$).

Signs of an additional heavy neutral boson (Z') were searched for, following the suggestion that the SM may be embedded in a larger gauge symmetry group. Three different scenarios were considered, referred as E(6) [4], Left-Right (L-R) [5] and Sequential SM (SSM) [6].

In absence of evidence for a Z' , lower bounds on the heavy boson mass ($M_{Z'}^{limit}$) were extracted. This was performed assuming there was no ZZ' mixing, as supported by the LEP-1 data. The results are illustrated in table 2. The E(6) fit outcome is shown for three conventional values of the angle^d θ_6 , while the L-R fit result is provided for the usual value of the angle^e α_{LR} .

Model	χ	ψ	η	L-R	SSM
$M_{Z'}^{limit}$ (GeV/c ²)	673	481	434	804	1787

Table 2: 95% C.L. lower limits on the Z' mass for χ , ψ , η , L-R and SSM models.

Fermion-pair production differential cross-sections are also quite sensitive to manifestations of low scale quantum gravity. The effect of the exchange of Kaluza-Klein excitations of gravitons in large extra dimensions is most visible at small polar angle. The most sensitive process is therefore Bhabha scattering. Its differential cross-section can be expressed as a expansion w.r.t. the gravitational mass scale (M_G), viz:

$$\frac{d\sigma}{dcos\theta_e} = A'(s, t) + B'(s, t) \cdot \frac{\lambda}{M_G^4} + C'(s, t) \cdot \frac{\lambda^2}{M_G^8}$$

where λ is a parameter expected to be of O(1), and where A' , B' and C' are well defined functions. The absence of deviations from the SM expectations

^dexpressing the mixing between the two gauge fields underlying the model.

^ewhich governs the Z' couplings to fermions.

was converted into lower bounds on M_G , obtained by fitting the expression above to the measured cross-section. The 95 % C.L. limits on M_G were found to be 1.2 TeV and 1.1 TeV for $\lambda = +1$ and -1 respectively.

3 Photon-pair production

3.1 General remarks

Photon-pair production provides a quite different insight to fundamental laws ruling nature than fermion-pair production, since it is mainly due to photon radiation by the incoming e^\pm , which is a purely electromagnetic process.

Besides the validity of QED, anomalous $e^+e^-\gamma$ couplings as well as the e^\pm elementarity can be scrutinised. The observables used for the studies are the total and differential cross-sections (σ_{tot} and $d\sigma/d\cos\theta_\gamma$). The (preliminary) results presented here are based on the almost complete LEP-2 data set, the only missing part being the DELPHI 2000 data.

3.2 Measured total and differential cross-sections

The total cross-sections obtained with each experiment at each collision energy from 1997 to 2000 are displayed on figure 3, normalised to the QED prediction. The stars show the LEP averages. No significant difference between the measurements and the theoretical values was observed.

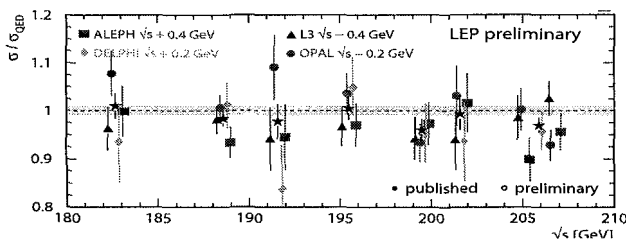


Figure 3: $\gamma\gamma$ -production total cross-section measurements normalised to the QED prediction.

3.3 Search for manifestations of new physics

The differential cross-sections measured by each collaboration were used to perform more refined QED tests by fitting them with an expression combining the SM term with a non-standard correction accounting for a well defined new physics framework. Since the observations confirmed QED, these fits were used to set limits on the energy scale at which nature may depart from the SM with an observable magnitude. The expressions fitted to the data are summarised hereafter. More details may be found in [7].

The agreement between the measurements and QED was converted into a limit on the cutoff parameter, Λ_{\pm} , representing the energy scale at which QED would break down [8]. In the corresponding fit formula below, the \pm sign is introduced to account explicitly for positive and negative deviations from the SM prediction.

$$\left(\frac{d\sigma}{d\Omega} \right)_{\Lambda_{\pm}} = \left(\frac{d\sigma}{d\Omega} \right)_{\text{Born}} \pm \frac{\alpha^2 s}{2\Lambda_{\pm}^4} (1 + \cos^2 \theta)$$

The fitted values of Λ_{\pm} allow also to test the existence of anomalous couplings (expressed by a dimension 6 term in the Lagrangian), which may be characterised by an energy scale Λ_6 related to Λ_{\pm} by the expression $\Lambda_{\pm}^4 = \frac{\alpha}{2} \Lambda_6^4$.

The differential cross-sections are also sensitive to contact interactions, which one may introduce through the expression [9]:

$$\left(\frac{d\sigma}{d\Omega} \right)_{\Lambda'} = \left(\frac{d\sigma}{d\Omega} \right)_{\text{Born}} \pm \frac{s^2}{32\Lambda'^6}$$

where Λ' is a characteristic energy scale fitted to the data. It corresponds to a dimension 7 term in the Lagrangian. In case of a dimension 8 term, the corresponding energy scale is related to Λ' by the relation $\Lambda_8^4 = m_e \Lambda'^3$.

Low scale quantum gravity was tested with the expression [10]:

$$\left(\frac{d\sigma}{d\Omega} \right)_{M_s} = \left(\frac{d\sigma}{d\Omega} \right)_{\text{Born}} - \frac{\alpha s}{2\pi} \frac{\lambda}{M_s^4} (1 + \cos^2 \theta)$$

where $\lambda = \pm 1$ and M_s stands for the gravitational mass scale.

Finally, the effects of excited electrons (mass M_{e^*}) were investigated by fitting the measured $d\sigma/d\cos\theta$ with the expression [11]:

$$\left(\frac{d\sigma}{d\Omega} \right)_{e^*} = \left(\frac{d\sigma}{d\Omega} \right)_{\text{Born}} + \frac{\alpha^2}{4} \frac{f_\gamma^4}{\Lambda_{\text{LSG}}^4} M_{e^*}^2 F(M_{e^*}, \cos\theta, s)$$

where the energy scale Λ_{LSG} may be set equal to M_{e^*} , f_γ is of order 1 and F is a well defined function. Fitted parameters were either M_{e^*} (with fixed f_γ and Λ_{LSG}) or $f_\gamma/\Lambda_{\text{LSG}}$ (with fixed M_{e^*}).

The limits extracted from the fits above are summarised in table 3.

4 Summary

Fermion- and photon-pair production were studied at LEP-2, based on data collected from 1995 through 2000 at collision energies ranging from ~ 130 to 208 GeV. The substantial integrated luminosity ($\sim 700 \text{ pb}^{-1}$) allowed to test

test framework	comment	95 % C.L. limit
QED break down	$> 0, < 0$ deviation	$\Lambda_+ > 392 \text{ GeV}, \Lambda_- > 364 \text{ GeV}$
anomal. coupling	derived from Λ_+	$\Lambda_6 > 1595 \text{ GeV}$
contact interact.	dimension 7 and 8	$\Lambda_7 > 831 \text{ GeV}, \Lambda_8 > 23 \text{ GeV}$
low scale gravity	$\lambda = +1$ and -1	$M_s > 933 \text{ GeV}, M_s > 1010 \text{ GeV}$
excited electron	$M_{e^*} = 200 \text{ GeV}/c^2$ $f_\gamma = 1, \Lambda_{LSG} = M_{e^*}$	$f_\gamma/\Lambda_{LSG} > 3.9 \text{ TeV}^{-1}$ $M_{e^*} > 248 \text{ GeV}/c^2$

Table 3: 95 % C.L. limits on basic parameters expressing physics beyond the SM.

the SM consistency at the per-cent level and to investigate potential signs of various new physics models well above the kinematical limit.

No significant discrepancy between the measurements and the SM predictions was observed, a feature which allowed to constrain quite severely basic parameters of models going beyond the SM. Due to space limitations, several studies could not be included in this article. More comprehensive reviews are available on the LEP-2 Working Group Web sites [12].

References

- [1] C.Geweniger et al., *CERN preprint LEP2FF/02-03* (2002), and references therein.
- [2] A.Leike et al., *Phys.Lett.* **B** 273, 513 (1991);
T.Riemann, *Phys.Lett.* **B** 293, 451 (1992).
- [3] E.Eichten et al., *Phys.Rev.Lett.* 50, 811 (1983).
- [4] P.Langacker et al., *Phys.Rev.* **D** 30, 1470 (1984);
D.London and J.Rosner, *Phys.Rev.* **D** 34, 1530 (1986).
- [5] J.Pati and A.Salam, *Phys.Rev.* **D** 10, 275 (1974);
J.Pati and A.Salam, *Phys.Rev.* **D** 11, 566 (1975).
- [6] G.Altarelli et al., *Z.Phys.* **C** 45, 109 (1989);
erratum *Z.Phys.* **C** 47, 676 (1990).
- [7] The LEP coll. et al., *CERN preprint LEP2FF/02-02* (2002), and references therein.
- [8] S.Drell, *Ann.Phys.(NY)* 4, 75 (1958);
F.E.Low, *Phys.Rev.Lett.* 14, 238 (1965).
- [9] J.P.Eboli et al., *Phys.Lett.* **B** 271, 274 (1991).
- [10] K.Agashe and N.G.Deshpande, *Phys.Lett.* **B** 456, 60 (1999).
- [11] B.Vachon, *preprint hep-ph/0103132* (2001).
- [12] <http://lepewwg.web.cern.ch/LEPEWWG/lep2/>

TAU AND TWO-PHOTON PHYSICS AT BABAR

J.Williams ^a

*Department of Physics and Astronomy, University of Manchester, Manchester,
M13 9PL, United Kingdom*

Abstract. The *BABAR* experiment at the PEP-II *B*-factory has collected over 100 M tau-pair events since its turn on in 1999. A review of various measurements in the tau sector at *BABAR* is presented, as well as results in two-photon physics from *BABAR*. Included in this review are the results of searches for lepton flavour violation in tau decays. Also discussed is a new precision measurement of the tau lifetime, a result made possible with *BABAR*'s high resolution silicon vertex tracker combined with the large tau data sample. The two-photon physics results include a discussion of a study of a candidate for the $\eta_C(2S)$ state.

1 Introduction

The *BABAR* experiment provides an ideal environment in which to study tau and two-photon physics. Millions of τ -pair events have been detected by the experiment, providing an excellent opportunity to search for rare or forbidden tau decay processes, as well as making possible high-precision measurements of τ physics quantities. Additionally, a large number of two-photon events are observed.

This paper is organised as follows: Section 2 contains a brief description of the *BABAR* detector and outlines the motivation for studying τ physics at the *BABAR* “*B* factory”. Section 3 contains a review of the search for lepton flavour violation in the neutrinoless decay $\tau \rightarrow \mu\gamma$, while Section 4 discusses a measurement of the tau lepton lifetime. Properties of the η_C meson were measured in two-photon interactions, as were those of a candidate for the excited state $\eta_C(2S)$. Results from these analyses are presented in Section 5. Finally, the analyses discussed in this paper are summarised in Section 6.

2 *BABAR* and τ physics

The *BABAR* detector [1] at the Stanford Linear Accelerator Centre (SLAC) is centred about the collision point of the electron and positron beams in the SLAC PEP-II storage rings [2]. The electrons are accelerated to 9.0 GeV and the positrons to 3.1 GeV before being injected into the PEP-II storage rings. The centre-of-mass (CMS) energy of the interaction is $\sqrt{s} = 10.58$ GeV – equal to the rest mass of the $\Upsilon(4S)$ (which predominantly decays into pairs of *B* mesons).

The *BABAR* detector [1] is essentially a *B* factory, producing approximately one million *B*-meson pairs for each inverse femtobarn of integrated luminosity. The asymmetric energy configuration of the experiment (the beam energies

^ae-mail: jenny@hep.man.ac.uk

correspond to a boost of $\beta\gamma = 0.55$) is required for measurements of the CP -violation parameter $\sin 2\beta$. This is because it is necessary to produce the $T(4S)$ with sufficient momentum in the laboratory frame that the B mesons it produces decay sufficiently far apart from each other that their decay products can be associated with one or other B meson.

PEP-II is also a τ factory: the cross section for $e^+e^- \rightarrow \tau^+\tau^-$ at a CMS energy of 10.58 GeV is about 0.90 nb, yielding just under a million τ -pair events per fb^{-1} of data logged. This means that *BABAR* observes a similar number of τ pairs to B pairs. With over 100 million τ -pair events logged to date, the *BABAR* experiment provides an ideal laboratory in which to seek rare decays and to make high-precision measurements of tau properties.

3 Search for lepton flavour violation in the decay $\tau \rightarrow \mu\gamma$

The decay $\tau \rightarrow \mu\gamma$ is a neutrinoless decay which is forbidden in the Standard Model [3], but which may be observable in some supersymmetric extensions to the Standard Model [4]. Supersymmetric models allow a branching ratio of up to $O(10^{-6})$, an enhancement of the limit for the decay $\mu \rightarrow e\gamma$ by $O(10^5\text{-}10^6)$ due to the tau lepton mass.

Present reported 90% confidence level limits on the branching ratio $\tau \rightarrow \mu\gamma$ are 1.1×10^{-4} (CLEO [5] on 13.8 fb^{-1}) and 3.2×10^{-7} (BELLE [6], preliminary result on 86.3 fb^{-1}).

The *BABAR* measurement of the branching ratio for $\tau \rightarrow \mu\gamma$ [7] was made using 56 million τ pairs from the 1999-2000 *BABAR* data set. A sample of 40,000 Monte Carlo signal events was generated using KORALB [8]. The taus were decayed using 2-body phase space with no polarisation and using the GEANT detector simulation. The signal sample was used for efficiency studies and to develop the event selection procedure.

Other simulated events included radiative muon pairs which were used for efficiency studies, and quark-pair events and tau pairs with Standard Model decays which were used to optimise background rejection. Bhabha and two-photon backgrounds were studied in the data.

Events selected as signal events had one τ decaying to a charged particle which was identified as a muon and a photon with energy at least 400 MeV in the same hemisphere (a “signal” decay), as well as a “tag” decay in the opposite hemisphere. The tag decay in this case is either an electron and no other observed energy deposits, or a reconstructed neutral pion and a track identified as coming from a charged pion.

Since there are no neutrinos produced in the signal decays, the invariant mass of the $\mu\gamma$ system of a properly reconstructed event should be equal to the τ mass, and the $\mu\gamma$ CMS energy should be equal to the beam CMS energy.

The analysis variables used are the mass of the $\mu\gamma$ system calculated from

a kinematic fit made using the beam energy as a constraint on the energy of the system, m_{EC} , and the difference between the reconstructed $\mu\gamma$ energy and the beam energy, ΔE . These two variables are uncorrelated in the absence of initial state radiation.

By fitting the ΔE and m_{EC} distributions in the Monte Carlo signal events, the resolutions were determined to be $\sigma_{\Delta E} = 88 \text{ MeV}$ and $\sigma_{m_{EC}} = 19 \text{ MeV}/c^2$. These resolutions were used to define signal and sideband regions, shown in Fig. 1, which were used to carry out a blinded analysis. The distribution in ΔE and m_{EC} of the simulated signal events is also shown in Fig. 1. The signal region is defined by an ellipse centred on $(\Delta E, m_{EC}) = (0, m_\tau)$ with half axes at $-2\sigma_{\Delta E}$ and $3\sigma_{\Delta E}$ in ΔE and $-3\sigma_{m_{EC}}$ and $3\sigma_{m_{EC}}$ in m_{EC} . A region slightly larger than the signal ellipse was blinded and was not studied in the data until the final event sample had been selected. Sideband regions near the signal region were studied in the blinded analysis in order to estimate the background present in the signal, and the selection procedure was developed using a broad region about the signal ellipse, excluding the blinded region.

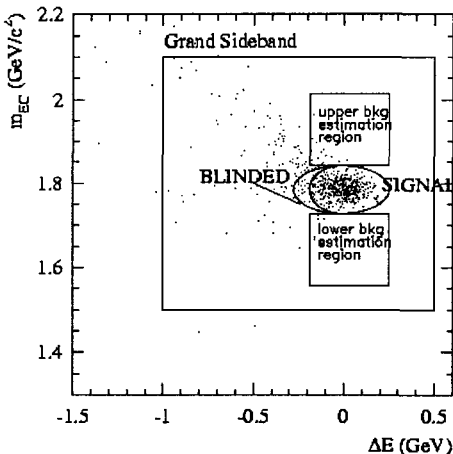


Figure 1: Definition of signal ellipse and sideband regions in the ΔE and m_{EC} plane. Points show the distribution for simulated signal events.

The main non- τ background which passes the initial selection cuts is from radiative μ -pair production, $e^+e^- \rightarrow \mu^+\mu^-\gamma$. This is largely removed by the particle identification requirement on the tag side, and there is very little non- τ background remaining after all cuts have been imposed. The particle identification requirements and 400 MeV signal-side photon energy cut strongly reduce all other non- τ backgrounds. An irreducible τ -pair background is present in the form of $\tau \rightarrow \mu\nu\nu\gamma$ events in which the two neutrinos carry off very little energy. The contribution from such events is estimated by looking in the

sideband regions. After all other cuts were applied, excellent agreement was observed between the data and Monte Carlo in both shape and scale over a wide range of event variables.

In the background region, the ratio of the number of observed events to the number of expected events is $1.022 \pm 0.069(\text{stat}) \pm 0.025(\text{norm})$. From Monte Carlo studies, the signal efficiency is found to be $5.2 \pm 0.1(\text{MCstat}) \pm 0.5(\text{syst})\%$.

The distribution in ΔE and m_{EC} for data events passing all event selection cuts, after unblinding, is shown in Fig. 2. There are 13 events in the signal region, to be compared with an expectation from a sideband analysis of 7.8 ± 1.4 events in the absence of a signal. This leads to a limit of

$$\mathcal{BR}(\tau \rightarrow \mu\gamma) < 2.0 \times 10^{-6} \text{ at } 90\% \text{ CL} \quad (1)$$

The probability for 7.8 ± 1.4 events to fluctuate to 13 or more events in the absence of a signal is 7.6 %.

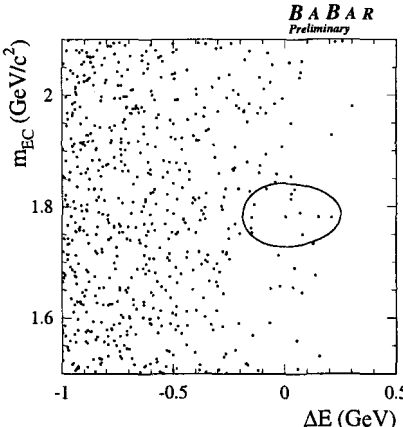


Figure 2: Distribution in ΔE and m_{EC} for final selected events in data.

4 Measurement of the tau lepton lifetime

In order to test lepton universality, namely that the W couples to all leptons with equal strength, precise measurements are required of the branching ratios for the processes $\tau \rightarrow \mu\bar{\nu}\nu$ and $\tau \rightarrow e\bar{\nu}\nu$ as well as measurements of the mass of the tau lepton and the tau lifetime. The current world average value for the tau lifetime is [10] $290.6 \pm 1.1\text{ fs}$. This result is based on results from CLEO and from the LEP experiments.

The tau lifetime was measured at *BABAR* using a sample of 27 million τ -pair events [9]. In this study a “signal” decay is one where the tau decays to three charged pions and a neutrino, and in a “tag” decay the τ decays to an electron and two neutrinos with no other observed neutral energy. For each event the tau decay length is reconstructed in the CMS system by measuring the distance between the nominal beam spot point and the position of the vertex formed by fitting the three signal-side tracks.

The lifetime of the tau lepton, τ_τ , is then extracted using the equation

$$\tau_\tau = \frac{M_\tau}{p_\tau} \lambda_\tau , \quad (2)$$

where the tau mass, M_τ , is taken to be the Particle Data Group (PDG) value [10], λ_τ is the average tau decay length which is measured in the *BABAR* detector, and p_τ is the average τ momentum. p_τ cannot be reliably reconstructed as some momentum is carried off by the neutrino, so Monte Carlo studies are used to predict the average tau momentum.

The tau decay length is first measured in the plane transverse to the boost direction. The measurement in this plane is less sensitive to local alignment errors and avoids boost complications. The beam spot centroid and the vertex from the three tracks are projected onto the transverse plane and the transverse decay length is defined in this plane to be the distance between the beam spot and the three-track vertex.

The polar angle of the tau candidate with respect to the transverse plane is approximated by the polar angle to the three-track total momentum. Dividing the transverse decay length by the polar angle gives the space decay length, λ_τ . The *BABAR* measurement of the tau decay length is shown in Fig 3.

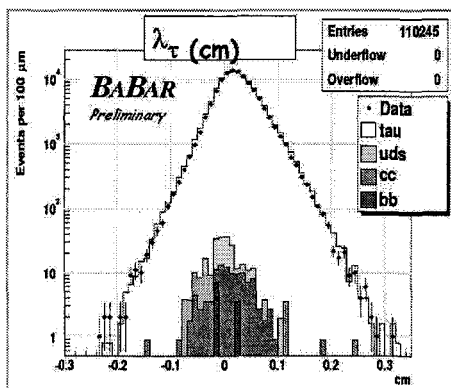


Figure 3: *BABAR* measurement of the tau decay length.

The preliminary result for the mean decay length extracted from this distribution is $\lambda_\tau = 240.72 \pm 1.26 \mu m$. The tau lifetime is extracted using this result, and the *BABAR* preliminary result for the measurement of τ_τ is

$$\tau_\tau = 290.8 \pm 1.5 \text{ (stat)} \pm 1.6 \text{ (syst)} \text{ fs} \quad (3)$$

A comparison of this result with previous tau lifetime measurements is shown in Fig. 4. The *BABAR* result is consistent the world average (which is based on CLEO and LEP results), and the current precision is comparable with the LEP experiments. The largest contributions to the systematic error on this analysis are from Monte Carlo bias subtraction, local alignment uncertainties and absolute scale uncertainty.

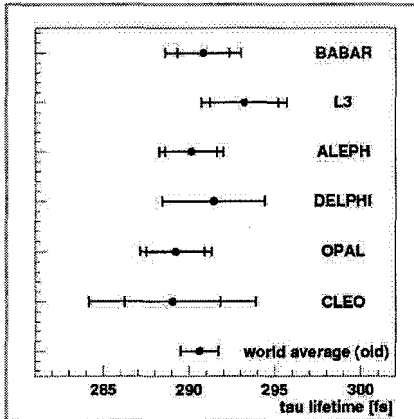


Figure 4: Comparison of *BABAR* tau lifetime measurement with previous results.

5 Study of η_C and $\eta_C(2S)$ production in two-photon interactions

The η_C meson is the lowest lying charmonium state. It is produced in photon-photon interactions in the *BABAR* detector, as illustrated in Fig. 5(a). The properties of the first radial excitation, the $\eta_C(2S)$, are not well established and existing measurements [13–15] are inconsistent. Experiment and theory [11, 12] predict the mass of the $\eta_C(2S)$ to be between about $3.55 \text{ GeV}/c^2$ and $3.65 \text{ GeV}/c^2$, and the total width to be less than $55 \text{ MeV}/c^2$.

The properties of the η_C meson and a candidate for the $\eta_C(2S)$ have been studied in two-photon production events using 88 fb^{-1} of *BABAR* data [16]. The η_C and $\eta_C(2S)$ were studied through the decays

$$\gamma\gamma \rightarrow \eta_C \rightarrow K_SK^\pm\pi^\mp, \quad \text{where } K^S \rightarrow \pi^+\pi^- \quad (4)$$

This decay mode of the η_C has a branching ratio of $(1.8 \pm 0.6)\%$.

The final state $K_S K^\pm \pi^\mp$ is also seen in J/ψ production through initial state radiation, as shown in Fig. 5(b). Properties of the η_C can be determined by measuring mass and width differences between the J/ψ and η_C , as the J/ψ mass is well measured and its width is much smaller than the detector resolution.

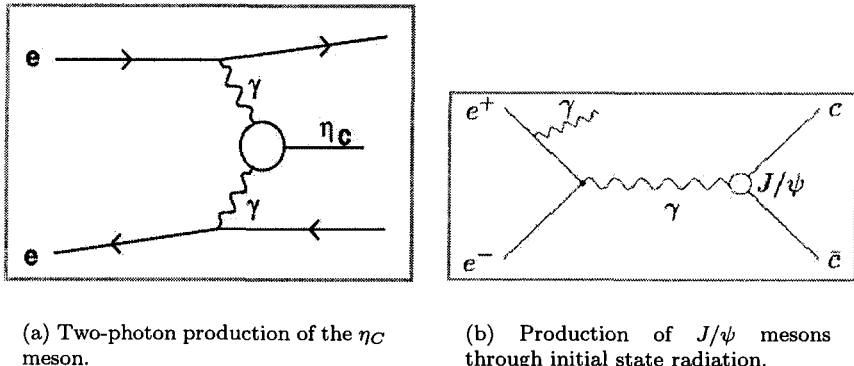


Figure 5: Production mechanisms for η_C and J/ψ mesons studied at *BABAR*.

The invariant mass spectrum for the $K_S K^\pm \pi^\mp$ final state in the region about the J/ψ and η_C masses is shown in the top plot of Fig. 6. The spectrum for the $K_S K^\pm \pi^\mp$ final state in the region about the candidate $\eta_C(2S)$ mass is shown in the bottom plot of Fig. 6.

The η_C peak is fitted with the convolution of a Gaussian for detector resolution and a Breit-Wigner to describe the natural line-shape, while the J/ψ peak is fitted with a Gaussian alone to describe detector resolution. The background is fitted with an exponential. Fit parameters include the J/ψ mass and the $J/\psi - \eta_C$ mass difference, the J/ψ resolution and the η_C width, as well as the background and the number of events in each peak.

Due to their different production mechanisms, the decay products of the J/ψ and the η_C have different angular distributions. As a result, the resolutions in J/ψ and η_C are expected to be different. Following Monte Carlo studies, the η_C width is taken to be $0.8 \text{ MeV}/c^2$ less than that of the J/ψ .

The total width of the η_C is taken to be the measured width of the η_C peak minus the resolution as determined from the fit of the J/ψ peak. The mass of the η_C is taken to be the PDG value [10] of the J/ψ mass minus the $(J/\psi - \eta_C)$ mass difference from the fit. The preliminary results of the *BABAR* measurement of the η_C mass and width are

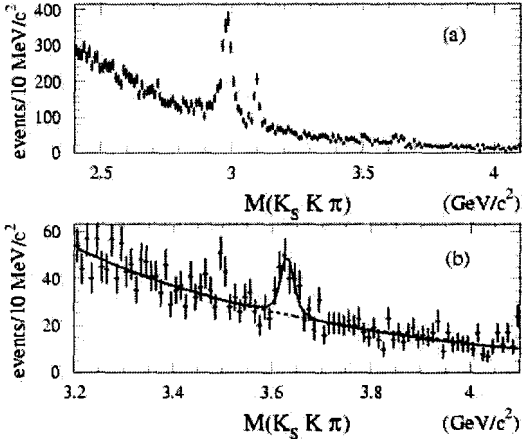


Figure 6: The $K_S K^\pm \pi^\mp$ invariant mass in the J/ψ and η_C regions (top, the left-hand peak is due to the η_C , while the right-hand peak is the J/ψ), and in the $\eta_C(2S)$ mass region (bottom).

$$\begin{aligned} M(\eta_C) &= 2983.3 \pm 1.2(\text{stat}) \pm 1.8(\text{syst}) \text{ MeV}/c^2 \\ \Lambda_{\text{tot}}(\eta_C) &= 33.8 \pm 2.6(\text{stat}) \pm 0.6(\text{syst}) \text{ MeV}/c^2 \end{aligned} \quad (5)$$

The mass measurement is consistent with the PDG value and with most previous η_C mass measurements, while the measured width is consistent with the Belle result but larger than some earlier measurements.

A search for the $\eta_C(2S)$ was carried out by studying the $K_S K^\pm \pi^\mp$ final state in the mass region above the η_C . The same analysis method was used as for the η_C study, and a peak was found just above $3.6 \text{ GeV}/c^2$ with 111 ± 23 events. The significance of this signal is 4.9σ . The quantum numbers of this candidate state need to be measured before it can be conclusively identified as the $\eta_C(2S)$. However, the transverse momentum spectrum of the events in the bump is peaked at 0, suggesting that it originates from two-photon resonance production, and the decay products have an angular distribution similar to that of the η_C .

The mass and width of the $\eta_C(2S)$ candidate have been measured, and the preliminary *BABAR* results are

$$\begin{aligned} \text{mass} &= 3632.5 \pm 3.5(\text{stat}) \pm 1.8(\text{syst}) \text{ MeV}/c^2 \\ \text{decay width} &= 18.5 \pm 8.4(\text{stat}) \pm 2.0(\text{syst}) \text{ MeV}/c^2 \end{aligned} \quad (6)$$

This represents the most precise measurement of the $\eta_C(2S)$ candidate, and is consistent with expectations from theory.

6 Summary

Preliminary measurements of results in tau and two-photon physics from the *BABAR* detector have been presented. A measurement of the tau lifetime was described as well as a search for lepton flavour violation in the decay $\tau \rightarrow \mu\gamma$. Two-photon production of the η_C meson was used to study the properties of the η_C , and the mass and width of a candidate for the $\eta_C(2S)$ were measured.

References

- [1] BaBar, B. Aubert *et al.*, Nucl. Instrum. Meth. **A479**, 1 (2002).
- [2] PEP-II: An Asymmetric b Factory. Conceptual Design Report, 1993, SLAC-R-418.
- [3] D. Black *et al.*, Phys. Rev. **D66**, 053002 (2002).
- [4] J. Hisano, hep-ph/0209005, 3rd Workshop on Higher Luminosity B Factory, Shonan Village, Kanagawa, Japan, 6-7 Aug 2002. Published in *Shonan Village 2002, Higher luminosity B factories* 166-174.
- [5] CLEO, S. Ahmed *et al.*, Phys. Rev. **D61**, 071101 (2000).
- [6] Belle, K. Abe *et al.*, hep-ex/0310029.
- [7] BaBar, C. Brown, eConf **C0209101**, TU12 (2002).
- [8] Z. Was, Nucl. Phys. Proc. Suppl. **98**, 18 (2001).
- [9] BaBar, G. Wagner, hep-ex/0305083.
- [10] K. Hagiwara *et al.*, Phys. Rev **D66**, 010001 (2002).
- [11] D. Ebert *et al.*, Phys. Rev. **D62**, 034014 (2000).
- [12] A. M. Badalian and B. L. G. Bakker, Phys. Rev. **D67**, 071901 (2003).
- [13] Crystal Ball, C. Edwards *et al.*, Phys. Rev. Lett. **48**, 70 (1982).
- [14] Belle, S. K. Choi *et al.*, Phys. Rev. Lett. **89**, 102001 (2002).
- [15] Belle, K. Abe *et al.*, Phys. Rev. Lett. **89**, 142001 (2002).
- [16] BaBar, B. Aubert *et al.*, hep-ex/0311038.

INITIAL STATE RADIATION STUDIES AT THE $\Upsilon(4S)$ USING THE BABAR DETECTOR

Janis McKenna ^a representing the BABAR Collaboration

*Department of Physics and Astronomy, University of British Columbia, Vancouver,
V6T 1Z1, Canada*

Abstract. An analysis of e^+e^- annihilation processes at a center of mass energy near the $\Upsilon(4S)$ resonance with initial state radiation has been performed using the BABAR detector at the PEP-II asymmetric electron-positron collider. Final states consisting of a hard photon plus either a $\mu^+\mu^-$ pair or a pair of oppositely charged hadrons were considered. Using a dataset corresponding to an integrated luminosity of 88.4 fb^{-1} , we measure the product $\Gamma(J/\psi \rightarrow e^+e^-) \cdot B(J/\psi \rightarrow \mu^+\mu^-) = 0.330 \pm 0.008 \pm 0.007 \text{ keV}$. Using the PDG values of the branching fractions $B(J/\psi \rightarrow \mu^+\mu^-)$ and $B(J/\psi \rightarrow e^+e^-)$ [4], the J/ψ electron and total widths may be derived: $\Gamma(J/\psi \rightarrow e^+e^-) = 5.61 \pm 0.20 \text{ keV}$ and $\Gamma = 94.7 \pm 4.4 \text{ keV}$.

1 Introduction and Motivation

With recent results of electroweak physics at LEP and the TeVatron, and new measurements of the muon magnetic anomaly $(g-2)_\mu$ from Brookhaven [1], we have entered a new era in precision tests of the Standard Model. Some of these tests are presently limited by uncertainties in hadronic vacuum polarization, which rely upon the measurement of of R , the ratio of the hadronic e^+e^- cross-section to the Born cross-section for $e^+e^- \rightarrow \mu^+\mu^-$ [2].

Precise measurements of the electroweak parameters in the Standard Model have put improved constraints on interpretation of electroweak parameters and the indirect determination of the mass of the Higgs boson. A goal is to predict the Higgs mass indirectly and precisely, much as was done with the top quark before its direct discovery. But knowledge of the hadronic vacuum polarization contributions to the running of the electromagnetic coupling constant $\alpha(q^2)$, from $q^2 = 0$, up to $q^2 = M_Z^2$, dominate uncertainty in the indirect determination of the Higgs mass [3]. Additionally, the recent precise measurements of the the muon magnetic anomaly, $(g-2)_\mu$ present an extremely sensitive probe to physics beyond the Standard Model [1]. At present, the largest contribution to the uncertainty in the theoretical prediction of $(g-2)_\mu$ is due to hadronic vacuum polarization. In both of these critical tests of the Standard Model, knowledge of the hadronic vacuum polarization contributions are necessary input, and can be related to R through dispersion relations. R may be obtained using a combination of theoretical calculations based on perturbative QCD and improved experimental measurements of R :

$$R = \frac{\sigma(e^+e^- \rightarrow \text{hadrons})}{\sigma_{\text{Born}}(e^+e^- \rightarrow \mu^+\mu^-)} \quad (1)$$

^ae-mail: janis@physics.ubc.ca

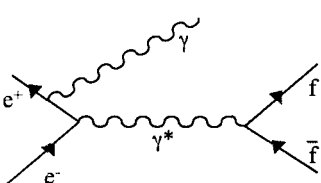


Figure 1: The diagram for $e^+e^- \rightarrow f\bar{f}\gamma$ with ISR to study $e^+e^- \rightarrow f\bar{f}$ at lower effective center-of-mass energies.

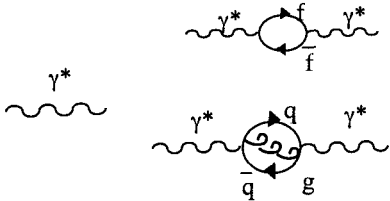


Figure 2: The virtual photon from Figure 1 has well understood QED contributions, as well as hadronic contributions to the QED process.

R is presently reliably calculated at energies above 10 GeV using perturbative QCD, but at lower energies, we must rely on precise measurements of R , as theoretical input alone is inadequate in this non-perturbative low energy region.

At the present time, our knowledge of R at low energies comes largely from a variety of experiments at different accelerator laboratories, each optimized and operating over a specific (and often small) center of mass energy range, thus introducing systematic uncertainties when datasets from these different experiments are combined. A precise measurement of R , preferably from a single experiment and over a wide range of center of mass energies, will improve the precision of input parameters in the aforementioned tests of the Standard Model.

With the advent of the high luminosity e^+e^- storage rings, such as PEP-II, it is now possible to have one experiment operating at **fixed** center-of-mass energy measure R over a broad range of energies using e^+e^- annihilation with initial state radiation (ISR). This procedure greatly minimizes systematic uncertainties in R which result from combining R measurements from many different experiments.

In addition to the precise measurement of R over a range of energies, initial state radiation processes are also of interest as a means of studying low mass particle spectroscopy: using ISR, improvements can be made to the current PDG world average values for branching fractions, mass and width measurements of low mass hadrons. *BABAR* results which improve upon world average J/ψ partial widths are presented here.

2 Initial State Radiation

The initial state radiation process, $e^+e^- \rightarrow X\gamma$, where X is a charged fermion pair $f\bar{f}$, is shown in Figure 1.

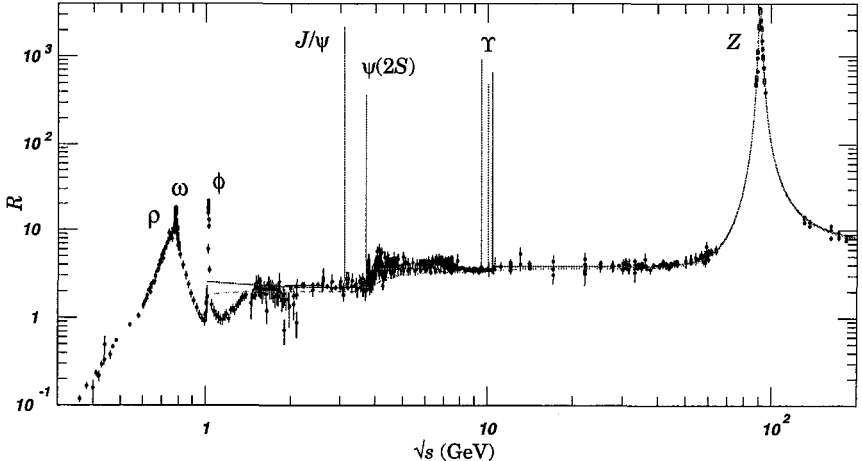


Figure 3: World data on ratio R of hadronic to muon pair cross-section in e^+e^- collisions [4].

The fundamental tests of the Standard Model introduced in the previous section require detailed measurements of $(g - 2)_\mu$ and $\alpha(M_Z^2)$, which in turn require knowledge of the hadronic vacuum polarization of the photon propagator in Figure 1, which can't be calculated perturbatively at low energies. Figure 2 depicts such hadronic correction to the virtual photon.

World data on the ratio R (Equation 1) are shown in Figure 3 [4]. Note that statistics are particularly low in the 1.4–3.5 GeV center-of-mass region, a region in which BABAR can contribute significantly.

2.1 ISR Cross-sections

The differential cross-section $\frac{d\sigma(s,x)}{dx}$ for the ISR process $e^+e^- \rightarrow X\gamma$ may be deduced from the direct $e^+e^- \rightarrow X$ annihilation cross-section, σ_X , for the final state X :

$$\frac{d\sigma(s,x)}{dx} = W(s,x) \cdot \sigma_X[s(1-x)] \quad (2)$$

where $x = 2E_\gamma^*/\sqrt{s}$, \sqrt{s} is the center-of-mass energy of the collider, E_γ^* is the energy of the ISR photon in the center-of-mass frame, and $W(s,x)$ is the probability function for ISR photon emission. The quantity $s' = s(1-x)$ is denotes the mass-squared of the final state system X . The effective ISR luminosity is obtained using the $e^+e^- \rightarrow \mu^+\mu^-\gamma$ process, and hence the Born cross-section $\sigma_X(s')$ is obtained by normalizing to the $e^+e^- \rightarrow \mu^+\mu^-$ cross-

section, $\sigma_{\mu\mu}(s')$:

$$\sigma_X(s') = \frac{N_{X\gamma} \cdot \epsilon_{\mu\mu}(1 + \delta_{FSR}^{\mu\mu})}{N_{\mu\mu\gamma} \cdot \epsilon_X(1 + \delta_{FSR}^X)} \cdot \sigma_{\mu\mu}(s') \quad (3)$$

where $N_{X\gamma}$ and $N_{\mu\mu\gamma}$ are the numbers of detected $X\gamma$ and $\mu^+\mu^-\gamma$ events in the energy bin of width $\Delta s'$ centered at energy s' , ϵ_X and $\epsilon_{\mu\mu}$ are the detection efficiencies for the final states, and $(1 + \delta_{FSR}^{\mu\mu})$ and $(1 + \delta_{FSR}^X)$ are final state radiative correction factors. The radiative corrections to the initial state, acceptance and efficiency for the ISR photon, and vacuum polarization effects cancel in the ratio.

3 BABAR ISR Analysis

The data in this analysis represent 88.4 fb^{-1} taken at $\Upsilon(4S)$ resonance and at slightly lower nearby continuum energies. Details of the *BABAR* detector may be found elsewhere [5].

3.1 Event Selection

ISR events were selected by requiring a well-measured high energy photon plus two oppositely charged tracks. The photon was required to have center-of-mass energy of at least 3 GeV and polar angle in the range $0.35 < \theta < 2.4$ radians. The two oppositely charged tracks were required to each have $p_T > 0.1 \text{ GeV}/c$. Energy and momentum balance were ensured by the conditions $|E_{total} - E_{beams}| < 1.5 \text{ GeV}$ and $\Delta\Psi < 0.07$, where E_{total} is the summed energy of the charged tracks (assuming a muon particle hypothesis) and the photon. $\Delta\Psi$ is the angle between the photon and the direction of the missing momentum, $\mathbf{P}_{miss} = \mathbf{P}_{e^+} + \mathbf{P}_{e^-} - \mathbf{P}_{trk^+} - \mathbf{P}_{trk^-}$.

The large background resulting from radiative Bhabha events ($e^+e^- \rightarrow e^+e^-\gamma$) was removed by requiring that both charged tracks in the final state have $p > 0.5 \text{ GeV}$ and small associated energies in the electromagnetic calorimeter, $E_{EMC} < 0.4 \text{ GeV}$. Final state radiation events (FSR) were suppressed by requiring a large angular separation in the center-of-mass frame between the photon and each of the two charged tracks, $|\cos\theta^*_{\gamma-trk}| < 0.5$.

Monte Carlo simulation of data and backgrounds included initial state radiation, final state radiation, with QED and hadronic final states using the AFKQED Monte Carlo generator package [6]. The JETSET [7] event generator was used to simulate the hadronic channel $e^+e^- \rightarrow q\bar{q}\gamma$.

Note that at this point, no particle identification, other than the elimination of electrons from the final state, has been performed. A detailed description and discussion of cuts and efficiency may be found elsewhere [8].

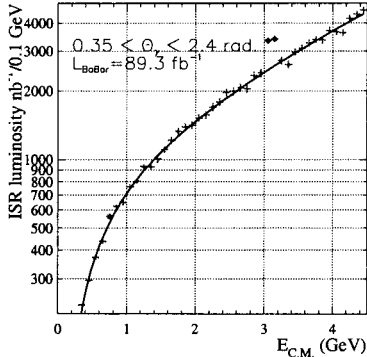


Figure 4: The effective ISR luminosity in 100 MeV bins, with effective $E_{CM} = \sqrt{s'}$, obtained using $e^+e^- \rightarrow \mu^+\mu^-\gamma$. (Points near the $\rho(770)$ and the J/ψ have been excluded from the plot.)

3.2 $\mu^+\mu^-\gamma$ Final State

The process $e^+e^- \rightarrow \mu^+\mu^-\gamma$ is used to deduce the effective ISR luminosity, using Equation 3. In order to remove backgrounds, in particular those arising from $e^+e^- \rightarrow \tau^+\tau^-\gamma$, a 1-C kinematic fit is performed. No muon identification is performed. The effective ISR luminosity for the 88.4 fb^{-1} of *BABAR* data corresponds to an e^+e^- energy scan with $0.7 \text{ pb}^{-1}/100 \text{ MeV}$ at 1 GeV, continuing up to $3.6 \text{ pb}^{-1}/100 \text{ MeV}$ at 4 GeV, as is shown in Figure 4.

Three processes which contribute to the $\mu^+\mu^-\gamma$ final state are shown in Figure 5: initial state radiation, final state radiation and resonant J/ψ production. The Born cross-section for J/ψ production, $e^+e^- \rightarrow J/\psi \rightarrow \mu^+\mu^-$ is given to first order by:

$$\sigma_{J/\psi} = \frac{12\pi^2 \Gamma_{ee} B_{\mu\mu}}{ms} W(s, x_0); \quad x_0 = 1 - m^2/s \quad (4)$$

where m and Γ are the mass and total width of the J/ψ , and B_{ee} and $B_{\mu\mu}$ are the branching fractions $B(J/\psi \rightarrow e^+e^-)$ and $B(J/\psi \rightarrow \mu^+\mu^-)$, respectively, and Γ_{ee} and $\Gamma_{\mu\mu}$ are the partial widths $\Gamma(J/\psi \rightarrow e^+e^-)$ and $\Gamma(J/\psi \rightarrow \mu^+\mu^-)$, respectively, so that $\Gamma_{ee} = \Gamma \cdot B_{ee}$. The mass spectrum is modified slightly when the interference between resonant J/ψ and the direct QED amplitudes is included, as shown in Figure 6.

The *BABAR* $\mu^+\mu^-$ invariant mass in ISR events near the J/ψ resonance is shown in Figure 7, and using the J/ψ peak and continuum, $\Gamma_{ee} \cdot B_{\mu\mu}$ may be deduced:

$$\Gamma_{ee} \cdot B_{\mu\mu} = (0.330 \pm 0.008_{stat} \pm 0.007_{syst}) \text{ keV} \quad (5)$$

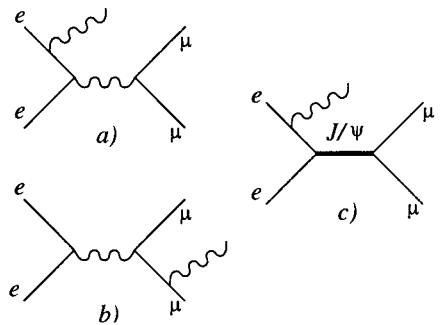


Figure 5: Three processes contribute to the $e^+e^- \rightarrow \mu^+\mu^-\gamma$ final state: a) initial state radiation, b) final state radiation c) J/ψ production.

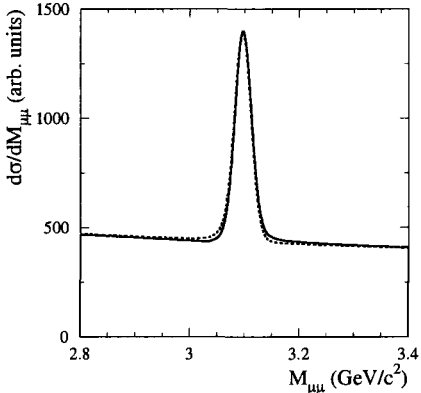


Figure 6: The dimuon mass spectrum calculated with(solid) and without(dashed line) interference between resonant J/ψ and QED amplitudes.

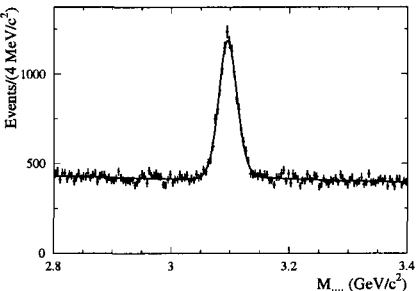


Figure 7: The $\mu^+\mu^-$ invariant mass spectrum. The curve is the result of a maximum likelihood fit to the data.

The world averages for the branching fractions B_{ee} and $B_{\mu\mu}$ are dominated by BES Collaboration measurements [9], and may be used to derive the total width of the J/ψ , $\Gamma = (94.7 \pm 4.4)$ keV and the electronic width $\Gamma_{ee} = (5.61 \pm 0.20)$ keV. These results agree with and significantly improve upon existing world averages for these quantities, $\Gamma = (87 \pm 5)$ and $\Gamma_{ee} = (5.26 \pm 0.37)$ respectively [4].

3.3 Hadronic Final States

One strategy to measure R is to examine exclusive hadronic final states with charged tracks and an ISR photon. Preliminary studies of the $\pi^+\pi^-$, K^+K^- , $p\bar{p}$ final states have been performed with BABAR, using a 1-C fit for each mass hypothesis and requiring particle identification in the K^+K^- and $p\bar{p}$ final states. Additionally investigations of final states with 4 charged hadrons plus a photon are underway. The statistics in each case are sufficient so that BABAR results compare favourably with existing results from CMD-2, DM-2 and ADONE in the 1.4-2.5 GeV energy region, and will improve upon world average values for J/ψ decays to two hadrons and four hadron final states. Full analysis for these channels is in progress.

4 Summary and Conclusions

B Factories are not only for B physics! Initial state radiation luminosity at PEP-II/BABAR is sufficient to use as a great tool for measuring e^+e^- cross-

sections over a range of center-of-mass energies, while operating at a fixed energy storage ring. *BABAR* will soon contribute to measurement of R , enabling critical and precise tests of the Standard Model. Additionally, *BABAR* currently has performed the most precise determination of the electronic and total J/ψ widths and very soon measurements of several more J/ψ partial widths will improve upon the world average values for these quantities.

Acknowledgments

I would like to thank the hosts of the 11th Lomonosov Conference on Elementary Particle Physics for their warm hospitality and an interesting conference.

References

- [1] G. W. Bennett *et al.* [Muon g-2 Collaboration], *Phys. Rev. Lett.* **89**, 101804 (2002), [Erratum-*ibid.* **89**, 129903 (2002)].
- [2] S. Binner, J.H. Kühn, K. Melnikov, *Phys. Lett. B* **459**, 279 (1999).
- [3] U. Baur *et al.* [The Snowmass Working Group on Precision Electroweak Measurements Collaboration], *Proc. of the APS/DPF/DPB Summer Study on the Future of Particle Physics (Snowmass 2001)* ed. N. Graf, eConf **C010630**, P1WG1 (2001)
- [4] K. Hagiwara *et al.* [Particle Data Group Collaboration], *Phys. Rev. D* **66**, 010001 (2002).
- [5] B. Aubert *et al.* [*BABAR* Collaboration], *Nucl. Instrum. Meth. A* **479**, 1 (2002)
- [6] A. B. Arbuzov, G. V. Fedotovich, E. A. Kuraev, N. P. Merenkov, V. D. Rushai and L. Trentadue, *JHEP* **9710**, 001 (1997), and A. B. Arbuzov, E. A. Kuraev, N. P. Merenkov and L. Trentadue, *JHEP* **9812**, 009 (1998).
- [7] T. Sjöstrand, *Comput. Phys. Comm.*, **82** 74 (1994).
- [8] B. Aubert *et al.* [*BABAR* Collaboration], *Phys. Rev. D* **69**, 011103 (2004).
- [9] J. Z. Bai *et al.* [*BES* Collaboration], *Phys. Rev. D* **58**, 092006 (1998).

SEMILEPTONIC B DECAYS IN BABAR

A.Sarti^a

Dep. of Physics, The University of Ferrara and INFN, I-44100 Ferrara, Italy

Abstract. *BABAR* measurements involving semileptonic decays of B mesons are reviewed. Attention is focused on the extraction of $|V_{ub}|$ and $|V_{cb}|$ elements of the Cabibbo-Kobayashi-Maskawa quark mixing matrix. Recent results of inclusive and exclusive approaches are presented.

The study of semileptonic B decays provides observables for the extraction of $|V_{ub}|$ and $|V_{cb}|$ elements of Cabibbo-Kobayashi-Maskawa matrix, the measurement of the b -quark mass and the extraction of non-perturbative QCD parameters ($\bar{\Lambda}, \lambda_1$). The theoretical framework for such measurements consists mainly of two different approaches: the Operator Product Expansion (OPE)[1], used for the extraction of inclusive semileptonic rates, and the Heavy Quark Effective Theory, providing the tools for handling exclusive decays. Both approaches need corrections when used in real measurements: the analysis cuts, used to reject background events, are reducing the decay kinematic phase space and thus have to be included in the OPE. The uncertainty on those corrections is currently giving the higher contribution to the systematic error. Similarly, in $|V_{cb}|$ exclusive measurements, an extrapolation to a phase space boundary is needed when using HQET.

From the experimental point of view the reconstruction of a large B meson sample ($\text{BR}(b \rightarrow u\bar{v}) \sim 10^{-3}$) and an accurate reconstruction of the B decay chain (the current relative error on $|V_{cb}|$ is $\sim 2\%$) are main issues. A dedicated B meson reconstruction technique has been set up in *BABAR* to fulfill the following requirements. A large sample of B mesons can be collected by selecting hadronic decays $B_{\text{reco}} \rightarrow D^{(*)}X$, where X represents a collection of hadrons composed of π, K, K_s^0, π^0 mesons. The kinematic consistency of B_{reco} candidates is checked with two variables, the beam energy-substituted mass $m_{ES} = \sqrt{s/4 - \vec{p}_B^2}$ and the energy difference $\Delta E = E_B - \sqrt{s}/2$. Here \sqrt{s} is the total energy in the $\Upsilon(4S)$ center of mass frame, and \vec{p}_B and E_B denote both the momentum and energy of the B_{reco} candidate, in the same frame. The advantages of fully reconstructing one B meson in the event are: an easier subtraction of the continuum background, the knowledge of decay kinematics of the other B (the only missing particle should be the neutrino) and the possibility to request flavor and charge correlations between the fully reconstructed B meson and the one decaying semileptonically (B_{recoil}). On the recoil side, semileptonic events can be selected using a cut on the lepton momentum ($\sim 0.5 \div 1 \text{ GeV}/c$) and on the neutrino four-momentum. The efficiency of this reconstruction technique is $\sim 0.1 \div 0.4\%$.

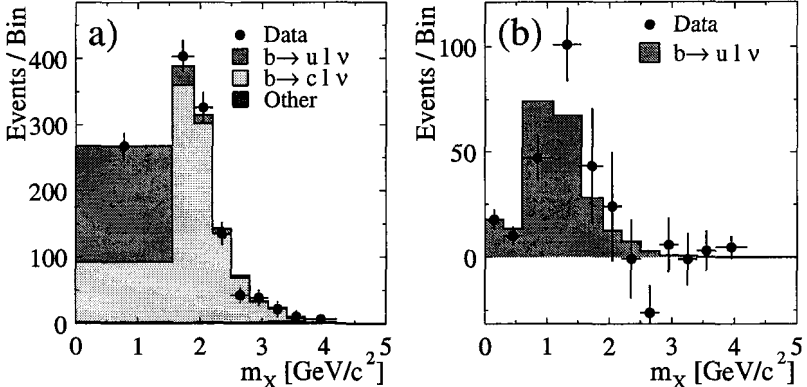


Figure 1: The m_X distribution for $\bar{B} \rightarrow X \ell \bar{\nu}$ candidates for *BABAR* inclusive analysis: a) data (points) and fit components, and b) data and signal MC after subtraction of the $b \rightarrow c \ell \nu$ and the “other” backgrounds.

1 Inclusive $|V_{ub}|$ measurement

The main experimental issue of this analysis is the rejection of the huge $\bar{B} \rightarrow X_c \ell \bar{\nu}^b$ background ($\mathcal{B}(\bar{B} \rightarrow X_c \ell \bar{\nu}) \sim 60 \times \mathcal{B}(\bar{B} \rightarrow X_u \ell \bar{\nu})$). The B_{recoil} charmless semileptonic decays are selected with a cut on the lepton momentum, a cut on the neutrino mass and a veto on neutral and charged kaons. The residual background is determined from a fit of the hadronic invariant mass (m_X) distribution and $|V_{ub}|$ is extracted from the measured semileptonic rate using the OPE relation [2]: $|V_{ub}| = 0.00445 \sqrt{\frac{B(b \rightarrow u \ell \nu) \cdot 1.55 ps}{0.002 \tau_B}} \times (1.0 \pm 0.020_{pert} \pm 0.052_{1/m_b^3})$. In order to reduce systematic uncertainties, the ratio of branching ratios $R_{u/sl} = \mathcal{B}(\bar{B} \rightarrow X_u \ell \bar{\nu}) / \mathcal{B}(\bar{B} \rightarrow X \ell \bar{\nu})$ is determined from N_u , the observed number of $\bar{B} \rightarrow X_u \ell \bar{\nu}$ candidates with $m_X < 1.55 \text{ GeV}/c^2$, and N_{sl} , the number of events with at least one charged lepton: $R_{u/sl} = \frac{N_u / (\varepsilon_{sel}^u \varepsilon_{m_X}^u)}{N_{sl}} \times \frac{\varepsilon_l^{sl} \varepsilon_{reco}^{sl}}{\varepsilon_l^u \varepsilon_{reco}^u}$. Here ε_{sel}^u is the efficiency for selecting $\bar{B} \rightarrow X_u \ell \bar{\nu}$ decays once a $\bar{B} \rightarrow X \ell \bar{\nu}$ candidate has been identified, $\varepsilon_{m_X}^u$ is the fraction of signal events with $m_X < 1.55 \text{ GeV}/c^2$, $\varepsilon_l^{sl} / \varepsilon_l^u$ corrects for the difference in the efficiency of the lepton momentum cut for $\bar{B} \rightarrow X \ell \bar{\nu}$ and $\bar{B} \rightarrow X_u \ell \bar{\nu}$ decays, and $\varepsilon_{reco}^{sl} / \varepsilon_{reco}^u$ accounts for a possible efficiency difference in the B_{recoil} reconstruction in events with $\bar{B} \rightarrow X \ell \bar{\nu}$ and $\bar{B} \rightarrow X_u \ell \bar{\nu}$ decays. N_{sl} is derived from a fit to the m_{ES} distribution. N_u is extracted from the m_X distribution by a minimum χ^2 fit to the sum of three contributions: the signal, the background N_c from $\bar{B} \rightarrow X_c \ell \bar{\nu}$, and a background of < 1% from other sources (misidentified leptons, secondary τ and charm decays). Fig. 1a shows the fitted m_X distribution. Fig. 1b shows the m_X dis-

^ae-mail: asarti@slac.stanford.edu

^bCharge conjugation is implied.

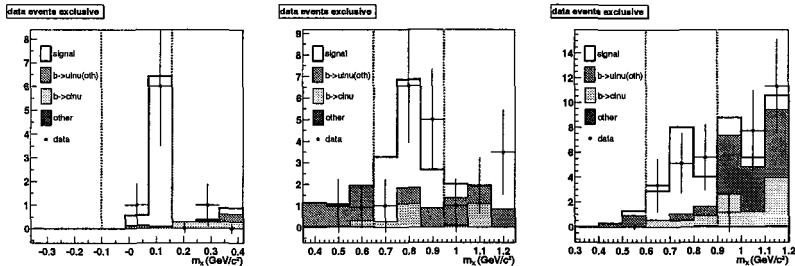


Figure 2: Projections in the m_X variable for the $BABAR$ $|V_{ub}|$ exclusive analysis. Vertical dotted lines represent the signal region. Left: $B^\pm \rightarrow \pi^0 l \bar{v}$; middle: $B^\pm \rightarrow \rho^0 l \bar{v}$; right: $B^\pm \rightarrow \omega l \bar{v}$.

tribution after background subtraction. By using 82 fb^{-1} integrated luminosity on the $\Upsilon(4S)$ peak, $BABAR$ obtains $|V_{ub}| = (4.62 \pm 0.28 \pm 0.27 \pm 0.40 \pm 0.26) \times 10^{-3}$, where errors are respectively statistical, detector systematic, theoretical model and propagation of error from the OPE relation [2]. The signal over background ratio (S/B) is 1.7 (higher than any previous inclusive analysis) and the main error comes from the parametrization of the b -quark Fermi motion inside the B meson parametrization. Reduction of theoretical systematic error, related to the shape function parameterization of the Fermi motion, can be achieved by adding a cut on the di-lepton pair invariant mass (q^2), to the m_X one, which allows for a reduction of systematic error of $\sim 35\%$ on $|V_{ub}|$.

2 Exclusive $|V_{ub}|$ measurement

Using the same B meson reconstruction technique as in the inclusive analysis, and with a similar analysis strategy and signal events selection, it is possible to study the exclusive $\bar{B} \rightarrow X_u \ell \bar{v}$ decays. The high purity of the sample of reconstructed B mesons makes possible to use the mass of the hadronic system (m_X) to separate the resonances. $B^\pm \rightarrow \pi^0 l \bar{v}$, $B^\pm \rightarrow \rho^0 l \bar{v}$ and $B^\pm \rightarrow \omega l \bar{v}$ decays are selected applying constraints on the missing mass and m_X . The measured exclusive branching ratios are: $\mathcal{B}(B^\pm \rightarrow \pi^0 l \bar{v}) = (0.78 \pm 0.32_{\text{stat}} \pm 0.13_{\text{syst}}) 10^{-4}$, $\mathcal{B}(B^\pm \rightarrow \rho^0 l \bar{v}) = (0.99 \pm 0.37_{\text{stat}} \pm 0.19_{\text{syst}}) 10^{-4}$ and $\mathcal{B}(B^\pm \rightarrow \omega l \bar{v}) = (2.20 \pm 0.92_{\text{stat}} \pm 0.57_{\text{syst}}) 10^{-4}$, where the main contribution to the systematic error comes from the uncertainty on signal MC modeling and the fit to the m_{ES} distributions used to extract the number of signal events. The $\mathcal{B}(B^\pm \rightarrow \rho^0 l \bar{v})$ result is obtained applying a cut on the two pions invariant mass ($0.65 \text{ GeV}/c^2 \leq m_{\pi^+\pi^-} \leq 0.95 \text{ GeV}/c^2$). In Figure 2 the projection of the results on the m_X variable is shown.

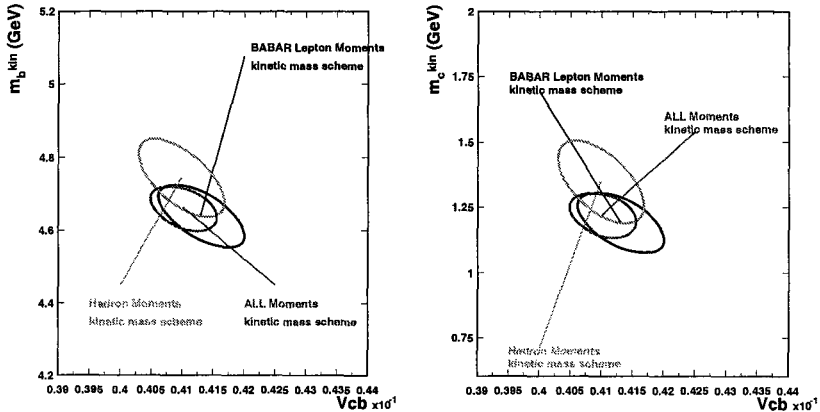


Figure 3: Fit results with contours corresponding to $\Delta\chi^2 = 1$ for (left) $|V_{cb}|$ versus m_b , and (right) $|V_{cb}|$ versus m_c , separately for fits using the hadron mass, the lepton energy, and all moments.

3 Inclusive $|V_{cb}|$ measurement

By measuring the first few moments $\langle m_\chi^n \rangle$ of the hadronic mass distributions in $\bar{B} \rightarrow X_c \ell^- \bar{\nu}_\ell$ decays, it is possible to constrain the OPE parameters and extract $|V_{cb}|$ and the heavy quark masses m_b and m_c . The measurement of the lepton energy moments can also improve the determination of $|V_{cb}|$ [3]. B mesons have been fully reconstructed with the technique discussed above. The semileptonic events selection proceeds using a cut on the lepton momentum and on the missing mass. Charge and flavor correlations are requested. The main sources of systematic errors are the precision in the modeling of the detector efficiency and particle reconstruction, the subtraction of the combinatorial background of the B_{reco} sample, the residual background estimate and the uncertainties in the modeling of the hadronic states. The results do not depend on assumptions for branching fractions and mass distributions for higher mass hadronic states. Using a Heavy Quark Expansion in the kinetic mass scheme to order $1/m_b^3$, we extract the branching fraction, $\mathcal{B}_{c\ell\nu} = (10.62 \pm 0.16_{\text{exp}} \pm 0.06_{\text{HQE}})\%$, and the CKM matrix element, $|V_{cb}| = (41.25 \pm 0.45_{\text{exp}} \pm 0.41_{\text{HQE}} \pm 0.62_{\text{theory}}) \times 10^{-3}$, with significantly reduced uncertainties. Figures 3(left) and 3(right) are showing the $\Delta\chi^2 = 1$ ellipses for $|V_{cb}|$ versus m_b and $|V_{cb}|$ versus m_c for the standard fit to all data and separate fits of the hadron and lepton moments, but including the truncated branching fractions in both.

4 Exclusive $|V_{cb}|$ measurement

A measurement of exclusively reconstructed $\bar{B}^0 \rightarrow D^{*+} \ell^- \bar{\nu}_\ell$ decays rate (Γ) can be used to extract $|V_{cb}|$ [4] by measuring the decay rate $d\Gamma/dw$ for $w > 1$, where w is

the Lorentz boost of the D^{*+} in the \bar{B}^0 rest frame, and extrapolating the rate to the kinematic limit corresponding to $w=1$. The analysis is based on a data sample of 79 (9.6) fb^{-1} recorded on (40 MeV below) the $\Upsilon(4S)$ resonance. We select events containing a D^* and an oppositely-charged electron or muon with momentum in the range $(1.2 < p_\ell < 2.4 \text{ GeV}/c)$. For each decay candidate we compute the cosine of the angle between momentum of the \bar{B}^0 and of the $D^{*+}\ell^-$ pair, $\cos\theta_{B^0,D^*\ell} = \frac{2E_{B^0}E_{D^*\ell}-M_{B^0}^2-M_{D^*\ell}^2}{2p_{B^0}p_{D^*\ell}}$, that we fit in the range $-10 < \cos\theta_{B^0,D^*\ell} < 5$ to determine the signal contribution and the normalization of the uncorrelated and $B \rightarrow D^{*+}\pi\ell^-\bar{\nu}_\ell$ backgrounds. To extract $|V_{cb}|$, we compare the signal yields to the expected differential decay rate $\frac{d\Gamma}{dw} = \frac{G_F^2}{48\pi^3} \mathcal{G}(w) [|V_{cb}| \mathcal{H}(w)]^2$, where $\mathcal{G}(w)$ is a known phase space factor and $\mathcal{H}(w)$ is the form factor. We consider two different parameterization of $\mathcal{H}(w)$. A simple Taylor expansion with three parameters (the extrapolation $\mathcal{F}(w=1)|V_{cb}|$, the slope $\rho_{\mathcal{F}}^2$, and the curvature c) and a parameterization with two parameters (the extrapolation $|V_{cb}|\mathcal{A}_1(w=1)$ and the slope $\rho_{\mathcal{A}_1}^2$). The two functions have different slopes, but in the limit $w \rightarrow 1$, we expect $\mathcal{A}_1(1) = \mathcal{F}(1)$. We perform a least-squares fit of the sum of the observed signal plus background yields to the expected yield in ten bins of w . Figure 4 compares the observed yield of signal and background events summed over all data samples with the result of the fit and illustrates the extrapolation to $w=1$ for the two form factor parameterizations. A major source of uncertainty is the reconstruction efficiency of the low-momentum pion from the D^{*+} decay. Furthermore, there are several uncertainties related to the form factors and their parameterization. The fit results for the two different parameterizations of the dependence of the form factors on w give consistent results. We adopt the result based on the more recent parameterization by Caprini *et al.* [5] and assign the observed difference in the extrapolation to $w \rightarrow 1$ as an additional systematic error. Using the recent lattice calculation [4], we obtain $|V_{cb}| = (38.03 \pm 0.68 \pm 1.07 {}^{+1.25}_{-1.15} {}^{+1.45}_{-1.25}) \times 10^{-3}$, where the first error is statistical, the second systematic, the third the model uncertainty (including the choice of the form factor expansion) and the fourth reflects the uncertainty in $\mathcal{A}_1(1)$.

5 Conclusions and outlook

BABAR studies of semileptonic B decays have given a significant contribution to the understanding of the theoretical framework used to describe $b \rightarrow u$ and $b \rightarrow c$ transitions (OPE and HQET) and resulted in a consistent reduction of the error on the $|V_{ub}|$ and $|V_{cb}|$ CKM matrix elements. The $|V_{ub}|$ inclusive analysis result is currently the best single measurement with a relative error on $|V_{ub}|$ of $\sim 14\%$ and $S/B \sim 1.7$ while the exclusive analysis gave promising preliminary results. The $|V_{cb}|$ exclusive analysis is currently the most precise single measurement and is consistent with results from Belle and LEP, while the preliminary result of the moment analysis will soon become public still reducing the uncertainty on $|V_{cb}|$.

^cMomenta are measured in the $\Upsilon(4S)$ rest frame, unless explicitly stated otherwise.

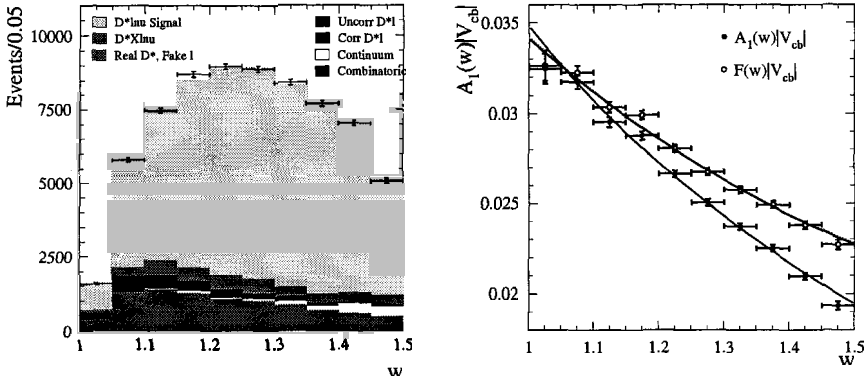


Figure 4: Left: Result of the fit (histograms) to the observed w distribution (data points). Right: Form factor dependence on w , fits (lines) and data corrected for background and efficiency, all the terms in the decay rate except for $|V_{cb}|F(w)$ for two different parameterizations (see text for details).

References

- [1] I. I. Y. Bigi, M. A. Shifman, N. G. Uraltsev, and A. I. Vainshtein, Phys. Rev. Lett. **71**, 496 (1993); A. V. Manohar and M. B. Wise, Cambridge Monogr. Part. Phys. Nucl. Phys. Cosmol. **10**, 1 (2000).
- [2] K. Hagiwara *et al.* [Particle Data Group Collaboration], Phys. Rev. D **66**, 010001 (2002).
- [3] B. Aubert *et al.* (BABAR Collaboration), “*Measurement of $|V_{cb}|$ using Lepton Energy and Hadronic Mass Moments in Semileptonic B Decays.*” (2003), to be submitted to Phys. Rev. Lett.
- [4] S. Hashimoto *et al.*, Phys. Rev. D **66**, (2002) 014503.
- [5] I. Caprini, L. Lellouch, M. Neubert, Nucl. Phys. B **530** (1998) 153; C. G. Boyd, B. Grinstein, R. F. Lebed, Phys. Rev. D **56** (1997) 6895.
- [6] R.A. Briere *et al.* [CLEO Collaboration], Phys. Rev. Lett **89** (2002) 081803; N.E. Adam *et al.* [CLEO Collaboration], Phys. Rev. D **67** (2003) 032001.

PERSPECTIVES OF THE STUDY OF DOUBLE POMERON EXCHANGE AT THE LHC

J.P.Guillaud ^a, A.Sobol ^b

*Laboratoire d'Annecy-le-Vieux de Physique des Particules (LAPP), IN2P3-CNRS,
Chemin de Bellevue, BP110, F-74941, Annecy-le-Vieux, FRANCE*

Abstract. We discuss the theoretical estimates and perspectives of the measurements of doubly diffractive production in central proton-proton collisions, $pp \rightarrow pXp$ at LHC energy, where a pure double Pomeron exchange is predicted. Such study can be done by measurements using one of the two general-purpose LHC detectors, CMS or ATLAS, and with a set of special tracking detectors located close to the beam at distances more than 100 meters from the interaction point to detect the diffractively scattered protons. This study is interesting due to the intensive glueball production expected in the mass region below 10 GeV and due to the unique possibility of the measurements of exclusive Higgs production in double Pomeron exchange.

1 Introduction

The talk is devoted to the exclusive measurements of central production in proton-proton collisions:



Figure 1: Diagram of the central production in proton-proton collisions.

The X , produced in the interaction of the two exchanged particles which can be Reggeons (R) or Pomerons (P), is called a central particle (or system) due to its pseudorapidity which is close to 0. Such reactions are predicted to be a source of glueballs or gluonic rich states when both of the exchanged particles are Pomerons (Double Pomeron Exchange (DPE)).

Theoretical predictions [1] for the intensities of the different types of exchange in function of the centre of mass energy:

$$\begin{aligned} \sigma(RR) &\sim s^{-1}, \\ \sigma(RP) &\sim s^{-0.5}, \\ \sigma(PP) &\sim \text{constant}, \end{aligned} \quad (2)$$

^ae-mail: Jean-Paul.Guillaud@cern.ch

^be-mail: Andrei.Sobol@cern.ch

where RR , RP and PP mean respectively Reggeon-Reggeon, Reggeon-Pomeron and Pomeron-Pomeron exchanges. These show that the contribution of the double Pomeron exchange in relation to the Reggeon-Reggeon and Pomeron-Pomeron exchanges in the cross-section of reaction 1 increases with the increase of the energy. So the production of central resonances with a rich gluon component becomes dominant. The cross-section for DPE at the LHC energy, $\sqrt{s} = 14\text{TeV}$, is equal around 0.37 mb and the X production concentrates in the mass region below 10 GeV dominantly.

The advantages of a study of the central production (reaction 1) at the LHC energy are more striking if one shifts the study of low X mass (several GeV) to much heavier objects. One of the main goal of the LHC is the search of the Higgs boson. It turns out, that Higgs can be produced in the central proton-proton collisions (reaction 1) by DPE exchange. Some estimates of the cross-section for the exclusive central Higgs production at LHC energy are listed in the table below:

Year	Publication	M_H , GeV	σ_H , fb
1991	[2]	[100,400]	$100 \div 200$
1995	[3]	[100,400]	$1000 \div 2000$
2000	[4]	100	$10 \div 270$
2001	[5]	[100,400]	$80 \div 140$
2002	[6]	120	≈ 3

Table 1: Theoretical predictions for Higgs production in DPE at $\sqrt{s}=14\text{ TeV}$.

If we consider a cross-section $\sigma_H = 100\text{ fb}$ as an optimistic estimate given by the table 1 one will get more than 30000 exclusive Higgs/year produced by DPE at the nominal LHC luminosity $L = 10^{34}\text{cm}^{-2}\text{s}^{-1}$.

2 Perspectives of the measurements

2.1 Low luminosity physics

To study an exclusive central production (reaction 1) we should measure the central particle X or its decay products and the 2 protons of the final state of the reaction. X , which has a rapidity from -3 to 3, is efficiently detected by the CMS [7] electromagnetic calorimeters (BARREL and ENDCAP) and tracker. But CMS cannot trigger on the protons scattered with small angles ($10 \leq \eta \leq 14$). This can be made using the TOTEM [8] forward tracking detectors located inside the beam-pipe, the so-called Roman Pots (RP). TOTEM will install several RP stations at distance from 100 to 215 meters along the beam. The general scheme of the measurements is shown in fig.2. Using the CMS+TOTEM facilities could be an unique opportunity to study the DPE reactions at LHC.

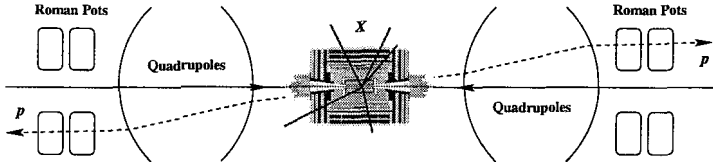


Figure 2: Scheme of the forward protons measurement using Roman pots stations.

To perform successful measurements at very small scattered angles TOTEM needs some special parameters for the beam, which are different from the nominal LHC conditions. It requires to:

- run with high- β optics ($\beta_{TOTEM}^* = 1000 \div 1500\text{m}$), instead of the nominal LHC $\beta_{nom}^* = 0.5\text{m}$ ^c;
- decrease the number of bunches, $n_{TOTEM}/n_{nom} \approx 10^{-2}$.

Such conditions led to the decline of the luminosity from $L_{nom} = 10^{34}\text{cm}^{-2}\text{s}^{-1}$ to $L_{TOTEM} = 10^{28}\text{cm}^{-2}\text{s}^{-1}$. The measurements can be performed in special runs during the early running-in phase of the LHC, taking periods of a few days. The estimated number of DPE events (non-corrected by any efficiency) is about ≈ 350000 per day at this low luminosity.

We made an estimates of the efficiency of DPE registration, resolution and background conditions for the neutral and charged decay channel of the X in the reaction 1. The mass dependence of the efficiency for the reaction $pp \rightarrow pXp, X \rightarrow 2\pi^0 \rightarrow 4\gamma$ is shown in fig.3. The low energy gammas decrease the efficiency essentially because the noise terms in the resolution of the electromagnetic calorimeters are rather large. One can see on this figure that the gamma conversion and the energy cut in the Barrel ECAL strongly suppress the detection of the events. The mass resolution of the calorimeter has been studied as a function of the X mass. The relative resolution on the X mass, $d\sigma_M/dM$, decreases from 25% at 1 GeV to 10% at 5 GeV.

The same study has been performed for the charged decay channel of the X particle: $pp \rightarrow pXp, X \rightarrow \pi^-\pi^+$. It was required that 2 charged pions should be detected by the CMS tracker and the 2 protons by the Roman Pots. The result for the efficiency is shown in fig.4.

The efficiency for tracks detection increases rapidly and becomes higher than the efficiency of the proton detection above 2.5 GeV. Thus, above 3 GeV the efficiency is very high (close to 90%) and is only limited by the efficiency for proton detection. The mass resolution is about 0.7% above 2 GeV and rises up to $\approx 1.2\%$ at 1 GeV, which is much better than in the case of neutral decays.

^cThe β -function is an optical function of the collider defining the transverse size of the beam ($\sigma_{x,y}^* \sim \sqrt{\beta^*}$). β^* is the value of the β -function at the interaction points.

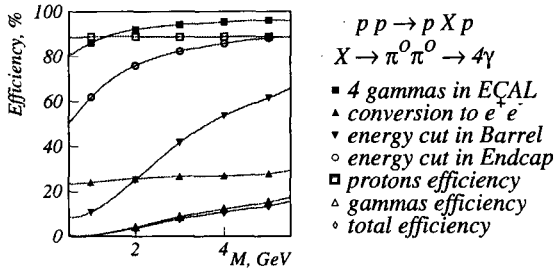


Figure 3: Mass dependence of the efficiency for the reaction $pp \rightarrow pXp, X \rightarrow 2\pi^0 \rightarrow 4\gamma$. The curves show the contribution to the total efficiency of the different factors suppressing the registration of events.

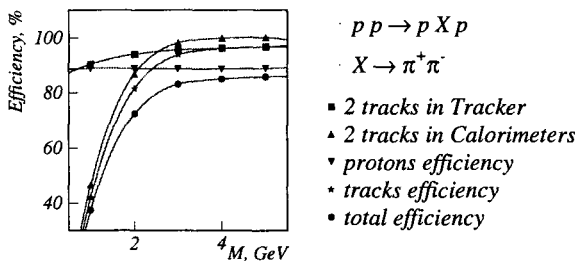


Figure 4: Mass dependence of the efficiency for the reaction $pp \rightarrow pXp, X \rightarrow \pi^-\pi^+$. The curves show the contribution to the total efficiency of the different factors suppressing the registration of events.

In order to investigate the background to the central production, we use the standard CMS set of PYTHIA's parameters for minimum bias^d. In addition the processes which have similar kinematics to double Pomeron exchange (DPE), such as elastic scattering, single diffraction, double diffraction, are included in the background.

We suggest some requirements for the DPE selection which can be used for the trigger or for the off-line event analysis. The main one is the detection of one track in the forward Roman pots and one track in the backward ones. We use also different energy deposits in the CMS calorimeters for the background and for the DPE events and the absence of tracks in the TOTEM inelastic tracking detectors T1 and T2 covering a pseudorapidity region from 3 to 7. Such selection requirements allow a very effective background suppression, saving more than 85% of the DPE events. The ratio of DPE to background before

^dhttp://cmsdoc.cern.ch/cms/Physics/btau/www/MB_cards.html

and after selections is the following:

$$\left(\frac{N_{DPE}}{N_{bg}} \right)_{\text{before selection}} \approx 0.004, \quad \left(\frac{N_{DPE}}{N_{bg}} \right)_{\text{after selection}} \approx 20.$$

2.2 High luminosity physics

Measurement of the high mass central system in reaction 1, for example Higgs, which has an extremely small cross-section is impossible at the luminosity $L_{TOTEM} = 10^{28} \text{ cm}^{-2} \text{s}^{-1}$. But they can be made at the nominal LHC luminosity 10^{34} . Taking into account the most pessimistic estimates of the cross-section for the central Higgs production, 3 fb, one expects 600 events per year (without taking in account any efficiency). The increase of the luminosity should offset by a decrease in β^* ($\beta_{\text{nom}}^* = 0.5 \text{ m}$) and, as a consequence, the worsening of some beam parameters, as the beam momentum and angular spread. The transverse size of the beam becomes larger at the distances $100 \div 200$ meters, where TOTEM's RPs are located, and one can not use them for measurements of the diffractive scattered protons flying inside the beam. For the high luminosity runs it is suggested to install several additional RP stations at distances $300 \div 450$ meters. One of the possible setup is shown in fig.5.

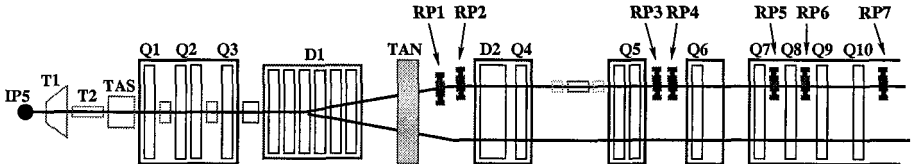


Figure 5: LHC beam line with the 7 RPs. Here, IP5 is the CMS interaction point, T1 and T2 are inelastic tracking detectors of TOTEM, TAS and TAN are collimators, D_i and Q_i are dipole and quadrupole magnets of LHC, RP_i are Roman Pot stations of TOTEM.

The trajectory of the proton (as scattered as beam) is defined exclusively by 6 parameters at the interaction point. One can choose, for example, the following set: $(x^*, y^*, \theta_x^*, \theta_y^*, \xi)$, where (x^*, y^*) are the transverse coordinates at the IP, (θ_x^*, θ_y^*) are the production angles, $\xi = \frac{\delta p}{p}$ is the relative momentum loss of the proton. If one measures the (x_i, y_i) coordinates of the proton by the RPs tracking detectors at different points z_i along the beam and if one knows all trajectories for different initial parameters with MC one can reconstruct the parameters of the proton at the interaction point. The most important of them, defining the diffractive process, are $t = p^2(\theta_x^{*2} + \theta_y^{*2})$, the transverse momentum squared, and ξ . ξ is very important and should be measured for reaction 1, because if one measures ξ_1 for the forward proton and ξ_2 for the backward proton one can calculate the mass of the central system X by the

simple formula (*Missing Mass Method*):

$$M_X^2 = s\xi_1\xi_2. \quad (3)$$

We made an estimate of the efficiency for proton detection by RPs located as shown on fig.5 and of the ξ resolution assuming a $30\text{ }\mu\text{m}$ coordinate resolution for the RPs tracking detectors. The calculations were made for an LHC optic related to $\beta^* = 0.5\text{ m}$. The result is shown in fig.6. The green area on the (z, ξ) 2D plot shows the region of a non-zero efficiency for the proton detection. One can see that RP 5, 6 and 7 cover together the ξ interval from 0.002 to 0.02. Using equation 3 one can calculate the interval of the central masses which is measured by the missing mass method: from 28 to 280 GeV. This interval widely covers the limits on the Higgs mass obtained by LEPII and by a global fit of the Standard Model parameters [9]. The relative ξ resolution and, accordingly, mass resolution in this interval vary from 2 to 5% depending on the ξ value, as can be seen in fig.6. This is a first rough estimate which can be improved, but it is already promising for such a method. This has to be compared with the most optimistic estimate of the Higgs mass resolution via the $H \rightarrow \gamma\gamma$ measurement that gives 1%.

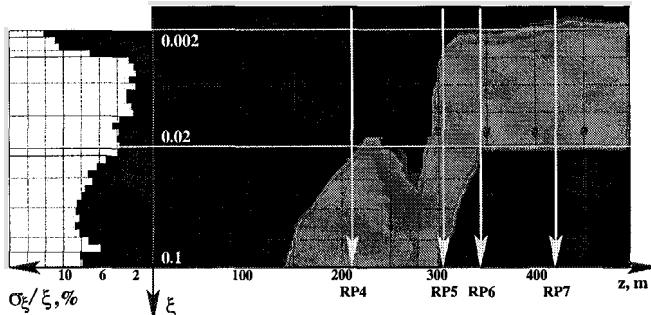


Figure 6: The right 2D histogram shows the efficiency for forward proton detection as a function of ξ , the relative proton momentum loss, and z , the distance along the beam. The RPs positions are shown by arrows. The left histogram presents relative resolution of the ξ measurements by RPs 4, 5, 6 and 7.

At present the analytical estimates of the background to the exclusive Higgs production in the reaction $pp \rightarrow pHp, H \rightarrow b\bar{b}$ have been made in the reference [10]. The significance $S/\sqrt{S+B}$ of the Higgs observation during one year LHC run at a luminosity 10^{33} is estimated to be about 3σ even for the more pessimistic (3 fb) Higgs cross-section. It makes the reaction 1 competitive to the other methods of Higgs measurements (for example, for the channel $H \rightarrow \gamma\gamma$: $S/\sqrt{S+B} \approx 4\sigma$).

3 Conclusion

We conclude that the CMS+TOTEM facility gives an unique opportunity to study the double Pomeron exchange at the LHC. Low mass central systems, having a high cross-section production in DPE (about 0.37 mb) can be studied at low luminosity ($L_{TOTEM} = 10^{28}\text{cm}^{-2}\text{s}^{-1}$) in CMS and TOTEM common runs in the early running-in phase of the LHC. High mass central objects, like Higgs produced diffractively in DPE, have smaller cross-section (a few fb) and can be studied at the nominal LHC luminosity ($L_{nom} = 10^{34}\text{cm}^{-2}\text{s}^{-1}$). Such study needs additional Roman Pots tracking detectors located at distances 300-400 m along the beam on both sides of CMS.

The study of the central production reaction at the LHC energy, where a pure double Pomeron exchange is predicted, gives a feeling of great achievement to understand the nature of the Pomeron and the underlying dynamics of the DPE, to solve the "glueball puzzle" and it gives an unique opportunity to make measurements of the exclusive Higgs production in DPE at LHC.

In this talk, CMS is given as an example but is also valid for ATLAS. In this context, BARREL and ENDCAP (two sub-detectors of CMS) should be replaced by their equivalent sub-detectors of ATLAS (with their pseudorapidity limits). In this way, TOTEM (an experiment with Roman pots in the beam pipe) should be understood, in the case of ATLAS, as Roman pots in the beam pipe on both sides of ATLAS.

Acknowledgments

We thank Pr. V.Petrov and Dr. R.Ryutin for their valuable discussions.

References

- [1] S.N.Ganguli and D.P.Roy, *Phys.Rep.* **67** 203 (1980).
- [2] A. Bialas and P.V. Landshoff, *Phys.Lett.* **B256** 540 (1991).
- [3] J.R.Cudell, O.F.Hernandez, *Nucl.Phys* **B471** 471 (1996).
- [4] D.E.Kharzeev and E.Levin, *Phys.Rev.* **D63** 073004 (2001).
- [5] V.Petrov and R.Ryutin, Talk on the CMS-TOTEM diffraction meeting, 8 March, 2002; <http://totem.web.cern.ch/Totem/cms/meeting.html>
- [6] V.A.Khoze, A.D.Martin and M.G.Ryskin, *Eur.Phys.J.* **C23** 311 (2002).
- [7] CMS Technical Proposal, CERN/LHCC 94-38, December 1994.
- [8] TOTEM Technical Proposal, CERN/LHCC 99-7, March 1999.
- [9] M.S.Chanowitz, LBNL-52452, Feb 2003.
- [10] A.De Roeck et.al., *Eur.Phys.J.* **C25** 391 (2002).

DISCREET HEAVY PHYSICS

José Wudka ^a

*Physics Department, University of California, Riverside
Riverside, CA 92521-0413, U.S.A.*

Abstract. In this talk I review the conditions under which heavy physics *virtual* effects are naturally suppressed without requiring a large scale for new physics.

1 The prophecies

Though there are no clear indications of a deficiency in the Standard Model, it is generally believed that this theory does not represent the most fundamental description of nature. This belief is supported by a variety of arguments. Examples are (*i*) the unexplained origin and enormous range of Yukawa couplings (within the pure Standard Model with the addition of right-handed neutrinos they range over almost 12 orders of magnitude [1]); (*ii*) the unexplained origin of the gauge group and the rationale for its particular structure; (*iii*) possible stability and triviality problems within the scalar sector suggest that there is an upper scale Λ beyond which the Standard Model must be modified. This scale depends on the details of the scalar sector and, in particular, is very sensitive to the masses of the physical scalars [2]; (*iv*) the unexplained origin of discrete symmetries, such as lepton and baryon number conservation, that are conserved within the Standard Model (up to non-perturbative effects, [3]), or almost conserved, such as CP. In addition the Standard Model has a relatively large number of unknown constants which is perceived as undesirable.

The above arguments suggest that the Standard Model is in fact an effective theory, obtained from a more fundamental one in the limit where all external particles have energies below $\sim 1\text{TeV}$. This idea has led to an intense study of the possible physics underlying the Standard Model. These investigations can be divided into two groups: (*i*) those that are based on specific models [4]; and (*ii*) those using an effective Lagrangian to describe new physics at low energies [5].

The second possibility attempts to constrain the heavy physics using the existing experimental constraints and is relatively model-independent. It does, however, assume that the underlying physics respects the Standard Model local symmetry and that underlying physics becomes manifest at a scale Λ which is significantly above the Fermi scale: $\Lambda^2 G_F \gg 1$ [5]. In addition the underlying dynamics might be strongly or weakly coupled.

In this talk I will consider the second possibility and attempt to describe the constraints on the heavy physics that can reconcile the absence of any deviation from the Standard Model predictions with the possibility of a relatively small

^ae-mail: jose.wudka@ucr.edu

value of $\Lambda < \mathcal{O}(10\text{TeV})$. In addition I will assume that the heavy physics is weakly coupled and it decouples [6]

2 Effective Lagrangians and small effects

The decoupling assumption implies that all observable heavy-physics effects vanish as $\Lambda \rightarrow \infty$ and this suggests one simple way of suppressing the effects generated by the heavy particles: one simply assumes that Λ is large enough. This sometimes puts the heavy physics out of LHC's reach. For example, the experimental constraints on the $e_L e_L u_L u_L$ 4-Fermi interaction generated by a heavy vector-boson exchange of mass Λ , leads to $\Lambda > 25\text{TeV}$ [1]

There is, however, a second option, assuming first that Λ is large enough to avoid direct particle production, and second, that all leading virtual effects are absent. The first condition leads to limit on Λ derived from the absence of direct observation of the heavy particles and correspond to $\Lambda \gtrsim \text{CM}$ collider energy. The second condition requires appropriate particle content and symmetries to insure the absence of the leading graphs. In this talk I will consider this option.

2.1 Hierarchy of virtual effects

Adopting the above assumptions it follows that at low energies (small compared to Λ) all virtual effects generated by the heavy physics can be reproduced by an effective Lagrangian that consists of a linear combination of an infinite series of local effective operators involving only the Standard Model fields and which respect all the local symmetries of the Standard Model. The coefficients of these operators are calculable if the heavy physics action is known; if this is not the case these coefficients are left free and parameterize *any* type of new physics satisfying the above conditions..

The weak-coupling requirement insures that all the anomalous dimensions will be small and so one can classify the operators according to their naive mass dimension: an operator \mathcal{O} of dimension n will appear with a coefficient f/Λ^{n-4} in the effective Lagrangian. The constant f is given by a product of coupling constants when \mathcal{O} is tree-level-generated (TLG); for operators that are generated via loops, f receives an additional suppression factor $\sim 1/(4\pi)^2$. Leading heavy physics effects are then produced by the lowest dimensional tree-level generated operators.

For example, operators of dimension 6 will generate percentile corrections of order $1/(G_F \Lambda^2)$ to Standard Model processes if they are generated at tree-level, or of order $1/(16\pi^2 G_F \Lambda^2)$ if loop generated. In this last case the heavy physics corrections are of the order of the Standard Model radiative corrections suppressed by an additional factor of $1/(G_F \Lambda^2)$. For $\Lambda > 1\text{TeV}$ the observation of the effects of loop-generated operators requires a precision of $\sim 0.02\%$.

The above arguments single out tree-level generated operators as being phenomenologically interesting. These operators can be characterized as follows. Imagine a vertex of in the full theory that has h_n heavy particle legs and ℓ_k light legs. If a graph has V_n vertices of this type and I heavy internal lines then it will contain no loops provided $\sum V_n = I + 1$; also, since there are no heavy external lines and no light internal lines, $\sum h_n V_n = 2I$. It follows that

$$\sum (h_n - 2)V_n = -2 < 0 \quad (1)$$

from which it follows that all tree-level generated operators are generated by graphs containing a vertex with $h_n = 1$

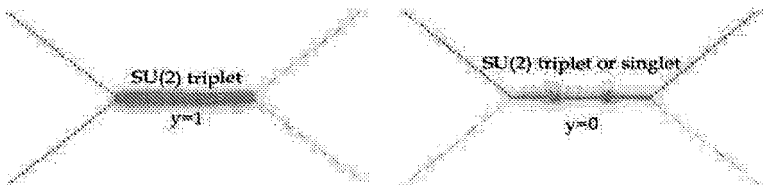
3 Eliminating tree-level generated operators

In the following I will denote heavy fermions, scalars and gauge bosons by Ψ , Φ and X respectively, while ψ , ϕ , and A will represent their light counterparts.

Using the previous characterization it is easy to see that all tree-level generated operators will contain one of the following vertices

$$\psi\psi\Phi \quad \phi\phi\Phi \quad \phi\phi\Phi \quad \psi\phi\Psi \quad \psi\psi X \quad \psi A\Psi \quad \phi\phi X \quad (2)$$

For example, the dimension 5 operator [7] $(\bar{\ell}\hat{\phi})(\phi^\dagger\ell^c)$ (where ℓ denotes a left-handed lepton doublet and ϕ the Standard Model scalar doublet and the superscript c denotes the charge conjugate field) is generated by the exchange of a scalar iso-triplet or a fermion iso-triplet or iso-singlet:



Similarly, the operator $(\bar{\nu}\nu^c)(\phi^\dagger\phi)$ (where ν denotes a right-handed neutrino singlet) is generated by the exchange of a scalar iso-singlet or a fermion iso-triplet.

Aside from these operators there is only one more dimension 5 operator, namely, $\bar{\nu}\sigma_{\alpha\beta}\nu^c B^{\alpha\beta}$ where $B^{\alpha\beta}$ denotes the $U(1)$ field strength.

Operators of dimension 6 are much more numerous: there are 82 operators (for 1 family) [8], of which 45 are tree-level generated operators [9]. These take the generic forms

$$\phi^6 \quad D^2\phi^2 \quad \psi^2\phi^3 \quad D\psi^2\phi^2 \quad (\bar{\psi}\psi)^2 \quad (\bar{\psi}\gamma\psi)^2 \quad (3)$$

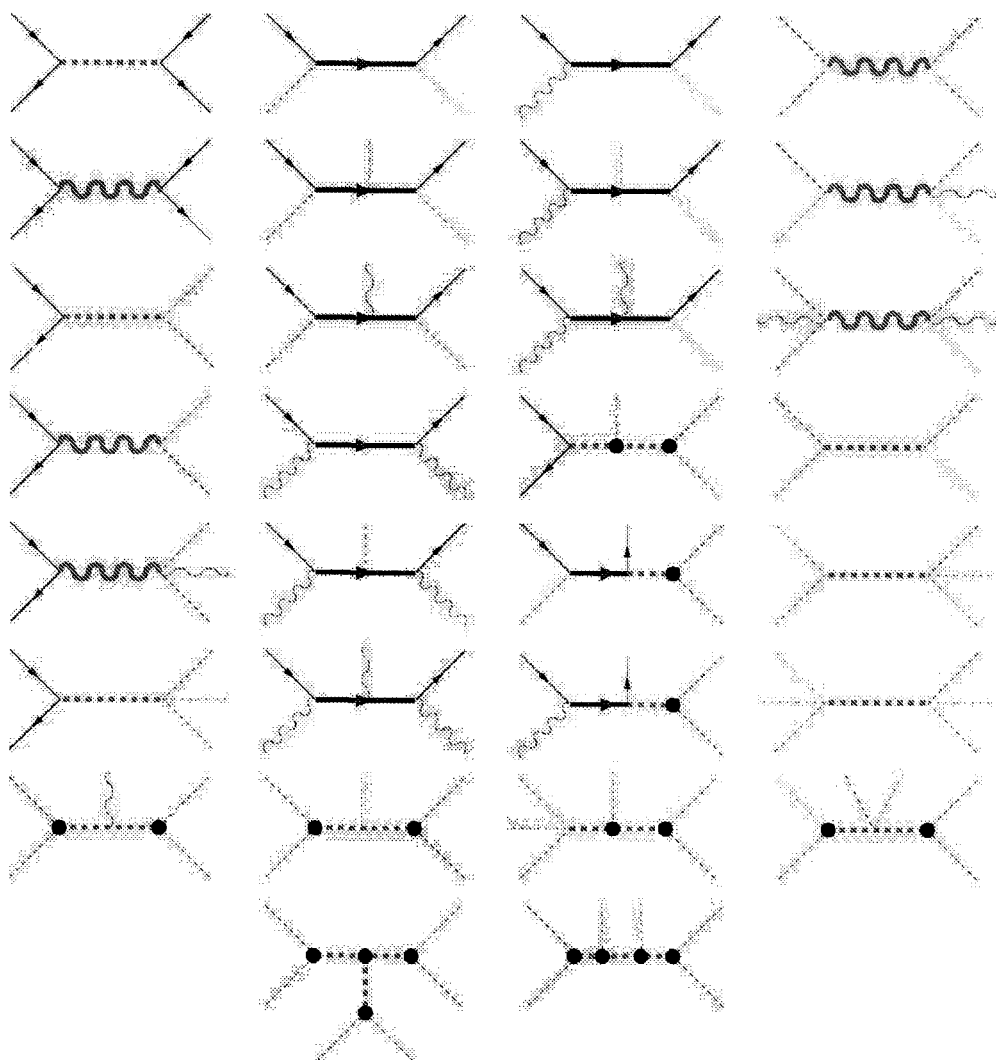


Figure 1: Graphs responsible for the dimension 6 tree-level generated operators

and are generated by the graphs in fig. 1

Note that there are no tree-level generated operators of dimension 6 containing only vectors and fermions. For example the operator $(\bar{\ell}\sigma^I\gamma^\mu D^\nu\ell)W_{\mu\nu}^I = (\bar{\ell}\sigma^I\gamma^\mu\partial^\nu\ell)(\partial_\mu W_\nu^I - \partial_\nu W_\mu^I) + \dots$ where W denotes the $SU(2)$ gauge field, cannot be generated at tree level since the first term it contains has 3 external legs and any graph with zero loops and three external lines has no internal lines. Because of this the vertex $\Psi\psi A$ is irrelevant when considering only operators of dimension ≤ 6 .

4 Eliminating tree-level generated operators

In this section I will describe a simple set of conditions that guarantee the absence of tree-level generated operators and, therefore of all leading new physics virtual effects.

4.1 Discrete symmetry

Since all tree-level generated operators contain at least one vertex with a single heavy leg one can eliminate them by requiring that the Lagrangian of the full theory be invariant under a Z_2 symmetry where all heavy fields are odd and all light fields are even. This is what occurs in the MSSM [10] where all s-fermions and bosinos are odd while the Standard Model (including both scalar doublets) are even [11].

4.2 Space-time symmetry

An alternative way of eliminating all tree-level generated operators is realized in models with universal extra dimensions [12]. In these theories space is assumed to be $4 + d$ -dimensional, and compactified into $\mathbb{R}^4 \times \mathcal{M}$, where \mathcal{M} compact of size $\sim R$; all fields are assumed to propagate in all the $4 + d$ dimensions. In a mode expansion a generic field χ can be expanded in terms of the spherical harmonics for \mathcal{M} , namely,

$$\chi = \sum_n \chi_n(x) q_n(y) \quad \nabla_{\mathcal{M}}^2 q_n = c_n q_n, \quad q_0 = 1$$

where x and y denote, respectively, the coordinates of \mathbb{R}^4 and \mathcal{M} , and where the eigenvalues $c_n \sim 1/R^2$ for $n \neq 0$. In this case only χ_0 is light while $\chi_{n \neq 0}$ have masses $\sim 1/R$.

Because of this expansion any vertex containing a single heavy field will be proportional to one of the q_n with $n \neq 0$. Its contribution to the action then vanishes because

$$\int_{\mathcal{M}} q_{n \neq 0} = 0$$

(which can be interpreted as momentum conservation along \mathcal{M} when this manifold has translation symmetry)

4.3 Gauge symmetry

It is also possible to eliminate all tree-level generated operators in a gauge theory by appropriately choosing the particle content and couplings. Here I will only consider a toy model where (i) all scalars s are assumed to get a vacuum expectation value $\langle s \rangle = O(\Lambda)$; (ii) all fermion and vector masses are generated through spontaneous symmetry breaking; and (iii) all physical scalars are heavy.

With these assumptions and using generic properties of spontaneously broken gauge theories (such as the fact that the unbroken generators close into an algebra, and that they annihilate the vacuum expectation values), it is easy to see that all undesirable vertices are eliminated except $\Psi\psi A$ and $\psi\psi X$. The first, however is irrelevant for dimension 6 operators, as mentioned earlier; the second is more problematic and can be eliminated only though appropriate choice of fermion representations. For example if the left-handed fermions (in the underlying theory) carry the adjoint representation, while right-handed fermions and scalars carry the fundamental representation ad the full gauge group is $SU(N)$ (broken to $SU(N-1)$), then all vertices of the form $\psi\psi X$ are disallowed. This type of model will not contain tree-level generated operators, but it is rather trivial having only massless fermions and gauge bosons in the light sector.

4.4 Standard Model gauge symmetry

The vertices we need to eliminate, $\psi^2\Phi$, $\phi^2\Phi$, $\phi^3\Phi$, $\psi\phi\Psi$, ψ^2X , $\psi A\Psi$, ϕ^2X can be used to determine the $SU(2)_L \times U(1)_Y$ representations that the heavy fields would carry:

heavy particle	weak isospin	hypercharge
X, Φ	0, 1	$n/3, 0 \leq n \leq 5$
Φ	$1/2, 3/2$	$1/2, 3/2$
Ψ_L	0, 1	$n/3, 0 \leq n \leq 3$
Ψ_R	1/2	1/6, 1/2

If we now use this to *forbid* such representations, the vertices would not occur and there would be no tree-level generated operators.

Note however that this conditions forbids the presence of heavy $SU(2)_L \times U(1)_Y$ singlet vector-bosons. In this case the underlying group must be of rank 2 (ignoring color), so either the Standard Model gauge group is the group for the full theory, or else the underlying group is $SU(3)$. This last case presents serious problems (*e.g.* anomalies)

5 Comments and conclusions

It is worth noting that the elimination of tree-level generated operators can be done selectively in sectors distinguished by some global symmetries. For example one can require that all baryon and lepton number conserving tree-level generated operators be absent, while allowing lepton number violating tree-level generated operators (whose effects are small presumably because they are generated at a scale Λ that is very large).

The absence of tree-level generated operators changes the the relationship between the experimental limits and the physical value of Λ . For example, a limit $\Lambda > M_{\text{exp}}$ obtained for a tree-level generated operator, becomes $\Lambda > M_{\text{exp}}/(4\pi)$. In particular the limit derived for the scale at which $(\bar{\psi}\gamma^\mu\psi)^2$ is generated drops to $\Lambda > 360\text{GeV}$, with similar results for non-Standard Model Z couplings.

The above arguments indicate that, at least partly, the phenomenological success of the MSSM and the universal-extra-dimensions theories due to the absence of tree-level generated operators in these theories.

Finally, it is worth emphasizing that there are sensible models which would exhibit no significant deviations from the Standard Model through radiative corrections. If such models are realized in nature it is quite possible for the LHC to uncover new physics without any premonition from LEP or the Tevatron.

References

- [1] K. Hagiwara *et al.* [Particle Data Group Collaboration], Phys. Rev. D **66**, 010001 (2002).
- [2] L. Maiani, G. Parisi and R. Petronzio, Nucl. Phys. B **136**, 115 (1978). N. Cabibbo, L. Maiani, G. Parisi and R. Petronzio, Nucl. Phys. B **158**, 295 (1979). M. Lindner, Z. Phys. C **31**, 295 (1986). M. Sher, Phys. Rept. **179**, 273 (1989). G. Isidori, G. Ridolfi and A. Strumia, Nucl. Phys. B **609**, 387 (2001) [[arXiv:hep-ph/0104016](#)]. T. Hambye and K. Riesselmann, Phys. Rev. D **55**, 7255 (1997) [[arXiv:hep-ph/9610272](#)]. J. A. Casas, J. R. Espinosa, M. Quiros and A. Riotto, Nucl. Phys. B **436**, 3 (1995) [Erratum-*ibid.* B **439**, 466 (1995)] [[arXiv:hep-ph/9407389](#)]. B. Grzadkowski and J. Wudka, Phys. Rev. Lett. **88**, 041802 (2002) [[arXiv:hep-ph/0106233](#)].
- [3] G. 't Hooft, Phys. Rev. Lett. **37**, 8 (1976).
- [4] See, for example, P. Langacker, M. x. Luo and A. K. Mann, Rev. Mod. Phys. **64**, 87 (1992).
- [5] . Weinberg, PhysicaA **96**, 327 (1979); [arXiv:hep-th/9702027](#). M. S. Chanowitz and M. K. Gaillard, Nucl. Phys. B **261**, 379 (1985). H. Georgi, Nucl. Phys. B **361**, 339 (1991); Nucl. Phys. B **363**, 301 (1991). J. Wudka, Int. J. Mod. Phys. A **9**, 2301 (1994) [[arXiv:hep-ph/9406205](#)].

- [6] T. Appelquist and J. Carazzone, Phys. Rev. D **11**, 2856 (1975).
J. C. Collins, F. Wilczek and A. Zee, Phys. Rev. D **18**, 242 (1978).
- [7] S. Weinberg, Phys. Rev. Lett. **43**, 1566 (1979).
- [8] W. Buchmuller and D. Wyler, Nucl. Phys. B **268**, 621 (1986). W. Buchmuller, B. Lampe and N. Vlachos, Phys. Lett. B **197**, 379 (1987).
- [9] C. Arzt, M. B. Einhorn and J. Wudka, Nucl. Phys. B **433**, 41 (1995) [arXiv:hep-ph/9405214].
- [10] H. P. Nilles, Phys. Rept. **110**, 1 (1984). H. E. Haber and G. L. Kane, Phys. Rept. **117**, 75 (1985). R. Barbieri, Riv. Nuovo Cim. **11N4**, 1 (1988). J. F. Gunion and H. E. Haber, Nucl. Phys. B **272**, 1 (1986) [Erratum-ibid. B **402**, 567 (1993)]; Nucl. Phys. B **278**, 449 (1986); Nucl. Phys. B **307**, 445 (1988) [Erratum-ibid. B **402**, 569 (1993)]. J. Rosiek, Phys. Rev. D **41**, 3464 (1990).
- [11] P. Fayet and J. Iliopoulos, Phys. Lett. **51**, 461 (1974). G. Ferrar and P. Fayet, Phys. Lett. **76B**, 575 (1978), *ibid.* **79B**, 442 (1978).
- [12] T. Appelquist, H. C. Cheng and B. A. Dobrescu, Phys. Rev. D **64**, 035002 (2001) [arXiv:hep-ph/0012100].

THE PROBLEM OF MONOPOLES IN THE STANDARD AND FAMILY REPLICATED MODELS

L. V. Laperashvili^{1 a}, H. B. Nielsen^{2 b}

¹ Institute of Theoretical and Experimental Physics, 117218 Moscow, Russia

² The Niels Bohr Institute, DK-2100 Copenhagen, Denmark

Abstract

The aim of the present talk is to show that monopoles cannot play any role in the Standard Model (SM) and in its usual extensions up to the Planck scale: $M_{Pl} = 1.22 \cdot 10^{19}$ GeV, because they have a huge charge and are completely confined or screened. The possibility of the extension of the SM with a Family Replicated Gauge Group (FRGG) symmetry of the type $(SMG)^N = [SU(3)_c]^N \times [SU(2)_L]^N \times [U(1)_Y]^N$ is briefly discussed. In this model monopoles can appear at high energies and provide for the phase transition into the phase with $[SU(5)]^3$ or $[SO(10)]^3$ gauge symmetry (SUSY or not SUSY).

1 The Problem of Monopoles in the Standard Model

The gauge symmetry group in the SM is :

$$SMG = SU(3)_{c(\text{color})} \times SU(2)_{L(\text{left})} \times U(1)_{Y(\text{hypercharge})}, \quad (1)$$

which describes the present elementary particle physics up to the scale ≈ 100 GeV. The aim of the present talk is to show that monopoles cannot be seen in the Standard Model and in its usual extensions, known in the literature, up to the Planck scale [1,2]: $M_{Pl} = 1.22 \cdot 10^{19}$ GeV, because they have a huge magnetic charge and are completely confined or screened. Supersymmetry does not help to see monopoles.

Let us consider the "electric" and "magnetic" running constants:

$$\alpha = \frac{g^2}{4\pi} \quad \text{and} \quad \tilde{\alpha} = \frac{\tilde{g}^2}{4\pi}, \quad (2)$$

where g is the coupling constant, and \tilde{g} is the dual coupling constant (in QED: $g = e$ is an electric charge, and $\tilde{g} = m$ is a magnetic charge.)

The renormalization group equation (RGE) for monopoles is:

$$\frac{d(\log \tilde{\alpha}(t))}{dt} = \beta(\tilde{\alpha}). \quad (3)$$

Here t is the evolution variable: $t = \log(\frac{\mu^2}{\mu_R^2})$, where μ is the energy scale and μ_R is the renormalisation point.

^ae-mail: laper@heron.itep.ru

^be-mail: hbech@alf.nbi.dk

The scalar monopole beta-function is taken from the dual scalar electrodynamics of Ref. [3]:

$$\beta(\tilde{\alpha}) = \frac{\tilde{\alpha}}{12\pi} + \left(\frac{\tilde{\alpha}}{4\pi}\right)^2 + \dots = \frac{\tilde{\alpha}}{12\pi}(1 + 3\frac{\tilde{\alpha}}{4\pi} + \dots). \quad (4)$$

The last equation shows that the theory of monopoles cannot be considered perturbatively at least for

$$\tilde{\alpha} > \frac{4\pi}{3} \approx 4. \quad (5)$$

And this limit is smaller for non-Abelian monopoles.

Let us consider now the evolution of the SM running fine structure constants $\alpha_i(t)$, where $i=1,2,3$ correspond to U(1), SU(2) and SU(3) gauge groups of the SM. The usual definition of the SM coupling constants is given in the *Modified minimal subtraction scheme* (\overline{MS}):

$$\alpha_1 = \frac{5}{3}\alpha_Y, \quad \alpha_Y = \frac{\alpha}{\cos^2 \theta_{\overline{MS}}}, \quad \alpha_2 = \frac{\alpha}{\sin^2 \theta_{\overline{MS}}}, \quad \alpha_3 \equiv \alpha_s = \frac{g_s^2}{4\pi}, \quad (6)$$

where α and α_s are the electromagnetic and QCD running constants, respectively, Y is the weak hypercharge, and $\theta_{\overline{MS}}$ is the Weinberg weak angle in \overline{MS} scheme. Using RGEs with experimentally established parameters, it is possible to extrapolate the experimental values of three inverse running constants $\alpha_Y^{-1}(\mu)$ and $\alpha_i^{-1}(\mu)$ (for $i=2,3$) from the Electroweak scale to the Planck scale (see Fig.1).

Assuming the existence of the Dirac relation for renormalised charges [4]: $g\bar{g} = 2\pi n$ ($n \in Z$), we have for minimal charges ($n=1$) the following expression: $\alpha(t)\tilde{\alpha}(t) = \frac{1}{4}$. Using this relation, it is easy to estimate (in the simple SM) the Planck scale value of $\tilde{\alpha}(\mu_{Pl})$ (minimal for $U(1)_Y$ gauge group):

$$\tilde{\alpha}(\mu_{Pl}) = \frac{5}{3}\alpha_1^{-1}(\mu_{Pl})/4 \approx 55.5/4 \approx 14. \quad (7)$$

This value is really very big compared with our previous estimate (5). Clearly we cannot make a perturbation approximation with such a strong coupling $\tilde{\alpha}$. But there is an interesting way out of this problem if one wants to have the existence of monopoles, namely to extend the SM gauge group so cleverly that certain selected linear combinations of charges get bigger electric couplings than the corresponding SM couplings. Then monopoles interact more weakly and thus have a better chance of being allowed "to exist". An example of such an extension of the SM that can impose the existence of free monopoles is just Family Replicated Gauge Group Model (FRGGM).

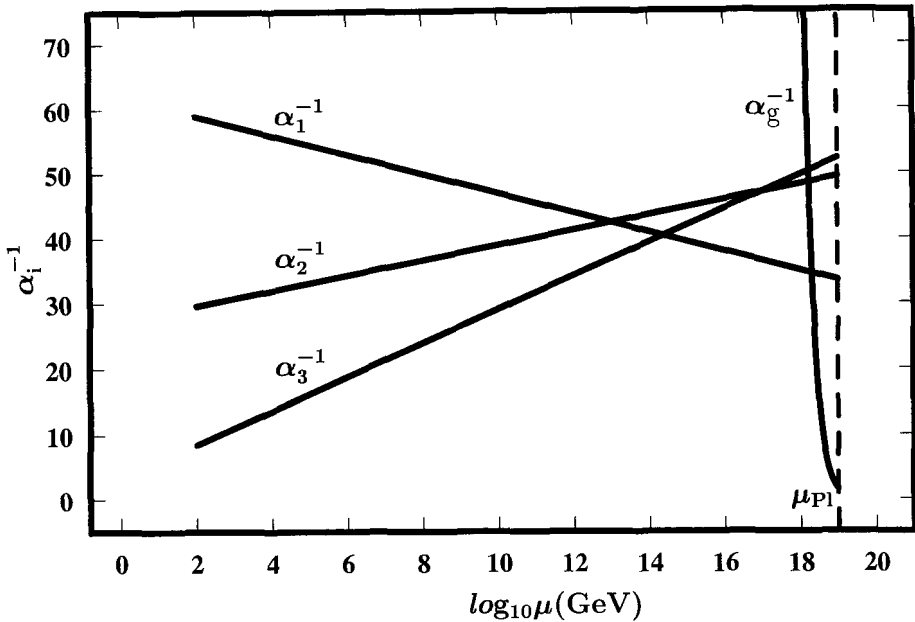


Figure 1:

2 Family Replicated Gauge Group as an extension of the Standard Model

The extension of the Standard Model with the Family Replicated Gauge Group (FRGG):

$$G = (SMG)^{N_{fam}} = [SU(3)_c]^{N_{fam}} \times [SU(2)_L]^{N_{fam}} \times [U(1)_Y]^{N_{fam}} \quad (8)$$

was first suggested in [5] and developed in [6]. Here N_{fam} designates the number of quark and lepton families. If $N_{fam} = 3$ (as our theory predicts [6] and experiment confirms), then the fundamental gauge group G is:

$$G = (SMG)^3 = SMG_{1st\ fam.} \times SMG_{2nd\ fam.} \times SMG_{3rd\ fam.}, \quad (9)$$

or

$$G = (SMG)^3 = [SU(3)_c]^3 \times [SU(2)_L]^3 \times [U(1)_Y]^3. \quad (10)$$

A new generalization of our FRGG-model was suggested in Refs. [7], where

$$\begin{aligned} G_{\text{ext}} &= (SMG \times U(1)_{B-L})^3 \\ &\equiv [SU(3)_c]^3 \times [SU(2)_L]^3 \times [U(1)_Y]^3 \times [U(1)_{(B-L)}]^3 \end{aligned} \quad (11)$$

is the fundamental gauge group, which takes right-handed neutrinos and the see-saw mechanism into account. This extended model can describe all modern neutrino experiments, giving a reasonable fit to all the quark-lepton masses and mixing angles in the SM.

The gauge group $G_{\text{ext}} = (\text{SMG} \times U(1)_{B-L})^3$ undergoes spontaneous breakdown (at some orders of magnitude below the Planck scale) to the Standard Model Group SMG which is the diagonal subgroup of the group G_{ext} . As was shown in [7], 6 different Higgs fields: $(\omega, \rho, W, T, \phi_{WS}, \phi_{B-L})$ break our FRGG-model to the SM. The field ϕ_{WS} corresponds to the Weinberg-Salam Electroweak theory. Its vacuum expectation value (VEV) is fixed: $\langle \phi_{WS} \rangle \approx 246$ GeV, so that we have only 5 free parameters – five remaining VEVs – to fit the experiment in the framework of the SM. These five adjustable parameters were used with the aim of finding the best fit to experimental data for all fermion masses and mixing angles in the SM, and also to explain the neutrino oscillation experiments.

3 Monopoles in the Family Replicated Gauge Group Model.

In theories with the FRGG symmetry the charge of monopoles is essentially diminished, and monopoles can appear near the Planck scale and change the evolution of the running constants $\alpha_i(t)$. FRGG of type $[SU(N)]^{N_{fam}}$ leads to the lowering of the magnetic charge of the monopole belonging to one family: $\tilde{\alpha}_{\text{one family}} = \frac{\tilde{\alpha}}{N_{fam}}$. For $N_{fam} = 3$ (for $[SU(2)]^3$ and $[SU(3)]^3$) we have: $\tilde{\alpha}_{\text{one family}}^{(2,3)} = \frac{\tilde{\alpha}^{(2,3)}}{3}$. But the FRGG $[U(1)]^{N_{fam}}$ gives: $\tilde{\alpha}_{\text{one family}} = \frac{\tilde{\alpha}}{N^*}$, where $N^* = \frac{1}{2}N_{fam}(N_{fam} + 1)$. For $[U(1)]^3$ we have: $\tilde{\alpha}_{\text{one family}}^{(1)} = \frac{\tilde{\alpha}^{(1)}}{6}$ (six times smaller!) This result was obtained previously in the paper [8].

According to the FRGG model, at some point $\mu = \mu_G < \mu_{Pl}$ the fundamental group $G \boxtimes G_{\text{ext}}$ undergoes spontaneous breakdown to its diagonal subgroup:

$$G \longrightarrow G_{\text{diag. subgr.}} = \{g, g, g | g \in \text{SMG}\}, \quad (12)$$

which is identified with the usual (low-energy) group SMG.

The aim of this investigation is to show that monopoles with masses $M_{mon} > 10^{14}$ GeV have the influence on running constants, if G -group undergoes the breakdown to its diagonal subgroup (that is, SMG) at $\mu_G \sim 10^{14}$ or 10^{15} GeV, that is, before the intersection of $\alpha_2^{-1}(\mu)$ with $\alpha_3^{-1}(\mu)$ at $\mu \approx 10^{16}$ GeV. In this case, in the region $\mu_G < \mu < \mu_{Pl}$ there are three $\text{SMG} \times U(1)_{B-L}$ groups for the three FRGG families, and we have a lot of new fermions, mass protected or not mass protected, belonging to usual families or to mirror ones, because in the FRGGM the additional 5 Higgs bosons, with their large VEVs, are responsible for the mass protection of a lot of new fermions appearing in the region $\mu > \mu_G$, and the total number of fermions N_F is different to N_{fam} .

Also the role of monopoles can be important in the vicinity of the Planck scale: they can give contributions to the corresponding beta-functions and change the evolution of $\alpha_i^{-1}(\mu)$. Here it is necessary to comment: in the FRGG model near the Planck scale monopole charges, together with electric ones, are sufficiently small, and their β -functions can be considered perturbatively. As was shown in the paper [4], there exists a region when both running constants α and $\tilde{\alpha}$ are perturbative. Approximately this region is given by the following inequalities: $0.2 \lesssim (\alpha, \tilde{\alpha}) \lesssim 1$. It is very interesting that the above-mentioned region coincides with the region of critical couplings for the phase transition "confinement-deconfinement" obtained in the lattice compact QED [9]:

$$\alpha_{crit}^{lat} \approx 0.20 \pm 0.015, \quad \tilde{\alpha}_{crit}^{lat} \approx 1.25 \pm 0.10, \quad (13)$$

what confirms the idea of Ref. [8] that at the Planck scale we have the multiple critical point.

4 The Evolution of Running Fine Structure Constants

Finally, we obtain the following RGEs:

$$\frac{d(\alpha_i^{-1}(\mu))}{dt} = \frac{b_i}{4\pi} + \frac{N_M^{(i)}}{\alpha_i} \beta^{(m)}(\tilde{\alpha}_{U(1)}), \quad (14)$$

where b_i are given by the following values:

$$b_i = (b_1, b_2, b_3) = \\ (-\frac{4N_F}{3} - \frac{1}{10}N_S, \quad \frac{22}{3}N_V - \frac{4N_F}{3} - \frac{1}{6}N_S, \quad 11N_V - \frac{4N_F}{3}). \quad (15)$$

The integers N_F , N_S , N_V , N_M are respectively the total numbers of fermions, Higgs bosons, vector gauge fields and scalar monopoles in the FRGGM considered in our theory. In our FRGG model we have $N_V = 3$ and one Higgs scalar monopole in each family.

We have obtained the evolutions of $\alpha_i^{-1}(\mu)$ near the Planck scale by numerical calculations for: $\mu_G = 10^{14}$ GeV, $M_{mon} > 10^{14}$ GeV, $N_F = 18$, $N_S = 6$, $N_M^{(1)} = 6$, $N_M^{(2,3)} = 3$. Fig.2 shows the existence of the unification point.

In this connection, it is very attractive to include gravity. The quantity $\alpha_g = \left(\frac{\mu}{\mu_{Pl}}\right)^2$ plays the role of the running "gravitational fine structure constant" and the evolution of its inverse is presented in Fig.2 together with the evolutions of $\alpha_i^{-1}(\mu)$. In Fig.2 we see that in the region $\mu > \mu_G$ a lot of new fermions and a number of monopoles near the Planck scale change the one-loop approximation behaviour of $\alpha_i^{-1}(\mu)$ which we had in the SM. Near the Planck scale these

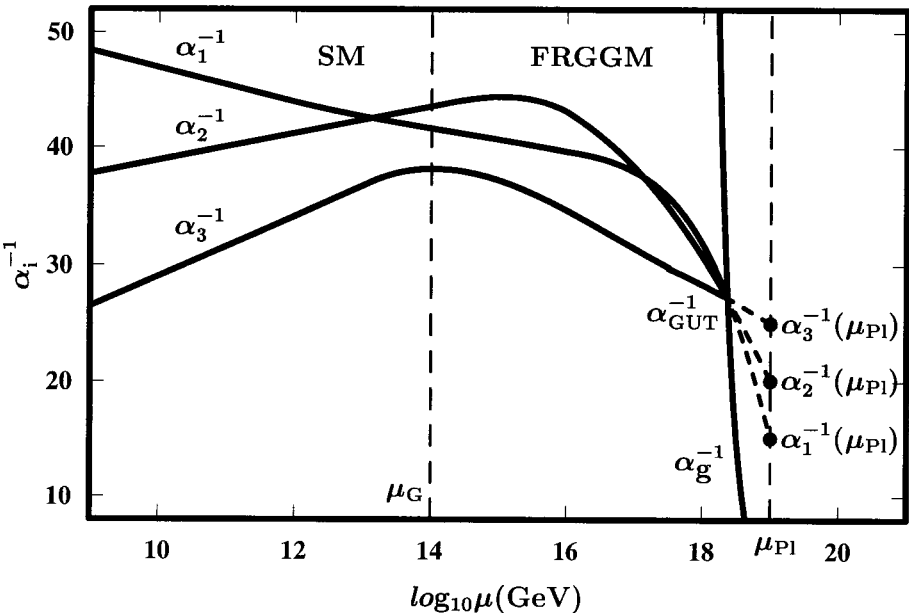


Figure 2:

evolutions begin to decrease, implying the suppression of asymptotic freedom in the non-Abelian theories.

Fig.2 demonstrates the unification of all gauge interactions, including gravity (the intersection of α_g^{-1} with α_i^{-1}), at $\alpha_g^{-1} \approx 27$ and $x_{GUT} \approx 18.4$. It is easy to calculate that for one family we have:

$$\tilde{\alpha}_{GUT,onefam.} = \frac{\alpha_{GUT,onefam.}^{-1}}{4} = \frac{\alpha_{GUT}^{-1}}{4 \cdot 6} \approx \frac{27}{24} \approx 1.125, \quad (16)$$

and $\alpha_{GUT,onefam.} \approx 0.22$, what means that at the GUT scale electric and monopole charges are not large and can be considered perturbatively.

Here we can expect the existence of $[SU(5)]^3$ or $[SO(10)]^3$, SUSY or not SUSY unification.

This investigation was supported by the grant RFBR 02-02-17379.

- [1] L.V.Laperashvili, D.A.Ryzhikh and H.B.Nielsen, *Yad.Fiz.* **66**, 1 (2003); [arXiv:hep-th/0212213].
- [2] L.V.Laperashvili, D.A.Ryzhikh and H.B.Nielsen, *Int.J.Mod.Phys. A* **18**, 4403 (2003); preprint DESY-02-188.
- [3] S.Coleman and E.Weinberg, *Phys.Rev. D* **7**, 1888 (1973).
- [4] L.V.Laperashvili and H.B.Nielsen, *Mod.Phys.Lett. A* **14**, 2797 (1999).
- [5] D.L.Bennett, H.B.Nielsen and I.Picek, *Phys.Lett. B* **208**, 275 (1988).

- [6] C.D.Froggatt and H.B.Nielsen, "*Origin of Symmetries*" (World Scientific, Singapore) 1991.
- [7] H.B.Nielsen and Y.Takanishi, Phys.Lett. **B** 543, 249 (2002); Nucl.Phys. **B** 604, 405 (2001); C.D.Froggatt, H.B.Nielsen and Y.Takanishi, Nucl.Phys. **B** 631, 285 (2002).
- [8] D.L.Bennett and H.B.Nielsen, Int.J.Mod.Phys. **A** 9, 5155 (1994).
- [9] J.Jersak, T.Neuhaus and P.M.Zerwas, Phys.Lett. **B** 133, 103 (1983); H.G.Everetz, J.Jersak, T.Neuhaus and P.M.Zerwas, Nucl.Phys. **B** 251, 279 (1985).

CONDITIONAL DENSITY MATRIX in the CONTEXT of NONCONTEXTUALITY

V.Belokurov , O.Khrustalev ^a, V.Sadovnichy, O.Timofeevskaya ^b

Moscow State University, 119992 Moscow, Russia

Abstract. Conditional density matrix represents a quantum state of subsystem in different schemes of quantum communication. Here we discuss some properties of conditional density matrix and its place in general scheme of quantum mechanics.

1 Introduction

A problem of a correct quantum mechanical description of divisions of quantum systems into subsystems and reunification of subsystems into new joint systems attracts a great interest due to the present development of quantum communication.

In principle the theory of such processes was created in general by von Neumann in 1927 [1] when he constructed deductive scheme of quantum mechanics.

Nevertheless until now the description of similar processes and their interpretation involves some problems. For example, a recent entanglement swapping experiment raised discussion. The authors [2] finished their interpretation of experimental results about entanglement swapping and teleportation by quotation: *this paradoxes do not arise if the correctness of quantum mechanics is firmly believed.* (*A.Peres*). This statement does little to explain why there is no paradox and it is difficult to agree with it because quantum mechanics is a science.

Quantum mechanics predicts probabilities for various possible outcomes of measurement once we specify the procedure used for preparation of the physical system. In quantum mechanics the important assumption, which might be called the "noncontextuality" of probabilities, means that probabilities are consistent with the Hilbert-space structure of the observable. With these assumptions the probabilities for all measurements can be derived from a density operator $\hat{\rho}$ associated by von Neumann with quantum mechanical state.

The quantum states of subsystem of complicated system are described by reduced and conditional density matrices. This approach helps to avoid difficulties and paradoxes in interpretation of some delicate experiments in different schemes of quantum communication.

2 The State in Quantum Mechanics

2.1 Kinematic Quantum Mechanics Postulate

In quantum mechanics

^ae-mail: khrust@goa.bog.msu.ru

^be-mail: olga@goa.bog.msu.ru

each dynamical variable \mathcal{F} of a system S corresponds to a linear operator \hat{F} in Hilbert space \mathcal{H}

$$\text{dynamical variable } \mathcal{F} \iff \text{linear operator } \hat{F}.$$

To compare predictions of the theory with experimental data it was necessary to understand how one can determine the values of dynamical variables in the given state. W.Heisenberg [3] gave a partial answer to this problem:

If matrix that corresponds to the dynamical variable is diagonal, then its diagonal elements define possible values for the dynamical variable, i.e. its spectrum.

$$(\hat{F})_{mn} = f_m \delta_{mn} \iff \{f_m\} \text{ is spectrum } \mathcal{F}.$$

2.2 Quantum State

The general solution of the problem was given by von Neumann in 1927. He proposed the following procedure for calculation of average values of physical variables:

$$\langle \mathcal{F} \rangle = \text{Tr}(\hat{F}\hat{\rho}). \quad (1)$$

It is possible to represent the operator \hat{F} in the form

$$\hat{F} = \sum_{n,m} |\psi_n\rangle\langle\psi_n|\hat{F}|\psi_m\rangle\langle\psi_m| = \sum_{n,m} F_{nm}\hat{P}_{mn},$$

where $\{|\psi_m\rangle\}$ is a basis in Hilbert space and

$$\hat{P}_{mn} = |\psi_n\rangle\langle\psi_m|.$$

The average value of the variable \hat{F} is

$$\langle \hat{F} \rangle = \sum_{n,m} F_{nm}\rho_{mn},$$

where

$$\rho_{mn} = \langle \hat{P}_{mn} \rangle.$$

If we suppose that the numbers ρ_{mn} define the operator $\hat{\rho}$: $\langle\psi_n|\hat{\rho}|\psi_m\rangle = \rho_{mn}$ then the average of the variable \hat{F} is represented in the form (1).

Really, when they suppose that the operator $\hat{\rho}$ does not depend of the variable \hat{F} but only depends on the physical state of the quantum system they introduce the proposition that the theory is noncontextual. All subsequent experiments confirmed quantum mechanical theory.

Operator $\hat{\rho}$ have to satisfy three conditions:

$$1) \quad \hat{\rho}^+ = \hat{\rho},$$

$$\begin{aligned} 2) \quad Tr\hat{\rho} &= 1, \\ 3) \quad \forall \psi \in \mathcal{H} \quad <\psi|\hat{\rho}\psi> &\geq 0. \end{aligned}$$

By the formula for average values von Neumann found out the correspondence between linear operators $\hat{\rho}$ and states of quantum systems:

$$\text{state of a system } \rho \iff \text{linear operator } \hat{\rho}.$$

In this way, the formula for average values becomes quantum mechanical definition of the notion "a state of a system". The operator $\hat{\rho}$ is called **Density Matrix**.

If \hat{F} is an observable with pure discrete spectrum

$$\hat{F} = \sum_n f_n \hat{P}_n,$$

then

$$\langle \hat{F} \rangle = \sum_n f_n Tr(\hat{P}_n \hat{\rho}).$$

Therefore, $Tr(\hat{P}_n \hat{\rho})$ is a probability of an observable \hat{F} gets a value f_n in the state $\hat{\rho}$.

Since density matrix is a positive definite operator and its trace equals 1, we see that its spectrum is pure discrete and it can be written in the form

$$\hat{\rho} = \sum_n p_n \hat{P}_n,$$

where \hat{P}_n is a complete set of self-conjugate projective operators:

$$\hat{P}_n^+ = \hat{P}_n, \quad \hat{P}_m \hat{P}_n = \delta_{mn} \hat{P}_m, \quad \sum_n \hat{P}_n = \hat{E}.$$

Numbers $\{p_n\}$ satisfy the condition

$$p_n^* = p_n, \quad 0 \leq p_n, \quad \sum_n p_n Tr \hat{P}_n = 1.$$

It follows that $\hat{\rho}$ acts according to the formula

$$\hat{\rho}\Psi = \sum_n p_n \sum_{\alpha \in \Delta_n} \phi_{n\alpha} \langle \phi_{n\alpha} | \Psi \rangle.$$

The vectors $\phi_{n\alpha}$ form an orthonormal basis in the space \mathcal{H} . Sets $\Delta_n = \{1, \dots, k_n\}$ are defined by degeneration multiplicities k_n of eigenvalues p_n .

2.3 Dispersion and Pure States

From the properties of density matrix and the definition of positively definite operators:

$$\hat{F}^+ = \hat{F}, \quad \forall \psi \in \mathcal{H} \quad \langle \psi | \hat{F} \psi \rangle \geq 0,$$

it follows that the average value of nonnegative variable is nonnegative. Moreover, the average value of nonnegative variable is equal to zero if and only if this variable equals zero. Now it is easy to give the following definition:

variable \mathcal{F} has a definite value in the state ρ if and only if its dispersion in the state ρ is equal to zero.

The dispersion of a quantum variable \mathcal{F} in the state ρ has the form:

$$\mathcal{D}_\rho(\mathcal{F}) = \text{Tr}(\hat{Q}^2 \rho),$$

where \hat{Q} is an operator:

$$\hat{Q} = \hat{F} - \langle \mathcal{F} \rangle \hat{E}.$$

If \mathcal{F} is observable ($\hat{F} = \hat{F}^+$) then \hat{Q}^2 is a positive definite variable. It follows that the dispersion of \mathcal{F} is nonnegative. This makes clear the above-given definition.

The dispersion of the observable \mathcal{F} in the state ρ is given by the equation

$$\mathcal{D}_\rho(\mathcal{F}) = \sum_n p_n \sum_{\alpha \in \Delta_n} \|\hat{Q}\phi_{n\alpha}\|^2.$$

All terms in this sum are nonnegative. Hence, if the dispersion is equal to zero, then

$$\text{if } p_n \neq 0, \text{ then } \hat{Q}\phi_{n\alpha} = 0.$$

Using the definition of the operator \hat{Q} , we obtain

$$\text{if } p_n \neq 0, \text{ then } \hat{F}\phi_{n\alpha} = \phi_{n\alpha}\langle \mathcal{F} \rangle.$$

In other words, *if an observable \mathcal{F} has a definite value in the given state ρ , then this value is equal to one of the eigenvalues of the operator \hat{F} .*

In this case we have

$$\hat{\rho}\hat{F}\phi_{n\alpha} = \phi_{n\alpha}p_n\langle \mathcal{F} \rangle, \quad \hat{F}\hat{\rho}\phi_{n\alpha} = \phi_{n\alpha}\langle \mathcal{F} \rangle p_n,$$

that proves the commutativity of operators \hat{F} and $\hat{\rho}$.

It is well known, that if \hat{A} and \hat{B} are commutative self-conjugate operators, then there exists self-conjugate operator \hat{T} with non-degenerate spectrum such that \hat{A} and \hat{B} are functions of \hat{T} .

Suppose \hat{F} is an operator with non-degenerate spectrum. Then,

if the observable \mathcal{F} with non-degenerate spectrum has a definite value in the state ρ , then it is possible to represent the density matrix of this state as a function of the operator \hat{F} .

The operator \hat{F} can be written in the form

$$\hat{F} = \sum_n f_n \hat{\Pi}_n,$$

$$\hat{\Pi}_n^+ = \hat{\Pi}_n, \quad \hat{\Pi}_m \hat{\Pi}_n = \delta_{mn} \hat{\Pi}_m, \quad \text{tr}(\hat{\Pi}_n) = 1, \quad \sum_n \hat{\Pi}_n = \hat{E}.$$

The numbers $\{f_n\}$ satisfy the conditions

$$f_n^* = f_n, \quad f_n \neq f_{n'}, \quad \text{if } n \neq n'.$$

From

$$\langle F \rangle = \sum_n p_n f_n = f_N, \quad \langle F^2 \rangle = \sum_n p_n f_n^2 = f_N^2$$

we get

$$p_n = \delta_{nN}.$$

In this case density matrix is a projective operator satisfying the condition

$$\hat{\rho}^2 = \hat{\rho}.$$

It acts as

$$\hat{\rho}\Psi = \hat{\Pi}_N|\Psi\rangle = |\Psi_N\rangle\langle\Psi_N|,\quad$$

where $|\Psi_N\rangle$ is a vector in Hilbert space. It is so-called *pure* state.

2.4 Density Matrix and Gleason Theorem

To each observable there corresponds a set of orthogonal projection operators $\{\hat{\Pi}_i\}$ over a complex Hilbert space \mathcal{H} that form a decomposition of the identity

$$\sum_n \hat{\Pi}_n = \hat{E}.$$

Quantum mechanics dictates that it is expected the various outcomes with a probability

$$p_n = \text{Tr}(\hat{\rho}\hat{\Pi}_n).$$

It was assumed by von Neumann and then was finally proven by Gleason [6] in 1957 as the following theorem:

Assume there is a function f from the one-dimensional projectors acting on a Hilbert space of dimension greater than 2 to the unit interval, with the property that for each orthonormal basis $\{|\psi_k\rangle\}$,

$$\sum_k f(|\psi_k\rangle\langle\psi_k|) = 1.$$

Then there exists a density matrix operator $\hat{\rho}$ such that

$$f(|\psi\rangle\langle\psi|) = \langle\psi|\hat{\rho}|\psi\rangle.$$

It assumes that each orthonormal basis corresponds to mutually exclusive results of measurement of some observable. The task is to derive the probabilities for the measurement outcomes. The only requirement is that the probability for obtaining the result corresponding to a normalized vector $|\psi\rangle$ depends only on $|\psi\rangle$ itself, not on the other vectors in the orthonormal basis defining a particular measurement. This important assumption is called the "noncontextuality". It means that the probabilities are consistent with the Hilbert-space structure of observables. With these assumptions the probabilities for all measurements can be derived from a density matrix using the standard quantum probability rule.

3 Conditional Density Matrix

3.1 Composite System and Reduced Density Matrix

Suppose that the Hilbert space \mathcal{H} is a direct product of two Hilbert spaces \mathcal{H}_1 , \mathcal{H}_2 :

$$\mathcal{H} = \mathcal{H}_1 \otimes \mathcal{H}_2.$$

Suppose the composite indexes m, n, \dots are divided into two parts: $m = \{r, u\}; n = \{s, v\}, \dots$ So, there is a basis in the space that can be written in the form

$$|\phi\rangle_n = |f\rangle_r |g\rangle_v.$$

In quantum mechanics it means that the system S is a unification of two subsystems S_1 and S_2 :

$$S = S_1 \cup S_2.$$

The Hilbert space \mathcal{H} corresponds to the system S and the spaces \mathcal{H}_1 and \mathcal{H}_2 correspond to the subsystems S_1 and S_2 .

If quantum state of the composite system is density matrix ρ_{1+2} then the state of the subsystem S_1 is defined by **Reduced Density matrix**

$$\hat{\rho}_1 = Tr_2 \hat{\rho}_{1+2},$$

the reduced density matrix for the subsystem S_2 is

$$\hat{\rho}_2 = Tr_1 \hat{\rho}_{1+2}.$$

Quantum states ρ_1 and ρ_2 of subsystems are defined uniquely by the state ρ_{1+2} of the composite system.

3.2 Conditional Probabilities

We recall some definitions of probability theory.

Let h be an event with positive probability. For any event A we define

$$P\{A|h\} = \frac{P\{Ah\}}{P\{h\}}.$$

This is conditional probability of the event A for given event h .

This formula can be written in the form:

$$P\{Ah\} = P\{A|h\}P\{h\}.$$

Let h_1, \dots, h_n be a set of mutually exclusive events such that one of them takes place necessarily. Then any event A can take place only with one of the events h_j . It can be written as

$$A = Ah_1 \cup Ah_2 \cup \dots \cup Ah_n.$$

Since Ah_j are mutually independent their probabilities are added. Thus,

$$P\{A\} = \sum_j P\{A|h_j\}P\{h_j\}. \quad (2)$$

This is well-known formula for total probability in terms of conditional probabilities.

3.3 Conditional Density Matrix

Let the operators $\hat{P}_n^{(2)}$ be the projections on certain basis states in the Hilbert space \mathcal{H}_2 of pure states of subsystem S_2 :

$$\hat{P}_n^{(2)} = |u_n\rangle\langle u_n|, \quad \sum_n \hat{P}_n^{(2)} = \hat{E}.$$

According definition the reduce density matrix for subsystem S_1 is

$$\rho_{sr}^{(1)} = \sum_{uv} \delta_{uv} \rho_{sv;ru} = \sum_{uv} \sum_n (\hat{P}_n^{(2)})_{uv} (\hat{\rho})_{sv;ru} =$$

$$\sum_n \sum_u (\hat{P}_n^{(2)} \hat{\rho})_{su;ru} = \sum_n p_n \frac{\sum_u (\hat{P}_n^{(2)} \hat{\rho})_{su;ru}}{p_n}.$$

Therefore, the reduced density matrix $\rho^{(1)}$ is written in the form:

$$\hat{\rho}^{(1)} = \sum_n p_n \hat{\rho}_n^{(c)}, \quad (3)$$

where

$$p_n = \sum_{uv} P_n^{(2)}(u|v) \sum_r \rho_{rv;ru} = \sum_{uv} P_n^{(2)}(u|v) \hat{\rho}^{(2)}(v,u)$$

or

$$p_n = Tr_2(\hat{P}_n^{(2)} \hat{\rho}^{(2)}).$$

If the set of projections $\hat{P}_n^{(2)}$ is associated with some observable in the subsystem S_2

$$\hat{G} = \sum_n g_n \hat{P}_n^{(2)},$$

then p_n is a probability of the variable \hat{G} gets a value g_n in the state $\hat{\rho}^{(2)}$.

The operator $\hat{\rho}_n^{(c)}$ equals:

$$\rho_n^{(c)}(r|s) = \frac{1}{p_n} \sum_{uv} P_n^{(2)}(u|v) \rho_{rv;su}$$

and satisfies all conditions (1). It is **density matrix** or quantum state.

Since $w_r = \hat{\rho}_{rr}^{(1)}$ is a probability to find a subsystem S_1 in the state $|r\rangle$, we see that an equality

$$w_r = \sum_n p_n \rho_n^{(c)}(r|r),$$

is formula(2).

Then the operator $\hat{\rho}_n^{(c)}$ is called **conditional density matrix** and is written [5]

$$\hat{\rho}_{1/2n}^{(c)} = \frac{Tr_2(\hat{P}_n^{(2)} \hat{\rho})}{Tr(\hat{P}_n^{(2)} \hat{\rho})} = \frac{Tr_2(\hat{P}_n^{(2)} \hat{\rho})}{w_n}. \quad (4)$$

This is a **conditional density matrix**, i.e. a **quantum state**, for subsystem S_1 under condition that the subsystem S_2 is selected in **pure state** $\hat{P}_n^{(2)}$. It is the most interesting case for quantum communication. This definition of the quantum state of quantum subsystem assumes noncontextual approach in quantum mechanics.

It is necessary to note that although formula (4) arose in description of measurement, for example in papers [11], [8] and et. , it was presented as the result of transformation of quantum state of the system during measurement. Here, conditional density matrix is the definition of a new quantum state of the subsystem that is selected under definite physical condition.

3.4 Conditional Density Matrix in Case of Generalized Measurement

It was recently shown [9] that a Glison-like theorem can be easily proved (and also extends to the case of 2-dimensional Hilbert space) on a set of effects $\{E\}$. It is a set of projections but commutativity (or orthogonality) is no longer necessary. According to this theorem

any generalized probability measure is of the form $E \rightarrow v(E) = \text{tr}[\rho E]$ for all E , for some density operator ρ .

While we consider a generalized measurement [8] in the subsystem S_2 we suppose that a set of projections $\{\hat{E}_b\}$ exists and satisfies the properties

$$\langle \psi | \hat{E}_b | \psi \rangle \geq 0, \quad \forall |\psi\rangle, \quad \sum_b \hat{E}_b = \hat{I}^{(2)}.$$

The probabilities of outcomes are equal

$$P(b) = \text{tr}(\hat{\rho} \hat{E}_b).$$

We don't suppose that condition $\Pi_i \Pi_j = \delta_{ij} \Pi_i$ is fulfilled.

In this case the decomposition (3) is also valid and quantum state of subsystem S_1 under condition that the subsystem S_2 is selected in pure state \hat{E}_b is

$$\hat{\rho}_{1/2b}^{(c)} = \frac{\text{Tr}_2(\hat{E}_b \hat{\rho})}{\text{Tr}(\hat{E}_b \hat{\rho})}.$$

4 Conditional Density Matrix Description of Entanglement Swapping

In the experiments [2] with installation two pairs of correlated photons are emerged simultaneously. The polarization state of the system is being described by the simultaneous wave function

$$|\Psi(\sigma_1, \sigma_2, \sigma_3, \sigma_4)\rangle = \Psi_-(\sigma_1, \sigma_2) \Psi_-(\sigma_3, \sigma_4),$$

where Ψ_- is antisymmetric state of pair of photons

$$\Psi_-(\sigma_i, \sigma_j) = \frac{1}{\sqrt{2}} (\chi_0(\sigma_i) \chi_1(\sigma_j) - \chi_1(\sigma_i) \chi_0(\sigma_j))$$

and $\chi_s(\sigma)$ are two basis states with orthonormal polarization. Reduced density matrix of subsystem S_{1-4} is proportional to unity

$$\rho_{14} = \frac{1}{2} \hat{I}^{(1)} \otimes \frac{1}{2} \hat{I}^{(4)}.$$

But if we select the pair of photons 1-4 only under condition that pair 2-3 is in the pure state $\Psi_-(\sigma_2, \sigma_3)$ then quantum state of pair 1-4 is conditional density matrix

$$\hat{\rho}_{14/23}^c = \frac{Tr_{23}(\hat{P}_{23}\hat{\rho}_{1234})}{Tr(\hat{P}_{23}\hat{\rho}_{1234})},$$

where operator \hat{P}_{23} selects pair 2-3 is pure state $\Psi_-(\sigma_2, \sigma_3)$. Direct calculation shows that the pair of the photons (1 and 4) has to be in pure state with the wave function $\Phi(\sigma_1, \sigma_4) = \Psi_-(\sigma_1, \sigma_4)$. As the system S_{1234} is described by simultaneous wave function the time order of measurements has no importance.

Other examples demonstrating the utilization of conditional density matrix in different schemes of quantum communication are represented in [10].

5 Conclusion

Provided that the subsystem S_2 of composite quantum system $S = S_1 + S_2$ is selected in a pure state \hat{P}_n the quantum state of subsystem S_1 is conditional density matrix $\hat{\rho}_{1c/2n}$. Reduced density matrix $\hat{\rho}_1$ is connected with conditional density matrices by an expansion (3).

References

- [1] J.von Neumann, Gött. Nach. pp. 1–57, 245 – 272, **1927**. See, also, J. von Neumann, "Mathematische Grundlagen der Quantenmechanik", (Berlin) 1, 1932.
- [2] T. Jennewein, G. Weihs, J.-W. Pan and A. Zeilinger, *Phys.Rev. Lett.* **88**, 017903 (2002).
- [3] W.Heisenberg, *Zeits.f.Physik* **43** , 172, (1925).
- [4] V.V.Belokurov, O.A.Khrustalev, O.D.Timofeevskaya, "Quantum Teleportation: an ordinary miracle", (Izhevsk, Regular and Haotic Dynamics) 1, 2000.
- [5] V.V.Belokurov, O.A.Khrustalev, V.A.Sadovnichy, O.D.Timofeevskaya in *System and subsystems in quantum communication*, (Proceedings of XXII Solvay Conference on Physics, Delphi Latin, 2001), World Scientific Publishing, 555, 2003.
- [6] A.M.Gleason, *J.Math.Mech.* **6**, 885 (1957).
- [7] H.Barnum, C.M.Caves, J.Finkelstein, C.A.Fuchs and R.Schack, arXive: quant-ph/9907024 (1999).
- [8] C.A.Fuchs, arXive: quant-ph/0106166 (2001).
- [9] P.Busch, arXive: quant-ph/9909073 (2003).
- [10] V.V.Belokurov, O.A.Khrustalev, V.A.Sadovnichy, O.D.Timofeevskaya, *Partcules and Nuclei*, *Lett.* **1**, 116 (2003).
- [11] A.Barchielly, *Phys.Rev D* **32**, 347 (1985).

HYPERFINE SPLITTING OF THE GROUND STATE IN MUONIC HYDROGEN

A.P.Martynenko^a

*Samara State University, Theoretical Physics Department,
Pavlov Street 1, 443011 Samara, Russia*

Abstract. Corrections of order α^5 , α^6 are calculated in the hyperfine splitting of muonic hydrogen ground state. Nuclear structure effects are taken into account in one- and two-loop Feynman amplitudes by means of the proton electromagnetic form factors. The modification of the hyperfine splitting part of the Breit potential due to electron vacuum polarization is considered. Total numerical value of the 1S state hyperfine splitting 182.725 meV in μp can play the role of proper estimation for the corresponding experiment with the accuracy 30 ppm.

Precision measurements of the energy spectra of the simplest atomic systems are of great importance for high accuracy verification of the Standard Model and the theory of bound states. Two particle bound states represent important tool for refining the values of fundamental physical constants [1]. The observation of fine effects in low energy physics of simple atoms can be considered as necessary supplement to the construction of large particle colliders for deep penetration to the structure of elementary particles and the search for new fundamental interactions. Such atomic experiments can improve our knowledge about elementary particle interactions at small distances that can only be observed at very high energies [2].

The effects of strong interactions play essential role in the energy spectrum of muonic hydrogen just as electronic hydrogen. On one hand, they are connected with two electromagnetic proton formfactors (electric G_E and magnetic G_M) describing the distributions of the electric charge and magnetic moment. In the Lamb shift case the main contribution to the energy spectrum of order $(Z\alpha)^4$ is determined by the proton charge radius r_p which appears as differential parameter of these distributions. So, the comparison of the experimental data and theoretical value for the Lamb shift obtained with the corrections of high order over α gives the effective approach to obtain more reliable value of the r_p . The measurement of 2P-2S Lamb shift in μp with the precision 30 ppm allows to obtain the value of the proton charge radius which is an order of the magnitude better in the comparison with different methods [3]. The calculation of nuclear structure corrections in the hyperfine splitting of the energy levels (see [4-8]) can be done only on the basis of whole proton electromagnetic form factors. Last experimental measurements of G_E and G_M were carried out in Mainz 20 years ago [9].

On the other one, important contribution of strong interactions to the hydrogen spectrum is connected with the proton polarizability [10]. It appears already in one-loop amplitudes of the muon (electron) proton electromagnetic

^amart@ssu.samara.ru

interaction when different baryonic resonances can be produced in the intermediate states as a result of virtual Compton scattering on the proton. Exact calculation of such effect can be done by means of experimental data and theoretical models for the polarized nucleon structure functions. The proton structure and polarizability effects lead to main theoretical uncertainty in the expressions for different energy levels including the hyperfine splitting of the hydrogen ground state:

$$\Delta E_{theor}^{HFS} = E^F (1 + \delta^{QED} + \delta^{str} + \delta^{pol} + \delta^{HVP}), \quad E^F = \frac{8}{3} \alpha^4 \frac{\mu_P m_1^2 m_2^2}{(m_1 + m_2)^3}, \quad (1)$$

where μ_p is the proton magnetic moment in nuclear magnetons, m_1 is the muon mass, m_2 is the proton mass, δ^{QED} represents the QED contribution, δ^{HVP} is the contribution of hadronic vacuum polarization (HVP), the corrections δ^{str} and δ^{pol} are the proton structure and polarizability contributions. The expression (1) is valid both for muonic and electronic hydrogen but the exact value of these corrections is essentially different for such atoms. The ground state hydrogen hyperfine splitting measurement was made many years ago with very high accuracy [11]:

$$\Delta\nu_{exp}^{HFS}(ep) = 1\ 420\ 405.751\ 766\ 7(9) \text{ kHz}. \quad (2)$$

Existing difference between the theory and experiment without accounting the proton polarizability contribution can be expressed as follows [12]:

$$\frac{\Delta E_{theor}^{HFS}(e p) - \Delta E_{HFS}^{exp}(e p)}{E^F(e p)} = -4.5(1.1) \times 10^{-6}, \quad (3)$$

This quantity contains one of the main uncertainties connected with inaccuracies of the proton form factor determination. Dominant part of one loop proton structure correction is defined by the following expression (the Zemach correction) [4]:

$$\Delta E_Z = E^F \frac{2\mu\alpha}{\pi^2} \int \frac{d\mathbf{p}}{(\mathbf{p}^2 + W^2)^2} \left[\frac{G_E(-\mathbf{p}^2) G_M(-\mathbf{p}^2)}{\mu_P} - 1 \right] = E^F (-2\mu\alpha) R_p, \quad (4)$$

where $W = \alpha\mu$, μ is the reduced mass of two particles, R_p is the Zemach radius. In coordinate representation the Zemach correction (4) is determined by the contraction of the charge ρ_E and magnetic moment ρ_M distributions. The Zemach radius represents the integral characteristic of the proton structure effects in the hyperfine splitting of the energy levels. It may be considered as new fundamental proton parameter in hydrogen atom. Numerical value of the Zemach contribution is equal

$$\Delta E_Z = -1.362 \pm 0.068 \text{ meV}, \quad (5)$$

where the 5% estimation of the uncertainty is connected with the measurement of the proton electromagnetic form factors [9]. So, the measurement of muonic hydrogen hyperfine splitting as for electronic hydrogen with similar accuracy 30 ppm as in the case of the Lamb shift can give new information about possible value of the contributions δ^{str} and δ^{pol} [13].

Such experiment demands corresponding theoretical study of different order corrections with the same precision. Analytical calculation of the hydrogen hyperfine splitting was carried out during many years [12, 14] and reached the accuracy 10^{-8} . But these calculations can not be used directly for muonic hydrogen after the replacement electron mass to muon mass. The reason consists in the proton structure effects. Indeed in the case of muonic hydrogen the dominant region of intermediate loop momenta is of order muon mass. So the calculation of the higher order amplitudes with good accuracy can be based only on their direct integration with the account of experimental data on the proton electromagnetic form factors.

The investigation of different contributions to the muonic atoms energy levels was done many years ago in Ref. [15]. So, at present there is need for new more complete analysis of all possible corrections in the HFS of μp with the declared accuracy 30 ppm. Main corrections of order α^5 to the hyperfine splitting of 2S state in μp were studied in Ref. [16]. They are very important for the extraction of the Lamb shift value 2P-2S in the experiment. In this study we calculate different contributions of order α^5 and α^6 to the muonic hydrogen HFS which are determined by the effects of electromagnetic and strong interactions. The aim of the work consists in obtaining the numerical value of the ground state HFS in muonic hydrogen with designated accuracy which can be serve as reliable guide for corresponding experiment.

The increasing of the lepton mass when we change electronic hydrogen to muonic hydrogen leads to decreasing the Bohr radius in μp . As a result the electron Compton wave length and the Bohr radius are of the same order: $\frac{\hbar^2}{\mu e^2} : \frac{\hbar}{m_e c} = 0.737384$ (m_e is the electron mass, μ is the reduced mass in the atom μp). As an important consequence of last relation is increasing the role of electron vacuum polarization effects in the energy spectrum of μp .

To obtain the contribution of the electron vacuum polarization to the interaction operator there is need to make the following substitution in the photon propagator:

$$\frac{1}{k^2} \rightarrow \frac{\alpha}{\pi} \int_0^1 dv \frac{v^2 \left(1 - \frac{v^2}{3}\right)}{k^2(1 - v^2) - 4m_e^2}. \quad (6)$$

The contribution of electron vacuum polarization to the hyperfine splitting of

the ground state of order α^5 can be written as follows:

$$\Delta E_{1\gamma, VP}^{HFS} = \frac{8\mu^3(Z\alpha)^4(1+\kappa)}{3m_1m_2} \frac{\alpha}{\pi} \frac{m_e^3}{3W^3} \int_{m_e/W}^{\infty} \frac{\sqrt{\frac{W^2}{m_e^2}\xi^2 - 1}}{\xi^4} \left(2\frac{W^2}{m_e^2}\xi^2 + 1 \right) d\xi \times \\ \times \left[1 - \int_0^{\infty} e^{-rm_e(\xi+1)/W\xi} r dr \right] = 0.398 \text{ meV.} \quad (7)$$

Table 1: Corrections of order α^5, α^6 to the ground state HFS in muonic hydrogen.

Contribution to HFS of μp	Numerical value in meV
The Fermi energy E^F	182.443
Muon AMM correction $a_\mu E^F$ of order α^5, α^6	0.213
Relativistic correction $\frac{3}{2}(Z\alpha)^2 E^F$ of order α^6	0.015
Relativistic and radiative recoil corrections with the account proton AMM of order α^6	0.014
One loop electron vacuum polarization contribution of 1γ interaction of order α^5	0.398
One loop muon vacuum polarization contribution of 1γ interaction of order α^6	0.004
Second order vacuum polarization corrections of order α^5, α^6	0.797
Proton structure corrections of order α^5	-1.215
Proton structure corrections of order α^6	-0.014
Electron vacuum polarization contribution + proton structure corrections of order α^6	-0.021
Two loop electron vacuum polarization contribution of 1γ interaction of order α^6	0.003
Muon self energy + proton structure correction of order α^6	0.008
Vertex corrections + proton structure corrections of order α^6	-0.014
"Jellyfish" diagram correction + proton structure corrections of order α^6	0.004
HVP contribution of order α^6	0.004
Proton polarizability contribution of order α^5	0.084
Weak interaction contribution	0.002
Summary contribution	182.725 ± 0.062

The contribution of muon vacuum polarization (MVP) of order α^6 can be found by means (7) after the substitution $m_e \rightarrow m_1$. Numerical value is 0.004

meV. The two loop electron vacuum polarization gives the contributions of the same order α^6 . The modification of the photon propagator in this case is more complicated [12]. Omitting intermediate expressions we present corresponding numerical value with the accuracy 0.001 meV:

$$\Delta E_{1\gamma, \text{2-loop VP}}^{HFS} = 0.003 \text{ meV}. \quad (8)$$

The corrections of the second order of the perturbation theory (SOPT) in the energy spectrum are defined by reduced Coulomb Green function (RCGF) $\tilde{G}_1(\mathbf{r}, \mathbf{r}')$. Some terms of the quasipotential contain the $\delta(\mathbf{r})$ so we must know the quantity $\tilde{G}_1(\mathbf{r}, 0)$. The expression for the RCGF was found in this case in Ref. [18] on the basis of the Hoestler representation for the Coulomb Green function after the subtraction of the pole term:

$$\tilde{G}_{1S}(\mathbf{r}, 0) = \frac{Z\alpha\mu^2}{4\pi} \frac{2e^{-x/2}}{x} [2x(\ln x + C) + x^2 - 5x - 2], \quad (9)$$

where $C = 0.5772\dots$ is the Euler constant. Numerical value of the total contribution of the SOPT is presented in the Table.

The proton structure corrections in μp are relatively large in the comparison with electronic hydrogen. In the HFS of μp these corrections are defined by the following expression:

$$\Delta E_{str}^{HFS} = -E^F \frac{Z\alpha}{8\pi n^3(1+\kappa)} \delta_{l0} \int_0^\infty \frac{dk}{k^2} V(k), \quad (10)$$

$$\begin{aligned} V(k) = & \frac{2F_2^2 k^3}{m_1 m_2} + \frac{\mu}{(m_1 - m_2)(k + \sqrt{4m_1^2 + k^2})} [16F_1^2 k^2 - 128F_1^2 m_1^2 - 128F_1 F_2 m_1^2 + \\ & 64F_1 F_2 k^2 + 16F_2^2 k^2 + \frac{32F_2^2 m_1^2 k^2}{m_2^2} + \frac{4F_2^2 k^4}{m_1^2} - \frac{4F_2^2 k^4}{m_2^2}] + \frac{\mu}{(m_1 - m_2)(k + \sqrt{4m_2^2 + k^2})} \\ & \times [128F_1^2 m_2^2 + 128F_1 F_2 m_2^2 - 16F_1^2 k^2 - 64F_1 F_2 k^2 - 48F_2^2 k^2]. \end{aligned}$$

Extracting infrared divergence in Eq.(10) by means of the iteration term of the quasipotential we obtain the numerical result -1.215 meV. Moreover, the effects of the proton structure must be taken into account carefully in the amplitudes of higher order over α containing the vacuum polarization, muon self energy and muon vertex corrections. Radiative corrections of these amplitudes including recoil effects were studied earlier both in the Lamb shift and HFS of hydrogen-like systems [12, 21, 22]. Radiative photons were taken in the Fried-Yennie (FY) gauge where the mass shell amplitudes don't contain infrared divergences. Infrared finiteness of the Feynman diagrams in this gauge gives the possibility to make standard subtraction on the mass shell without introducing the photon

mass. Renormalizable mass operator and one particle vertex operator in the FY gauge are [12]

$$\Sigma^R(p) = \frac{\alpha}{\pi} (\hat{p} - m)^2 \int_0^1 dx \frac{-3\hat{p}x}{m_1^2 x + (m_1^2 - p^2)(1-x)}, \quad (11)$$

$$\Lambda_\mu^R(p, p-k) = \frac{\alpha}{4\pi} \int_0^1 dx \int_0^1 dz \left[\frac{F_\mu^{(1)}}{\Delta} + \frac{F_\mu^{(2)}}{\Delta^2} \right], \quad (12)$$

where $\Delta = m_1^2 x + 2pk(1-x)z - k^2 z(1-xz)$, the functions $F_\mu^{(1)}$, $F_\mu^{(2)}$ were determined in Ref. [22]. The numerical values of corresponding corrections are written in the Table.

The calculation of different quantum electrodynamical effects, effects of the proton structure and polarizability, the hadron vacuum polarization to HFS of muonic hydrogen was carried out here. The corrections of order α^5 and α^6 were considered. Working with the vacuum polarization diagrams we take into account that the ratio $\mu\alpha/m_e$ is very close to 1 and don't increase the order of corresponding contributions. Obtained numerical results are presented in the Table. We include here also QED corrections to the Fermi energy which are determined by muon anomalous magnetic moment $a_\mu E^F$ [12], the Breit relativistic correction of order $(Z\alpha)^6$, relativistic and radiative recoil effects of the same order $(Z\alpha)^6 m_1/m_2$ with the account of the proton anomalous magnetic moment [19], the proton structure corrections of order $(Z\alpha)^6 \ln(Z\alpha)^2$ [7], the hadron vacuum polarization contribution [20] and the proton polarizability correction [10], the weak interaction contribution due to Z boson exchange [12].

Let point out some peculiarities of this investigation.

1. The effects of the vacuum polarization play very important role in the case of muonic hydrogen. They lead to essential modification of the spin-dependent part of the quasipotential of one photon interaction.

2. We took into account consistently the proton structure in the loop amplitudes by means of electromagnetic form factors. The point-like proton approximation gives essentially increased results (approximately twofold).

3. The calculation of muon self-energy and vertex corrections of order $\alpha(Z\alpha)^5$ was done on the basis of the expressions for the lepton factors in the amplitude terms of the quasipotential obtained by Eides, Grotch and Shelyuto. We supplemented these relations by the subtraction of the iteration terms of the potential.

Total value of the ground state HFS in muonic hydrogen shown in the Table can be considered as definite guide for the future experiment which is prepared [13]. Numerical values of the corrections were obtained with the accuracy 0.001 meV. Theoretical error connected with the uncertainties of fundamental physical constants (fine structure constant, the proton magnetic moment etc.) entering the Fermi energy composes the value near 10^{-5} meV. Other source of

theoretical uncertainty is connected with the corrections of higher order. Its estimation can be found from the leading correction of the next order on α and m_1/m_2 in the form: $\alpha(Z\alpha)^2 \ln(Z\alpha)^2/\pi \approx 0.0005$ meV. Further improvement of theoretical result presented in the Table is connected first of all with the corrections on the proton structure and polarizability which give the theoretical error near 340 ppm. The most part of this error is determined by the proton structure corrections of order $(Z\alpha)^5$ (the Zemach correction). So, the measurement of the hyperfine splitting of the levels 1S and 2S in muonic hydrogen with the accuracy 30 ppm will lead to more accurate value (with relative error 10^{-3}) for the Zemach radius which than can be used for the improvement of theoretical result for the ground state hydrogen hyperfine structure and more reliable estimation of the proton polarizability effect. Increasing the number of the tasks due to excited states of simple atoms and including new simple atoms where the hyperfine structure of the energy spectrum is studied will decrease the uncertainties in the determination of physical fundamental parameters and increase the accuracy for the check of the Standard Model in low energy physics.

References

- [1] P.J.Mohr, B.N.Taylor, *Rev. Mod. Phys.* **72**, 351 (2000).
- [2] Yu.L.Sokolov, *UFN* **619**, 559 (1999).
- [3] R.Pohl et al., *Hyperfine Interactions* **127**, 161 (2000).
- [4] A.C.Zemach, *Phys. Rev.* **104**, 1771 (1956).
- [5] G.M.Zinoviev et al., *Yad. Fiz.* **11**, 1284 (1970).
- [6] A.I.Milshtein et al. *JETP*, **109** 1146 (1996).
- [7] S.G.Karshenboim, *Phys. Lett.* **A225**, 97 (1997).
- [8] R.N.Faustov, A.P.Martynenko, *Phys. Rev.* **A67**, 052506 (2003).
- [9] G.G.Simon et al., *Nucl. Phys.* **A333**, 381 (1980).
- [10] E.V.Cherednikova et al., *Nucl. Phys.* **A703**, 365 (2002).
- [11] H. Hellwig et al, *IEEE Trans. IM-19*, 200 (1970).
- [12] M.I.Eides, H.Grotch, V.A.Shelyuto, *Phys. Rep.* **342**, 62 (2001).
- [13] A.Adamczak et al., *Hyperfine Interactions* **136**, 1 (2001).
- [14] G.T.Bodwin, D.R.Yennie, *Phys. Rev.* **D37**, 498 (1988).
- [15] E.Borie, G.A.Rinker, *Rev. Mod. Phys.* **54**, 67 (1982).
- [16] K.Pachucki, *Phys. Rev.* **A53**, 2092 (1996).
- [17] M.I.Eides, H.Grotch, V.A.Shelyuto, *Phys. Rev.* **D65**, 013003 (2001).
- [18] V.G.Ivanov, S.G.Karshenboim, *JETP* **109**, 1219 (1996).
- [19] G.T.Bodwin et al., *Rev. Mod. Phys.* **57**, 723 (1985).
- [20] A.P.Martynenko, R.N.Faustov, *Yad. Fiz.* **61**, 471 (1998).
- [21] M.I.Eides, H.Grotch, V.A.Shelyuto, *Phys. Rev.* **A63**, 052509 (2001).
- [22] M.I.Eides, V.A.Shelyuto, *Eur. Phys. Jour.* **C21**, 489 (2001).

EVOLUTION OF ANGULAR DISTRIBUTION OF POLARIZATION COMPONENTS FOR SYNCHROTRON RADIATION UNDER CHANGES OF PARTICLE ENERGY

V.G. Bagrov^{a 1}, D.M. Gitman³,
V.B. Tlyachev², A.T. Jarovoi¹

Abstract

In the framework of classical theory, a complete analysis of the behavior of angular profiles for synchrotron radiation under a change of the particle energy is carried out. For the description of previously known qualitative features of synchrotron radiation, exact quantitative characteristics are introduced.

1 Angular distribution of σ -component of linear polarization of synchrotron radiation

In this paper, we introduce new quantitative characteristics of synchrotron radiation in the framework of classical theory. The initial expressions can be found in papers [1–5]. We adopt the notation of [5].

The angular distribution of the σ -component of synchrotron radiation has the simplest behavior under a change of the particle energy.

The function $F_2(\beta, \theta)$ reaches its extremal values only at $\theta = 0, \pi/2, \pi$. At the same time, $\theta = 0, \pi$ are points of minimum, but at $\theta = \pi/2$ a maximum is reached at every β . The minimal values $F_2(\beta, 0) = F_2(\beta, \pi) = 1/4$ do not depend on β . The maximal value $F_2(\beta, \pi/2) = \gamma^3(7\gamma^2 - 3)/16$ is reached at $\theta = \pi/2$ and behaves at large energies as γ^5 . Inside the interval $0 < \theta < \pi/2$, the function $F_2(\beta, \theta)$ monotonously increases, but at $\pi/2 < \theta < \pi$ it monotonously decreases with the growth of θ . Fig. 1 shows the behavior of $F_2(\beta, \theta)$ as the particle energy increases.

2 Angular distribution of π -component of linear polarization for synchrotron radiation

The turning points of $F_3(\beta, \theta)$ are $0, \pi/2, \pi$. At the same time, $F_3 = 0$ reaches the absolute minimum at $\theta = \pi/2$. If $\beta < \beta_3$ ($\gamma < \gamma_3$), where

$$\beta_3 = 2/\sqrt{15} \approx 0,5164, \quad \gamma_3 = \sqrt{15/11} \approx 1,1678, \quad (1)$$

the absolute maximum is reached at $\theta = 0, \pi$. If $\beta > \beta_3$ ($\gamma > \gamma_3$), the absolute maximum is reached at $\theta = \theta_3(\beta)$, $\theta = \pi - \theta_3(\beta)$, where $\theta_3(\beta)$ is defined by

$$6\beta^2 \sin^2 \theta_3(\beta) = 5\beta^2 - 24 + \sqrt{5(5\beta^4 + 24\beta^2 + 96)}, \quad \beta \geq \beta_3. \quad (2)$$

^aCorresponding author. Tel. +7-3822-529-843. E-mail address: bagrov@phys.tsu.ru.

Consequently, in the region $0 < \theta < \pi/2$ the function $F_3(\beta, \theta)$ has a maximum at $\theta = 0$ when $\beta \leq \beta_3$, ($\gamma < \gamma_3$) and monotonously decreases with the growth of θ ; if $\beta > \beta_3$, ($\gamma > \gamma_3$), then $F_3(\beta, \theta)$ has a minimum at $\theta = 0$ and monotonously increases with the growth of θ up to the point of maximum $\theta = \theta_3(\beta)$. The function $F_3(\beta, \theta)$ monotonously decreases with the growth of θ when $\theta_3(\beta) < \theta \leq \pi/2$. Consequently, if we denote by $\theta_3(\beta)$ the maximum of $F_3(\beta, \theta)$ in the region $0 \leq \theta \leq \pi/2$, then

$$\theta_3^m(\beta) = \begin{cases} 0, & \beta \leq \beta_3, \\ \theta_3(\beta), & \beta \geq \beta_3. \end{cases} \quad (3)$$

In particular, at $\beta \rightarrow 1$ ($\gamma \rightarrow \infty$) from (2) follows the well-known asymptotic formula [1]

$$\theta_3^m(\beta) \approx \pi/2 - \gamma^{-1} \sqrt{2/5}, \quad \gamma \gg 1. \quad (4)$$

The plot of $\theta_3^m(\beta)$ is presented on fig. 5. The plot of the family $F_3(\beta, \theta)$ at different β is presented on fig. 2. Thus, we have two types of plots: the first type (at $\beta \leq \beta_3$) is represented by curves 1,2,3 on fig. 2, with the maximums at $\theta = 0, \pi$; the second type (at $\beta > \beta_3$) is represented by curves with the maximums shifted from $\theta = 0, \pi$ with the growth of β , and simultaneously approaching $\theta = \pi/2$.

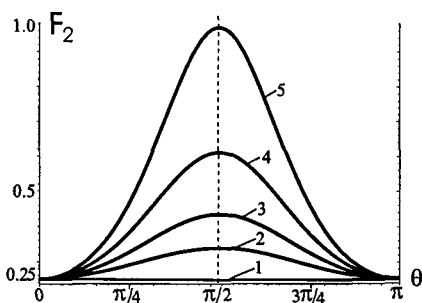


Figure 1: The angular profiles of the σ -component of radiation at different β : 1 - 0.0; 2 - 0.3; 3 - 0.4; 4 - 0.5; 5 - 0.6.

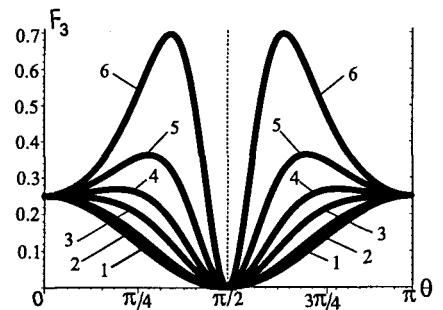


Figure 2: The angular profiles of the π -component of radiation at different 1 - 0.0; 2 - 0.3; 3 - 0.5; 4 - 0.6; 5 - 0.7; 6 - 0.8.

3 Angular distribution of total radiating intensity

Let us introduce the values

$$\begin{aligned} \beta_0^{(1)} &= 1/\sqrt{7} \approx 0,3379, & \gamma_0^{(1)} &= \sqrt{7/6} \approx 1,0801; \\ \beta_0^{(2)} &= \sqrt{(\sqrt{6}-2)2/3} \approx 0,5474, & \gamma_0^{(2)} &= (\sqrt{3}+3\sqrt{2})/5 \approx 1,1949. \end{aligned} \quad (5)$$

An elementary analysis shows that for every value of the particle energy the function $F_0(\beta, \theta)$ has the turning points $\theta = 0, \pi/2, \pi$. Given this, a maximum is reached at $\theta = 0, \pi$, while a minimum is reached at $\theta = \pi/2$. If $\beta > \beta_0^{(2)}$, we have minimums at $\theta = 0, \pi$, and a maximum at $\theta = \pi/2$.

If $\beta_0^{(1)} < \beta < \beta_0^{(2)}$ ($\gamma_0^{(1)} < \gamma < \gamma_0^{(2)}$), the function $F_0(\beta, \theta)$ has minimums at $\theta = 0, \pi/2, \pi$ and a maximum at $\theta = \theta_0(\beta), \theta = \pi - \theta_0(\beta)$, where $\theta_0(\beta)$ is defined by the condition $B_- = 0$. It follows that

$$\begin{aligned} 3(1 + 3\beta^2)\beta^2 \sin^2 \theta_0(\beta) &= 2\sqrt{15(2 + 4\beta^2 + 9\beta^4)} - 6(2 + \beta^2), \\ 0 \leq \theta_0(\beta) \leq \pi/2, \quad \beta_0^{(1)} \leq \beta \leq \beta_0^{(2)}. \end{aligned} \quad (6)$$

It is easy to see that if $\gamma < \bar{\gamma}$, where $\bar{\gamma}$ is a root of the algebraic equation

$$\bar{\gamma}^3(7\bar{\gamma}^2 - 3) - 8 = 0, \quad \bar{\gamma} \approx 1,1172; \quad \bar{\beta} \approx 0,4459; \quad \gamma_0^{(1)} < \bar{\gamma} < \gamma_0^{(2)}, \quad (7)$$

then $F_0(\beta, 0) = F_0(\beta, \pi) > F_0(\beta, \pi/2)$; if $\bar{\gamma} < \gamma$, then $F_0(\beta, 0) = F_0(\beta, \pi) < F_0(\beta, \pi/2)$. Thus, denoting by $\theta_0^m(\beta)$ the point of absolute maximum of $F_0(\beta, \theta)$ in the region $0 \leq \theta \leq \pi/2$, we have

$$\theta_0^m(\beta) = \begin{cases} 0, & \beta \leq \beta_0^{(1)}; \\ \theta_0(\beta), & \beta_0^{(1)} \leq \beta \leq \beta_0^{(2)}; \\ \pi/2, & \beta_0^{(2)} \leq \beta. \end{cases} \quad (8)$$

The plot of $\theta_0^m(\beta)$ is presented on fig. 5. The family of $F_0(\beta, \theta)$ at different β is presented on fig. 3. Thus, there are four types of plots: the first type ($\beta \leq \beta_0^{(1)}$) is represented by curves 1,2 on fig. 3, with the maximums at $\theta = 0, \pi$, so that the behavior of $F_0(\beta, \theta)$ is similar to the behavior of $F_2(\beta, \theta)$ (fig. 1); the second type is defined by the condition ($\beta_0^{(1)} < \beta \leq \bar{\beta}$) and the third type, with the condition ($\bar{\beta} \leq \beta < \beta_0^{(2)}$), is represented by curves 3, 4, 5 on fig. 3, with the maximums shifted from $\theta = 0, \pi$ and approaching $\theta = \pi/2$ as β increases. The plots of the second (curve 3) and third (curves 4,5) types differ in the mutual location of the values F_0 at $\theta = 0, \pi$ and $\theta = \pi/2$, according to the above description; the fourth type ($\beta > \beta_0^{(2)}$) is represented by curve 6 on fig. 3; it has the property that its point of maximum is $\theta = \pi/2$, and the plot of $F_0(\beta, \theta)$ is again similar to that of $F_2(\beta, \theta)$ on fig. 1.

4 Angular distribution of right-polarized radiation

The points $\theta = 0, \pi$ are turning points of $F_1(\beta, \theta)$, and the absolute minimum $F_1(\beta, \pi) = 0$ is reached at $\theta = \pi$.

Denoting by $\theta_1^m(\beta)$ the point of maximum of the function $F_1(\beta, \theta)$, we find after a simple analysis that

$$\theta_1^m(\beta) = \begin{cases} 0, & \beta \leq \beta_0^{(1)}; \\ \theta_1(\beta), & \beta_0^{(1)} < \beta. \end{cases} \quad (9)$$

The function $\theta_1(\beta)$ is equal to zero at $\beta \leq \beta_0^{(1)}$ and is more than zero at $\beta > \beta_0^{(1)}$. There is no closed analytical form of $\theta_1^m(\beta)$; however, this does not prevent one from calculating $\theta_1(\beta)$ using a computer. The plot of $\theta_1^m(\beta)$ is presented on fig. 5. The family of $F_1(\beta, \theta)$ at different β is presented on

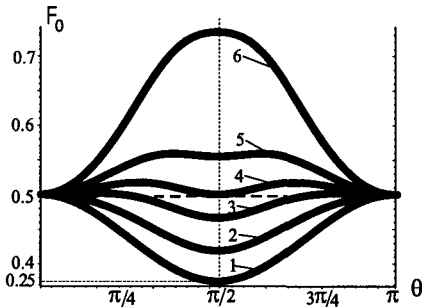


Figure 3: The angular profiles of total radiation at different β : 1 - 0.0; 2 - 0.3; 3 - 0.4; 4 - 0.4458; 5 - 0.5; 6 - 0.6.

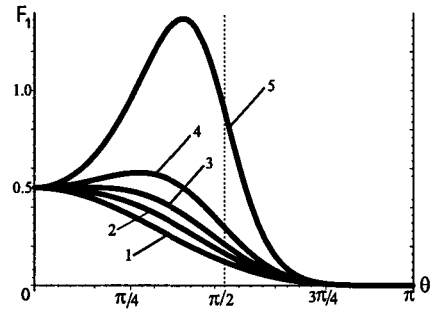


Figure 4: The angular profiles of the right-polarized radiation component at different β : 1 - 0.0; 2 - 0.3; 3 - 0.4; 4 - 0.5; 5 - 0.6.

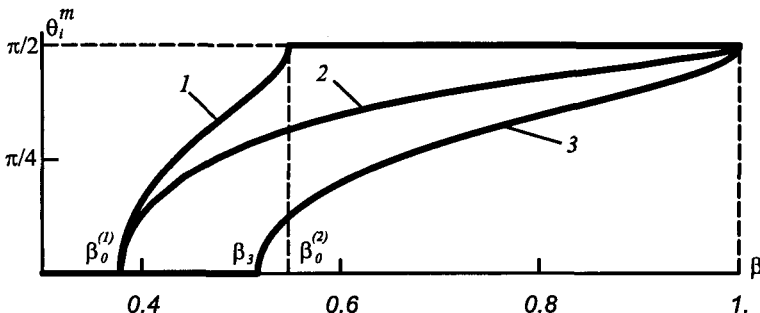


Figure 5: Profiles of function $\theta_i^m(\beta)$: 1 - $\theta_0^m(\beta)$, 2 - $\theta_1^m(\beta)$, 3 - $\theta_3^m(\beta)$

fig. 4. In this case, we have two types of plots: the first type ($\beta < \beta_0^{(1)}$) is represented by curves 1,2 on fig. 4, with the maximums at $\theta = 0$; the second

type ($\beta > \beta_0^{(1)}$) is represented by curves 3,4,5 on fig. 4; it has the property that the maximums shift from $\theta = 0$ and approach $\theta = \pi/2$ as β increases.

In the ultrarelativistic case ($\gamma \rightarrow \infty$), we have

$$F_0^m/F_1^m \approx 1.6042, \quad F_0^m/F_3^m = \frac{2401\sqrt{35}}{1250} \approx 11.3636. \quad (10)$$

5 Effective angle of radiation. Deviation angle

The behavior of the profiles of $F_i(\beta, \theta)$ with the growth of the particle energy confirms the well-known fact [1-4] concerning the concentration of almost entire amount of ultrarelativistic radiation in a narrow cone located close to the plane of the particle orbit ($\theta = \pi/2$). The effective angle of this cone is $\Delta\theta \sim \gamma^{-1}$. This statement has a qualitative character, and until recently no quantitative formulation has been suggested.

The quantitative characteristics of the degree of radiation concentration (effective radiation angle), and its direction in the region of concentration (deviation angle), will be given below. From the beginning, we introduce the effective angle of radiation and the deviation angle, using the example of the function $F_1(\beta, \theta)$ (this function does not possess the mirror symmetry with respect to the direction $\theta = \pi/2$).

The plot of this function at $\beta = 0.6$ is presented on fig. 7. Let us consider the points $0 \leq \theta_1^{(1)} < \theta_2^{(1)} \leq \pi$ which obey the relation

$$\int_{\theta_2^{(1)}}^{\theta_1^{(1)}} F_1(\beta; \theta) \sin \theta d\theta = \frac{1}{2} \int_0^\pi F_1(\beta; \theta) \sin \theta d\theta. \quad (11)$$

In other words, one half of radiation intensity of the right-polarized component is radiated through the angle $\overline{\Delta}_1 = \theta_2^{(1)} - \theta_1^{(1)}$. It is evident that the relation (11) does not determine the values $\theta_1^{(1)}$ and $\theta_2^{(1)}$ (and consequently $\overline{\Delta}_1$) in a unique manner; however, it establishes a relation between them (e.g., it establishes a functional dependence $\overline{\Delta}_1 = \Delta(\theta_1^{(1)})$). Let us now select θ_1 in $\overline{\Delta}_1$ to be a minimum (i.e., we look for a minimum of the function $\overline{\Delta}_1(\theta_1^{(1)})$). It is easy to see that if the value $\theta_2^{(1)}$ is not in agreement with the right end of the interval ($\theta_2^{(1)} \neq \pi$), then the condition of a minimum $\overline{\Delta}_1$ can be written in the form

$$F_1(\beta; \theta_1^{(1)}) \sin \theta_1^{(1)} = F_1(\beta; \theta_2^{(1)}) \sin \theta_2^{(1)}. \quad (12)$$

From the system of two equations (11) and (12) one can uniquely determine $\theta_1^{(1)}$ and $\theta_2^{(1)}$; thereby, one can find the minimal value $\overline{\Delta}_1^{\min} = \Delta_1$.

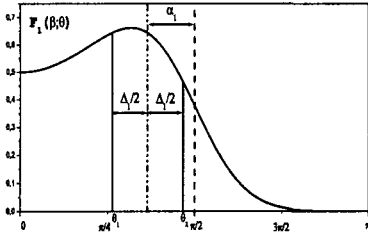


Figure 6: To the definition of the effective angle and the deviation angle for the function $F_1(\beta; \theta)$

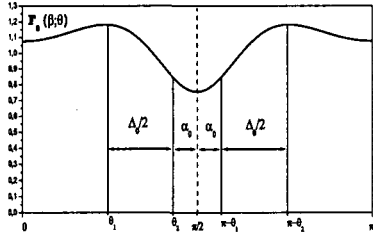


Figure 7: To the definition of the effective angle and the deviation angle for the function $F_0(\beta; \theta)$

We shall refer to Δ_1 as the effective angle of the right-polarized radiation component. The location of the interval $[\theta_1^{(1)}, \theta_2^{(1)}]$ on the axis θ will be characterized by the angle

$$\alpha_1 = (\pi - \theta_1^{(1)} - \theta_2^{(1)})/2, \quad (13)$$

which will be called the deviation angle (the point α_1 divides the interval Δ_1 in half). The introduced values are illustrated by fig. 7.

Considering the functions $F_k(\beta, \theta)$ for $k = 0, 2, 3$, we can see that their plots are mirror-symmetrical with respect to $\theta = \pi/2$. As an example, the plot of $F_0(\beta; \theta)$ and $\beta = 0.55$ is presented on fig. 8. In this case, it is appropriate to apply the above definition to the interval $0 < \theta < \pi/2$, so as to determine the deviation angle in a somewhat different manner:

$$\begin{aligned} \int_{\theta_1^{(k)}}^{\theta_2^{(k)}} F_k(\beta; \theta) \sin \theta d\theta &= \frac{1}{2} \int_0^{\pi/2} F_k(\beta; \theta) \sin \theta d\theta, \quad F_k(\beta; \theta_1^{(k)}) \sin \theta_1^{(k)} = \\ &= F_k(\beta; \theta_2^{(k)}) \sin \theta_2^{(k)}, \quad \Delta_k/2 = \theta_2^{(k)} - \theta_1^{(k)}, \quad \alpha_k = \pi/2 - \theta_2^{(k)}, \quad k = 0, 2, 3. \end{aligned} \quad (14)$$

At $\alpha_k > 0$, the effective angle is divided into two equal parts, located symmetrically with respect to the line $\theta = \pi/2$, and separated by the interval $2\alpha_k$, as shown on fig. 8. In some cases (e.g., for $F_2(\beta; \theta)$ at every β , and for $F_0(\beta; \theta)$ at β close to 1). With the value $\theta_2^{(0,2)} = \pi/2$ (in agreement with the right end of the integration interval), in order to determine Δ_k , it is sufficient to use only the first equation in (14), where one has to set $\theta_1^{(k)} = (\pi - \Delta_k)/2$, $\theta_2^{(k)} = \pi/2$, with the deviation angle $\alpha_k = 0$. Two parts of the effective angle merge, and the effective angle is located so that it is divided in two by the vertical line. It is evident that the effective angles and the deviation angles are functions of the particle energy (or β) $\Delta_i = \Delta_i(\beta)$, $\alpha_i = \alpha_i(\beta)$.

The plots of $\Delta_i(\beta)$ and $\alpha_i(\beta)$ are presented on figs. 8, 9, respectively ($\alpha_2(\beta) = 0$).

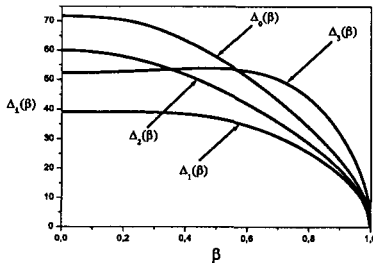


Figure 8: The dependence of the effective angle on β for the polarization component.

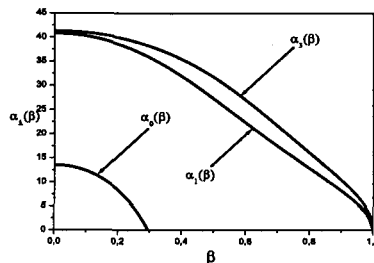


Figure 9: The dependence of the deviation angle on β for the polarization component.

6 Conclusion

The above consideration shows that the angular profiles of synchrotron radiation have a rather complicated behavior with respect to the growth of the particle energy. The previously known qualitative statements concerning the preferred circular polarization in the upper (lower) half-plane, as well as concerning the concentration of ultrarelativistic radiation in the region of the orbit plane, are given an exact quantitative formulation.

Acknowledgments

This work was partially supported by RFBR grant 03-02-17615 and Russia President grant SS-1743.2003.2.

References

- [1] A.A. Sokolov and I.M. Ternov, *Synchrotron Radiation*, (Akademie Verlag, Berlin; Pergamon Press, New York, 1968).
- [2] A.A. Sokolov, I.M. Ternov, *Radiation from relativistic electrons*, (American Institute of Physics, New York, 1986).
- [3] I.M. Ternov, V.V. Mihailin, *Synchrotron Radiation. Theory and experiment* (Energoatomizdat, Moscow, 1986) in Russian.
- [4] *Synchrotron Radiation Theory and its Development*, (Editor V.A. Borodovitsyn. World Scientific. Singapore • New Jersey • London • Hong Kong, 1999).

- [5] V.G. Bagrov, V.G. Bulenok, D.M. Gitman, Jose Acosta Jara, V.B. Tlyachev, A.T. Yarovoi, Phys. Rev. E, 2004, V. 69, No. 4–2, 046502 (1–8).

SYNCHROTRON RADIATION OF RELATIVISTIC ELECTRON BUNCHES

V.A.Bordovitsyn ^a, V.G.Bulenok ^b, T.O.Pozdeeva

Tomsk State University, Lenin Ave. 36, 634050 Tomsk, Russia

Abstract. The possibility of super-power short-wavelength coherent synchrotron radiation from a train of bunches is discussed.

1 Introduction

For a long time the traditional way to consider coherent synchrotron radiation (CSR) has been the following: first a facility for emission of SR (betatron, microtron, synchrotron, undulator) was designed, then a possibility of CSR-effect observation for the formed density distributions of electron bunches was discussed. This situation might have been conditioned by the commonly accepted and experimentally confirmed view that ordinary SR is incoherent, and the CSR peak is known to be shifted to long wavelength regions of the spectrum [1].

The first manifestation of the coherence effect of SR was recorded in 1984 at the synchrotron SRS at Daresbury [2]. In 1989 some especial experiments for observation of CSR from electron bunches in the far-infrared region were fulfilled on the base of the 300-MeV linear accelerator Tohoku [3]. The results of the experiments turned out to be in good agreement with the theory of CSR by L.J. Schiff [4] and J.Schwinger [5] (see also [6–11]). In particular, it was shown that the spectral peak of CSR power as compared to ordinary SR of a single electron (SESR) falls on the millimeter region according to the longitudinal bunches length l and in comparison with incoherent SR of bunches increases proportionally with the number Z of electrons in the bunch.

The purpose of our work is a detailed analysis of possibilities for generation of super-power CSR emitted from the electron bunches and from a bunch train of relativistic electrons in a more wide range of SR up to the critical wavelength.

2 The spectral composition of radiation from an electron bunch

In a pioneering work on CSR from the electron bunches of spherical shape [8] it was shown that the CSR power depends only on longitudinal bunch length at a circle, and so simplicity further we consider only one-dimensional bunch with zero cross-section. The relevant formulas are known in literature (see, for example [1]). The CSR power for one such bunch at frequency $\tilde{\omega}$ is determined by the following expression:

$$W_{nB} = W_n^1 Z F_n(\alpha). \quad (1)$$

^ae-mail: bord@mail.tomsknet.ru

^be-mail: vadim@tspu.edu.ru

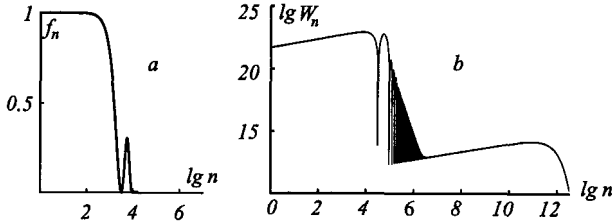


Figure 1: a. Spectral shape functions f_n of CSR for $\alpha = 10^{-3}$ (left); b. Spectral distribution of CSR power for $Z = 10^{11}$ and $\gamma = 5.87 \cdot 10^3$ (right).

Spectral power of SESR W_n^1 and the shape functions

$$F_n(\alpha) = 1 + Zf_n(\alpha) \quad (2)$$

are depending on probability $w(\varphi)$ that a given electron is found in the angular interval between φ and $\varphi + d\varphi$ on a circle orbit in electron bunches of various configurations. The normalized function $w(\varphi)$ used here has the form

$$w(\varphi) = \frac{1}{\alpha} \sin^2 \frac{\pi \varphi}{\alpha}. \quad (3)$$

The value of the azimuthal parameter α included in $w(\varphi)$ determines the effective longitudinal size of an electron bunch $l = \rho\alpha$. For example, for $l = 1\text{cm}$ and $\rho = 10\text{m}$ we shall have $\alpha = 10^{-3}$. Note that this value of α for electrons with energy 3GeV is in the limits of the synchrotron radiation formation length (see [12]) $\tilde{l} = 4\pi\rho/\gamma$ which corresponds to $\tilde{\alpha} = 4\pi/\gamma$ and for electrons with the same energy we shall have $\alpha < \tilde{\alpha} = 2.14 \cdot 10^{-3}$.

The second terms in (1) describe the spectral distribution of coherent radiation from bunched electrons

$$W_n^{Coh} = Z^2 W_n^e f_n(\alpha), \quad (4)$$

where

$$W_n^e = W_{SR}^e \frac{\sqrt{3}}{2\pi} \frac{n}{\gamma^6} \int_{2n/3\gamma^3}^{\infty} K_{5/3}(x) dx, \quad W_{SR}^e = \frac{2}{3} \frac{e^2 c}{\rho^2} \gamma^4 \quad (5)$$

is the spectral distribution of SR, and the SESR power correspondingly.

We can find the spectral shape functions of coherent radiation $f_n(\alpha)$ using the relations (see e.g. [1, 6])

$$f_n(\alpha) = \left(\int \cos n\varphi w(\varphi) d\varphi \right)^2 \quad (6)$$

for the symmetrical bunches. The spectral shape function $f_n(\alpha)$ corresponding to (6) and (3) is

$$f_n = \frac{\sin^2 n\alpha}{(n\alpha)^2} \frac{1}{[1 - (n\alpha/2\pi)^2]^2}.$$

This function is shown in Fig. 1a. To capture large values of n characteristic of radiation from one electron, we use logarithmic scale in this figure. The spectral distribution of the total radiation power, including its incoherent part for electrons with energy 3GeV ($\gamma = 5.87 \cdot 10^3$) is shown in Fig.1b.

The corresponding to CSR range of effective values for parameter α falls, by Fig.1a, onto harmonics $n \leq 2\pi/\alpha$. It follows that radiation frequency of coherent radiation $\tilde{\omega}^{Coh} = nc/\rho \leq 2\pi c/l$, and the corresponding wavelength $\lambda \geq l$. Thus, CSR should be observed at wavelength of order of bunch size, i.e. in the long-wavelengths region. It is obvious that CSR peak shifts to the short wavelength region as longitudinal bunch length decreases and at the region $\lambda = \lambda_c \approx 4\pi R/\gamma^3$ it comes into the region of SESR peak frequency.

To receive the total power of coherent radiation it is necessary to integrate a spectral distribution of this radiation. On doing the integrating, consideration should be given to the fact that low-frequency approximation of a spectrum of synchrotron radiation of one electron $W_n \sim n^{1/3}$ is well enough fulfilled in the whole spectral range of coherent radiation (see Fig.2a). Therefore the total power of coherent radiation considering the stepped character of functions f_n (see also Fig.1a) can be received by integrating of expression (4) over the whole spectrum. Integrating by a numerical method we obtain

$$W^{Coh} = Z^2 \frac{e^2 c}{\rho^2} \frac{1.49}{\alpha^{4/3}}. \quad (7)$$

If we normalize the value of α to the formation length of synchrotron radiation, i.e. accept $\alpha = 4\pi/\gamma$ (see above), formula (7) can be given in a practical more convenient form

$$W^{Coh} = 8.63 \cdot 10^{-20} Z^2 \frac{E^{4/3}(GeV)}{\rho^2(m)} \text{ kWatt.} \quad (8)$$

With $E = 3GeV$, $\rho = 10m$, and $Z = 10^{11}$ it takes the value 37.32 kWatt.

3 CSR from a train of bunched electrons

We shall also consider coherent synchrotron radiation from a train of N bunches, each of which has the angular size $\alpha = 2\pi/m$ where m is a number not necessary an integer. In this case the normalized probability of electron distribution is

$$w(\varphi) = \frac{2}{N\alpha} \sin^2 \frac{\pi\varphi}{\alpha}, \quad (9)$$

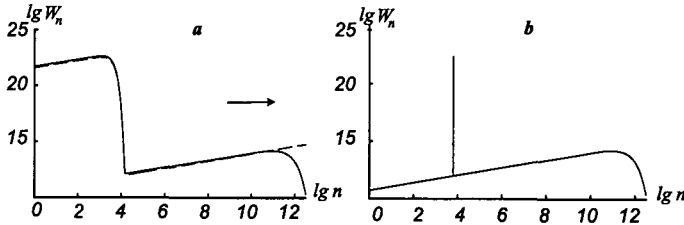


Figure 2: a. The validity of approximation $W_n^{Coh} \sim n^{1/3}$ in the short-wave limit of CSR;
b. Spectral distribution of CSR power from a train of bunched electrons.

and the spectral function $f_n(\alpha)$ is equal to

$$f_n(\alpha) = \frac{\sin^2(nN\alpha/2)}{(nN\alpha/2)^2} \frac{1}{[1 - (n\alpha/2\pi)^2]^2}. \quad (10)$$

With $\alpha = 2\pi/N$, i.e. when $m = N$ is an integer, all bunches are uniformly distributed on a circle orbit. Thus only one harmonics with the number $n = N$ equal to the number of bunches in a train is radiated, since the spectral function f_n does not equal zero only with the given value of n . With the latter it equals $(1/4)\delta_{n,n}$. From this by means of (4) and (5) it is easy to verify, that the power of coherent radiation on N -th harmonics with frequency $\tilde{\omega} = (c/\rho)N$ is defined by expression

$$W_{n=N}^{Coh} = Z_B^2 N^{7/3} W_{SR}^e \frac{3^{7/6} \Gamma(2/3)}{8\pi\gamma^4}, \quad (11)$$

where $Z_B = Z/N$ is the number of electrons in one bunch. The total radiation spectral distribution with the parameters of Fig.1 ($N = 2\pi\rho/l = 6283$) for this case is shown in Fig.2b.

If the angular sizes of bunches correspond to the synchrotron radiation formation length (see above), $N = 2\pi/\alpha = \pi\gamma/2 \gg 1$. Then almost all power of coherent radiation falls on frequency $\tilde{\omega} = cN/\rho$ and wavelength $\lambda = 2\pi\rho/N$, which makes approximately 0.68 cm. for energy $E = 3GeV$ and $\rho = 10m$.

The spectral distribution of radiation is described by one formula

$$\frac{dW^{Coh}}{dx} = Z^2 W_{SR}^e \frac{2^{1/3} 3^{7/6} \Gamma(2/3)}{\pi} \frac{x^{1/3} f(x)}{\gamma^4 \alpha^{4/3}}, \quad (12)$$

where

$$f(x) = \frac{\sin^2 2x}{(2x)^2} \frac{1}{[1 - (x/\pi)^2]^2}, \quad x = \frac{n\alpha}{2} = \frac{3}{4}\alpha\gamma^3.$$

Of course, further integration over x according to (12) gives the former expressions for the total power of coherent radiation.

In conclusion, we shall consider an opportunity of deriving short-wavelength CSR when the longitudinal sizes of bunches $l \rightarrow \lambda_c$. In this case approximation $W_n^e \sim n^{1/3}$ as it follows from Fig.2a, remains valid almost up to the critical value of $l = \lambda_c = 4\pi\rho/\gamma^3$.

According to (7), the total power of coherent radiation takes in this limit the following form:

$$W^{Coh} \approx 0.07Z^2 W_{SR}^e, \quad (13)$$

which is the analogue to the synchrotron radiation power of a single particle with the charge $q = Ze$.

In the practical units we have

$$W^{Coh} = 5.45 \cdot 10^{-11} Z^2 \frac{E^4(GeV)}{\rho^2(m)} \text{ kWatt.}$$

For the same parameters as in the above examples we obtain $W^{Coh} = 441 \text{ TWatt.}$

Certainly, for the present, it is only an exotic case, but it specifies an opportunity of deriving super-power CSR in a short-wave range of a spectrum. Further progress in this direction depends on successes in deriving more compact electron bunches.

Acknowledgments

This work was supported by RF president grant no. SS 1743.2003.2, by RFBR grant no. 03-02-17 615, and partially by grant of "Dynasty" fond.

References

- [1] I.M. Ternov, V.M. Mihailin, "*Synchrotron Radiation. Theory and Experiment*", (Moscow, Energoatomizdat), 1986.
- [2] J.Y. Yarwood, T. Shuttlewarth, J.B. Hasted, and T. Nanba, *Nature* (London) 312, 742 (1984).
- [3] T. Nakazato, T. Nanba, Y. Kondo, Y. Shibata et al., *Phys. Rev. Lett.* 63, 1254 (1989).
- [4] L.J. Schiff, *Rev. Sci. Instrum.* 17, 6 (1946).
- [5] J. Schwinger, *Phys. Rev.* 75, 1912 (1949).
- [6] J.S. Nordvick, D.S. Saxon, *Phys. Rev.* 96, 180 (1954).
- [7] A.M. Prohorov, *Radiotekhnika i elektronika* No. 1, 71 (1956).
- [8] S.P. Kapitza, L.A. Weinstein, *J. Exp. Teor. Fiz. (JETP)* 42, 821 (1962).
- [9] F.C. Michel, *Phys. Rev. Letters* 48, 580 (1982).
- [10] A.M. Kondratenko, E.L. Saldin. *DAN Nauk SSSR* 249, 843 (1979).
- [11] M.P. Klepikov, I.M. Ternov, *Izv. Vuz. Fiz.* 33, No. 3, 9 (1990).
- [12] "*Synchrotron Radiation and Its Development.*" Ed. V. Bordovitsyn, (World Scientific, Singapore), 1999.

NEW APPROACH FOR DESCRIPTION OF P-, T-NON-INVARIANT STATES IN ELEMENTARY PARTICLE PHYSICS

O.Kosmachev ^a

*Joint Institute for Nuclear Research, Laboratory of High Energies, 141980, Moscow
Region, Dubna, Russia*

Abstract. It is shown that P-,T- (PT)-conjugate irreducible representations of Lorentz group exist. Their inclusion in theoretical schemes leads to substantial reconsideration of processes between elementary particles.

1 Introduction

Main peculiarities of proposed approach are:

1.A necessity to specify Lorentz invariance is shown. It means, that description of physical objects necessary to connect with quite definite irreducible representations of Lorentz group from infinite series of irreducible representations (IR). It allows more completely and deeply to analyze structure of objects and their interactions.

2.It is shown, that besides the known P-,T-invariant or ordinary IR's of Lorentz group, P-,T-conjugate IR's exist as well. It is naturally to connect them with P-,T-non-invariant physical objects or interactions.

3.A relativity and a mutuality of such notions as P-,T-invariance and non-invariance are emphasized. Objects become such by relations between themselves.

2 Dirac equation and irreducible representations of Lorentz group

All completeness of information, which is contained in Dirac equation, is determined by structure of γ -matrix group.

One can show [1], that γ -matrix group contains two subgroups d_γ and b_γ . Both have order -16 , number of conjugate classes -10, eight 1-dimension IR's and two 2-dimension IR's.

If to construct IR's and to define algebras on elements of these groups, one can derive such commutative relations (CR).

Commutative relations on the base of d_γ are:

$$\begin{aligned} [a_1, a_2] &= 2a_3, & [a_2, a_3] &= 2a_1, & [a_3, a_1] &= 2a_2, \\ [b_1, b_2] &= -2a_3, & [b_2, b_3] &= -2a_1, & [b_3, b_1] &= -2a_2, \\ [a_1, b_1] &= 0, & [a_2, b_2] &= 0, & [a_3, b_3] &= 0, \\ [a_1, b_2] &= 2b_3 & [a_1, b_3] &= -2b_2, \\ [a_2, b_3] &= 2b_1, & [a_2, b_1] &= -2b_3, \\ [a_3, b_1] &= 2b_2, & [a_3, b_2] &= -2b_1. \end{aligned} \tag{1}$$

^ae-mail: kos@thsun1.jinr.ru

where: $a_1 \sim \gamma_3\gamma_2$, $a_2 \sim \gamma_1\gamma_3$, $a_3 \equiv a_1a_2 \sim \gamma_2\gamma_1$, $a_2a_1a_2^{-1} = a_1^{-1}$, $b_1 \sim \gamma_1$, $b_2 \sim \gamma_2$, $b_3 \sim \gamma_3$.

Here following definitions are used [2]

$$[i(\gamma_\mu p_\mu) + mc]\Psi = 0, \quad \gamma_\mu\gamma_\nu + \gamma_\nu\gamma_\mu = 2\delta_{\mu\nu}, \quad \mu, \nu = 1, 2, 3, 4. \quad (2)$$

Commutative relations on the base of b_γ are:

$$\begin{aligned} [a_1, a_2] &= 2a_3, & [a_2, a_3] &= 2a_1, & [a_3, a_1] &= 2a_2, \\ [b'_1, b'_2] &= 2a_3, & [b'_2, b'_3] &= 2a_1, & [b'_3, b'_1] &= 2a_2, \\ [a_1, b'_1] &= 0, & [a_2, b'_2] &= 0, & [a_3, b'_3] &= 0, \\ [a_1, b'_2] &= 2b'_3, & [a_1, b'_3] &= -2b'_2, & & \\ [a_2, b'_3] &= 2b'_1, & [a_2, b'_1] &= -2b'_3, & & \\ [a_3, b'_1] &= 2b'_2, & [a_3, b'_2] &= -2b'_1, & & \end{aligned} \quad (3)$$

where; $b'_1 \equiv c'a_1 \sim -\gamma_1\gamma_4$, $b'_2 \equiv c'a_2 \sim -\gamma_2\gamma_4$, $b'_3 \equiv c'a_3 \sim -\gamma_3\gamma_4$, $c' = a_3b_5$.

Commutative relations for d_γ coincide with commutators for infinitesimal matrices of proper Lorentz transformations [3]. Whence it follows physical interpretation: operators $b_1 \sim \gamma_1$, $b_2 \sim \gamma_2$, $b_3 \sim \gamma_3$ have the sense of infinitesimal operators of Lorentz transformations along axes 1, 2, 3.

Both expressions for two types of commutators are differed only by a sign of the second upper row. The time parameter starts to act just from here. The difference between CR is such as if substitution was made $b_k \rightarrow b'_k = ib_k$, ($k = 1, 2, 3$). It is usual to suppose in physics, that the positron is the electron moves in opposite direction in the time. Therefore we will call IR's connected with b_γ as T-conjugate with respect to d_γ 's one.

Now for obtaining a next equation it is necessary to note important property of d_γ -subgroup namely - dichotomy. It means that under another generator choosing we shall have another commutative relations. We shall note their as (CR) for f_γ :

$$\begin{aligned} [a_1, a'_2] &= 2a'_3, & [a'_2, a'_3] &= -2a_1, & [a'_3, a_1] &= 2a'_2, \\ [b'_1, b'_2] &= -2a'_3, & [b'_2, b'_3] &= 2a_1, & [b'_3, b'_1] &= -2a'_2, \\ [a_1, b'_1] &= 0, & [a'_2, b'_2] &= 0, & [a'_3, b'_3] &= 0, \\ [a_1, b'_2] &= 2b'_3, & [a_1, b'_3] &= -2b'_2, & & \\ [a'_2, b'_3] &= -2b'_1, & [a'_2, b'_1] &= -2b'_3, & & \\ [a'_3, b'_1] &= 2b'_2, & [a'_3, b'_2] &= 2b'_1. & & \end{aligned} \quad (4)$$

where $a'_2 = a_2c$, $a'_3 = a_1a_2c$.

Transition from (1) to (4) or $d_\gamma \rightarrow b_\gamma$ is such as substitutions were made: $a_2 \rightarrow ia'_2$, $a_3 \rightarrow ia'_3$, $b_1 \rightarrow -b'_1$, $b_2 \rightarrow -ib'_2$, $b_3 \rightarrow -ib'_3$.

All outlined here is a statement of the facts, following from Dirac equation. They are not connected with any assumptions or additions.

3 Wave equation for P-non-invariant doublet states

Here the theorem on three kinds of matrix groups [4] will be used.

Theorem. If $D = \{\gamma_1, \dots, \gamma_n\}$ is irreducible matrix group, then

$$\text{In}[D] = \frac{1}{n} \sum_{i=1}^n Sp(\gamma_i^2) = \begin{cases} 1 \\ -1 \\ 0 \end{cases} \quad (5)$$

Here n - is the order of the group and $Sp(\gamma_i^2)$ - is a trace of i -matrix squared.

This value ($\text{In}[\dots]$) will be called structural invariant below. Dirac equation has structural invariant $\text{In}[D_\gamma(II)] = -1$. The matter of this section is equation with $\text{In}[D_\gamma(I)] = +1$. The theorem predicates in this case, that the group of this kind is equivalent to a group of real matrices.

In order to obtain equation different from Dirac one, it is necessary to refuse of definitions: $\gamma_\mu \gamma_\nu + \gamma_\nu \gamma_\mu = 2\delta_{\mu\nu}$, $\mu, \nu = 1, 2, 3, 4$. $\gamma_\mu^2 = 1$.

One of the possible variant looks as

$$\begin{aligned} \gamma_s \gamma_t + \gamma_t \gamma_s &= 2\delta_{st}, & \gamma_{s,t}^2 &= 1 & (s, t = 1, 2, 3), \\ \gamma_s \gamma_4 + \gamma_4 \gamma_s &= 0, & (s &= 1, 2, 3), \\ \gamma_4^2 &= -1. \end{aligned} \quad (6)$$

The obtained group very similar to Dirac γ -matrix group, but differs in structure. The Dirac group $D_\gamma(II)$ has 20 elements of fourth order and 12 elements of second order. Situation is inverse in the new equation $D_\gamma(I)$: 12 elements have fourth order and 20 elements have second order. It leads to another value of structural invariant

$$\text{In}[D_\gamma(I)] = +1 \quad (7)$$

Important distinction consists of $D_\gamma(I)$ has two maximal invariant subgroups: d_γ and c_γ .

I wish emphasize that $D_\gamma(II)$ contains only d_γ and b_γ , but $D_\gamma(I)$ contains only d_γ and c_γ .

If to construct an algebra on c_γ , we obtain commutative relations:

$$\begin{aligned} [a_1, a'_2] &= 2a'_3, & [a'_2, a'_3] &= -2a_1, & [a'_3, a_1] &= 2a'_2, \\ [b''_1, b''_2] &= 2a'_3, & [b''_2, b''_3] &= -2a_1, & [b''_3, b''_1] &= 2a'_2, \\ [a_1, b''_1] &= 0, & [a'_2, b''_2] &= 0, & [a'_3, b''_3] &= 0, \\ [a_1, b''_2] &= 2b''_3, & [a_1, b''_3] &= -2b''_2, \\ [a'_2, b''_3] &= -2b'_1, & [a'_2, b''_1] &= -2b''_3, \\ [a'_3, b''_1] &= 2b''_2, & [a'_3, b''_2] &= 2b''_1, \end{aligned} \quad (8)$$

where $b''_1 \sim \gamma_4$, $b''_2 \sim \gamma_2 \gamma_4$, $b''_3 \sim \gamma_3 \gamma_4$,

$a_1 \sim \gamma_3 \gamma_2$, $a'_2 \sim \gamma_2$, $a_3 \sim \gamma_3$.

All these operators have the same physical sense as previously. Situation is such with respect to commutative relations for d_γ as if substitutions was made: $a_2 \rightarrow ia'_2, a_3 \rightarrow ia'_3; b_2 \rightarrow ib''_2, b_3 \rightarrow ib''_3$.

Evidently distinction arises at first row, i.e. at the level of 3-rotation subgroup. Therefore we will call objects, which are described by this representation, P-non-invariant objects. And we will call this representation P-conjugate one with respect to d_γ .

If transition from (1) to (3) to denote as $\langle T \rangle$, then one can obtain equalities

$$b_\gamma = \langle T \rangle d_\gamma, \quad d_\gamma = \langle T^{-1} \rangle b_\gamma, \quad (9)$$

where $\langle T^{-1} \rangle$ corresponds transformations $b'_1 = ib_1, b'_2 = ib_2, b'_3 = ib_3$.

Let us introduce notation $\langle P \rangle$ for transition from (1) to (8), then

$$c_\gamma = \langle P \rangle d_\gamma, \quad d_\gamma = \langle P^{-1} \rangle c_\gamma. \quad (10)$$

Here $\langle P^{-1} \rangle$ corresponds transformations: $a'_2 = ia_2, a'_3 = ia_3, b'_2 = ib_2, b'_3 = ib_3$.

If to denote combined sequential action of these transformations $\langle P \rangle \langle T \rangle \equiv \langle PT \rangle$ and $\langle T \rangle \langle P \rangle \equiv \langle TP \rangle$, then we have

$$\langle TP \rangle d_\gamma = \langle PT \rangle d_\gamma \equiv f_\gamma. \quad (11)$$

As a corollary with the preceding notation we have a set of equalities:

$$\begin{aligned} \langle T \rangle d_\gamma &= b_\gamma, & \langle P \rangle d_\gamma &= c_\gamma, & \langle PT \rangle d_\gamma &= f_\gamma, \\ \langle T^{-1} \rangle b_\gamma &= d_\gamma, & \langle P \rangle b_\gamma &= f_\gamma, & \langle T^{-1} P^{-1} \rangle b_\gamma &= c_\gamma, \\ \langle T \rangle c_\gamma &= f_\gamma, & \langle P^{-1} \rangle c_\gamma &= d_\gamma, & \langle TP \rangle c_\gamma &= b_\gamma, \\ \langle T^{-1} \rangle f_\gamma &= c_\gamma, & \langle P^{-1} \rangle f_\gamma &= b_\gamma, & \langle P^{-1} T^{-1} \rangle f_\gamma &= d_\gamma. \end{aligned}$$

Analysis of the weight numbers for f_γ and c_γ leads to conclusion, that spin of the particles are connected with $D_\gamma(I)$ -equation, is directed along momentum or opposite one. Spin orientation is not defining condition for distinction particle-antiparticle. Such is a transition between substructures $f_\gamma \leftrightarrow c_\gamma$ in the frame of $D_\gamma(I)$ -group, namely $\langle T \rangle$ -transformation.

Evidently the case of $m \neq 0$ does not cause a complication like in Dirac case. Here we have the doublet of massive, stable, P-non-invariant particles. They have spin 1/2 and longitudinal polarization.

4 Wave equation for the quartet state

Naturally question arises on existence of a group with $\text{In}[D_\gamma(III)] = 0$. One can show, that impossibly to obtain anything different from $D_\gamma(I)$ and $D_\gamma(II)$ by changing of the generator orders (i.e. $\gamma_1, \gamma_2, \gamma_3, \gamma_4$).

If to omit all details of solution [5,6], than the answer is that. One can obtain equation with $\text{In}[D_\gamma(III)] = 0$ in particular under following determining

relations:

$$\begin{aligned}\gamma_s \gamma_t + \gamma_t \gamma_s &= 2\delta_{st}, \quad (s, t = 1, 2, 3) \\ \gamma_s \gamma_4 - \gamma_4 \gamma_s &= 0, \quad \gamma_\mu^2 = 1 \quad (\mu = 1, 2, 3, 4).\end{aligned}\tag{12}$$

Evidently relations are not completely anti-commutative. As a consequence structure of the group is rebuild very essentially. The order is equal 32 as previously. Center contains eight elements. Therefore number of conjugate classes is became 20 instead of 17 as previously.

According to Burnside theorem we have in this case 16 1-dim. IR's and 4 nonequivalent 2-dim. IR's. Thus we have here spinor states, but not bispinor states. Most important structural peculiarity is that new equation includes three kinds of subgroups $d_\gamma, b_\gamma, c_\gamma$ at once. It provides presence of two pairs of particles and their antiparticles. From the requirement of reduction of quartet equation $D_\gamma(III)$ to Klein-Gordon equation we obtain, that particles have mass $m = 0$. By analogy with Dirac equation we shall suppose, that two subgroups, which are connected between themselves by $\langle T \rangle$ -transformation, are responsible for doublet particle-antiparticle. Evidently one pair is connected with subgroups d_γ, b_γ and second one with f_γ, c_γ . Therefore spin properties for first pair coincides with doublet of e^+e^- . Spin properties for second pair coincides with doublet of neutral leptons (see sec. 3).

The quartet equation is closed with respect to any $\langle T \rangle$ -, $\langle P \rangle$ -, $\langle TP \rangle$ -transformations. It means, that we have here necessary conditions for oscillations.

References

- [1] O.Kosmachev, "Covariant Formulation of the Wave Equation for a Doublet of Massive Neutral Leptons". (Preprint JINR P4-2003-127), Dubna,(2003) (in russian).
- [2] P.Dirac, *Proc.Roy.Soc. A*,vol.117, 113, (1928).
- [3] M.Naimark,"Linear representations of Lorentz group", (Fizmat, Moskow) 88, 1958 (in russian).
- [4] J.Lomont "*Applications of finite groups*" (Academic Press, New York, London) 51, 1959.
- [5] O.Kosmachev, "On Invariants of Dirac type Equations". (Preprint JINR P2-2002-217), Dubna,(2002) (in russian).
- [6] O.Kosmachev, "Wave Equation for a Quartet of Neutrinos". (Preprint JINR P2-2003-224), Dubna, (2003) (in russian).

THE GENERATION OF EXOTIC QUASIPARTICLES

V. Skvortsov ^a, N. Vogel ^b

*Moscow Institute for Physics and Technology, 141700, Moscow region, Dolgoprudny,
Institutsky lane 9, Russia (a); University of Technology Chemnitz, 09107 Chemnitz,
Germany (b)*

Abstract. The nonlinear phenomena in dense plasma of laser-induced discharges in vacuum and gases are considered. They are accompanied by matter transition to extreme states, miniature black holes creation, ignition of different nuclear reactions, gamma-ray radiation and exotic quasiparticles generation with extremely high magnetic charges. Its main physical parameters are first determined experimentally. Quarks as quasi-free particles within hadrons are most likely to be detected for the first time too.

1 Introduction

This paper deals with the experimental investigation of nonlinear phenomena in dense plasma produced by picosecond laser beams in vacuum and in air. Sofar it has been concluded that superhigh laser intensities $I = 10^{25} \text{ W/cm}^2$ (for photoexcitation of nucleus) or $I = 10^{18} \text{ W/cm}^2$ (for direct excitation of nucleus by accelerated ions in laser plasmas) are needed for nuclear excitation. This threshold in laser intensities can be reduced by 3-4 orders of magnitude if the resonance self-channeling of directed energy flows [2, 3] is taken into account. We found that under moderate initial intensities of laser beams ($I = 10^{14} - 10^{15} \text{ W/cm}^2$) due to cumulative processes of electro-magnetic fields transformation in the small limited space it is possible to create a unique "magnetic anvil". With the aid of this "magnetic anvil" it is possible to disturb the vacuum and generate electromagnetic quasiparticles (magnetic monopoles) which can, in turn, be used in processes of nuclear excitations and reactions accompanied by different elementary particles generation [4, 5]. Moreover, it is not possible to obtain, in principle, some of them in modern accelerators because the cross-section of the magnetic monopole generation in proton-proton collisions is very small and proportional to its mass in the state of "boring" $\sigma \sim m_g^3$ [6]. The mass of the studied systems of magnetic monopoles can be very small ($m_g \rightarrow 0$) as it was first determined in our experiments [4]. We consider the ultrafast nonlinear processes in laser-induced discharges in vacuum and gases which are accompanied by matter transition to extreme states and exotic quasiparticles generation. The magnitudes of electric fields tensions reach 1-10's GV/cm and the inductance of magnetic fields is 10-100's MGauss and higher! The ion (protons) temperatures are up to 10 MeV, its pressures increasing up to a few Gbar. Under this conditions (of relatively "low" electron temperatures about 1-10 keV only) the state of matter is similar to the state of

^ae-mail: skv@pop3.mipt.ru

^be-mail: n.vogel@physik.tu-chemnitz.de

a miniature black hole. In our case the size of black holes is very small (their radius in the range $10^{-6} - 0.5$ cm). During the evaporation of these miniature black holes the magnetic monopoles are generated in accordance with the available theoretical predictions (see, e.g., [7]). But only in our case we observe the effect of multiple magnetic monopoles generation, which has some specific features associated with the mass reduction of magneto-monopole system due to its collective interaction (like a massive particle — a maximon, its rest mass is about 10^{-5} g, which can be reduced up to 0 under a certain condition [8], this particle let us call "monopolino"). The discovered quasiparticles have the large magnetic charge $q \leq 100 - 200$ CGSEq) and the small mass $m_q \sim 2 \cdot 10^{-31} q^{-2}$. Thus, its de Broil wavelength must also be large: $\lambda_q \sim 1 - 5$ mm, as can be seen! However, it is not possible to generate such "big" particles in proton-proton collisions. It is necessary to take into account not only the energy concentration but also the space-time conditions (see below). Note also that our method of elementary particle generation (our "magnetic anvil") is different from the meson and neutrino generation method proposed by Askar'jan [9]. In view of this, we first produce the necessary conditions for the generation of magnetic charges (or monopoles), viz quasiparticles of an essentially electromagnetic nature which were predicted by Heaviside [10] and Dirac [11, 12].

2 Experimental details and results

The experimental scheme was the same as in [13]. Only instead of copper electrodes used in the above paper, we used tantalum-181, tungsten and aluminum electrodes in this work. The Nd: YAG-laser was used with active modes synchronization. The laser beam (of wavelength $\lambda = 1064$ nm) was focused by a spatial lens (with focus path of about 25 cm) on the surface of metallic targets, i.e. electrodes with a small (50 micro meters) interelectrode gap. In one of the electrodes (in the anode) there is a small hall (with its diameter equal to 300 micrometers) through which the laser radiation penetrates into the cathode. The externally applied voltages were varied in the range: 0-3.0 kV. In some cases, a simpler geometric experimental scheme could be used. In particular, all experiments in air were carried out by using a single metallic target under different conditions (with external electric or magnetic fields and in the absence of them). In all cases, the multiple generation of magnetic monopoles occurs if the energy of a laser beam is greater than 50 mJ (the energy of the main laser pulse was generally about 50-100 mJ, its duration —100 ps, i.e. a maximum value of the intensity of focusing the laser beams (in a vicinity of a focal spot in diameter 40 micrometers) was about 10^{14} W/cm². The values of gas pressure in a vacuum chamber were not larger than 10^{-7} mbar. The X-ray and gamma-ray radiation from dense laser produced plasmas were detected by the X-ray streak camera RFR-4 [14] with a golden photocathode on a carbon

film. The X-ray (or gamma-ray) image from an exit screen (a fiber-optic plate) was registered by cooling the CCD-camera (Cordin CCD). The external slit of a photocathode in RFR-4 (of 200 micrometers width and 15 mm height) was located at a distance of about 23,8 cm from the target surface. The images of the slit are registered in mode without sweep with the total time exposition equal to 0.5-1.0 sec. The different dielectric track detectors (CR-39, PMMA, glass) were used to register the energetic particles. The CR39 detectors were developed in 6.25 N suspension of NaOH during 20, 40, 60 minutes at temperature $(55 \pm 10)^\circ$ C. The detectors were located in vacuum or in air at a distance of about 1-2 cm (or 5-10 cm as in the case of diamond synthesis in carbon dust under the influence of magnetic poles).

In the mode when magnetic monopole spinning rays and tops were generated (see, e.g., Figures in [4, 5]). Due to the plasma configuration produced by a prepulse and following a heating beam we could create a magnetic anvil in front of shock waves. In this case, the enormous energy input in a very thin plasma layer is produced. In the following we tried to detect accelerated particles from laser-produced plasma in air and in vacuum and used a plastic nuclear detector CR-39. Our aim was to register the typical tracks for accelerated ions for comparison. However, the first experiments showed that a number of long caterpillar tracks and circlelike tracks were visible on the detector surface without etching [4, 15]. The caterpillar tracks were also registered on the metallic surface (see Figure in [16] on which the track is on the surface of a semiconductor gamma-ray detector SPPD-1). The measurement signal of gamma-ray radiation is shown in Fig.1. The preliminary calibration by using wellknown Co-sources (in the gamma-quanta range: from 50 keV to 1.5 MeV) was produced by our SPPD-1 detector by which the gamma-ray radiation flux can be measured. The maximum value of this flux is $2 \cdot 10^{12}$ quanta/cm²s. Massive blocks of foil material were removed from the tracks [16]. The precise investigation of these tracks produced by the exotic quasiparticles in metals allows us to estimate the characteristic magnitude of its energy loss: $dE/dx = (0.5 - 2) \cdot 10^4$ GeV/cm. The lengths of these tracks reaches a few mm. The length of the observed analogous tracks in CR39 was about a few cm. The gamma-ray radiation passing through 3.2 mm steel and 3 cm lead was observed in the experiments in vacuum [4]. Since the first ones can be due to the nuclear excitation of Ta-181 (for Ta-181 nuclei, there exist the corresponding energy level $E_\gamma = 136.3$ keV with lifetime 30 ps [17]). Probably, we had the first tabletop gamma-ray laser pumping by magnetic monopoles [4, 5] and the second one with protons decay due to magnetic monopoles catalysis (Callan-Rubakov's effect [18, 19]) when gamma-ray radiation with energy quantum $E_\gamma \gg 1$ MeV takes place. In Fig.2) we can see Shrodinger's "Zitterbewegung" of Dirac's particle [20]. This trace was observed on the CR39 plate after 20-minute chemical etching in an alkali suspension (this picture was produced by the laser

scanning microscope LSM-510). In the lower part of this picture we can see a horizontal line. This may be a locus forbidden for electrons — the so-called "Dirac fibers"? We find very many analogous traces. It is easy to estimate the mass of Dirac's particle if the amplitude of its oscillation is $2\delta r \sim 100$ micrometers (see, e.g., [19]): $m_q = h/(2\delta rc) \approx 2.0 \cdot 10^{-35}$ g (the corresponding de Broil wavelength of this particle is 0.8–8.0 mm depending on its observed velocities). The value of the magnetic charge of the observed monopoles is : $q = n(137/2)e \approx 100 - 200$ CGSEq, where e is the charge of an electron and hence $n \approx (3 - 6) \cdot 10^9$ is a topological charge. Here we used the well known relationship for the classical radius of a monopole ([21], p. 117): $r = q^2/E_m$. For the maximum energy of the observed monopoles: $E_m = 10^{-2}$ J, and for its visible radius $r \approx 0.1 - 0.5$ cm (see, [5]). Indeed, following to Dirac's hypothesis that the magnetic monopole is a fermion particle with spin 1/2, we can conclude that these fermions (or the system of collective interacting magnetic charges, i.e. the monopolino) like (maybe) neutrino have a very small mass. But if they (like photons) have no rest mass in this case, we have probably an unique experimental observation when a magnetic monopole interacts with a neutrino. For this light quasiparticles (with their masses are 5-8 orders of magnitude smaller than the mass of an electron) Compton's wavelengths are 5-8 orders of magnitude greater than those of an electron so that the red light of the scattered light radiation in the visible region can be seen. It is remarkable that this fact was observed too. The color of most visible particles is red (or pink) in our experiments ($\Delta\lambda_{\text{Compton}} \sim 2 \cdot 10^{-5} - 5 \cdot 10^{-3}$ cm, including infraredshift). As observed in the experiments, the redshift of visible light due to Compton scattering on light quasiparticles is one of the main reasons for us to conclude that we really deal with very light particles (with masses which are about 100 000 - 20 000 000 times lighter than the electron mass). The predicted [22] tubularlike tracks (with diameter $\approx 50\mu$) produced by the magnetic monopoles are shown in Fig.3 (the traces of magnetic monopoles in PMMA without chemical etching). The diamond synthesis was produced by the magnetic monopoles (diamonds of characteristic dimensions from a few to 100-200 micrometers were obtained in our experiments [15, 16]). By the way, the same value of the magnetic charge $q \approx 100$ CGSEq can be obtained by simple estimations. We take into account that the needed value of pressure P for the production of diamonds with approximate character size $R \sim 100 \mu$ is 100 kBar (or 10^{11} dyn/cm²). Thus, it is easy to determine the magnitude of q by the relation (in the CGS system of units):

$$P = \frac{H^2}{8\pi} = \frac{(q/r^2)^2}{8\pi}.$$

The behavior of magnetic monopoles in the applied external electric and magnetic fields was studied too. In particularly, the distinct separation of magnetic charges into two parts moving to the opposite magnetic poles was observed.

Note, that despite the massive magnetic monopoles predicted in [23], in modern theory there is prediction of massless magnetic monopoles [24], but the discovered magnetic monopoles with these high topological numbers have not been predicted yet. Strictly speaking, in [23] three new particles (the so-called "extremons" or "hedgehog") were predicted, one of them later renamed by the author of [25] a "magnetic monopole". However, two other "extremons" must be massless particles in accordance with the theoretical prediction [23]. To explain the obtained results we can give the following simple model. In principle, the magnetic monopoles could really have a large enough mass, but in the case of its multiple generation the total mass of this system (referred to as "magneto-monopole maximon" or "monopolino") must be very small. For this reason, the magnetic charges can be generated under our conditions. The typical X-ray image of this monopolino was shown in [26]. It was obtained in the experiment when after this quasiparticle generation in a laser-induced discharge it began to fly in air (approximately 10 cm), penetrated a steel plate 14 mm thick (which closed the window of RFR-4) and after its flight in a vicinity of the vacuum chamber of an autonomous working X-ray streak camera along 30 cm it produced the shown image without the vacuum destruction of the used camera. This ultrahigh penetration of our quasiparticles in matter is very similar to the behavior of maximons [8]. We emphasize that due to the monopolino interaction with matter in external magnetic fields acting as a "magnetic lock", a strong gamma-ray (or hard X-ray) radiation is generated. Figure 4 demonstrate the registered hard radiation from the studied system, which is about 40 s. It is remarkable that no soft X-ray radiation was detected (the slit of an X-ray device was opened but soft X-ray radiation was not detected). In addition, we registered radioactive radiation by TLD-detectors (transmitted luminescence detectors), which shows that in a definite direction the typical total doze measured during 30-45 minutes of our device operation can be 7 times as much as the natural (earth) radioactive doze per year. Thus, we observed very many interesting physical effects in our experiments which must of course be repeated in analogous experiments in other laboratories. We hope they will be carried out before long. It is very interesting to note that in parallel we solved the paradox of the relict magnetic monopoles [27]. Namely, in view of the remarkable possibility for magnetic monopoles to diminish their masses due to collective interactions, it is understandable why our Universe has existed up to now. The other explanation of our results is that the observed magnetic monopoles are very light particles. In this case, it will be necessary to reconsider the fundamentals for modern elementary particle physics. Besides, the magnetic monopoles were most probably first produced in the detection of quarks too (see, e.g., Fig.5). The parallel tracks in matter can be produced by quarks (as quasi-free particles within hadrons under the influence of the magnetic monopoles) in accordance with the predictions [22]. The behavior of the

magnetic monopoles (monopolino) is similar in turn to the other kind (state) of black holes [30] with specific space-time effects which will be considered in greater detail in our other papers. Here we demonstrate the observed plate of "censure" (see, e.g., Fig.6) and some space-time effect near the region of miniature black holes. It is remarkable, that the Vavilov-Cherenkov's radiation of magnetic charges has the direction which is opposite to the direction of its motion (see,e.g.,Fig.6).

3 Mathematical model and results of computer simulation

The detailed numerical calculations based on a 2D-magneto-hydrodynamical model (ZEVS-2D, [28] generalized to the case of laser interaction with solid targets(Al, W, see, e.g., [16])in the hydrogen atmosphere) were carried out under concrete experimental conditions. We take into account three angles of radiation transfer, with the radiation spectra divided into a several groups (up to 20 groups, therefore in the corresponding calculations of radiation transfer we actually solved the six-dimensional problem: in r,z - geometry with 3 angles, and a several groups in spectra radiation). The absorption of laser radiation was calculated by taking into account the laser beam propagation in plasma channels with its fast changing parameters. Thus, we have the situation when the laser intensity can increase in small volume in the region of resonance absorption, where the compression of a laser beam occurs (in other words, we must take into account the effect of optimal filtration [29]). In view of this effect, the real intensity of our laser beam in the resonance absorption region was very high (much higher than the averaged laser beam intensity).

Our computer simulation shows that in the laser-produced plasma (in vacuum and in different gas atmospheres) we can obtain the conditions for the solitonlike behavior of a strong magnetic field. In these calculations we assumed that the intensity of laser beams has the time distributions: $I(t) = I_0 \cdot \exp \{-[10 \cdot ((t - t_0 - \tau)/\tau)]^2\}$, where $\tau \sim 190$ ps on the basis of the laser pulse (so that on the half pulse width we have a strong pulse duration of about 100 ps. For the main pulse with maximum intensity $I_0 = 6.35 \cdot 10^{13} \text{ W/cm}^2$, which starts at $t_0 = 7.4$ ns after the prepulse. The intensities of laser beam in plasma channel were recalculated with taken into account a processes of radiation absorption at every time step.In result of calculations we obtain that the matter transition to extreme states with pressures up to a few 100's Mbar takes place during the laser beam interaction with matter. However, the most interesting physical phenomenon occurs after the switching (disruption) of our laser beam. Figures 7-8 demonstrate how the main plasma parameters are evaluated at later times. We can see that the spatial distribution of the electron temperature has a complicated form with its maximum in the centre of a laser spark, where the plasma densities are not very high and the strong magnetic

and electric fields are observed (see Fig.8 (a-b)), and ion temperatures (for protons) reach 8 MeV. Thus, we have the extreme states of matter at the stage of an electromagnetic collapse, which is initiated in our case in approximately 300 ps after the laser pulse disruption (at 53 ps). Note that in Figures 7-8 the numbers of cells on a calculated grid are indicated along directions r and z . This grid was nonequidistant and had a small cell size near the target. The maximum radius of considered systems was 0.02 cm and the length about 0.13 cm. Note that the observed behavior of our laser-induced system is very similar to the behavior of the prime black holes, which also must be accompanied by the magnetic monopoles generation [7], as well as by hot gas creation moving with the extremely high velocity (up to $\sim (1/4)c$). Our calculation demonstrates the same effect (see Fig.8, c), which is in a good agreement with the observed phenomena: our spinning tops have velocities $v \sim 40000 \text{ km/s}$ [4].

4 Summary

Let us summarize all the evidence of the enormous concentration of electromagnetic field energy in a small volume for a short time, energy deposition in tracks , the form of tracks, as well as the presence of these tracks on the metallic surface, the production of diamonds and long polymer fibers, which can be produced in a very strong magnetic field beforehand. We can infer that the so-called "quasiparticle" must be Dirac's monopole and of an essentially electromagnetic nature with initial "rest mass" $m_q \simeq 2 \cdot 10^{-35} \text{ g}$ and magnetic charge $q \sim 100\text{-}200 \text{ CGSEq}$. We have very many observations of the strange physical properties of our electromagnetic quasiparticles, some of them are in good agreement with the available theoretical results. However the others invite further investigation and the development of magnetic monopoles theory. The main conclusion is: the magnetic monopole exists! Note also, that the discovered magnetic monopole maybe corresponds to the new fermion family which is solution of the multitime Dirac equation [31](if the time multidimensionality exists indeed in Nature). Besides, the magnetic monopoles were most probably first produced in the detection of quarks too. Thus, it is remarkable that now in high energy physics the table top devices like those considered in this work may be more useful than large and very expensive particle accelerators.

Acknowledgments

We would like to thank Professor A.I. Studenikin for discussions and attention to this work.

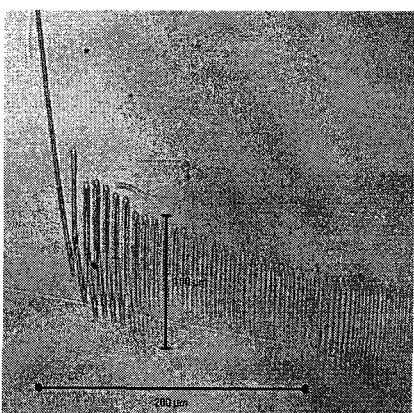
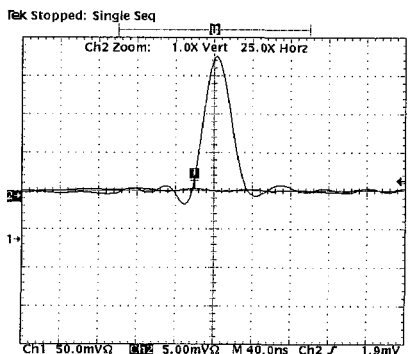


Fig. 1(left), Fig. 2(right)

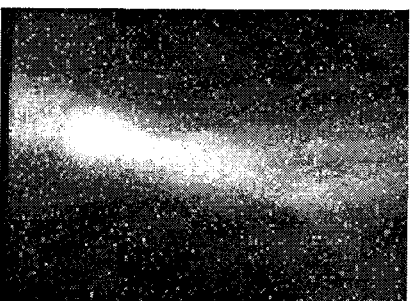
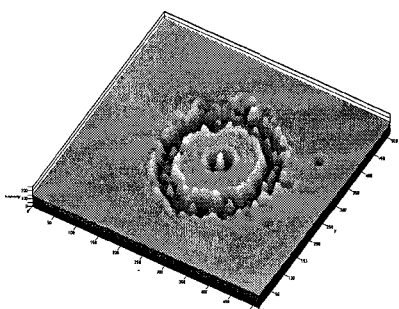


Fig. 3 (left), Fig. 4 (right)

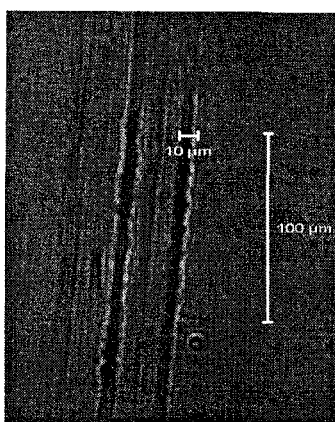


Fig. 5 (left) Fig. 6 (right)

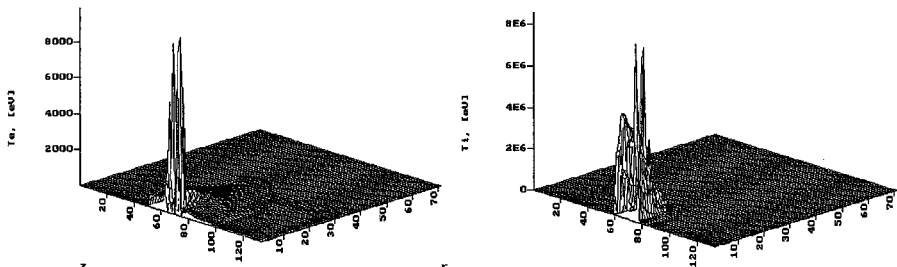


Fig.7 a (left), Fig.7 b (right)

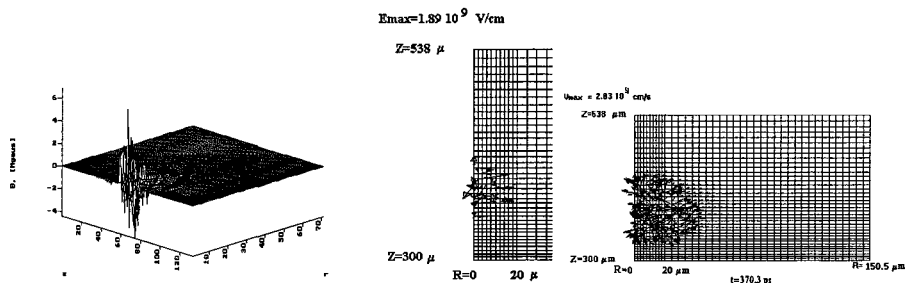


Fig.8 a (left), Fig.8 b (center), Fig.8 c (right)

References

- [1] V. Korobkin, M. Romanovsky, "Interaction of ultrashort pulses with matter", (Proc. IOFAN, Nauka, Moscow), **57**, 3 (2000).
- [2] N. Vogel, V. Skvortsov, *Phystech Journal*, **3**, No. 3, 71 (1997).
- [3] N. Vogel , V. Skvortsov, *Electromagnetic waves and electronic systems*,**3**, No.1-2, 100 (1998).
- [4] V. Skvortsov, N. Vogel, *Electromagnetic waves and electronic systems*,**7**, No.7, 64 (2002).
- [5] V. Skvortsov, N. Vogel, "Physics of extreme states of matter-2002", ed. by V.E. Fortov and et al., Inst. Problem Chem. Phys., Chernogolovka, 136, 2002.
- [6] "Diracs Monopole", (Mir, Moscow), 214, 1970.
- [7] A. Sakharov, "Scientific Proceedings", (CENTRCOM, Moscow) 1995.
- [8] M. Markov, *Zh.E.T.F.*, **51**, No.9, 878 (1966).
- [9] G. Askar'jan, *Pis'ma v Zh.E.T.F.*,**28**, No 5, 322 (1978).
- [10] O. Heaveside, "Electrical papers", (London, N.Y.,Macmillan and Co.),**2**, 521, 1892.
- [11] P. Dirac, *Proc. Roy. Soc.*, **A133**, 60 (1931).
- [12] P. Dirac, *Phys. Rev.*, **74**, 817 (1948).
- [13] N. Vogel, *Pis'ma v Zh.E.T.F.*, **67**, No. 9, 622 (1998).

- [14] S. Petrov, Lazarchuk V.P., Murugov V.P. et. al., *Proc. of 22 nd Intern. Congress on High-Speed Photography and Photonics. Santa Fe, USA, 27 Oct.-1 Nov., 1996.*
- [15] V. Skvortsov, N. Vogel, "The Magnetic Monopoles Generation in Laser-Induced Discharges", (Proc. 29th EPS Conf. on Plasma Physics and Contr. Fusion, Montreux, 17-21 June), **26B**, D-5.013, 2002.
- [16] N. Vogel, V. Skvortsov, "Diagnostics of Laser-Induced Spark Discharges in Air and Vacuum", i.b.i.d., O-2.30, 2002.
- [17] G. Baldwin, J. Solem, V. Gil'danskii, *Rev. of Modern Physics*, **53**, Part 1, 687 (1981).
- [18] V. Rubakov, *Pis'ma v Zh.E.T.F.*, **33**, 658 (1981).
- [19] C. Callan, *Phys. Rev.*, **D25**, 2141 (1982).
- [20] I. Ternov, "Introduction in physics of spin of relativistic particles, (Moscow. Publ. in Moscow State University), 45, 1997.
- [21] E. Arnoldi et al., "Serch for Dirac magnetic poles", (CERN, Report), No.**63-13**, 1963.
- [22] L. Schiff, *Phys.Rev.* **160**, No. 5, 1257 (1967).
- [23] A. Poljakov, *Pis'ma v Zh.E.T.F.*, **20**, No.6, 430 (1974).
- [24] N. Seiberg, H. Witten, *Nuclear Physics* **B-431**, 484 (1994).
- [25] L. Okun, "Physics of elementary particles", (Nauka, Moscow), 183, 1988.
- [26] V. Skvortsov, N. Vogel, "Else time about monopole", (Proc. XXX Zvenigorodsky Conf. on Plasma Physics and Contr. Fusion, 24-28 Febr. Zvenigorod, The Russian Academy of Sciences, Moscow), 198, 2003.
- [27] A. Linde, "Elementary Particle Physics and Inflationary Cosmology", (Moscow. Nauka), 30, 1990.
- [28] V. Skvortsov, B. Etlicher, A. Krukovsky, *J. Phys. IV. France*, **10**, No.pr.5, 263 (2000).
- [29] V. Vakman, "The complicated signals and princip of undefinitivity", ("Sov. Radio", Moscow), 1965.
- [30] K. Lee, V. Nair, E. Weinberg, *Phys. Rev.*, **D.45**, No.8, 2751 (1992).
- [31] V. Barashenkov, M. Yuriev, *Particles and Nuclei, Letters*, **No.6 (115)**, 38 (2002).

NEW KIND OF ELECTROMAGNETIC RADIATION

N.Perevozchikov^a, V.Sharichin

Moscow power institute (technical university), 109117, Moscow, Russia

Abstract. The new kind of electromagnetic radiation of the Sun of an optical range, distinguished from known radiation by presence of weight of rest photon is found out. The speed of propagation of new radiation, which equal to 0.91 from speed of light is measured. Determined are weight of rest of photon and spectral range of radiation. Established is, that the electromagnetic field of a new kind of radiation differs the Maxwellian.

1 Introduction

During realization of researches on of radiation of the Sun with the help gas-filled photocells, we found out unexpectedly high sensitivity of these devices to radiation of the Sun. Already in the first experiments was established, that the registered radiation of the Sun differs from known optical radiation.

2 Technique and results of researches

The detector of a new kind of radiation is gas-filled photocell, in which on an axis of the copper cylindrical cathode the anode is located. The electrodes are placed in a glass cylinder with a face window from glass, transparent to UV radiation.

In a Fig. 1 the spectral dependences of the response of a photocell on radiation of a deuterium lamp (curve 1) and halogen lamp (curve 2) are submitted. For registration of spectra was used monochromator with a holographic grating. The short-wave border of spectral sensitivity of a photocell is determined by transparency of a glass, and long-wave is an output work function of a copper, which is equal to 4.68 eV [1].

The first found out feature of the solar radiation registered by a described photocell, is its spectral characteristic (Fig. 1, curve 3). It is visible, that the registered spectrum lays outside of region of sensitivity of a photocell to usual radiation. For usual UV-radiation of a spectral interval 295–390 nm the energy of quantum is estimated 3.0–4.0 eV, that it is not enough for a photo effect from a copper. The second feature of a new kind of radiation is small coherence length, no more than 0.2 microns. This estimation is made by results of measurements of spectra in the first and second order of diffraction grating. For used monochromator the value of a signal from usual UV-radiation in the first and second orders is approximately identical (coherence length not less than 5 microns). For a new kind of radiation the signal is observed only in the first order and is not observed in second.

^ae-mail: bioph@pop3.mipt.ru

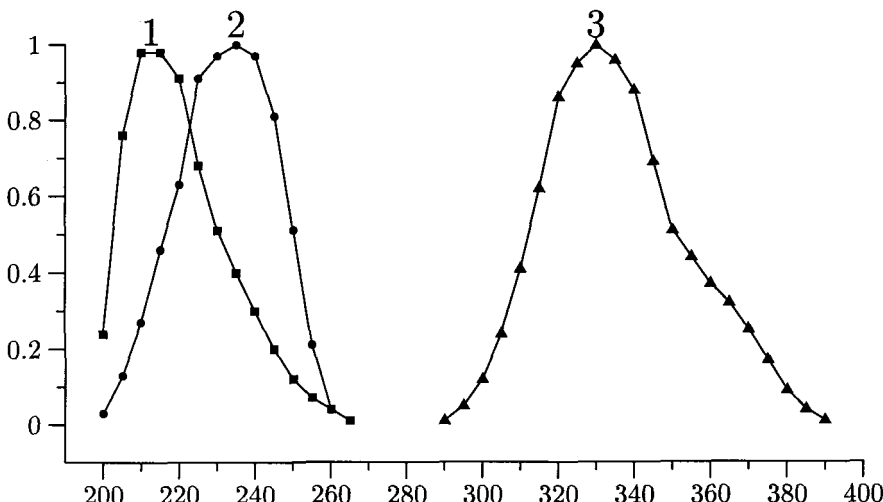


Figure 1:

The third and main feature of a new kind of radiation is the velocity of it's propagation, smaller than the velocity of light. This velocity is determined on delay of a new kind of radiation relatively usual photon radiation of the Sun. For measurement of this delay the solar rays are directed on the input slit of the monochromator by the mirror. Because of rotation of the Earth there is a moving of the rays across the input slit. Complete time of illumination of a slit makes up about six minutes. The simultaneous measurement of two signals was made. One signal represents the response of photodiode, which is placed in zero order of diffraction. Other signal registered in the first order of diffraction. It is the response of photocell, received the new kind of radiation.

The numerous measurements give constant value of a delay of a signal of a photocell—48 seconds with an error no more than 1%. This delay within the limits of an error of measurements is constant in a spectral interval 295–390 nm. The received meaning of a delay allows to calculate speed of propagation of a new kind of radiation $V = 0.91c$, where c —speed of light.

With the purpose of finding out of a nature and features of a new kind of radiation the numerous experiments were carried out, which have shown the following. The radiation scatters in an atmosphere and clouds and is registered at various orientation of a photocell. The scattering radiation is much less than direct radiation of the Sun. The radiation is observed at any weather, though are weakened clouds and aerosols. The intensity of scattering radiation depends from zenith distance of the Sun and is registered in twilight, i.e. up to sunrise and after sunset.

The radiation undergoes not elastic scattering in various mediums. The spectral characteristics of absorbing mediums are similar to the characteristics of these mediums for UV-radiation. The color glass filters, polymeric film, water and water solutions of salts and biomolecules, crystals are tested.

The radiation undergoes elastic scattering similar to scattering of UV-radiation. As an example it is possible to name reflection of radiation as mirror surfaces of metals, semiconductors, dielectrics, refraction of radiation in transparent dielectrics such as quartz, glass, water. The radiation can be polarized.

The set of the listed properties of the founded out radiation of the Sun allows approving, that this radiation has practically all characteristics of usual UV-radiation of the appropriate range, but it has three impotence differences. The energy of quantum of new radiation should be not less than 4.68 eV (the output work function of the copper photocathode), i.e. surpasses energy of quantum of UV-radiation with same wavelength. The second difference is a small coherence length, and as a consequence, limited opportunities of the observations of an interference and diffraction. The third difference is a velocity of propagation. These differences allow consider, that the founded out radiation represents a flow of particles participating in electromagnetic interactions substantially similarly to usual photons, but distinguished from them by presence of weight of rest.

Let's name these particles massive photons, and their weight we shall determine as follows. In a spectrum of radiation (Fig. 1, curve 3) the maximum of the response is observed for length of a wave $\lambda = 330$ nm. At known velocity massive photons V this wavelength can compare energy $E = hV/\lambda = 3.42$ eV. Obviously, this energy cannot be complete energy massive photons, since it is insufficient for a photo effect from copper. In expression for complete energy of a particle with weight of rest m_0

$$E_R = \frac{m_0 c^2}{\sqrt{1 - \left(\frac{V}{c}\right)^2}}$$

dimension of energy has only multiplier $m_0 c^2$, i.e. we believe, that $m_0 c^2 = hV/\lambda = 3.42$ eV. In this case $E_R = 8.26$ eV. Thus, the photo effect from copper is possible not only by transfer of complete energy massive photon, but even parts of kinetic energy, i.e. at a photo effect massive photon can be kept, having lost a part of the energy and having reduced speed. Similarly massive photon can be kept at any not elastic processes; for example, at absorption of a new kind of radiation there is accumulation the massive photons in an absorber.

The unexpected result turns out at account of de Broglie wavelength λ_{dB} for massive photon. It appears to an equal half of electromagnetic wavelength

λ_{em} of registered solar radiation:

$$\lambda_{dB} = \frac{1}{2} \lambda_{em} \quad (1)$$

Let's express equality (1) through the ratio of speeds V/c , using a known expression for $\lambda_{dB} = h/mV$ and expression entered by us, for weight of rest photon $m_0 c^2 = hV/\lambda_{em}$. Let's receive the equation

$$\left(\frac{V}{c}\right)^4 + \left(\frac{V}{c}\right)^2 - 4 = 0.$$

Taking into account, that $(V/c)^2 > 0$, we shall receive

$$\left(\frac{V}{c}\right)^2 = \sqrt{8} - 2 = 0.828427\dots, \quad \frac{V}{c} = 0.910179\dots \quad (2)$$

The equality (2) means, that the speed of solar massive photon does not depend on weight of rest of photon, i.e. from wavelength of radiation that corresponds to results of experiments on measurement.

The ratio (2) is received from a condition (1), reflecting display in experiment of fundamental properties of internal structure massive photons. The condition (1) is a condition harmonic resonance for oscillations of two wavelengths describing massive photons. The further researches have shown, that generally should be satisfied condition

$$\lambda_{dB} = \frac{n}{4} \lambda_{em}, \quad n = 1, 2, 3, \dots \quad (3)$$

The condition (3) is a condition of quantization of a pulse and complete energy massive photons. The value of quantum number $n = 2$ there corresponds a "soft" mode of solar radiation, which spectrum is submitted in a Fig. 1. At value $n = 1$ we have $V/c = 0.9717$ and the complete energy massive photons exceeds 10 eV. In solar radiation more "rigid" modes are found out also.

Acting on the Earth from the Sun massive photons at not elastic scattering, in particular, in clouds, in a spreading surface of the Earth and waters of world ocean, lose or part of a pulse, or completely pulse at accumulation in an absorber.

Saved by condensed mediums massive photons can be released at change of a phase condition of this medium. The chain reaction of burning (oxidation) of organic materials is most effective for this process. Released as a result of such reaction massive photons get additional energy, sufficient for a photoeffect in gas-filled photocell. The experiments with radiation of a flame have shown, that at burning are radiated massive photons with quantum numbers of $n = 5; 6; 7; 8$; (see ratio (3)). For such meaning of quantum number n

de Broglie wavelength λ_{dB} exceeds electromagnetic length of a wave λ_{em} , that allows observe diffraction not only in first, but also in the second order. Thus visibility of interference picture it appears the better, than more λ_{dB} in relation to λ_{em} . It will completely correspond with representation of a new kind of radiation as flow photons, having weight of rest. According to the modern quantum theory of a field (see, for example, [2]), radius of interaction of particles having weight of rest is determined by Compton length of a wave. However, for massive photons radius of interaction, that coherence length is equivalent to λ_{dB} , depends on speed of particles.

3 Conclusion

The submitted above results of experiments unequivocally show, that in a nature besides known electromagnetic interaction, transferring ordinary photons, there is also the electromagnetic interaction, transferring massive photons. The basic source such photons are the Sun. Is established also, that the field of a new kind of radiation differs from Maxwellian. This field acts in a short distance, approximately equals to de Broglie wavelength. That is found out first of all in the phenomena diffraction and interference.

References

- [1] P. Gerlich, "*Photocells, their manufacturing and properties*", (OGIZ-GITTL, Moscow), 1948.
- [2] M. Peskin, D. Shreder, "*Introduction in the quantum theory of a field*", (Regular and chaotic dynamics, Izhevsk), 2001.

THE INTELLIGENTSIA & PROGRESS

John Kuhn Bleimaier ^a

15 Witherspoon Street, Princeton, New Jersey 08542 USA

Progress is the result of a communal effort. While invention and discovery may be the products of individual genius, the attainment of social advancement is invariably a collaborative achievement. Just as a single scientist cannot land a man on the moon, so an individual reformer may not single-handedly precipitate social change. The intelligentsia is a more or less cohesive grouping within society characterized by intellectual curiosity and social engagement. The intelligentsia can be the prime mover in bringing about progress within society.

The intelligentsia as we know it came into existence in the 19th Century with the evolution of a large cadre of educated people possessed of wide ranging interests and sharing a fundamental moral consciousness. The development of a complex technological community requiring trained manpower coupled with the proliferation of a morally grounded literature and art created the 19th Century intelligentsia. This social class conceived the programs which brought about universal literacy, social welfare and democratic government in much of the western world.

However, the intelligentsia as we know it had its historic predecessors. As far back as the classical eras in Greece and Rome there existed groupings of intellectuals who provided a level of moral leadership. The spiritual leaders of the Protestant Reformation and the men of the Renaissance were respectively intelligentsias of their times. The French bourgeois revolutionaries of 1789 and the Biedermeier middle class were immediate precursors of the intelligentsia.

The intelligentsia which developed in the 19th Century was rooted in the ethics and morality of western, Christian culture. Intellectual foment was engendered by the writings of novelists, philosophers and social scientists. Representative thinkers who had a critical impact were Darwin, Nietzsche and Marx. These three towering figures introduced unsettling and radical concepts which were seemingly at odds with the fundamental precepts of contemporary social structure. However, as radical as the ideas of Darwin, Nietzsche and Marx may have seemed when promulgated, they were firmly grounded in the western ethos. Darwin's theory of evolution had great appeal because it was premised on the notion of progress. The belief in improbability has been central to western culture from its earliest Christian genesis. The idea that nature evolves from primitive to complex, from common to specialized, held enormous intellectual attraction. While ostensibly contradicting a Biblical notion of creation, the theory of evolution was consistent with society's faith in historic betterment. In fact Darwin's theory could be found to be consistent with the Old

^aB.A., M.I.A., J.D.; Member of the New York, New Jersey & US Supreme Court bars; Fellow of Mathey College, Princeton University; e-mail: BLEIMAIER@aol.com

Testament description of God's creation first of the lower orders of creatures with homo sapiens as the final product.

Nietzsche's philosophy premised on the emergence of a superman with prerogatives of leadership is completely consistent with the Darwinian concept of survival of the fittest. It should be noted that a social structure based on Nietzschean principles might not be that different from a Calvinist one with the "elect" in command.

Marx, on the other hand, while dismissing religion as the opiate of the masses, had based his entire structure of a classless society on fundamental Christian notions of equality before God and charity to ones neighbor. Marx's communist society has a basic appeal to those who were brought up on Christ's admonition to give all to the poor and follow Him. The dismantling of capitalist structure can hardly offend those who believe that it is easier for a camel to go through the eye of a needle than for a rich man to go the heaven.

Fired by idealism the intelligentsia sought to attain progress through ideology. The philosophical movements of the 19th Century spawned the ideologies of the 20th. Members of the intelligentsia attempted to attain social advances through communism, fascism and liberalism. These mass movements were the intellectual constructs created by groups of members of the intelligentsia. Indeed there was also a conservative intelligentsia which sought to preserve the tried and true institutions of an earlier era. However, the conservative members of the intelligentsia were not themselves reactionaries. They were rather convinced that true progress could only be achieved through gradual enlightenment in the absence of societal upheaval. Spokesmen for the conservative intelligentsia included Fyodor Dostoyevsky and Henry Adams. The idealism of the intelligentsia is fired by the conviction that there is objective truth and there is objective beauty. The concept of progress presupposes that an ideal exists and that it is, at least in theory, capable of attainment. This is the *raison d'être* of the intelligentsia. However, in chronicling the history of the intelligentsia and progress it must be noted that there has been a significant solecism.

The Great War of 1914 to 1918 represented a critical watershed in the history of western culture. The unprecedented carnage of that international conflict kindled the spark of doubt in relation to the inevitability of progress. The fact that the forces of scientific advancement, technological development and organizational sophistication could lead to a war of horrendous proportions shook the faith of many thinking people. This led to the development of a "lost generation" of moral relativism and aesthetic indifference.

However, over the long run, the fundamental values of western Christendom have proven more resilient than the despair of negation. The idealism of the intelligentsia has reemerged and continues in our time. Environmentalism, sustainable economic development, self determination are just random examples of progressive causes which have served to galvanize the forces of the intelli-

gentsia in our time. This is a reaffirmation of the concept of progress and of the categorical imperative of idealism.

Whither the intelligentsia and progress in the 21st Century? While there are those who would claim that there is but a single super power in the world community at the dawning of the Third Millennium, a kind of geopolitical law of nature dictates that the planet is always bipolar. Despite the demise of the Soviet Union, the Russian Federation continues to loom large on the strategic, economic, cultural and spiritual horizons. The fate of western civilization continues to depend on internal developments within Russia and the United States. Thus it is to America and Russia that we must look when we ponder the contributions of the intelligentsia to the attainment of progress.

An examination of the current American political environment will lead to the inescapable conclusion that American democracy has failed. The government of the United States has for over a half century become ever less representative of the will of the people and ever more beholden to moneyed, special interests. Idealistic intellectuals have attempted to reform the political structure to no avail. The reconstruction of the American republic is the primary task presently facing the American intelligentsia. The road to social progress leads through massive political restructuring.

Modern students of political science are surprised to learn that the framers of the American Constitution never envisioned the evolution of a two party system. Far from it, the Founders inveighed at length against the ills of political faction and its negative impact on the governance of a democracy.

Whatever the merits and defects of party politics in general, the two party system is surely the greatest foe of democracy in the contemporary republic. This is most obviously demonstrated when we realize that in a society of 280 million individuals two parties cannot fairly represent the spectrum of ideas and ideals espoused by the citizenry. Are there but two sides of every issue before the legislature? Even if, in a simplistic world, there were only two alternatives for addressing every problem, how can two parties speak simultaneously for one side or another on an infinite number of controversies? The two party system actually thwarts the cogent presentation of all the alternatives for society.

The two party system gives the impression that there exists representative government because voters select legislators and a chief executive. However, this is but a chimera as the party machinery actually controls who is put up for election. As Boss Tweed of New York's corrupt Tammany Hall said in the 19th Century, "Let the people select their leaders, so long as I select the candidates!" In a two party system there is always change in leadership as one organization or the other takes control of the helm when the pendulum makes its invariable swings. However, today's majority is always tomorrow's minority and vice versa. With the inevitable ebb and flow of political fortunes it does not take long for the politician to realize that one hand washes the other. While the two parties may rant and rail against one another in the annual electoral

circus, they know full well that they would be ill advised to attack each other's sacred cows. The maverick politico who "takes no prisoners" is the enemy of the entire system and will be surely excoriated by both sides.

The two party system as it has evolved in the United States of America has created the rather anomalous institution of "government by splinter group." In a simplified overview let us postulate that 45 will select a Democrat for office virtually regardless of his or her stand on the issues. Conversely 45 will select a Republican, no matter what. Thus the government is effectively run by the 10 voters. Well organized, minuscule pressure groups in society who can influence the swing vote can effectively rule. Thus, the enormous influence of "political action committees" and lobbyists in American government. The interests and values of the majority are of no significance whatsoever in a two party system where only the swing of the fringe spells the margin of victory or defeat. From foreign policy to insurance, from military spending to public morality, it is the organized swing voters who can effectively thumb their noses at the will of the majority when there are but two political parties.

Much has been made of the concept that the two political parties of the American republic must be "inclusive." By this it is contemplated that the mass parties must embrace among their adherents individuals who personally espouse a vast divergence of social, economic and political views. At first glance this seems a reasonable and fair proposition. After all, since we have only two parties which govern the country, why shouldn't these parties be broad based and "representative?"

A thoughtful analysis reveals that "inclusive" political parties constitute the sure road to corruption in government. Let us look at human nature. An individual will donate money to a cause with which he or she is strongly in agreement. For example, environmentalists support green organizations with donations. Advocates of one side or the other in the abortion debate send money to the organizations which advance the agendas with which they agree. This is natural and logical. Now, who will provide the financial support for the "inclusive" political party which is for and against abortion; for and against environmental protection; for and against affirmative action; for and against increased military spending; for and against entitlement programs? The answer is simple. The "inclusive" political party will be funded by those with a financial interest in issues before government. The "inclusive" party can claim no idealistic or ideological basis for financial support, thus it is the cynical advocates of their own selfish ends who will buy influence with donations to the "inclusive" party. This is the unerring road to corruption. This is the story of contemporary American government.

Similarly, what sort of individual will seek out the career of public service in the world of the "inclusive" party? It will surely not be the idealist. Those possessed of strong convictions are not likely to be willing to speak for all sides of all the issues; to represent the pro and the con on every controversy. Thus,

in the absence of the idealists, who will be our leaders. Surely leadership in the context of the two, "inclusive" party system will go to those motivated either by self enrichment or self aggrandizement. Can we expect good government from those for whom greed or ego are the prime sources of motivation?

A democracy must be a multi-party state as long as mankind is possessed of a multiplicity of ideas and ideals. The idealistic or ideological political party can combat corruption because it is founded on the basis of principle. Idealistic leaders are capable of honest compromise, but they will never sell out their most dearly held beliefs.

A multi-party system demands proportional representation. Theoretically, in the context of our present American system of government a particular point of view may command the loyalty of 49 of the population in every state, county and city across the country, while yet not being represented in the government anywhere. Is this democracy? Popular government, self government, demands that political parties be represented in the legislature in proportion to their presence in the population at large. If 5 people are socialists, 5 members of congress should be socialists. This is representative government, anything less is not.

When we realize that multi-party government is democracy we must conclude that two party government is indeed dictatorship. The burden of the American intelligentsia is to recreate democracy, representative government, a pluralistic system, free of corruption.

The Russian intelligentsia faces a parallel assignment. The collapse of the Soviet Union has been followed by a period of unparalleled banditry and corruption. The trappings of democracy have been artfully laid upon a grinding oligarchy which has denuded the nation of its economic and natural resources while sapping its moral strength and fiber. Cynical forces have paid lip service to free market concepts while imposing monopolistic constraints designed for personal enrichment.

While the economic system has been transformed from inefficient communism to dishonest capitalism, the political environment has been cleverly shaped to give the appearance of self government while ensuring the concentration of power in a small number of hands.

As in America, the machinations of a media controlled by oligarchs may deceive a substantial component of the general population. However, it is inconceivable that the majority of the intelligentsia should be taken in by clever ruses and slights of hand. Thus it is the burden of the intelligentsia to stake out the high ground and to enter the fray on the side of progress.

I am an optimist. I believe in progress. I anticipate that the intelligentsia will play a vital role in attaining that progress. I expect that the current moral relativism and societal corruption will be definitively overcome. This is not merely an article of blind faith. It is a reasoned conclusion.

If we extrapolate all the present social, political, economic, environmental

and technological trends into the future, they all lead to disaster. We are headed on a collision course with the end of civilization. Moral ambivalence has resulted in the demise of trust in human relationships. Political entities were founded on the basis of a social compact. That compact has now been breached by leaders corrupted by selfish interests. Monetary systems and financial institutions are hopelessly compromised. The natural environment is being polluted without regard to the welfare of future generation. Technology is consuming the future of mankind rather than enhancing it.

Once we recognize that the follies of the present are leading inevitably to disaster we must realize that a radical change of course is compelled in the interests of self preservation. This radical change is itself inevitable. The survival instinct of the species is tenacious and will prevail. At some point in time between where we find ourselves today and the cataclysm ahead, radical change will be implemented by a cadre of idealistically motivated individuals. It is the destiny of the intelligentsia to reassert progress.

The solecism of the 20th Century with its consuming self doubt and concurrent rise of cynicism will be banished. Sneering corruption will be replaced with principled dedication. Self serving cronyism will be displaced by compassionate altruism. The ideal of a Christian culture grounded on brotherhood and sisterhood will become the lodestar of civilization. Temporal society may never attain perfection. However, those who have ceased to strive for realization of the dream have always been bound to descend into the nightmare. Whereas, those who commit themselves to a better future will, surely, reap the harvest of progress.

During the 20th Century in both Russia and the United States the advance toward the attainment of progress was derailed. The guiding principles of western civilization, founded upon Christian faith and charity, were abandoned and replaced by secular materialism. Both societies have experienced consequent upheavals and dislocations. Atheistic communism and amoral laissez-faire capitalism, the false gods of the last century, have proven themselves to be flawed and bankrupt.

During the 20th Century interregnum the very survival of the intelligentsia has been imperiled as education shifted its mission from the provision of enlightenment to imparting of technocratic skills. Membership in the intelligentsia dwindled as the number of individuals possessed of general knowledge and intellectual curiosity has declined. Yet a sophisticated society demands a leadership group comprised of individuals capable of seeing the big picture. Thus a resurgence of the classic intelligentsia is indicated.

The intelligentsia's mission in the attainment of progress is a foregone conclusion.

THE DEVELOPING OF THE SCIENTIFIC KNOWLEDGE AND THE CHANGE OF THE HUMAN CONDITION

Giordano Diambrini Palazzi ^a

Departement of Physics,

University of Rome P.zza A. Moro 5 00185 Rome, Italy

Abstract. In this short review we will show how the new scientific development mainly born in the western countries has produced since the end of 1700s an enormous increase in the level of life and of the number of their inhabitant, as never happened since the beginning of the human species. With the export of the scientific and technological culture in the other countries, like eastern Europe, in north and south America, and later in China and India (to quote the main examples), also their welfare condition have increased or are developing now. For what is concerning the second part of this short review, we try to explain why the most important future needs would be to insert, step by step, the developing countries inside the community of "interacting minds", in order to propagate the scientific culture (but not only) and to make it evolving by the contribution of the full humanity.

1 The scientific and technological development

1.1 *The origins*

The origins of the technological development can be defined as a way by which the Homo Sapiens could be able to simulate, extend and increase the capability typical of his nature, like muscle work, the movement, the language and his memory and certain aspects of his intelligence. The commitment by the man to simulate and increase such capabilities is the main motivation for a technological development since the neolitical age started around 5000 - 10000 years b.C. In fact the installation of the social urban life and the relative economical and cultural development started at the beginning of the historical times is essentially due to the so called neolitical revolution, i. e. the transition from the hunting and food collection economy to the agriculture and animal breeding age. In such a way the work of a single tiller , was producing more food than needed for sustaining himself and or his family. So such a nutritive surplus allowed the survival of individuals who were able to make different activities, in the field of building making, mechanics, figurative arts. All this implied the installation of the first stable urban communities where the man minds were free to communicate each other with a language of semantic contents quite soon codified in writing. Therefore the neolitical revolution was able allowing the change from the biological Darwinian revolution to the cultural revolution, typical product of an ensemble of interacting minds. Some main features of the modern aspects of the cultural evolution can be shortly synthesized as follows.

^ae-mail: giordano.diambrini@roma1.infn.it

- It is of *Lamarkian* type, which means that cultural notions are transmitted from one generation to the next.
- The environment is placed under control.
- More protection of the species through the social self-planned organization.
- Transposition of the biological evolution mechanism at the level of the mind-nature interaction. The rule of the modern scientific and technological development of the last 500 years can be defined as: experimental selection of mutating theories . It is historically evident that inside these kinds of ensembles of interacting minds a kind of cultural, economic and self-organizing structure is growing up, some time more or less suddenly and with different duration times. But the progress of technology and the consequent social economic level was very low up to the end of the middle age and the birth of the modern science.
- Another important reason is the falling down of a barrier which has forbidden, in the Hellenic age, a science development with the modern features, notwithstanding the birth of an outstanding science and philosophy school, from pre-Socratic to the Athens School . This barrier was due to the repulsion of practical-experimental activity by the Greek philosophers . Instead in Europe, since the first middle age, a great interest raised for mechanical inventions and for the engineering, mainly because of their impact on the economy, and military applications . The interactions of such activities and products, with the Greek philosophy and mathematics, mainly with Aristotelian philosophy and the neoplatonism, brot to a dramatic comparison and finally to the beginning of the modern science (ref 3). This new approach is usually synthesized with reference to the scientific work by Galileo and Newton. With Galileo the experimental method of the physical science assumes a new well definite content and meaning . He shows that the essential feature in the knowledge process of the Nature, or the physical world, is NOT only to make a set of experimental measurements, but to do this inside a preordered logical and mathematical structure. Therefore the coherence between a theoretical model and the experimental measurements (or observation), establish a unique not splittable element of knowledge [1]. With the success of effort to fit natural phenomena to theoretical and mathematical structures, industrial engineers ,medical doctors ,biologists have become transmitters and users of scientific knowledge and methods. In XXth century western science become inseparable from industry and economy developments.

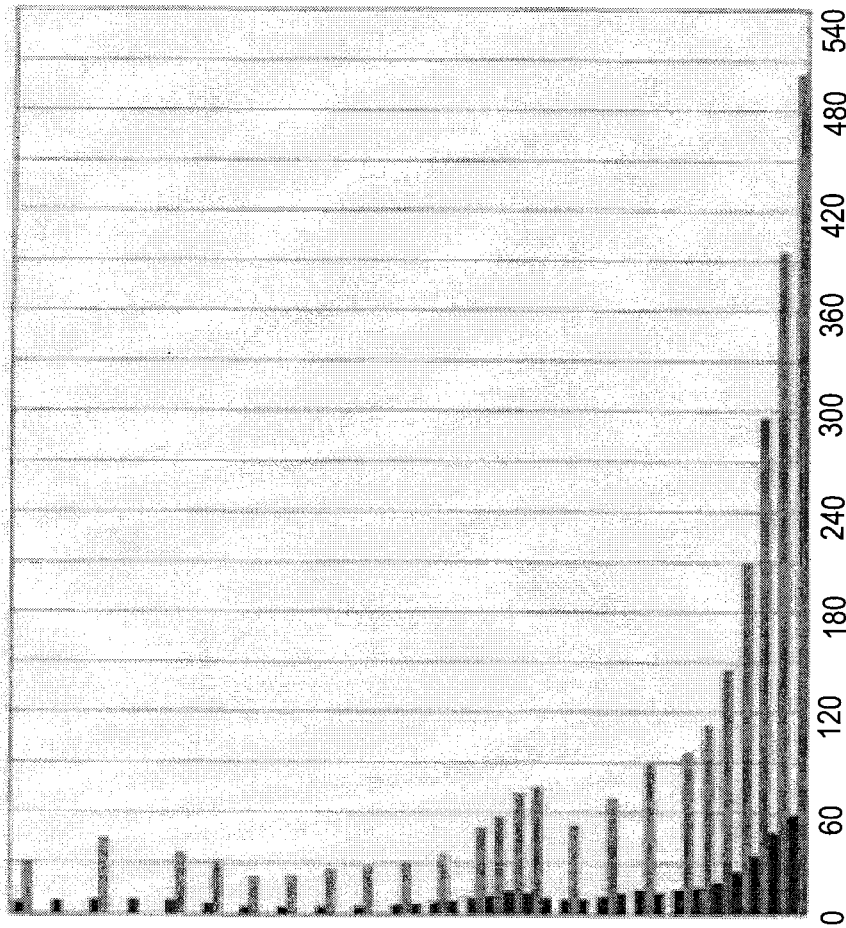


Figure 1: Europe population growth in coincidence with the born of the modern science (millions of inhabitants from the year 0 to 1990); from: L.Del Panta, M.Livi Bacci, G.Pinto, E.Sonnino, "The Italian Population from Middle Age up Today", Editor Laterza, 1996.

2 The scientific-technological development in the modern age, and the consequences for the human life

Perhaps the first more important discovery at the end of the XVth century was the printing invention.

- The manuscript were precious and rare before the printing invention, also if they were reaching the cultural European centers quite fast with respect to the available means of that time. But the print invention multiplied the information store capacity, and the copies available by very big factors and so also the number of possible mental connections in a given time; Numerical example:
- On 1450 AC the number of manuscript present in Europe is estimated to be around few ten-thousands
- But only 50 years later , just after the printing invention, there were more than 10 millions of books.

The great 'explosion' of the modern technological development in the first decades of the XIXth century is mainly due to the basic scientific research up to the discoveries of the fundamental physics laws, in the field of classical mechanics, thermodynamics and classical electromagnetism. All these allowed a great number of technological applications, which have been the sources of the new industrial civilization of the western world [1]. Let us make a brief review Up to the mid 1700s the average inhabitant of the western Europe had a material welfare not too different from that of ancient Rome. Only a minority of the population enjoyed an income in excess of the minimum required to sustain life. By about 1800, however, become apparent that the above minority in Europe was growing up because science and technology were progressing faster than elsewhere. The increase of the number of factories and of the use of mechanically powered machinery causes the so called *industrial revolution*. The process of growth and change accelerated during the 19th century and has continued through the 20th. As a consequence we assisted to an enormous increase of the life level in the western countries after de development of the modern scientific knowledge. This revolutionary change can be synthesized in the following list. List of the main changes on the human life of the western countries from middle of the 18th century to the present :

- Population growth fivefold.
- Infant mortality declined drastically.
- Per capita gross product increased tenfold
- Famine banished. -Plagues disappeared

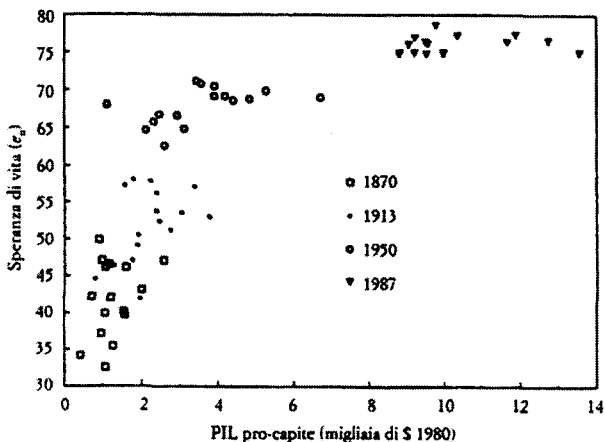


Figure 2: From: A.Maddison, "The World Economy in the 20th Century", Paris, OCDE, 1989; Idem, "Monitoring the World Economy, 1820-1992", Paris, OCDE, 1995.

- Average life span increased by a factor 3

Table I: The World demographic transition (ONU)

Year	World	Growth rate per year	Doubling time
1650	500 millions	0.3%	250 years
1900	1600 millions	0.5%	140 years
1970	3600 millions	2.1%	33 years
1991	5400 millions	1.7%	41 years
2025	Forecast by ONU: 7937 millions(?)		

Now we will show some graphics of social-economical data on which such a list is based. First let us consider the population growth—In the graphic of fig 1 we can see the impressive increasing of the western countries population (excluded Russia) from the middle of the XVIII century. This was the consequence of the mortality decline, while the fertility was almost stable for a long time, so that the life span was increasing very fast, as never happen before. The graphic in fig 2 shows that the life hope at the birth increase very fast with the growth of the gross domestic product per capita (in dollar 1980), between 1870 and 1987, up to rich a stable value around 75 years. This is due to the fast decreasing of the enfance mortality. This shows as the life span increase is due to the economic growth, but up to a certain limit; to go over this limit what needs is, of course, the progress of medical science, in order to defeat the diseases, up to the human genetic limit. It is important that if we look to the full world population, we have quite similar outstanding results, (see the graphic of fig 3).

Let us look to the number of inhabitant of the world after the born of modern science: From the graphic of fig 3 it is clear that speed of the exponential increase of the population depend on the difference between the natality and mortality. Infact while the mortality index is decreasing quite fast, the natality index remains to much high mainly in developing countries. But after 1950, see fig 3 , also the fertility is going down so that population grows less faster. One of the more debated problems is to forecast the consequences of this exponential world population increase. For example from 1960 up to the 1990 in several countries where the food production is at a terrible low level the total food production is doubled or tripled, but the food per capita remained the same or decreased, because the population increased of the same or higher rate. For example in Africa, the total production of food increased by a factor 2 in this 30 years but the food per capita decreased by 15%, and the famine increase As we have seen, the scientific and technological development has improved the life condition in many countries. But as soon as such outstanding advantage have been reached, new problems of difficult solution cams out. Perhaps the most important problem aroused is: the limited resources available in our planet will determine a limit to the population growth; how far away is this limit, and how it will be possible to put it under control

3 Possible scenaries for the future life in our planet

3.1 First approaches by simulations

The first attempt to give an answer was made in the years 1970s , after e proposal made by an association called Club of Rome founded by Aurelio Peccei. On the year 1972 was published the first report realized by a researcher group of MIT under the direction of Jay Forrester and Dennis H Meadows. This group was specialized in computer simulations on the field of the dynamics systems. The title of the book was "The Limit of Growth". It was translated in 30 languages, with a total of 10 millions of copies.

This simulation is based on a mathematical [2-4] model of the world economical system schematised in only 5 independent variables, like:

- 1) world population numbers;
- 2) per capita industrial product;
- 3) pollution production (1970=1);
- 4) natural not renewable resources (1900=1, 1970= 0,95)
- 5) feeding, (per capita Kg of weath per year).

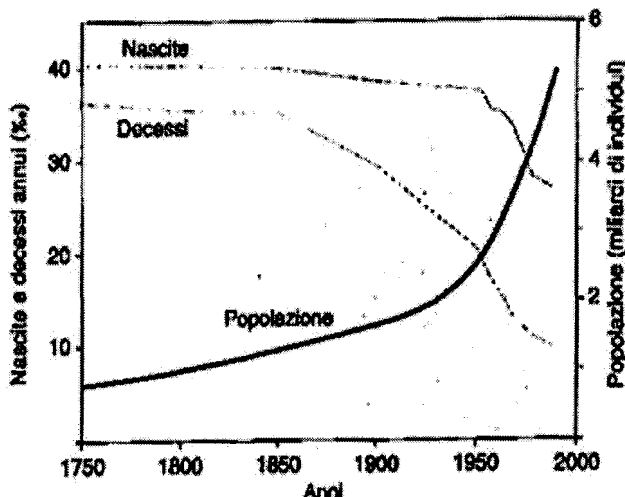


Figure 3: Birth and death rate (left), and world population (right), from the year 1750.

The interdependence of such variables in this model is represented by feed back rings based on acceptable suppositions, but with great incertitudes. The 4 of 5 kinds of simulations (each with different values of the variables) gave results consistent with a collapse of the human conditions already on 2050. We skip details and go to the final very pessimistic conclusions synthesized by the authors as follows. By assuming that the to day increasing of the 5 variables will continue without change, the humanity will reach the growth limit on the next 100 years. The consequences would be a decline of the life level and of the industrial production. This report was very much criticized by the economists and managers, with justified arguments. Nevertheless such first approach was very useful to rise up an alarm signal for all the human collectivity, and for stimulating further approaches to these kind of studies.

4 Critical revisions and forecasting at the beginning of XXIth century

One important argument on which the criticism is based, is concerning the oversimplification of that model, who schematise the world as a unique system with only 5 independent variable. Infact this model is not able to be representative of the real world dynamics. The reasons are that the inadequate availability

of the not renewable energy sources, the difficulty for the developing countries (mainly African countries) for independent developing of new technology due to the absence of the scientific knowledge inside their culture, make impossible the growth rates obtained by the elaboration of the first Forrester-Meadows model.

But the consequences of this 'stand by' of the developing countries would be also quite dramatic. Infact the alternative to a global development would be a dramatic contrast between the developing and developed countries [5].

In the second half of the last century was evident the following behaviour for the natality rate. According a social-economic model based by the population data, up to the middle of the last century, such a behaviour would be due to the fact that in the rich countries to take care of a son, for his health and instruction is much more expensive than in the poor ones. So the developed countries have already reached a level of stable population, with more or less fixed number of inhabitant; to the contrary, in developing countries the natality rate was remaining much higher than the mortality rate. As a consequence the fraction of the "poor" population will increase more and more, while the fraction of the rich population would decrease at the same rate. The graphic of fig 4 shows the data from which such a conclusion can be inferred. The graphic shows the birth rate (yearly new born for 1000 inhabitants), as a function of per capita gross product (US dollar of 1989). It can be seen that the poor countries have a birth rate between 20 and 50, while the richer countries have birth rate no larger than 20 (with exception of the patrol states of middle east). If such a situation should continue for a long time, will bring the humanity to the an unacceptable diversity, from an ethical profile, and for possible political conflicts. But now, at the beginning of the XXI century, we are able to look to a much more optimistic view of our future. By concluding, let us try to synthesize such perspectives. Let us update the problem of the exponential increase of the developing countries populations. We can register positive signals concerning the birth rates in developing countries. According to the conclusions of a group of experts of demographic studies (ref. 6), the birth rate in many of these countries is going down, also because it is no more so strictly dependent on the inverse of economical level. We recall some important data, taken from ref. 6. In comparison with the years 1970s, birth rates declined of 26% on the Botswana, of 35% on Kenya, of 18% on the Zimbabwe, while in one of the poorer country of the world, the Bangladesh, the decline was, between 1970 and 1991, of 21%: from 7 to 5,5 children per woman. We want to underline that the graphic of fig 4 rephers to the birth rates only of the year 1989, and so do not emphasize the change of the birth rates during the previous years. For example the Shri Lanca in fig 4 show a fertility index of 2.1%, but from 70 to 89 the total fertility index changed from 4 to 2,6 per woman children. One very important case is that concerning the great country like China, who on

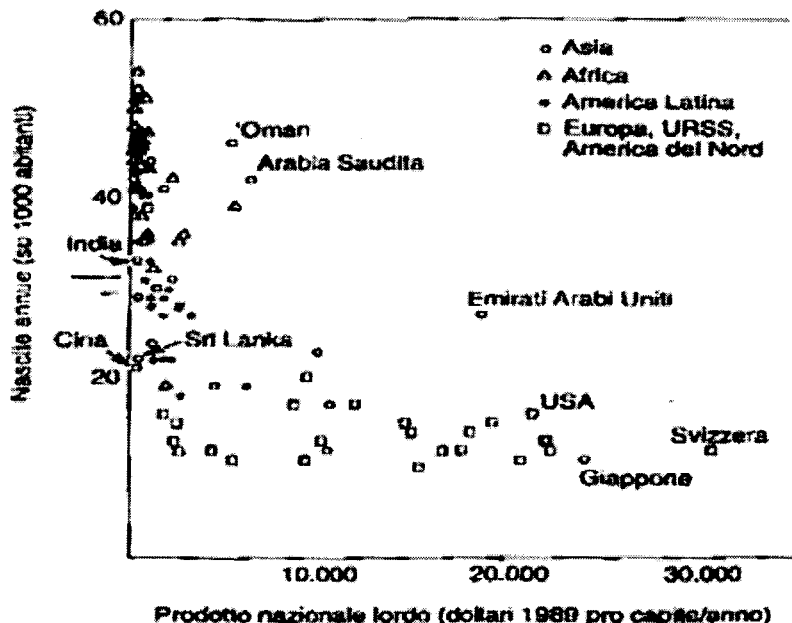


Figure 4: Birth rate (number of new yearly born) as a function of Gross National Product pro capita on 1989.

1989 had a very low per capita product , but a birth rate nearby to 2%. This is due to the policy of the previous government to decrease the birth rates. The China is an example of the greatest developing country of the world (population of 1285 millions of inhabitant, see the next table) who, after imported basic science and technology in his schools and industries, was able to perform an outstanding increasing of his economy and population welfare.

5 Conclusions

We have shown how the new scientific development mainly born in the western countries has produced since the end of 1700s an enormous increase in the level of life and of the number of their inhabitant, as never happened since the beginning of the human species. With the export of the scientific and technological culture in the other countries, like eastern Europe, in north and south America, and later in China and India (to quote the main examples) , also their welfare

Table II: According this table, the product per capita since 1980 to 2001 in China increased by a factor 8,5, life span from 65,9 to 71,2 years (from "State of the World-2003", Hoepli Editor www.hoepli.it).

	1980	1990	2000	2001
Population (million)	998,9	1155,3	1275,1	1285,0
Population yeary growth%	1,4	1,3	0,9	0,7
Birth rate (childrenper wooman)	2,9	2,2	1,8	1,8
Infant mortality (for 1000 born)	52,0	48,3	41,4	38,5
Product pro capite (PPA)	464	1394	3643	3976
Life Span	65,9	67,7	69,8	71,2
		Sociocultural index		
University schoolboys %	1,7	3,0	6,1 (data 1997)	6,2 (data 1998)

condition have increased or are developing now. For what is concerning the second part of this short review, the most important needs would be to insert, step by step, the developing countries inside the community of "interacting minds", in order to propagate the scientific culture (but not only) and to make it evolving by the contribution of the full humanity. For this aim, the more developed countries should committee themselves to help the other countries in developing: a cultural education, by installing primary schools and universities; increase their economic levels and by installing industrial enterprises. So this aim should be a primary commitment for the countries as depository of scientific and technological knowledge, without which it would be impossible any evolution toward a society with a good level of life for all the inhabitants

References

- [1] G. Diambrini-Palazzi - Modello epistemologico e formale dello sviluppo scientifico - Physis - Rivista Intern. di Storia della Scienza), anno XIV (1972), p. 375 - Olschki Ed. - Firenze; G. Diambrini-Palazzi On Features and Meaning of scientific Knowledge Proceedings of the third International Symposium on Conceptual tools for understanding nature - Trieste-21-23 Juin 1995 Editors G.Costa, G.Calucci,M.Giorgi- By World Scientific.
- [2] System Dynamics Group (MIT) Toward global equilibrium, Papers collected by Dennis Meadows and Donella Meadows; Editor Wrigth -Allen Press, Cambridge (Mass.)1973
- [3] M. Mesarovic E. Pestel - Strategie per sopravvivere - Mondadori - Milano 1975.

- [4] J. Timberg - Club di Roma - Progetto Rio (Reshaping the International Order) - Mondadori Ed. - 1976.
- [5] Donella H. Meadows, Dennis L. Meadows, Jorgen Randers - Oltre i limiti dello sviluppo - Ed. Il Saggiatore - Milano - 1993.
- [6] Bryant Robey, Shea O. Rutstein, Leo Morris -Le Scienze - Edizione Italiana di Scientific American- Vol LII -(1994) 306,16.

A BOOK: HAS IT GOT A FUTURE ?

H.Westerheide^a

Gartenstrasse 23, D - 07389 Ranis/Theuringen, Germany

Abstract. Books are the door to a new world. Is a Book an object with Future?

The German Minister of Education, Mrs.Buhlman, told in the summer of 2003, that only 40 % of the adolescent uncalled seize for books. That is why the question is authorized: is the book an object with future? In the present time with multiplicity of mediums and a vast variety of the world information being spread in different visual forms, reading a book for many people has become a great exertion; but it is necessary to reproduce the contents in the train of thought!

Let us have a look at a book of today. We can recognize that in fact the function and construction of a book have not change for many centuries. A view back: at the beginning to collect information human used Stones, wooden sticks, boards of wax etc, that for sure are far not comfortable to be transported. With invention of paper and development of Latin type the transport of information became more comfortable.

The edition of handwriting information where only few in number because of big expense and high costs. As a result, a limited editions of books were only accessible for a small group of people.

With invention of the movable bookmarks and, in particular, after the first Bible was printed by Gutenberg in 1454, a new epoch has started. Since then it has become possible to prepare books and printed papers in a bigger quantity combined with low costs. More and more people has got information from books.

During the centuries of industrialization the new printing technologies were development, and as a result prints became cheaper. The books changed their view and adapt the new production possibilities.

With further development, with again new technologies the books changed into payable books for everybody. To get a direction in the future we have asked the students of the Academy of Art in Shtuttgart on what is their idea for the book in the future. In which form can it encounter side by side with the new mediums? What are the students ideas on the storage, transportation and use of information? Is it possible to change the design, to give a new construction, to give a useful change to a book? What can be done to make a book more attractive? What can be done to crack old rules? So that it becomes desirable.

The fundamental construction of a book has not changed in the students vision. All parts of a book: the cover and the block inside (forever bound in

^ae-mail: Westerheide-Ranis@t-online.de

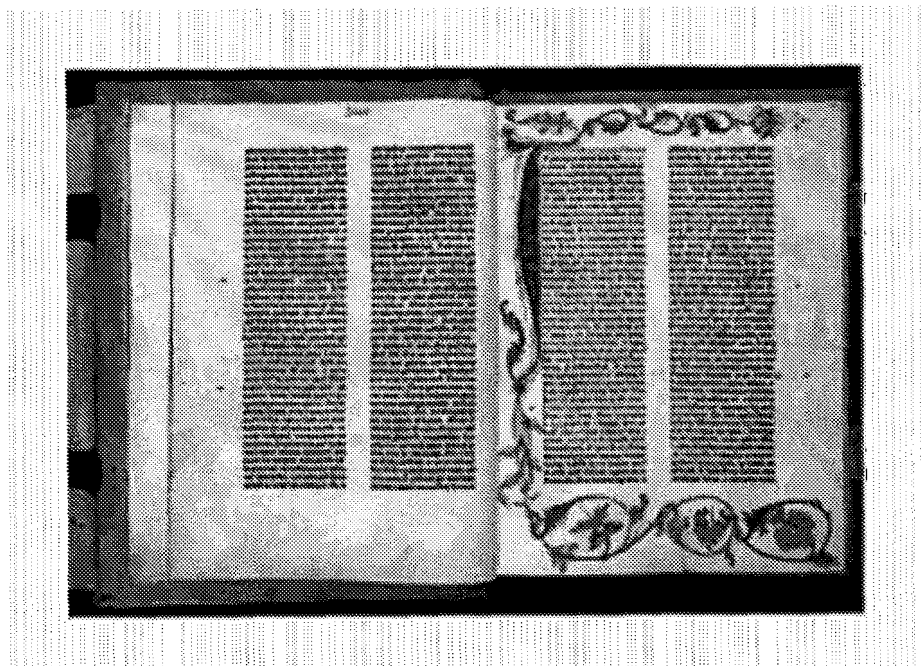


Figure 1: With the Bible into a new era: Johannes Gutenberg, together with Johannes Faust and Peter Scheuffer, printed the Bible in 1454.

the back) have remained unchanged like since the beginning. Only a book's design has changed and gave new fields of application.

Although a book stands in need of no corrections, can it exist in the contest with internet, the E-book or developments in future? Is the development of Print on Demand a possibility for the books?

It is my opinion, that Print on Demand, with all its possibilities of data using in combination with internet and preparation of data for special demands gives the book a chance to survive. The big unit of digital data quantity will save the books survive!

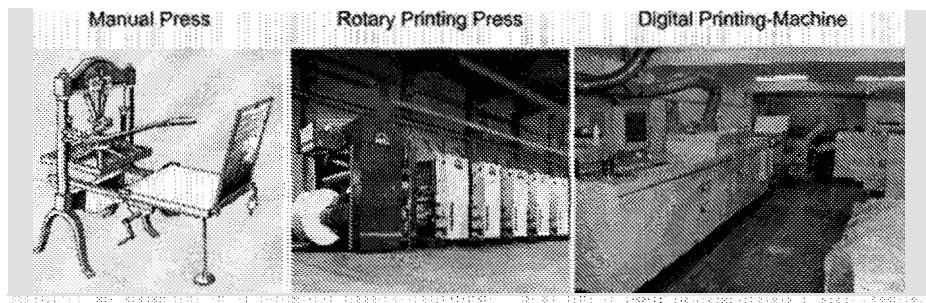


Figure 2: Along with industrialization the printing technique grew faster and the printed information became cheaper.

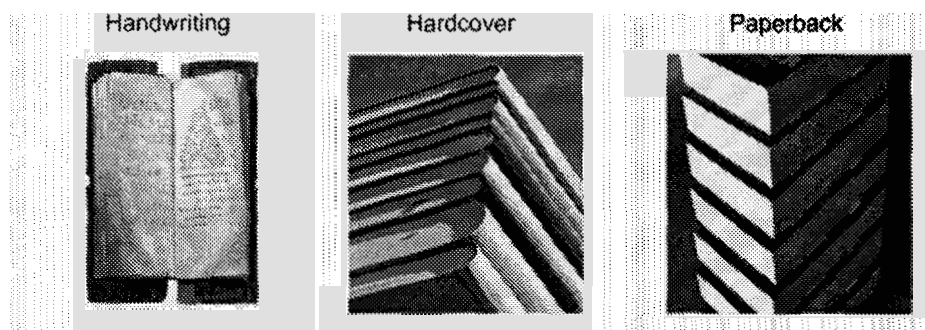


Figure 3: Along with industrialization the mounting of books began to change.

With the technology of Print on Demand it is possible to estimate exactly the number of the needed copies of a printing book, like it was just at the beginning with the handwriting books. A Book or some books can be produced individually for costs that makes it possible for everybody to get these books.

SCIENTIFIC SOCIETIES IN MOSCOW UNIVERSITY

V. Mikhailin^a

Physics Faculty of Moscow State University, 119992 Moscow, Russia

The natural-scientific societies appeared in Russia at the end of the XVIIIth century and at the beginning of the XIXth due to the changes in the system of people education, to the expansion of the network of the universities. Unlike the latter oriented mainly to the teaching, scientific societies should become the main concentration places of the scientific life.

Originally these societies were universal that is involved sections of different natural sciences, including the section of physics.

The first attempt to create the natural scientific society at Moscow University was made by I.I.Milissino in 1789. The society was called "The society of amateurs of the Russian erudition" and survived only one session. Then it was closed down by the empress Catherine the Great.

Fifteen years later, under Alexander the First, the situation essentially changed. The new university statutes required the members of universities to carry out their scientific investigations in such a way that the ordinary members of human community could take part in this process. It was believed that organizing scientific societies and instituting the prizes for the best works on the themes given by universities would be very helpful in this respect.

So, in 1804 the first stable scientific society was established at the Imperial Moscow University on the initiative of its warden (administrator) M.N.Muraviov under the title " The Society of medical and physical sciences competition". Then this society was called the Moscow Physical-Medical Society. The Honored Professor of medicine F.F.Keresturi was its President. Professor of Physics P.I.Strakhov and Professor of Astronomy Ch.F.Goldbach and other physicists and physicians were the members of the this society.

The well-known European scientists such as A.Volta, P.S.Laplace and many others were the honored members of the Moscow Physical Medical Society.

This association of physician and natural scientists organized the workshops and meetings where important questions and points of their studies were discussed. The results of the investigations were published in their journal printed in two languages: Russian and Latin.

Despite its double title the Physical Medical Society paid more attention to medicine, and the problems of natural sciences were discussed mainly with their respect to medicine. Therefore with time the medical problems became the main object of its activity.

The natural scientists could not satisfy with such states of affairs. So in 1805 also at Moscow University another natural scientific association was established. It was called the Moscow Society of Nature Testers (MSNT).

^ae-mail: mikh@opts.phys.msu.ru

This Society has almost two hundred years history, it exists now and has as its President Academician V.A.Sadovnichy.

During so long period of its existence the Moscow Society of Nature Testers knows its best times and its hard times. However, as a whole it played and plays very important role in the investigations of nature, in the progress of human knowledge of the world in which all human beings live.

The Section of Physics and Astronomy was formed in MSNT in 1851, and from 1897 the society was headed by outstanding Russian physicist N.A.Umov.

The members of the Moscow Society of Nature Testers were many well-known and famous Russian scientists: A.M.Butlerov, D.I.Mendeleev, K.A.Timiryasev, I.P.Pavlov, I.M.Sechenov, V.I.Vernadskii, N.A.Uhmov, P.L.Kapitza and others. Famous European scientists such as P.S.Laplace, A.Gumboldt, M.Faraday, E.Rutherford et al were also the members of the Moscow Society of Nature Testers.

The Moscow Society of Nature Testers had its own journal "Notes of the Society", printed in French, and in 1829 "The Bulletin of the Society" appeared. It was also published in French.

Later (in 1863) there appeared the Society of lovers of natural sciences, anthropology and ethnography arranged as well at Moscow university. Physical Section of the Society was founded in 1867, and from 1881 the Section was headed by famous Russian physicist A.G.Stoletov.

The process of apportionment of narrow-special societies from the universal ones started at the second half of the XIX century. The highest activity in their organization showed physicists, mathematicians and chemists. One of the most important, having played an outstanding role in the development of physics in Russia, was the Physical society at the Imperial St.Petersburg university. It was organized in 1872. One of the main organizer and the first president was well-known Russian physicist Petrushevsky, who remained at this post up to 1901.

In the scientific works of the Physical society actively took part its member D.I.Mendeleev. According to his suggestions the Physical society was united in 1878 with the Russian chemical society into a joint Russian physical-chemical society (RPCS). The society consisted of two sections: physics and chemistry. The post of president of the RPCS was hold in turn during a year by the chairmen of the sections. During a long time the section of physics of the RPCS was the center of the Russian investigations in physics. In different years its members were I.I.Borgman, O.D.Chwolson, N.A.Umov, A.G.Stoletov, A.F.Ioffe, and many other outstanding Russian physicists.

In 1895 A.S.Popov demonstrated the action of his wireless telegraph. The society had its magazine "The Journal of RPCS" (in 1930 this magazine was replaced by the Journal of Experimental and Theoretical Physics).

A new wave in the creation physical societies in Russia came during the

second decade of the XX century. In 1911 at Moscow University was organized the Moscow physical society which after the death of P.N.Lebedev (March 14, 1912) was named after him.

After the October revolution the process of creation of new societies was strongly activized.

In 1919 the physical section of the RPCS presents the statute of the Russian association of physicists which was confirmed in 1922 by the State Scientific Council, but the final mounting of the Association (RAP) took place in 1924. In 1924-25 RAP was able to satisfy the needs of the most standing in need scientific schools and laboratories belonging to it.

In 1930 the activity of all physical societies in the USSR was stopped. The attempts to restore their work which were made in 1946 and 1971 ended in failure.

In 1988 in the new year issue of the physical department newspaper was published the article "Let resuscitate the physical society" and as early as the February of the next year the activity of the Physical society Moscow University was restored.

Professor I.M.Ternov was elected the first chairman of the society, and after his death in 1996 professor A.F.Tulinov acted as the chairman.

In November 1989 the Constitutive congress of the Physical Society of the USSR was held. Above 800 delegates took part in this congress. Professor S.P.Kapitza was elected the President of the PS of the USSR. The Russian Physical Society was restored in 1991.

The Russian Physical Society (The Physical Society of Russia) and the Physical Society of Moscow University as its very important component do their best to preserve the scientific potential and high level of physical education in Russia. The Bulletin of Physical societies is published. Several scientific and popular scientific books were published by the Society and with its support. National and international conferences are held. Young physicist Schools are paid special attention. The Russian Physical Society was the founder of Russian Association of physical students which is the organizer of the Annual scientific conferences of physical students and young scientists. In 2003 the conference was held in Krasnoyarsk, and the next one will be in Moscow in 2004.

In 2000 under the aegis of the Russian Physical Society the Congress of physics teachers was held, and at that time the section of physics teachers was organized.

Russian Physical Society and the Physical Society of Moscow University hold the regular meetings where the well-known Russian scientists give their talks and important physical problems are discussed. Some meeting are devoted to significant dates of the physics history. In 2003 the special session of the Russian Physical Society dedicated to the 70th Anniversary of the Physics Faculty was

planned to be held.

At present, when the System of Education in Russia is being reformed, the role of intelligentsia and therefore of Scientific Societies grows dramatically. One can hope that at that crucial moment intelligentsia does not remain aside.

References

- [1] N.Gesekhus, *A historical sketch of the 10-year activity of the Physical society*, Moscow, 1882
- [2] S. P. Kapitza, *Bull.Phys.Soc.* No 2, 3 (1992).
- [3] D. D. Ivanenko, I. Pomeranchuk *Phys.Rev.* **65**, 343 (1944).
- [4] A.A. Sokolov, I.M. Ternov *Synchrotron Radiation*,(Academie - Verlag, Berlin) 1968.
- [5] I.M. Ternov, V.V. Mikhailin, and V.R. Khalilov *Synchrotron Radiation and Its Applications*, (Harwood Academic Publishers, NY) 1985.

This page intentionally left blank

**Programme of 11th Lomonosov Conference on
Elementary Particle Physics
and
5th International Meeting on Problems of Intelligentsia**

21 August, THU

- 08.00 - 09.30** **Registration** (Auditorium 1-31, Faculty of Physics,
Moscow State University)
- 09.30 - 09.45** **Opening** (Conference Hall)
A.Studenikin, MSU
V.Belokurov, Vice Rector of MSU
A.Slavnov, Head of Department of Theoretical Physics of MSU
V.Matveev, Director of Institute for Nuclear Research of Russian Academy of Sciences

- 09.45 - 13.50 MORNING SESSION** (Conference Hall)

Chairman: V.Belokurov

- 09.45** N.Krasnikov, V.Matveev (INR) *Search for new physics at LHC* (35 min)
10.20 G.Martinelli (Univ. of Rome-I) *CP violation in the Standard Model and beyond* (35 min)
10.55 A.Slavnov (Steklov Math. Inst & MSU) *Renormalization in model with internal symmetries* (35 min)
11.30 M. Panasyuk (Skobeltsyn Inst. Nuc. Phys., MSU) *Physics of cosmic rays: perspectives of space and on-ground experiments* (35 min)

- 12.05-12.40** Tea break

Chairman: A.Slavnov

- 12.40** A.Cherepashchuk (Sternberg Astron. Inst.) *The search of black holes* (35 min)
13.15 G.Lafferty (Univ. of Manchester) *Hadron physics in BaBar* (35 min)

- 13.50 - 15.00** Lunch

- 15.00–18.10 AFTERNOON SESSION** (Conference Hall)

Chairman: N.Krasnikov

- 15.00** A.Kaidalov (ITEP) *Diffractive processes at high energies* (30 min)
15.30 Y.Kwon (Yonsei Univ.) *New Results from Belle* (35 min)
16.05 I.Arefeva (Steklov Math. Inst.) *Recent progress in string field theories* (35 min)

- 16.40 - 17.00** Tea break

- 17.00** V.Zhukov (Univ. of Karlsruhe) *Astroparticle physics with AMS-02* (35 min)
17.35 J.Wudka (Univ. of California) *Discreet new physics: evading the limits on the scale of heavy particles* (35 min)

- 18.10 - 22.30 SPECIAL SESSION** (40⁰)

Reception banquet will be held on board of a ship that will stream along the river across the central part of Moscow

22 August, FRI

9.00 - 13.55 MORNING SESSION (Conference Hall)

Chairman: G.Martinelli

9.00 D.Cebra (California State Univ.) *Recent results of STAR* (30 min)**9.30** S.Gerassimov (Tech. Univ. of Munchen & Lebedev Phys. Inst.) *COMPASS experiment at CERN: status and perspectives* (20 min)**9.50** M.Sapozhnikov (JINR) *Polarized intrinsic strangeness of the nucleon* (30 min)**10.20** M.Polikarpov (ITEP) *Confining strings and temperature phase transition in lattice QCD with dynamical quarks* (30 min)**10.50 - 11.10** Tea break

Chairman: A.Kaidalov

11.10 G.Pivovarov (INR), *Duality condition for ϕ^4 in 1+1 and the light-front quantization* (25 min)**11.35** E.Leader (Univ. of London), A.Sidorov (JINR), D.Stamenov (INR, Sofia) *On the role of higher twist in polarized deep inelastic scattering* (20 min)**11.55** M.Greco (Univ. of Rome-III) *Singlet structure function g_1 at small x* (20 min)**12.15** A.Kataev (INR) *The Gottfried sum rule for F_2 function of DIS: theory vs. experiment* (20 min)**12.35** S.Kulagin (INR) *Nuclear effects in neutrino DIS and the extraction of weak mixing angle* (20 min)**12.55** A.Illarionov, A.Kotikov (JINR) *Small x behaviour of parton distributions. A study of higher twist effects* (15 min)**13.10** I.Bogolubsky (JINR) *Stable extended strings in anisotropic gauged sigma model* (15 min)**13.25** A.Zakharov (ITEP) *Gravitational microlensing and dark matter problem: 10 years later* (30 min)**13.55 - 15.00** Lunch**15.00 - 18.45 AFTERNOON SESSION** (Conference Hall)

Chairman: A.Kataev

15.00 Yu.Simonov (ITEP) *Recent results on chiral symmetry breaking from confinement* (30 min)**15.30** J.Manjavidze, N.Shubitidze, A.Sissakian (JINR) *Low of large number and asymptotic phase-space integral* (25 min)**15.55** A.Badalyan (ITEP) *Determination of α_s and heavy quark masses from $b\bar{b}$ and $c\bar{c}$ spectra* (25 min)**16.20** M.Iori (INFN-Roma-I & FNAL) *Results on doubly charm baryons* (25 min)**16.45** I.Narodetskii (ITEP) *Light and heavy baryons in the nonperturbative QCD* (20 min)**17.05 - 17.25** Tea break**17.25** V. Shevchenko (ITEP) *Static potentials in QCD; what information we can get* (20 min)**17.45** I.Solovtsov (Univ. of Gomel) *Integral representation for structure functions and target mass effects* (15 min)**18.00** M.Osipenko (INFN-Genova, SINP MSU) *Evaluation of the higher twist contribution to the moment of proton structure functions F_2 and g_1* (15 min)**18.15** O.Solovtsova (Univ. of Gomel) *Analytic approach in QCD and inclusive tau-decay* (15 min)**18.30** N.Agasian, S.Fedorov (ITEP) *Thermal QCD condensates in the hadron resonance gas model* (15 min)**19.00 - 22.00** Sight-seeing bus excursion in Moscow

23 August, SUT**9.00-13.50** **MORNING SESSION** (Conference Hall)

Chairman: V.Rubakov

9.00 A.Smirnov (ICTP & INR) *The present status of neutrino physics* (40 min)**9.40** C.Giunti (INFN-Torino) *Theory of Neutrino Oscillations* (35 min)**10.15** K.Ganezer (California State Univ.) *Neutrino oscillations and neutrino physics at Super-Kamiokande* (35 min)**10.50** T.Kobayashi (Inst. of Part. and Nucl. Studies) *Long baseline neutrino experiments* (35 min)**11.25** E.Yakushev (Univ.of Alabama) *KamLAND antineutrino detector - status and perspectives* (35 min)**12.00 - 12.20** Tea break**12.20** K.Abazajian (FNAL) *Precision cosmological measurements of neutrino mass* (35 min)**12.55** S.Turck-Chieze (Saclay) *Quiet and active Sun and the solar neutrino puzzle* (35 min)**13.30** A.Studenikin (MSU) *New effects in neutrino oscillations* (20 min)**13.50 - 15.00** Lunch**15.00 - 18.15** **AFTERNOON SESSION** (Conference Hall)

Chairman: A.Smirnov

15.00 D.Fargion (Univ. of Rome-I) *Neutrino induced horizontal-upward tau air shower* (25 min)**15.25** A.Barabash (ITEP) *Double beta decay experiments: present and future* (35 min)**16.00** F.Villante (INFN-Ferrara) *BBN bounds on neutrino oscillations* (25 min)**16.25** P.Spillantini (INFN-Florence) *Observation of UHE neutrinos* (20 min)**16.45** R.Petti (CERN) *Precision measurements from the NOMAD experiment* (15 min)**17.00 - 17.20** Tea break

Chairman: P.Spillantini

17.20 A.Ali (DESY), A.Borisov, D.Zhuridov (MSU) *Effects of heavy Majorana neutrinos at lepton-proton and proton-proton colliders* (15 min)**17.35** O.Kosmachev (JINR) *New approach for description of P- and T - non-invariant states of elementary particles* (15 min)**17.50** M.Winter (IN2P3/CNRS) *Fermion- and photon-pair production at LEP-2* (25 min)**24 August, SUN****9.00-19.00** Bus excursion to Sergiev Posad

25 August, MON

9.00-13.35 MORNING SESSION (Conference Hall)

Chairman: K.Abazajian

9.00 D.Galtsov (MSU) *Black holes, gravitational waves and cosmology: new ideas from string theory* (30 min)

9.30 V.Lukash (Astro Space Centre of Lebedev Phys. Inst.) *Formation of structure in the Universe and the role of dark matter* (30 min)

10.00 F.Ricci (Univ. of Rome-I) *The status of art of the gravitational wave detectors* (30 min)

10.30 V.Muchanov (Ludwig-Maximilian-Univ.) *CMB fluctuations* (30 min)

11.00 I.Ciufolini (Univ. of Lecce) *Frame-dragging: theory and experiment* (30 min)

11.30 - 11.50 Tea break

11.50 V.Berezinsky (LNGS), V.Dokuchaev, Yu.Eroshenko (INR) *Neutralino annihilation in small-scale galactic halo clumps* (25 min)

12.15 V.Pervushin, (JINR) *Early Universe as W,Z-factory* (20 min)

12.35 Yu.Dumin (IZMIRAN) *Testing the "dark-energy"-dominated cosmological models by searching for the local hubble expansion* (20 min)

12.55 M.Fil'chenkov (Peoples' Friendship Univ. of Russia) *Quantum tunnelling of a rotating Universe* (20 min)

13.15 A.Nikishov (Lebedev Phys. Inst.) *The problem of uniqueness of energy-momentum tensor of gravitational field* (20 min)

13.35 - 15.00 Lunch

15.00 - 18.30 AFTERNOON SESSION (Conference Hall)

Chairman: A.Borisov

15.00 L.Laperashvili (ITEP), H.Nielsen (N. Bohr Inst.) *The problem of monopoles in the standard and family replicated models* (25 min)

15.25 V.Skvortsov (MIPT), N.Vogel (Univ. of Tech. Chemnitz) *The generation of exotic quasi-particles* (20 min)

15.45 O.Teplov (Inst. of Metallurgy and Material Science) *The quantization and precise values of quark masses* (25 min)

16.10 - 16.30 Tea break

16.30 V.Bagrov, A.Yarovo (Univ.of Tomsk) *New results in synchrotron radiation theory* (20 min)

16.50 V.Bordovitsyn, V.Bulenok, T.Pozdeeva (Univ. of Tomsk) *Coherent synchrotron radiation of relativistic electron bunches* (20 min)

17.10 O.Dorofeev, A.Lobanov (MGU) *Beta-decay in external field and neutrino mass* (20 min)

17.30 A.Martynenko (Univ.of Samara) *Hyperfine splitting of the ground state in muonic hydrogen* (20 min)

17.50 N.Perevozchikov (MPTI), V. Sharichin (MPEI) *The new kind of electromagnetic radiation* (20 min)

18.10 S.Kopylov ("Brainstorm"), G.Cherny (BMSTU) *Singularities of electrodynamics with a magnetic charge in spaces of various dimension* (20 min)

26 August, TUE**9.00-13.50 MORNING SESSION (Conference Hall)**

Chairman: G.Lafferty

9.00 M.Scarpa (INFN and Univ. of Ferrara) *Direct CP violation measurements with the NA48 experiment: status and perspectives* (35 min)

9.35 A.Kiiskinen (Helsinki Inst. of Phys.) *Higgs searches at LEP* (35 min)

10.10 S.Gentile (Univ. of Rome-I) *Higgs search in ATLAS* (35 min)

10.45 E.Graziani (INFN-Rome-III) *4-fermion physics at LEP* (25 min)

11.10 O.Yushchenko (IHEP) *Gauge boson couplings at LEP* (25 min)

11.35 – 12.00 Tea break

12.00 J.Salt (Univ. of Valencia) *B physics at LEP* (35 min)

12.35 J.Williams (Univ. of Manchester) *Tau physics in BaBar* (35 min)

13.10 A.Sarti (INFN-Ferrara) *Semileptonic B decays in BaBar* (20 min)

13.30 G.Ricciardi (Univ. of Naples) *The structure function of B mesons* (20 min)

13.50 – 15.00 Lunch

15.00 – 18.00 AFTERNOON SESSION (Conference Hall)

Chairman: M.Iori

15.00 A.Sobol (LAPP & IHEP) *Diffraction program at CMS and TOTEM (LHC): physical tasks and perspectives of measurements* (20 min)

15.20 F.Ambrosino (Univ. of Naples) *Recent results from the KLOE experiment* (35 min)

15.55 E.Shabalin (ITEP) *On the relative strength of direct CP violation in $K \rightarrow 2\pi$ and charged $K \rightarrow 3\pi$ decays* (20 min)

16.15 G.Collazuol (Univ.of Pisa) *Rare K_s decays in the CERN NA48 experiment* (20 min)

16.35 - 17.10 Tea break

Chairman: J.Salt

17.10 G.H.A.Vasseur (Saclay) *Inclusive spectra at $Y(4S)$* (25 min)

17.35 J.McKenna (Univ. of British Columbia) *Initial state radiation studies at $Y(4S)$* (25 min)

27 August, WED

9.30-14.10 MORNING SESSION (Conference Hall)

Chairman: K.Ganezer

9.30 V.Belokurov, O.Khrustalev, V.Sadovnichy, O.Timofeevskaya (MSU) *Conditional density matrix and quantum communication* (40 min)

10.10 V.Rubakov (INR) *Long distance modification of gravity: is it possible?* (40 min)

10.50-11.10 Tea break

FIFTH INTERNATIONAL MEETING ON

PROBLEMS OF INTELLIGENTSIA:

"Intelligentsia and Education"

11.10-11.30 Opening (Conference Hall)

A.Studenikin, MSU

N.Khrustaleva, Director of Centre of International Educational Projects,
Ministry of Education of Russia

Chairman: A.Studenikin

11.30 S.Kapitza (RAS) *"Intelligentsia" and responsibility?* (30 min)

12.00 D.Shirkov (JINR) *The intelligentsia, its merits, problems and destination* (20 min)

12.20 H.Westerheide (Ranis, Germany) *The Book – has it got a future?* (20 min)

12.40-13.10 Tea break

13.10 G.Diambriini-Palazzi (Univ. of Rome-I) *Scientific development and human conditions* (20 min)

13.30 V.Mikhailin (MSU) *Scientific societies in Moscow University (18-20 Centuries)* (20 min)

13.50 J.Bleimaier (Princeton) *The intelligentsia & reform* (30 min)

Closing of the 11th Lomonosov Conference on Elementary Particle Physics

and

the 5th International Meeting on Problems of Intelligentsia

SPECIAL SESSION (40 °)

**List of participants of the 11th Lomonosov Conference
on Elementary Particle Physics and the 5th International Meeting on Problems
of Intelligentsia**

Abazajian Kevork	FNAL	aba@fnal.gov
Agasian Nikita	ITEP	agasian@heron.itep.ru
Akhmedov Evgeny	ICTP & KINR	akhmedov@ictp.trieste.it
Arefeva Irina	Steklov Math. Inst.	arefeva@mi.ras.ru
Badalian Alla	ITEP	
Bagrov Vladislav	Univ. of Tomsk	pecher@ido.tsu.ru
Barabash Alexander	ITEP	alexander.barabash@itep.ru
Belokurov Vladimir	MSU	belokur@rector.msu.ru
Berezinsky Venya	LNGS	venya.berezinsky@lngs.infn.it
Bilenky Samoil	JINR	bilenky@to.infn.it
Bilokon Halina	LNF	halina.bilokon@lnf.infn.it
Bleimaier John	Princeton	bleimaier@aol.com
Bogolubsky Igor	JINR	bogolubs@cv.jinr.ru
Bordovitsyn Vladimir	Univ. of Tomsk	bord@mail.tomsknet.ru
Borisov Anatoly	MSU	borisov@ave.phys.msu.su
Cebra Daniel	STAR	cebra@nuclear.ucdavis.edu
Cherepashchuk Anatoly	Sternberg Astronomical Institute, MSU	cher@sai.msu.ru
Chieze Philippe	Saclay	turck@discovery.saclay.cea.fr
Ciufolini Ignazio	Univ. of Lecce	ciufoli@ifsi.rm.cnr.it
Collazuol Gianmaria	Univ. of Pisa	gianmaria.collazuol@cern.ch
Danilov Mikhail	ITEP	danilov@iris1.itep.ru
Diambrini-Palazzi Giordano	Univ. of Rome	diambrini@roma1.infn.it
Dokuchaev Vladislav	INR	dokuchaev@inr.npd.ac.ru
Dolgov Alexander	INFN-Ferrara & ITEP	dolgov@fe.infn.it
Dumin Yurii	IZMIRAN	dumin@cityline.ru
Dvornikov Maxim	MSU	maxim_dvornikov@aport.ru
Egorov Andrey	ICAS, Moscow	ane@srdlan.npi.msu.su
Eroshenko Yury	INR	erosh@inr.npd.ac.ru
Fargion Daniele	Univ. of Rome-I	daniele.fargion@roma1.infn.it
Fedorov Sergei	ITEP	fedorov@heron.itep.ru
Fil'chenkov Mikhail	Peoples' Friendship University of Russia	fil@crosna.net
Galtsov Dmitry	MSU	galtsov@grg.phys.msu.ru
Ganezer Kenneth	California State Univ.	kganezer@csudh.edu
Gentile Simonetta	Univ. of Rome-I	simonetta.gentile@cern.ch
Gerassimov Sergei	Tech. Univ. of Munchen	sergei.gerassimov@cern.ch
Giunti Carlo	INFN-Torino	giunti@to.infn.it
Graziani Enrico	INFN-Rome-III	graziani@roma3.infn.it
Greco Mario	Univ. of Rome-III	greco@fis.uniroma3.it

Grigoriev Alexander	MSU	ax.grigoriev@mail.ru
Iori Maurizio	INFN-Roma-I & FNAL	maurizio.iori@roma1.infn.it
Ishhanov Boris	NPI-MSU	bsi@depni.npi.msu.su
Kadyshevsky Vladimir	JINR	kadyshev@jinr.dubna.ru
Kaidalov Alexey	ITEP	kaidalov@vitep5.itep.ru
Kapitza Serguey	Russian Academy of Sciences	sergey@kapitza.ras.ru
Kataev Andrei	INR	kataev@ms2.inr.ac.ru
Khrustalev Oleg	MSU	timofod@mail.ru
Khrustaleva Nelli	Ministry of Science (RU)	hns@mail.ru
Kiiskinen Ari	Helsinki Inst. of Phys.	ari.kiiskinen@cern.ch
Kobayashi Takashi	Inst.of Part.&Nucl. Studies	takashi.kobayashi@kek.jp
Kopylov Sergey	STE "Brainstorm"	fil@crospa.net
Kosmachev Oleg	JINR	kos@thsun1.jinr.ru
Kotikov Anatoly	JINR	kotikov@thsun1.jinr.ru
Krasnikov Nikolai	INR	krasniko@ms2.inr.ac.ru
Kulagin Sergey	INR	kulagin@ms2.inr.ac.ru
Kwon Youngjoon	Yonsei Univ.	yjkwon6@yonsei.ac.kr
Lafferty George	Univ. of Manchester	george.lafferty@man.ac.uk
Laperashvili Larisa	ITEP	laper@heron.itep.ru
Lobanov Andrey	MSU	lobanov@th466.phys.msu.su
Lukash Vladimir	Astro-Space Centre, LPI	vladimir@lukash.asc.rssi.ru
Manjavidze Joseph	JINR	joseph@nursun.jinr.ru
Martinelli Guido	Univ. of Rome-I	guido.martinelli@rome1.infn.it
Martynenko Alexei	Univ.of Samara	mart@ssu.samara.ru
Matveev Victor	INR	matveev@ms2.inr.ac.ru
McKenna Janis	Univ. of British Columbia	janis@physics.ubc.ca
Mikhailin Vitaly	MSU	mikh@srl.phys.msu.su
Muchanov Vjaceslav	Ludwig-Maximilian-Univ.	mukhanov@theorie.physik.uni-muenchen.de
Narodetskii Ilya	ITEP	naro@heron.itep.ru
Nikiforova Nataliya	MSU	inter@phys.msu.su
Nikishov Anatoly	Lebedev Phys. Inst.	nikishov@lpi.ru
Okun Lev	ITEP	okun@heron.itep.ru
Osipenko Mikhail	MSU-INFN	osipenko@ge.infn.it
Panasyuk Mikhail	SINP, MSU	panasyuk@sinp.msu.ru
Perevozchikov Nikolay	MPTI	bioph@pop3.mipt.ru
Pervushin Victor	JINR	pervush@thsun1.jinr.ru
Petti Roberto	CERN	roberto.petti@cern.ch
Pivovarov Alexei	INR	aapiv@ms2.inr.ac.ru
Polikarpov Mihail	ITEP	polykarp@heron.itep.ru
Popov Yurii	MSU	popov@srdlan.npi.msu.su
Pozdeeva Tatyana	Univ. of Tomsk	bord@mail.tomsknet.ru

Ricci Fulvio	Univ. of Rome-I	fulvio.ricci@roma1.infn.it
Ricciardi Giulia	Univ. of Naples	giulia.ricciardi@na.infn.it
Ritus Vladimir	LPI	ritus@lpi.ru
Rubakov Valery	INR	rubakov@minus.inr.ac.ru
Salt Jose	Univ. of Valencia	jose.salt@ific.uv.es
Sapozhnikov Mikhail	JINR	mikhail.sapozhnikov@sunse.jinr.ru
Sarti Alessio	INFN-Ferrara	asarti@roma1.infn.it
Savrin Vladimir	MSU	savrin@theory.sinp.msu.ru
Scarpa Marcella	INFN & Univ. of Ferrara	marcella.scarpa@cern.ch
Shabalin Evgeny	ITEP	shabalin@vxitep.itep.ru
Sharichin Valentin	MPEI	bioph@pop3.mipt.ru
Shevchenko Vladimir	ITEP	shevchen@heron.itep.ru
Shirkov Dmitry	JINR	shirkovd@thsun1.jinr.ru
Shubitidze Nodar	JINR	shubi@nusun.jinr.ru
Sidorov Alexander	JINR	sidorov@thsun1.jinr.ru
Simonov Yury	ITEP	simonov@heron.itep.ru
Sissakian Alexey	JINR, Dubna	sisakian@jinr.ru
Skrinsky Alexander	INP, Novosibirsk	skrinsky@inp.nsk.su
Skvortsov Vladimir	MIPT	skv@pop3.mipt.ru
Slavnov Andrey	MSU& Steklov Math. Inst.	slavnov@mi.ras.ru
Smirnov Alexei	ICTP, Trieste & INR	smirnov@ictp.trieste.it
Sobol Andrei	LAPP & IHEP	sobol@cern.ch
Solovtsov Igor	Univ. of Gomel	solovtsov@gstu.gomel.by
Solovtsova Olga	Univ. of Gomel	solovtsov@gstu.gomel.by
Spillantini Piero	INFN-Florence	piero.spillantini@fi.infn.it
Studenikin Alexander	MSU	studenik@srd.sinp.msu.ru
Teplov Oleg	Inst. of Metallurgy and Material Science	teplov@ultra.imet.ac.ru
Timofeevskaya Olga	MSU	timofod@mail.ru
Turck-Chieze Sylvaine	Saclay	turck@discovery.saclay.cea.fr
Vasseur Georges	Saclay	vasseur@hep.saclay.cea.fr
Villante Francesco	INFN-Ferrara	villante@fe.infn.it
Vogel Nadeshda	Univ. of Tech. Chemnitz	n.vogel@physik.tu-chemnitz.de
Westerheide Hans	Ranis, Germany	westerheide-ranis@t-online.de
Williams Jennifer	Univ. of Manchester	jenny@hep.man.ac.uk
Winter Marc	IN2P3/CNRS	marc.winter@cern.ch
Wudka Jose	Univ. of California	jose.wudka@ucr.edu
Yakushev Evgueni	Univ.of Alabama	yakushev@bama.ua.edu
Yushchenko Oleg	IHEP	oleg.iouchtchenko@cern.ch
Zakharov Alexander	ITEP	zakharov@vitep5.itep.ru
Zhukov Valery	AMS	joukov@cern.ch
Zhuridov Dmitry	MSU	jouridov@mail.ru

World Scientific
www.worldscientific.com
5754 hc

ISBN 981-256-162-5



9 789812 561626